NUMERICAL SIMULATIONS OF THE MICRO FLOW FIELD IN THE HINGE REGION OF BILEAFLET MECHANICAL HEART VALVES

A Thesis
Presented to
The Academic Faculty

by

Hélène Anne Simon

In Partial Fulfillment
of the Requirements for the Degree
Doctor of Philosophy in the
School of Chemical and Biomolecular Engineering

Georgia Institute of Technology

August 2009

NUMERICAL SIMULATIONS OF THE MICRO FLOW FIELD IN THE HINGE REGION OF BILEAFLET MECHANICAL HEART VALVES

Approved by:

Dr. Ajit P. Yoganathan, Advisor
The Wallace H. Coulter Department of Biomedical Engineering
Georgia Institute of Technology

Dr. Fotis Sotiropoulos, Co-Advisor
Saint Anthony Falls Laboratory
University of Minnesota

Dr. Hang Lu
School of Chemical and Biomolecular Engineering
Georgia Institute of Technology

Dr. Sue Ann Bidstrup Allen
School of Chemical and Biomolecular Engineering
Georgia Institute of Technology

Dr. Ari Glezer
The George W. Woodruff School of Mechanical Engineering
Georgia Institute of Technology

Date approved: June 11th, 2009

One may not reach the dawn save by the path of the night.

- Khalil Gibran

ACKNOWLEDGEMENTS

There are so many people whom I would like to acknowledge for their support, encouragement, guidance and friendship during my stay at Georgia Tech. First, I would like to thank my advisor, Dr. Ajit Yoganathan who supported me during my Master's of Science and then convinced me to stay for a PhD. He gave me the best of the opportunities to discover the fascinating world of Biomedical Engineering. I would like to thank Dr. Sotiropoulos for allowing me to perform this numerical work under his supervision. I am also grateful to Dr. Lu, Dr. Glezer and Dr. Allen for serving in my thesis committee and taking the time to read and critically review this thesis.

I would like to thank all the past and present members of the Cardiovascular Fluid Mechanics Lab, without whom nothing would have been possible. Each of them, in their own way, helped me go through the frustrating times of doing research: Hiroumi Kitajima, Kartik Sundareswaran, Kartik Balachandran, Diane de Zelicourt, Dave Frakes, Hwa-Liang Leo, Kerem Pekkan, Philippe Sucosky, Anna Fallon, Lakshmi Prasad, Murali Padala and also David Murphy, Chris Haggerty, Erin Spinner, Choon Hwai Yap, Maria Restrepo, Brandon Chaffins, David Icenogle and Jean-Pierre Rabbah.

Special thanks go to Dr Liang Ge, who was always so patient with me and taught me so much about numerical simulations. I am more than deeply thankful to Diane for being the best officemate and helping me throughout the completion of this thesis. She is a never-ending source of wise advices, good ideas, and fun time! Your help and enthusiasm were and are invaluable. Merci!

I would like to express my gratitude to the staff of Chemical Engineering and Biomedical Engineering that have helped me one way or another. I would like to

especially thank Steven Marzec and Jesus Mata-Acosta for always being ready to provide technical assistance during all computer crises.

I would like to thank each and every one of my friends. I had so much fun outside the lab with you all: Matthieu, Reah, Nathalie, Christophe, Florent, Aurelija, Remi, Alpha, Teresa, Cedric, Diane, Franklin, Leon, Jenn, Yannick, and Callie. Many thanks for making my time in Atlanta so enjoyable. I would have liked to list here all the good times I shared with you. They are all in mind… So many fun times, so many good memories… Thank you all.

My gratitude goes to my family for helping me take the opportunity I was given to pursue my graduate studies at Georgia Tech. They thought I would go to the United States for a year but I ended up staying a little big longer… Thank you for your patience. Finally, last but not least, I would like to thank Pedro. You were always there for me, ready to listen, give wise advices, cheer me up. Thank you for your support, your patience, your help… and for just being you. Muchas gracias!

To all of you, thank you!

TABLE OF CONTENTS

LIST OF TABLES

LIST OF FIGURES

SUMMARY

Native heart valves with limited functionality are commonly replaced by prosthetic heart valves in patients with valvular heart disease. Bileaflet mechanical heart valves (BMHVs) are currently the most widely implanted mechanical heart valve design owing to their long-term durability, with over 130,000 implants every year worldwide. However, despite the widespread clinical use of these valves and considerable improvement over the last two decades, the function of these devices remains imperfect. Recent studies have shown that BMHVs can still cause major complications, including promote hemolysis, platelet activation, and thromboembolic events. To avoid thromboembolic complications, patients with a BMHV must undergo lifelong anticoagulant therapy. However, side effects include significant risk of hemorrhage, infection, and autoimmune responses. Clinical reports and recent *in vitro* experiments suggest that the thrombogenic complications caused by BMHVs are mainly associated with the hemodynamic stresses imposed on blood elements by the complex non-physiologic flow through the valve and in particular through the hinge regions.

Therefore, full three dimensional characterization of the flow through the hinge region of prosthetic heart valves is essential to explore the dynamics of hinge flow structures and quantify their thrombogenic potentials based on shear stress history of blood elements combined with hinge residence times.

To date, flow phenomena occurring in the hinge region of BMHVs have largely been studied experimentally, but these studies provided only limited information. This study aims at numerically simulating the flow through the hinge region of a BMHV under physiologic pulsatile conditions so as to quantitatively and accurately predict the hinge

flow features at a level that cannot be assessed by experiments alone. This research proposes to 1) develop an efficient and accurate computational fluid dynamics solver specifically tailored to simulate the pulsatile three-dimensional flow through the hinge region of BMHVs under physiologic conditions, 2) develop a Lagrangian framework to estimate the thromboembolic potential associated with the hinge region of BMHVs, and 3) apply the developed framework to assess the influence of hinge design on the blood damage potential associated with the hinge region of BMHV.

Accurate computational meshes of the hinge region of clinical valves are obtained from X-ray micro-computed tomography scans. The hinge flow solver is based on a hybrid Cartesian/Immersed Boundary approach specifically tailored to handle moving and colliding boundaries. The accuracy of the solver is assessed by comparing the simulated velocity field with earlier experimental data obtained using Hydrogen Bubble Flow visualization and two-component Laser Doppler Velocimetry techniques. Finally, a particle tracking method, coupled with existing blood damage models, is implemented to predict blood element trajectories through the hinge region and estimate the associated shear stress histories. This approach allows for the analysis of the computed hinge flow field as they are experienced by the blood cells flowing through the hinge and for an estimation of the potential for hemolysis and platelet activation.

Computational fluid dynamic simulations and Lagrangian particle tracking are performed on three different hinge configurations subjected to aortic conditions to provide new insights into the influence of hinge design on hemodynamics, hemolysis, platelet activation, and thrombus formation. The influence of the hinge gap width is studied by simulating the flow in the hinge region of two identical St Jude Medical (SJM) hinges with varying hinge gap width. The influence of wall curvature is investigated by comparing the performance of a SJM hinge and a CarboMedics (CM) valve.

Calculations reveal complex, unsteady and highly 3D flow fields, with flow patterns known to be detrimental to blood elements throughout the hinge and cardiac cycle. In particular zones of flow stagnation and recirculation, favorable to thrombosis, are identified. Elevated shear stresses, which may induce platelet activation, are seen in the hinge and near-hinge region. Hinge gap width and, more importantly, the shape of the hinge recess and leaflet ear are found to impact the levels of shear stresses experienced by the blood cells. In particular avoiding sharp corners or sudden shape transitions appears as a key geometrical design parameter to minimize flow disturbances and thromboembolic potential.

The implications of the present study are two folds. First, the computed flow fields underscore the need to perform full 3D pulsatile simulations throughout the cardiac cycle in order to fully capture the complexity and unsteadiness of the hinge flows. Then, though based only on three different hinge designs, this study provides general guidelines to optimize the hinge design based on hemodynamic performance and thromboembolic potential. The developed framework enables rapid and cost-efficient pre-clinical evaluation of prototype BMHV designs prior to valve manufacturing. Application to a wide range of hinges with varying design parameters will eventually help in determining the optimal hinge design.

CHAPTER 1

BACKGROUND AND SIGNIFICANCE

1.1 Heart Valve Replacement and Prosthetic Heart Valves

1.1.1 Heart valve replacement

Function of native human heart valves may be compromised by congenital birth defects or disease. When a heart valve does not work properly and surgical repair is contraindicated, a natural heart valve may be replaced by a prosthetic one. The first heart valve replacement took place in 1960 and was performed using an artificial caged-ball valve. Since then, valve designs have improved considerably, and heart valve replacement has become a remarkably successful clinical procedure. To date, more than 50 prosthetic heart valve designs have been developed, and over 182,000 heart valves are implanted in the world each year [1, 2]. In 2005, an estimated 106,000 heart valve procedures were performed in the United States alone [3]. Nearly three million prosthetic heart valves have been implanted worldwide since the first heart valve replacement, and demand for these devices continues to expand at a rate of 10-12% per year [4].

1.1.2 Current heart valve prostheses

Existing heart valve prostheses can be divided into three categories, namely mechanical, bioprosthetic and polymeric heart valves. The mechanical heart valves are fabricated entirely from synthetic material and include caged-ball, caged-disk, tilting disc, and bileaflet designs. The first mechanical heart valve was the Starr Edward caged-ball

valve developed in 1960. This valve was composed of a ball retained in a sub-cage on the proximal side of the valve. Caged-ball valves are rarely used today due to their high pressure drop and elevated levels of turbulent stresses produced by the ball obstructing the flow. The development of tilting disc valves in the late 1960s made a notable contribution to the advancement of valve replacement. The tilting disc design is based on the concept of a free-rotating disc, which in the open position tilts to a particular angle. Improvements to this design focused mainly on disc geometry and disc-retaining mechanisms. Although the tilting disc valve offers a decreased amount of wake turbulence and less pressure drop across the heart valve compared to the caged-ball model, metal fatigue sometimes caused the struts to break, resulting in a fatal embolization of the disc. Today, caged-ball and tilting disc valves have been superseded by bileaflet mechanical heart valves (BMHVs). The BMHV design consists of two semicircular, hinged pyrolytic carbon occluders, called leaflets, which regulate the flow. These valves offer the benefit of greater durability, superior bulk flow hemodynamics, and better functional safety than the single leaflet of a tilting disc valve. They also provide a relatively larger effective orifice area than the other valve designs for a same valve size, and therefore have a smaller transvalvular pressure drop.

The primary disadvantage of mechanical valves is the need for long term anticoagulation therapy to prevent thrombosis and thromboembolic complications. Furthermore, the hemodynamics of these prostheses differs significantly from that of natural valves. An alternative approach is the development of a valve that resembles the native valves. The second category of prostheses thus include the bioprosthetic or tissue valves, which are made from a combination of synthetic material and chemically treated animal tissues, commonly porcine valve or pericardial tissues. The main benefits of these valves are that lifelong anticoagulant therapy is usually not required and that they offer natural form and function, thus reducing blood damage. However, their durability is

limited and they are prone to time-dependent structural changes such as calcification and leaflet wear leading to ultimate valve failure [4]. The mechanical properties of tissue valves degrade rather rapidly and these valves are prone to calcification [4]. Often, implanted tissue valves fail in less than ten years and reoperation is necessary.

The search for a non-thrombogenic prosthesis mimicking the natural valve function has led to the development of a third heart valve type, the polymeric heart valves**.** Polymeric valves utilize synthetic materials to mimic the natural valve function. They are commonly made of polyurethane material, which is known to be an excellent non-thrombogenic material. Conceptually, these valves combine the best features of both tissue and mechanical heart valves, but they are still in development and clinical trials are yet to be conducted.

1.2 Bileaflet Mechanical heart valves

1.2.1 Overall design

Fifty-five percent of defective native valves are currently replaced by a mechanical heart valve. Of all available mechanical heart valve designs, the bileaflet valve design (Figure 1-1) is currently the most implanted design, accounting for nearly 80% of implanted mechanical heart valves [5].

The BMHV design is composed of two semicircular occluders, called leaflets, which pivot about hinges machined into an annular housing (Figure 1-2). The axis of rotation of the leaflets does not bisect the leaflet area equally, thereby enabling the leaflets to open and close passively with the dynamic cross-valvular pressure variations generated by the contraction and relaxation of the heart chambers. When the leaflets are open, the blood flows through the central rectangular orifice and two lateral orifices. The open occluders form an angle with respect to the plane of the valve housing. An opening

angle greater than 80° is commonly incorporated in order to minimize flow disturbances. When the leaflets are fully closed, small gaps exist where the leaflets meet in the central region of the valve, called the b-datum line, and between the closed leaflets and the housing. These small gaps allow leakage flow and are incorporated into the design to washout critical areas and prevent blood element buildup.

A sewing cuff made of Dacron cloth is attached to the valve housing to facilitate the suturing of the prosthetic heart valve to the surrounding heart tissue. The leaflets and housing are usually made of pyrolytic carbon, which is biocompatible and wear-resistant over the patient lifetime and holds a highly polished finish for increased thromboresistance.

After the introduction of the St Jude Medical (SJM) bileaflet valve in 1977, the bileaflet valve became the most commonly used mechanical heart valve design on the market. This valve poses little threat to the patient because its components have little chance of detaching from the device and its design allows a small amount of backflow. This backflow prevents flow stasis, thereby minimizing blood element buildup and the required dose of anticoagulation drugs. Several BMHV designs are currently available and the variations in design are often slight, such as subtle differences in housing shape or hinge design.

Figure 1-1: Different types of bileaflet mechanical heart valve designs

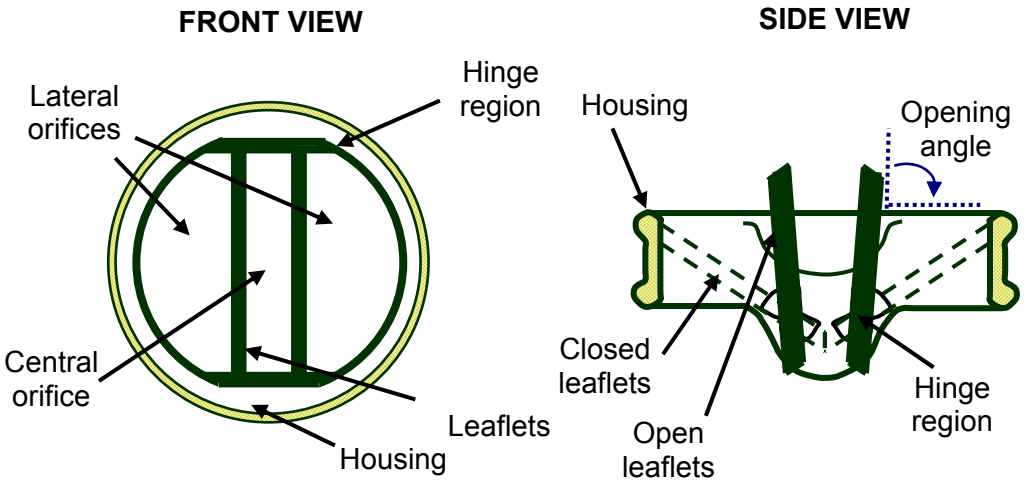

Figure 1-2: Characteristics of a bileaflet mechanical heart valve prosthesis

1.2.2 Hinge Region Design

1.2.2.1 St Jude Medical Heart Valve Design

The most widely used BMHV is currently the SJM valve. The design of the SJM valve exhibits two semicircular protrusions called pivot guards (Figure 1-3). The four hinges are machined within these two pivot guards, which are designed to protect the pivot mechanism from intrusion by sutures or calcium buildup and to reduce interference with subvalvular structures. The hinge design consists of a semicircular projection of the leaflet, called an ear, which mates to a recess of similar shape in the valve housing. The SJM hinge recess is characterized by a streamlined butterfly geometry with smooth contours (Figure 1-4). During opening and closing, the flat areas of the leaflets contact the flat areas of the orifice. This flat-to-flat contact is designed to evenly distribute pyrolytic carbon load and wear. Moreover, the mated-sphere pivot design allows the leaflet appendage to sweep all areas of the pivot depression. The opening and closing angles of the leaflet relative to the plane of the valve housing are 84° and 29°, respectively, leading to a sweep angle of 55°. The SJM valve features an expansion region, called the thumbnail, located downstream of the hinge mechanism. The thumbnail is a small region of slight expansion machined into the housing to further increase the orifice area.

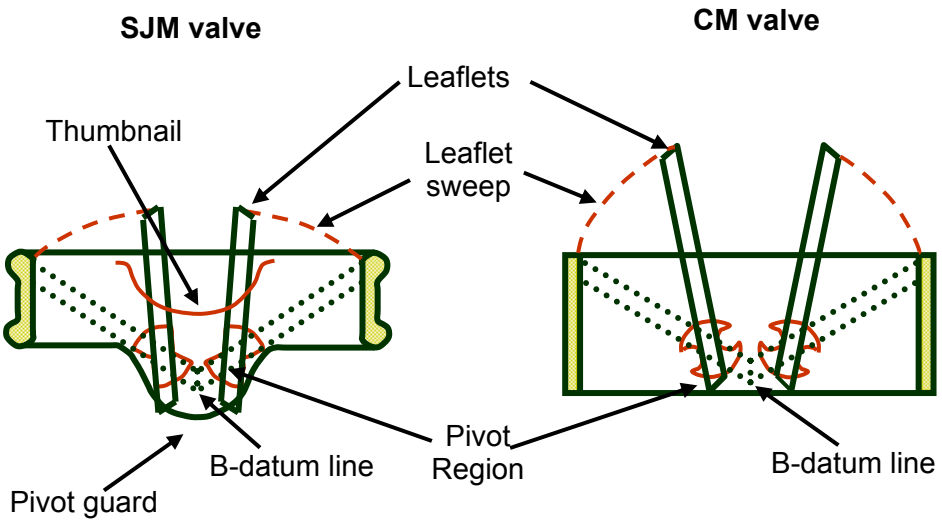

Figure 1-3: Side view of the SJM valve (left) and CM valve (right)

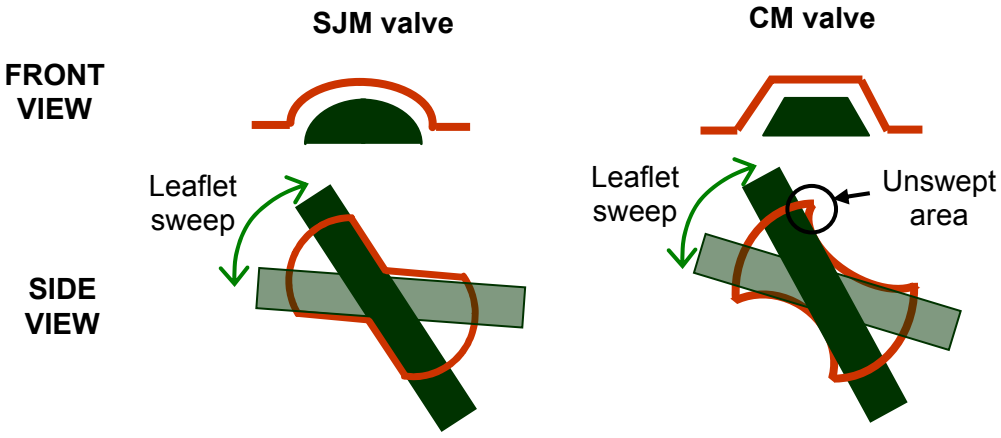

Figure 1-4: Pivot mechanism of the SJM valve (left) and the CM valve (right)

1.2.2.2 CarboMedics Heart Valve Design

The second most widely used BMHV design is the CarboMedics (CM) valve which exhibits an angulated recess and a butterfly geometry with sharper corners and less streamlined edges than the SJM hinge design (Figure 1-4). Contrary to the SJM valve, the CM valve design doesn't include a pivot guard (Figure 1-3). The CM valve has a maximum opening angle of 78°. When the valve is fully open the flat angular leaflet ear rests on the curved profile in the pivot recess. This point of contact has the potential to generate increased stress, thus creating pyrolytic carbon wear. Also, the pivot recess of the CM valve does not allow complete sweeping by the leaflet appendage, leaving an unswept area in each of the four corners of the hinge (Figure 1-4). The CM valve design, like the SJM design, is able to rotate within its sewing ring.

1.3 Complications Related to Bileaflet Mechanical Heart Valve

Despite the widespread clinical use of BMHVs, the function of these devices is far from perfect. The survival rate is approximately 80% five years after surgery, 60% after ten years, and only 50% after fifteen years. Heart valve complications are divided into six categories: structural valvular deterioration, non-structural dysfunction, valve thrombosis, embolism, bleeding, and endocarditis [6]. The major complications that contribute to valve failure are hemolysis, platelet destruction, and thromboembolic events arising from the formation of clots and their subsequent detachment. Prevention of these complications requires lifelong anticoagulation therapy. However, such treatment increases the risk of hemorrhage, infection, and autoimmune response [7]. Prosthetic heart valve failure may also occur due to tissue overgrowth, paravalvular leaks associated with healing defects, material fatigue, or material chemical property change.

Sublethal and lethal trauma to blood elements and thromboembolic events remain the major complications with current heart valve designs and are the major obstacles toward the realization of the ideal mechanical heart valve. The non-physiological geometries of the mechanical heart valve generate abnormal velocity profiles and high shear rates, which may cause blood cell damage. Shear stresses including Reynolds stresses have been studied extensively as possible sources of blood trauma. These forces, imposed by non-physiological flow, can lyse blood cells or change their conformation, acting as a signal to promote coagulation, and ultimately promote thrombus formation. A study performed as early as 1970 showed that patients with first-generation mechanical valves such as the caged-ball and tilting disc had a shortened platelet half-life due to increased incidence of platelet destruction and activation [8]. Direct impacts of the cells on the valve surface as well as shear stresses of the turbulent flows are two possible initiators of this blood cell damage. A 1978 study of patients with first-generation prosthetic heart valves showed that the elevated levels of the enzyme lactate dehydrogenase could be correlated with a decreased red cell half-life. More recently, Skoularigis *et al.* evaluated the hemolysis levels in 170 patients with SJM valves and 80 patients with Medtronic Hall tilting disc valves [9]. It was shown that the presence and severity of hemolysis was related to high levels of serum lactic dehydrogenase and blood hemoglobin. By doing so, the authors established a relation between the severity of hemolysis and the type, position, and size of prosthetic heart valves [9].

Despite the changes and improvement of prosthetic heart valve designs over the years and the development of new drug therapies, the problems of thromboembolism still persist. During clinical trials, the Medtronic Parallel (MP) valve was found to have an unacceptable thrombosis complication rate, and explants showed the presence of thrombi in the hinge regions. The hinge region was found to directly influence the valve

durability, functionality and success rate [10] and thus is considered as the most critical part of the BMHV. The valve-related thromboembolic complications, which include hemolysis, platelet activation, and thrombosis, are believed to be induced by altered flow conditions such as elevated shear stresses, high shear rates and flow stasis. Predicting thromboembolic complications and improving current valve designs therefore require a characterization and quantification of the flow field in the immediate vicinity of the prosthetic heart valves, and in particular inside the hinge recess.

1.4 Blood Damage

1.4.1 Blood

In order to understand some of the valve-related complications associated with prosthetic heart valves, it is necessary to consider the biological origins of thromboembolic events.

1.4.1.1 Red Blood Cells and Hemolysis

Red blood cells, or erythrocytes, are the most abundant cell type in the blood, and their primary function is to carry oxygen and carbon dioxide between the lungs and the tissues. They are a simple, membranous “bag” filled with enzymes and hemoglobin. The permeable membrane is composed of a lipid bilayer in association with protein molecules. Red blood cells have a biconcave discoid shape with a diameter of approximately 7.6 μm and a thickness of about 2.8μm. Despite their complex cytoskeleton, which holds the membrane in place, the red blood cells have an extraordinary ability to deform. Because they have an excess of membrane in relation to their volume, the membrane can tolerate large uniaxial strain without tearing. However,

the physical properties of the membrane are not isotropic, and the membrane cannot tolerate areal strain. The red blood cell membrane is a non-homogeneous material, especially in the direction normal to the surface. When the membrane is subjected to shear, initially the membrane is viscoelastic (reversible deformation under load), but after a transition region, it becomes viscoplastic (non-linear irreversible deformation under load) [11]. The typical life span of a red blood cell is about 120 days.

During normally occurring hemolysis, the older red cells rupture and many components of hemoglobin are recycled. Hemolysis is the consequence of cumulative or instantaneous damage to the red cell membrane and corresponds to the release of hemoglobin from the red cells. When a red blood cell is stretched, the membrane develops 'holes' large enough for the diffusion of hemoglobin into the extracellular fluid. Once the pores are open, the protein molecules may pass through. If a large enough stretch is applied and the stretch required for lysis is exceeded, the membrane tears, spilling the cell contents and leaving the membrane fragments.

1.4.1.2 Platelets and Coagulation Cascade

Another important blood cell type is the platelet. Platelets are produced in the bone marrow by megakaryotes. Platelets are colorless cell fragments with no nucleus and contain a cytoskeleton consisting of microtubules, actin filaments, and other binding proteins. They are smaller than red blood cells with a diameter of approximately 2.5 μm. They have a typical life span of about 10 days. Inactive platelets are small disk-like cells that are extremely responsive to alterations in the surrounding medium. Platelets constitute the principal line of defense against bleeding, and therefore become active in response to stimuli like a vessel wall injury. Active platelets lose their discoid form and extend long pseudopods in response to a change in their cytoskeleton. They also

release a great number of vasoactive substances and adhere to any exposed collagen. This liberation of chemicals attracts additional platelets, which aggregate thus enlarging the forming plug. A series of reactions initiated by exposed collagen and tissue factors occurs and corresponds to the coagulation cascade during which inactive plasma proteins are converted into active enzymes. This cascade converts fibrinogen into fibrin fibers which are the major structural component of blood clots [12].

1.4.2 Shear Stress and Blood Damage

1.4.2.1 Red Blood Cell and Shear Stress

In 1968 Nevaril used a modified Couette viscometer to investigate the effects of a nearly uniform laminar stress field on hemolysis. For a 2-min exposure time, the threshold shear stress for the onset of red blood cell lysis was about 1,500 dyn/cm^2. When the shear stress exceeded 3,000 dyn/cm^2, many cells were lysed. Nevaril also demonstrated that the normal stress, which corresponds to pressure, was of secondary importance; this implied that shear stress effects were the primary mechanism of hemolysis [13]. The instrument of choice to investigate blood damage by shear stress was a rotational viscometer, as it allowed a known shear stress to be applied to certain fluid regions. However, the secondary physical effects such as cell-solid surface interaction appeared to induce major errors. Nevertheless, the threshold value of 1,500 dyn/cm^2 was considered to be a realistic estimation and correlated well with Nevaril's results [14]. It was also concluded that under low shear stress conditions hemolysis was directly proportional to cell-solid surface interactions. Leverett emphasized the importance of exposure time and established that disagreements between previous results were due to the investigation of different regimes of the exposure time-stress domain [14]. Blackshear noticed that mechanical hemolysis could be divided into three

classes: hemolysis induced by surface interaction, hemolysis occurring in the bulk fluid at medium stress (1,000-2,000 dyn/cm^2 applied for several seconds), and hemolysis occurring in the bulk fluid at high stress (about 40,000 dyn/cm^2 applied for milliseconds). According to Blackshear, a medium shear induced a gradual fragmentation of the cells depending on the exposure time, whereas the third class seemed to be associated with an instantaneous rupture of the cell membrane [15]. In order to study the changes in cell shape under bulk stress condition, Sutera fixed red cells directly in the fluid by adding glutaraldehyde [16]. At 37°C after 4 minutes of turbulent conditions at 100 dyn/cm^2, the cells had a bulbous shape. At around 1,500 dyn/cm^2, cells began to lose their concavity and exhibited an ellipsoidal shape. At about 2,500 dyn/cm^2, fragmentation became apparent. At 4,500 dyn/cm^2, more fragmentation was visible. The degree to which the reversibility of the damage varied with shear stress was investigated using a fixed recovery period of one minute. Cells sheared at 2,000 dyn/cm^2 could almost recover their normal shape, but cells sheared at 3,500 dyn/cm^2 were fragmented irreversibly. At high shear stress, the deformation through the entire population seemed to be uniform. According to Sutera, the shear flow, and hence the turbulent characteristics of the flow, must be completely determined in order to obtain realistic data describing the relationship between shear stress and hemolysis. Hellums carried out studies on the effect of pressure changes, impact due to the crushing of red cells between solid surfaces, and shear stress. The hemolysis rate was found to be approximately linear with time at low hemolysis rates with an increase in morphological changes with time. The concept of threshold shear stress was therefore justified. Hellums concluded that the time *vs.* shear stress plane could be divided into two regimes. In the first regime with low shear stress and short exposure time, there was little damage, and this damage was influenced by surface interaction effects. In the second regime corresponding to high

shear stress and long exposure time, very high hemolysis occurred and shear stress was the dominant factor of hemolysis [17].

In 1984 Sallam and Hwang used a submerged axisymmetric jet flow field to investigate the effect of shear on red blood cells [18]. A technique was developed to allow the collection of samples directly in the jet flow field at locations corresponding to known values of mean velocity, turbulence intensity, and shear stress. Using this technique, local shear stress and blood cell damage could be related. The incipient hemolysis was associated with a shear stress of 400 N/m^2 for an exposure time of 1 ms. Below this level, no free hemoglobin was detectable. Beyond the threshold level, hemolysis increased with increasing shear stress. Sallam and Sutera investigated the additional effect of turbulence on red blood cell tolerance to shear flow. They found that a laminar shear stress and a fluctuating turbulent shear stress may not have the same impact on the cells [16, 18]. Lu reevaluated the threshold limit for hemolysis in a turbulent shear flow and showed that the values found by Sallam were an underestimation due to experimental methodology and calculations. The value determined by Lu was 800 N/m^2 with an exposure time of 1 ms [19].

1.4.2.2 Platelets and Shear Stress

Before 1960 there was no intensive research activity in the field of thrombosis, and the mechanism of coagulation was not well understood. In 1962, Born developed a method measuring platelet aggregation in order to characterize the influence of shear stress on platelet-platelet interaction. The applied shear stress was however not uniform and conclusions on the effect of specific shear stress levels on platelet aggregation could not be drawn [20, 21]. Thirteen years later, Brown *et al.* hypothesized that shear stress may have hemolytic effects on blood as a result of its thrombogenic effect on

platelet activation [22]. They performed controlled shear stress experiments where platelet rich plasma was exposed to shear stresses from 5 to 900 dyn/cm^2. The platelets exhibited biochemical and morphological changes when subjected to shear stress as low as 50 dyn/cm^2. In addition it was shown that platelet function was altered when a shear stress exceeding 100 dyn/cm^2 was applied for five minutes. These experiments demonstrated that shear stress could induce platelet aggregation; however no attempt was made to establish a relation between platelet aggregation and exposure time.

In 1977, Bernstein *et al.* attempted to separate the blood damage resulting from shear stress within the bulk fluid from that related to surface interaction by using two devices to selectively impose different forms of damage [23]. The authors showed that high wall impact had no real influence on activation or aggregation of the platelets as evidenced by a moderate decrease in serotonin uptake, which might indicate cellular destruction. However, experiments demonstrated that high shear forces applied for a few milliseconds within the bulk flow partially affected platelet function. No significant change in platelet adhesion and aggregation was observed for shear stresses below 10^5 dyn/cm^2; however, structural and functional changes as well as serotonin release were detected at a shear stress of 10^6 dyn/cm^2. No abnormal platelet aggregation was observed. Following these observations, Hellums undertook a study of platelet ultrastructure to determine a correlation between morphologic changes and functional abnormalities [17]. At low shear stresses, he observed that platelet aggregates began to form. However the level of aggregates decreased after a period of 2 to 4 hours, indicating that low shear stress could biochemically alter platelet function. At higher shear stresses, some platelets were fragmented and distorted but did not aggregate. Despite the discrepancies observed between these findings and previous experiments, it can be seen that factors such as exposure time and cell-solid surface interactions may contribute to blood damage. In another study, Anderson demonstrated that platelet

surface interaction had no real influence on platelet aggregation or lysis since shear stress of 50-75 dyn/cm^2 applied for a duration of five minutes resulted only in reversible swelling and aggregation of platelets. Some aggregation and fragmentation occurred under a shear stress of 100 dyn/cm^2, but the change was greatest at a shear stress level of 150 dyn/cm^2 where the platelet count drastically dropped. Thus, 150 dyn/cm^2 was considered to be the threshold for incipient lysis. Anderson showed that for platelet damage threshold shear stress increased with decreasing exposure time. He also underlined the fact that laminar and turbulent flows might not have the same impact on cell damage [24].

1.4.2.3 Comparison of Shear Stress Effects on Red Cells and on Platelets

A good agreement between studies supports the findings that shear stress does not have the same effect on red blood cells and platelets. Platelets are much more fragile than red blood cells when subjected to long exposure times. Bernstein's results indicate that for a 2-min exposure time, the shear stress threshold for hemolysis was around 1500 dyn/cm^2; whereas it was tenfold lower for platelet lysis [17, 23]. Brown *et al*. also showed that the leakage of hemoglobin by red cells was not significant compared to the leakage of ADP by sheared platelets [22]. However, it seems that the reverse is true at very short exposure times, when platelets are observed to be more resistant to stress than the red blood cells [24].

The observed differences in the way red blood cells and platelets react to different shear stress exposure times most likely stem from their structural differences. One major structural difference between red blood cells and platelets is in the deformability properties of erythrocytes, which platelets do not have. It is hypothesized that for short but intense stress exposures, the stiff membrane of the platelet offers more

resistance to shear than that of the red blood cells. On the other hand, when undergoing prolonged exposure to shear stress, the erythrocyte membrane may deform thereby allowing the red blood cells to adapt their shape to minimize surface tearing, whereas the platelets, unable to deform, lyse.

1.5 Previous Hinge Investigations

1.5.1 Experimental studies

The hinge region of BMHVs is a crucial point where fluid shear stress and material wear are concentrated. In addition, the hinge region was also found to be one of the most critical components of a BMHV, directly affecting valve durability, fluid dynamics, functionality, and thrombus formation [10]. Shipkowtiz *et al.* evaluated the performance of BMHVs and pointed out that even though ATS and SJM valves only differed by the design of the hinge region, the leaflets of the former did not open completely while those of the latter did [25]. It is generally agreed that valves with large opening angles have better hemodynamics, a less perturbed flow pattern, and less wake turbulence. Further delving into the topic, Shipkowtiz *et al.* concluded that hinge location, leaflet position and outflow orifice dimension influence the pressure distribution across the valve and therefore the opening angle [25].

Bearing in mind the importance of the hinge region, researchers have tried to characterize and compare the hinge flow fields of various BMHV to elucidate the effect of the hinge design on the fluid dynamic performance.

Investigation of flow structures within the hinge of a Medtronic Parallel (MP) valve in the mitral position revealed a vortex in the inflow channel, disturbed flow, and multiple stagnation zones [26]. These flow conditions were hypothesized to inhibit washing in the MP pivot and thus contribute to thrombus formation. This hypothesis corroborated well

with clinical explant data that had revealed high early thrombus formation within the MP hinge recess. These flow phenomena were also observed by Ellis *et al.* and were found to correspond to regions of elevated shear stress [27]. Reynolds shear stresses near the inflow channel wall were greater than 6,000 dyn/cm^2, which is significantly greater than the accepted threshold level of blood damage of 4,000 dyn/cm^2 [28]. Undesirable flow phenomena such as vortex formation and stagnation regions were observed in the MP hinge region but not in the SJM hinge region [29]. The differences in flow patterns were attributed to variations in pivot geometry, since the MP hinge exhibits abrupt changes in geometry while the SJM pivot has relatively smooth contours. The active leaflet motion of the SJM valve and streamlined hinge design were shown to restrict the persistence of separation zones and regions of flow stagnation, thereby leading to reduced levels of mechanically induced thromboembolic events. Moreover, the SJM valve design exhibits a slight expansion region, called the thumbnail, situated downstream of the hinge mechanism and machined into the housing to act as a means of increasing the orifice area. Studies have shown that, during the forward flow phase, the thumbnail region is characterized by two recirculation zones, which bound a skewed forward flow jet. This complex and unsteady flow field was hypothesized to reduce the residence time of stagnant flow and clear any forming clots from the region [30, 31]

The comparative study of Leo *et al.* measured the velocity magnitudes and the turbulent shear stress levels within three different hinge recesses in the mitral position, namely a 23mm CM, a 23m SJM and a 27mm MP valve [32]. Velocity and turbulent shear stress magnitudes up to 3.17 m/s and 5,640 dyn/cm^2, respectively, were recorded within the CM hinge, while corresponding values of 1.5 m/s and 2,600 dyn/cm^2, respectively, were found in the SJM Regent hinge. The abrupt changes in the hinge geometry of the MP valve lead to even higher leakage velocities and turbulent shear stresses of 4 m/s and 8,000 dyn/cm^2, respectively. Leo *et al.* concluded that the

hemodynamic performance of the 23 mm CM hinge is between that of a 27 mm MP and a 23 mm SJM Regent hinge.

A number of studies have sought to isolate the most critical design parameters. For instance, Ellis *et al.* assessed the effect of the overall valve design on the hinge flow fields by comparing the performance of three generations of SJM valves, namely the SJM Standard, the SJM Hemodynamic Plus (HP) and the SJM Regent valves. Briefly, the HP valve design achieves a larger effective orifice area compared to that of the Standard valve, for an equivalent valve annulus diameter. The hemodynamic performance of a SJM HP is thus equivalent to that of the next size larger SJM Standard. As for the SJM Regent valve, it includes an increase in the orifice diameter over the HP series. Ellis *et al.* showed that the hinge flow dynamics of the 23 mm SJM Regent under mitral conditions were superior to those of the 25 mm SJM Standard [33]. The peak leakage velocity and Reynolds shear stress recorded in the 25 mm SJM Standard valve were 3.42 m/s and 7,400 dyn/cm^2, respectively, while the 23 mm SJM Regent valve achieved lower leakage velocity of 1.52 m/s and Reynolds shear stress of 2,600 dyn/cm^2. Ellis *et al.* also evaluated the hinge flow dynamics of the 17 mm SJM HP and the 17 mm SJM Regent valves and concluded that the flow performance of the Regent valve was at least equivalent, and possibly superior, to those of the HP valve [31] .

Travis *et al.* studied different aspects of pivot geometry that could influence thrombogenic valve potential [34]. The valve size and pivot geometry was found to have only limited impact on platelet disruption while the hinge gap width had, in comparison, a significant effect on platelet secretion and anionic phospholipid expression. Studies by Leo revealed that Travis' findings could be related to a change in hinge micro-flow fields as the hinge gap width was shown to clearly influence washout and shear stress levels inside the hinge recess [35]. Studies by Leo and Travis *et al*. suggested the possible

existence of a hinge gap width with optimum hemodynamic performance and minimal thromboembolic potential.

Simon *et al.* examined the influence of implant location on the hinge micro-flow field [36]. Aortic and mitral hinge flow fields were found to be similar but with a more dynamic forward flow pattern in the aortic position. This flow pattern was expected to ensure an effective washout and thus limit the propensity for blood element buildup in the hinge region. Relatively higher velocity magnitudes and shear stresses were measured under mitral conditions and were hypothesized to contribute to the higher rates of thromboembolism in the mitral implants when compared with the aortic implants. The authors concluded that the geometry of the hinge region as well as the implant location are critical valve design parameters.

Clinical studies combined with *in vitro* experiments have highlighted the importance of the hemodynamics in the hinge region in determining the overall success of BMHVs. However, due to the small dimensions of the hinge region and the motion of the leaflet, experimental measurements are limited. Thoroughly validated numerical simulations could yield descriptions of the three dimensional hinge flow fields at a level of detail not accessible by experimental techniques alone.

1.5.2 Numerical studies

Computational fluid dynamic (CFD) tools have been used widely to numerically simulate the flow fields proximal and distal to prosthetic heart valves [37-42]. However, only few numerical studies have focused on the hinge region and the importance of modeling accurately its highly complex and unsteady flow fields.

The first unsteady three dimensional numerical simulation to reveal the hinge flow fields of a BMHV was reported in 1996 [26]. Gross performed an experimental and

numerical study of the flow through a 27 mm Medtronic Parallel valve model under mitral conditions. The bulk flow through the valve housing and the flow in the vicinity of the valve hinge were simulated separately. The bulk flow domain consisted of approximately 66,000 cells while approximately 45,000 cells were generated inside the hinge region. Assuming two planes of symmetry for the valve, Gross at al. simulated the bulk flow using a commercial code CFD2000 STORM and used the calculated flow field near the hinge to specify the boundary conditions for the local hinge model. The full Navier Stokes equations were solved using a finite volume method (FVM) with a pressure-based algorithm for continuity, a Pressure-Implicit with Splitting of Operators (PISO) algorithm for pressure-velocity coupling, an implicit scheme for spatial discretization and a second order accurate hybrid scheme for time marching. The turbulence $k-\varepsilon$ model was also incorporated. The leaflet motion, provided as prescribed boundary conditions, was based on experimental measurements. The mass flow rate was prescribed at the domain inlet and the pressure was fixed at the outlet surface. The numerical simulation was further simplified by modeling a single cardiac cycle. The macroscopic flow field was validated based on a comparison of CFD velocity profiles and experimental velocity measurements using echo Doppler and Laser Doppler Velocimetry. Results revealed several zones of flow stagnation, vortical flow and disturbed flow throughout the entire cardiac cycle, and the authors hypothesized that these complex flow structures contribute to thrombus formation and valve failure. Similar computational fluid dynamic simulations have since been used to evaluate flow phenomena within the hinge regions of other BMHVs.

Gao *et al.* simulated the hinge flow fields in the On-X® bileaflet valve [29] using the finite element method provided by the commercial code CFD2000 STORM. A numerical approach similar to that employed by Gross *et al.* was used to solve the time-dependent, three dimensional Navier-Stokes equations. Boundary conditions were

obtained experimentally from a 5x scale-up model of the valve constructed using laser stereolithography. Symmetry was assumed and only half of the valve was modeled. A moving grid methodology was employed to simulate the periodic leaflet motion. The simulation domain was discretized with 30x42x17 cells (21,420 cells), arranged with a power law distribution, and distributed over 6x10x6 sub-volumes for grid moving control purposes. The capability of moving a point along a predefined surface or curve was incorporated in the code to keep the geometry unchanged while the leaflet was moving. A time-varying velocity profile, based on experimental measurements, was prescribed at the upstream inlet while the pressure at the outlet was set constant. The CFD results showed transient vortices and strong flow washout that eliminate any region of flow stagnation during both the opening and closing phases. These results suggested that the design of the On-X hinge region does not favor thrombosis.

Wang *et al.* investigated the flow fields of a protruded hinge under steady flow conditions, with the leaflet in the fully open position [43]. The authors employed the commercial code Fluent 4.4.7 using a standard FVM and a semi-implicit method for pressure linked equation (SIMPLE) schemes to replicate the flow in the vicinity of the protruded hinge. Two symmetrical planes were assumed and the flow domain reduced to a quadrant. A body fitted grid, optimized by a power law distribution, was generated over the entire computational flow domain. A total of 56x38x80 mesh cells (170,240 cells) was used for the whole domain while approximately 10,000 cells were generated in the hinge region. Newtonian fluid and steady flow conditions were assumed. The simulations were performed for Reynolds number (Re) ranging from 1,000 to 8,000 and the turbulence k-ε model was applied for Re values greater than 4,000. A flat flow profile was applied at the inlet while the axial gradient of all fluid properties except pressure was set to zero across the outlet plane. No slip and impermeable boundary conditions were defined on the wall boundary. The steady flow results showed three dimensional

washout flows with vortices developing behind the protruded leaflet stopper. However, there are two main limitations to this study: the simulations were performed under steady conditions with non-moving leaflet and the results were not validated against experimental findings.

Kelly *et al.* simulated the flow in the recessed hinge region of a 25 mm ATS valve placed under physiological aortic conditions [44, 45]. The flow was calculated by the commercially available CFD package FLUENT/UNS. Second order upwind discretization was used for the convective terms. Because *in vitro* results revealed an unsteady vortex shedding occurring from the leaflets, a fully implicit time integration was employed to model the flow. Symmetry was assumed and only one quarter of the flow domain was modeled. An unstructured computational mesh of approximately 110,000 tetrahedral cells was fitted to the geometry. The mesh was locally refined in areas of geometrical complexity and in regions where unsteadiness was expected. An important limitation of this work is that only the acceleration phase of forward flow was modeled and not the entire cardiac cycle. Additionally, the pulsatile inlet flow conditions were simplified and modeled as a sinusoidal pulse wave.

Shu *et al.* developed an integrated macro/micro approach to evaluating the hinge flow within a 29 mm ADV bileaflet valves [46]. The simulations were conducted in the mitral position using the commercial code CFD2000 STORM. The model was created using only one quarter of the valve housing and a total of approximately 40,000 cells was generated using the transfinite interpolation technique. To eliminate potential acceleration errors imposed on the pressure and flow fields at the beginning of the valve opening, the governing equations were calculated twice. To simulate the valve leaflet motion through the cardiac cycle, the CFD tool incorporated a 3D moving cell technique. Hydrogen bubble visualization was used to acquire two dimensional images of the microscopic hinge flow field, which defined the CFD inlet flow boundary conditions while

zero pressure was fixed at the outlet. Laser Doppler velocimetry (LDV) measurements within the hinge region provided velocity validation of the CFD simulations. Flow visualization, LDV and CFD techniques revealed that the ADV design permitted continuous flow washing of the hinge region and eliminated any persistent hinge flow stases.

One of the latest numerical study was performed by Shu *et al.* [47]. The hinge flow and pressure fields of the ADV and the SJM bileaflet valves were characterized using the commercial code CFD2000 STORM. The Navier Stokes equations were solved using a FVM with a pressure-based algorithm for continuity and a PISO algorithm for pressure-velocity coupling. The solution scheme was based on a strongly conservative formulation for the Navier Stokes equations, and the turbulence k-ε model was incorporated. The two computational grids, comprising approximately 40,000 mesh cells, were created according to the dimensions of an *in vitro* experimental aorta model. The simulations were carried out using the flow boundary conditions obtained experimentally and the simulation results were validated by the experiment. The measured leaflet motion was supplied as a prescribed leaflet movement boundary condition. The flow fields and flow features of both hinges were compared at specific instances of the cardiac cycle. The simulations demonstrated the presence of a waterhammer effect upon valve closure and retrograde flow at the bottom of the hinge recesses during valve opening. No persistent flow stasis was observed in the hinge region of either valve. The bi-level butterfly hinge design of the ADV valve was shown to provide relatively easy passage for hinge flow washout and to produce more dynamic flow activity within the valve pivots than did the SJM valve's single level butterfly pivot design. However, because of the lack of published clinical data, the authors could not relate the computed enhanced ADV hinge flow dynamic with valve clinical outcome.

1.6 Lagrangian Studies

Previous blood studies (see section 1.4) have shown that platelet activation and hemolysis not only depends on the forces experienced by the blood elements but also on the exposure time. Both a long exposure to low level of shear stresses and a short exposure to high level of shear stresses may lead to blood cell trauma. Moreover, entrapment of activated elements in regions of low flow favors cell-to-cell contact and therefore promotes thrombus formation. With these observations in mind, many researchers have sought to analyze the blood flow structures from a blood cell's perspective to better understand the relationship between thromboembolic potential and hemodynamics.

Researchers in recent studies have tried to develop complex blood models [48] with cell-to-cell interaction and deformable cells, but to date these studies have been limited to two-dimensional models and dilute blood flow with a red blood cell concentration below the normal level of hematocrit. Most detailed analysis up till now have thus resorted to a more global point of view, where blood-elements are modeled as point-like particles and their path through time is reconstructed via Lagrangian analysis. Such an approach has widely been used to estimate flow-induced blood cell trauma in complex systems (such as centrifugal blood pumps, Ventricular Assist Devices (VAD), coronary stenoses or artificial heart valves) [49-51].

Balducci *et al.* focused on analyzing the flow through a BMHV [52]. Using particle image velocimetry (PIV) and particle tracking velocimetry (PTV), the authors experimentally measured the velocity and stress fields downstream of the valve and computed particle trajectories. To assess the particle exposure time to specific flow conditions, the authors defined a mean residence time as the ratio of the total time spent by the particles in a given region to the number of trajectories crossing the same region.

By dividing the cardiac cycle into forward and leakage flow phases, the authors plotted a contour map of the mean residence time downstream of the valve for each phase. However, they did not attempt to correlate residence time to shear stress levels, and thus to blood damage potential.

In a later study, Krishnan *et al.* numerically simulated the flow at valve closure through a BMHV in the mitral position [53]. Platelets, modeled as point-particles, were tracked by a Lagrangian particle method. A platelet activation parameter, defined as the integral of the fluid shear stress acting on each particle over the time taken by the particle to cross the computational domain, was computed to approximate the cumulative effect of the shear stress magnitude and the exposure time. The time history of platelets exposed to shear stress was tracked to define regions associated with elevated potential for platelet activation. However, as in the previous study by Balducci *et al*. [52], no direct correlation with blood trauma was attempted. It should also be noted that both of these studies [52, 53] were limited to the analysis of two-dimensional flow fields. The computed trajectories were therefore not a true representation of the three-dimensional paths of the blood cells.

Other researchers have tried to overcome these limitations by considering three-dimensional particle paths and either performing specific blood experiments or using existing blood damage models to relate their shear stress-exposure time results with blood trauma potential. In a recent study, Raz *et al*. experimentally and numerically assessed the platelet activation induced by the flow through an axisymmetric and an eccentric coronary stenosis models [54]. By summing the local shear stress multiplied by the local residence time along selected trajectories, the authors computed an activation level parameter, which was compared to platelet activation threshold determined from *in vitro* platelet activation state assay measurements. The authors showed that the numerical and experimental results were in good agreement with the *in vitro* blood

results and therefore concluded that assessing a first estimate of platelet activation levels using solely fluid mechanics information was possible. To fully comprehend any flow-induced platelet activation, the authors acknowledged that a more sophisticated model, accommodating any stress threshold-exposure time and shear stress history, was needed.

Song et al. evaluated the red blood cell damage induced by a continuous flow left ventricular assist device (VAD) [50]. Using a Lagrangian tracking approach, the authors computed streaklines and obtained the shear history of particles flowing along these trajectories. The cumulative effect of stress on red blood cell trauma along each particle trajectories, dubbed blood damage index (BDI), was estimated by integrating a power law hemolysis model along each trajectory. This power law model was based on the experimental model developed by Heuser and Opitz [55] which relates hemoglobin release, shear stress and exposure time. Comparison of the computed BDI with clinical data proved that numerical approaches could be used to obtain an order of magnitude of the hemolysis level induced by VADs. It should be pointed out that the experimental model proposed by Heuser and Opitz [55] and used in this study was obtained with a Couette viscometer and its range of applicability (including exposure time and shear tress level ranges) is limited. This model was found suitable for VADs but not for blood pumps or artificial heart valves for which the models proposed by Bludszuweit [56] and Giersiepen *et al*. [57] were preferred.

Chan *et al.* simulated the blood flow through different centrifugal blood pumps under steady state conditions and applied a Lagrangian analysis to compute streaklines and estimate the effect of blade geometry on red blood cell trauma [49]. Particles were released at the pump inlet and the shear history experienced by these particles was computed. Using the instantaneous blood trauma model proposed by Giersiepen *et al*. [57] and the linear cumulative hemolysis model proposed by Bludszuweit [56], the

authors computed and compared the percent of hemoglobin released by each particle crossing the centrifugal pump. However, it should be pointed out that the comparison of the pump performance from a blood damage perspective was performed by considering only a selected number of particle trajectories. Moreover, the authors didn't attempt to validate the computed blood trauma levels by comparing them to blood experiment results.

Lim *et al.* also used the model proposed by Giersiepen *et al*. [57] to characterize the blood damage induced by a porcine bioprosthetic heart valve [58]. The velocity fields immediately downstream of the valve were obtained from PIV measurements and were used to calculate shear stress fields and particle trajectories. The authors estimated the particle shear history and used the model developed by Giersiepen *et al* [57] to compute the percentage of platelets and red blood cell damaged by the shear stress levels experienced. This study, along with the ones by Krishnan *et al.* [53] and Balducci *et al.* [52], are to date the only studies that have tried to analyze the flow through a prosthetic heart valve using Lagrangian analysis tools. These studies [52, 53, 58] provided important information on the approach to be taken to predict flow-induced blood cell trauma but were limited to the analysis of two-dimensional flow fields. A blood damage model applied to three-dimensional flow fields would provide a more in-depth understanding of artificial valve-induced blood trauma.

1.7 Significance of the Study

Nearly 45 percent of all failing native heart valves are currently replaced by a bileaflet mechanical heart valve (BMHV). However, despite their widespread use, BMHVs are not complication-free and are still associated with high levels of hemolysis, platelet activation and thromboembolic events. Clinical reports and recent *in vitro*

experiments suggest that these complications are associated with the fluid stresses imposed on blood elements by the non-physiological hemodynamics induced by the hinge region of the BMHV.

With that observation in mind, numerous researchers have sought to characterize the flow field inside the hinge region in an effort to better understand the relationship between hinge design and thromboembolic potential. Numerical studies, in particular, have gained interest as a mean to probe the hinge flow fields with high spatial and temporal resolution. However, the relevance of most of the numerical simulations to date is insufficient due to a lack of spatial resolution, a lack of experimental validation, or the use of non-physiologic flow conditions (as described in section 1.5.2).

The present study aims at addressing the shortcomings of previous numerical studies. A pseudo multi-scale approach is implemented to simulate the three-dimensional pulsatile physiologic flow in the hinge region of a BMHV. This is achieved by performing a one-way coupling between large-scale and small-scale simulations consisting of extracting the boundary conditions for the hinge simulations from the Fluid-Structure-Interaction simulations of a BMHV bulk flow. This approach ensures not only that realistic physiologic flow conditions are applied in the small-scale solver but also that the complex hinge flow features are correctly reproduced by using dense grid with high spatial resolution.

Simulating the flow in realistic hinge geometry is essential to understand the thromboembolic potential associated with currently used hinges and subsequently improve upon their design. The present study thus undertakes a reverse engineer approach to obtain, from actual clinical BMHVs realistic numerical models of the hinge region. The leaflet motion, the intricate geometry of the hinge, and the pulsatility of the flow induce complex three dimensional unsteady flows within the hinge recess. As a result, the capability of numerical approaches to simulate such complex flow needs to be

tested by comparing the numerical simulations with experimental measurements. The accuracy of the numerical flow solutions is addressed through experimental validation. The numerical results are here compared to the findings of Laser Doppler Velocimetry experiments performed under the same physiologic flow conditions and with a similar valve configuration.

Finally, this study relates for the first time the Eulerian flow solutions to Lagrangian statistical characteristics by implementing a Lagrangian particle tracking methodology. Previous studies have primarily focused on the maximum shear stress present within the hinge recess to estimate the hinge clinical performance. Yet, it is essential to analyze the flow fields from a blood cell standpoint to relate hinge geometry to its respective flow patterns and thromboembolic potential. Knowledge of the blood element trajectories, combined with existing blood damage model, provides meaningful measure, such as mean residence time (propensity for blood clot formation) or the cell shear histories (propensity for hemolysis and platelet activation). This analysis of the hinge flow fields aims at providing a framework to gain new insight into the thromboembolic potential of the hinge.

The developed approach is demonstrated on two existing hinge designs with varying configurations to assess the effect of curvature and hinge gap with on the hinge performance. Such an approach, applied to a wide range of hinges, with varying design parameters would allow for a rapid and cost-efficient assessment of the fluid dynamics performance of the different designs and eventually help in determining the optimal hinge design. The developed numerical framework thus has the potential to reduce the duration and cost of pre-clinical evaluation of new BMHV designs and accelerate the development of new valve with improved hinge design.

CHAPTER 2

HYPOTHESIS AND SPECIFIC AIMS

Bileaflet mechanical heart valves, despite their widespread use, can still cause major life-threatening complications, including platelet activation, hemolysis, and thrombogenic and thromboembolic events. These complications are thought to be associated with the non-physiologic hemodynamic stresses imposed on blood elements by the flow in the hinge region of the valves. The hemodynamics of the hinge flow is characterized by complex spatial and temporal three-dimensional structures that arise from the pulsatility of the flow, the complexity of the geometry, and the flow-dependent motion of the valve leaflets. Given the nature of the hinge hemodynamics, accurate-characterization of the hinge flow fields throughout the cardiac cycle is required to improve and refine existing hinge designs so as to ultimately develop bileaflet mechanical heart valves with minimal thromboembolic complications. This could be achieved with a computational fluid dynamics (CFD) tool specifically tailored to the heart valve hemodynamics.

The hypothesis of this research is that: **Accurate simulations of the complex three-dimensional flows in the hinge region of bileaflet mechanical heart valves require a sophisticated computational fluid dynamics tool implemented at the micro-scale.** This hypothesis will be addressed by the following Specific Aims:

<u>Specific Aim 1:</u> To adapt a hybrid Cartesian/immersed boundary method to accurately and efficiently simulate the three-dimensional pulsatile micro-flow fields within the hinge region of bileaflet mechanical heart valves. This aim will be achieved by tailoring an existing general hybrid Cartesian/immersed boundary algorithm to accurately resolve high velocity unsteady flows in micro-gaps, such as those encountered in the hinge region. The necessary boundary conditions for this micro hinge flow solver (i.e. flow boundary conditions and dynamic leaflet motion) will be obtained from an existing 3D macro-scale fluid-structure interaction model of the bulk flow through a bileaflet mechanical heart valve. This approach will ensure an appropriate one-way coupling of the macro- and micro-scale models and guarantee a detailed modeling of the micro hinge flow fields.

The accuracy with which the numerical simulations predict the micro-flow fields within the hinge region will be investigated by comparing the simulated flow fields with two-component Laser Doppler Velocimetry velocity measurements. The validation will be performed with a 23 mm St. Jude Medical (SJM) Regent valve subjected to physiological aortic flow conditions. The experimental measurements will be acquired in the hinge recess and the near-hinge region of a clear-housing clinical-quality replica of the valve. The numerical simulations will be performed using a highly spatially refined computational mesh of the hinge region of the same valve. Exact leaflet, housing and hinge geometries will be obtained from X-ray micro-computed tomography scans. The computed results will then be compared to the experimental velocity data to evaluate the ability of the numerical tool to capture the hinge flow fields.

<u>Specific Aim 2:</u> To develop a framework to estimate the thromboembolic potential associated with the hinge region of bileaflet mechanical heart valves. Non-physiologic fluid forces, and in particular fluid shear stresses, are known to lyse red

blood cells and activate platelets, thereby starting the coagulation cascade and promoting thrombus formation. Therefore, in order to understand thromboembolic complications, it is critical to estimate the shear stress forces experienced by blood elements as they flow through the hinge. To achieve this specific aim, a two-step approach will thus be followed by first calculating the shear stress fields across the hinge using the simulated three-dimensional velocity fields and, then implementing a particle tracking algorithm to estimate the trajectories of blood elements through the hinge region. Knowledge of the particle trajectories will enable the estimation of the flow environment experienced by each particle and the calculation of thromboembolically relevant parameters, such as residence time and shear stress levels along each particle trajectory. These quantities, combined with existing blood damage models, will be used to assess the role of specific hinge flow structures in inducing platelet activation, hemolysis and/or thrombus formation and provide surrogate measures of the thromboembolic potential associated with the hinge region.

Specific Aim 3: ***To examine the influence of hinge design on the blood damage potential associated with the hinge region of bileaflet mechanical heart valves.*** This aim will be achieved by applying the CFD tool developed in Specific Aim 1 on three different hinge designs and computing the associated thromboembolic potential using the analysis framework developed in Specific Aim 2. All three configurations will be studied under physiologic aortic conditions. More precisely, we will study a 23 mm SJM Regent hinge with a normal hinge gap width, a 23 mm SJM Regent hinge with a larger-than-normal hinge gap width, and a 23 mm CarboMedics hinge with a normal hinge gap width. This flow analysis, along with the three-component velocity fields and the shear stress fields, will provide new insights into the influence of dimensional (hinge gap width) and geometrical (hinge design) parameters on the hinge thromboembolic potential.

CHAPTER 3

METHODS

In this section, the numerical methods used to simulate and analyze the complex pulsatile three-dimensional hinge flow fields are described. The chapter is divided into two main sections. The numerical methodology employed to simulate the hinge flow fields is presented first and is followed by a description of the flow analysis performed.

The numerical flow solver is an extension of the methodology developed by Sotiropoulos and co-workers [59-61]. This methodology was applied to carry out high-resolution Fluid-Structure Interactions (FSI) simulations of the bulk of the flow through bileaflet mechanical heart valves under physiologic aortic conditions [61] and yielded results in excellent agreement with *in vitro* measurements [62]. First the governing equations are presented. The numerical solver for integrating numerically the time-accurate governing equations is then described along with the immersed boundary approach employed to take into account the effects of the moving leaflet on the flow fields. A detailed description of the numerical geometry and the boundary conditions is provided next.

The chapter ends with a description of the Lagrangian particle tracking methodology and the clinically-relevant parameters extracted to gain a better insight into the thromboembolic potential of the hinge region.

3.1 Numerical Flow Solver

3.1.1 The Navier-Stokes equations in Cartesian and Contravariant Coordinates

By considering that a fluid is a continuum and that the principles of conservation are to be satisfied at all times, the Navier-Stokes equations can be derived and used to describe the motion of this fluid. For a finite arbitrary control volume Ω bounded by a closed surface S (Figure 3-1), the general integral form of the conservation law for the quantity ϕ may be written as:

$$\frac{\partial}{\partial t}\iiint_{\Omega}\Phi d\Omega+\iint_{S}\vec{\mathrm{H}}.d\vec{S}=\iiint_{\Omega}Q_{\Omega}d\Omega+\iint_{S}\vec{F}Q_{s}.dS \qquad \text{Equation 3-1}$$

The first term of Equation 3-1 corresponds to the temporal variations of the quantity ϕ inside the control volume Ω. With H the flux associated with the quantity ϕ, the second term represented the net flow of the quantity ϕ into or out of the control volume Ω through the control surface S. Finally, the quantity Q_{Ω} and Q_s are any possible source of the quantity ϕ inside the control volume Ω and on the control surface S, respectively.

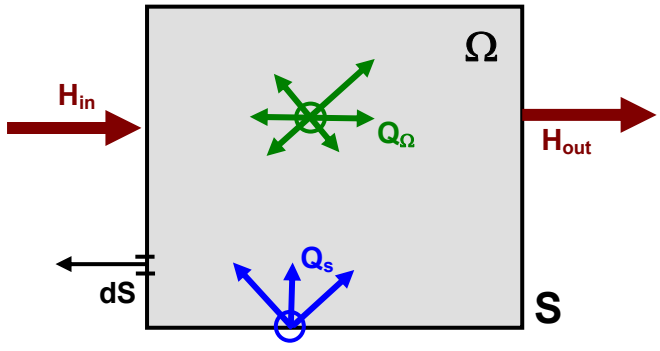

Figure 3-1: Finite arbitrary control volume Ω and its bounding surface S.

If the quantity ϕ is the mass, the equation for the conservation of mass, also known as the continuity equation, may be derived from Equation 3-1 and reads as:

$$\frac{\partial}{\partial t}\iiint_{\Omega}\rho d\Omega+\iint_{S}\rho\vec{V}d\vec{S}=\mathbf{0} \qquad \text{Equation 3-2}$$

where ρ is the fluid density and $\vec{V}$ is the fluid velocity.

Similarly, three equations of conservation of momentum, one for each space direction, may be obtained. For instance, for a coordinate system defined by the unit vector ($\vec{e_i}$, $\vec{e_j}$, $\vec{e_k}$),the fluid velocity component along the k-axis is denoted as U_k and the k-component of the momentum equation is:

$$\frac{\partial}{\partial t}\iiint_{\Omega}\left(\rho U_k\right)d\Omega+\iint_{S}\left(\rho U_k\vec{V}\right).d\vec{S}= \iiint_{\Omega}\left(f_k\right).d\Omega+\iint_{S}\left(-P\vec{n}.\vec{e_k}+\sigma_n\vec{n}.\vec{e_k}+\sigma_s\vec{t}.\vec{e_k}\right).dS \qquad \text{Equation 3-3}$$

where $\vec{n}$ and $\vec{t}$ are two unit vectors perpendicular and tangent, respectively, to the infinitesimal control surface dS. P is the static pressure, σ_s and σ_n are the normal stress and tangential stress that acts on the surface dS, and f_k represents other body forces, such as gravity or centrifugal forces, along the k-direction.

Finally, if the quantity ϕ represents the total energy of the system (defined as the sum of the thermodynamic internal energy and the kinetic energy), the equation for the conservation of energy can be obtained from Equation 3-1. The set of momentum equations (1, 2 or 3 equations depending on the number of spatial dimensions considered) together with the continuity equation and the energy conservation equation constitute the so-called Navier-Stokes equations.

In this thesis, the fluid of interest is assumed to be incompressible and Newtonian. The effect of gravity or all other body force is neglected and no heat transfer

occurs. The fluid motion can thus be fully described by the continuity and momentum equations (Equations 3-2 and 3-3). These two equations are the well-known incompressible, Newtonian form of the time-dependent Navier-Stokes equations. Using Einstein's notation, these equations in adimensional form are:

$$\frac{\partial u_i}{\partial x_i} = \mathbf{0} \qquad i=1,2,3 \qquad \text{Equation 3-4}$$

$$\frac{\partial u_i}{\partial t} + \frac{\partial \left(u_i u_j\right)}{\partial x_j} = -\frac{\partial p}{\partial x_i} + \frac{\mathbf{1}}{\mathrm{Re}} \frac{\partial^2 u_i}{\partial x_j \partial x_j} \qquad i=1,2,3 \qquad \text{Equation 3-5}$$

where x_i are the normalized Cartesian coordinates, u_i the normalized Cartesian velocity components, *Re* the Reynolds number of the flow and *i,j*=1,2,3 index three orthonormal directions in space. The terms $\partial\left(u_i u_j\right)/\partial x_j$ and $\mathrm{Re}^{-1}.\partial^2 u_i/\partial x_j \partial x_j$ denote the convective and viscous contributions, respectively, while the term $\partial p/\partial x_i$ is the pressure gradient term. The different variables are non-dimensionalized with:

$$u_i = \frac{u_i}{U^*} \qquad \text{Equation 3-6}$$

$$x_i = \frac{x_i}{L^*} \qquad \text{Equation 3-7}$$

$$t_i = \frac{t_i}{T^*} \qquad \text{Equation 3-8}$$

$$p = \frac{P}{\rho U^* U^*} \qquad \text{Equation 3-9}$$

where u_i, x_i, t_i, and p are the non-dimensional velocities, positions, time, and pressure, respectively. U*, T* and L* are the characteristic velocity, time, and length, respectively. More details on the choice for these constants are given in section 3.4.4.

When non-uniform and/or body-fitted grids are used to discretize the fluid domain, the Cartesian equations are typically transformed into a generalized curvilinear

coordinate system where $\xi^k = \xi^k(x_1, x_2, x_3)$ with *k*=1,2,3 for each of the three-directions. The Contravariant velocity components U^j are related to the Cartesian velocity u_i components by:

$$U^i = u_j \xi^i_{x_j} = u_1 \xi^i_{x_1} + u_2 \xi^i_{x_2} + u_3 \xi^i_{x_3} \qquad \text{Equation 3-10}$$

Transforming the independent variables (x_i) but keeping the component of the velocity fields (u_i) expressed in terms of their Cartesian components where needed, the partially transformed governing equations read as:

$$J \frac{\partial}{\partial \xi^i}\left(\frac{U^i}{J}\right) = \mathbf{0} \qquad \text{Equation 3-11}$$

$$\frac{\mathbf{1}}{J}\frac{\partial u_i}{\partial t} + Conv(u_i) = -Grad_i(p) + \frac{\mathbf{1}}{\mathrm{Re}} Visc(u_i) \qquad \text{Equation 3-12}$$

where J is the Jacobian of the geometric transformation, defined as $J = \partial(\xi_1, \xi_2, \xi_3)/\partial(x_1, x_2, x_3)$. With g^{kl} the Contravariant metric tensor $g^{kl} = \xi^k_{x_j} \xi^l_{x_j}$, the operators for the convective $Conv(u_i)$, viscous $Visc(u_i)$, and pressure $Grad_i(p)$ terms can be expressed, respectively, as:

$$Conv(\alpha) = \frac{\partial}{\partial \xi^j}\left(\frac{U^j}{J}\alpha\right) \qquad \text{Equation 3-13}$$

$$Visc(\alpha) = \frac{\partial}{\partial \xi^j}\left(\frac{g^{jl}}{J}\frac{\partial}{\partial \xi^l}\alpha\right) \qquad \text{Equation 3-14}$$

$$Grad_i(\alpha) = \frac{\partial}{\partial \xi^j}\left(\frac{\xi^j_{x_i}}{J}\alpha\right) \qquad \text{Equation 3-15}$$

Because of the relationship between the Cartesian and Contravariant velocities (Equation 3-10), the time derivative in the momentum equation can be expressed as:

$$\frac{\partial u_i}{\partial t} = \frac{\partial}{\partial t}\left(\frac{U^j}{\xi^j_{x_i}}\right) = \frac{\partial U^j}{\partial t}\frac{\partial}{\partial t}\left(\frac{1}{\xi^j_{x_i}}\right) = \frac{\partial U^j}{\partial t}\frac{1}{\xi^j_{x_i}} = \frac{\partial\left(V^j J\right)}{\partial t}\frac{1}{\xi^j_{x_i}} = \frac{\partial\left(V^j\right)}{\partial t}\frac{J}{\xi^j_{x_i}} \quad \text{Equation 3-16}$$

with V^i the surface flux defined as $V^i = U^i / J$. The governing equations (Equations 3-11 and 3-12) can then be rewritten as:

$$J\frac{\partial}{\partial \xi^i}\left(V^i\right) = \mathbf{0} \quad \text{Equation 3-17}$$

$$\frac{\partial\left(V^j\right)}{\partial t} = -\xi^j_{x_i}\left(Conv\left(u_i\right) + Grad_i\left(p\right) - \frac{\mathbf{1}}{\mathrm{Re}}Visc\left(u_i\right)\right) \quad \text{Equation 3-18}$$

Because in the present thesis stretched orthogonal fluid grids are considered rather than arbitrary grids, it is worth noting that only the terms $\xi^i_{x_i} = \partial\xi^i / \partial x_i$ are non-zero, while the terms $\xi^i_{x_j} = \partial\xi^i / \partial x_j$ equal zero (with $i \neq j$). $\xi^k = \xi^k\left(x_1, x_2, x_3\right)$ thus simplifies to $\xi^k = \xi^k\left(x_k\right)$, the transformation Jacobian to $J = \xi^{\mathbf{1}}_{x_1} . \xi^{\mathbf{2}}_{x_2} . \xi^{\mathbf{3}}_{x_3}$, the Contravariant metric tensor $g^{kl} = \xi^k_{x_k}\xi^l_{x_l}$ and the Contravariant velocities to $U^i = u_i\xi^i_{x_i}$.

3.1.2 Discretization approach to solve the Navier-Stokes equations

As discussed in detail by Sotiropoulos and Abdallah [63], discretization of the governing equations on a non-staggered grid using a three-point central differencing scheme leads to spurious non-physical oscillations in the pressure field. Adding artificial dissipation terms, explicitly or implicitly, in the discrete continuity equations has been proposed in the literature to eliminate these odd-even decoupling [63-65]. However,

such artificial dissipation terms could lead to unacceptably high errors in the satisfaction of the continuity equation near rapidly accelerating immersed bodies. A staggered grid arrangement may circumvent these issues, satisfying the discrete continuity equation to machine zero and leading to smooth discrete pressure fields. However, a staggered grid is burdensome to implement in conjunction with immersed boundary methods due to the difficulty of appropriately applying the boundary conditions at the body surface.

In order to combine the versatility and convenience of implementing a non-staggered variable arrangement with the superior accuracy of staggered mesh approaches, a hybrid staggered/non-staggered method has been developed by Gilmanov and Sotiropoulos [59, 66]. This combined approach has been successfully applied to simulate a wide range of flows, such as the flow fields around fishes, around planktonic copepod or through artificial heart valves [59-61, 66].

A hybrid staggered/non-staggered control volume approach is therefore employed to discretize the governing equations. In this approach the pressure *p* and the Cartesian velocities are stored at the control volume centers (*i,j,k*) while the surface fluxes V^i are stored at the respective surface centers (*(i+1/2,j,k), (i,j+1/2,k),(i,j,k+1/2)*), as shown in Figure 3-2. The boundary conditions are prescribed using the non-staggered layout with collocated pressures and Cartesian velocities, while the Navier-Stokes equations are solved using the more stable staggered layout. When needed in the bulk of the flow, the Cartesian cell-centered velocity components are reconstructed from the surface-centered surface fluxes by interpolation.

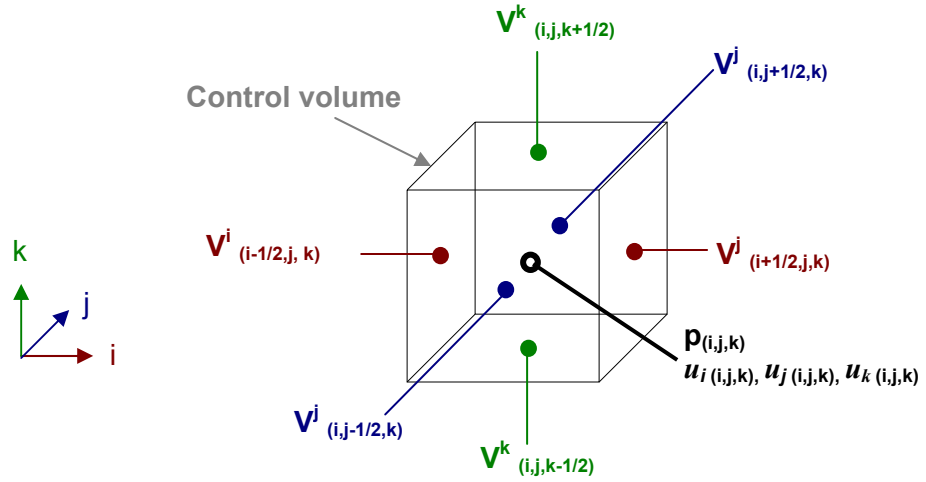

Figure 3-2: Surface fluxes, Cartesian velocities and pressure storage arrangement for the staggered/non-staggered control volume approach

The three momentum equations (Equation 3-18) should thus be recast from the volume centers to the surface centers. This is done as follows:

$$\frac{\partial\left(V^1_{i+1/2,j,k}\right)}{\partial t} = -\xi^1_{x_1} RHS^1_{i+1/2,j,k} \qquad \text{Equation 3-19}$$

$$\frac{\partial\left(V^2_{i,j+1/2,k}\right)}{\partial t} = -\xi^1_{x_1} RHS^1_{i+1/2,j,k} \qquad \text{Equation 3-20}$$

$$\frac{\partial\left(V^3_{i,j,k+1/2}\right)}{\partial t} = -\xi^3_{x_1} RHS^3_{i,j,k+1/2} \qquad \text{Equation 3-21}$$

where RHS^i is the right-hand side of the i^{th} momentum equation (with i=1,2,3) and corresponds to the sum of the viscous, convective and pressure terms.

Computation of the RHS^i at the surface centers would require the evaluation of the viscous and convective fluxes at the control volume centers, so that the central differentiation stencil may be centered on the desired surfaces. In practice, it is more convenient to compute the right-hand-side terms RHS^i at the volume center and then interpolate each component of RHS^i into the corresponding surface centers using either

QUICK or central differencing (see Appendix A.4 for more details on the interpolation schemes). As a result, the viscous and convective fluxes are first evaluated at the surface centers and their derivative is then computed at the control volume centers. Each component of the cell-centered viscous and convective terms is then interpolated onto the corresponding surface centers. As for the pressure gradient term, it can be directly computed at the surface centers since the pressure variable is stored at the volume centers. At that point, the convective, viscous and pressure terms are known at all surface centers and thus, the term RHS^i can be estimated at the surface centers.

For clarity, a flow chart summarizing the numerical approach to obtain the Contravariant fluxes and the right-hand-side of Equations 3-19, 3-20 and 3-21 is provided in Appendix A.3. Using the pressure values stored at the volume center, the pressure gradient $Grad(p)$ is finally obtained at the surface center using a central differencing scheme.

3.1.3 Solving the discretized Navier-Stokes equations

The momentum equations (Equation 3.18) may be rewritten, for simplicity as:

$$\frac{\partial\left(V^j\right)}{\partial t} = -F^j - G\left(p\right) \qquad \text{Equation 3-22}$$

with $$F^j = \xi_{x_i}^j \left(Conv^j\left(u_i\right) - \frac{\mathbf{1}}{\mathrm{Re}} Visc^j\left(u_i\right) \right) \qquad \text{Equation 3-23}$$

$$G(p) = \xi_{x_i}^j Grad_i\left(p\right) \qquad \text{Equation 3-24}$$

These governing equations are integrated in time using a fractional-step method, which comprises two main steps, a momentum step followed by a pressure correction step.

1- Momentum step: Intermediate surface fluxes $V^{j(*)}$ are obtained by solving the following momentum equations at the surface centers.

$$\frac{\mathbf{1}}{\mathbf{2}\Delta t}\left(\mathbf{3}V^{j(*)} - \mathbf{4}V^{j(n)} + V^{j(n-\mathbf{1})}\right) = -F(V^{j(*)}) - G\left(p^{(n)}\right) \qquad \text{Equation 3-25}$$

where the indices n and (n-1) denote the time step *n* and the previous time step (*n-1*) and $V^{j(n)}$ is the solution at time step *n*. The above equations (Equation 3-25) correspond to the momentum equations (Equation 3-22) where the time derivative is discretized with a second-order backward Euler scheme. The right-hand side is calculated at the surface centers using the hybrid staggered/non-staggered approach described in the previous section (section 3.1.2). Note that the solution $V^{j(*)}$ satisfies the Navier-Stokes equations with the pressure $p^{(n)}$ and not $p^{(n+1)}$.

2- Pressure correction step: The momentum step, often dubbed prediction step, is followed by a pressure correction step where the following equation is solved:

$$\frac{2}{3\Delta t}\left(V^{j(n+1)} - V^{j(*)}\right) = G(\varphi) \qquad \text{Equation 3-26}$$

where $V^{j(*)}$ is the previously predicted velocity, $V^{j(n+1)}$ is the solution at time step (*n+1*) that satisfies the continuity equation (Equation 3-17). The pressure correction term φ is obtained by solving the following Poisson equation:

$$J\frac{\partial}{\partial \xi^j}\left(G(\varphi)\right) = \frac{3}{2\Delta t}J\frac{\partial V^{j*}}{\partial \xi^j} \qquad \text{Equation 3-27}$$

The pressure and velocity at the time step (*n+1*) are finally obtained by:

$$p^{n+1} = p^n + \varphi$$ Equation 3-28

$$V^{j(n+1)} = G(\varphi)\frac{3\Delta t}{2} + V^{j(*)}$$ Equation 3-29

Once the Contravariant fluxes $V^{j(n+1)}$ are computed at the surface centers, the Cartesian velocity at the volume center can be recovered using QUICK interpolation scheme (Appendix A.4). The numerical algorithms used for solving the two above steps are described in the following sections (sections 3.1.3.1 and 3.1.3.2, respectively).

3.1.3.1 Momentum step

The intermediate velocity fluxes are obtained by solving the momentum equations using a Newton method. Explicit schemes, such as explicit Runge-Kutta method, impose severe restrictions on the physical time steps and thus reduce drastically the overall efficiency of the solver. This issue may be circumvented by using a Newton solver. Newton solvers are used to solve iteratively systems of non-linear equations of the form $f(x) = 0$. The general form of the Newton method for solving this equation is:

$$x_{k+1} = x_k - f(x_k) / f'(x_k) \qquad \text{with k=0,1,2…}$$ Equation 3-30

In this equation, x_0 is an initial approximation to the solution and $f'(x_k)$ is the Jacobian. In practice, the Newton iteration is implemented by the following steps:

1. Solve $f'(x_k)\Delta x_k = -f(x_k)$
2. Update $x_{k+1} = x_k + \Delta x_k$.
3. Iterate until the difference (x_{k+1} - x_k) is relatively small.

A graphical illustration of the iterative approach used in the Newton method to solve the equation $y=f(x)$ is given in Figure 3-3.

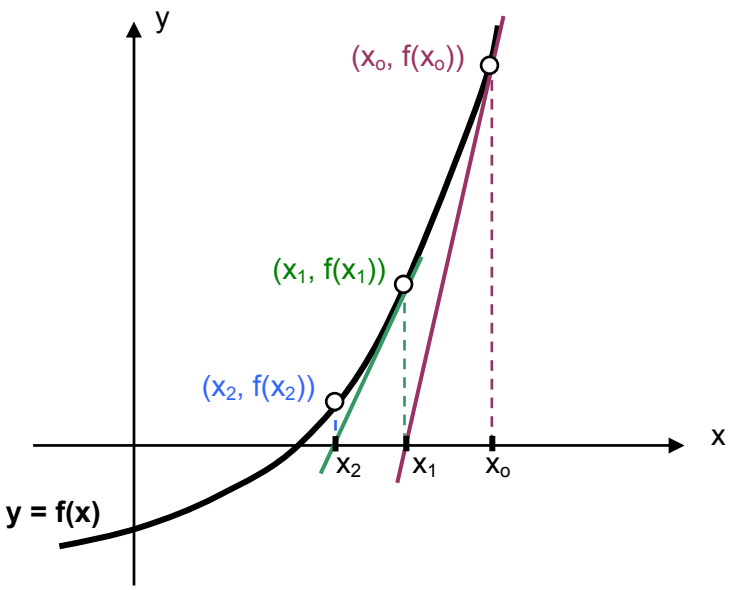

Figure 3-3: Illustration of the Newton method. The red line shows the first Newton iteration with the point x_1 closer to the root of the function *y=f(x)* than the initial guess x_0. The point x_2 obtained at the second iteration is closer to the function root than the point x_1 and the initial guess.

However, it should be noted that the Newton's methods are generally very costly and inexact Newton techniques are often preferred as they reduce these expenses (in particular matrix storage requirements) and retain the rapid convergence of Newton's method [67]. In such methods, the above first step is replaced by a series of iterations (indexed by *i*) until the residuals:

$$r_k^{(i)} = f'(x_k)\Delta x_k + f(x_k) \qquad \text{with } i=1,2,\ldots \qquad \text{Equation 3-31}$$

satisfy the following condition:

$$\frac{\| r_k^{(i)} \|}{\| f(x_k) \|} < 1 \qquad \text{with } i=1,2,\ldots \qquad \text{Equation 3-32}$$

More details on the Newton and inexact Newton methods may be found in the literature[67, 68].

Since the momentum equations, given in Equation 3.21, may be written as $\mathcal{G}(V^{j^*}) = \mathbf{0}$, this non-linear system of equations can be solved using an inexact Newton method. The equations to be solved at the first step of the Newton method are therefore:

$$\frac{\partial \mathcal{G}}{\partial V}.\Delta V = -\mathcal{G}(V) \qquad \text{Equation 3-33}$$

where the left hand side $\partial \mathcal{G}/\partial V$ is the Jacobian matrix. These equations were solved using a Newton-Krylov subspace method [67-69] which belongs to the class of inexact Newton methods. The selected solver was the restarted Generalized Minimal Residual Method (GMRES) solver (see section 3.1.3.2 for more details on GMRES methods) with a block Jacobi preconditioner. This methodology for solving the momentum equations was implemented using the libraries available in PETSC (Portable, Extensible Toolkit for Scientific Computation) [67, 69].

3.1.3.2 Pressure correction step

The pressure correction step requires solving a system of equations of the type:

$$A.x = b \qquad \text{Equation 3-34}$$

where A is a N x N matrix operator representation, b is vector of size N that is given and the vector x is to be found. An overview of the different methods available to solve such systems will be presented first, followed by a detailed description of the method retained in this thesis.

Available methods to solve linear systems of equations

Direct methods attempt to solve the problem with a finite number of operations and an exact solution, notwithstanding rounding errors, would be obtained. However, in cases of large systems, direct methods are extremely expensive and often not applicable as the matrix A might be singular and thus not invertible. Other methods have therefore been developed to overcome this issue. Iterative methods, unlike direct methods, attempt to solve the system of equations by finding from an initial guess a sequence of approximate solutions that converges to the exact solution. The iterative methods generally end when the residual defined by $r = b - A.x$ is sufficiently small. There are two main classes of iterative methods: the stationary iterative methods and the non-stationary iterative methods (also known as the Krylov subspace (KSP) method).

Methods that can be expressed in the form of $x^{(K+1)} = Bx^{(K)} + C$, where $x^{(K)}$ is the approximate solution at the K^{th} iteration and B and C are two constants which do not depend on the iteration K, are called stationary iterative methods. While these methods are simple to implement, convergence may be very slow to reach. If, on the other hand, B and C are changing during the iteration process, the methods are considered non-stationary iterative methods. The non stationary methods, or KSP methods, form an orthogonal basis of the sequence of successive matrix A power times the initial residual. They minimize at the Kth iteration the error over the affine space defined as $x_o + \mathcal{K}_K$ where x_o is the initial guess and $\mathcal{K}_K$ is the K^{th} Krylov subspace:

$$\mathcal{K}_R = span\left\{r_o, Ar_o, A^2 r_o, ..., A^{R-1} r_o\right\} \qquad \text{Equation 3-35}$$

The approximations of the solution are thus obtained by minimizing the residual over the subspace formed. The KSP methods were found to be more efficient than the simple

stationary methods [68] and thus this class of methods was selected to solve the pressure correction step.

One of the most commonly used KSP methods is the General Minimal Residual (GMRES) method. The generalized minimal residual (GMRES) method was first proposed by Saad and Schultz in 1986 [70] and is essentially an extension of the minimal residual method (MINRES). While the MINRES is only applicable to symmetric systems, the main advantage of the GMRES method is to be applicable to asymmetric systems. One of the main issues of GMRES methods is the storage requirement as the memory cost increases with the number of GMRES iterations. The method is therefore often restarted after a number, for instance *q*, of iterations, with the solution x_q as the initial guess. The resulting method, called restarted GMRES, has reduced storage requirements.

So as to speed-up convergence, GMRES is usually combined with a preconditioning method, such as Jacobi, Successive Over Relaxation (SOR) or Multigrid. The preconditioner may be fixed or it may change from one iteration to the next. In this last case, where variable preconditioning operators are used, the methods are referred to as Flexible methods. More details on the GMRES method and the advantages of using variable preconditioners are available in the literature [70, 71]. Because of the enhanced performance of the GMRES method compared to other iterative methods, this approach was chosen to solve the pressure correction equation.

Iterative approach used to solve the pressure correction equation

The pressure-correction equation (Equation 3-26) is solved using the Flexible Generalized Minimal Residual Method (FGMRES) [71] combined with a Multigrid approach. As shown previously in the literature [60], a Multigrid preconditionner is superior to other preconditioners such as Jacobi or Incomplete Lower Upper (LIU)

decomposition) in enhancing the convergence performance of the GMRES for higher mesh resolution. It has also been shown that FGMRES solver preconditioned with a Multigrid approach is very robust [60] and has better performance than a Multigrid method alone used as a solution method as demonstrated by OOsterlee and Washio [72]. Thus a cell-centered Multigrid preconditioned FGMRES solver is employed to solve the pressure Poisson equation. The solver was implemented using the library readily available on the Krylov Suspace package offered by PETSC [67, 69]. Since an overview of GMRES method has already been presented in the above section, the following section will focus solely on describing the Multigrid approach.

Multigrid preconditioner: In order to speed the convergence, a multigrid preconditioner was combined to the iterative solver. The multigrid approach uses a family of grids of differing mesh sizes (from fine to coarse grids) to discretize and solve complex non-symmetric systems of partial differential equations. The overall approach depends on two main basic principles:

- *Principle of smoothing:* Iterative methods appropriately applied to discrete elliptic problems have a strong smoothing effect on the error of any approximations and a rapid reduction of the overall error can be achieved.

- *Principle of coarse grid:* A smooth error term is well approximated on a coarse grid. A coarse grid procedure is less expensive than a fine grid procedure.

The Multigrid approach therefore uses a few iterations of an inexpensive smoothing (or relaxation) scheme on each grid level to attenuate the approximation error components introduced by using an under-refined mesh grid. The smoothing schemes are performed for equations defined on each grid level that approximate a suitable finest-grid error equation. The results are eventually interpolated into the finest grid level. Speed and accuracy are the two main advantages of the Multigrid method as this

method has been shown to produce results whose accuracy were comparable to the finest-grid discretization error at a cost equivalent to a few smoothing steps [73]. Figure 3-4 and Figure 3-5 show a schematic illustrating the overall Multigrid approach for two-, three- and four-grid cycles.

The main components of the Multigrid method used in the present solver are given below.

- *Grid coarsening strategy:* A semi-coarsening strategy along the valve axis (z-direction here) is employed. Figure 3-6 shows a two-dimensional schematic of this strategy where the mesh size h is doubled in only one direction, i.e. (H_y ,H_z)= (h_y, 2.h_z). Such coarsening methodology imposes the use of a mesh such that the number of nodes N_i in the coarsening direction satisfies the condition:

$$N_i = \mathbf{4}.\,Int + \mathbf{1} \qquad \text{Equation 3-36}$$

where i indicates the direction (i=1,2,3) and *Int* is an integer. A three-level Multigrid method is used in this thesis.

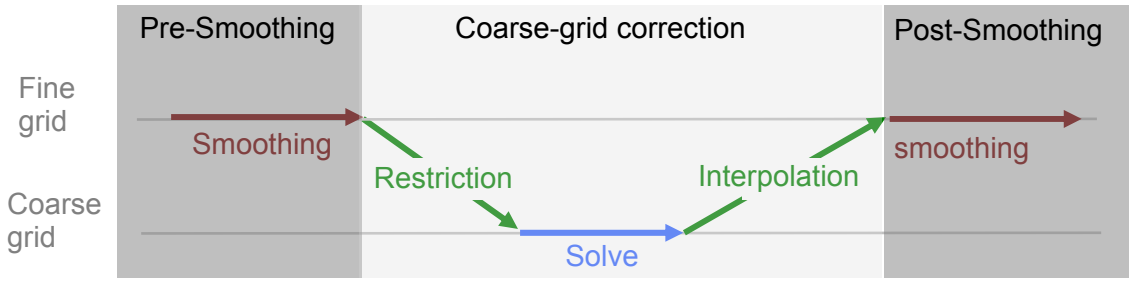

Figure 3-4: Illustration of the Multigrid approach for a two-grid cycle

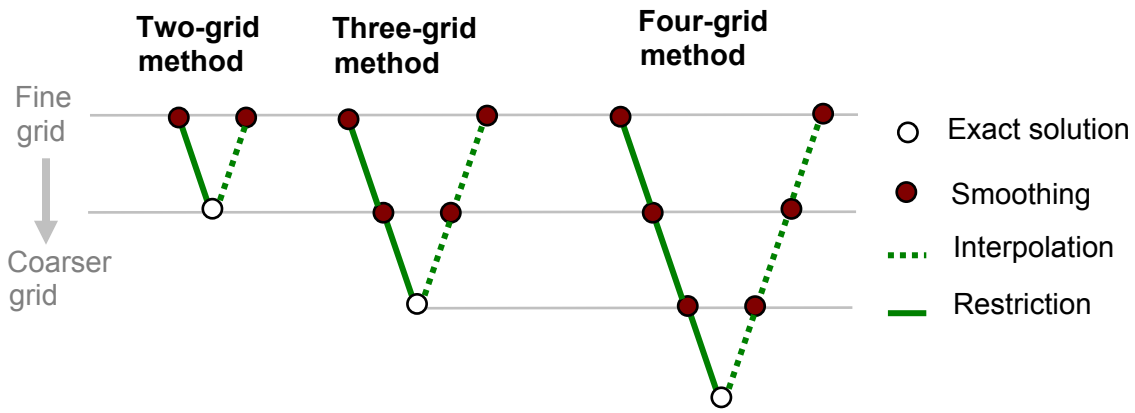

Figure 3-5: Examples of Multigrid V-cycle structures for three different numbers of grids.

- *Smoothing procedure:* The smoothing is done, for both pre-and post-smoothing correction steps, using an Incomplete Lower Upper (ILU) decomposition approach, which has been shown to have good smoothing properties [73].

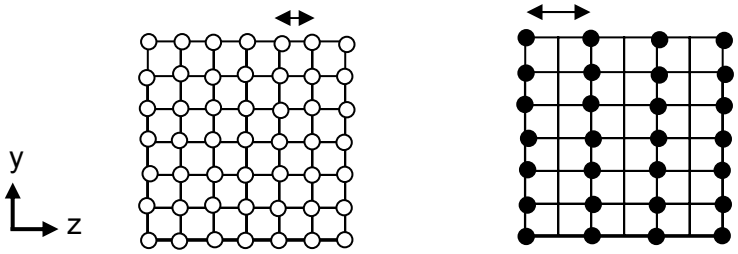

Figure 3-6: Example of semi-coarsening strategy, left panel: fine grid (o) and right panel: x-semi-coarse grid (•)

- *Coarsest grid level solver:* The Poisson equation is solved at the coarsest level using a FGMRES solver.

- *The restriction and interpolation operators:* The restriction and interpolation between the different levels of the Multigrid approach are done using a standard tri-linear interpolation operator [73].

3.2 Sharp Interface Immersed boundary method

3.2.1 Node classification

The immersed boundaries, here the leaflet and the valve housing surfaces, are discretized using unstructured triangular meshes and are treated as sharp interfaces immersed in a background non-uniform Cartesian grid. At every time step, the computational nodes of the Cartesian mesh are sorted into three categories based on their location relative to the immersed surfaces: 1) near-boundary (*nb*) nodes; 2) nodes in the fluid, called *fluid* nodes; and 3) nodes in the solid body, called *inner body* nodes.

3.2.1.1 Preliminary classification

The method employed to sort the different nodes is based on a general mathematical theory. Consider a two-dimensional problem where a body surface is immersed in a Cartesian background mesh as shown in Figure 3-7.

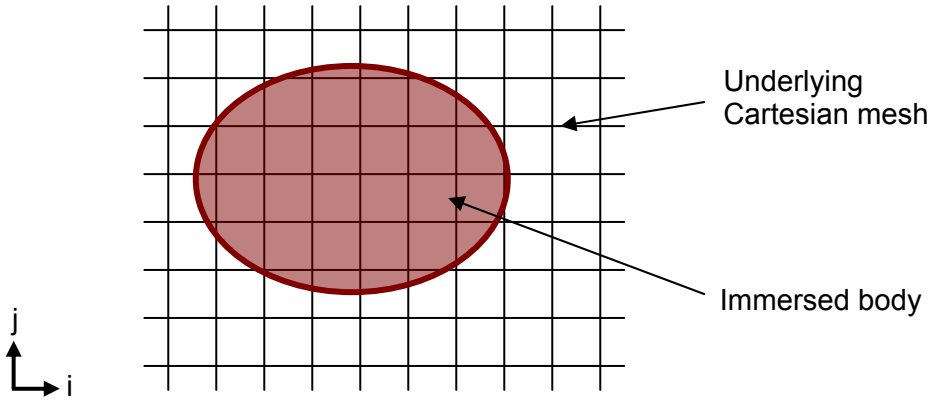

Figure 3-7: Two-dimensional schematic illustrating a body immersed into an underlying Cartesian rectangular background mesh

A Cartesian grid node n_g (*i,j*) will be internal to the body (*inner node*) if the number of intersections of any half-line (starting at node n_g and of random direction) with the immersed body surface is odd (Figure 3-8A). On the other hand, if the number of intersection is null or even (Figure 3-8B) then the Cartesian grid node n_g will be considered as external to the body (*outer node*). A first classification, separating *inner nodes* from *outer nodes*, is therefore performed based on the number of intersection points. It is important to note that even though such a procedure only holds in the case of closed bodies, it has the main advantage of not being dependent upon the resolution of the Cartesian mesh or the unstructured mesh.

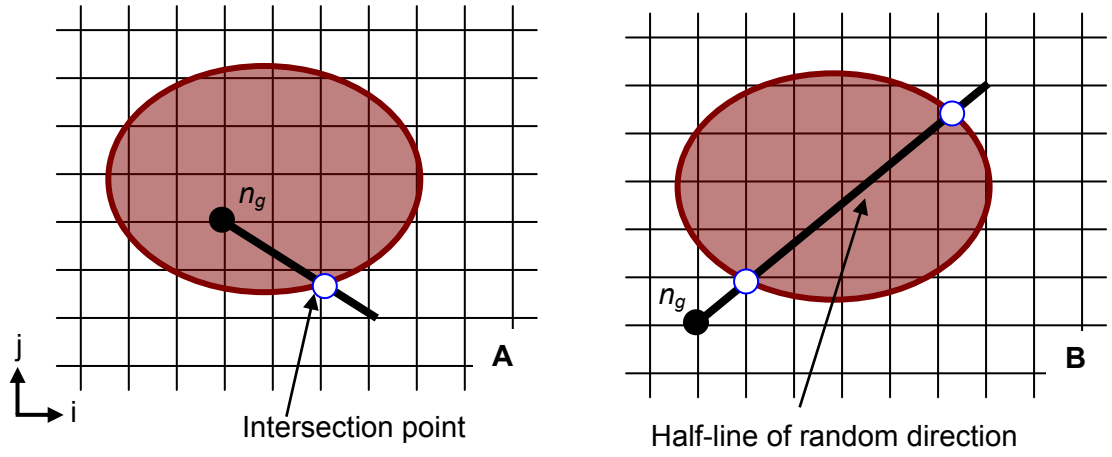

Figure 3-8: Two-dimensional schematic illustrating the search algorithm for sorting the nodes into *inner body* nodes (A) or *outer body* nodes (B). The node of interest n_g is shown with a filled black circle, while the intersections of the random half-line with the immersed body surface are shown with open circles

3.2.1.2 Special cases

To avoid erroneous classification of the Cartesian nodes and ensure the appropriate handling of the immersed body surfaces even in the case of complex geometries or colliding bodies, special conditions in the node classification algorithm have to be included:

Complex body shapes: In the case of complex body shapes such as concave bodies, a node lying outside of the body may be associated with an odd number of intersections and might be incorrectly classified as an *inner node* as the random direction half-line might intercept the edge of a body triangle or a body triangle vertex (Figure 3-9). Counting the number of intersection in such cases becomes problematic. A check is therefore performed to ensure that each intersection point belongs to only one triangular body element. If at least one of the intersection points of a particular half-line

with the immersed body can't be associated with a single triangle but instead to several, another half-line of random direction is selected.

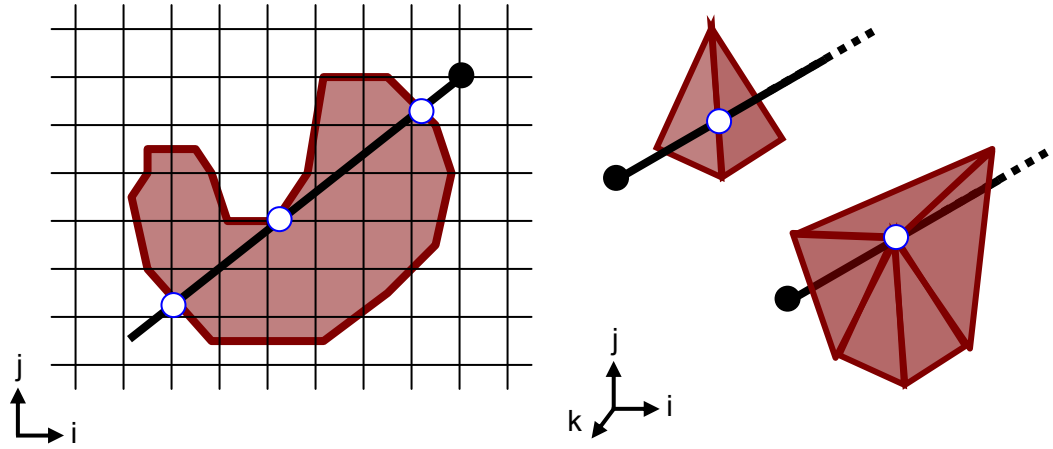

Figure 3-9: Left panel: Two-dimensional schematic showing the case of a concave body. Right panel: Three-dimensional schematic illustrating two singularity cases occurring when an intersection point lies on a triangle edge or vertex (for clarity the underlying Cartesian mesh is not shown). In both panels, the node of interest is shown with a filled black circle, while the intersections of the random half-line with the immersed body surface are shown with open circles

Random direction parallel to body surface: If the random direction is in the same plane as that defined by the considered body triangle, defining the number of intersection points is also challenging. Such a situation corresponds to the case where:

$$\left|\vec{N} \,.\, \vec{dir}\right| < \varepsilon \qquad \text{Equation 3-37}$$

with $\vec{N}$ the normal of the body triangle, $\vec{dir}$ a vector defining the random search direction, and $\varepsilon = 10^{-6}$. If for a specific half-line, such a case is encountered, another half line oriented along a new randomly-selected direction is used.

Adjacent bodies: Erroneous classification of the nodes might occur where the boundary surfaces of two immersed bodies are immediately adjacent, as illustrated in Figure 3-10. Appropriate classification of the node in this particular case is of prime importance in the simulation of the hinge region as the leaflet ear surface enters into contact with the hinge recess wall at some instances of the cardiac cycle. In Figure 3-10, two of the intersection points have the same coordinates and thus only one of them is counted. The node of interest n_g, denoted as a filled black circle, is thus associated with three intersection points (open circles) and classified as an *inner node* instead of *outer node*. To avoid such possible confusion, the normal of the body surfaces at the overlapping intersection points ($\overrightarrow{N_A}$ and $\overrightarrow{N_B}$ in Figure 3-10) are also taken into consideration.

If two intersection points have the same coordinates but the normal of the body at the intersection points are not the same then the two intersection points A and B are taken into account and summed. This can be summarized by the following "non-colinear normal" condition that is to be satisfied:

$$\overrightarrow{N_A} . \overrightarrow{N_B} < \mathbf{1} - \delta \qquad \text{Equation 3-38}$$

where δ was arbitrarily set to 0.03.

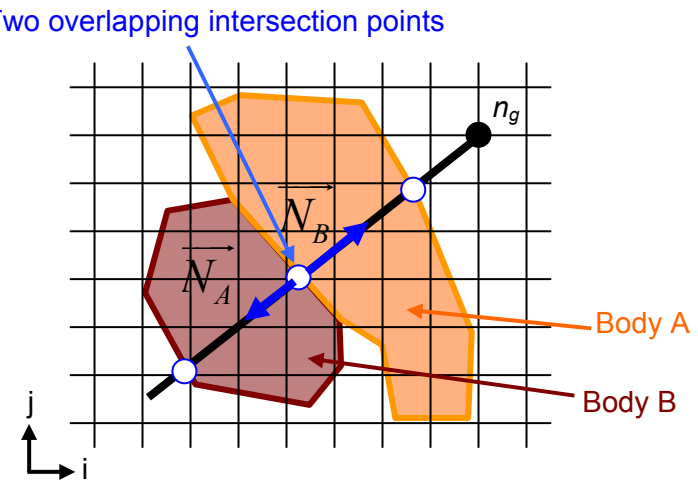

Figure 3-10: Two-dimensional schematic illustrating a singularity case occurring when two bodies have an adjacent boundary. The node of interest n_g is shown with a filled black circle, while the intersections of the random half-line with the immersed body surface are shown with open circles

3.2.1.3 Classification verification

Because of the complexity of the hinge geometry and the motion of the leaflet in the hinge recess, the classification is verified to ensure appropriate node sorting. At the end of the preliminary node classification, each node is associated with a real *nvert* whose value depends on the location of the node with respect to the body surface: if a node is outside of the body, *nvert* value is 0; otherwise it equals 3. To check that the node classification is correctly performed, the sorting is done twice and the results compared. If the node category (and thus the *nvert* value for a particular node) differs, a third sorting is performed and the node of interest is eventually sorted as follows:

If ($nvert_1 + nvert_2 + nvert_3 = 3$), then $nvert = 0$ (*outer node*).

If ($nvert_1 + nvert_2 + nvert_3 = 6$), then $nvert = 3$ (*inner node*).

where $nvert_i$ corresponds to the nvert value of the i^{th} sorting.

3.2.1.4 Final Classification

At this point, the Cartesian grid nodes are classified into two broad categories, nodes located inside or outside of the body (*inner vs. outer nodes)*. All *inner nodes* are then considered as *inner body nodes*, while the outer nodes are divided into either *fluid nodes* or *near-boundary* (*nb*) nodes. To appropriately apply the necessary boundary conditions at the wall of the immersed body, it is important to identify the nodes located in the fluid domain but also in the immediate vicinity of the body surface. These nodes, known as *near-boundary nodes*, can easily be found by considering the neighboring points of the *outer nodes*. Consider a node n(i,j,k) located outside of the body. If any of its immediate neighbor nodes ((i±1,j,k) or (i,j±+1,k) or (i,j, k±+1)) are classified as *inner body nodes*, the node *n*(*i,j,k*) is considered as a *near-boundary node*.

The final classification of the nodes therefore contains three categories, each associated with a different $nvert$ value: the *near-boundary (nb)* nodes (*nvert*=1), the inner *fluid* nodes (*nvert*=0) and the *body* nodes (*nvert*=3) as shown in Figure 3-11. The overall methodology used to classify the nodes of the Cartesian mesh is provided in Appendix A.2.

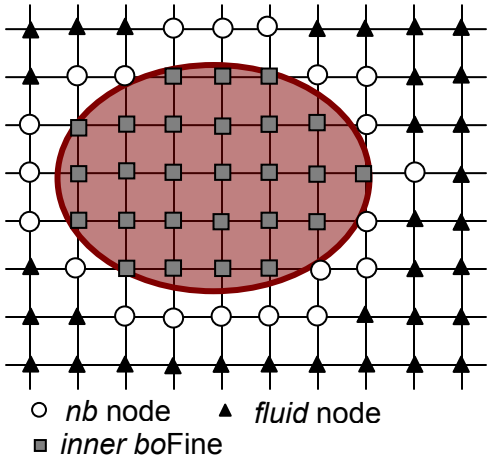

Figure 3-11: Classification of the Cartesian nodes in three categories

Performing a node classification at every time step is costly. The node classification is therefore divided into two main steps so as to minimize computational time. At the first time step, the entire Cartesian grid is considered and all Cartesian nodes are classified based upon their location with respect to the immersed body surfaces. At all following time steps, however, the classification is limited to the nodes in the immediate vicinity of the moving leaflet. All nodes that are far from the leaflet and thus whose classification will not be changed keep the node category allocated at the first time step. Therefore it is only at the first iteration that several million grid nodes are analyzed. At all other iterations, the search is limited to a few thousand nodes.

3.2.2 Velocity Reconstruction

Once all Cartesian nodes have been classified, the governing equations are solved at all *fluid* nodes with all *inner body* nodes excluded from the computational domain. Given the solution at all *fluid* nodes, advancing the velocity and pressure field at the next time step *r*equires specifying the boundary conditions at all *near-boundary nb* nodes.

The immersed boundaries are tracked as sharp interfaces and no-slip boundary conditions for the velocity field are applied at all vertices of the unstructured triangular mesh. Velocities are reconstructed by interpolation between the closest body triangular element and fluid Cartesian cell, along the normal to the closest body mesh element. According to the notation shown in Figure 3-12, the boundary conditions at the *near-boundary nb* node *G* associated with the m^{th} triangular body element are defined as follows. Let $f_{k,m}^{n+1}$ denote one of the three velocity components of the k^{th} vertex of the m^{th} triangular interface element at the time step *n+1*. Since the normal $\overrightarrow{N}_m^{n+1}$ of the m^{th}

element is known, the line that passes through node *G* and is parallel to the normal $\overrightarrow{N}_m^{n+1}$ can be constructed. This line intersects the surface triangular element *m* at point *F* and the Cartesian grid element (defined by the nodes $\alpha,\beta,\chi,$ and δ) at point *H*.

Since the velocity component $f_{k,m}^{n+1}$ is known at all vertices of the m^{th} surface element, the velocity components at point *F*, f_F^{n+1}, can be computed by linear interpolation among the vertices of the m^{th} triangular surface element as follows. Consider the triangle *m* defined by its three vertices m_1, m_2, and m_3 (Figure 3-12). Three coefficients Cr_1, Cr_2, and Cr_3 can be defined as:

$$Cr_1 = \left(\overrightarrow{m_3m_2} \times \overrightarrow{m_3F}\right) / A_{Tot} \qquad \text{Equation 3-39}$$

$$Cr_2 = \left(\overrightarrow{m_3m_1} \times \overrightarrow{m_3F}\right) / A_{Tot} \qquad \text{Equation 3-40}$$

$$Cr_3 = 1 - Cr_2 - Cr_1 \qquad \text{Equation 3-41}$$

with $A_{Tot} = \overrightarrow{m_3m_1} \times \overrightarrow{m_3m_2}$.

The velocity components at point F then read as:

$$f_F^{n+1} = \sum_{k=1,3} f_{k,m}^{n+1}.Cr_k \qquad \text{Equation 3-42}$$

where *k* corresponds to one of the three vertices of the m^{th} triangular element within which point *F* lies and Cr_k are the coefficients previously described.

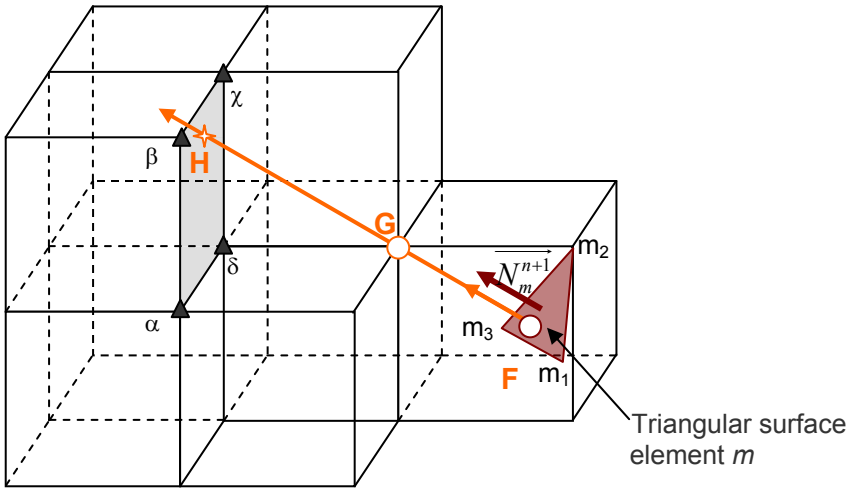

Figure 3-12: Three-dimensional schematic of the velocity reconstruction at a near-boundary node by interpolating along the normal to the surface of the body. The near-boundary node is represented by the node G. The point H corresponds to the intersection of the normal with the Cartesian grid. The triangle is a typical element of the unstructured mesh used to discretize the immersed body.

A similar interpolation procedure is employed to obtain the velocity components of point *H* at the physical time *n+1*. Point H, which belongs to a rectangular element defined by the nodes $\alpha,\beta,\chi,$ and $\delta,$ lies in a triangle defined by three of these four nodes. The coefficients Cr_i (with i=1,2,3) are calculated using Equations 3-39 thru 3-41 and the velocity at point H is obtained by interpolating between the three appropriate Cartesian grid nodes α,β,χ,δ where the solution is known at time step *n*.

Assuming that the velocity components vary in a quadratic manner along the line joining *H* and *F,* the velocity components at the *near-boundary nb* node *G*, $f_G^{n+1,\ell+1}$ can be computed by interpolation between the known velocity components at point *H* and point *F*:

$$f_G^{n+1} = \frac{f_H^{n+1}.d_{GF} + f_F^{n+1}\,d_{GH}}{d_{GF} + d_{GH}} \qquad \text{Equation 3-43}$$

where d_{il} is the distance between the points *i* and *l*.

The overall accuracy of the resulting solver, with the above reconstruction algorithm, has been shown to be second-order in space [66].

3.3 Final remarks on the numerical solver

The numerical solver, which comprises a hybrid staggered/non-staggered flow solver coupled with a sharp interface immersed boundary approach, is fully parallelized and written in C. The solver is implemented using Petsc libraries [67, 69]. Petsc is a suite of data structures and routines for the parallel solution of scientific applications modeled by partial differential equations. It employs the Message Passing Interface (MPI) standard for all message-passing communication and includes support for parallel vectors, parallel matrices but also Krylov subspace approaches and parallel Newton-based nonlinear solvers.

The overall structure of the flow solver is provided in Appendix A.1. Details on the different setting parameters, such as convergence criteria or maximum number of iterations, are provided in Appendix A.5.

3.4 Numerical geometry and boundary conditions

3.4.1 Hinge recess and leaflet geometries

The exact designs of the hinge recess and leaflet ear were not known *a priori* and therefore micro-Computed Tomography (μCT) was used to obtain three-dimensional geometric information. Computed tomography imaging is a radiographic method that permits the non-destructive characterization of the internal structure of materials. A high speed, high resolution *in vivo* microCT scanner with a cone-beam geometry, VivaCT40 (Scanco USA, Inc, Southeastern, PA), was used to scan the hinge region of the valve of

interest. The radiation source was a microfocus X-ray source with a peak X-ray energy of 50 to 70 kVp and a spot size of 5 μm. Cross-sectional images of the hinge region were produced by scanning transverse slices from different angular positions while the radiation source and detectors rotated 360^{o} around the prosthetic valve.

The hinge regions of clinical bileaflet mechanical heart valves were scanned using μCT and the resulting scans, after being post-processed in Geomagics (see Appendices C.1 and C.2 for a detailed description of the Geomagics protocol) , were imported into ProE (Pro|Engineer Wildfire 3.0 M020) as IGES files so as to generate the overall numerical model described in section 3.4.2. The following sections provide details on the hinge and leaflet geometries used in this thesis. Appendix B.4 gives the detailed dimensions of the hinge geometries.

3.4.1.1 Geometry of the hinge recess

The hinge region of a clear housing 23 mm St. Jude Medical (SJM) Regent valve was scanned at a resolution of 18 μm (Figure 3-13A). Geomagics (Geomagics Studio 10 SR2) was used to clean-up the scan, extract the hinge recess and eliminate any unnecessary information, such as the leaflet geometry. However, as can be seen in Figure 3-13B, some data was lost within the hinge recess itself due to the radio-opaque leaflet material. Therefore, the missing section of the hinge geometry had to be reconstructed based on the available surrounding information. This was performed using the tools readily available in Geomagics, such as mirroring and surface merging. Once reconstructed, the hinge recess surface was smoothened using Geomagics. The final surface of the SJM hinge recess is shown in Figure 3-13C.

The hinge region of a clinical CarboMedics (CM) valve was scanned using μCT. However, because of the poor resolution of the scan due to the radio-opaque properties

of the valve housing, a second scan was performed, at a resolution of 18 μm, on a clear-housing 23 mm CM clinical valve replica. In this valve, contrary to the SJM clear-housing valve, the leaflets could be taken out of the housing. As a result, no loss of data was observed and the μCT scan of this valve provided good quality images of the whole hinge recess. As done with the SJM hinge recess, Geomagics software was used to clean-up the scan, extract the hinge recess, and smoothen the hinge recess surface.

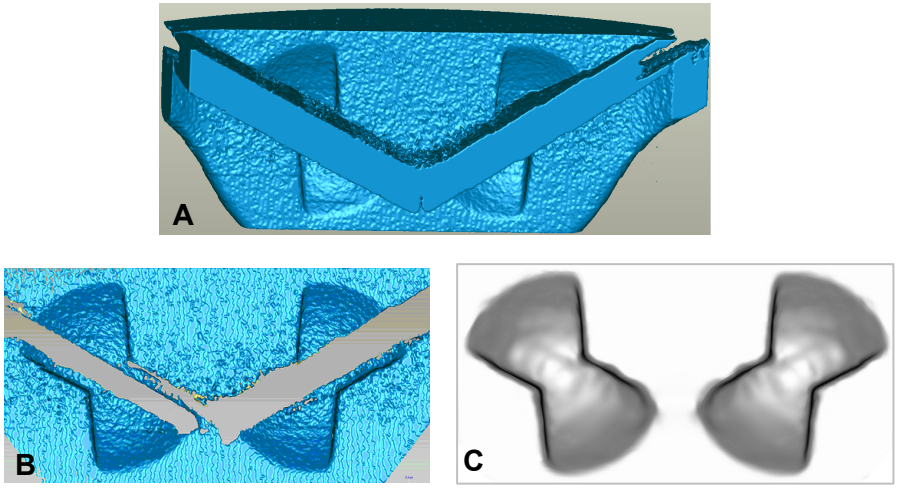

Figure 3-13: Reconstruction of the hinge recess of a 23 mm SJM Regent valve scanned with 18 μm resolution. A: Original micro Computed Tomography scan, B: Hinge region extracted from the original scan. Loss of data is clearly visible and can be attributed to the presence of the valve leaflets. C: Reconstructed hinge recess.

3.4.1.2 Geometry of the leaflet ear

For the present study, not only is the hinge surface important but also the leaflet ear geometry. However, Figure 3-13 clearly shows that obtaining the leaflet ear geometry bileaflet valve from μCT scan is challenging due to the material property of the

leaflet. In order to minimize interferences and optimize data acquisition, the leaflet geometry, without the valve housing, was scanned.

For the SJM valve, the leaflet ear of a broken 17 mm SJM Standard pediatric valve was scanned at a resolution of 15 μm. The leaflet and hinge recess geometries are similar across valve sizes but their dimensions vary. For instance, the dimensions of the hinge region is identical for the 23 mm, 25 mm and 27 mm valves but those of the pediatric 17 mm valve are smaller. The scanned pediatric leaflet was therefore scaled-up, based on the relative dimensions of the hinge, to obtain a leaflet ear whose dimensions correspond to that of an adult valve size**.**

As for the CM valve, the leaflets could be taken out of the clear housing valve and thus be placed in the scanner without the valve housing. The leaflet of the 23 mm clear housing CM valve was scanned at a resolution of 21 μm.

As done with the hinge recesses, the tools available in Geomagics software were used to clean-up the scans, extract the leaflet ear geometry and smoothen the surface.

3.4.2 Numerical model

This thesis focuses on the flow through the hinge region of BMHVs. Obtaining accurate and relevant flow results requires imposing realistic boundary conditions at the fluid domain edges. These boundary conditions were obtained from large-scale simulations of the bulk of the flow through a SJM BMHV placed under aortic physiologic flow conditions (see section 3.4.4 for more details). To allow this one-way coupling between the large-scale solver and the hinge flow solver, particular care regarding the numerical valve and hinge models had to be taken.

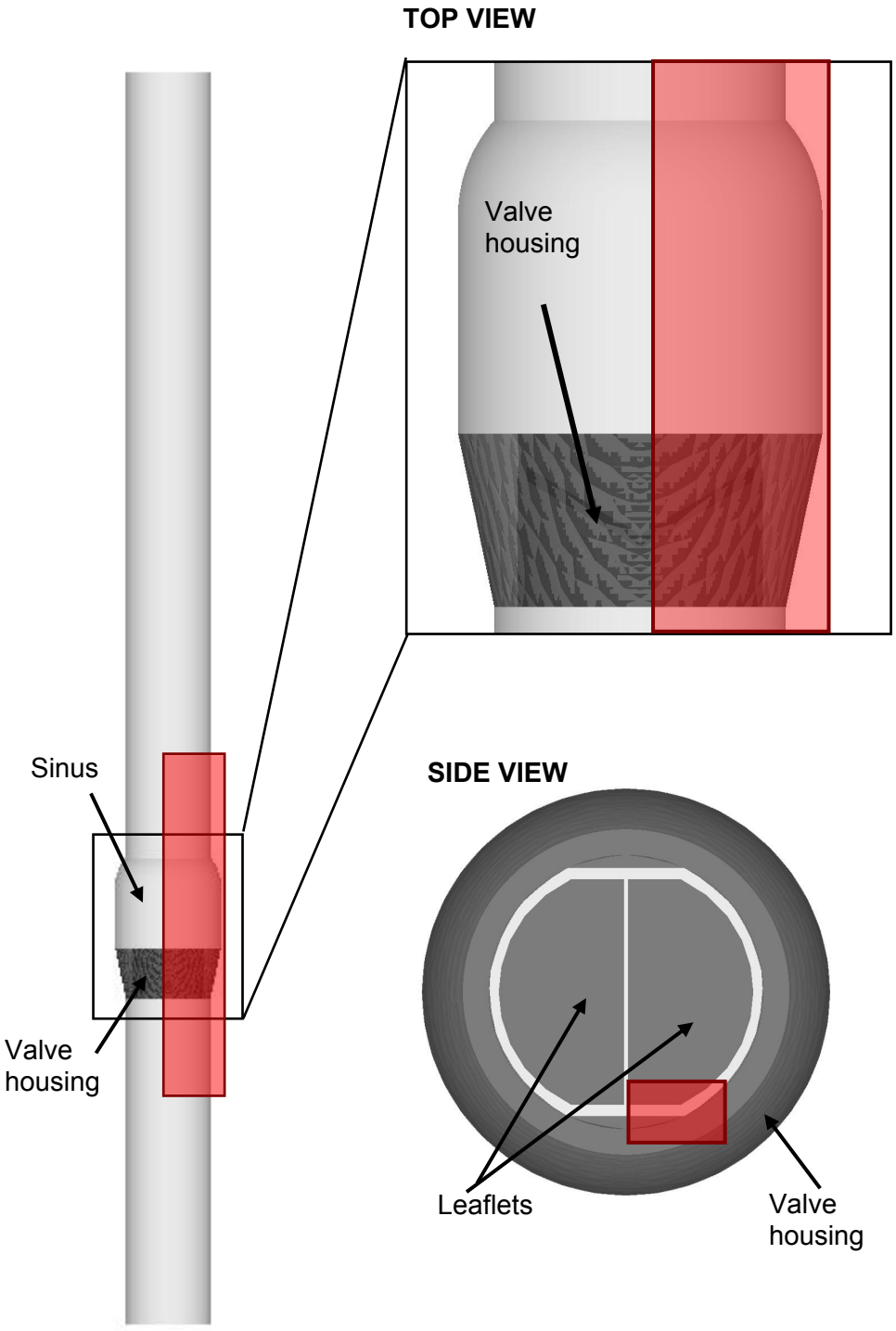

Figure 3-14: Large-scale numerical model. A bileaflet valve model is inserted into a simplified aorta consisting of a straight tube with an axisymmetric expansion representing the sinus region. The left column shows the overall geometry while the right column focuses on the valve and sinus region. The red area corresponds to the region modeled in the hinge simulations.

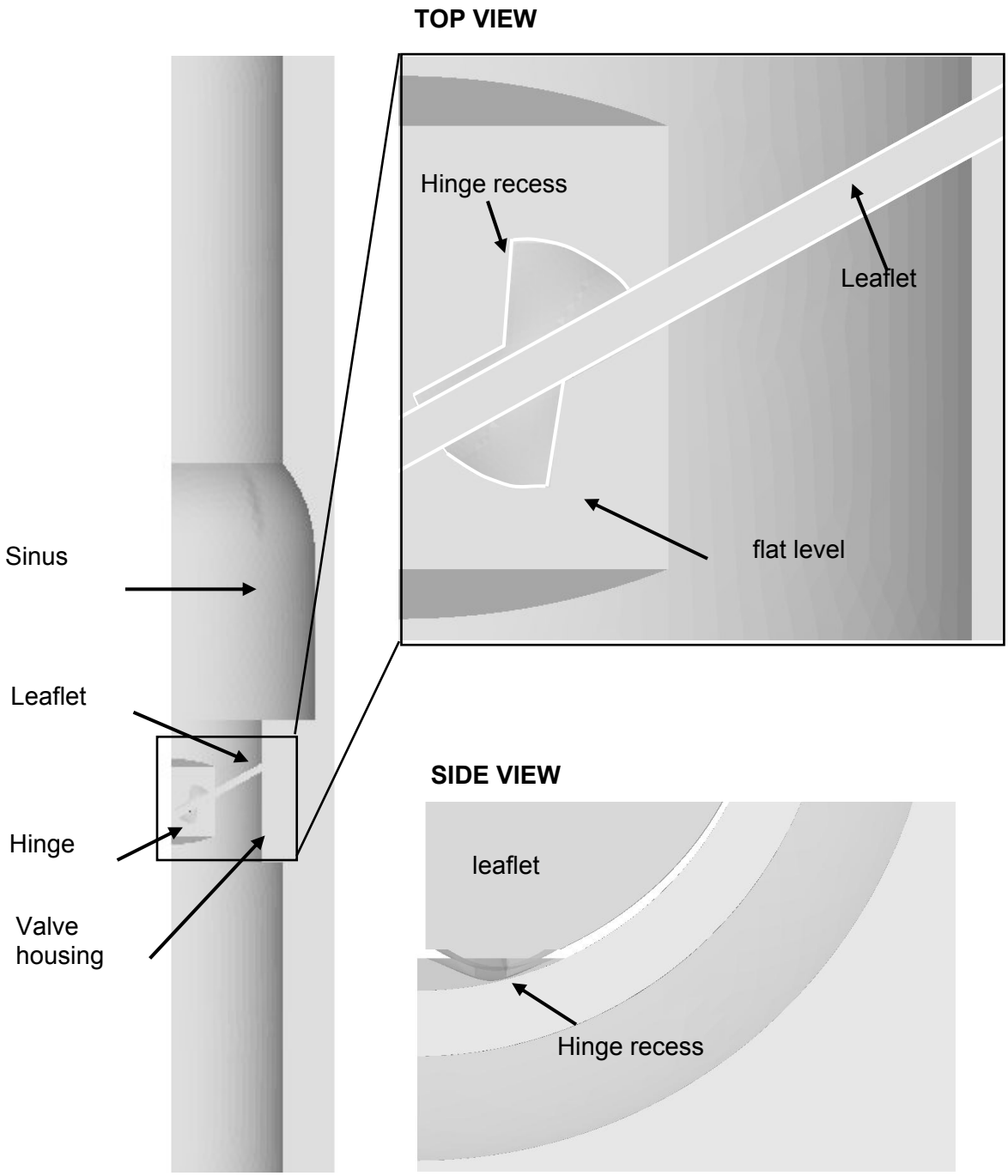

Figure 3-15: Hinge numerical model

In the large-scale simulation, a BMHV model was inserted into a simplified aorta model consisting of a straight tube with an axisymmetric expansion representing the sinus region (Figure 3-14). In the hinge simulation, the hinge domain was set so as to correspond to a section of the large-scale domain, as shown in Figure 3-14 where the area shaded in red corresponds to the hinge domain. Figure 3-15 shows the final hinge model, where the hinge recess, characterized by its butterfly shape, is clearly visible. Dimensions of both the large-scale and hinge models are provided in Appendices B.1 and B.2. Only one of the four hinges was modeled and thus the model corresponds to only a section of the large-scale geometry model. Identical valve housing/aorta geometry was used throughout all hinge simulations, but the hinge recess was selectively modified to include the hinge recess of interest (either SJM or CM design). The leaflet ear was positioned within the hinge recess such that the hinge gap width (defined as the distance between the bottom of the hinge recess and the tip of the leaflet ear, as shown in

Figure 3-16 was set to the desired value (150 or 250 μm). Details on the three hinge configurations investigated in this study are given in Appendix B.3. The model geometry was generated with Pro|Engineer (Pro|Engineer Wildfire 3.0 M020) and meshed, using triangular elements, in Gambit (Gambit 2.4.6, Fluent Inc) software. (See Appendix B.4 for a schematic illustrating the overall approach to generate the numerical meshes).

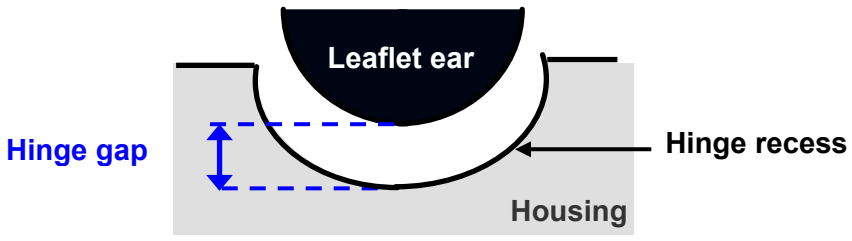

Figure 3-16 : Cross-sectional close-up view of the hinge region. The hinge gap width is defined as the distance between the tip of the leaflet ear and the bottom of the hinge recess

3.4.3 Fluid domain

The geometry of the valve chamber, housing and leaflet was immersed into a fluid domain composed of a non-uniform Cartesian grid of approximately 6 million grid nodes. Identical mesh was used to discretize the fluid domain in all simulations (Figure 3-18). The fluid domain was first generated using ProE (Pro|Engineer Wildfire 3.0 M020) and was subsequently meshed using Gridgen (Gridgen 15.11 release 1, Pointwise Inc). The Cartesian grid was discretized with 217 nodes along the x-direction (leaflet axis), 133 nodes along the y-direction and 205 along the z-direction (main flow direction). The fluid grid was stretched so as to optimize the grid refinement within the hinge and resolve all details of the hinge structure. If the local grid stretching ratio r_i (Figure 3-17) is defined as:

$$r_i = \left(x_i - x_{i-1}\right) / \left(x_{i+1} - x_i\right) = \Delta x_i / \Delta x_{i+1} \qquad \text{Equation 3-44}$$

the range of stretching ratios used in the x-, y- and z-direction are [0.88;1.09], [1.00;1.09] and [8.87;1.13], respectively. Figure 3-19 shows the mesh resolution in the hinge region for the SJM hinge geometry set with a 150 μm hinge gap width.

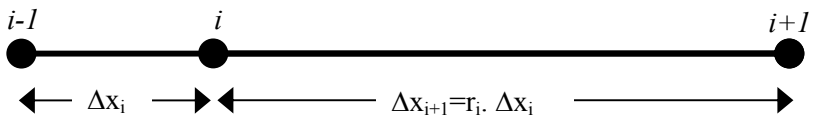

Figure 3-17: Definition of the grid stretching ratio r of a non uniform grid layout

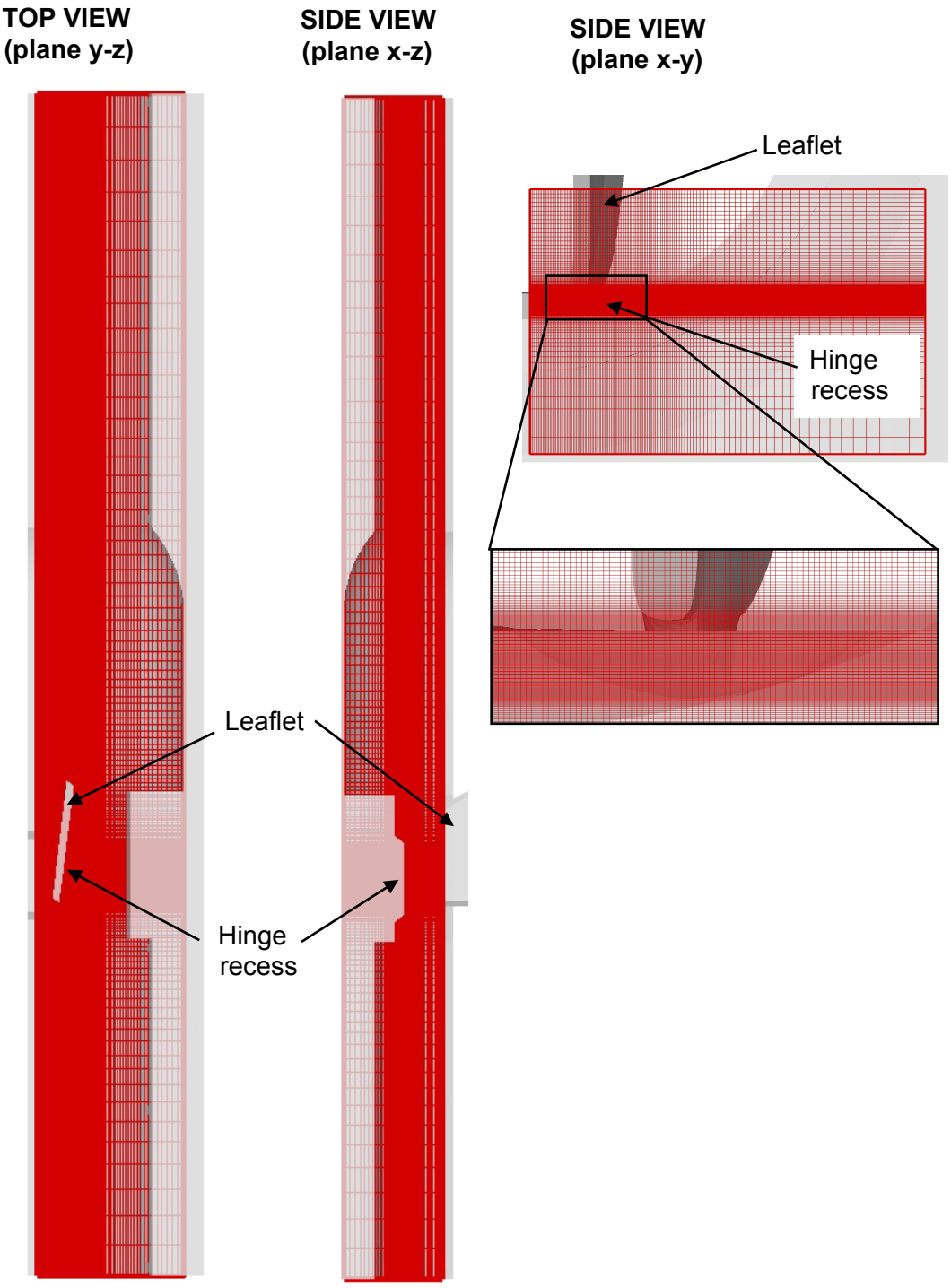

Figure 3-18 : Non-uniform Cartesian fluid mesh

TOP VIEW (Flat Level)

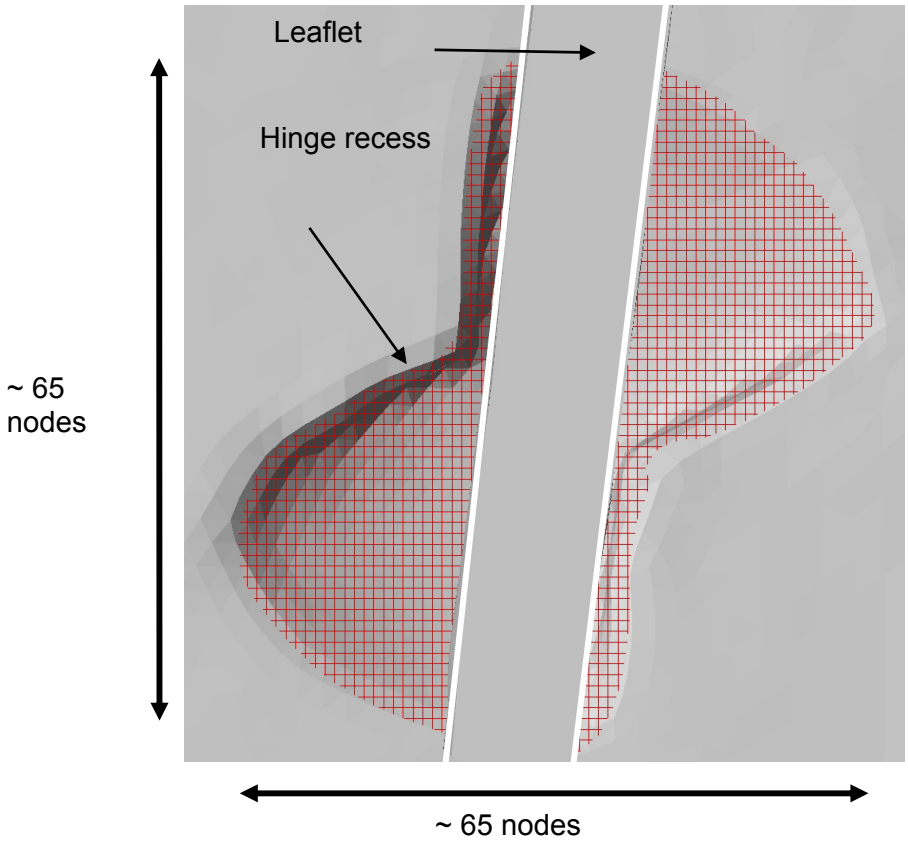

SIDE VIEW (hinge center plane)

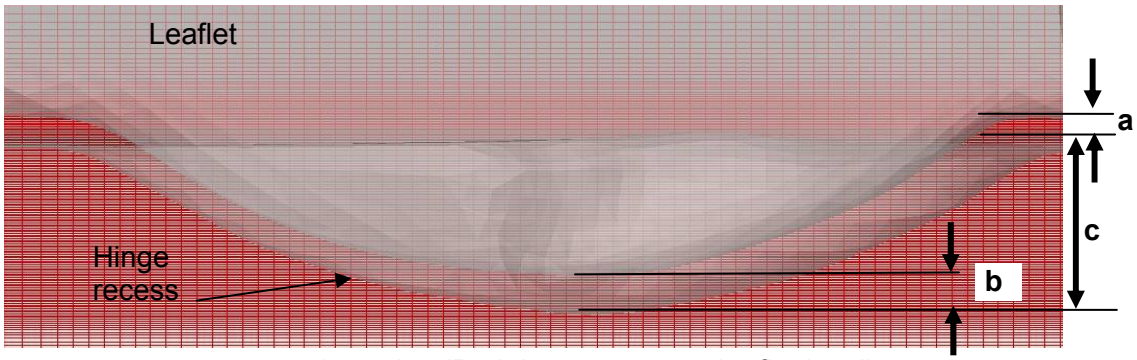

a: ~ 15 nodes (Periphery gap near the flat level)

b: ~ 25 nodes (Hinge gap width)

c: ~ 95 nodes (Hinge recess)

Figure 3-19 : Mesh refinement in the hinge recess. The hinge shown here is the SJM hinge recess with a regular hinge gap width of 150 μm.

3.4.4 Flow and boundary conditions

This thesis focuses on the BMHV hinge region and requires realistic boundary conditions to be applied at the fluid domain boundaries. As previously mentioned in section 3.4.2, these boundary conditions were obtained from the large-scale simulations of the bulk of the flow through a SJM BMHV placed under aortic physiologic flow conditions, where the leaflet motion was computed using a Fluid-Structure Interaction (FSI) model [61]. It should be pointed out that the large-scale computations did not model the details of the hinge geometry and the damping due to the friction of the hinge was neglected. Nonetheless, the computed FSI leaflet motion was found to be in good agreement with experimental data throughout the cardiac cycle. There also was an excellent match between the flow fields computed and experimentally measured downstream of the valve [61] during the forward flow phase. The velocity fields and the leaflet position calculated using the large-scale CFD-FSI solver were therefore deemed suitable to be used as boundary conditions of the refined numerical hinge flow solver during systole. During this phase, velocity profiles were therefore extracted from the large-scale simulation and used as boundary flow condition for the ventricular plane of the hinge domain (see Figure 3-20 for the different planes defining the boundaries of the fluid domain). During diastole on the other hand, a plug flow profile was imposed on the aortic plane of the domain to ensure a physiologic pressure gradient across the closed valve. Zero-flux was enforced across the top and b-datum planes while zero-velocity conditions were applied at the bottom and housing planes. The flow at the outlet plane of the domain (the aortic/ventricular planes during systole/diastole, respectively) was scaled to ensure mass conservation throughout the domain. More details on these boundary conditions are provided below.

3.4.4.1 Inlet Boundary conditions

Forward Flow Phase:

As previously stated, in order to impose realistic boundary conditions at the edge of the hinge fluid domain, a one-way coupling was performed between the large- and micro-scale models by using the computed large-scale velocity profile as boundary conditions for the micro-scale model during the forward flow phase. More details on the treatment of the boundary conditions during the leakage flow phase are given in the next section.

The large-scale simulations were run with the following normal aortic physiologic flow conditions: peak flow rate of approximately 25 L/min, systolic duration of one third of the cardiac cycle, a cardiac cycle of 860 ms, and a heart rate of 70 beats/min. Figure 3-21 shows the valvular flow rate and leaflet position as a function of time. Using the valve diameter (25.4 mm) and the peak systolic flow rate (24.27 L/min), the Reynolds number was 6,000. Because of the coupling of the large-scale model with the small scale simulations, similar flow conditions are imposed on the hinge model. It should be noted that the characteristic velocity and length used to non-dimensionalize the governing equations in the hinge simulations were the same as those of the large-scale dimensions: the peak valvular systolic velocity (0.80 m/s) and the valve diameter (25.4 mm), respectively. The peak valvular systolic velocity is based on the peak valvular flow rate (24.27 L/min) imposed in the large-scale simulations.

The large-scale velocity components computed along the plane corresponding to the ventricular plane of the hinge model were used as inlet boundary conditions for the hinge solver during the forward flow phase. Figure 3-22 shows the relative position of the large-scale model (valve model shown in red) with the hinge model (in grey). Also shown is a cross-sectional view of the large-scale and hinge grids at the inlet plane of the hinge

model. Because of the difference in grid resolution between the large-scale body-fitted grid and the hinge Cartesian grid, the velocity profile computed on the large-scale grid were interpolated onto the highly refined hinge fluid grid using linear interpolation. Figure 3-23 shows the profiles of all three velocity components along a selected line on the ventricular plane of the hinge model for both the large-scale and hinge models at three instances of systole. It should be noted that while the large-scale simulations were conducted using a body-fitted curvilinear grid, the hinge computations were carried out using a non-uniform Cartesian grid. As a result not all grid nodes at the inlet ventricular plane of the hinge domain fall within the fluid domain. Velocities at these non-fluid inlet nodes were set to zero.

In the large-scale simulations, the cardiac cycle was discretized into 2,500 time steps. At each of these time steps, the flow profiles along the plane corresponding to the ventricular plane of the hinge domain were extracted and interpolated onto the fine mesh of the hinge domain. However, because the hinge simulations were run with more time steps (up to 40,000 during peak systole and down to 10,000 during the rest of systole), linear interpolation was subsequently performed between time steps to compute the velocity profiles at the intermediate time steps. The temporally and spatially interpolated velocity components were used as velocity boundary conditions at the ventricular plane throughout the forward flow phase of the cardiac cycle.

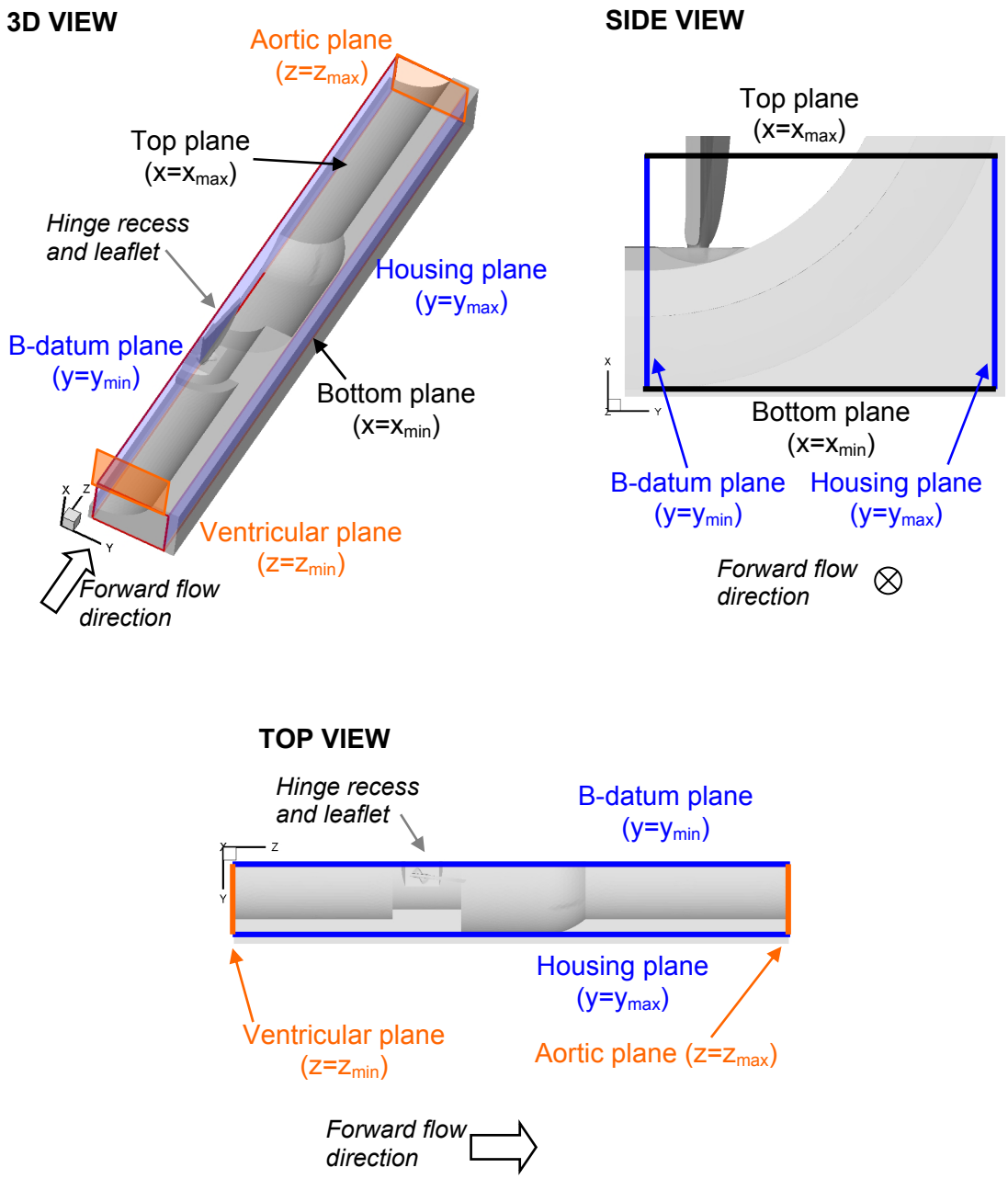

Figure 3-20: The hinge domain and its boundary planes

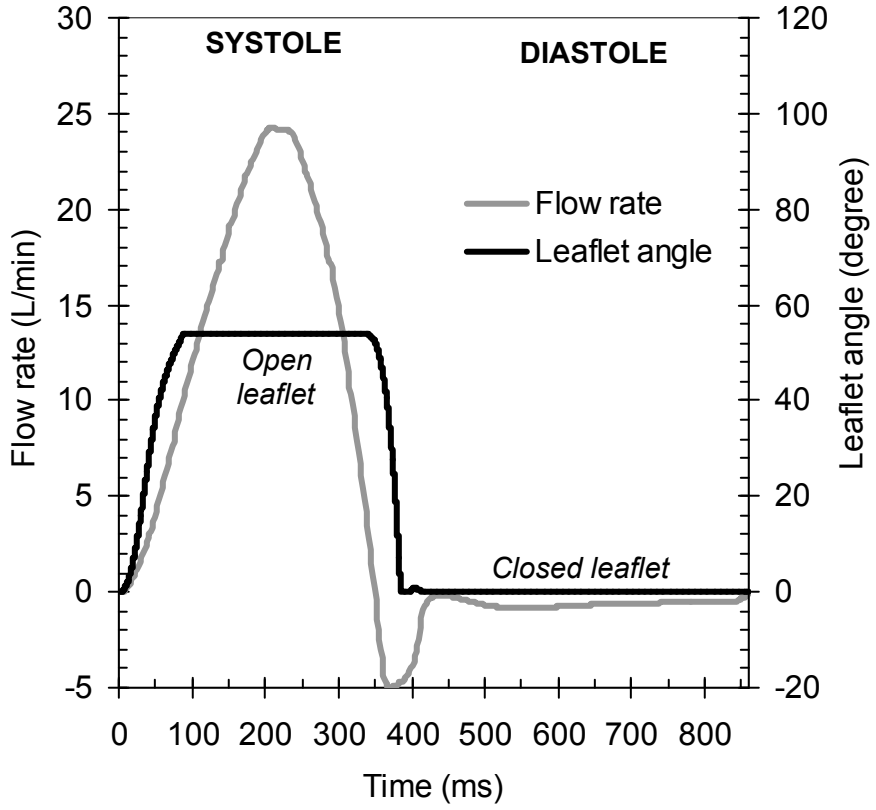

Figure 3-21: Temporal variation of the cross-valvular flow rate and the leaflet position in the large-scale numerical simulations [61]

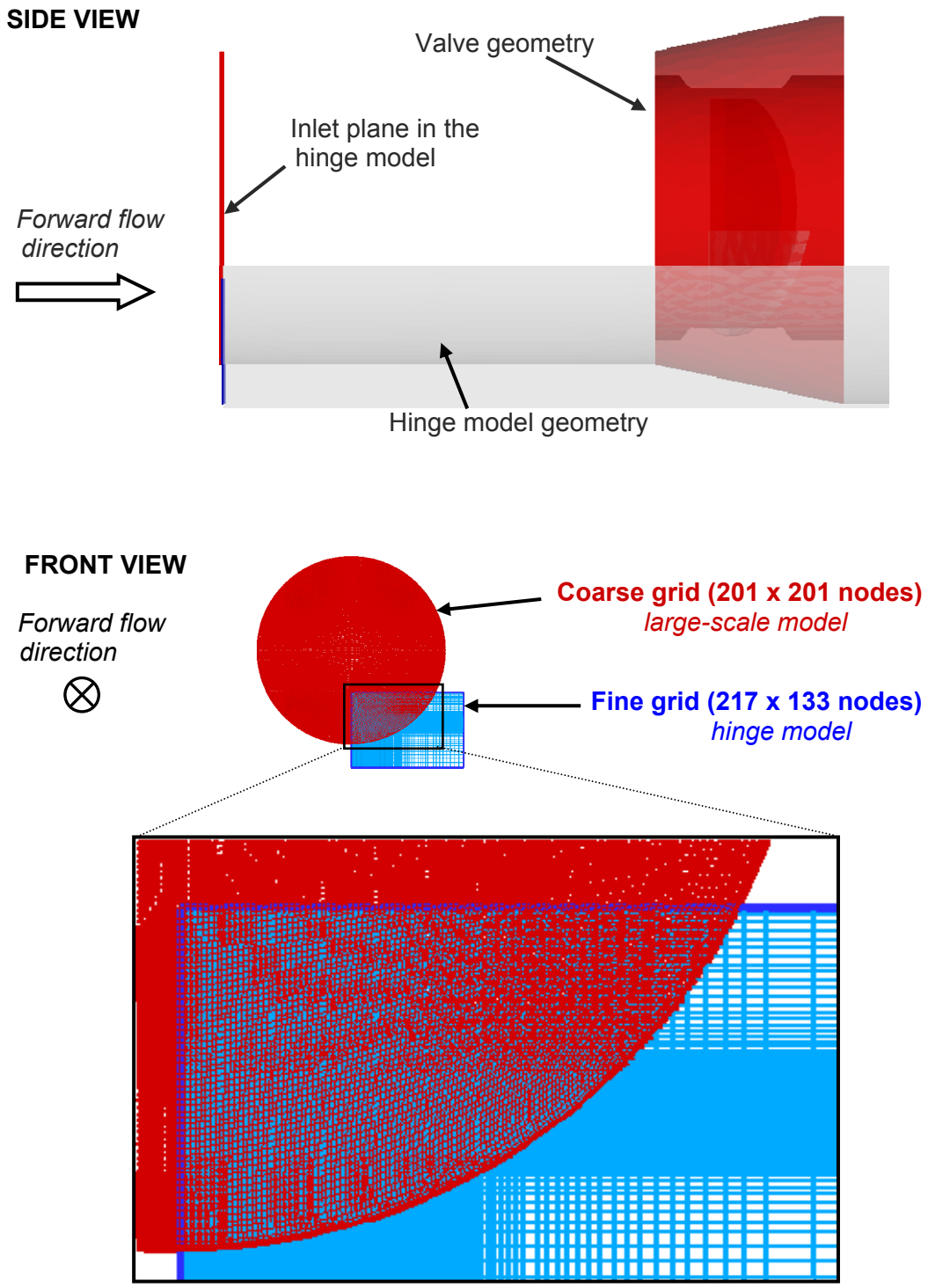

Figure 3-22: Relative position of the large-scale and hinge models. The top panel shows the side view of the hinge model (its geometry being shown in grey), with the position of the inlet plane, along with the large-scale valve (geometry shown in red). The bottom panel shows a cross-sectional view of the large-scale and hinge computational grids at the inlet plane of the hinge model. The number of grid nodes on the plane displayed is included for each model.

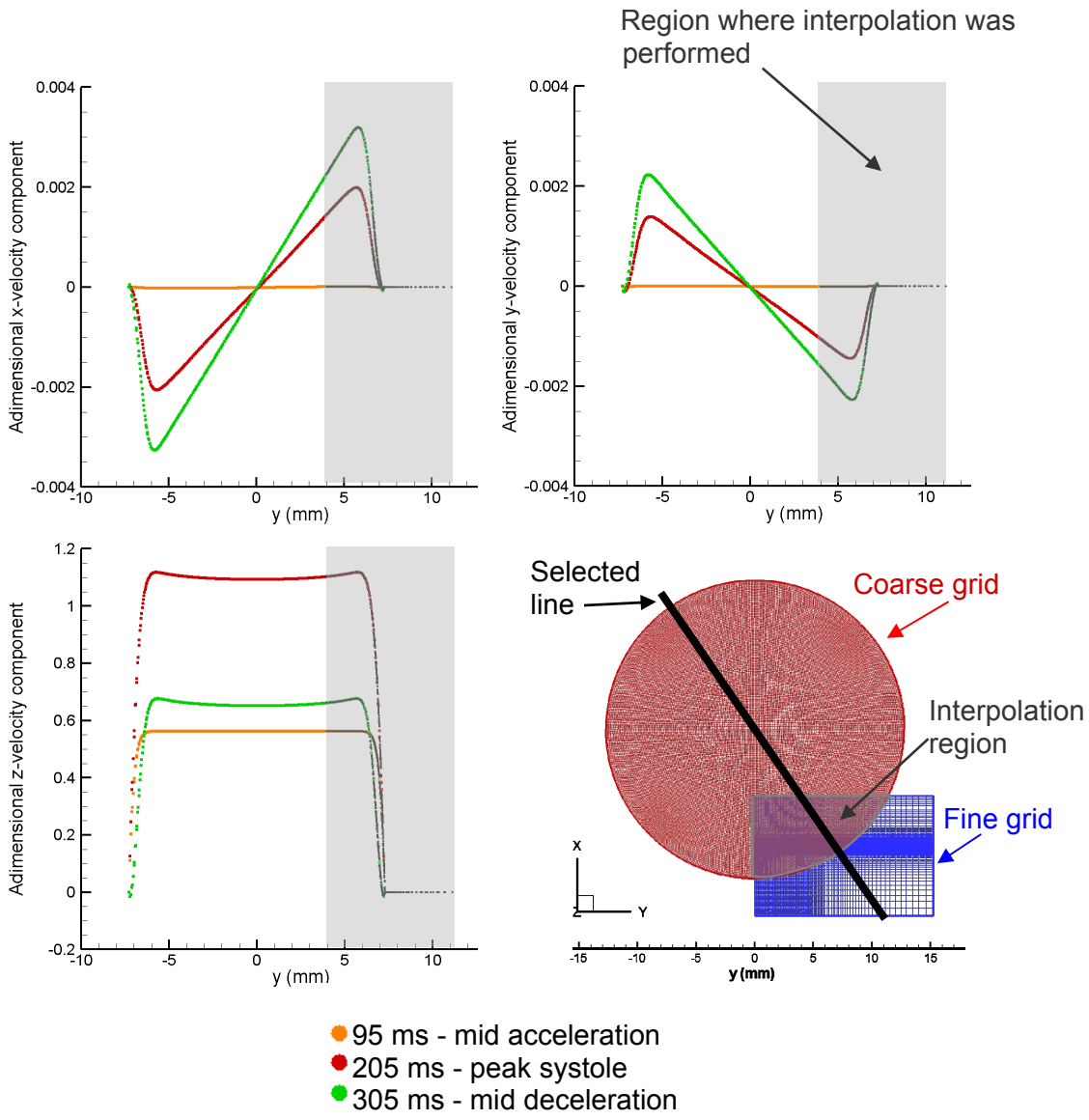

Figure 3-23: Profiles of velocity components along a selected line on the hinge model inlet plane (as shown in the bottom right panel) for both the large-scale (color) and hinge models (black). All three velocity components are plotted as a function of y (mm) at three instances of the cardiac cycle.

Leakage Flow Phase:

While the large-scale FSI simulations provided the boundary conditions for the hinge model during the forward flow phase, such a methodology couldn't be applied during the leakage flow phase. During this phase, because of resolution and size limitations of the large-scale computational grid, the gap formed between the closed leaflets and the valve housing was increased (Figure 3-24). The distance between the leaflet edge and the flat housing in the large-scale simulation was consequently approximately 900 μm while it is generally about 150 μm in clinical valves. The over-sized gap is likely to create unrealistic leakage flow rate and cross-valvular pressure gradient during diastole. The velocity profiles computed during the leakage flow phase by the large-scale model thus couldn't be directly used as boundary conditions for the hinge simulations.

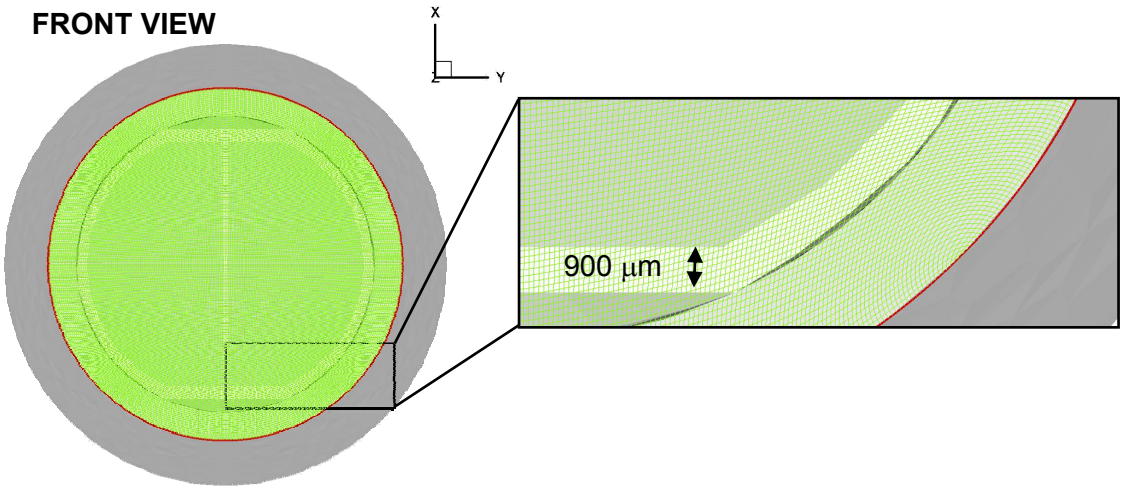

Figure 3-24: Resolution of the large-scale computational grid in the near-hinge region. The computational grid is shown in green, while the leaflets and valve housing are shaded in grey.

Starting at the instance of time when the valvular flow rate is zero at the end of systole (t=344 ms as shown in Figure 3-21), a plug flow profile was applied at the aortic plane of the hinge domain. The magnitude of this plug flow was linearly increased from 0 at the time of zero-flow-rate to a maximum value of V^p_{max} at the instance of valve closure (t=384 ms as shown in Figure 3-21). After valve closure and throughout diastole, the magnitude of the plug flow was kept constant at V^p_{max}. The value of V^p_{max} was set so as to reach a physiologic pressure gradient of 80 mmHg across the closed valve at mid-diastole. A series of steady leakage simulations was performed with the leaflet in the closed position and a steady leakage plug flow profile imposed at the aortic plane of the domain. The magnitude of the plug flow was varied until a cross-valvular pressure gradient of 80 mmHg was reached at convergence. This value of the plug flow magnitude was then used as V^p_{max} in the pulsatile simulations. For the SJM hinge design, this value was -0.11 m/s and -0.16 m/s for the normal hinge gap width and the larger-than-normal hinge gap width cases, respectively, while for the CM hinge design, V^p_{max} equaled -0.11 m/s.

3.4.4.2 Outlet Boundary conditions

The numerical model was set such that the flow entered and exited the domain only through the ventricular and aortic planes. During systole, the inlet plane located upstream of the open valve was the ventricular plane while the outlet plane was the aortic plane. During diastole, the inlet and outlet planes were reversed, the aortic plane being the inlet and the ventricular plane the outlet.

Assuming that the outlet plane is located at k_{max}, the velocity components at this plane were obtained from the velocity components at the plane immediately upstream of it (k_{max-1}) as follow:

$$u_{[k\max,j,i]} = u_{[k\max-1,j,i]} \quad \text{Equation 3-45}$$

$$v_{[k\max,j,i]} = v_{[k\max-1,j,i]} \quad \text{Equation 3-46}$$

$$w_{[k\max,j,i]} = w_{[k\max-1,j,i]} \quad \text{Equation 3-47}$$

where (i,j,k_{max}) are the indices of the point of interest located on the outlet plane k_{max}, (i,j,k_{max-1}) are the indices of the same point on the plane k_{max-1} and u,v,w represent each of the three-velocity components.

However, in order to ensure mass conversation throughout the domain, the axial velocity component at the outlet plane had to be scaled such that the inlet flow rate (Q_{in}) evaluated at the inlet plane (k_{min}) was equal to the outlet flow rate (Q_{out}) at the outlet plane (k_{max}). Assuming that the velocity component w lying along the z-axis is the axial velocity, the axial velocities at the outlet plane were then obtained based on the difference between these two flow rates with:

$$w^{out}_{[i,j,k_{\max}]} = w^{out}_{[i,j,k_{\max-1}]} + \Delta w = w^{out}_{[i,j,j,k_{\max-1}]} + \frac{Q_{out} - Q_{in}}{A_{out}} \quad \text{Equation 3-48}$$

where A_{out} is the area offered to the flow at the outlet plane.

This scaling approach guaranteed mass conservation in the numerical model throughout the simulations and was applied at the outlet plane of the domain, the aortic plane during systole and the ventricular plane during diastole.

3.4.4.3 Remaining Boundary conditions

Zero-flux conditions were enforced across the top plane as well as the b-datum plane (j_{min} and j_{max} planes). For instance, the velocity boundary conditions on the plane j_{min} read as:

$$u^{out}_{[k,j\min,i]} = u^{out}_{[k,j\min+1,i]}$$ Equation 3-49

$$v^{out}_{[k,j\min,i]} = 0$$ Equation 3-50

$$w^{out}_{[k,j\min,i]} = w^{out}_{[k,j\min+1,i]}$$ Equation 3-51

It should be noted that both the bottom and housing planes (Figure 3-20) were totally immersed into the body and thus the boundary conditions chosen for these planes didn't affect the overall solution. Nonetheless, the velocity components along these planes were set to zero.

3.4.4.4 Prescribed leaflet motion

The motion of the leaflet was prescribed based on the results of the large-scale FSI simulations. In these simulations, the leaflets were assumed to have only one degree of freedom: any translation motion was neglected and only a rotation motion around a fixed hinge axis was modeled. The FSI solver was found to accurately capture the leaflet motion throughout the cardiac cycle [61]. Thus, the computed FSI leaflet angle variation as shown in Figure 3-21 was used to prescribe the leaflet motion in the hinge model. Note that in the hinge simulations, the leaflet rebounds present after valve closure (at approximately t=405 ms and t =415 ms) were neglected.

Because the leaflet motion was prescribed in the hinge model, the velocity of all the body vertices of the unstructured triangular mesh defining the leaflet surface were known at all time and, thus, the shape and location of the boundaries (of both the leaflet and non-moving housing) were known at every physical time step. A no-slip boundary condition could therefore be enforced along all body surfaces by reconstructing the velocity at all near-boundary nodes as described in section 3.2.2.

3.5 Point-Particle Trajectories

A better understanding of the thromboembolic potential associated with the hinge recess requires a better insight into the role of the hinge flow structures in inducing cell trauma, platelet activation, and thrombus formation. This could be achieved by assessing the Lagrangian transport of blood cells by the hinge flow fields. A Lagrangian method consisting of computing the trajectories of particles from pre-computed flow fields was therefore implemented to simulate the particle transport process by the flow through the hinge recess. The next section (section 3.5.1) gives an overview of the method and is followed by a detailed description of the numerical aspects of the particle tracking algorithm.

3.5.1 Overview of the particle tracking algorithm

The Lagrangian particle tracking code calculates particle paths representing cell trajectories. The blood elements are modeled by weight-less point particles and are assumed to be passively advected by the velocity field. Under this assumption the motion of each particle $\mathcal{P}$ in the flow is governed by the following three equations:

$$\frac{dx}{dt} = u\left(x, y, z, t\right) \qquad \text{Equation 3-52}$$

$$\frac{dy}{dt} = v\left(x, y, z, t\right) \qquad \text{Equation 3-53}$$

$$\frac{dz}{dt} = w\left(x, y, z, t\right) \qquad \text{Equation 3-54}$$

where *x*, *y*, and *z* are the Cartesian coordinates of the particle $\mathcal{P}$ at the instant *t* and (u , v , w) is the fluid velocity vector computed in (x,y,z) at instant t.

However, the governing equations of the fluid motion (the continuity equation and the momentum conservation equations) are solved on a discretized mesh and the velocity fields (pre-computed as described in section 3.1) are therefore known at discrete locations in space (corresponding to the nodes of the Cartesian numerical mesh) and at discrete time points in the cardiac cycle. An interpolation scheme is therefore required to estimate the particle velocity at any point in time and space.

Consequently, the numerical algorithm to integrate the equations of motion of the particles involves three main schemes: a particle location scheme, an interpolation scheme, and a temporal integration scheme (Figure 3-25). The particle location scheme identifies the computational grid cells where each particle $\mathcal{P}$ is located. The particle velocity is then obtained by interpolation of the known velocity components at the cell nodes. With the velocity of each particle known, the temporal integration scheme is executed to compute the new particle position after a small time step with high order of accuracy.

3.5.2 Details on the particle tracking method

3.5.2.1 Particle location scheme

The leaflet and hinge surfaces were immersed into non-uniform Cartesian meshes of approximately 5.9 million grid nodes. The fluid domain was therefore divided into several thousand orthogonal rectangular elements of varying dimensions. Checking each and every single one of these elements to assess whether they contain the particles would be a slow and time-consuming approach. In order to improve the speed of the particle location scheme, the entire domain was divided into large uniformly

distributed sub-domains Ω and the search algorithm was implemented as a three-steps approach: 1) create a set of sub-domains and identify all Cartesian cells within each sub-domain 2) perform a preliminary search to associate each particle with a particular sub-domain Ω and 3) carry out a refined search to determine which of the Cartesian cells within the sub-domain Ω contains the particles. Note that the Cartesian numerical mesh used to discretize the flow domain is the same throughout the cardiac cycle and thus the first step is only performed once. Each of these three steps is described below.

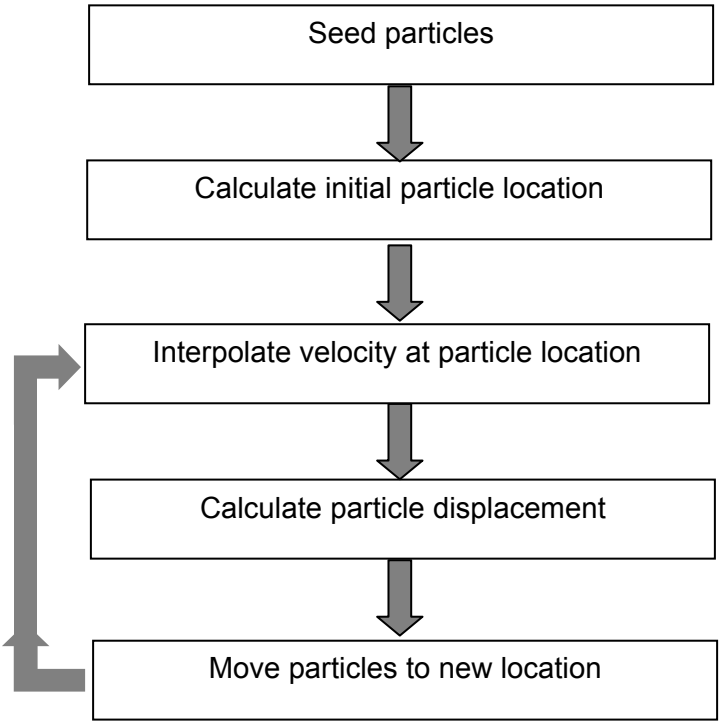

Figure 3-25: Overview of the particle tracking algorithm

The fluid domain is first divided into sub-domains Ω of dimensions Δa x Δb x Δc defined as:

$$\begin{aligned}\Delta a &= (x_{\max} - x_{\min}) / IM \\ \Delta b &= (y_{\max} - y_{\min}) / JM \\ \Delta c &= (z_{\max} - z_{\min}) / KM\end{aligned} \qquad \text{Equation 3-55}$$

where x_{min}, y_{min}, z_{min} and x_{max}, y_{max}, z_{max} are, the minimum and maximum coordinates of the fluid domain, respectively and *IM*, *JM* and KM define the total number of sub-domains. *IM*, *JM*, and *KM* were all set to 50.

Each sub-domain Ω is referenced by a set of indices $(i_\Omega, j_\Omega, k_\Omega)$ that corresponds to the vertex V_Ω of the subdomain that has the smallest coordinates: $\Omega(i_\Omega, j_\Omega, k_\Omega)$ thus depicts the volume $\left[i_\Omega \Delta a, (i_\Omega + \mathbf{1})\Delta a\right].\left[j_\Omega \Delta b, (j_\Omega + \mathbf{1})\Delta b\right].\left[k_\Omega \Delta c, (k_\Omega + \mathbf{1})\Delta c\right]$ where i_Ω, j_Ω, k_Ω may take any value between 0 and either (IM-1),(JM-1) or (KM-1), respectively. Once defined, each sub-domain is associated with the list of Cartesian cells that it contains. This is done only once at the first iteration.

The location of particle $\mathcal{P}$ at the time step (*n*) is known *a priori* and is denoted $\mathcal{P}^n = (\mathcal{P}_x^n, \mathcal{P}_y^n, \mathcal{P}_z^n)$. The sub-domain $\Omega_{\mathcal{P}}^n(i_\Omega, j_\Omega, k_\Omega)$ within which the particle $\mathcal{P}$ lays can be found using the following equations:

$$\begin{aligned}i_\Omega &= (\mathcal{P}_x^n - x_{\min}) / \Delta a \\ j_\Omega &= (\mathcal{P}_y^n - y_{\min}) / \Delta b \\ k_\Omega &= (\mathcal{P}_z^n - z_{\min}) / \Delta c\end{aligned} \qquad \text{Equation 3-56}$$

Once the sub-domain containing $\mathcal{P}$ has been identified, each Cartesian cell within the sub-domain $\Omega_{\mathcal{P}}^n(i_\Omega, j_\Omega, k_\Omega)$ is tested until the Cartesian cell containing the particle $\mathcal{P}$ is identified. Lets consider the Cartesian cell $\mathcal{C}$, within the sub-domain $\Omega_{\mathcal{P}}^n(i_\Omega, j_\Omega, k_\Omega)$, and

test if the particle $\mathcal{P}$ lays within this cell. The Cartesian cell is referenced, as previously done with the sub-domains, by a set of indices *(i, j, k*) that corresponds to the vertex of the cell that has the smallest coordinates. For ease of notation, lets name the eight vertices defining the Cartesian cell $\mathcal{C}$ as C_{000},C_{001},C_{110},C_{010},C_{001},C_{011},C_{111}, and C_{101} (Figure 3-26). The side of the Cartesian cell located along the plane (*i*) and noted $\mathcal{F}_{(i)}$ is defined by the two vectors $\overrightarrow{C_{000}C_{011}}$ and $\overrightarrow{C_{010}C_{001}}$. The normal direction to $\mathcal{F}_{(i)}$ is therefore:

$$\overrightarrow{n_1} = \frac{\overrightarrow{C_{000}C_{011}} \wedge \overrightarrow{C_{010}C_{001}}}{\left\| \overrightarrow{C_{000}C_{011}} \wedge \overrightarrow{C_{010}C_{001}} \right\|} \qquad \text{Equation 3-57}$$

The center of the side $\mathcal{F}_{(i)}$,is noted O_i and its coordinates are defined as:

$$x_{O_i} = \frac{1}{4}\left(x_{C_{000}} + x_{C_{010}} + x_{C_{001}} + x_{C_{011}} \right) \qquad \text{Equation 3-58}$$

$$y_{O_i} = \frac{1}{4}\left(y_{C_{000}} + y_{C_{010}} + y_{C_{001}} + y_{C_{011}} \right) \qquad \text{Equation 3-59}$$

$$z_{O_i} = \frac{1}{4}\left(z_{C_{000}} + z_{C_{010}} + z_{C_{001}} + z_{C_{011}} \right) \qquad \text{Equation 3-60}$$

Lets define the vector $\overrightarrow{O_i\mathcal{P}}$ from the center of the side $\mathcal{F}_{(i)}$ to the particle $\mathcal{P}$ and the parameter $Cond$ whose value depends on the dot product between the normal $\overrightarrow{n_i}$ of $\mathcal{F}_{(i)}$ and the vector $\overrightarrow{O_i\mathcal{P}}$:

If $\overrightarrow{O_i\mathcal{P}}.\overrightarrow{n_i} > \mathbf{0}$, $Cond(i) = \mathbf{0}$ and if $\overrightarrow{O_i\mathcal{P}}.\overrightarrow{n_i} \leq \mathbf{0}$, $Cond(i) = \mathbf{1}$

The value of the parameter $Cond$ is evaluated for each of the six faces of the Cartesian cell $\mathcal{C}$ and is eventually used to determine if the particle $\mathcal{P}$ is inside or outside of $\mathcal{C}$ (see below Equation 3-62).

Lets perform a similar analysis on the side of the Cartesian cell located at (*i+1*) and compute the value of *Cond(i+1)*. Lets consider $\mathcal{F}_{(i+1)}$ defined by $\overrightarrow{C_{110}C_{101}}$ and $\overrightarrow{C_{100}C_{111}}$. The normal direction to $\mathcal{F}_{(i+1)}$ is:

$$\overrightarrow{n_{i+1}} = \frac{\overrightarrow{C_{100}C_{111}} \wedge \overrightarrow{C_{110}C_{101}}}{\left\| \overrightarrow{C_{100}C_{111}} \wedge \overrightarrow{C_{110}C_{101}} \right\|} \qquad \text{Equation 3-61}$$

The coordinates of the center O_{i+1} of the side $\mathcal{F}_{(i+1)}$ can be computed by applying the three equations 3-58,3-59 and 3-60 to the nodes C_{100},C_{111},C_{110},and C_{101}. If $\overrightarrow{O_{i+1}\mathcal{P}}$ is the vector from the center O_{i+1} to the particle $\mathcal{P}$, the dot product between $\overrightarrow{O_{i+1}\mathcal{P}}$ and $\overrightarrow{n_{i+1}}$ can be computed.

If $\overrightarrow{O_{i+1}\mathcal{P}}.\overrightarrow{n_{i+1}} > \mathbf{0}$ $Cond(i+\mathbf{1}) = \mathbf{0}$ and if $\overrightarrow{O_{i+1}\mathcal{P}}.\overrightarrow{n_{i+1}} \leq \mathbf{0}$ $Cond(i+\mathbf{1}) = \mathbf{1}$

Such an analysis is done in all four remaining sides of the Cartesian cell $\mathcal{C}$, namely $\mathcal{F}_{(j)}$, $\mathcal{F}_{(j+1)}$, $\mathcal{F}_{(k)}$,and $\mathcal{F}_{(k+1)}$. The particle $\mathcal{P}$ is considered within the Cartesian cell $\mathcal{C}$ if the following is true:

$$\begin{array}{ll} Cond(i) = \mathbf{0} & Cond(i+\mathbf{1}) = \mathbf{1} \\ Cond(j) = \mathbf{0} & Cond(j+\mathbf{1}) = \mathbf{1} \\ Cond(k) = \mathbf{0} & Cond(k+\mathbf{1}) = \mathbf{1} \end{array} \qquad \text{Equation 3-62}$$

If any one of these conditions is violated, then the particle lies outside the Cartesian cell $\mathcal{C}$.

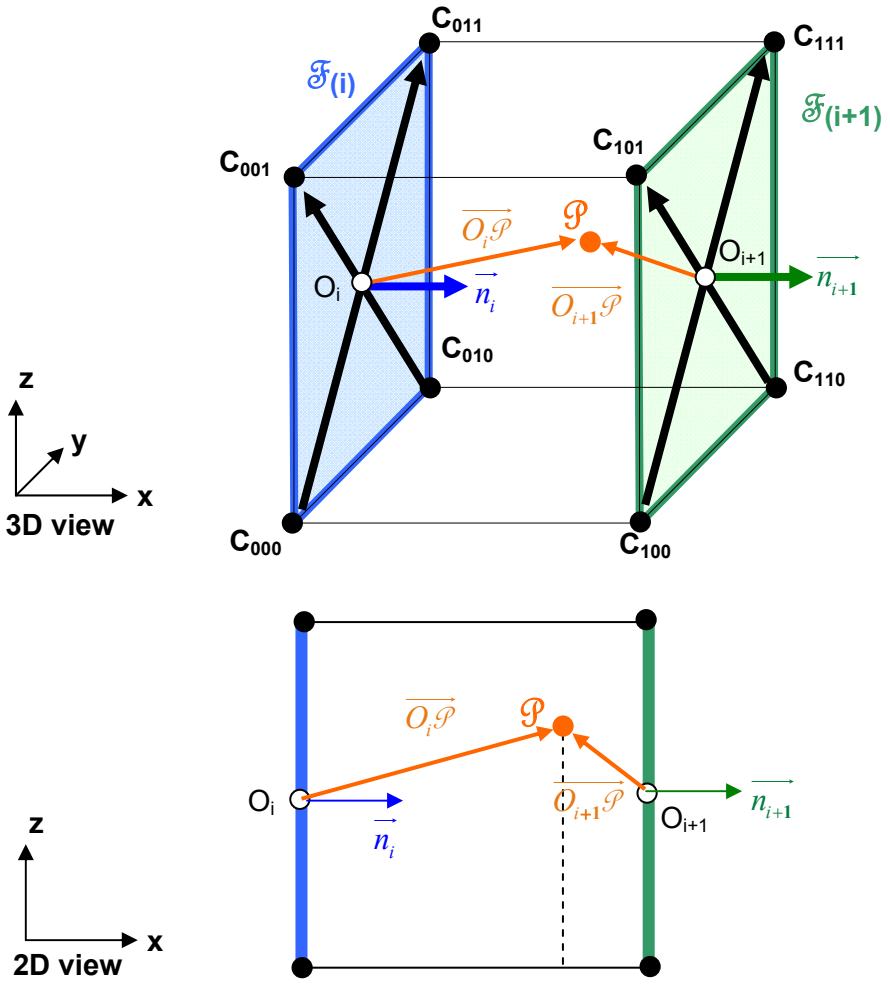

Figure 3-26: Three-dimensional (top) and two-dimensional (bottom) schematic illustrating the algorithm to check if the particle $\mathcal{P}$ is inside or outside a Cartesian cell $\mathcal{C}$.

3.5.2.2 Interpolation schemes

Spatial interpolation scheme: From the particle location scheme the particle location within a particular Cartesian cell $\mathcal{C}$ is known, and the velocity at the particle location may be reconstructed from the eight surrounding nodes using trilinear interpolation (Figure 3-27). However, the relative position of the particle $\mathcal{P}$ within the Cartesian cell $\mathcal{C}$ is needed to perform such an interpolation.

As noted in the previous section (section 3.5.2.1), the vertex of reference for the Cartesian cell $\mathcal{C}$ is the vertex with the lowest coordinates (C_{000} in Figure 3-27). The normalized distance along each coordinate axis between the particle $\mathcal{P}$ and this reference node can then computed with:

$$x_d = \frac{\overrightarrow{O_i\mathcal{P}}.\overrightarrow{n_i}}{\overrightarrow{O_i\mathcal{P}}.\overrightarrow{n_i} - \overrightarrow{O_{i+1}\mathcal{P}}.\overrightarrow{n_{i+1}}} \qquad \text{Equation 3-63}$$

$$y_d = \frac{\overrightarrow{O_j\mathcal{P}}.\overrightarrow{n_j}}{\overrightarrow{O_j\mathcal{P}}.\overrightarrow{n_j} - \overrightarrow{O_{j+1}\mathcal{P}}.\overrightarrow{n_{j+1}}} \qquad \text{Equation 3-64}$$

$$z_d = \frac{\overrightarrow{O_k\mathcal{P}}.\overrightarrow{n_k}}{\overrightarrow{O_k\mathcal{P}}.\overrightarrow{n_k} - \overrightarrow{O_{k+1}\mathcal{P}}.\overrightarrow{n_{k+1}}} \qquad \text{Equation 3-65}$$

where $\mathcal{P}$ is the particle of interest, O_i is the center of the face $\mathcal{F}_{(i)}$,and $\overrightarrow{n_i}$ is the normal of the face $\mathcal{F}_{(i)}$.

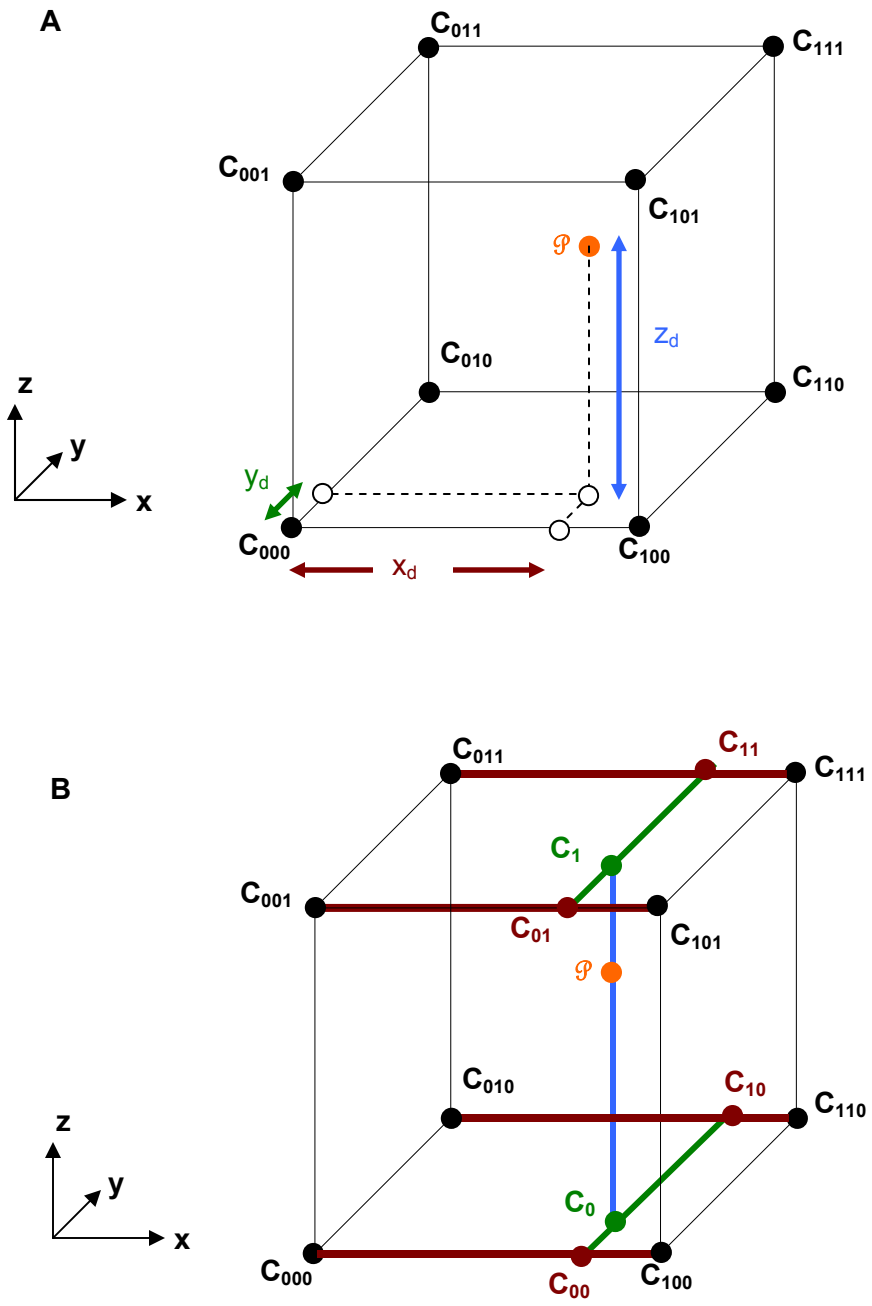

Figure 3-27: Illustration of the trilinear interpolation method. (A) Normalized distance (x_d, y_d and z_d) between the vertex of reference C_{000} and the particle $\mathcal{P}$. (B)Three linear interpolations are performed, one along the x axis(red), one along the y axis (green) and finally one along the z-axis(blue)

A first linear interpolation (Figure 3-27B) is performed along the x-direction to obtain the velocity at the nodes C_{01}, C_{00}, C_{10}, and C_{11}:

$$\vec{V}_{C_{00}} = (\mathbf{1} - x_d)\vec{V}_{C_{000}} + x_d\vec{V}_{C_{100}} \quad \text{Equation 3-66}$$

$$\vec{V}_{C_{10}} = (\mathbf{1} - x_d)\vec{V}_{C_{010}} + x_d\vec{V}_{C_{110}} \quad \text{Equation 3-67}$$

$$\vec{V}_{C_{01}} = (\mathbf{1} - x_d)\vec{V}_{C_{001}} + x_d\vec{V}_{C_{101}} \quad \text{Equation 3-68}$$

$$\vec{V}_{C_{11}} = (\mathbf{1} - x_d)\vec{V}_{C_{011}} + x_d\vec{V}_{C_{111}} \quad \text{Equation 3-69}$$

These velocities are then used to assess the velocity components at the nodes C_0 and C_1 using the following equations:

$$\vec{V}_{C_0} = (\mathbf{1} - y_d)\vec{V}_{C_{00}} + y_d\vec{V}_{C_{10}} \quad \text{Equation 3-70}$$

$$\vec{V}_{C_1} = (\mathbf{1} - y_d)\vec{V}_{C_{01}} + y_d\vec{V}_{C_{11}} \quad \text{Equation 3-71}$$

Similarly, the velocity at the location of the particle $\mathcal{P}$ can be computed by interpolating between C_0 and C_1 with:

$$\vec{V}_{\mathcal{P}} = (\mathbf{1} - z_d)\vec{V}_{C_0} + z_d\vec{V}_{C_1} \quad \text{Equation 3-72}$$

The result of the trilinear interpolation doesn't depend on the order of the different interpolation steps along the three axes. The series of interpolations can thus be summarized in a single equation:

$$\begin{aligned}\vec{V}_{\mathcal{P}} = {} & (\mathbf{1} - x_d)(\mathbf{1} - y_d)(\mathbf{1} - z_d)\vec{V}_{C_{000}} + x_d(\mathbf{1} - y_d)(\mathbf{1} - z_d)\vec{V}_{C_{100}} + \dots \\ & (\mathbf{1} - x_d)y_d(\mathbf{1} - z_d)\vec{V}_{C_{010}} + x_d y_d(\mathbf{1} - z_d)\vec{V}_{C_{110}} + \dots \\ & (\mathbf{1} - x_d)(\mathbf{1} - y_d)z_d\vec{V}_{C_{001}} + x_d(\mathbf{1} - y_d)z_d\vec{V}_{C_{101}} + \dots \\ & (\mathbf{1} - x_d)y_d z_d\vec{V}_{C_{011}} + x_d y_d z_d\vec{V}_{C_{111}}\end{aligned} \quad \text{Equation 3-73}$$

The above trilinear interpolation equation, applied to the pre-computed velocity fields, can be used to compute the velocity components of the particles at any desired location within the fluid domain.

Temporal considerations: The velocity fields are computed throughout the cardiac cycle and are outputted at regular time intervals. However, in order to compute the trajectories of the particle through these pre-computed flow fields, the velocity distribution has to be known at any instances of time. Thus, a temporal interpolation has to be performed between the velocity fields in order to determine the velocity at any specific instances of time.

Lets assume the particle position is updated at regular time interval Δt_p and the velocity fields are available at every Δt such that $\Delta t > \Delta t_p$. Lets consider a particle $\mathcal{P}$ at time $t_{\mathcal{P}}$ such that $t^{(n)} < t_{\mathcal{P}} < t^{(n+1)}$, where $t^{(n)}$ and $t^{(n+1)}$ correspond to two consecutive time points at which the velocity fields are available (Figure 3-28). The location of particle $\mathcal{P}$ is known and the Cartesian cell $\mathcal{C}$ containing this particle has been identified. By applying the aforementioned trilinear spatial interpolation to the velocity fields at times $t^{(n)}$ and $t^{(n+1)}$ described, the velocity components at the location of the particle $\mathcal{P}$ are reconstructed and the velocity vectors $\overrightarrow{V_{\mathcal{P}}}^{n}$ and $\overrightarrow{V_{\mathcal{P}}}^{n+1}$ are obtained.

The velocity of the particle at time $t_{\mathcal{P}}$ is then reconstructed using the following weighted linear interpolation:

$$\vec{V}_p(t_p) = coeff.\vec{V}_p^{n+1} + (1 - coeff).\vec{V}_p^{n} \qquad \text{Equation 3-74}$$

with $coeff = \dfrac{t_p - t^{(n)}}{t^{(n+1)} - t^{(n)}}$.

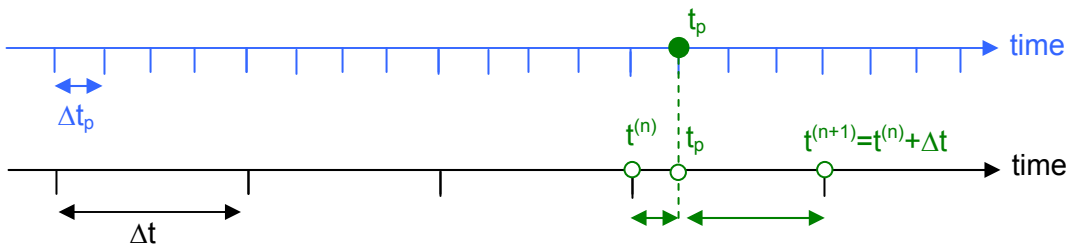

Figure 3-28: Illustration of the linear temporal interpolation

3.5.2.3 Temporal integration scheme

With the velocity of each particle $\mathcal{P}$ known, the position of the particles is updated as follows:

$$x_{\mathcal{P}}(t_{\mathcal{P}} + \Delta t_{\mathcal{P}}) = x_{\mathcal{P}}(t_{\mathcal{P}}) + \Delta t_{\mathcal{P}} . u_{\mathcal{P}}(t_{\mathcal{P}})$$ Equation 3-75

$$y_{\mathcal{P}}(t_{\mathcal{P}} + \Delta t_{\mathcal{P}}) = y_{\mathcal{P}}(t_{\mathcal{P}}) + \Delta t_{\mathcal{P}} . v_{\mathcal{P}}(t_{\mathcal{P}})$$ Equation 3-76

$$z_{\mathcal{P}}(t_{\mathcal{P}} + \Delta t_{\mathcal{P}}) = z_{\mathcal{P}}(t_{\mathcal{P}}) + \Delta t_{\mathcal{P}} . w_{\mathcal{P}}(t_{\mathcal{P}})$$ Equation 3-77

Where $x_{\mathcal{P}}(t_{\mathcal{P}}+\Delta t_{\mathcal{P}})$, $y_{\mathcal{P}}(t_{\mathcal{P}}+\Delta t_{\mathcal{P}})$ and $z_{\mathcal{P}}(t_{\mathcal{P}}+\Delta t_{\mathcal{P}})$ are the new coordinates of the particle $\mathcal{P}$ at time $t_{\mathcal{P}}+\Delta t_{\mathcal{P}}$ while $x_{\mathcal{P}}(t_{\mathcal{P}})$, $y_{\mathcal{P}}(t_{\mathcal{P}})$ and $z_{\mathcal{P}}(t_{\mathcal{P}})$ are the coordinates of the same particle $\mathcal{P}$ at time t_p. The velocity components of $\vec{V}_{\mathcal{P}}(t_{\mathcal{P}})$ are denoted here as $u_{\mathcal{P}}(t_{\mathcal{P}})$, $v_{\mathcal{P}}(t_{\mathcal{P}})$, and $w_{\mathcal{P}}(t_{\mathcal{P}})$.

3.6 Clinically-relevant parameters

The knowledge of the particle trajectories allows for the calculation of clinically-relevant parameters such as residence time (representative of the potential for platelet aggregation) or shear stress history and shear stress levels with their respective exposure time (indicating potential for blood cell trauma). The shear stress information

combined with existing blood damage models can be used to compute a surrogate measure, called blood damage index, for hemolysis and platelet activation induced by the hinge flow fields. The next section presents the shear stress calculation and is followed by a description of the blood damage index estimation.

3.6.1 Maximum Shear Stress

An important parameter in assessing the potential of blood cell trauma associated with a particular flow field is the shear stress. The three-dimensional Cauchy stress tensor is defined as:

$$\sigma_{ij} = \begin{pmatrix} \sigma_{xx} & \sigma_{xy} & \sigma_{xz} \\ \sigma_{xy} & \sigma_{yy} & \sigma_{yz} \\ \sigma_{xz} & \sigma_{yz} & \sigma_{zz} \end{pmatrix} \qquad \text{Equation 3-78}$$

where σ_{ii} are the normal stresses and σ_{ij} (with $i \neq j$) are the shear stresses.

The terms σ_{ii} are defined as:

$$\sigma_{ij} = \frac{\mathbf{1}}{\mathbf{2}} \mu \left(\frac{\partial u_i}{\partial x_j} + \frac{\partial u_j}{\partial x_i} \right) \qquad \text{Equation 3-79}$$

where μ is the dynamic viscosity, x_j and u_j (for j=1,2,3) are the coordinates and vector components, respectively. Note that the stress tensor is symmetric and thus, $\sigma_{xy} = \sigma_{yx}$, $\sigma_{xz} = \sigma_{zx}$, and $\sigma_{zy} = \sigma_{yz}$.

The components of this stress tensor depend heavily on the orientation of the chosen coordinate system, but the eigenvalues of the above matrix are known to be invariant. When the coordinate system coincides with the eigenvectors of the stress tensors, the stress tensor can be represented by the following diagonal matrix:

$$\sigma_{ij} = \begin{pmatrix} \lambda_1 & \mathbf{0} & \mathbf{0} \\ \mathbf{0} & \lambda_2 & \mathbf{0} \\ \mathbf{0} & \mathbf{0} & \lambda_3 \end{pmatrix} \qquad \text{Equation 3-80}$$

where λ_1, λ_2 and λ_3 are the eigenvalues of the tensor. These eigenvalues correspond to the largest components of the stress tensor and are called principal stresses. It is therefore required, to determine the physical maximum stress values, to perform a coordinate transformation and compute the tensor in the principal stress coordinate system.

Given the stress tensor defined above (equation 3.78), the eigenvalues λ of the tensor are obtained by solving the following equation:

$$\left|\sigma_{ij} - \lambda\delta_{ij}\right| = \begin{vmatrix} \sigma_{xx} - \lambda & \sigma_{xy} & \sigma_{xz} \\ \sigma_{xy} & \sigma_{yy} - \lambda & \sigma_{yz} \\ \sigma_{xz} & \sigma_{yz} & \sigma_{zz} - \lambda \end{vmatrix} = \mathbf{0} \qquad \text{Equation 3-81}$$

Expanding this determinant leads to the following characteristic equation:

$$\lambda^3 - I_1\lambda^2 + I_2\lambda - I_3 = \mathbf{0} \qquad \text{Equation 3-82}$$

with $$I_1 = \sigma_{kk} = \sigma_{xx} + \sigma_{yy} + \sigma_{zz} \qquad \text{Equation 3-83}$$

$$I_2 = \frac{\mathbf{1}}{\mathbf{2}}\left(\sigma_{ii}\sigma_{jj} - \sigma_{ij}\sigma_{ji}\right) = \sigma_{xx}\sigma_{yy} + \sigma_{yy}\sigma_{zz} + \sigma_{xx}\sigma_{zz} - \sigma_{xy}^2 - \sigma_{yz}^2 - \sigma_{xz}^2 \qquad \text{Equation 3-84}$$

$$I_3 = \det(\sigma_{ij}) = \sigma_{xx}\sigma_{yy}\sigma_{zz} + \mathbf{2}\sigma_{xy}\sigma_{yz}\sigma_{zx} - \sigma_{xy}^2\sigma_{zz} - \sigma_{yz}^2\sigma_{xx} - \sigma_{xz}^2\sigma_{yy} \qquad \text{Equation 3-85}$$

The general expression for the roots λ_1, λ_2, and λ_3 of a cubic polynomial of this form can be written as:

$$\lambda_1 = -\frac{\mathbf{1}}{\mathbf{3}}I_1 + (S + T) \qquad \text{Equation 3-86}$$

$$\lambda_2 = -\frac{\mathbf{1}}{\mathbf{3}} I_1 - \frac{\mathbf{1}}{\mathbf{2}}(S+T) + \frac{\mathbf{1}}{\mathbf{2}} i\sqrt{\mathbf{3}}(S-T) \qquad \text{Equation 3-87}$$

$$\lambda_3 = -\frac{\mathbf{1}}{\mathbf{3}} I_1 - \frac{\mathbf{1}}{\mathbf{2}}(S+T) - \frac{\mathbf{1}}{\mathbf{2}} i\sqrt{\mathbf{3}}(S-T) \qquad \text{Equation 3-88}$$

with $S = \sqrt[3]{R+\sqrt{D}}$, $T = \sqrt[3]{R-\sqrt{D}}$, $D = Q^3 + R^2$, $Q = \frac{\mathbf{3}I_2 - I_1^2}{\mathbf{9}}$ and

$R = \frac{\mathbf{9}.I_1 I_2 - \mathbf{27}.I_3 - \mathbf{2}.I_1^3}{\mathbf{54}}$.

The value of the polynomial discriminant D determines if a root is either real or complex.

- If D >0, one root is real while the other two are complex conjugates.
- If D=0, all roots are real and at least two of them are equal.
- If D<0, all roots are real and unequal.

In this last case, the real solutions of the equations are of the form:

$$\lambda_1 = \mathbf{2}\sqrt{-Q}\cos\left(\frac{\theta}{\mathbf{3}}\right) - \frac{\mathbf{1}}{\mathbf{3}} I_1 \qquad \text{Equation 3-89}$$

$$\lambda_2 = \mathbf{2}\sqrt{-Q}\cos\left(\frac{\theta + \mathbf{2}\pi}{\mathbf{3}}\right) - \frac{\mathbf{1}}{\mathbf{3}} I_1 \qquad \text{Equation 3-90}$$

$$\lambda_3 = \mathbf{2}\sqrt{-Q}\cos\left(\frac{\theta + \mathbf{4}\pi}{\mathbf{3}}\right) - \frac{\mathbf{1}}{\mathbf{3}} I_1 \qquad \text{Equation 3-91}$$

Note that the roots λ_1, λ_2, and λ_3 should satisfy:

$$I_1 = \lambda_1 + \lambda_2 + \lambda_3 \qquad \text{Equation 3-92}$$

$$I_2 = \lambda_1\lambda_2 + \lambda_2\lambda_3 + \lambda_3\lambda_1 \qquad \text{Equation 3-93}$$

$$I_3 = \lambda_1\lambda_2\lambda_3 \qquad \text{Equation 3-94}$$

The terms I_1, I_2 and I_3 are the first, second and third stress invariants, respectively and their values are the same regardless of the chosen coordinate system.

Once the three roots λ_1, λ_2, and λ_3 have been computed, the maximum shear stress τ_{max} can be obtained from the principal normal stresses as:

$$\tau_{\max} = \max\left(\left|\frac{\lambda_1 - \lambda_2}{2}\right|, \left|\frac{\lambda_1 - \lambda_3}{2}\right|, \left|\frac{\lambda_2 - \lambda_3}{2}\right|\right) \qquad \text{Equation 3-95}$$

3.6.2 Blood Damage Index

The knowledge of the particle trajectories enables the estimation of the forces experienced by each cell crossing the hinge region. This information, coupled with existing blood damage models, can provide a surrogate measure of the blood trauma potential induced by the hinge flow fields. It is acknowledged that the shear stress level is the primary biomechanical trigger for thromboembolic events. It is also well known that exposure time is a critical parameter for hemolysis and platelet activation (see background section). Accordingly, existing blood damage models not only take into account the level of shear stress but also the exposure time. Several blood damage models have been used in previous studies, from simplistic models to more realistic models, and are presented below.

The most simplistic approach in assessing blood damage is defined by a linear stress-exposure time model. Dumont et al. [74] used this approach to obtain a first approximation of platelet activation. Let's consider a particle $\mathcal{P}$ whose trajectory is known. The cumulative effects of shear stress and exposure time experienced by this particle $\mathcal{P}$ can be computed with:

$$BDI_{\mathcal{P}} = \sum_i \tau_i \,.\Delta t_i \qquad \text{Equation 3-96}$$

where $BDI_{\mathcal{P}}$ is the blood damage index along the trajectory of particle $\mathcal{P}$, τ is the principal shear stress (dyn/cm^2), Δt is the exposure time (s) and *i* denotes successive time points along the particle trajectory.

Previously published blood studies have however shown that a shear activation threshold exists for platelet activation to occur under physiological flow conditions. This threshold is independent of the length of time a platelet may be exposed to forces below the shear activation threshold [75]. Tambasco and Steinman therefore included this threshold τ_{thres} in their linear blood damage model [76] by only considering particles that have experienced significant stress trauma. The blood damage model then reads as:

$$BDI^*_{\mathcal{P}} = \sum_i \tau^*_i \,.\Delta t^*_i \qquad \text{Equation 3-97}$$

where $BDI^*_{\mathcal{P}}$ is the modified BDI, τ^* is the principal shear stress (dyn/cm^2) that exceeds the threshold τ_{thres} and Δt* is the exposure time (s). Tambasco and Steinman defined this threshold τ_{thres} for platelet activation as 105 dyn/cm^2 [76, 77] and a similar value was used in this thesis.

The two aforementioned models (Equation 3-96 and 3-97) assume a linear relationship between shear stress, exposure time and blood damage trauma. Blood studies have shown that this relationship is far more complex [78-80]. Wurzinger *et al.* [79, 80] experimentally measured, using isolated platelet-rich plasma, the amount of cytoplasm enzyme (LDH) released by platelets (which is proportional to the level of platelet activation) as a function of shear stress and exposure time using a Couette-viscometer. In a separate set of experiments, Wurzinger *et al.* [79, 80] used isolated washed human red blood cells to quantify the amount of hemoglobin (Hb) released by

red blood cells (which is representative of the amount of hemolysis) as a function of shear stress and exposure time. Giersiepen *et al* [78] incorporated these experimental data by Wurzinger *et al.* into a mathematical correlation and established the following two relationships:

$$\frac{\Delta LDH}{LDH}(\%) = 3.31x10^{-6}\Delta t^{0.77}\tau^{3.075} \qquad \text{Equation 3-98}$$

$$\frac{\Delta Hb}{Hb}(\%) = 3.62x10^{-5}\Delta t^{0.785}\tau^{2.416} \qquad \text{Equation 3-99}$$

where τ is the principal shear stress (N/m^2) and Δt is the exposure time (s). These equations were used to estimate the shear stress related blood damage induced by artificial heart valves [58, 78] and the estimated blood damage were found to be in good agreements with clinical results[78]. These correlations were therefore retained to analyze the hinge flow fields from a blood-cell standpoint. It should be noted that because weight-less point particles were used for the particle tracking algorithm, it was assumed that the particle trajectories were representative of both red blood cell and platelet trajectories. Assuming that the total damage is accumulated linearly [49, 56], the above relationships (Equations 3-98 and 3-99) were used to compute the blood damage index along each particle trajectory as follows:

$$BDI^{PL}{}_{\mathcal{P}} = \sum_i 3.31x10^{-6}\Delta t_i{}^{0.77}\tau_i{}^{3.075} \qquad \text{Equation 3-100}$$

$$BDI^{H}{}_{\mathcal{P}} = \sum_i 3.62x10^{-5}\Delta t_i{}^{0.785}\tau_i{}^{2.416} \qquad \text{Equation 3-101}$$

where BDI^{PL} is the blood damage index corresponding to platelet activation, while BDI^{H} refers to hemolysis and *i* denotes successive time points along the particle trajectory.

This concludes the description of the methodology used in this thesis to numerically simulate the flow fields in the hinge region and extract clinically-relevant parameters in order to better understand the thromboembolic potential associated with the hinge region of bileaflet mechanical heart valves.

CHAPTER 4

RESULTS

Thromboembolic complications of bileaflet mechanical heart valves (BMHV) are believed to be due to detrimental hemodynamic stresses imposed on blood elements by the hinge flows. These flow features are in turn dictated by the design retained for the hinge recess and the protruding leaflet ear. Detailed characterization of the hinge flow fields is therefore essential to understand the causes of blood damage and thrombus formation on the one hand, and improve hinge design on the other.

Two challenges are thus at stake: 1) to establish a relationship between hinge geometry and the resulting flow structures; and 2) to estimate the thromboembolic potential of these flow structures. To address the first of these challenges, we will scrutinize the simulated flow fields, focusing particularly on the flow patterns known to be detrimental to blood elements:

- Zones of recirculating flow and low velocities, which are favorable to platelet aggregation and thrombus formation.
- Regions of elevated velocities that washout the hinge and may dislodge thrombi.
- Regions of elevated shear stresses, which may induce platelet activation and hemolysis.

In order to get a thorough understanding of the flow patterns, the fluid dynamics of the hinge is presented at selected instances throughout the cardiac cycle. Three-dimensional instantaneous streamtraces are used to visualize the global hinge flow structures. Three-dimensional velocity magnitude contour plots and two-dimensional in-

plane velocity vectors with out-of-plane velocity component contours help in quantifying the unsteadiness and three-dimensionality of the flow. Out-of-plane vorticity contour plots are used to highlight key flow patterns revealed by the velocity vectors fields. In order to ease the analysis and comparison of the hinge flow fields throughout the forward flow phase, the color-scales are optimized for the flat level at peak systole and the same color-scales are used for all other systolic instances depicted. Similarly, for the leakage flow phase the color-scales are optimized for the flat level at mid-diastole.

Analysis of the shear stress distribution is essential to understand the forces experienced by blood cells crossing the hinge. Previous researchers have shown that shear stress as low as 100 to 1,000 dyn/cm^2, depending upon the exposure time, may induce platelet activation [79, 81-83]. Iso-surfaces for various shear stress levels starting at 100 dyn/cm^2 are thus provided to visualize the global shear stress distribution. Shear stress contour plots, with the color maximum set to 1,000 dyn/cm^2 are also included to gain deeper insight into the shear stress distribution and identify critical regions with elevated potential for blood damage.

This flow analysis will pinpoint the critical hinge flow features, but their actual impact on the blood cells cannot be grasped from a purely Eulerian description. This goes back to the second challenge raised earlier, namely, to relate the hinge flow structures to thromboembolic potential. Blood cell trauma does not depend solely on the levels of stress experienced by the cells, but also on the exposure duration. Thus, extended exposure of blood elements to low levels of shear stress or short exposure to high levels of shear stress might both lead to hemolysis or platelet activation. Furthermore, a region of low flow where residence time is elevated might favor aggregation of activated blood elements. Assessing the trajectory of blood elements flowing near the hinge region and estimating the shear stress history experienced by these elements are therefore essential to understand the risk for hemolysis, platelet

activation, and thrombus formation. This in turn will pinpoint geometrical features of the hinge design that are detrimental to blood elements. The second part of this chapter thus provides a detailed Lagrangian analysis of the hinge flow fields. The particle trajectories representing blood cells flowing through the hinge recess are examined to locate entrapment regions and estimate the overall potential of the hinge flow fields for inducing hemolysis and platelet activation.

This results chapter is structured in five sections, organized as follows. In the first section, we define the terminology pertinent to the hinge design. In the following three sections, we describe the flow fields in the three investigated hinge designs: the SJM hinge recess with a regular hinge gap width, followed by the SJM hinge recess with a large hinge gap width, and thirdly the CM hinge recess with a regular hinge gap width.

To ease the reader's understanding, description of the flow features in each one of these three hinges will follow the same scheme: an overview of the flow structures and shear stress distribution present within the hinge recess are described first and followed by a thorough description of the hinge hemodynamics throughout the cardiac cycle. The cardiac cycle is divided into four main phases based upon the leaflet position, which are presented in order: 1) the leaflet opening phase, 2) the fully-open leaflet phase, 3) the closing leaflet phase, and 4) the fully-closed leaflet phase. The result chapter ends with a fifth and final section on the Lagrangian analysis of the hinge flow fields and the estimation of the hinge thromboembolic potential for each hinge design.

4.1 Terminology used to describe the hinge recess

To illustrate the hinge terminology and present the planes along which the hinge flow fields are described, schematics representing the St. Jude Medical hinge design are

provided. Similar terms are used for the CarboMedics hinge design. Figure 4-1 shows the terminology used to describe the hinge recess. The forward flow direction goes from the ventricular to the aortic side of the hinge, i.e. from bottom to top of the figures. The ventricular and adjacent corners form the ventricular (upstream) pocket of the hinge. The corners in the aortic (downstream) pocket of the hinge are dubbed aortic and lateral corners.

Figure 4-2 illustrates the location of the different planes chosen to describe the hinge flow fields. For consistency and ease of comparison, the same planes are used to present all three hinges. The plane of reference is the flat level, which is the level flushed with the valve housing. The 195 μm-level, the 390 μm-level and 585 μm-level are three planes located within the hinge recess at 195 μm, 390 μm and 585 μm away from the flat level, respectively. In order to visualize and characterize the flow between the leaflet and the recess wall at the bottom of the hinge recess, cross sectional views of the hinge are presented along the adjacent, central and lateral planes identified in Figure 4-2. Figure 4-3 shows an example of the top view and cross-sectional planes displayed in the following sections. For clarity and ease of orientation in the subsequent images, Figure 4-3 illustrates the location of the housing, recess, and leaflet for each of these planes.

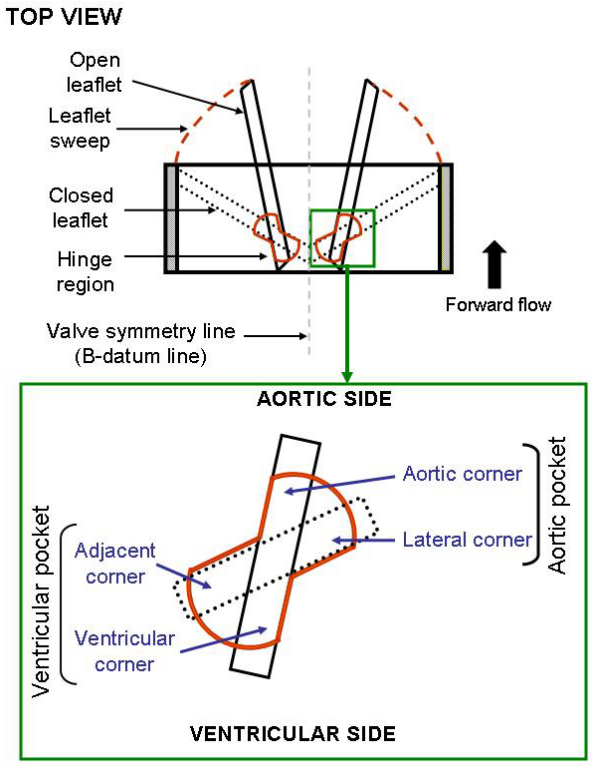

Figure 4-1: Pertinent terminology used to describe the hinge design

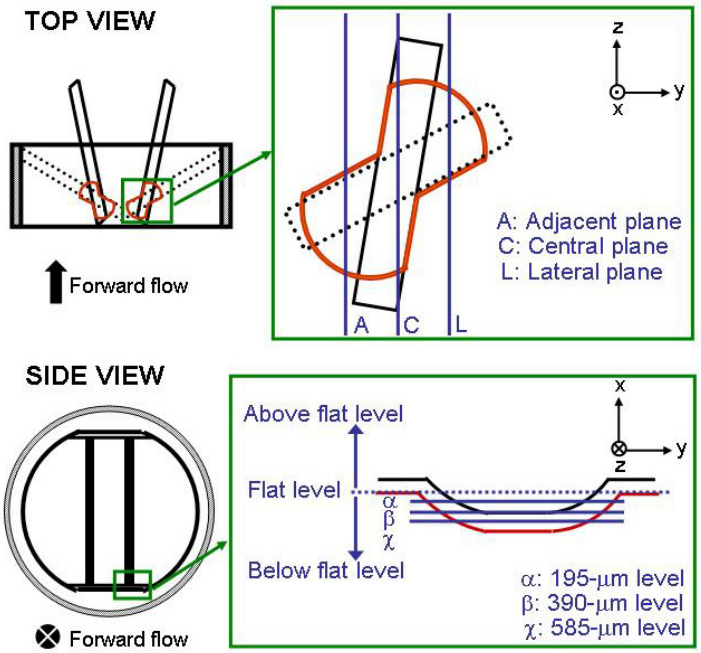

Figure 4-2: Schematic illustrating the location of the different planes chosen to describe the hinge flow fields.

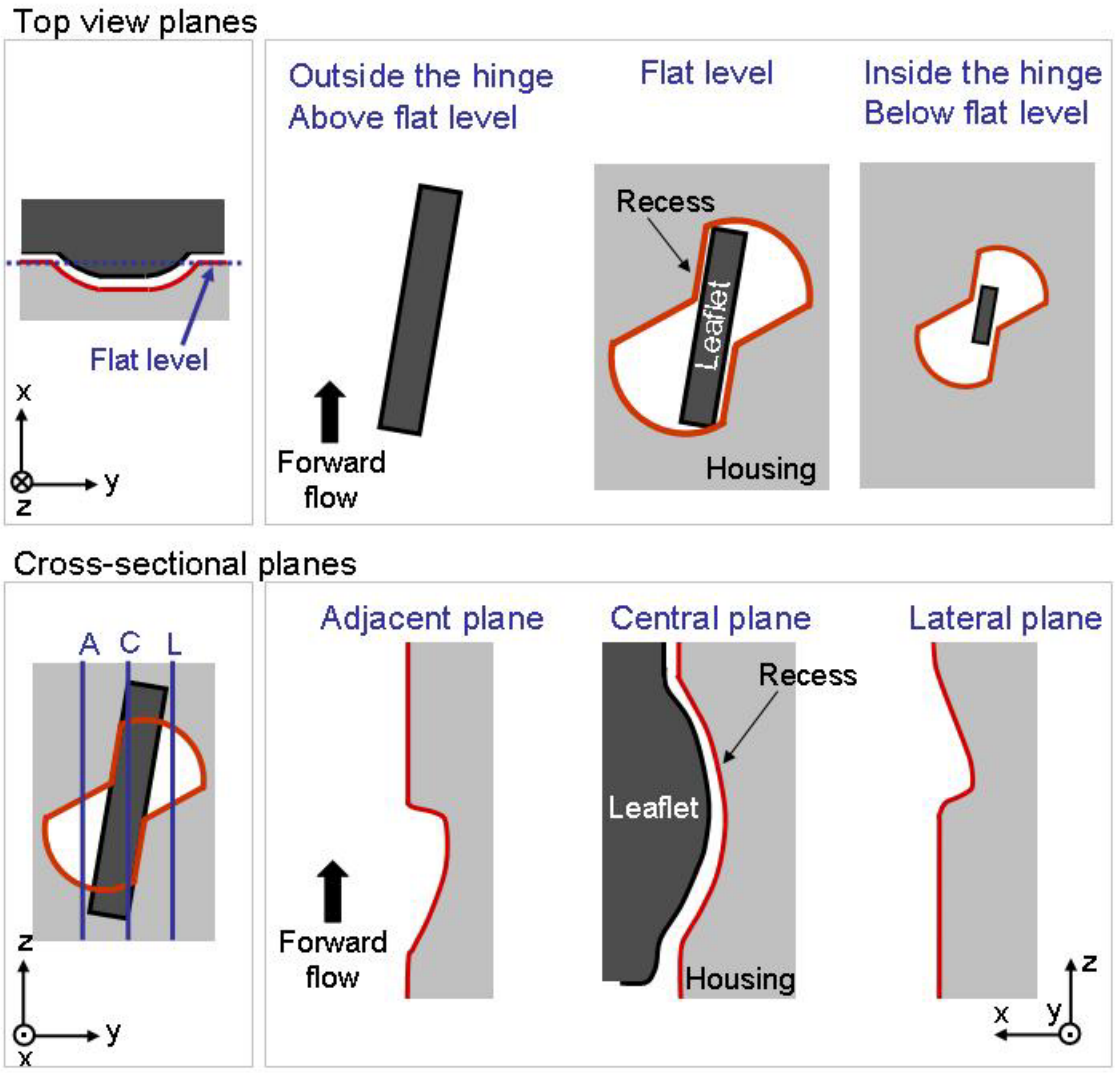

Figure 4-3: Examples of top view and cross-sectional planes.

4.2 Eulerian analysis of the SJM hinge design with a regular hinge gap width

4.2.1 Overview

Prior to diving into the detailed hinge flow features, it is important to first get a good understanding the global hemodynamics and identify the dominant flow structures. Visualization of the full three-dimensional and time-varying flow structures constitutes a challenge in itself. Two sets of images are thus provided that depict the global hinge flow structures at four instances of the cardiac cycle: first qualitatively, using three-dimensional instantaneous streamtraces (Figure 4-4); and then more quantitatively, using three-dimensional velocity vectors superimposed on the velocity magnitude contours (Figure 4-5). Note that in the latter figure, the x-axis is stretched to ease the visualization. The interested reader is referred to the animation SJMReg_3DView _3DVectors_3DVmag.mov for the visualization of the global hinge dynamics across the whole cardiac cycle.

Considering the flat level as the plane of reference, the streamtraces clearly reveal the existence of a highly three-dimensional flow with strong in- and out-of-plane motion throughout the cardiac cycle. The importance of the third velocity component, neglected in quite a few studies, is further highlighted in Figure 4-5 by the magnitude of the out-of-plane vector components, especially along the leaflet during systole and in the ventricular corner during diastole. The presence of the rapid upward flow motion on the ventricular side during systole may appear as counter-intuitive. Going back to Figure 4-4, the red streamtraces reveal that, during the forward flow phase, the flow consistently dives into the recess from the most lateral tip of the aortic pocket (right side) and goes toward the adjacent corner of the hinge, where it impinges on the recess wall. The blue streamtraces also dive inside the hinge recess towards the adjacent corner. Both streamtrace sets then exit the hinge recess from the downstream part of the adjacent

corner, thus yielding the strong out-of-plane component observed throughout systole in Figure 4-5. The local flow reversal observed at the bottom of the hinge recess corresponds to a momentum energy transfer from high to low pressures, from the right side of the leaflet where the forward flow impinges the recess wall, to the left side of the leaflet where flow separation leads to a local depressurization. Figure 4-5 shows that this reverse flow is of low magnitude throughout the forward flow phase and reaches its maximum magnitude at peak systole. The observed flow patterns are persistent throughout systole but vary in intensity with the magnitude of the incoming flow rate. A notable exception to this rule is the lateral corner of the hinge, which is characterized by a streamlined flow pattern at mid-acceleration that becomes unstable after peak systole. Flow deceleration gives rise to flow instabilities, demonstrated by the complex flow patterns and intertwined streamtraces observed in that region at mid-deceleration.

The diastolic phase is unique in its flow features. It is characterized by three-dimensional reverse leakage flows throughout the hinge. Three independent flow structures may be identified, which are depicted with three different colors in Figure 4-4. The blue streamtraces clearly show the fluid diving into the recess from the aortic side of the hinge, flowing underneath the leaflet ear and exiting the recess through the ventricular corner of the hinge. Two leakage jets form on either side of the leaflet ear: the first one, depicted in green in the figure, forms in the ventricular side of the adjacent corner and is characterized by a strong helical structure. The second one, depicted in red, forms in the lateral corner of the hinge and exits the recess with a more streamlined pattern. All three leakage jets exit the hinge recess with a strong out-of-plane motion as shown by the three-dimensional velocity vectors in Figure 4-5.

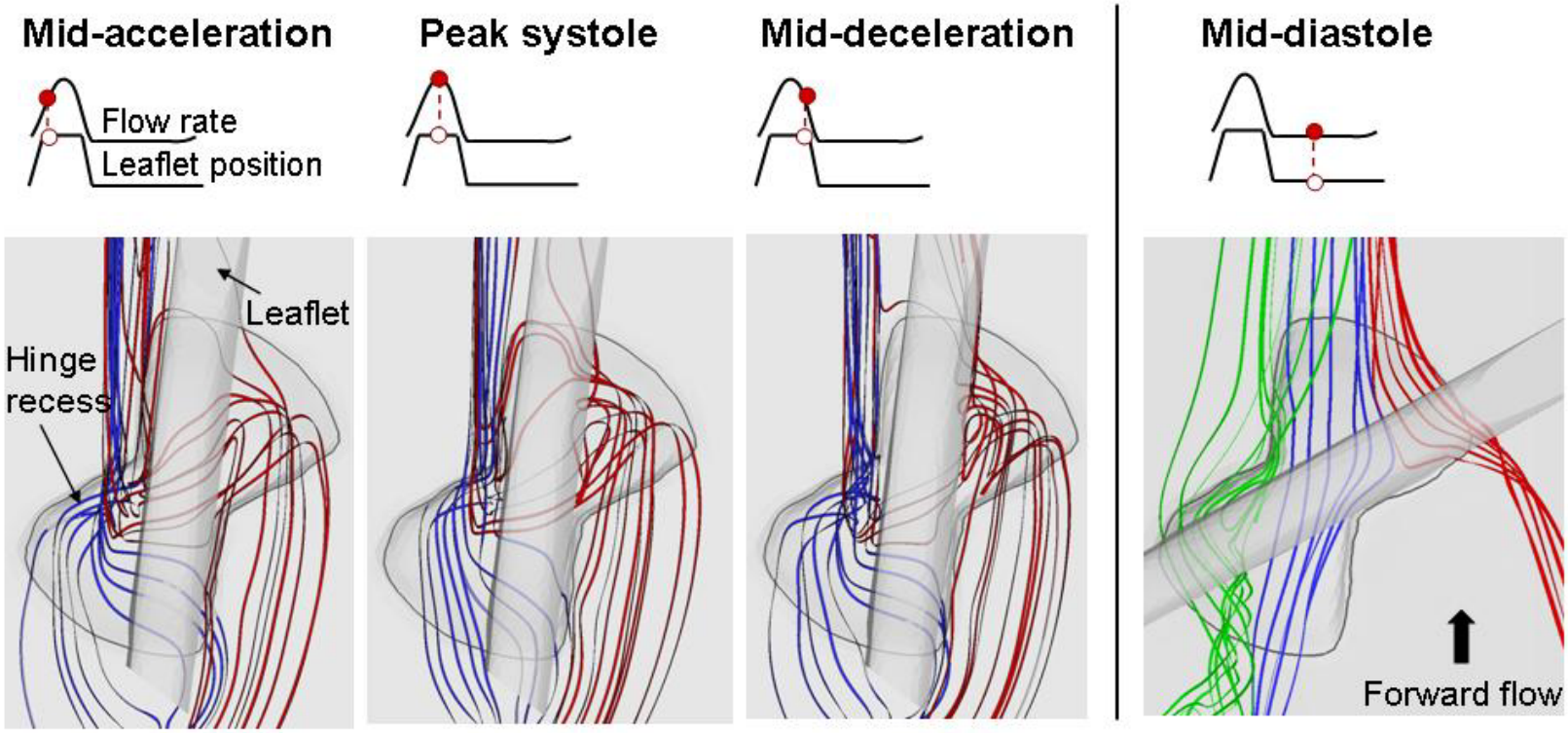

Figure 4-4: Three-dimensional instantaneous streamtraces at four instances of the cardiac cycle.
[SJM hinge design with a regular hinge gap width]

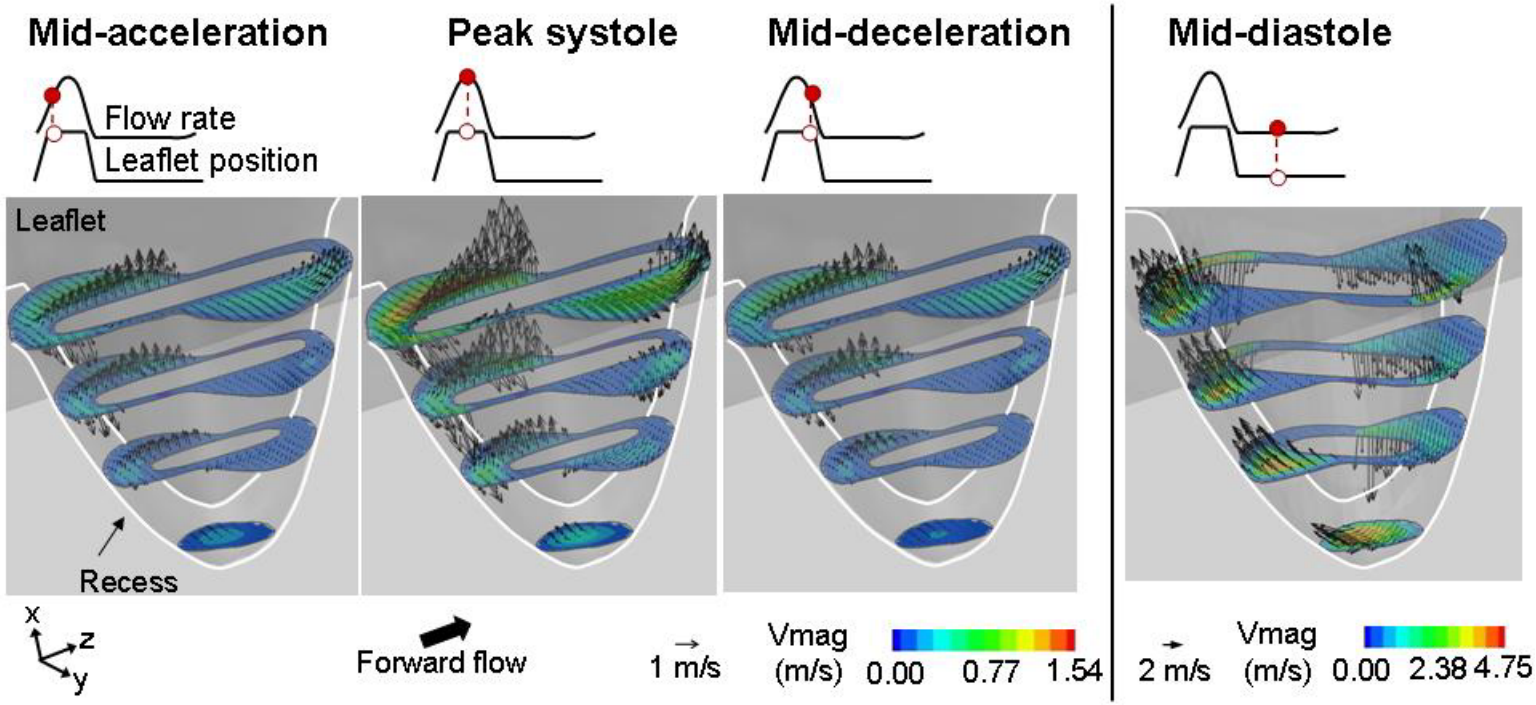

Figure 4-5: Three-dimensional velocity vectors with three dimensional velocity magnitude contour plots along four planes within the hinge recess and at four instances of the cardiac cycle. Note that the x-axis is not to scale and has been stretched to allow visualization of the flow fields [SJM hinge design with a regular hinge gap width]

During the forward flow phase, the velocity magnitudes inside the hinge recess are seen to vary with the cross-valvular flow rate. At peak systole, when the bulk valvular flow rate is at its peak, the velocity magnitude and each individual velocity component reach their maximum for the forward flow phase. However, it is during the leakage flow phase, when the leaflet is in its fully closed position that the velocity magnitude is the highest with a peak within the hinge recess of 4.75 m/s at mid-diastole. It should also be noted that the three-dimensionality of the flow is the most pronounced during the leakage phase as highlighted by the three-dimensional velocity vectors in Figure 4-5. Table 4-1 summarizes the maximum velocity magnitude and the range of velocity components computed within the hinge recess at each of the four depicted instances of the cardiac cycle.

Table 4-1: Maximum velocity magnitude and velocity component range throughout the hinge recess at mid-acceleration, peak systole, mid-deceleration, and mid-diastole [SJM hinge design with a regular hinge gap width]

		SJM hinge with a regular hinge gap width			
		Across entire hinge recess			
		Mid-acceleration	**Peak systole**	**Mid-deceleration**	**Mid-diastole**
Velocity range (m/s)	**u**	[-0.38; 0.31]	[-0.71; 0.71]	[-0.28; 0.34]	[-2.40;2.40]
	v	[-0.31; 0.38]	[-0.51; 0.72]	[-0.22; 0.46]	[-2.20;2.96]
	w	[-0.16; 0.75]	[-0.29; 1.53]	[-0.16; 0.88]	[-4.57; 0.70]
Max. velocity magnitude (m/s)		0.75	1.54	0.89	4.75

To help assess the shear stress distribution in the hinge and near hinge region, Figure 4-6 shows the iso-surfaces of the principal shear stress for the same four instants of time as before. Animations of the iso-surfaces at peak systole and mid-diastole are also provided (SJMReg_Isosurfaces_MidDiastole.mov and SJMReg_Isosurfaces _PeakSystole.mov). As expected from the flow structures observed above, the shear stress distribution is similar at mid-acceleration and mid-deceleration. The iso-surface downstream of the aortic pocket extends further downstream at mid-deceleration, which correlates with the presence of flow instabilities observed in the lateral corner of the hinge during flow deceleration. Similar shear-stress structures are also observed at peak systole, but with higher shear-stress values, due to the overall larger bulk valvular flow rate at this instance of time. For example, shear-stress iso-surfaces of 500 dyn/cm^2 at peak systole closely resemble those observed at mid-deceleration for 250 dyn/cm^2. Similarly, the shear-stress hot-spots identified with the 500 dyn/cm^2 iso-surfaces at mid-acceleration and mid-deceleration are also found in the same loci at peak systole but with threshold values of 1,000 dyn/cm^2. Throughout systole, the highest shear stress levels are thus observed in two main locations: near the downstream edge of the adjacent corner, immediately downstream of the region of flow impingement identified in Figure 4-4; and immediately upstream of the hinge ventricular pocket, where the flow is squeezed between the surface of the flat level and the leaflet surface.

At mid-acceleration and mid-deceleration, it is interesting to note that the hinge recess itself does not contain any 250 dyn/cm^2 iso-surface, indicating that the shear stresses within the hinge recess are lower than 250 dyn/cm^2. At peak systole, an iso-surface of 250 dyn/cm^2 is clearly visible within the hinge recess, underneath the leaflet ear. This iso-surface extends on either side of the open leaflet, clearly demonstrating the flow separation that takes place behind the leaflet. This flow separation is clearly observed throughout the forward flow phase with the 100 dyn/cm^2 iso-surfaces. Overall,

the iso-surfaces during the forward flow phase demonstrate that elevated shear stress levels above the threshold for platelet activation are present but localized in the near-hinge region rather than within the hinge recess.

The shear stress distribution during the leakage phase is drastically different from that observed during systole. As expected, the maximum shear stresses are seen on the wake of the leakage jets emanating from the gap formed by the hinge recess and the closed leaflet. The iso-surfaces at mid-diastole clearly pinpoint three regions associated with elevated shear stresses: the wake of the adjacent leakage jet, the wake of the lateral jet, and the central region of the hinge, underneath the closed leaflet. It is interesting to note that, while only localized regions of shear stress of 1,000 and 1,500 dyn/cm^2 could be identified during systole, large green (1,000 dyn/cm^2) and red (1,500 dyn/cm^2) iso-surfaces are present during diastole. Overall, the maximum shear stresses computed during the forward flow phase are 1.310 dyn/cm^2 and 2,080 dyn/cm^2 in the hinge and near hinge region, respectively. These maxima reach 6,515 and 8,535 dyn/cm^2, respectively during the leakage phase. This indicates that the leakage phase will be more detrimental to blood elements than the forward flow phase.

4.2.2 Detailed description of the hinge flow fields

Gaining further insights into the hemodynamics of the SJM hinge with regular gap width, the following section provides a detailed description of the fluid dynamics over multiple instants of the cardiac cycle. All explanations are supported by the combined use of multiple planar cross-sections and varying plane orientations. However, as for the global hemodynamic overview, the interested reader is referred to the accompanying animations (SJMReg_2Dvectors_Vmag.mov and SJMReg_2Dvectors_Vo-p.mov at

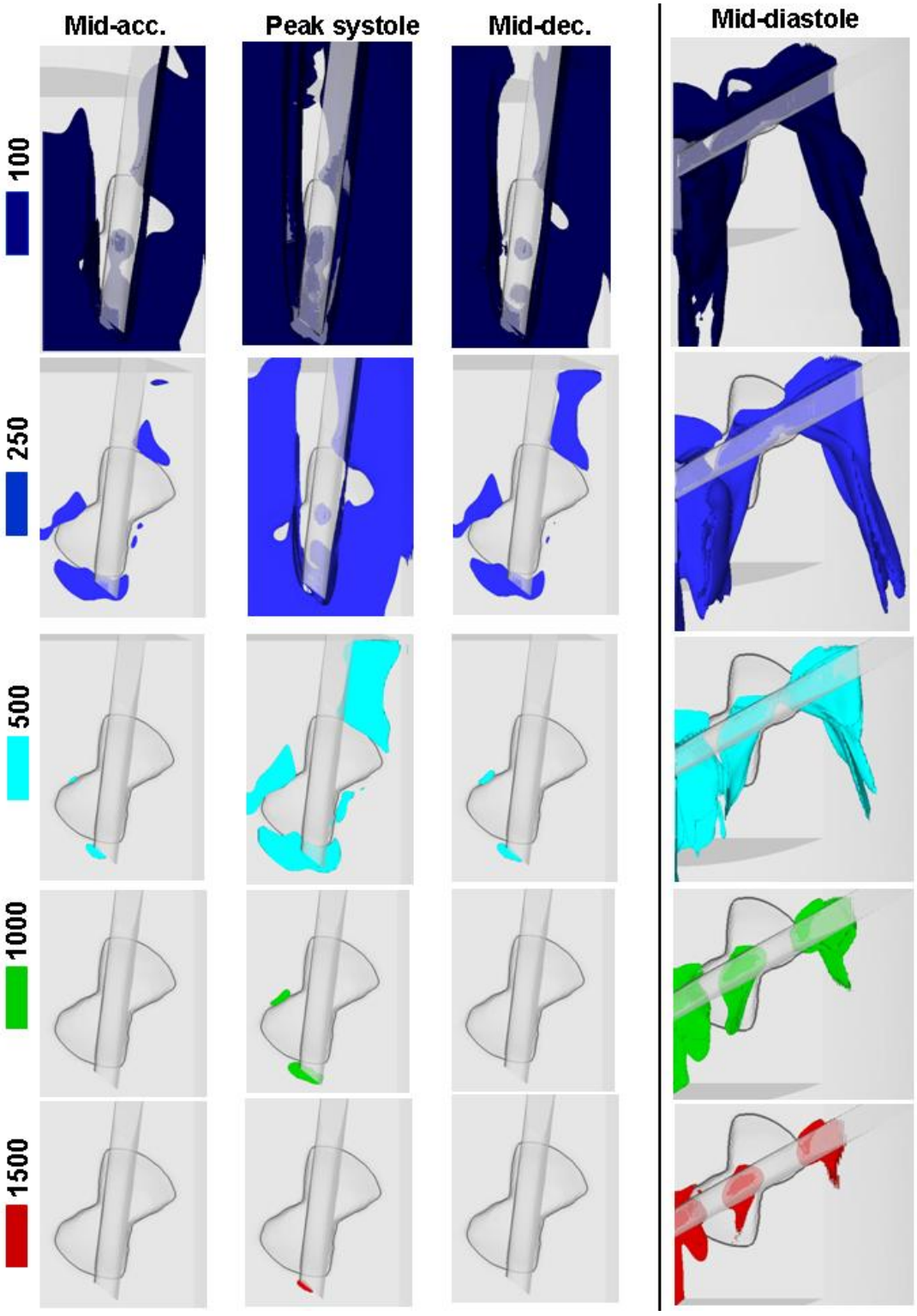

Figure 4-6: Iso-surfaces of shear stress levels at mid-acceleration, peak systole, mid-deceleration and mid-diastole. All shear stress levels are expressed in dyn/cm^2. [SJM hinge design with a regular hinge gap width]

different levels within the hinge recess) to better visualize the dynamics of the described flow structures.

Leaflet opening phase

Figure 4-7 and Figure 4-8 show the hinge flow fields at four instances of the leaflet opening, spanning from 20 ms to 88 ms into systole. Figure 4-7 places a special emphasis on the flat level, while Figure 4-8 shows these flow structures deeper into the hinge at 195, 390 and 585 μm below the flat level. The flow events depicted herein occur before the mid-acceleration phase described in the general overview. The flow features during the leaflet opening phase are strongly impacted by the motion of the leaflet that entrains fluid in its wake. As will be seen further along this subsection, when the leaflet reaches its fully opened position, the transient hinge flow structures reach a configuration that closely resembles that observed throughout the fully-open phase.

The leaflet opening motion is a rapid short-spanned event in the cardiac cycle. The dynamics prescribed in these simulations were obtained from large-scale fluid structure interactions that were deemed realistic because of good agreement with experimental measurements. The leaflet reaches its fully open position in 88 ms for a cardiac cycle duration of 860 ms. When the leaflet is still in the near-fully closed position (20ms), the flow goes around the surface of the closed leaflet and squeezes between the leaflet and the hinge recess wall. Flow structures at this instant of time, somewhat resemble those observed during the leakage phase, but with the opposite flow direction. Two forward flow jets of small magnitude are observed in the adjacent and lateral corners of the hinge. The maximum velocity magnitudes in these corners at the flat level are 0.43 m/s and 0.31 m/s, respectively, and the extremum out-of-plane u-velocity

components are 0.22 m/s and -0.23 m/s, respectively. At deeper levels within the hinge recess, a forward flow going around the leaflet is visible.

As the valve opens (42 ms), a strong forward flow pattern develops at the flat level in the ventricular and lateral corners of the hinge (on the right-hand side of the leaflet in Figure 4-7). The velocity magnitude in the lateral corner reaches 0.20 m/s at the flat level. As can be observed from Figure 4-8, this forward flow pattern is observed even at deeper levels into the hinge. While the flow direction at the flat level seems to be mainly dictated by the leaflet surface, flow vectors at deeper levels are seen to be oriented toward the aortic corner of the hinge as the flow follows the curvature of the hinge recess. In contrast to the fast-paced flow structures observed on the right-hand side of the leaflet, flow structures in the adjacent and aortic corners (i.e., on the left hand-side of the leaflet) display far smaller velocity magnitudes. These lower velocities testify to the flow separation that occurs behind the leaflet. As the flow impinges on the upstream edge of the leaflet surface on the ventricular pocket, it splits between the right and left sides of the leaflet. Due to the angle formed between the leaflet and the main flow direction, this leads to the formation of a large separation region behind the leaflet. Due to the ensuing depressurization, the flow that impinges the leaflet in the ventricular pocket of the hinge, dives under the leaflet and is redirected toward the adjacent corner. This is evidenced by the localized jet that is visible near the leaflet edge at the flat level (Figure 4-7, 42ms). In this region, the maximum velocity magnitude and out-of-plane component at the flat level are 0.23 m/s and -0.12 m/s, respectively. This jet is also identified at deeper levels in the adjacent corner.

At 57 ms, the leaflet has reached 65% of its opening. In the ventricular pocket of the hinge, the jet that forms due to the collision of the flow with the leaflet is still visible and leads to the formation of a clockwise recirculating flow in the adjacent corner as the flow impinges on the recess wall. This recirculating pattern develops throughout the

opening phase and is best seen at 88 ms when the leaflet is in its fully open position. At this instance of time, the velocity magnitude in the adjacent corner reaches 0.58 m/s. A region of elevated out-of-plane flow motion, with a maximum out-of-plane u-velocity component of 0.21 m/s is visible near the downstream-most wall of the adjacent corner. The lateral corner of the hinge is characterized by a forward flow pattern with a velocity magnitude up 0.41 m/s.

At the bottom of the hinge recess (585 μm below the flat level in Figure 4-8), the complete opening of the leaflet induces a reversal in flow direction. This change of flow direction is clearly seen in Figure 4-9, which shows in-plane velocity vectors along the hinge central plane. The strong forward flow pattern visible at 20 ms decreases in strength and reverses direction. As the leaflet reaches its fully open position (88 ms), a reversed flow of low magnitude may be identified throughout the 585 μm-level. At early systole (20 ms), the magnitude of the forward flow pattern is 0.34 m/s. At the end of the opening phase, the magnitude of the observed reverse flow pattern decreases to only 0.11 m/s.

Fully-open leaflet phase

Figure 4-10, Figure 4-11, and Figure 4-12 show the flow fields within the hinge recess during the fully-open leaflet phase. As was seen in the flow structure overview provided in section 4.2.1, flow structures during the fully-opened phase (spanning from 88ms to 330 ms) are fairly self-similar; the main difference from one instant to the next being that the velocity magnitudes scale with the magnitude of the bulk valvular flow rate. In addition, the de-stabilizing effect of flow deceleration gives rise to distinctive regions of flow instabilities in the later part of systole, especially in the lateral corner of the hinge. With these observations in mind, this section provides a thorough description

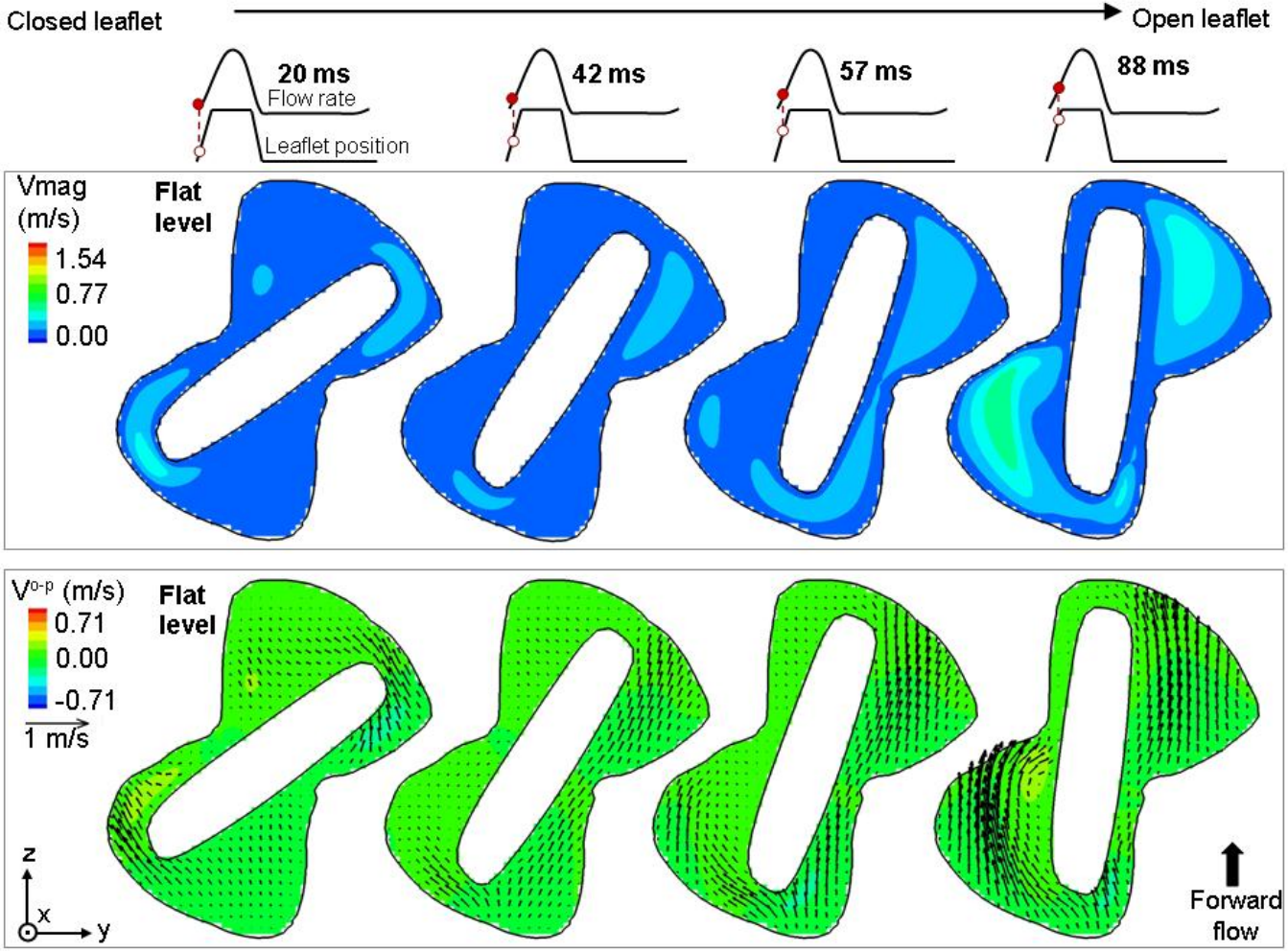

Figure 4-7: Three-dimensional velocity magnitude (top row) and two-dimensional in-plane velocity vectors with out-of-plane velocity contours (bottom row) at the flat level at four instances of the opening phase.
[SJM hinge design with a regular hinge gap width]

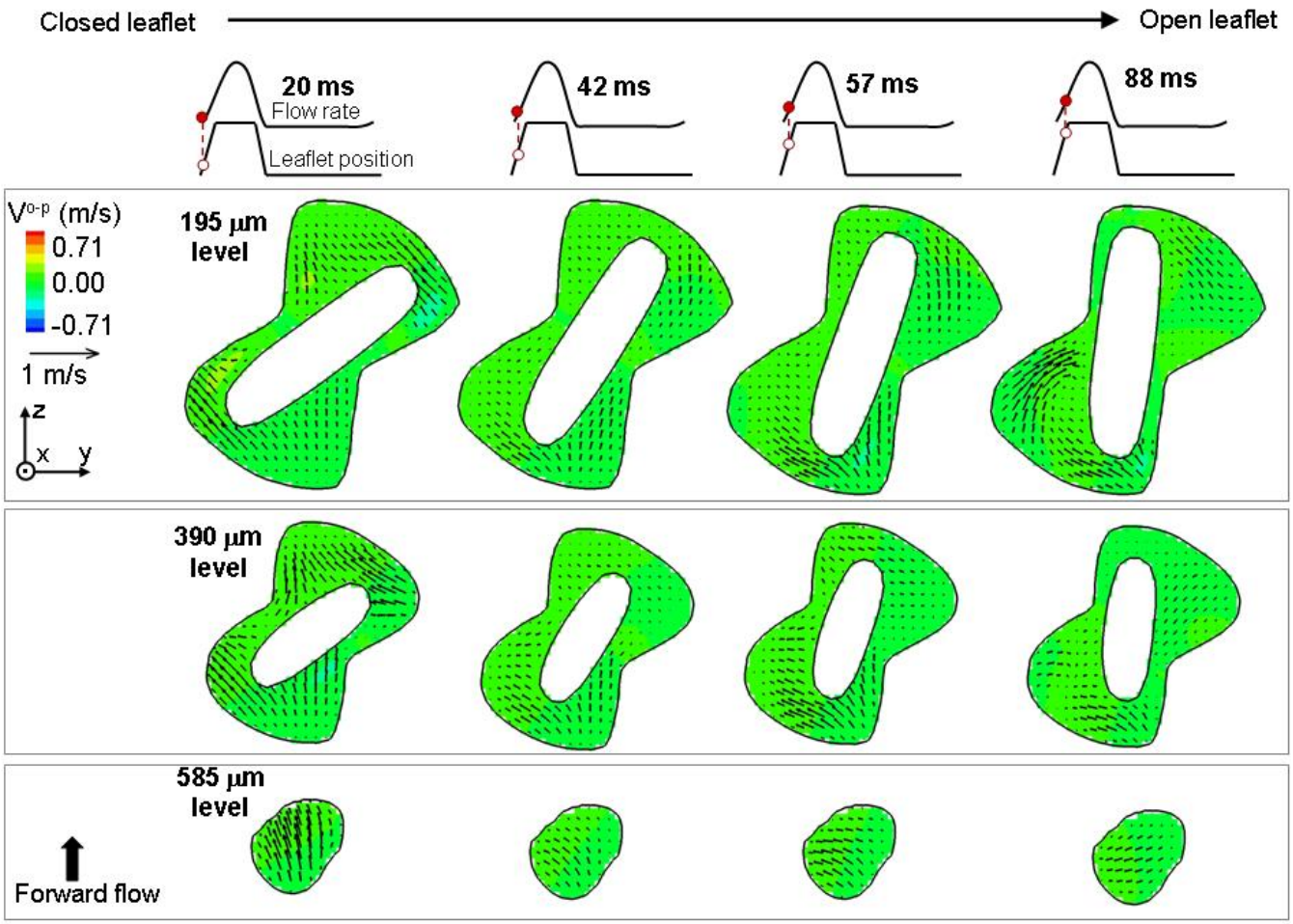

Figure 4-8: Two-dimensional in-plane velocity vectors with out-of-plane velocity contours at 195 μm, 390 μm, and 585 μm below the flat level during the leaflet opening phase. [SJM hinge design with a regular hinge gap width]

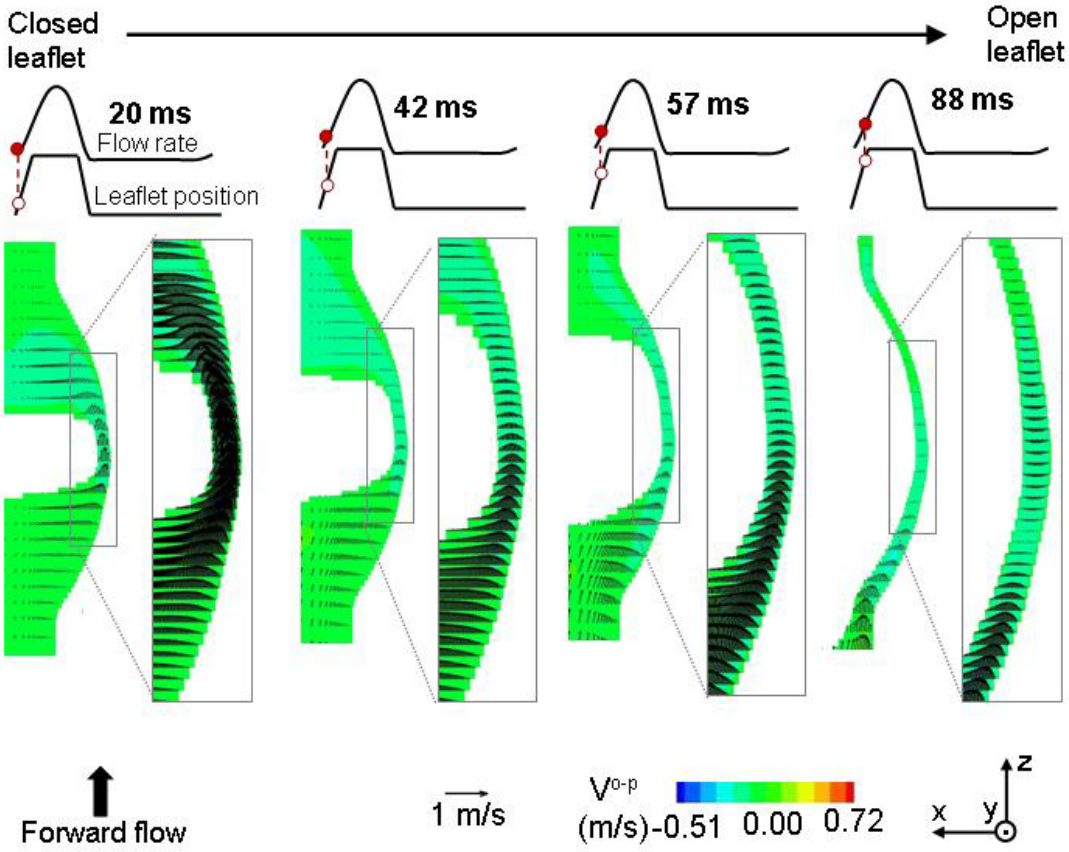

Figure 4-9: Two-dimensional in-plane velocity vectors with out-of-plane velocity contours along the central plane of the hinge recess during the leaflet opening phase. [SJM hinge design with a regular hinge gap width]

of the hinge flow structures at three instances of the fully-open phase (namely mid-acceleration, peak systole, and mid-deceleration) all together. Emphasis will be placed on specific differences observed between the three depicted instances.

The three-dimensional streamtraces depicted in Figure 4-4 from mid-acceleration to mid-deceleration show that the flow entering the hinge recess through the ventricular corner dives inside the hinge recess towards the adjacent (left) corner as it as it impinges the upstream edge of the leaflet. This flow pattern is visible in Figure 4-10 and Figure 4-11 where a region of elevated out-of-plane motion is present immediately upstream of the open leaflet. The out-of-plane u-velocity component at the flat level in

this region reaches up to -0.45 m/s, -0.29 m/s and -0.22 m/s at peak systole, mid-acceleration, and mid-deceleration, respectively.

As the flow dives inside the hinge recess towards the adjacent corner, it impinges on the wall of the corner and exits the recess in the downstream-most tip of the adjacent corner, as shown by the blue streamtraces in Figure 4-4. The impingement of the flow on the recess wall yields to the formation of a clockwise rotating flow pattern with elevated out-of-plane motion, that appears at the end of the opening phase (Figure 4-7 and Figure 4-8) and persists throughout the fully-open leaflet phase (Figure 4-10 and Figure 4-11). This flow pattern, which is clearly visible at the 195 μm-level shown in Figure 4-11 and in animation SJMReg_2Dvectors_Vmag_195micron.mov, is best seen when considering the vorticity field. Figure 4-13 shows the out-of-plane vorticity distribution within the hinge recess at peak systole. The clockwise rotating structure identified in Figure 4-11 is depicted by the blue area seen in the adjacent corner of the hinge at the 195 μm-level. The streamtraces in this region exits the hinge recess with a large out-of-plane component (Figure 4-4). This is further confirmed by the out-of-plane velocity distribution where the u-velocity component in this region reaches up to 0.71 m/s at the flat level at peak systole.

The streamtraces presented in Figure 4-4 underscore the presence of a reverse flow developing in the lateral corner of the hinge and extending to the bottom of the hinge recess towards the adjacent corner. This translates, near the recess surface, into a forward flow pattern with a strong axial velocity component that dives into the hinge recess near the downstream wall of the lateral corner of the hinge. At the flat level of the lateral corner, the maximum velocity magnitude is 1.02 m/s and the peak out-of-plane u-velocity -0.16 m/s at peak systole. At deeper levels within the hinge recess (390 μm-level shown in Figure 4-12), the reverse flow identified with the streamtraces is evident.

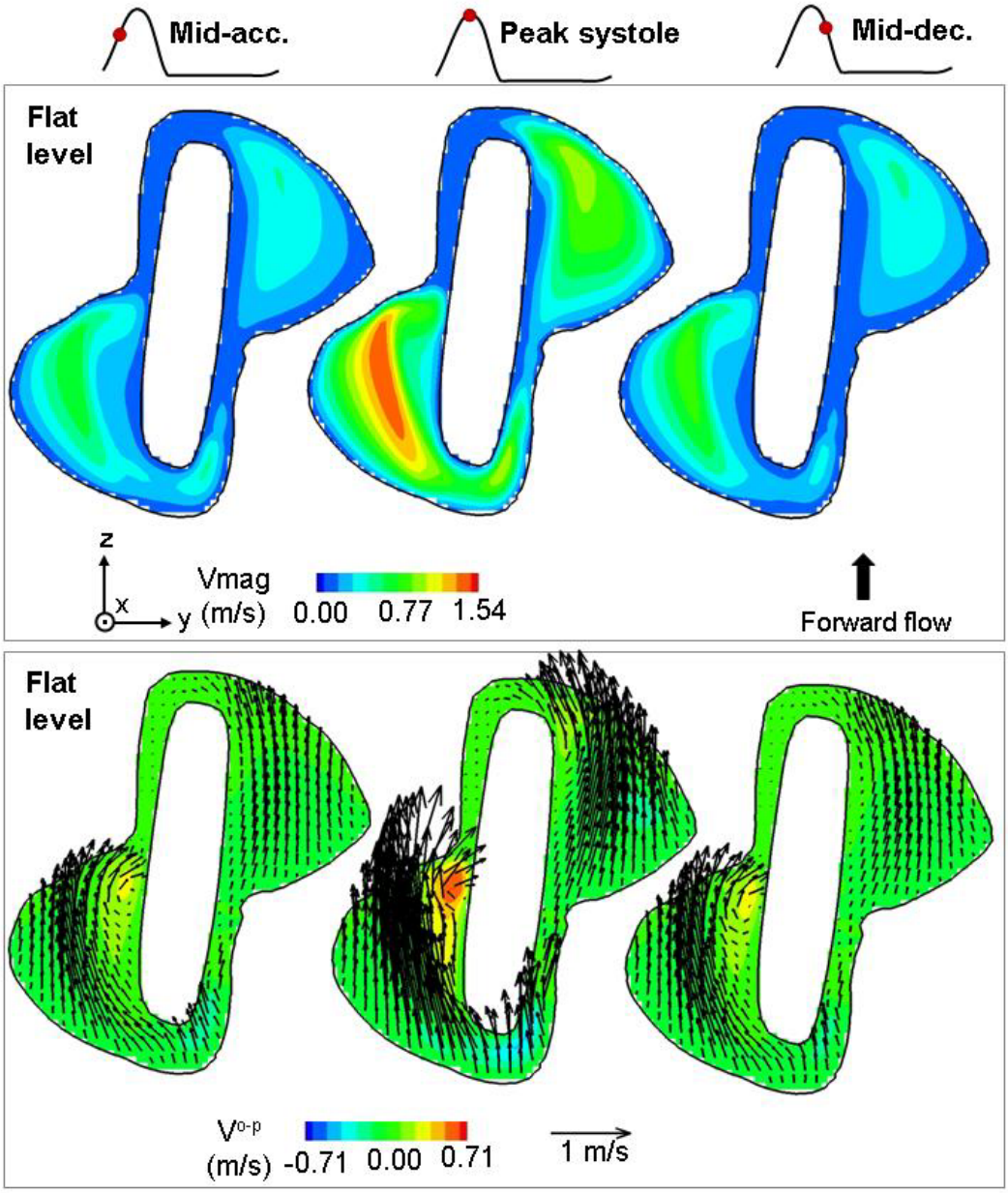

Figure 4-10: Three-dimensional velocity magnitude (top row) and two-dimensional in-plane velocity vectors with out-of-plane velocity contours (bottom row) at three instances of the fully-open leaflet phase at the flat level.
[SJM hinge design with a regular hinge gap width]

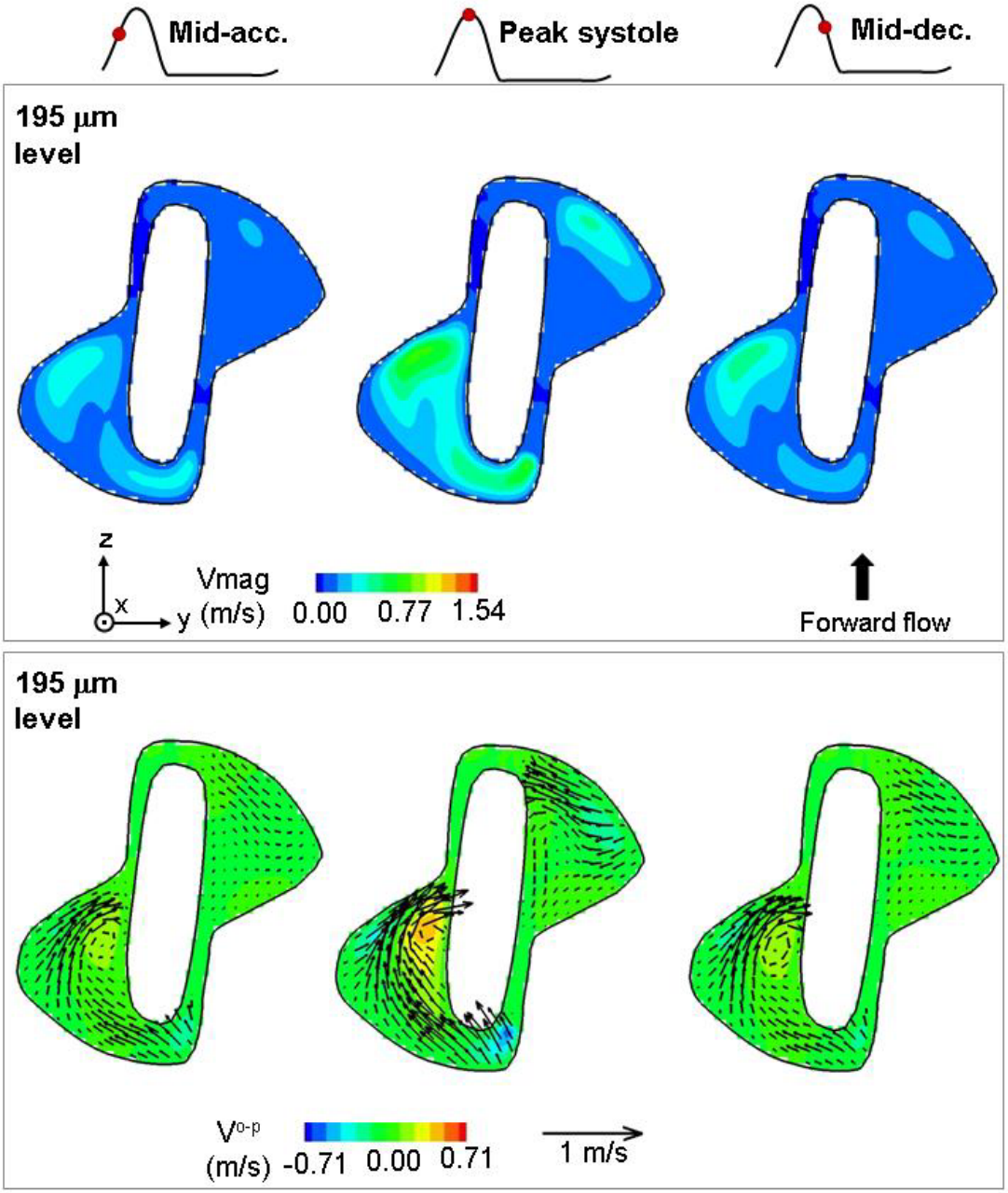

Figure 4-11: Three-dimensional velocity magnitude (top row) and two-dimensional in-plane velocity vectors with out-of-plane velocity contours (bottom row) at three instances of the fully-open leaflet phase along the plane located 195 μm below the flat level. [SJM hinge design with a regular hinge gap width]

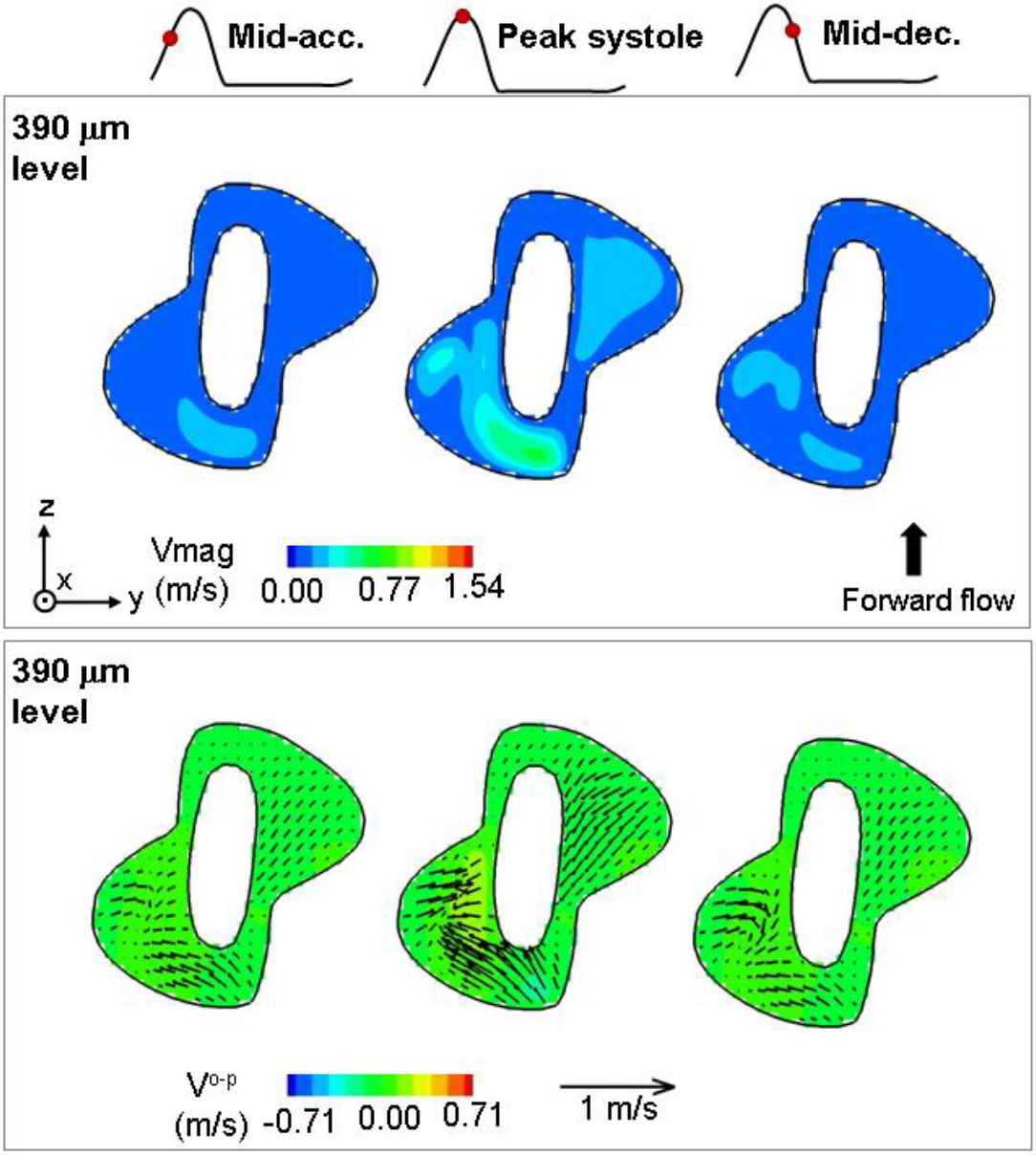

Figure 4-12: Three-dimensional velocity magnitude (top row) and two-dimensional in-plane velocity vectors with out-of-plane velocity contours (bottom row) at three instances of the fully-open leaflet phase along the plane located 390 μm below the flat level. [SJM hinge design with a regular hinge gap width]

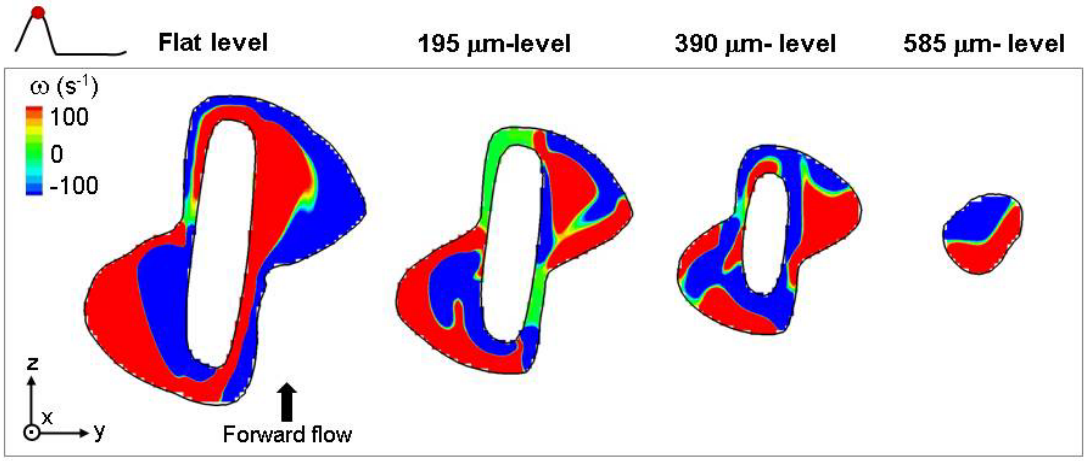

Figure 4-13: Out-of-plane vorticity contours along four planes parallel to the flat level at peak systole. [SJM hinge design with a regular hinge gap width]

It is interesting to note that, at the intermediate level (195 μm-level in Figure 4-11), the velocity vector distribution slightly differs at mid-acceleration, peak systole and mid-deceleration. At peak systole, the fluid along the downstream wall of the lateral corner collides with the leaflet and then flows back along the leaflet surface in the direction of the ventricular pocket of the hinge. This induces the formation of a slow counter-clockwise rotating flow structure. This flow structure, evident at peak systole, is also visible at mid-deceleration, but does not exist at mid-acceleration. This correlates with the streamtraces shown in Figure 4-4, which reveal the presence of a streamlined flow in the lateral corner at mid-acceleration and a more complex flow pattern at peak systole and mid-deceleration.

Cross-sectional views through the adjacent and lateral corners of the hinge help to explain the flow patterns observed inside the hinge region during systole. Figure 4-14 shows the flow patterns along the adjacent, central and lateral planes at peak systole. The two-dimensional velocity vector fields along the adjacent plane show a forward flow pattern throughout the adjacent corner with the largest flow magnitude seen near the flat

level. This flow pattern is in agreement with the streamtraces shown in Figure 4-4 that show a streamline flow pattern in the adjacent corner. The downstream region of the adjacent corner, as the flow impinges on the recess wall and is redirected towards the lateral side of the hinge, is associated with large out-of-plane v-velocity components up to 0.53 m/s. The lateral plane, on the other hand, shows a more complex flow pattern, characterized by a clockwise rotating structure. This rotating flow pattern may be attributed to the detachment of the main flow from the flat level, which induces a small recirculation region in the recess. The formation of such a structure is expected as the hinge geometry here resembles that of a backward-facing step. This specific flow structure is particularly visible in the vorticity contour plots at the lateral plane, where a region of positive vorticity, shown in red, is present along the wall of the lateral corner and corresponds to the region of reverse flow.

As previously underscored by the instantaneous 3D streamtraces shown in Figure 4-4 and despite the significant forward flow pattern present outside of the hinge recess during the forward flow phase, a reverse flow phenomenon is seen at the deepest level within the hinge recess through the gap formed by the leaflet ear and the recess wall. The two-dimensional velocity vectors along the central plane of the hinge indicate that this reverse flow has a nearly-parabolic profile and a large out-of-plane velocity component (extremum up to -0.38 m/s) (Figure 4-15). This reverse flow pattern underneath the leaflet ear is also visible in the out-of-plane vorticity contours displayed along the central plane of the hinge (Figure 4-14). It should also be noted that, because of the position of the fully-open leaflet within the hinge recess wall, no fluid may flow between the leaflet surface and the recess wall in the aortic pocket of the hinge. This is seen in the vorticity contour plot shown along the central plane of the hinge where a region of zero-vorticity is present immediately downstream of the region associated with the flow reversal.

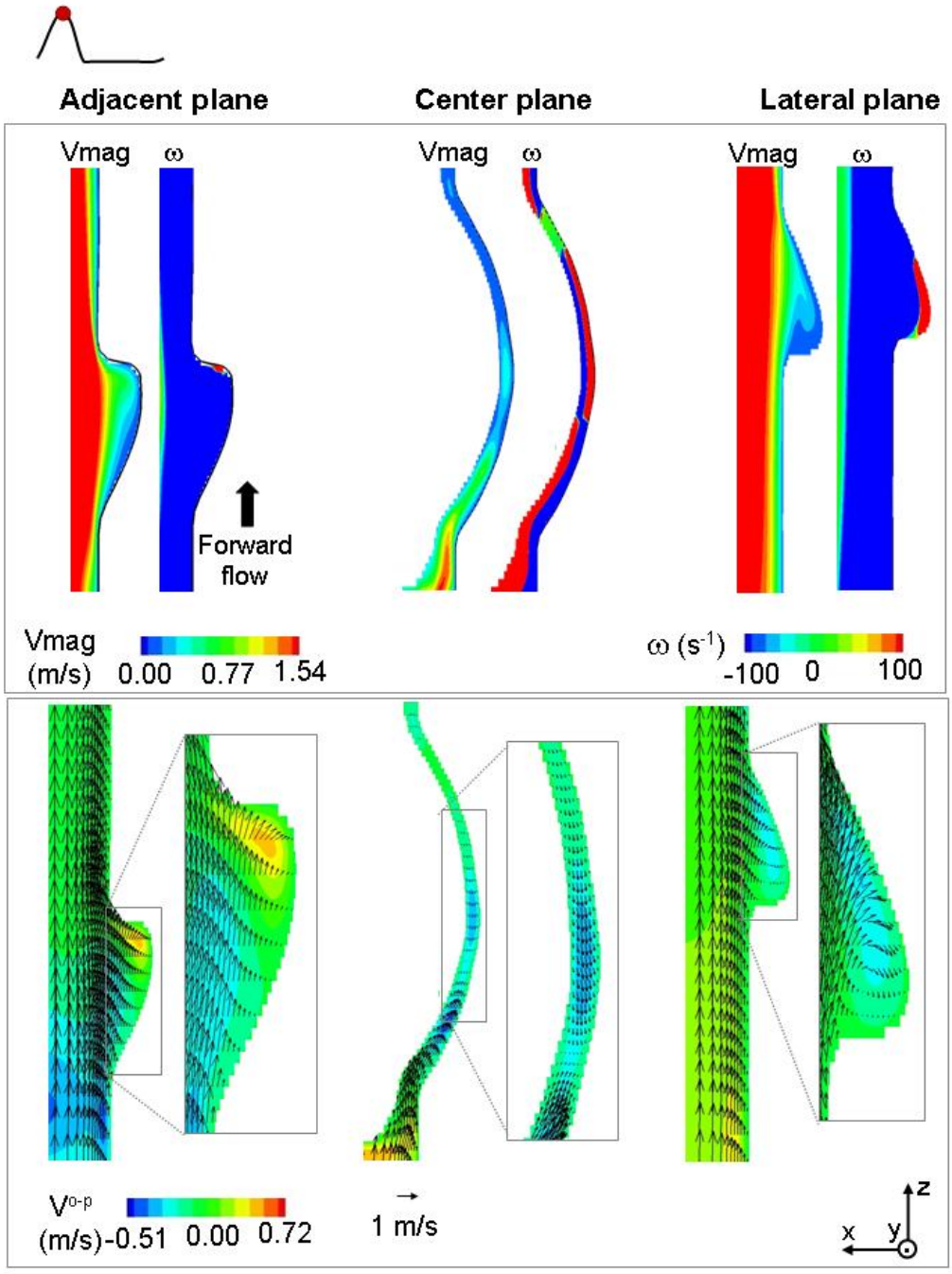

Figure 4-14: Cross-sectional views of the hinge recess at peak systole. Three-dimensional velocity magnitude and out-of-plane vorticity contours are shown on the top row. The bottom row displays the two-dimensional in-plane velocity vectors superimposed on the out-of-plane velocity contours.
[SJM hinge design with a regular hinge gap width]

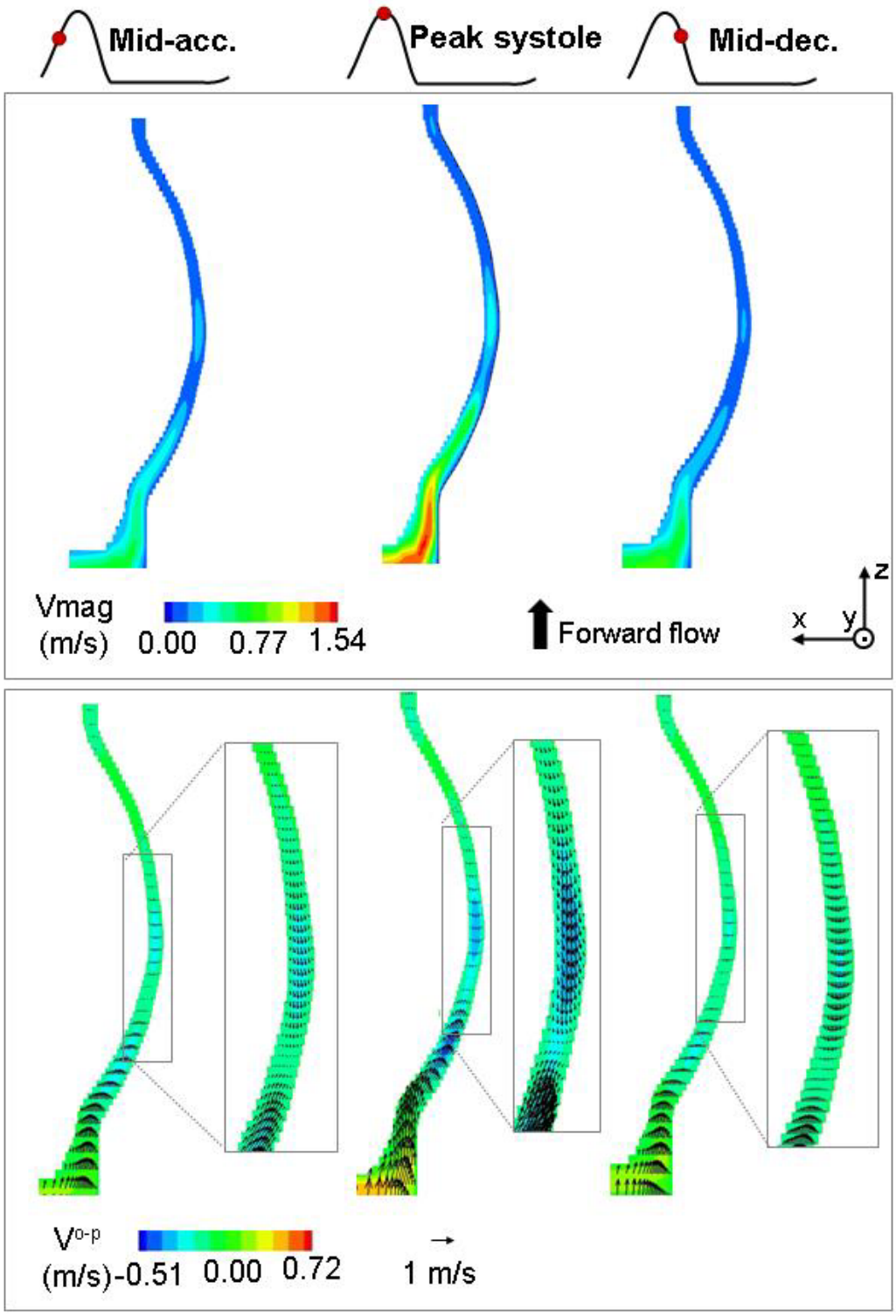

Figure 4-15: Three-dimensional velocity magnitude (top row) and two-dimensional in-plane velocity vectors with out-of-plane velocity contours (bottom row) along the central plane of the hinge at mid-acceleration, peak systole and mid-deceleration.
[SJM hinge design with a regular hinge gap width]

The flow structures within the hinge recess are overall similar throughout the fully-open phase, except in the lateral corner of the hinge, where the destabilizing effect of the decelerating flow leads to a less streamlined flow compared to mid-acceleration. The velocities on the other hand are seen to vary during the fully-open phase and depend upon the cross-valvular flow rate. During the acceleration and deceleration phases, the maximum velocity magnitudes within the hinge recess do not exceed 0.75 m/s and 0.88 m/s**,** respectively, while at peak systole, they reach a peak of 1.54 m/s and 1.02 m/s in the ventricular pocket and the aortic pocket, respectively. This global increase in flow rate toward peak systole also translates into a higher three-dimensionality of the flow within the hinge recess (Table 4-1).

The maximum velocity magnitude of the reversed flow identified at the bottom of the hinge recess is 0.41 m/s at peak systole and 0.22 m/s during the acceleration and deceleration phases. Moreover, comparison of the velocity magnitude contour plots at the different levels within the hinge recess (Figure 4-10, Figure 4-11, and Figure 4-12) highlights that the maximum velocity magnitudes vary as expected with the position within the hinge recess, the velocity magnitude being the lowest at the deepest level. It also reveals that the ventricular pocket of the hinge is consistently associated with stronger flow and larger velocity magnitude than the aortic pocket.

Leaflet closing phase

The flow events depicted here occur during the leaflet closing phase, that is, after the mid-deceleration phase but before the mid-diastole phase described in the general overview. Figure 4-16 and Figure 4-17 show the hinge flow fields at three instances of the leaflet closing phase, from 348 ms to 382 ms into systole. Figure 4-16 focuses on the flat level while Figure 4-17 presents the flow structures deeper into the hinge recess.

The leaflet closing is more abrupt and rapid than the opening as the leaflet moves from its fully-open to fully-closed position in only 55 ms, from 330 ms to 385 ms into the cardiac cycle. This motion, combined with the decelerating flow rate through the valve, has a strong impact on the hinge flow features.

At the onset of the leaflet closing phase (348 ms), the flow has already reversed throughout the hinge recess. The magnitude of this reverse flow, clearly visible in the lateral and adjacent corners, is the largest at the flat level and lowers at deeper levels within the hinge. As the leaflet closes further (372ms), the reverse flow in the adjacent and lateral corners of the hinge starts to accelerate but the velocity magnitude remains low with a maximum of less than 0.11 m/s at the flat level.

At the end of the leaflet closing phase (382 ms), the leaflet has nearly reached its fully closed position. The reverse flow is seen to squeeze between the leaflet and the recess wall. This yields the formation of two leakage jets, one in the adjacent corner and another in the lateral corner. The maximum velocity magnitudes are obtained in these jets, with a peak at the flat level of 0.36 m/s and 0.31 m/s in the aortic and lateral corners, respectively. Despite the increase in velocity magnitude, the out-of-plane motion at the flat level at this instant remains low. The extremum out-of-plane u-velocity components in the aortic and ventricular pockets are 0.27 m/s and -0.14 m/s, respectively. While the flow distribution appears to be similar at the flat level, the 195 μm- and the 390 μm-levels, the velocity magnitude is the largest at the flat level. At 382 ms, the maximum velocity magnitudes at the flat level, 195, and 390 below the flat level are 0.36 m/s, 0.34 m/s, and 0.33 m/s, respectively. It is interesting to note that the effect of the leaflet motion is clearly visible at this instant of time in the ventricular and aortic corners: the flow has an overall clockwise orientation, which corresponds to the clockwise rotating movement of the leaflet. This is particularly evident at the flat level (Figure 4-16).

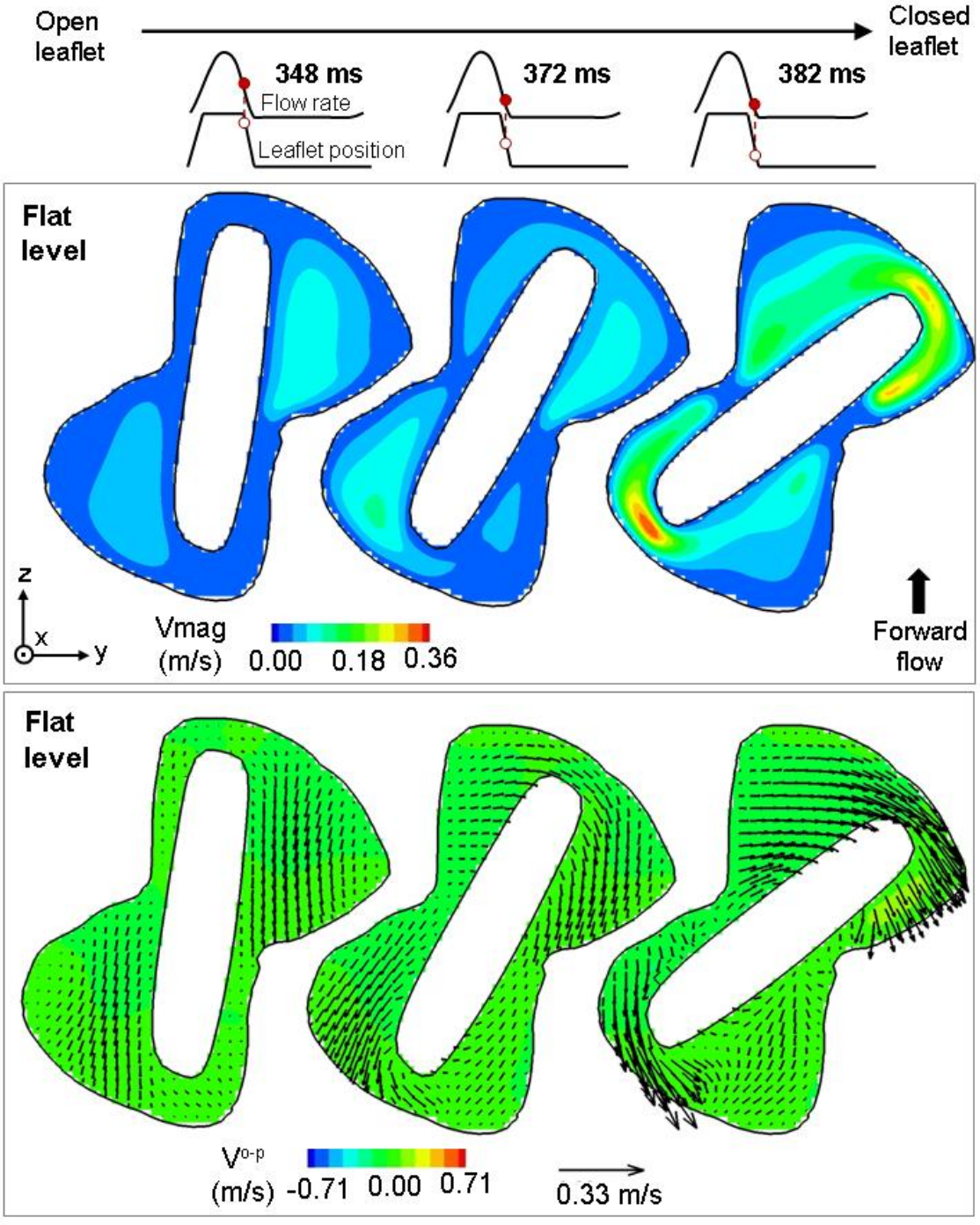

Figure 4-16: Three-dimensional velocity magnitude (top row) and two-dimensional in-plane velocity vectors with out-of-plane velocity contours (bottom row) at the flat level during the leaflet closing phase. [SJM hinge design with a regular hinge gap width]

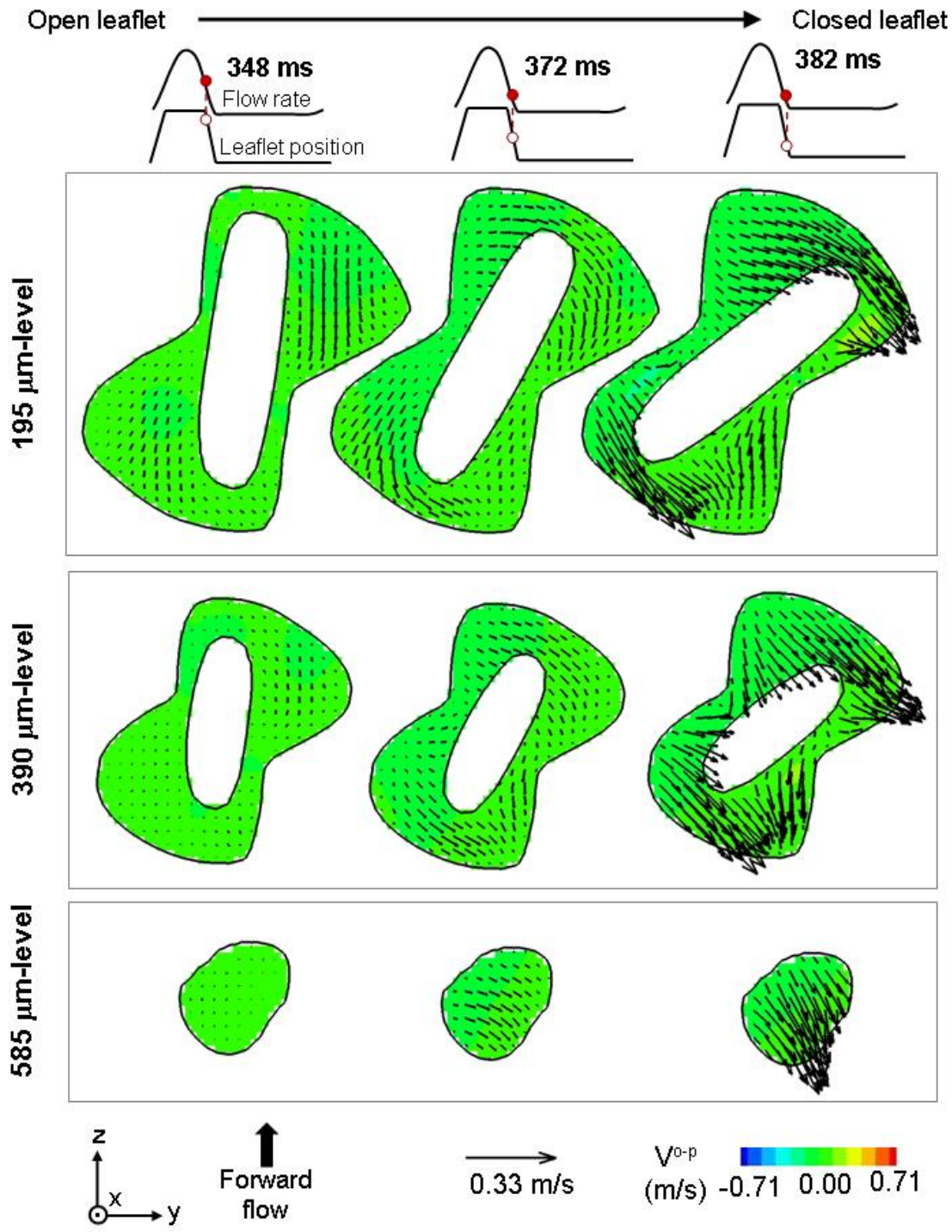

Figure 4-17: Two-dimensional in-plane velocity vectors with out-of-plane velocity contours at 195 μm, 390 μm, and 585 μm below the flat level during the leaflet closing phase. [SJM hinge design with a regular hinge gap width]

At the end of the leaflet closing phase, the flow vector distribution at the bottom of the hinge recess (585 μm-level in Figure 4-17) indicates that the leakage flow extends throughout the hinge. A cross-sectional view through the hinge central plane at this instance of time (Figure 4-18) shows a leakage flow with a parabolic-like profile developing in the gap formed by the closing leaflet and the hinge recess wall. Along the hinge central plane, the maximum velocity magnitude and out-of-plane v-velocity component are 0.30 m/s and 0.12 m/s, respectively, in the leaflet-recess gap.

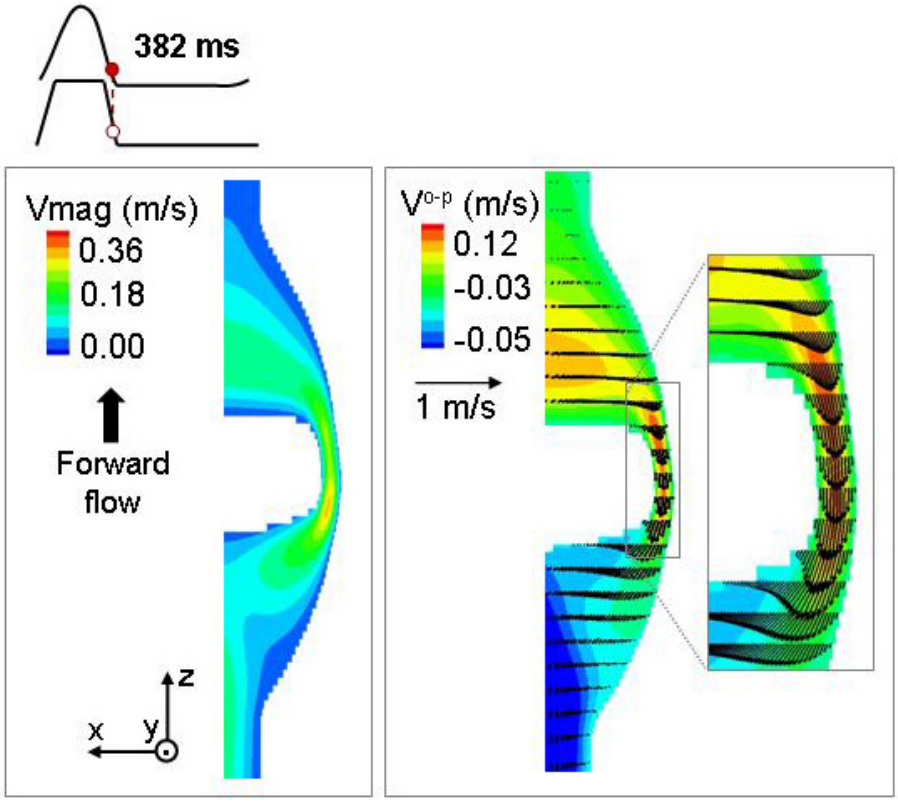

Figure 4-18: Three-dimensional velocity magnitude (left) and two-dimensional in-plane velocity vectors with out-of-plane velocity contours (right) through the hinge central plane at late systole (382 ms). [SJM hinge design with a regular hinge gap width]

Fully-closed leaflet phase

The leaflet reaches its fully closed position at 385 ms within the cardiac cycle. However, this particular instant in time when valve closure occurs can not be captured by the undertaken modeling approach. In this study, this instant is modeled by prescribing the leaflet kinematics from the large-scale fluid-structure interaction simulations, while pressure and flow smoothly transition towards their diastolic value. In reality, at this instance of time, the closing of the leaflets yields a sudden pressure build up, which would require a full two-way coupling between the large-scale and the hinge solvers to synchronize leaflet kinematics and the local hemodynamics. This limitation is addressed in detail in the discussion section.

The result presented here focuses on the phase after valve closure, when the leaflet is in its fully closed position and a constant leakage flow is leaking through the closed valve. At this instant in time, the configuration of the flow structures within the hinge recess resembles that observed at the end of the leaflet closing phase but with increased velocity magnitude: a fast-paced reverse flow is present throughout the recess and the two leakage jets identified in the lateral and adjacent corners of the hinge are still present but have gained in strength. A third leakage jet, not visible at the end of the closing phase, is observed in the ventricular corner of the hinge.

To best visualize this complex leakage flow pattern, Figure 4-19 shows the three-dimensional velocity magnitude and the two-dimensional velocity vectors superimposed on the out-of-plane velocity component contours along four planes within the hinge recess. As the flow goes around the leaflet ear, it squeezes between the leaflet edge and the housing surface and accelerates. This leads to the formation of two main leakage jets on either side of the leaflet. These two leakage jets (not shown) flow outside of the hinge recess through the gap formed by the leaflet and the housing. A close

inspection of the hinge recess (Figure 4-19) reveals that in the adjacent corner the flow dives inside the recess on the ventricular side of the leaflet and exits the hinge through the ventricular corner. Further on the left side of the adjacent corner, a flow with less out-of-plane motion is identified as the flow goes underneath the leaflet ear but without diving to the bottom of the hinge recess. This correlates with the trajectories of the green streamtraces (Figure 4-4) that show a complex flow pattern in the adjacent corner of the hinge. On the lateral corner on the other hand, the velocity vector distribution clearly indicate a strong jet with a large out-of-plane motion emanating from the hinge recess. This jet corresponds to the leakage flow pattern identified by the red streamtraces (Figure 4-4), where the flow is seen to dive in the recess in the aortic corner and exit the hinge through the tip of the lateral corner. In this tip, the out-of-plane u-velocity component reaches 2.41 m/s. The identified leakage flow patterns in the lateral and adjacent corner of the hinge are best seen at the flat level and the 195 μm-level (Figure 4-19). The velocity magnitude distribution at the flat level clearly shows that the adjacent flow is stronger than the lateral jet, with a maximum velocity magnitude at this level of 4.61 m/s and 3.96 m/s, respectively. Additionally these jets appear to be primarily oriented towards the lateral side (right side) of the hinge recess (flat level and 195 μm-level in Figure 4-19). These leakage jets can be identified in the out-of-plane vorticity contour plot shown in Figure 4-20, where the juxtaposed layers of negative and positive vorticity in the adjacent and lateral corners at the flat level and the 195 μm-level are characteristic of flow jets.

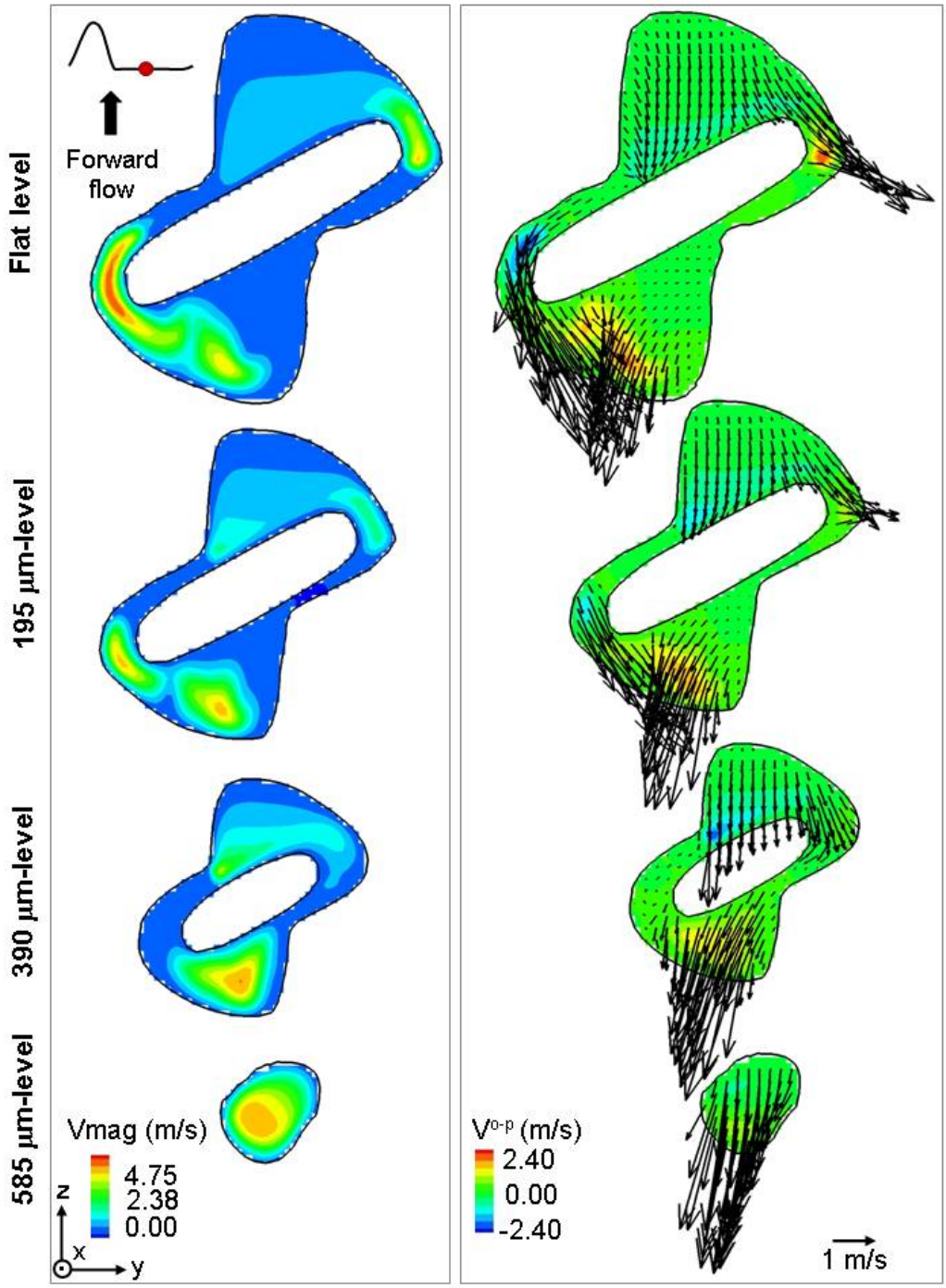

Figure 4-19: Two-dimensional in-plane velocity vectors with out-of-plane velocity contours at the flat level, 195 µm, 390 µm, and 585 µm below the flat level at mid-diastole. [SJM hinge design with a regular hinge gap width]

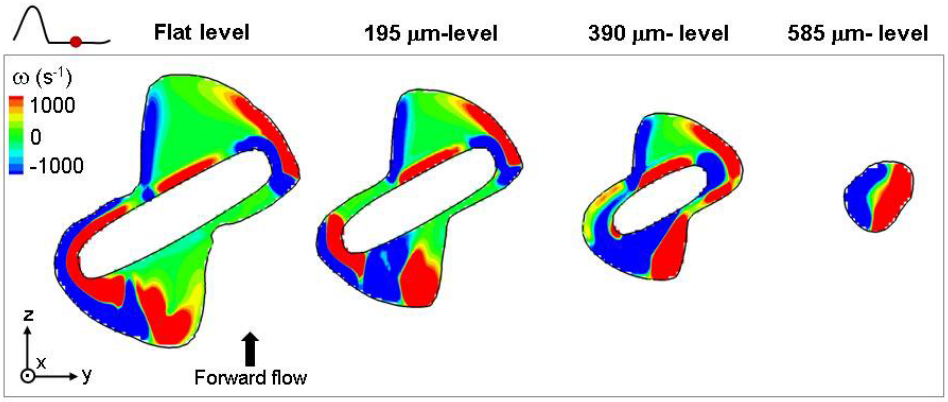

Figure 4-20: Out-of-plane vorticity contours along four planes parallel to the flat level at mid-diastole. [SJM hinge design with a regular hinge gap width]

The vorticity distribution in the ventricular corner of the hinge suggests the existence of an additional leakage jet. This ventricular jet is best seen in Figure 4-19 and results from the acceleration of the flow leaking through the gap formed by the leaflet ear and the bottom of the recess. The ventricular jet has a strong axial velocity component, as suggested by the direction of the two-dimensional velocity vectors at 390 and 585 μm below the flat level. The velocity magnitude of the ventricular jet is lesser than those reported in the adjacent and lateral corners with a maximum of 3.79 m/s at the flat level. The flow exits the ventricular corner with a large out-of-plane motion as indicated by the u-velocity component distribution that reaches 1.96 m/s in this corner at the flat level. The overall direction of the leakage flow patterns identified in Figure 4-19 is consistent with the orientation of the three-dimensional streamtraces shown in Figure 4-4.

Cross-sectional views through the hinge recess provide additional information on the flow structures present within the hinge recess. In particular the ventricular leakage jet (central plane in Figure 4-21) is seen to have a near-parabolic profile when flowing underneath the leaflet ear. Further on the lateral side (lateral plane in Figure 4-21), the ventricular jet has a profile skewed towards the leaflet ear. The two-dimensional velocity vectors along the adjacent plane, on the other hand, shows a leakage flow with a

parabolic-like profile and with an out-of-plane velocity component up to 2.16 m/s. This flow corresponds to the flow diving into the adjacent corner and exiting the hinge through the ventricular corner. A region of near-zero flow is present in the aortic (top) side of the adjacent corner. This region of low flow corresponds to the detachment of the flow as the strong leakage jet persists near the flat level in the adjacent corner. The out-of-plane v-velocity component is the smallest in the lateral plane compared to the adjacent and center planes. This correlates with the velocity vector distribution in Figure 4-19 which shows a more axial flow in the lateral corner compared to the adjacent corner.

4.2.3 Detailed description of the shear stress distribution

The iso-surfaces shown in Figure 4-6 and the animations SJM_Reg_Isosurfaces _MidDiastole.mov and SJM_Reg_Isosurfaces_MidDiastole.mov reveal the global shear stress distribution in the hinge and the near-hinge region at key instances of the cardiac cycle. In order to gain further insight into the shear stress associated with the hinge fluid dynamics, the following section provides a detailed description of the shear stress fields over multiple instants of the cardiac cycle. The explanations are here supported by the use of shear stress contour maps along five planes outside and within the hinge recess at four instances of the cycle, namely, mid-acceleration, peak systole, mid-deceleration, and mid-diastole (Figure 4-22 and Figure 4-23). The local shear stress maxima are indicated on each one of these contour maps. The reader is referred to the accompanying animations (SJMReg_Shear_Stress_Contours.mov at four planes within the hinge recess) to better visualize the temporal variations of the shear stress distribution.

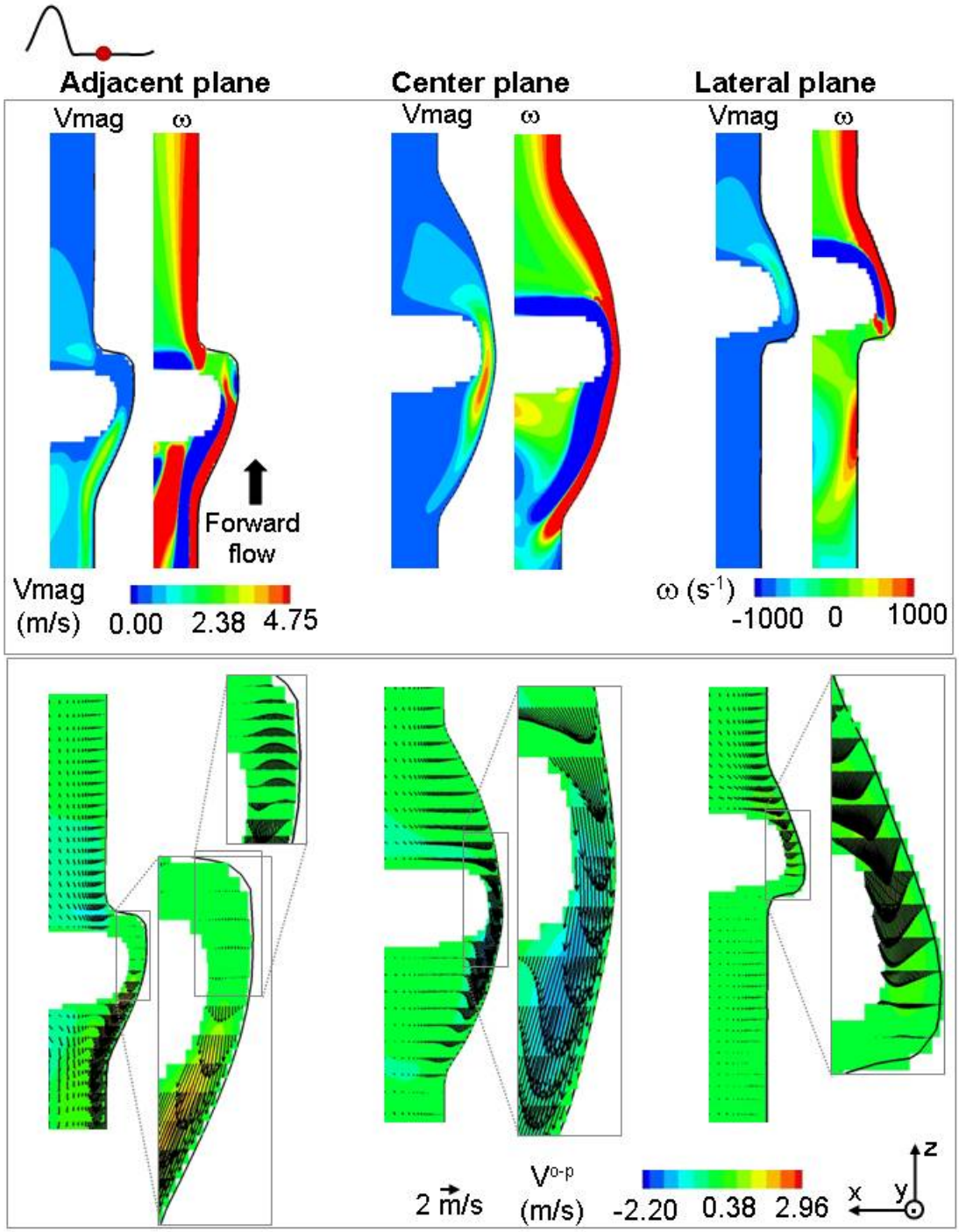

Figure 4-21: Three-dimensional velocity magnitude (top row) and two-dimensional in-plane velocity vectors with out-of-plane velocity contours (bottom row) along the adjacent, central, and lateral planes of the hinge at mid-diastole.
[SJM hinge design with a regular hinge gap width]

The iso-surfaces highlighted that, during the forward flow phase, the shear stress levels are closely related to the bulk valvular flow rates as the maximum shear stress levels were the highest at peak systole. This is further confirmed by the local maxima provided on the shear stress fields (Figure 4-22 and Figure 4-23). Moreover, the iso-surfaces also pinpointed two main regions associated with elevated shear stresses during systole: 1) near the downstream edge of the adjacent corner and 2) immediately upstream of the hinge ventricular pocket, where the flow is squeezed between the flat and the leaflet surfaces. These two regions are clearly seen along the plane located outside of the hinge recess along the leaflet surface (top row of Figure 4-22). Along this plane, the maximum shear stress level at peak systole is 565 dyn/cm^2 downstream of the adjacent corner and 1,170 dyn/cm^2 upstream of the ventricular corner. The hinge recess itself, as suggested by the absence of high shear stress iso-surfaces, is associated with lower shear stress values. Its shear stress distribution is characterized by higher levels in the ventricular pocket compared to the aortic pocket (Figure 4-22 and Figure 4-23). This correlates with the velocity magnitude distribution that shows higher velocity magnitude in the ventricular pocket compared to the aortic pocket (Figure 4-10). At the flat level (Figure 4-22), the maximum shear stress values are seen at peak systole, with a maximum of 720 dyn/cm^2 near the upstream wall of the ventricular corner. Shear stresses reported for deeper levels within the hinge recess (Figure 4-23) are systematically lower than at the flat level. The maximum shear stress value inside the hinge recess is 530 dyn/cm^2 observed at peak systole, 390 μm below the flat level (middle row, middle column in Figure 4-23). Overall, throughout the forward flow phase, the maximum shear stresses are observed at the flat level near the hinge recess wall. In particular, elevated shear stress levels are consistently observed along the upstream wall of the ventricular pocket; along the downstream wall of the adjacent corner; and near the aortic pocket wall. This is further confirmed when considering cross-sectional

planes through the hinge recess (Figure 4-24). The highest stress levels are located along the hinge, the leaflet and the housing surfaces. In both the lateral and adjacent planes, it is near the flat level, immediately upstream and downstream of the hinge recess that the maximum shear stresses are present. This is in agreement with the iso-surfaces presented in Figure 4-6. The peak shear stress appears to be consistently higher downstream than upstream of the hinge. At peak systole, the peak shear stress reaches 1,280 dyn/cm^2 and 900 dyn/cm^2 along the adjacent and lateral planes, respectively.

As underscored by the iso-surfaces, the shear stress distribution during the leakage phase is drastically different from that observed during the forward flow phase. Large shear stress levels are seen outside of the hinge recess on either side of the closed leaflet (top row in Figure 4-22). Along the plane located outside the hinge recess, along the leaflet surface, the shear levels reach 5,325 dyn/cm2. It is clear that these regions of high shear stresses correspond to the regions of leakage jet flows noted at mid-diastole (Figure 4-5). In the adjacent jet, shear stresses up to 2,715 dyn/cm^2 are computed at the flat level. The shear stresses in the lateral jet on the other hand are lower with a maximum of 2,200 dyn/cm^2 at the flat level. The slowest of the three jets, the ventricular jet, is associated with the lowest shear stress levels (maximum of 1,380 dyn/cm^2 at the flat level). However, at deeper levels within the hinge recess, the associated shear stress levels are much higher. At the bottom of the hinge recess near the tip of the leaflet, the shear stress levels reach up to 4,865 dyn/cm^2 due to the ventricular leakage jet flowing underneath the closed leaflet. Cross-sectional views through the hinge (Figure 4-24) clearly show that the regions of elevated shear stresses are located in the wake of the leakage jets.

Overall, the shear stress contour maps clearly highlight that during diastole, the regions of elevated shear stress are localized in the wake of the leakage jets and at the bottom of the hinge recess, in the gap formed by the closed leaflet and the recess wall.

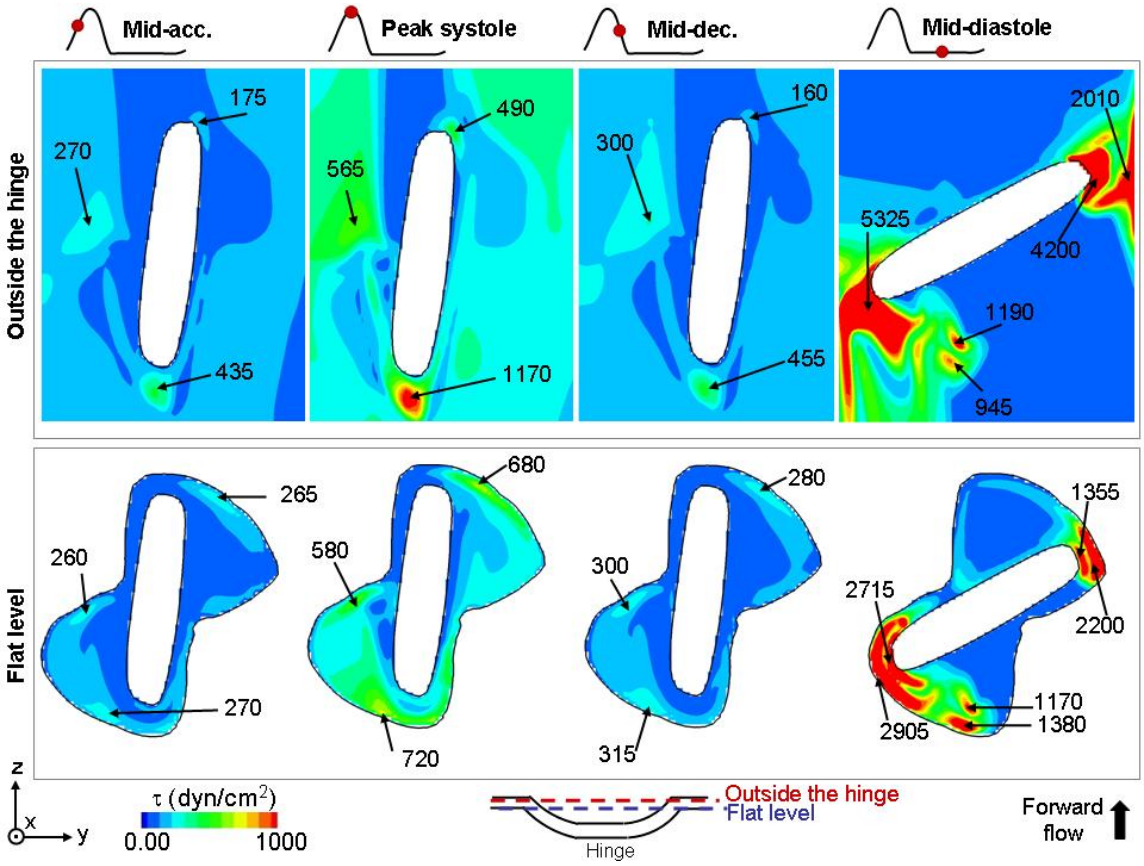

Figure 4-22: Shear stress distribution at mid-acceleration, peak systole, mid-deceleration, and mid-diastole. The top row shows a plane located outside the hinge recess, near the leaflet edge surface as depicted in the schematic. The bottom row corresponds to the flat level. [SJM hinge design with a regular hinge gap width].

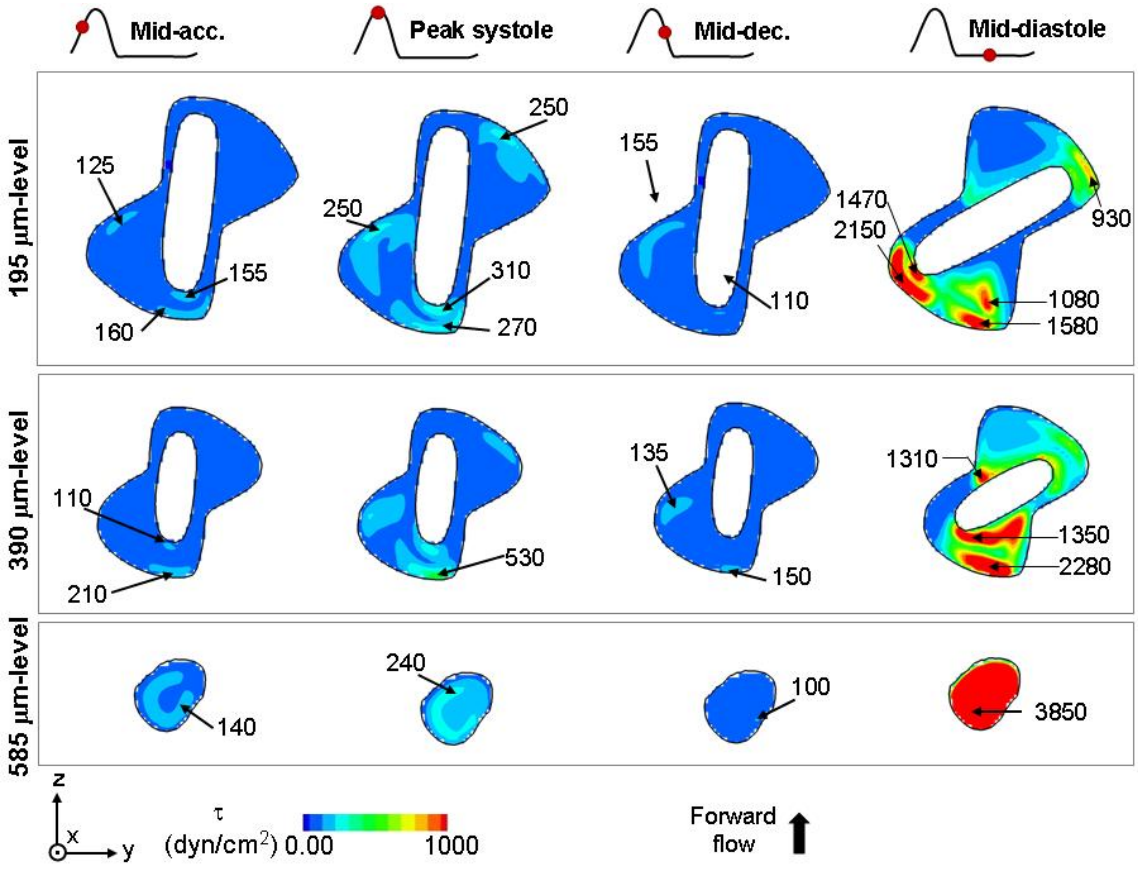

Figure 4-23: Shear stress distribution at four instants of the cardiac cycle at 195 μm, 390 μm and 585 μm below the flat level. [SJM hinge design with a regular hinge gap width].

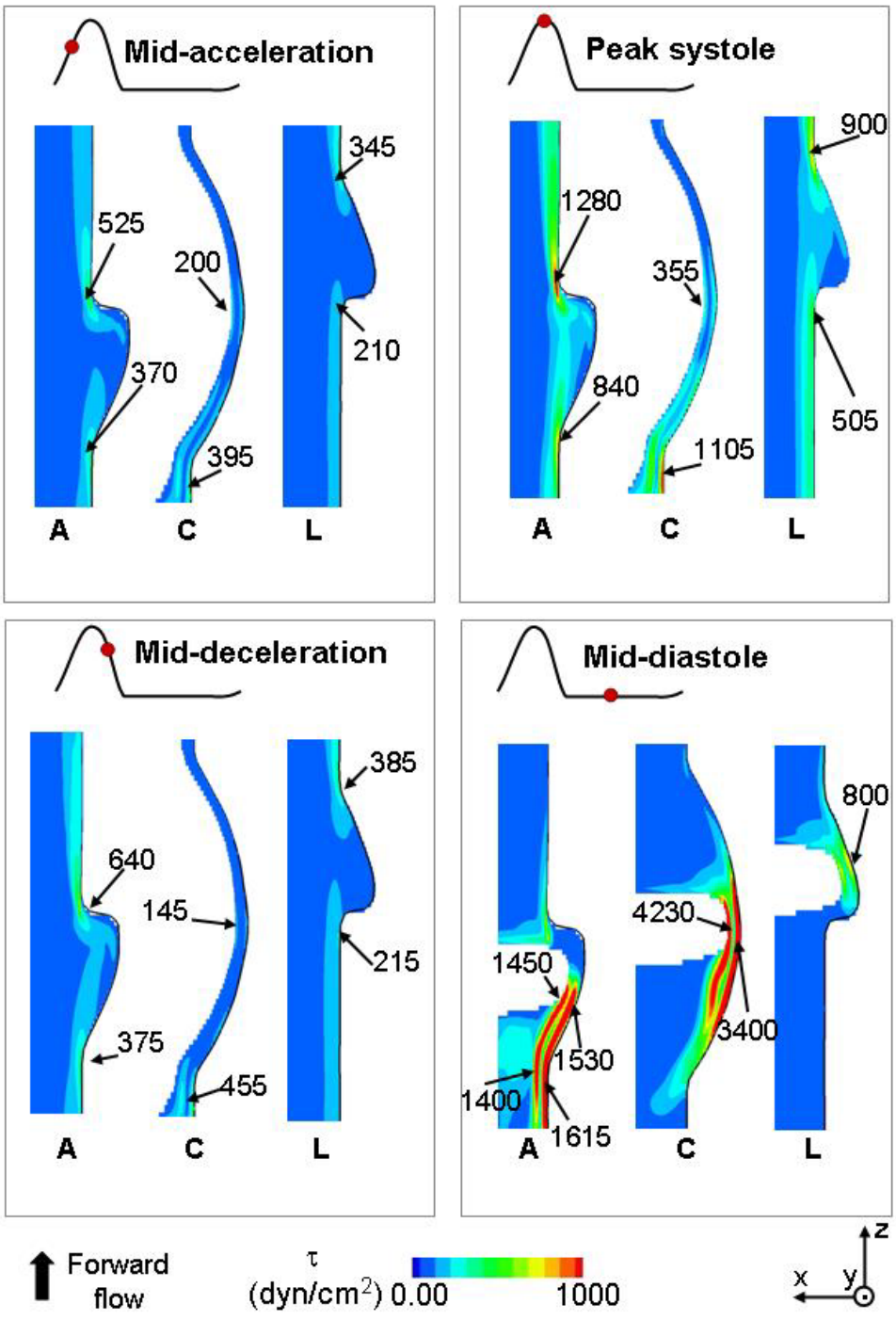

Figure 4-24: Shear stress distribution at four instants of the cardiac cycle along three cross-sectional planes: the adjacent (A) plane, the central (C) plane, and the lateral (L) plane. [SJM hinge design with a regular hinge gap width].

The shear stress contour maps clearly indicate large changes in the shear stress distribution throughout the cardiac cycle. In order to better visualize these changes, the temporal variations of the maximum shear stress in the hinge and near hinge regions are provided in Figure 4-25 during the first 550 ms of the cardiac cycle. The black curve depicts the global maxima for the hinge recess and its vicinity (zone depicted in blue in the two schematics shown below the graph), while the red curve depicts the maxima for the hinge recess alone. Both time traces follow a parabolic-like profile during systole, thus indicating that the maximum shear stress closely follows the variation in bulk valvular flow rate. On the other hand, during the leakage phase, the maximum shear stresses increase abruptly immediately after valve closure and then reach a plateau. Shear stress levels above the threshold for platelet activation are seen in the near-hinge region during the forward flow phase, and in particular at peak systole. However, it is during the leakage phase that the highest shear stresses are computed, with maximum shear stress levels over three times larger during the leakage phase compared to the forward flow phase.

It may be observed that the black curve lies above the red one throughout the cardiac cycle, indicating that the highest shear stress values are not observed within the recess, but rather in the hinge vicinity. These maximum shear stress values correspond, during the forward flow phase, to the region identified earlier, immediately upstream of the hinge, in the gap formed by the leaflet and the flat level. At peak systole, the maximum shear stress is 1,310 dyn/cm^2 inside the hinge recess and 2,080 dyn/cm^2 in the hinge vicinity. During the leakage phase, the maximum shear stress level reaches up to 6,515 in the hinge recess and 8,535 dyn/cm^2 in the hinge vicinity. These elevated shear stresses are located in the wake of the leakage jets as previously shown with the iso-surface plots provided in Figure 4-6.

Finally, Figure 4-25 underscores the differences in flow dynamics and associated shear stresses between the leaflet opening and closing phases. As was discussed in section 4.2.2, the opening of the leaflet takes place during the first 88 ms of the cardiac cycle and entrains fluid, yielding complex unstable flow patterns. This, in turn, induces a complex shear stress field distribution, with large variations in maximum shear stress levels as may be observed in Figure 4-25 at early systole (from 0 to 88 ms of the cardiac cycle).

During the leaflet closing phase (between 330 ms and 385 ms), the bulk valvular flow rate is lesser than during the leaflet opening phase. Furthermore, the effect of the leaflet motion on the flow structures is less pronounced during the closing phase. Both effects combined lead to smaller levels and lesser variations in the maximum shear stress compared to the leaflet opening phase.

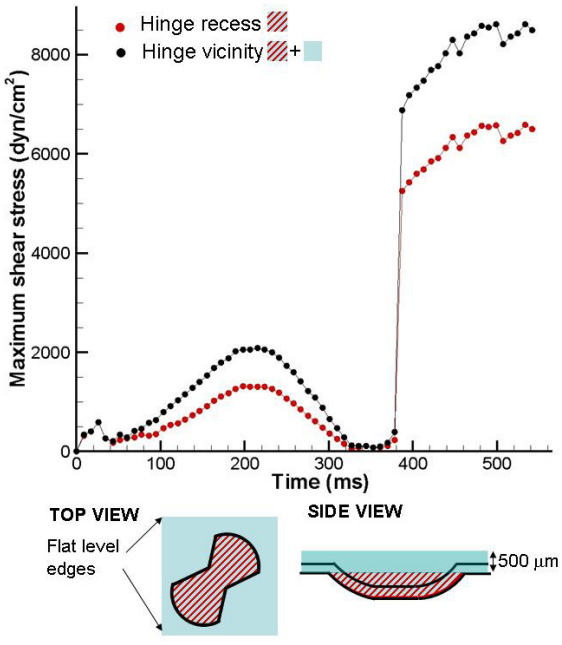

Figure 4-25: Variations of the maximum principal shear stress within the hinge recess (red) and in the hinge vicinity (black) as a function of time.
[SJM hinge design with a regular hinge gap width]

4.3 Eulerian analysis of the SJM hinge design with a large hinge gap width

Similar to the section describing the hinge flow fields for the SJM design with a regular hinge gap width (section 4.2), the following section provides an overview of the hinge flow fields and shear stress distribution throughout the cardiac cycle and is followed by a detailed description of the flow fields during 1) the leaflet opening phase, 2) the fully-open leaflet phase, 3) the leaflet closing phase, and finally 4) the leakage phase.

4.3.1 Overview

The global hinge flow structures are presented at four instances of the cardiac cycle first qualitatively, using three-dimensional instantaneous streamtraces (Figure 4-26); and then more quantitatively, using three-dimensional velocity vectors superimposed on the velocity magnitude contours (Figure 4-27). Note that in Figure 4-27 the x-axis is stretched to ease the visualization. Animation SJMLarge_3DView _3DVectors_3DVmag.mov provides the reader with the global hinge dynamics across the whole cardiac cycle for the SJM design with a large hinge gap width.

The streamtraces highlight the existence throughout the cardiac cycle of a highly three-dimensional and unsteady flow fields. The three-dimensionality of the flow is particularly evident along the leaflet surface during systole and in the ventricular and aortic corners of the hinge during diastole (Figure 4-27). Inspection of the streamtraces during systole reveals a similar flow distribution at mid-acceleration and mid-deceleration and a more complex flow pattern at peak systole. At mid-acceleration and mid-deceleration, the blue streamtraces indicate that the flow dives into the ventricular corner and goes underneath the open leaflet toward the adjacent corner where it impinges on the recess wall. These streamtraces underscore the presence of a streamlined flow that

follows the curvature of the recess wall. At peak systole, on the other hand, the same streamtraces are seen to form a large counter-clockwise recirculating flow pattern. Similarly, in the lateral corner of the hinge the streamtraces at peak systole show a complex, swirling flow pattern, which is not present at mid-acceleration and mid-deceleration. The most striking difference lies in the central region of the hinge where the streamtraces suggest a change of flow direction during systole: at mid-acceleration and mid-diastole, the streamtraces indicate the presence of a reverse flow underneath the leaflet ear; whereas, a forward flow pattern is clearly revealed by the direction of the blue streamtraces at peak systole. Figure 4-27 shows that the magnitude and three-dimensionality of the hinge flow during the forward flow phase is closely related to the cross-valvular flow rate as peak systole is associated with the largest velocities and out-of-plane motion. Table 4-2 Table 4-1summarizes the maximum velocity magnitude and the range of velocity components computed within the hinge recess at all instances depicted in Figure 4-26 and Figure 4-27.

The streamtraces during the leakage phase indicate the existence of drastically different flow features at mid-diastole. Highly three-dimensional reverse leakage flows are seen throughout the hinge. Three main flow structures may be identified within the hinge recess and are depicted using three different colors (Figure 4-26). The blue streamtraces clearly show a streamlined leakage flow pattern. Two leakage jets are seen on either side of the leaflet ear: the first one, depicted in green, is characterized by a strong helical structure; the second one, depicted in red, develops in the lateral corner and exits the recess with a more streamlined pattern. These ventricular, adjacent and lateral leakage jets exit the hinge recess with a strong out-of-plane motion as indicated by the three-dimensional velocity vectors in Figure 4-27. Comparison of the velocity vector fields at mid-diastole and during the systolic phase clearly indicate that it is at mid-diastole, when the leaflet is in its fully closed position, that the velocity magnitude is

the highest, with a peak within the hinge recess of 5.26 m/s. It should also be noted that the three-dimensionality of the flow is the most pronounced during the leakage phase (Figure 4-27 and Table 4-2).

Table 4-2: Maximum velocity magnitude and velocity component range throughout the hinge recess at mid-acceleration, peak systole, mid-deceleration, and mid-diastole [SJM hinge design with a large hinge gap width]

		SJM hinge with a large hinge gap width			
		Across entire hinge recess			
		Mid-acceleration	**Peak systole**	**Mid-deceleration**	**Mid-diastole**
Velocity range (m/s)	**u**	[-0.41; 0.37]	[-0.81;0.80]	[-0.34; 0.35]	[-2.90;2.97]
	v	[-0.29; 0.09]	[-0.58;0.30]	[-0.30; 0.12]	[-2.87;2.96]
	w	[-0.16; 0.57]	[-0.14;1.65]	[-0.14; 0.67]	[-4.91;1.55]
Max. velocity magnitude (m/s)		0.63	1.66	0.69	5.26

The global shear stress distribution in the hinge and near-hinge region is presented using iso-surfaces. Figure 4-28 shows the iso-surfaces for five principal shear stress levels ranging from 100 to 1,500 dyn/cm^2 for the same four points in time as previously described. Animations of the iso-surfaces at peak systole and mid-diastole are also provided (SJMLarge_Isosurfaces_MidDiastole.mov and SJMLarge_Isosurfaces _PeakSystole.mov). The streamtraces revealed similar flow structures at mid-acceleration and mid-diastole. It is therefore not surprising that the shear stress distribution is similar at these two points in time. The only major difference lies downstream of the aortic pocket where the iso-surfaces are seen to extend further downstream at mid-deceleration than at mid-acceleration. At these two points in time, the bottom of the hinge recess does contain 100 dyn/cm^2 iso-surfaces, but does not

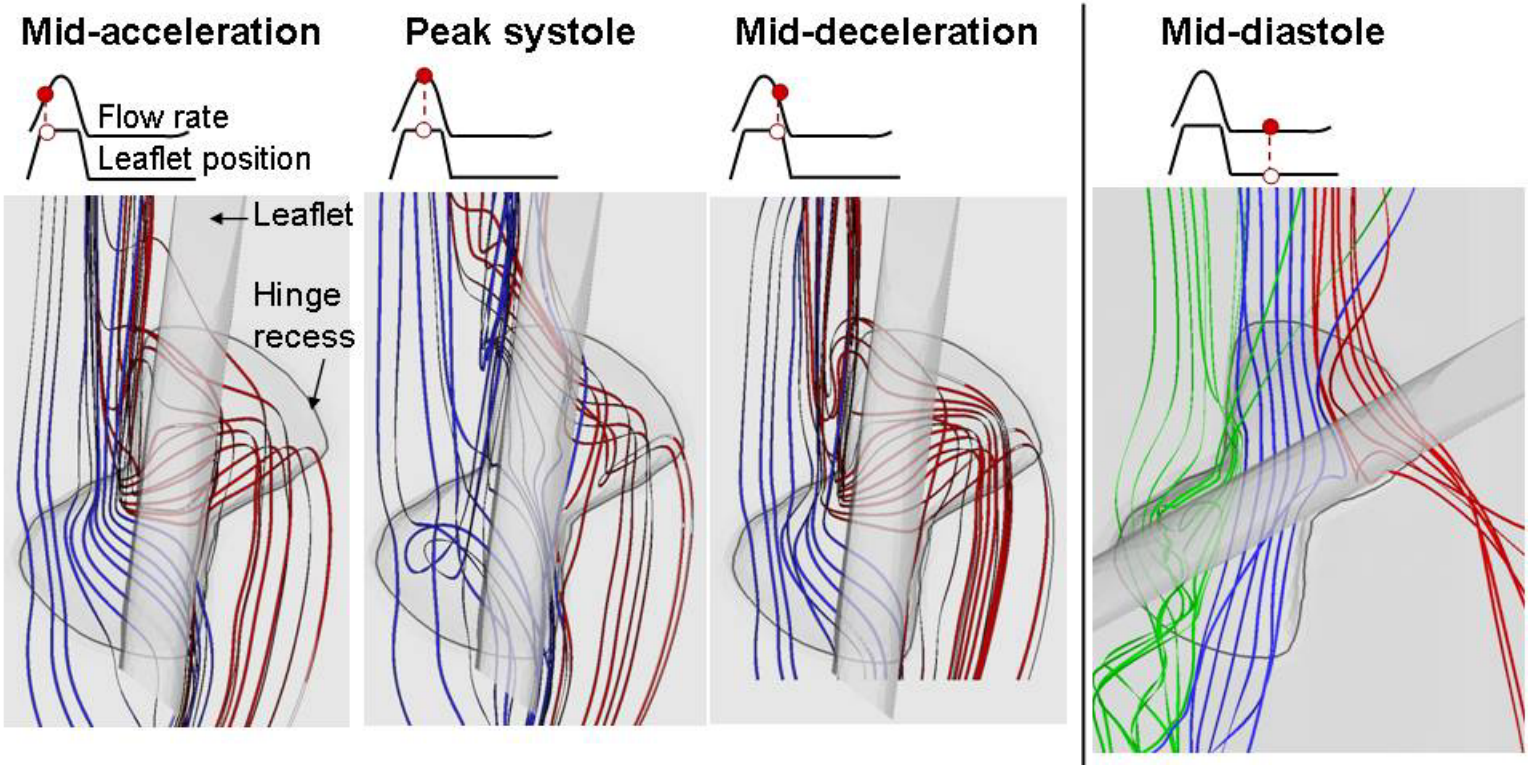

Figure 4-26: Three-dimensional instantaneous streamtraces at four instances of the cardiac cycle.
[SJM hinge design with a large hinge gap width].

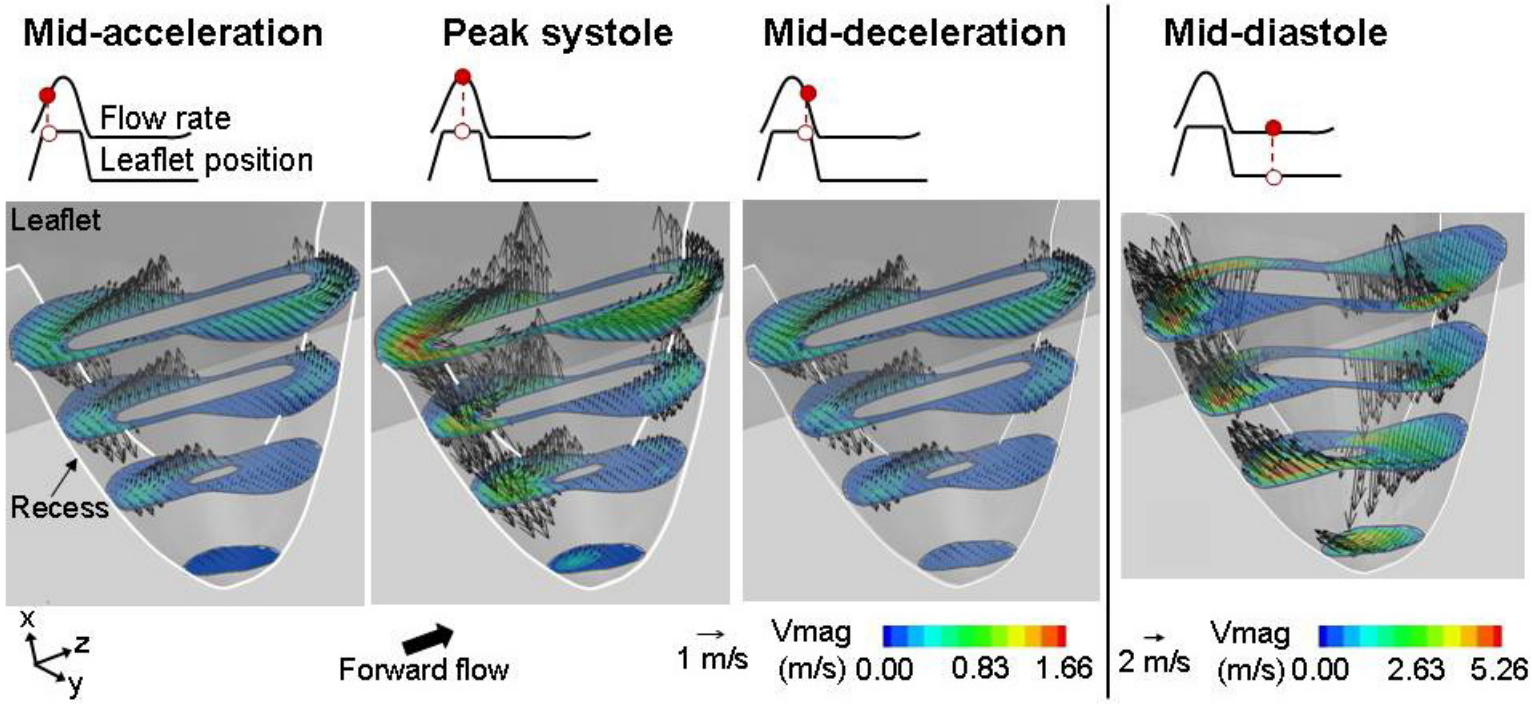

Figure 4-27: Three-dimensional velocity vectors with three dimensional velocity magnitude contour plots along four planes within the hinge recess and at four instances of the cardiac cycle. Note that the x-axis is not to scale and has been stretched to allow visualization of the flow fields [SJM hinge design with a large hinge gap width].

contain any iso-surfaces of 250 dyn/cm^2. This indicates that the shear stresses within the hinge recess are lower than 250 dyn/cm^2.

The iso-surface distribution at peak systole is similar to that seen at mi-acceleration and mid-deceleration for lower shear stress values. For instance, the iso-surfaces of 500 dyn/cm^2 at peak systole resemble those observed at mid-acceleration and mid-deceleration for 250 dyn/cm^2. This is also the case for the iso-surface of 1,000 dyn/cm^2 that is located in the same region as the 500 dyn/cm^2 iso-surfaces obtained at mid-acceleration and mid-deceleration. Throughout systole, the largest shear stress levels are therefore observed outside of the hinge recess rather than within. The main region of high shear stress is located immediately upstream of the open leaflet. This corresponds to the region where the incoming flow is squeezed between the housing surface and the leaflet surface.

During the leakage phase, the maximum shear stresses are seen on the wake of the leakage jets identified in Figure 4-26 and Figure 4-27. The iso-surfaces clearly pinpoint three regions associated with elevated shear stresses: the wake of the adjacent leakage jet, the wake of the lateral jet, and the central region of the hinge, underneath the closed leaflet. Comparison of the iso-surfaces at systole and mid-diastole shows significant differences in shear stress distribution and magnitude. Small and localized regions of shear stress of 1,000 and 1,500 dyn/cm^2 are identified during systole, whereas during mid-diastole the iso-surfaces for these same shear stress levels are very large. The maximum shear stress levels during the forward flow phase are observed at peak systole and reach 1,460 dyn/cm^2 within the recess and 1,730 dyn/cm^2 in near-hinge region. These maximum stresses reach 5,445 and 6,320 dyn/cm^2, respectively, during the leakage phase. This difference in shear stress distribution suggests that the leakage phase might be more detrimental to blood elements than the forward flow phase.

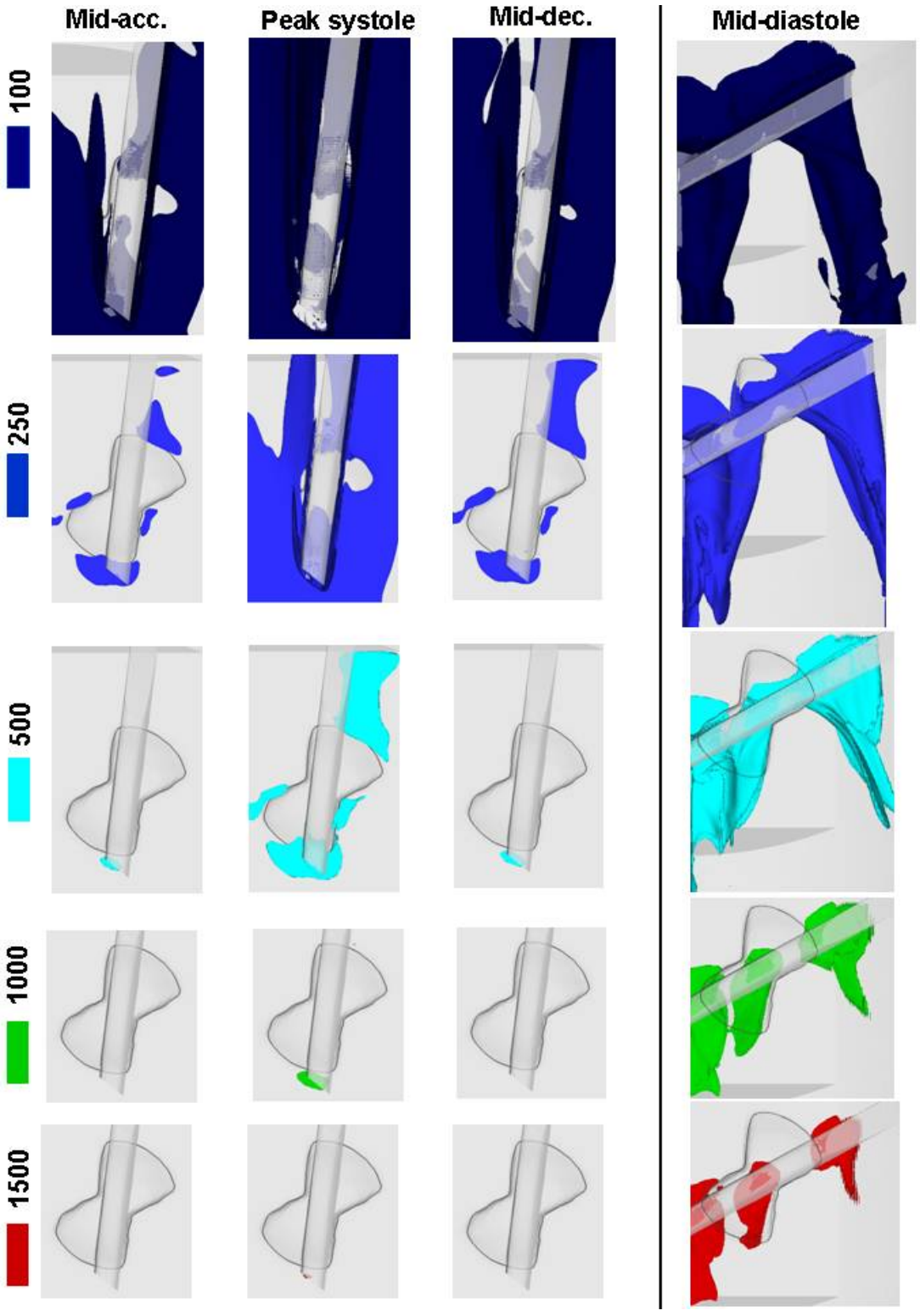

Figure 4-28: Iso-surfaces of shear stress levels at mid-acceleration, peak systole, mid-deceleration and mid-diastole. All shear stress levels are expressed in dyn/cm^2. [SJM hinge design with a large hinge gap width].

4.3.2 Detailed description of the hinge flow fields

The following section provides a detailed description of the hinge flow fields throughout the cardiac cycle by presenting the flow along selected planes at multiple instants of time. In order to gain further insight into the dynamic of the flow, the reader is referred to the accompanying animations (SJMLarge_2Dvectors_Vmag.mov and SJMLarge_2Dvectors_Vo-p.mov at the same planes within the hinge recess) to better visualize the temporal variations of the described flow structures.

Leaflet opening phase

This section focuses on the phase of the cardiac cycle during which the leaflet opens. The leaflet opening motion is a rapid event during which the leaflet travels 55^{o} in 88 ms. This abrupt motion combined with the slowly increasing bulk valvular flow rate leads to complex unsteady flow structures within the hinge recess. To best visualize the hinge flow dynamic during this phase, Figure 4-29 and Figure 4-30 show the hinge flow fields at four instances, spanning from 20 ms to 88 ms into systole. The first figure focuses on the flat level, while the later presents the flow structures deeper into the hinge at 195, 390 and 585 μm below the flat level.

At 20 ms, the leaflet is still in its near-fully closed position. A forward flow pattern of low magnitude is observed throughout the hinge region, except in the adjacent and lateral corners where a flow of stronger magnitude is present. In these corners, the flow goes around the leaflet and accelerates as it is being squeezed between the leaflet and the recess wall. Consequently, two forward flow jets, oriented toward the b-datum line, form. Flow structures at this instant of time somewhat resemble those observed during the leakage phase but with the opposite flow direction. The maximum velocity magnitude at the flat level is 0.46 m/s in the lateral corner and 0.50 m/s in the adjacent corner. The

out-of-plane u-velocity component reaches a maximum of 0.31 m/s in the adjacent corner and a minimum of -0.26 m/s in the lateral corner. At deeper levels within the hinge recess, a flow pattern similar to that observed at the flat level is observed as the flow goes around the leaflet.

As the valve opens further (42 ms), a strong forward flow pattern develops on the right side of the leaflet in the ventricular and lateral corners. As can be observed from Figure 4-29 and Figure 4-30, this forward flow pattern is primarily observed at the flat level. At this level, the flow direction seems to be mainly dictated by the leaflet surface. However, at deeper levels within the hinge recess the flow vectors are seen to follow the curvature of the recess. As the flow impinges on the upstream edge of the leaflet in the ventricular pocket of the hinge, it is deflected on the right and left sides of the leaflet. The flow redirected toward the adjacent corner is squeezed with the recess wall and a localized flow jet that dives into the recess forms near the upstream edge of the leaflet. The maximum velocity magnitude observed in this jet reaches 0.39 m/s. Due to the angle formed between the leaflet and the main flow direction, the impingement of the flow on the leaflet leads to the formation of a large separation region behind the leaflet, on the downstream-most part of the adjacent corner. In the aortic pocket, the velocity magnitudes are lower those seen in the ventricular pocket, with a maximum at 0.29 m/s. The out-of-plane velocity u-component throughout the flat level at this instant ranges from -0.21 m/s to 0.19 m/s.

At 57 ms, the leaflet has reached 65% of its opening. The flow patterns at this instant in time are similar to those observed at 42 ms, but the velocity magnitudes are larger. The forward flow pattern in the lateral corner increases in strength up to 0.39 m/s. At the end of the leaflet opening phase (88 ms), the region of flow separation identified earlier on the left side of the leaflet in the adjacent corner remains visible at the flat level. The incoming flow is seen to collide with the upstream edge of the leaflet and dive into

the hinge recess. The flow then follows the curvature of the hinge recess, goes towards the adjacent corner before being re-oriented towards the lateral corner after impinging on the recess wall. This flow pattern is particularly visible at the 195 μm-level (Figure 4-30). In the downstream-most tip of the adjacent corner, a region of small in-plane motion and large out-of-plane motion is present. This corresponds to the region where the flow exits the hinge recess. In this tip, the maximum velocity magnitude and out-of-plane u-velocity components are 0.31 m/s and 0.27 m/s, respectively. The lateral corner is characterized by a strong forward flow pattern whose maximum velocity magnitude reaches 0.47 m/s.

It is interesting to note that the velocity vector distribution at the deepest level within the hinge recess (585 μm-level in Figure 4-30) is characterized throughout the opening phase by a forward flow pattern of varying magnitude except when the leaflet reaches nearly its fully-open position. At early systole, this forward flow pattern has a strong axial component; but as the leaflet opens, it is seen to curve toward the b-datum plane of the valve (left side) and decreases in strength. The bottom of the hinge recess at 88 ms is characterized by a reverse flow pattern of very low magnitude. This change in magnitude and orientation of the flow can be best seen in Figure 4-31 that shows the in-plane velocity vector distribution along the central plane of the hinge during the leaflet opening phase. At the bottom of the hinge recess, underneath the leaflet ear, the maximum velocity magnitude is 0.42 m/s at 20 ms, but does not exceed 0.10 m/s at 88 ms. On the other hand, the out-of-plane flow motion in this region doubles during the opening phase. The out-of-plane v-velocity component, along the hinge central plane, ranges from -0.07 m/s to 0 m/s at early systole (20 ms) and from -0.14 to 0 m/s at the end of the opening phase (88 ms).

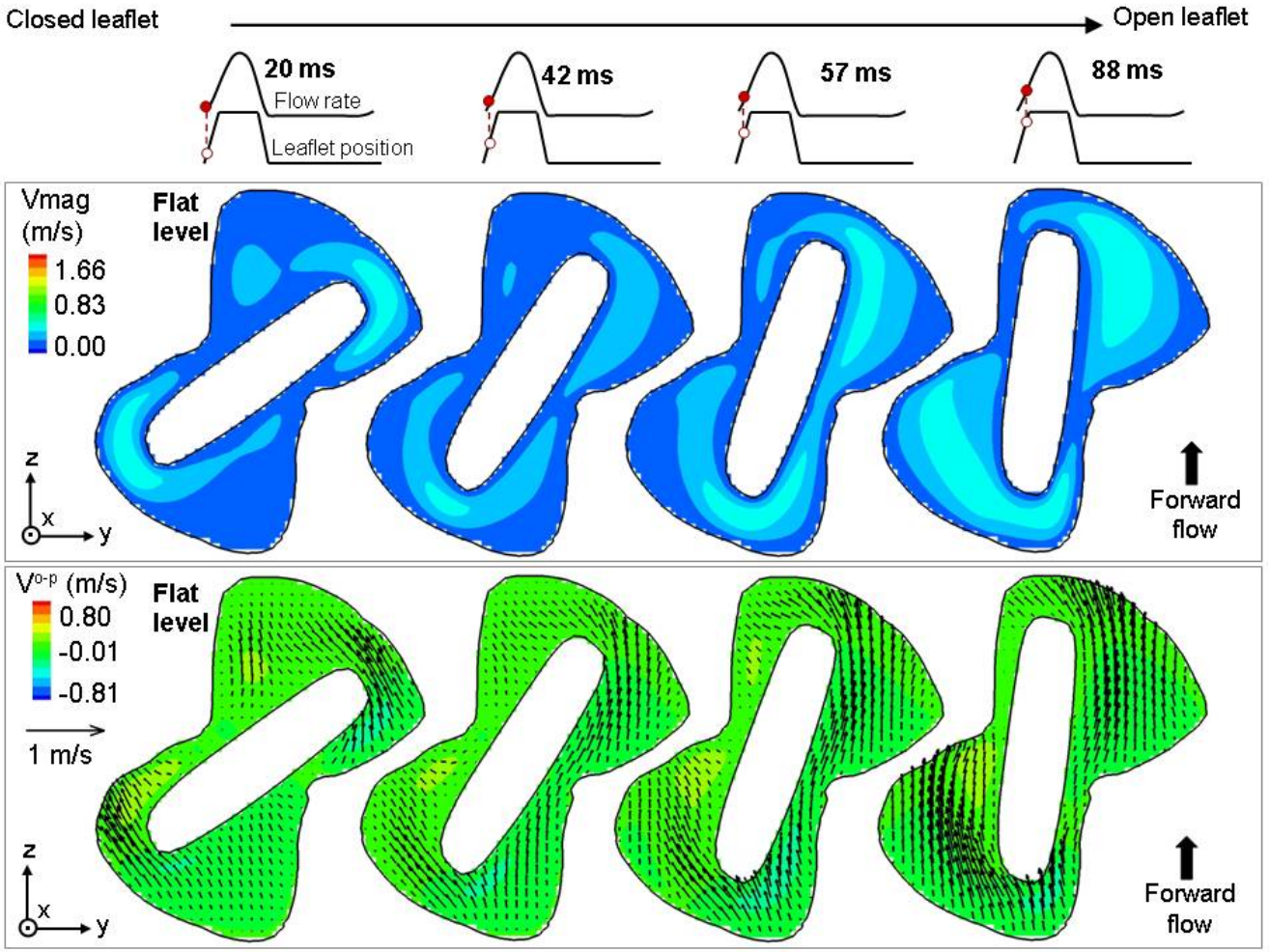

Figure 4-29: Three-dimensional velocity magnitude (top row) and two-dimensional in-plane velocity vectors with out-of-plane velocity contours (bottom row) at the flat level at four instances of the opening phase.
[SJM hinge design with a large hinge gap width]

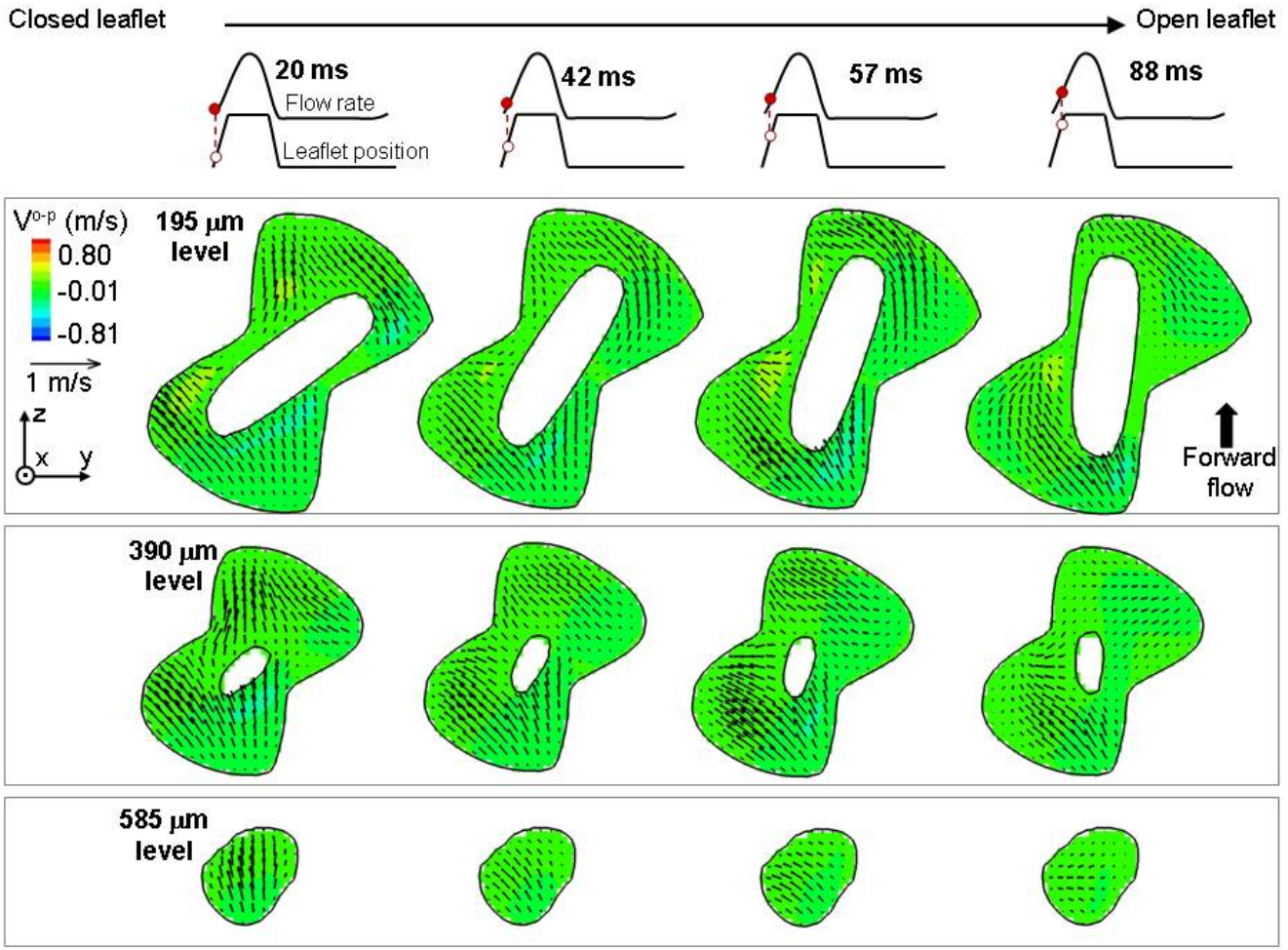

Figure 4-30: Two-dimensional in-plane velocity vectors with out-of-plane velocity contours at 195 μm, 390 μm, and 585 μm below the flat level during the leaflet opening phase. [SJM hinge design with a large hinge gap width]

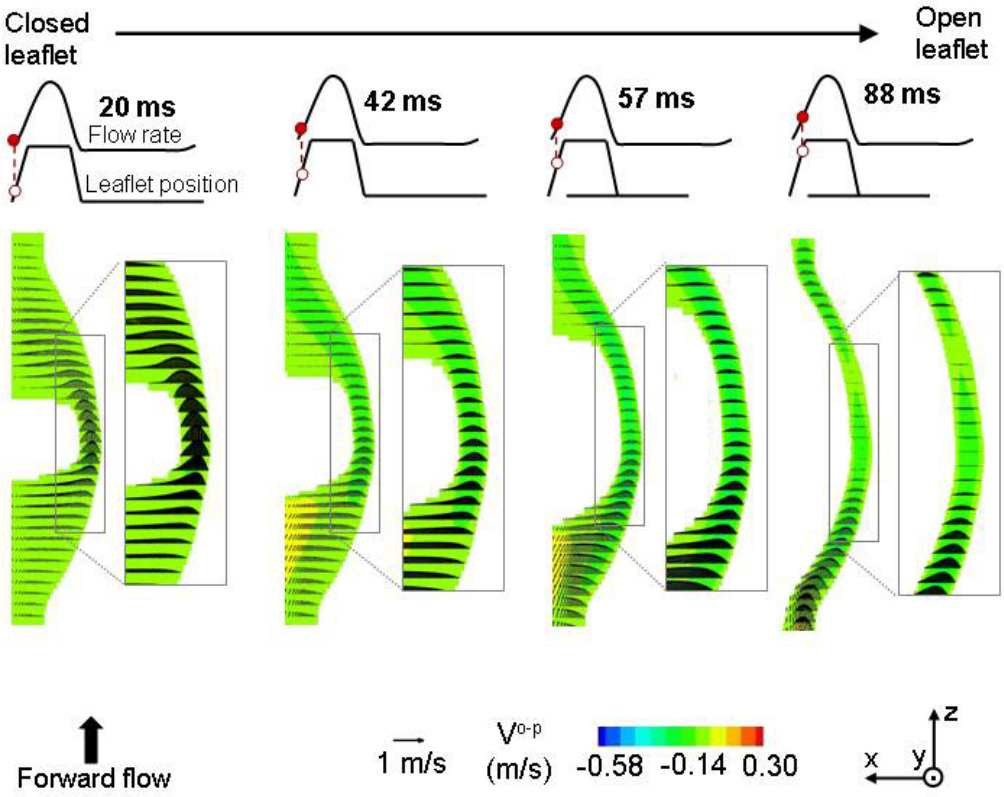

Figure 4-31: Two-dimensional in-plane velocity vectors with out-of-plane velocity contours along the central plane of the hinge during the leaflet opening phase. [SJM hinge design with a large hinge gap width]

Fully-open leaflet phase:

As seen in the hinge flow field overview provided in section 4.3.1, large difference in flow structures exists during the fully-open phase, the major difference being the change in flow direction observed at the bottom of the hinge recess at peak systole compared to mid-acceleration and mid-diastole. This section first provides a thorough description of the hinge flow structures at mid-acceleration, which is then followed by the flow fields at peak systole, and then at mid-deceleration. The description is supported by Figure 4-32, Figure 4-33, Figure 4-34 and Figure 4-35. These figures

present the flow fields at the flat level, the 195 μm, the 390 μm, and the 585 μm-levels, respectively.

Mid-acceleration: At mid-acceleration, the ventricular corner of the hinge is characterized by a velocity vector distribution that clearly suggests the diving of the flow inside the recess induced by the collision of the flow with the upstream surface of the leaflet ear. The trajectories of the streamtraces (Figure 4-26) underscore this flow pattern. This diving of the flow is associated with large out-of-plane motion which yields an extremum out-of-plane v-velocity component of -0.32 m/s at the flat level.

The streamtraces in the adjacent corner of the hinge show a streamlined flow that follows the curvature of the hinge recess. As the flow impinges on the upstream edges of the leaflet, it is seen to deflect towards the adjacent corner of the hinge where it impinges on the recess wall before turning towards the lateral side of the hinge. This smooth flow pattern is particularly visible at the 195 μm-level in Figure 4-33. A similar flow pattern is observed at the 390 μm-level, which is not shown. A region of elevated out-of-plane u-velocity component is seen at the downstream-most part of the adjacent corner. This region corresponds to the location where the flow exits the hinge recess.

The streamtraces in the lateral corner of the hinge reveal a more complex pattern where the flow dives in the hinge recess, reverses direction and goes back towards the adjacent corner of the hinge from where it exits the hinge. This flow pattern translates into a forward flow pattern at the flat level (Figure 4-32). The maximum velocity magnitude seen in this corner at the flat level at mid-acceleration is 0.72 m/s. At a deeper level within the hinge recess, the flow in the downstream part of the lateral corner is seen to follow the curvature of the recess wall. This corresponds to the streamtraces exiting the hinge recess from the tip of the aortic corner (shown in red in Figure 4-26). A reverse flow of low magnitude with low out-of-plane motion is visible immediately

downstream of the open leaflet. This corresponds to the flow reversal observed in the streamtraces. This flow reversal extends to the bottom of the hinge recess, as highlighted by the velocity vector fields at the 585 μm-level shown in Figure 4-35.

Peak systole: The hinge flow structures observed at peak systole are very different from those identified at mid-acceleration. This is underscored by the complex streamtraces observed at peak systole compared to the more streamlined flow seen at mid-acceleration. As seen at mid-acceleration, the flow in the ventricular corner of the hinge collides with the leaflet surface and dives into the hinge recess. While the flow pattern in this region is similar at mid-acceleration and peak systole, the three-dimensionality of the flow is larger at peak systole. The extremum out-of-plane u-velocity component in this region at the flat level is -0.32 m/s and -0.71 m/s at mid-acceleration and peak systole, respectively. The maximum velocity magnitude seen in this region at peak systole is 1.66 m/s. The adjacent corner, characterized by a streamlined flow at mid-acceleration, is characterized at peak systole by a complex flow pattern. At the flat level (Figure 4-32), the flow is dominated by the flow outside of the recess and is thus characterized by a forward flow pattern, only disrupted at the downstream-most part of the adjacent corner by a large out-of-plane flow motion. This region of elevated positive u-velocity component is due to the flow at the bottom of the recess exiting the hinge and is thus also visible at lower level within the recess (195 μm-level in Figure 4-33). The maximum out-of-plane u-velocity computed at the flat level in this region reaches 0.78 m/s at peak systole.

At a deeper level within the hinge recess, the influence of the flow outside the recess in the adjacent corner diminishes and the flow appears to be dictated by the geometry of the recess and the strong diving flow noted in the ventricular corner. This translated into the formation of a counter-clockwise rotating flow structure visible at the

195 μm-level shown in Figure 4-33. This rotating flow structures is best seen in the out-of-plane vorticity contour plot (bottom row in Figure 4-36) where a large region of positive vorticity, bounded by a layer of negative vorticity defines this rotating flow. This rotating flow vanishes at 390 μm below the flat level (Figure 4-34) and is replaced by a strong flow pattern slightly oriented towards the left.

In the lateral corner of the hinge, a strong axial flow with a lesser out-of plane velocity component compared to the ventricular pocket is seen at the flat level (Figure 4-32), indicating that the flow outside the hinge recess dictates the flow at this level. The velocity magnitude at the flat level reaches 1.15 m/s in the lateral corner. At 195 μm below the flat level, the velocity field distribution is more complex. It is characterized by a strong flow along the downstream wall of the hinge recess. Such a flow was visible at mid-acceleration but with reduced velocity magnitude compared to peak systole. As indicated by the three-dimensional streamtraces (Figure 4-26), the flow in the lateral corner exits the hinge from the tip of the aortic corner. This region is thus associated with large out-of-plane velocity component up to 0.47m/s at the flat level.

As previously suggested by the three-dimensional streamtraces (Figure 4-27), it is at the bottom of the hinge recess that the most striking difference in flow pattern between mid-acceleration and peak systole is visible. At peak systole (Figure 4-35), the 585 μm-level is characterized by a strong forward flow pattern of low magnitude and no out-of-plane motion. The maximum velocity magnitude at this level is 0.38 m/s and the out-of-plane u-velocity component ranges from -0.06 m/s to 0.03 m/s. At mid-deceleration and also at the end of the valve closing phase, on the other hand, a reverse flow of low magnitude was present throughout the bottom of the recess. This change in flow direction is clearly underscored by the out-of-plane vorticity contour plots shown in Figure 4-35.

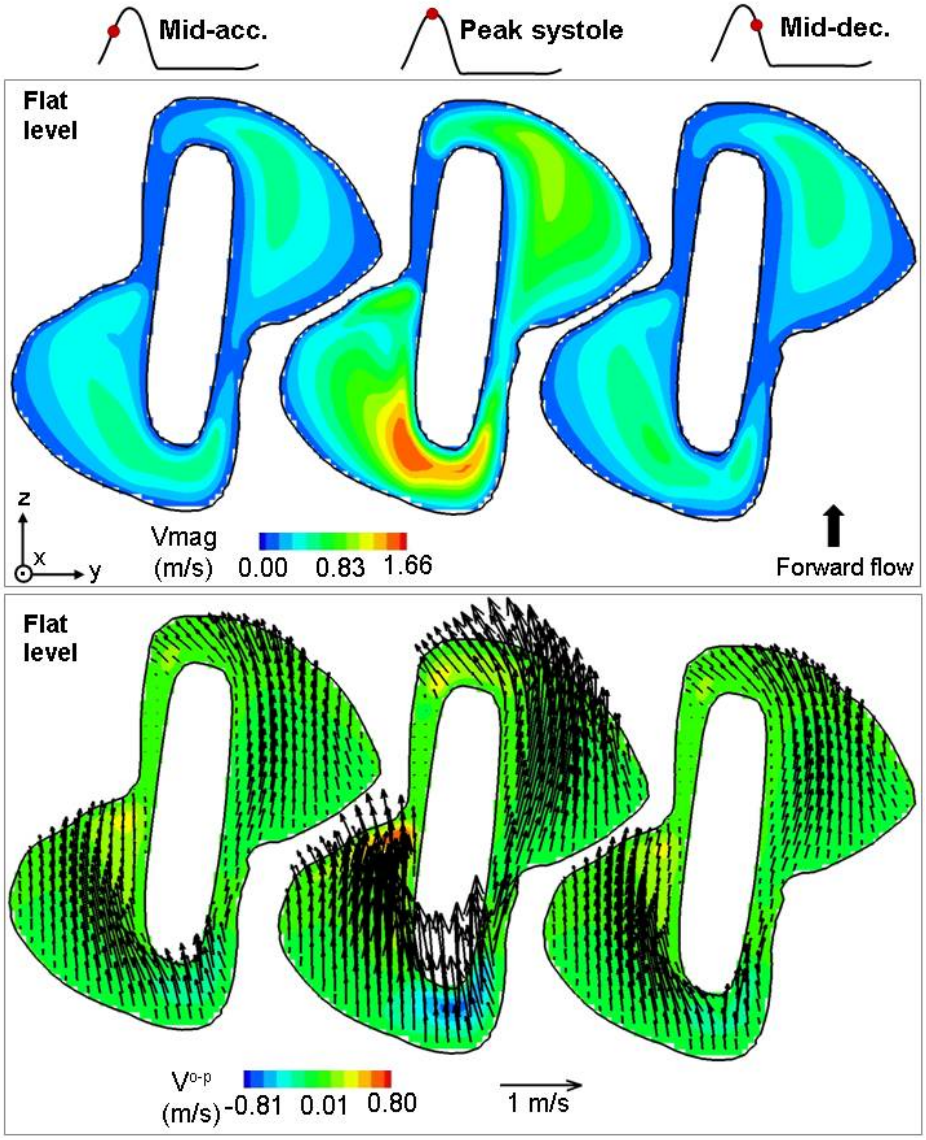

Figure 4-32: Three-dimensional velocity magnitude (top row) and two-dimensional in-plane velocity vectors with out-of-plane velocity contours (bottom row) at three instances of the fully-open leaflet phase at the flat level.
[SJM hinge design with a large hinge gap width]

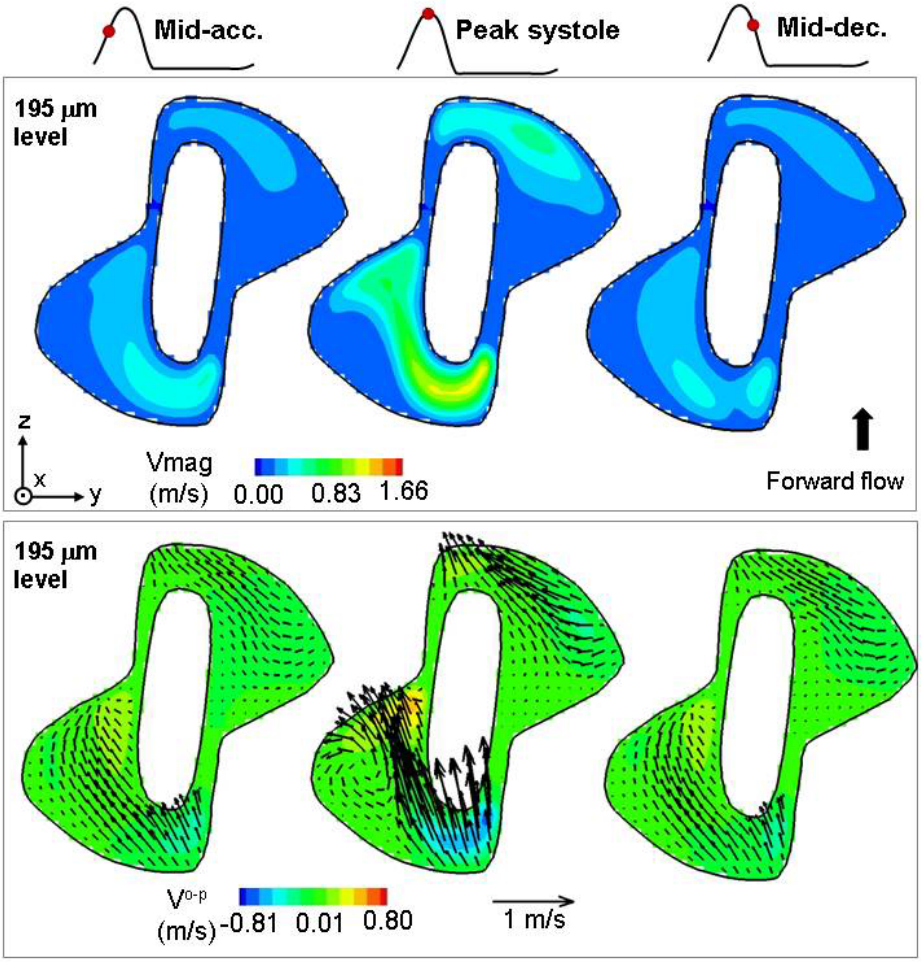

Figure 4-33: Three-dimensional velocity magnitude (top row) and two-dimensional in-plane velocity vectors with out-of-plane velocity contours (bottom row) at three instances of the fully-open leaflet phase along the plane 195 μm below the flat level.
[SJM hinge design with a large hinge gap width]

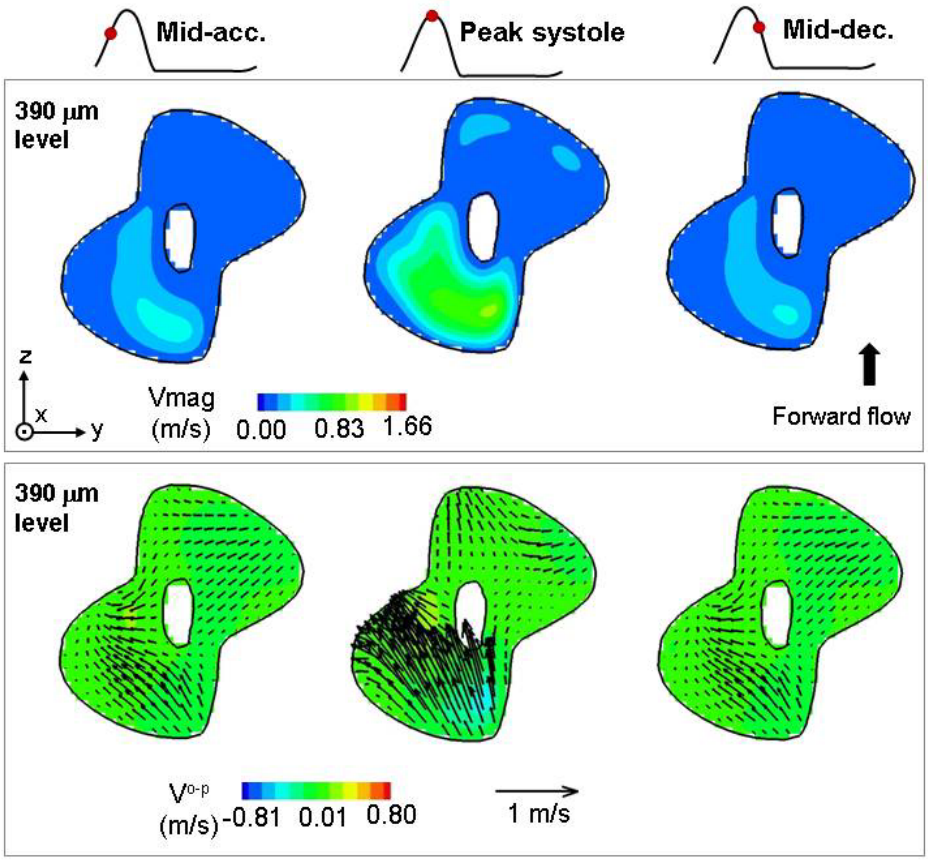

Figure 4-34: Three-dimensional velocity magnitude and two-dimensional in-plane velocity vectors with out-of-plane velocity contours at three instances of the fully-open leaflet phase at the 390 μm-level. [SJM hinge design with a large hinge gap width]

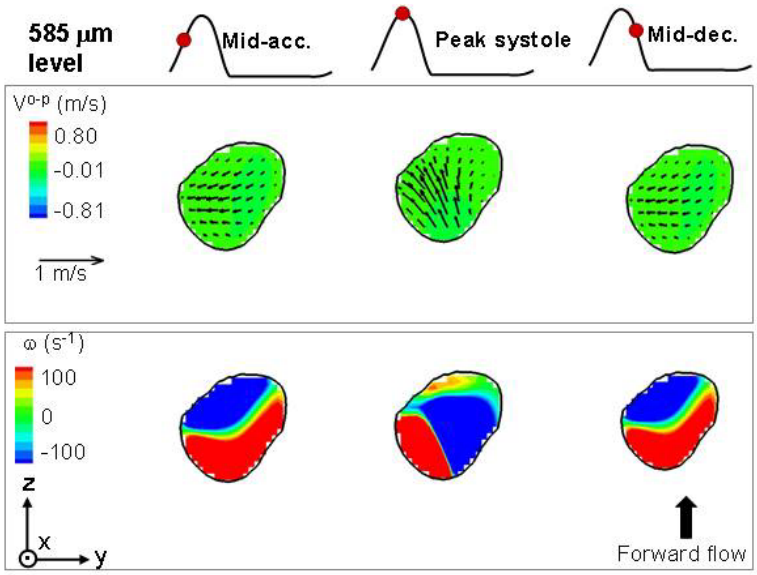

Figure 4-35: Three-dimensional velocity magnitude and two-dimensional in-plane velocity vectors with out-of-plane velocity contours at three instances of the fully-open leaflet phase at the 585 μm-level. [SJM hinge design with a large hinge gap width]

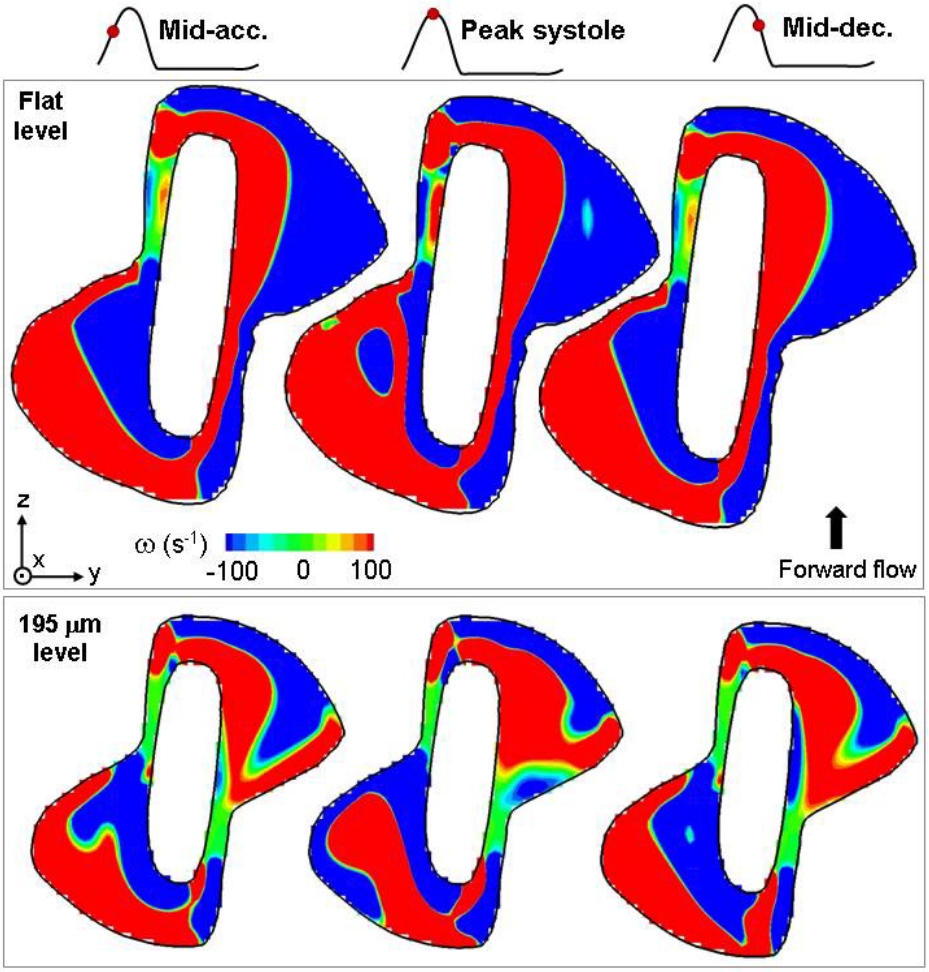

Figure 4-36: Out-of-plane vorticity contours at the flat level (top row) and at 195 μm below the flat level (bottom row) at mid-acceleration, peak systole, and mid-deceleration. [SJM hinge design with a large hinge gap width]

The change of flow direction underneath the leaflet ear is best seen in a cross-sectional view of the hinge through the hinge center plane (Figure 4-37). The velocity vector distribution clearly shows that at peak systole, a near-parabolic forward flow profile exists in the gap formed by the surface of the open leaflet and the hinge recess wall. The same gap is characterized at mid-acceleration by a reverse flow pattern with a parabolic-like profile. Moreover, at peak systole, the bottom of the hinge recess is characterized by near-zero out-of-plane motion (maximum v-velocity component of 0.02 m/s), while at mid-acceleration the out-of-plane motion in this region is larger with a maximum out-of-plane velocity v-component of -0.18. The change in flow direction at the bottom of the hinge recess during systole is also evident in the out-of-plane vorticity distribution in the center plane of the hinge (Figure 4-37).

In order to gain further insight into the flow fields present at peak systole, the flow fields along the adjacent, central, and lateral planes of the hinge are provided in Figure 4-38. The zoom-in panel of the adjacent plane shows a complex flow pattern in the adjacent corner of the hinge with the presence of a forward flow pattern near the flat level and a back flow near the upstream wall of the recess. Such a flow reversal is also visible in the lateral plane of the hinge. This flow pattern may be attributed to the detachment of the main flow from the flat level, which induces a small recirculation region in the recess. The formation of such a structure is expected as the hinge geometry here resembles that of a backward-facing step. The zoom-in panel in the center of the hinge underscores the parabolic profile of the forward flow seen at the bottom of the hinge recess. The velocity vector distribution along these cross-sectional planes correlates with the disturbed trajectories of the streamtraces observed in the adjacent and lateral corners and the more streamlined paths seen in the central section of the hinge.

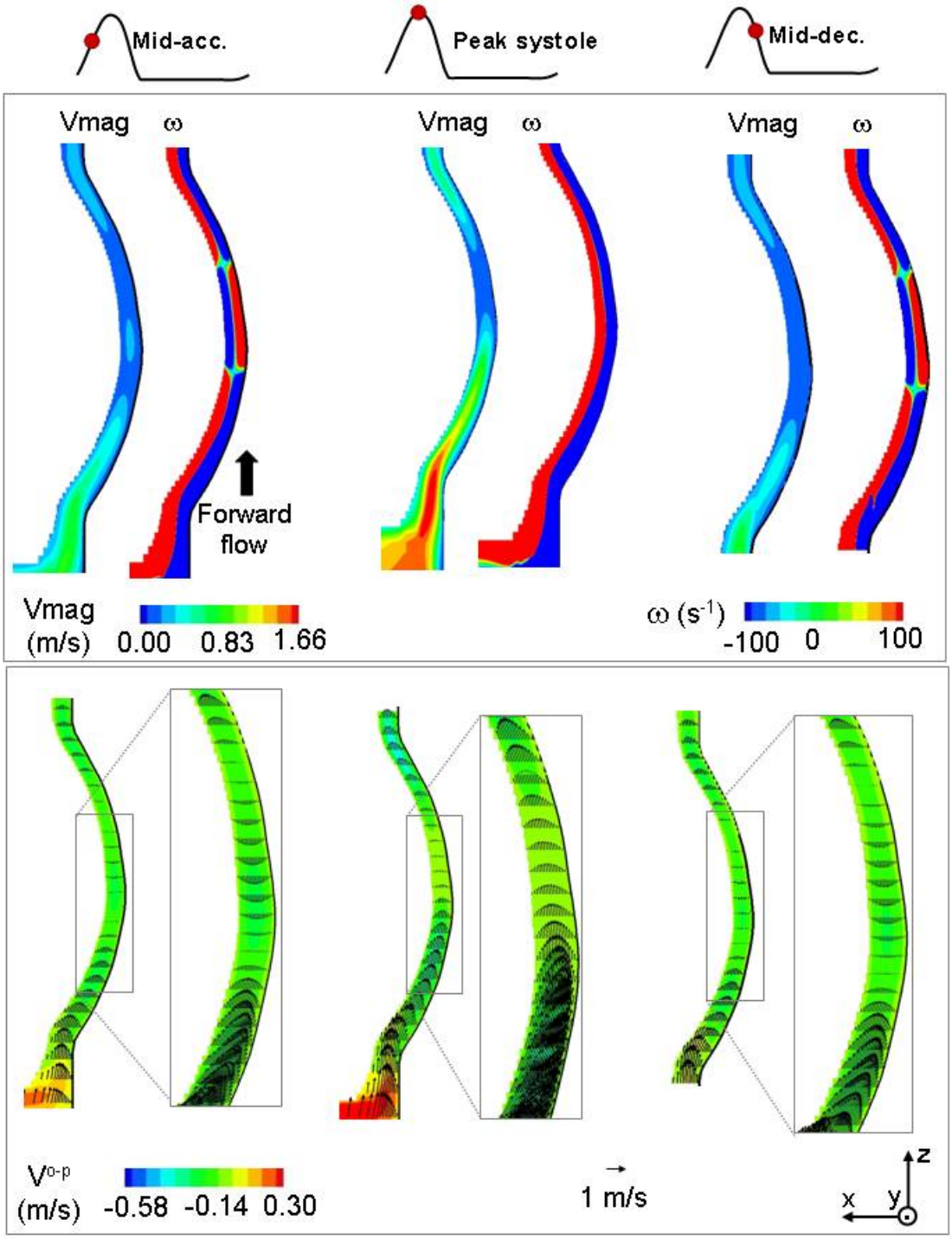

Figure 4-37: Three-dimensional velocity magnitude (top row) and two-dimensional in-plane velocity vectors with out-of-plane velocity contours (bottom row) along the central plane of the hinge at mid-acceleration, peak systole and mid-deceleration. [SJM hinge design with a large hinge gap width]

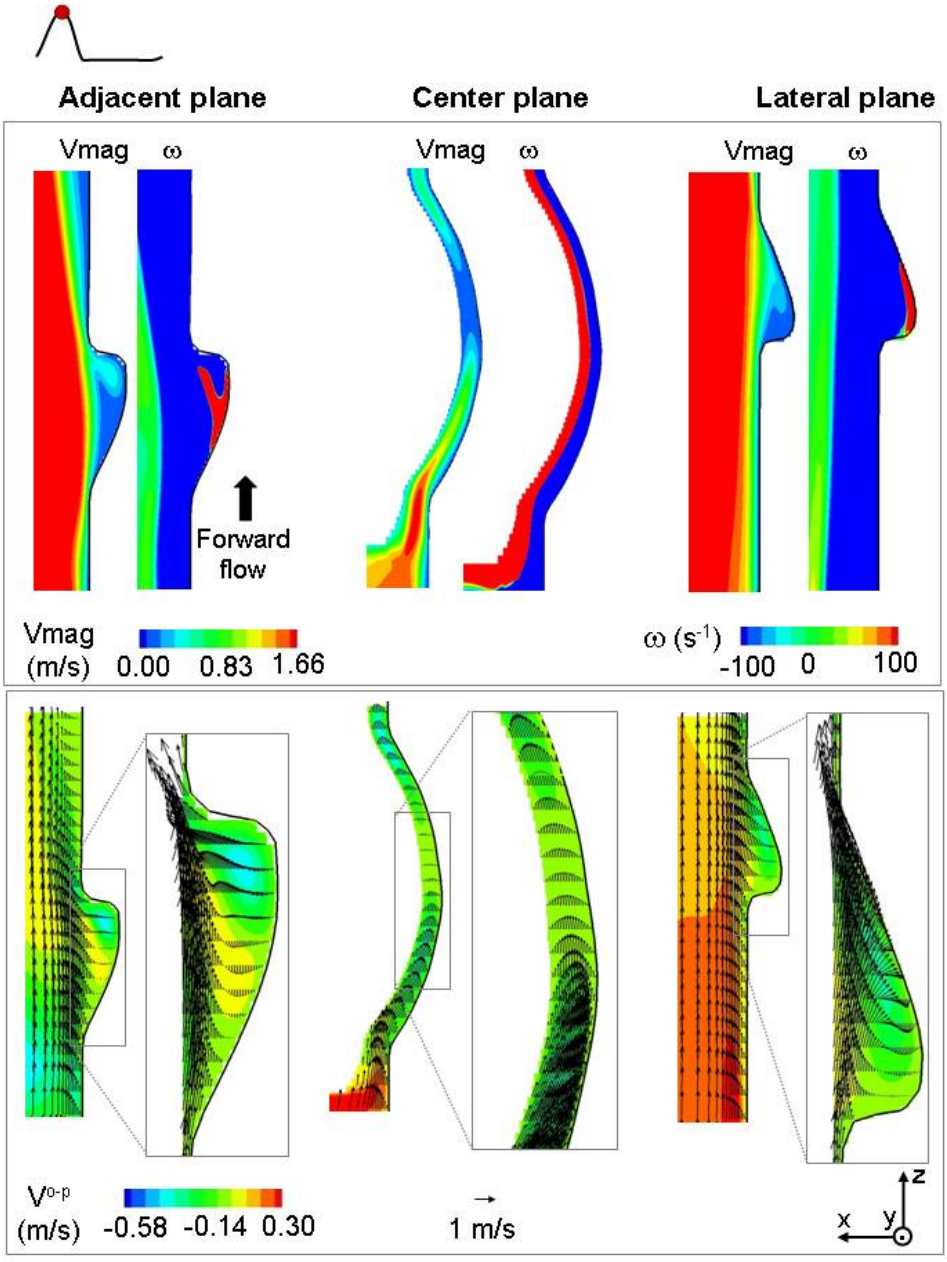

Figure 4-38: Cross-sectional views of the hinge recess at peak systole. Three-dimensional velocity magnitude and out-of-plane vorticity contours are shown on the top row. The bottom row displays the two-dimensional in-plane velocity vectors superimposed on the out-of-plane velocity contours.
[SJM hinge design with a large hinge gap width]

Mid-deceleration: At this instance of the cardiac cycle, the flow structures revert to a configuration similar to that observed at mid-acceleration. The counter-clockwise rotating flow that forms at peak systole vanishes and is replaced by a streamlined flow that follows the curvature of the hinge recess and thus resembles that seen at mid-acceleration. The similitude and differences in flow distribution in the hinge recess with those seen at mid-acceleration can be seen in the vorticity contour plots. At the flat level, the adjacent corner is characterized by a large region of positive vorticity and a small localized region of negative vorticity; whereas at mid-acceleration and mid-deceleration, this corner appears to be divided nearly equally by a region of positive vorticity and another region of negative vorticity. The change in flow structures during the fully-open leaflet phase in the adjacent corner of the hinge is best seen at the 195 μm-level. The rotating flow structure in the adjacent corner is only visible at peak systole and thus the large region of positive vorticity, surrounded by a layer of negative vorticity can only be observed at peak systole and not at mid-acceleration and mid-deceleration.

The forward flow pattern characterizing the aortic pocket of the hinge at the flat level at mid-acceleration and peak systole is still present at mid-deceleration. The vorticity distribution at the flat level in this corner is thus similar throughout the fully-open phase. However, the velocity magnitude changes with the cross-valvular flow rate and thus at the flat level, the maximum velocity magnitudes in the lateral corner are 0.72 m/s, 1.15 m/s and 0.60 m/s at mid-acceleration, peak systole, and mid-deceleration, respectively. It should be noted that while a similar vorticity distribution is seen at the flat level in the aortic pocket, small differences at deeper levels within the hinge recess exist, as highlighted in Figure 4-36.

The forward flow pattern characterizing the bottom of the hinge recess at peak systole vanishes and is replaced by a reverse flow similar to that observed at mid-acceleration. The similitude of this flow at mid-acceleration and mid-deceleration is best

seen in the velocity vector distribution and out-of-plane vorticity contours at the 585 μm-level (Figure 4-35) but also along the hinge center plane (Figure 4-37). The velocity magnitude of this reverse flow at 585 μm below the flat level is similar at mid-acceleration and mid-deceleration with a peak at 0.15 m/s and 0.13 m/s, respectively.

Leaflet closing phase

The fully open leaflet phase ends at 330 ms within the cardiac cycle. It is followed by the leaflet closing phase that lasts 55 ms. During this phase, the leaflet moves from its fully-open to its fully-closed position, thereby spanning an angle of 55^{o}. This rapid leaflet motion, combined with the decreasing bulk valvular flow rate, gives rise to complex unsteady flow structures within the hinge recess. In order to best visualize these time-dependent flow structures, Figure 4-39 and Figure 4-40 show the hinge flow fields at three instances of the leaflet closing phase, from 348 ms to 382 ms into systole. Figure 4-39 focuses on the flat level while Figure 4-40 presents the flow structures deeper into the hinge recess.

At the beginning of the leaflet closing phase (348 ms), a slow reverse flow with low out-of-plane motion is seen throughout the flat level. The velocity magnitude does not exceed 0.19 m/s and the out-of-plane u-velocity magnitude at this instance ranges from -0.05 m/s to 0.10 m/s. A similar flow pattern is seen at deeper levels within the hinge recess (Figure 4-40).

As the leaflet closes further (372ms), the reverse flow accelerates and elevated velocity magnitudes are seen throughout the flat level, in particular near the upstream and downstream edges of the leaflet where the flow squeezes between the leaflet and recess walls. The velocity magnitude reaches 0.61 m/s and 0.59 m/s in the aortic pocket and ventricular pocket, respectively. Comparison of the flow at the different levels within

the hinge recess shows a similar velocity vector distribution at the flat level and the 195 μm-level, but with stronger velocity magnitudes at the flat level. In the aortic corner, the incoming reverse flow impinges the leaflet and dives inside the hinge recess. Part of the incoming flow is deflected towards the lateral corner, inducing the formation of a fast-paced flow. In the adjacent corner, the flow follows the curvature of the leaflet and is then redirected towards the ventricular corner as it impinges the recess wall. The direction of the incoming reverse flow and the position of leaflet yields to a region of flow separation on right side of the leaflet characterized by a region of low flow. At deeper levels (390 μm and 585 μm-levels in Figure 4-40), the hinge recess is characterized by a strong reverse flow pattern oriented towards the lateral side of the hinge.

At the end of systole (382 ms), the leaflet has nearly reached its fully closed position. Two strong leakage jets are observed in the adjacent and lateral corners of the hinge. At the flat level, the velocity magnitude in these corners reaches 1.02 m/s and 1.07 m/s, respectively. These two leakage jet are predominantly oriented towards the lateral side of the hinge as indicated by the velocity vector distribution at the flat level (Figure 4-39), the 195 μm and the 390 μm-levels (Figure 4-40). A third leakage jet may be identified as the flow dives inside the hinge recess in the aortic corner and exits the hinge recess from the ventricular corner. This observation is supported by the orientation of the velocity vectors and by the out-of-plane velocity component distribution. The latter shows a region of elevated negative u-velocity (extremum u-velocity of -0.39 m/s) in the aortic corner that suggest diving of the flow inside the recess; and a region of elevated positive u-velocity (up to 0.48 m/s) in the ventricular corner indicating that the flow there exits the recess.

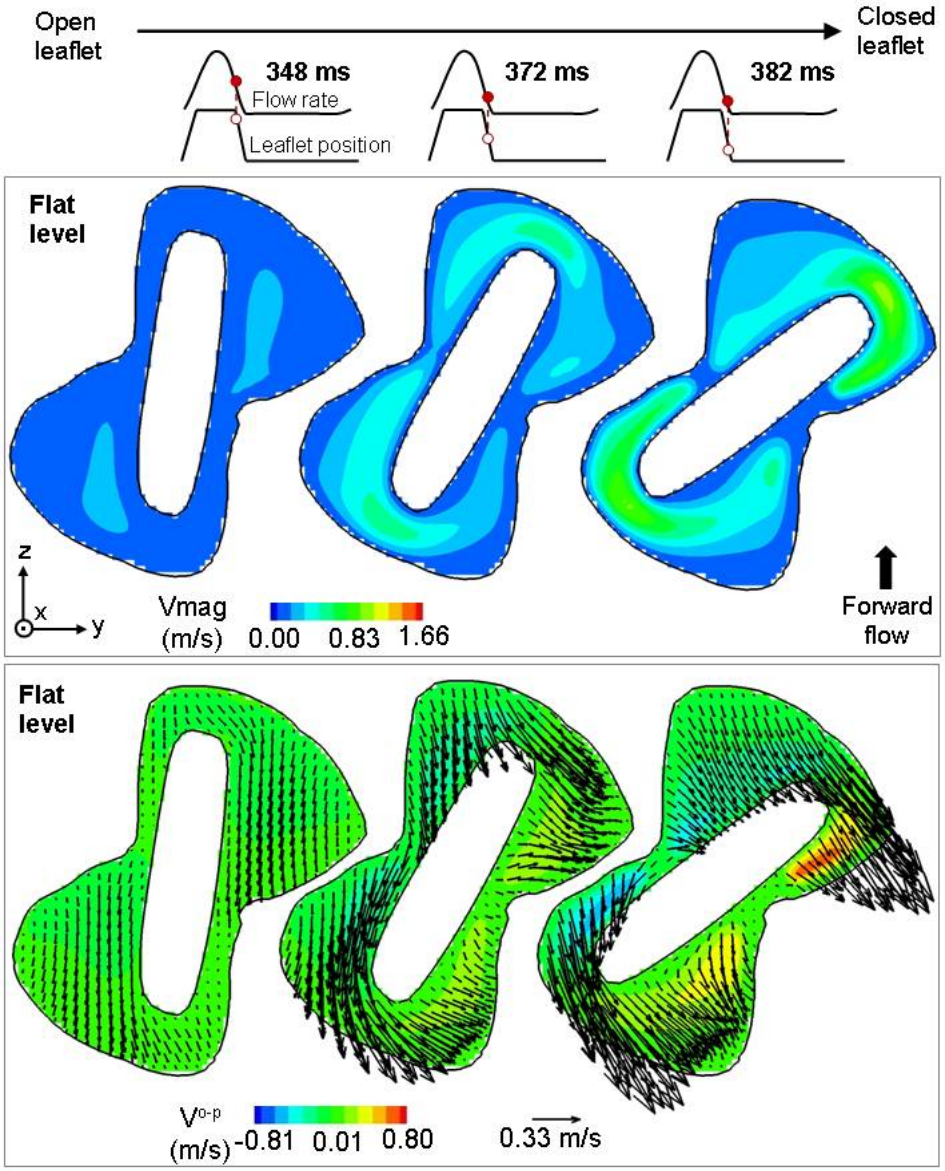

Figure 4-39: Three-dimensional velocity magnitude (top row) and two-dimensional in-plane velocity vectors with out-of-plane velocity contours (bottom row) at the flat level during the closing phase. [SJM hinge design with a large hinge gap width]

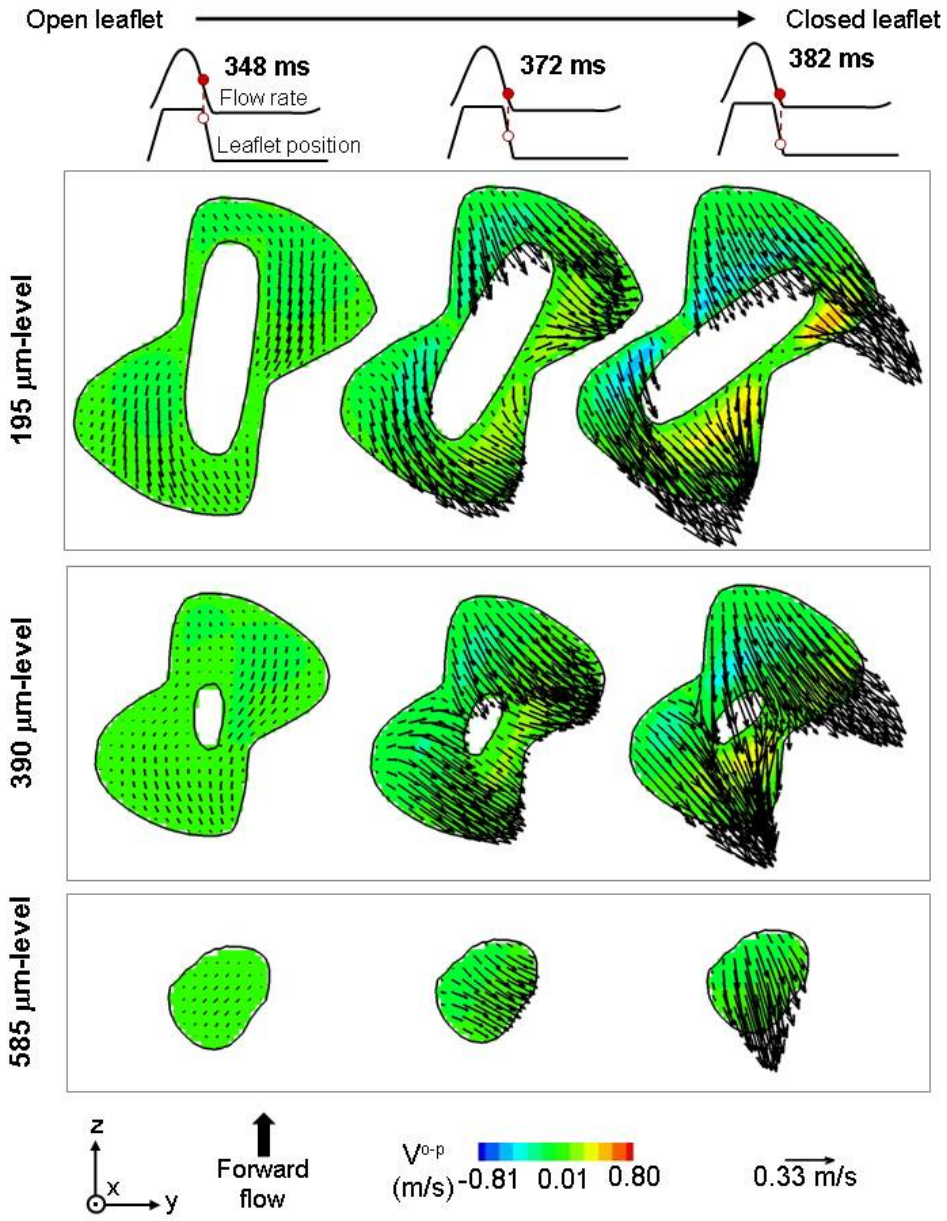

Figure 4-40: Two-dimensional in-plane velocity vectors with out-of-plane velocity contours at 195 μm, 390 μm, and 585 μm below the flat level during the leaflet closing phase. [SJM hinge design with a large hinge gap width]

This ventricular leakage jet is visible at the deepest level within the hinge recess (585 μm-level in Figure 4-40). The strength and orientation of the leakage flow at the bottom of the hinge recess are seen to change as the leaflet closes. At 372 ms, a leakage flow of low magnitude and oriented towards the lateral side of the hinge is observed. At the end of systole (382 ms), the velocity vector distribution shows a strong leakage flow which is primarily oriented towards the ventricular side of the hinge. A cross-sectional view through the hinge center plane at this instance of time (Figure 4-41) reveals that the leakage flow is characterized by a parabolic-like profile with relatively small out-of-plane motion. Along the hinge central plane, the maximum velocity magnitude is 0.80 m/s in the leaflet-recess gap and the maximum out-of-plane v-velocity component is 0.32 m/s.

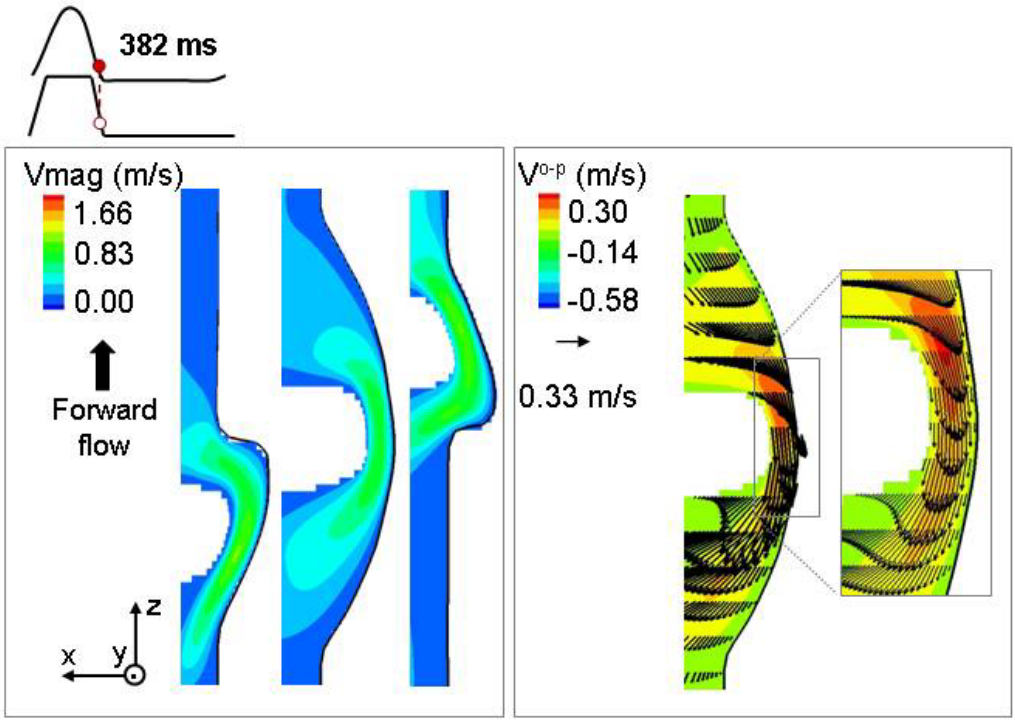

Figure 4-41: Three-dimensional velocity magnitude contours along three cross-sectional planes of the hinge (left) and the in-plane velocity vectors distribution along the hinge central plane (right) at late systole (382 ms).
[SJM hinge design with a large hinge gap width]

Fully-closed leaflet phase

The results presented here focus on the phase after valve closure, when the leaflet is in its fully closed position and a constant leakage flow is leaking through the closed valve. During the fully-closed leaflet phase, the configuration of the flow structures within the hinge recess resembles that observed at the end of the leaflet closing phase but with increased velocity magnitude. Three main flow structures are identified: a leakage jet in the lateral corner of the hinge, a second one in the adjacent corner, and a third one at the bottom of the hinge recess, exiting the hinge through the ventricular corner. Each of these jets corresponds to a set of streamtraces of different colors in Figure 4-26.

To gain further insight into the hinge flow fields during the fully-closed leaflet phase, Figure 4-42 shows the three-dimensional velocity magnitude along four planes within the hinge recess at mid-diastole. Two-dimensional velocity vectors superimposed on the out-of-plane velocity component contours along the same planes are also included. The flow is seen to accelerate as it squeezes between the closed leaflet and the housing surface. This leads to the formation of two leakage jets, one in the lateral corner and the other one in the adjacent corner of the hinge. The velocity magnitude of these two jets is high with, at the flat level, a peak at 4.63 m/s for the lateral jet and at 5.26 m/s in the adjacent jet. Both of these two jets are primarily oriented towards the lateral side (right side) of the hinge recess, as underscored by the direction of the velocity vectors in the lateral and adjacent corners at the flat level.

The velocity magnitude distribution along with the in-plane velocity vectors clearly highlight the existence of the third leakage jet that emanates from the hinge through the ventricular corner. This jet results from the flow in the aortic corner diving into the recess, accelerating in the gap formed by the leaflet ear and the recess, and finally exiting the

hinge from the ventricular corner. This jet exits the recess near the hinge wall and thus a region of low flow is visible at the flat level in the ventricular corner, near the leaflet surface. This ventricular jet has a strong axial velocity component as suggested by the direction of the in-plane velocity vectors provided in Figure 4-42. This is also seen in the trajectory of the streamtraces at mid-diastole in Figure 4-26. Moreover, this jet is observed to extend all the way to the bottom of the hinge recess. This is underscored by the presence of the large axial in-plane velocity vectors present at the deepest level within the hinge recess (the 585 μm-level). The velocity magnitude of the ventricular jet is less than that of the adjacent and lateral jets with a maximum of 4.78 m/s at the flat level. The ventricular jet exits the hinge with a strong out-of-plane motion. The maximum u-velocity component in the ventricular corner reaches 2.37 m/s at the flat level compared to 2.97 m/s in the lateral corner and 2.39 m/s in the adjacent corner.

Each of these three leakage jets can be identified in the out-of-plane vorticity contour plot shown in Figure 4-43. The juxtaposed layers of negative and positive vorticity along the wall of the adjacent and lateral corners correspond to the adjacent and lateral jet respectively. The shear layers along the upstream wall of the hinge recess appear to be disrupted. This is due to the ventricular jet exiting the hinge recess in this region. This leakage jet, as noted previously, extends to the bottom of the hinge recess and explains the vorticity distribution observed at the deepest level within the hinge recess (the 585 μm-level).

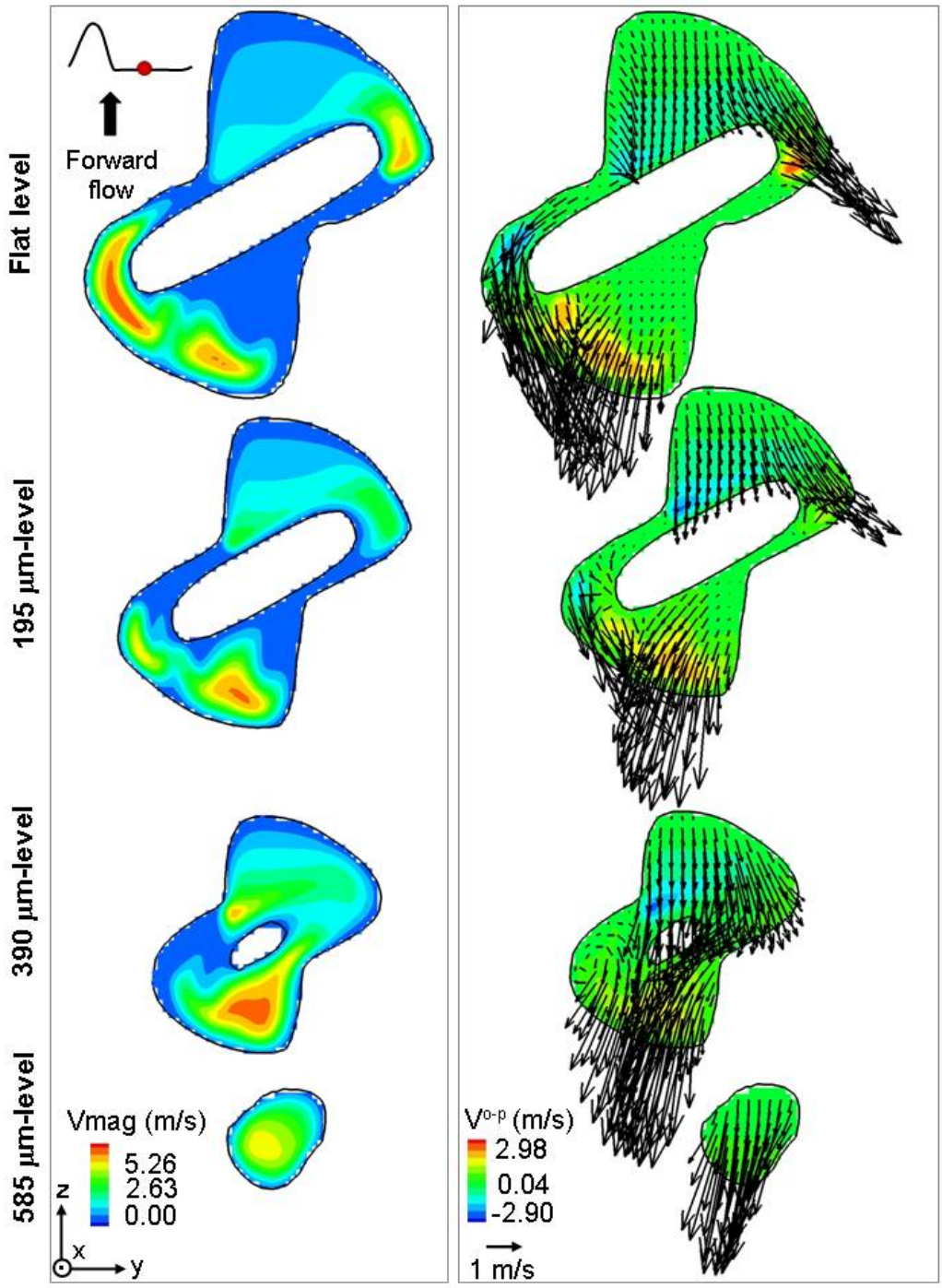

Figure 4-42: Two-dimensional in-plane velocity vectors with out-of-plane velocity contours at the flat level, 195 µm, 390 µm, and 585 µm below the flat level at mid-diastole. [SJM hinge design with a large hinge gap width]

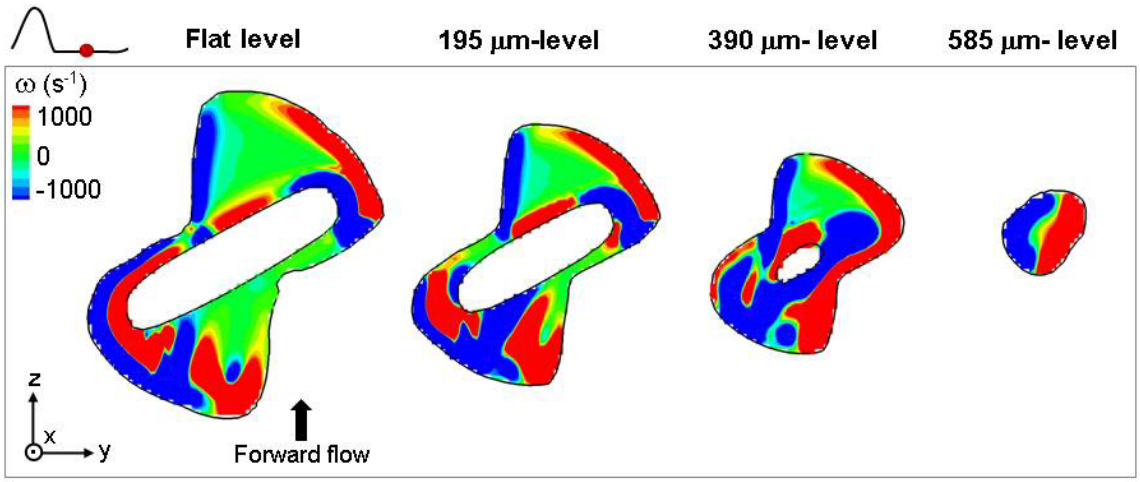

Figure 4-43: Out-of-plane vorticity contours along four planes parallel to the flat level at mid-diastole. [SJM hinge design with a large hinge gap width]

Cross-sectional views through the hinge recess provide additional information on the flow structures that exists within the hinge recess during the leakage phase. In particular the hinge center plane reveals that the ventricular leakage jet is characterized by a near-parabolic profile when flowing underneath the leaflet ear. However, the lateral plane indicates that further on the lateral side of the hinge, the ventricular plane has a profile skewed towards the leaflet ear.

The skewed parabolic profile shown in the lateral plane (Figure 4-44) corresponds to the adjacent jet. It is interesting to note that along this plane, in the aortic (top) part of the recess, a region of low reverse flow is present. This region of low flow is also visible at the 390 μm-level in Figure 4-42. This region of low flow corresponds to a region of flow separation due to the presence of the strong leakage jet that persists near the flat level in the adjacent corner.

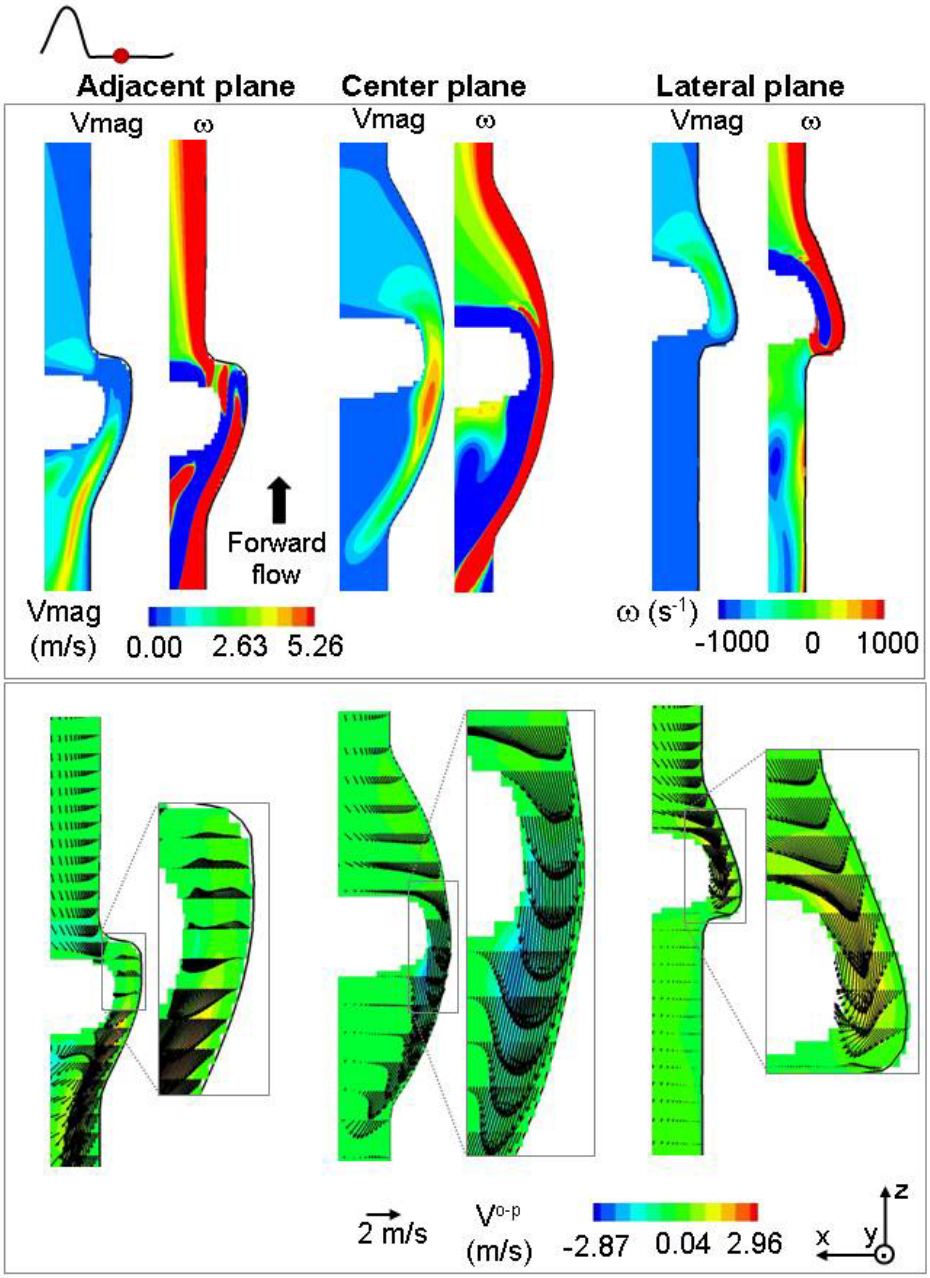

Figure 4-44: Three-dimensional velocity magnitude (top row) and two-dimensional in-plane velocity vectors with out-of-plane velocity contours (bottom row) along the adjacent, central, and lateral planes of the hinge at mid-diastole.
[SJM hinge design with a large hinge gap width]

4.3.3 Detailed description of the shear stress distribution

The iso-surfaces in Figure 4-28 and the animations SJMLarge_Isosurfaces_ MidDiastole.mov and SJM_Large_Isosurfaces_Peaksystole.mov show the global distribution of the shear stress in the hinge and near hinge region at key instances of the cardiac cycle. More details on the shear stress distribution are obtained by considering the shear stress contour maps along five planes outside and within the hinge recess at multiple instances of time (Figure 4-45 and Figure 4-46). Animations complement this figure by illustrating the temporal variations of the shear stress distribution throughout the cardiac cycle (SJMLarge_Shear_Stress_Contours.mov at four planes within the hinge recess). The local shear stress maxima are indicated on each one of these contour maps. In this section, the shear stress distribution is described first during the forward flow phase, and then during the leakage flow phase. The temporal variations of the maximum shear stress levels in the hinge and the near-hinge region throughout the cardiac cycle are presented last.

Forward flow phase: During the forward flow phase, the iso-surfaces showed that the shear stress levels in both the hinge and near-hinge region are dependent upon the bulk valvular flow rate. The maximum shear stress levels were seen at peak systole when the bulk valvular flow rate is the highest. This is further confirmed by the shear stress distributions presented in Figure 4-45 and Figure 4-46. Additionally, the iso-surfaces highlighted that the principal region of high shear stress during systole is located immediately upstream of the open leaflet. This corresponds to the region where the incoming flow is squeezed between the housing and the leaflet surface. This region is clearly seen along the plane located outside of the hinge along the leaflet surface (top row in Figure 4-45), where a localized region of elevated shear stress is seen

immediately upstream of the open leaflet. The peak shear stress in this region along the plane located outside of the hinge is 410 dyn/cm^2 at mid-acceleration, 900 dyn/cm^2 at peak systole, and 400 dyn/cm^2 at mid-deceleration. A second region of elevated shear stress is identified with the shear stress contour map outside of the hinge. This localized region is located outside of the hinge recess immediately downstream of the open leaflet. At all three depicted instances, the shear stress levels downstream of the leaflet are consistently smaller than those downstream of the leaflet.

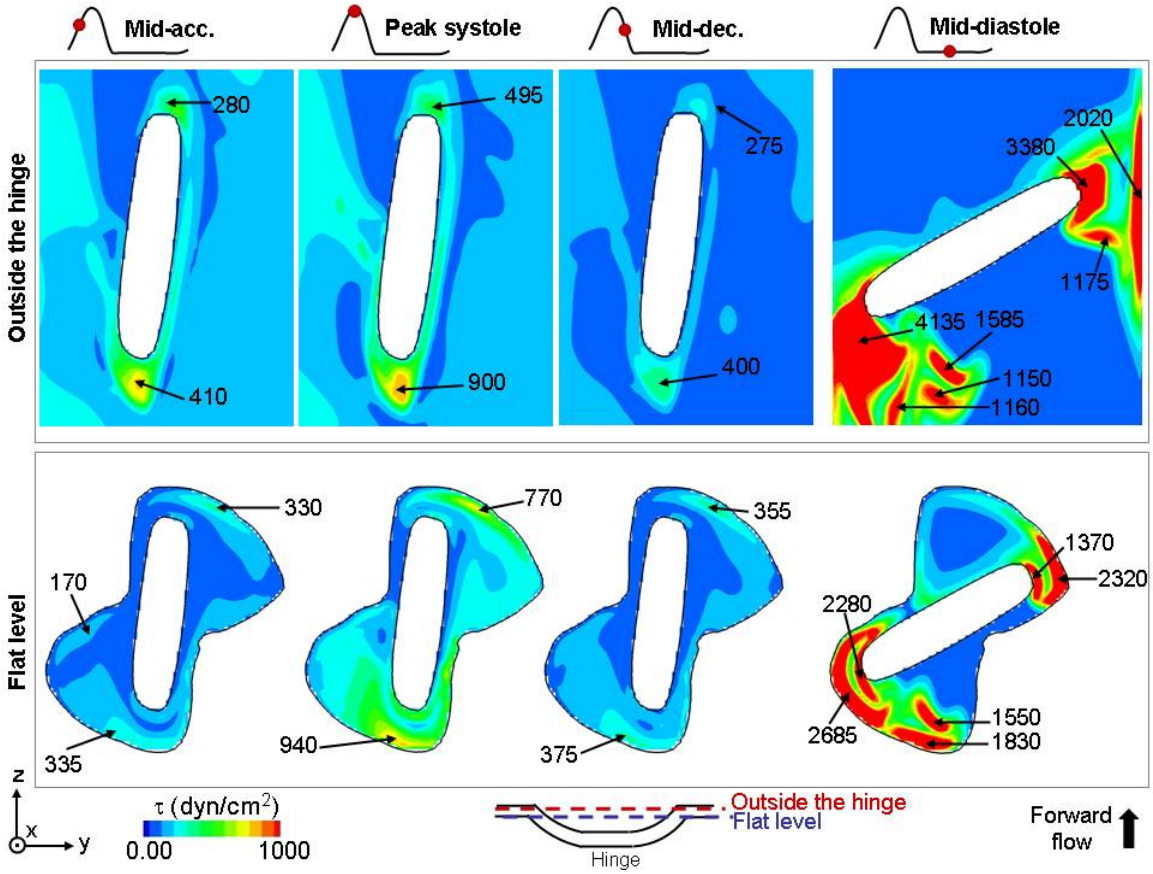

Figure 4-45: Shear stress distribution at mid-acceleration, peak systole, mid-deceleration, and mid-diastole. The top row shows a plane located outside the hinge recess, near the leaflet edge surface as depicted in the schematic. The bottom row corresponds to the flat level. [SJM hinge design with a large hinge gap width].

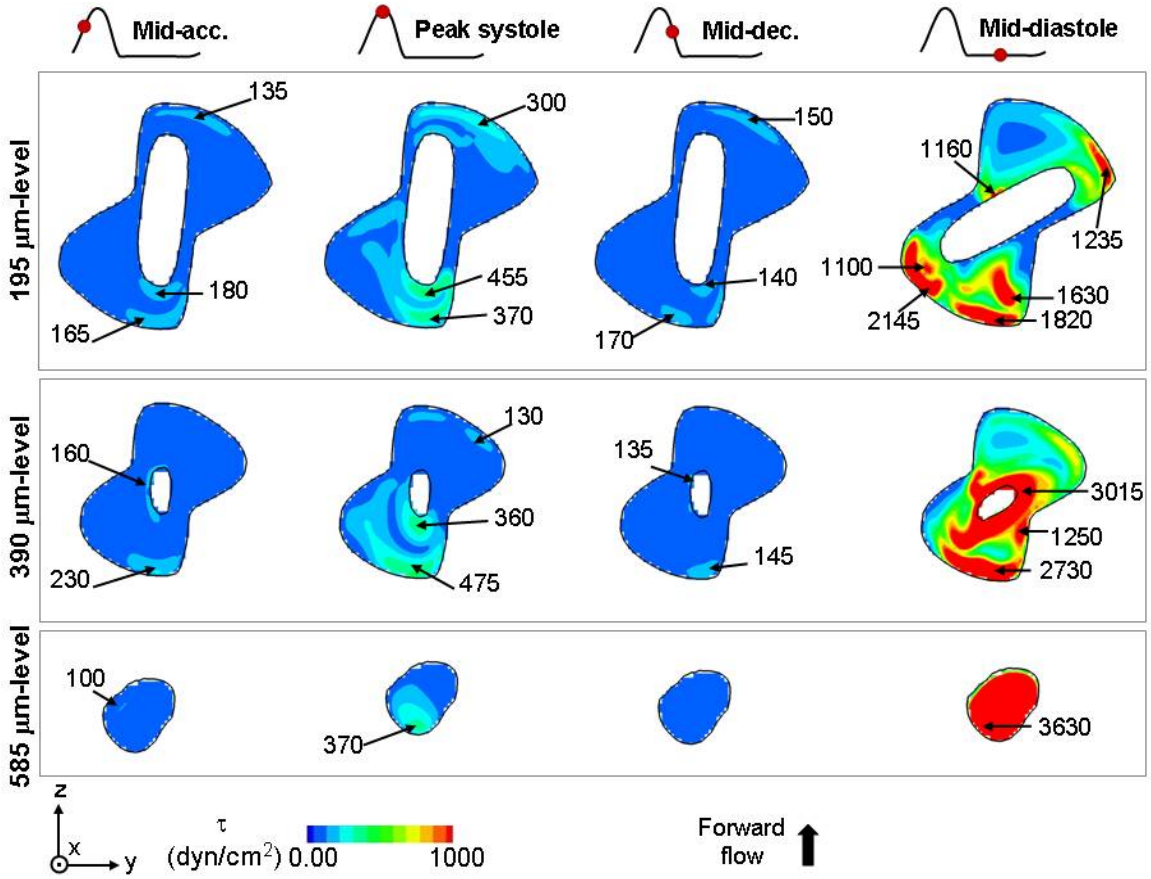

Figure 4-46: Shear stress distribution at mid-acceleration, peak systole, mid-deceleration, and mid-diastole at 195 μm, 390 μm and 585 μm below the flat level. [SJM hinge design with a large hinge gap width].

The maximum shear stress computed up to 500 μm outside of the hinge recess reaches 1,730 dyn/cm^2 at peak systole. This maximum reaches 1,460 dyn/cm^2 within the hinge recess (near the recess wall at the flat level) at the same instant in time. This clearly indicates that the maximum shear stress during the forward flow phase occurs outside of the hinge rather than within the hinge. This compares well with the absence of elevated shear stress iso-surfaces within the hinge recess during the forward flow phase.

At the flat level (bottom row of Figure 4-45), the maximum shear stress values are seen at peak systole, with a maximum of 940 dyn/cm^2 near the upstream wall of the ventricular corner and 770 dyn/cm^2 near the downstream wall of the aortic pocket. Overall, the shear stresses reported for the flat level are systematically greater than those obtained at deeper levels within the hinge recess (Figure 4-46). This correlates with the velocity magnitude distribution that showed faster-paced flow at the flat level than at the bottom of the hinge recess. Moreover, comparison of the shear stress distribution at the different levels within the recess (Figure 4-45 and Figure 4-46) highlights that during the forward flow phase the shear stresses in the ventricular pocket of the hinge are consistently higher than those computed in the aortic pocket. Three main regions of elevated shear stresses can be identified: along the upstream wall of the ventricular corner, along the downstream wall of the aortic corner, and near the upstream edge of the leaflet ear.

Figure 4-47 shows the shear stress distribution along the lateral, central and adjacent planes of the hinge at the same four instances in time as shown in Figure 4-45 and Figure 4-46. As previously noted, it is clear that it is at peak systole that the shear stress levels are the highest. The shear stress contour plots along these three cross-sectional planes further highlights that during systole, the maximum shear stress levels are not present inside the hinge recess, but near the valve housing surface, immediately upstream and downstream of the hinge. The central plane also underscores the existence of a region of elevated shear stress along the leaflet surface at peak systole. This is in agreement with the iso-surfaces presented in Figure 4-28. The peak shear stresses along the center plane of the hinge reach 1,040 dyn/cm^2 along the housing wall and 630 dyn/cm^2 along the leaflet wall at peak systole

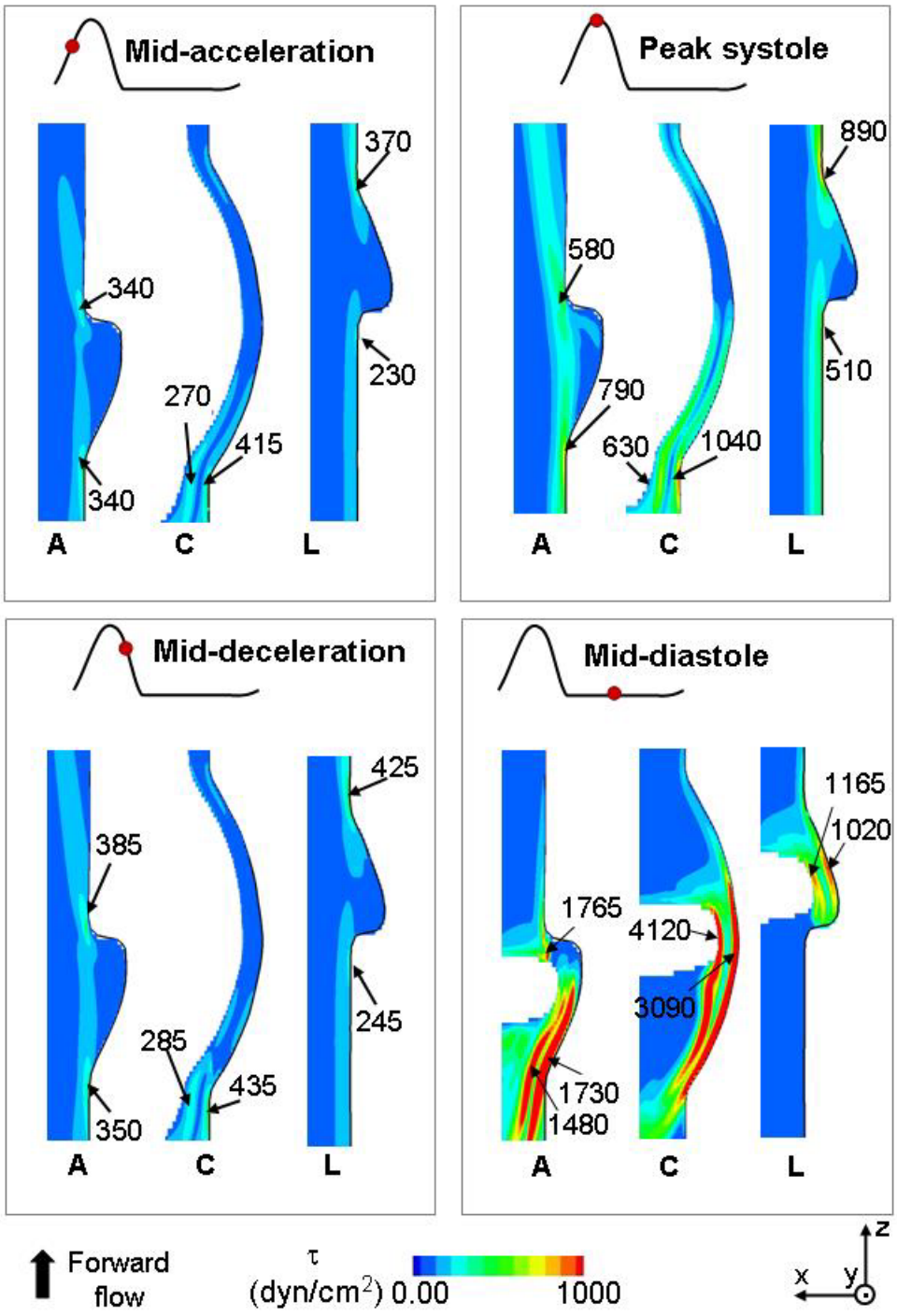

Figure 4-47: Shear stress distribution at mid-acceleration, peak systole, mid-deceleration, and mid-diastole along three cross-sectional planes: the adjacent (A) plane, the central (C) plane, and the lateral (L) plane.
[SJM hinge design with a large hinge gap width].

Leakage flow phase: The shear stress iso-surfaces shown in Figure 4-28 reveal that both the distribution and magnitude of the shear stress vary with time, with significant differences between the leakage and the forward flow phases. During diastole, large regions of elevated shear stress levels are seen on the wake of the leakage jets emanating from the gaps between the housing and the closed leaflet. This is clearly seen along the plane outside of the hinge recess, near the leaflet surface (top row in Figure 4-45). Regions of elevated shear stress levels (up to 4,135 dyn/cm^2) are seen on either side of the leaflet ear, where strong leakage flow jets exist. The effect of the jets originating from the hinge recess itself is also visible along this plane. The localized region of elevated shear stresses (up to 1, 595 dyn/cm^2) observed on the ventricular side of the leaflet corresponds to the leakage jet emanating from the ventricular corner of the hinge.

Within the hinge recess itself, the levels of shear stresses are lower than those reported outside of the hinge recess. Regions of high shear stresses are seen along the recess and leaflet walls in the lateral and adjacent corners where the flow squeezes between the leaflet and the hinge surface. At the flat level, the shear stress levels are the highest in the adjacent corner with a peak of 2,685 dyn/cm^2. Elevated levels of shear stresses are also seen in the ventricular corner at all levels within the hinge recess. These high shear stresses are associated with the ventricular leakage jet. Finally, it is interesting to note that while low shear stresses are seen at the bottom of the hinge recess throughout the forward flow phase, elevated shear stress levels are seen at mid-diastole (bottom row of Figure 4-46). These high levels are due to the ventricular leakage jet flowing underneath the closed leaflet. At 585 μm below the flat level, the maximum shear stress level reaches 3,630 dyn/cm^2.

Cross-sectional views through the hinge (Figure 4-47) highlight that the regions of elevated shear stresses are located in the wake of the leakage jets. This is particularly

visible along the adjacent and central planes. The maximum shear stress levels are seen in the central plane, along the leaflet and recess surfaces. In these region, shear stresses up to 4,120 dyn/cm^2 and 3,090 dyn/cm^2, respectively, are seen.

Overall, the shear stress contour maps emphasize that during the leakage flow phase the wake of the leakage jets and the bottom of the hinge recess are regions where large shear stresses above the threshold for platelet activation are computed.

Temporal variations: Both the iso-surfaces and shear stress contour maps show large changes in shear stress distribution with time. In order to better visualize these changes, Figure 4-48 shows the temporal variations of the maximum shear stress in the hinge and near hinge region during the first 550 ms of the cardiac cycle. The red curve depicts the global maxima computed within the hinge recess whereas the black curve corresponds to the global maxima observed in the hinge recess and its vicinity. This last zone is defined as the blue region in the schematic shown below the graph in Figure 4-48.

During the first 88 ms of the cardiac cycle, the leaflet moves from its fully-closed to its fully-open position. This leaflet motion entrains the surrounding fluid, thereby inducing complex and unstable flow patterns (see section 4.3.2). This induces in turn a complex shear stress field distribution, with noticeable variations in maximum shear stress (Figure 4-48). During this period, the red and black curves are superimposed, indicating that the maximum shear stress occur within the hinge recess.

Once the leaflet has reached its fully open position (after 88 ms), both curves exhibit a similar parabolic trend. This suggests that the maximum shear stress follows the variation of the bulk valvular flow rate. Consequently, the highest shear stress values during the forward flow phase are seen at peak systole, with a peak of 1,460 dyn/cm^2 inside the hinge recess and 1,730 dyn/cm^2 in the hinge vicinity.

From 330 ms to 385 ms, the leaflet closes and the valvular flow rate increases steadily to its constant diastolic value. This translates into an increase in the maximum shear stress values during the leaflet closing phase. At the instant in time when the leaflet reaches its fully-closed position the maximum shear stresses increase abruptly and then reach a plateau. Shear stress levels above the threshold for platelet activation are seen during the forward flow phase, and in particular at peak systole. However, it is during the leakage phase that the highest shear stresses are computed. The maximum shear stress levels are nearly 3.5 times larger during the leakage phase than during the forward flow phase. At mid-diastole, the shear stress levels reach 5,445 dyn/cm^2 inside the hinge recess and 6,320 dyn/cm^2 in the hinge vicinity. During the forward flow phase, the maximum shear stresses are lower with a peak of 1,430 dyn/cm^2 inside the recess and a peak of 1,730 dyn/cm^2 in the hinge vicinity.

It may be observed that the black curve lies above the red one throughout the cardiac cycle except during the leaflet opening and closing phases. This indicates that the highest shear stress values are observed for most of the cardiac cycle outside of the hinge recess rather than within. These elevated high shear stress levels during the forward flow phase correspond to the region identified earlier (Figure 4-28 and top row of Figure 4-45) immediately upstream of the hinge, in the gap formed by the leaflet surface and the flat level. During the leakage flow phase, the elevated shear stresses are located in the wake of the leakage jets as previously shown with the iso-surface plots and contour maps given in Figure 4-28, Figure 4-46 and Figure 4-47.

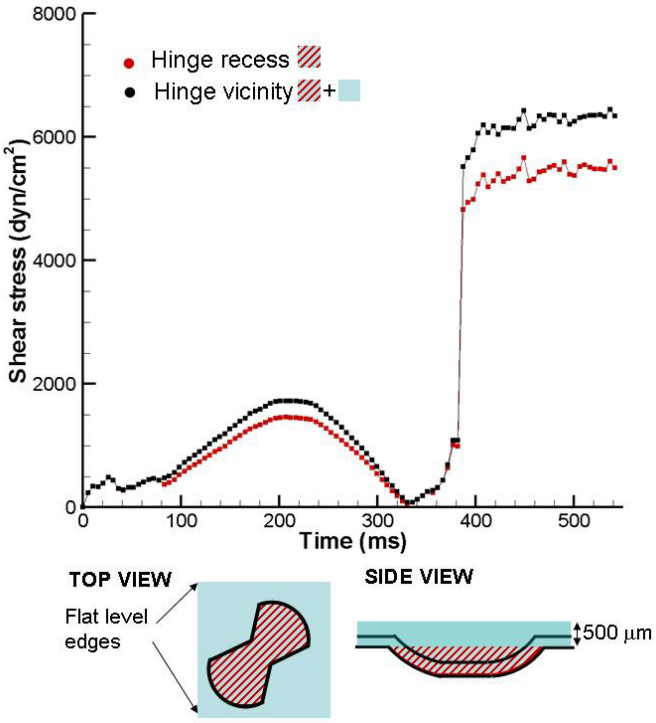

Figure 4-48: Variations of the maximum principal shear stress within the hinge recess (red) and in the hinge vicinity (black) as a function of time.
[SJM hinge design with a large hinge gap width].

4.4 Eulerian analysis of the CM hinge design with a regular hinge gap width

Following the same outline as in the two previous sections describing the hinge flow fields for the two SJM hinge designs (sections 4.2 and 4.3), the following section provides first an overview of the hinge flow fields and shear stress distribution throughout the cardiac cycle. A detailed description of the flow fields during 1) the leaflet opening phase, 2) the fully-open leaflet phase, 3) the leaflet closing phase, and finally 4) during the fully-closed leaflet phase then follows.

4.4.1 Overview

In order to get a good understanding of the global hinge hemodynamics and identify important flow features, two sets of images are provided. The three-dimensional instantaneous streamtraces (Figure 4-49) are used to qualitatively depict the flow features present within the hinge recess at mid-acceleration, peak systole, mid-deceleration, and mid-diastole. These flow features are then assessed quantitatively in Figure 4-50 using three-dimensional velocity vectors superimposed on the velocity magnitude contours. Animation CM_3DView_3DVectors_3DVmag.mov shows in details the temporal variations of the flow fields during the cardiac cycle.

The streamtraces (Figure 4-49) and the magnitude of the out-of-plane velocity component (Figure 4-50) underscore the three-dimensionality of the flow fields throughout the cardiac cycle. Comparison of streamtraces at mid-acceleration, peak systole and mid-deceleration does not indicate any large difference in flow features. The blue streamtraces reveal that, in the ventricular corner of the hinge, the flow dives into the hinge recess through the tip of the corner and goes underneath the leaflet towards the adjacent corner. These streamtraces then form, with the blue streamtraces that enter the hinge directly through the adjacent corner, a large recirculating flow pattern. All blue streamtraces exit the hinge recess from the downstream-most part of the adjacent corner, thus yielding a strong out-of-plane flow motion (Figure 4-50).

The red streamtraces on the other hand clearly show a more streamlined flow pattern and highlight the presence of a reverse flow pattern throughout the forward flow phase in the central region of the hinge. Figure 4-50 shows that this reverse flow is of low magnitude throughout the forward flow phase and reaches its maximum magnitude at peak systole. Additionally, the red streamtraces also suggest that part of the fluid dives into the lateral corner and follows the curved downstream wall of the hinge before

exiting the recess from the left-most tip of the aortic corner. The observed flow patterns are persistent throughout systole but vary in intensity with the magnitude of the incoming flow rate. The increase in flow rate towards peak systole also translates into a higher three-dimensionality of the flow, with larger out-of-plane velocity components seen at all levels within the hinge recess. The main difference in flow structure is seen in the lateral corner, where a small flow swirl exists near the leaflet surface at both peak systole and mid-deceleration, but is not visible at mid-acceleration. This may be due to the flow deceleration giving rise to flow instabilities.

The diastolic phase, on the other hand, shows extremely different flow features compared to the forward flow phase. Highly three-dimensional leakage flows are present throughout the hinge recess. Three main flow structures, each colored with a different color in Figure 4-49, may be identified. The blue streamtraces underscore the existence of a streamlined flow pattern in the central region of the hinge recess. The flow in the aortic corner is seen to dive into the recess, flow underneath the leaflet ear and exit the recess through the ventricular corner. Two additional leakage jets are seen on either side of the leaflet ear. The first one corresponds to the green streamtraces which clearly show the fluid diving into the left-most tip of the adjacent corner and exiting the recess from the ventricular corner. The second jet, depicted in red, is seen to form in the lateral corner of the hinge and exit the recess from the right-most tip of the adjacent corner with a more streamlined pattern. These three main flow structures are associated with a large out-of-plane motion as shown by the three-dimensional velocity vectors in Figure 4-50. Velocity vectors with large out-of-plane v-velocity components are clearly seen in the ventricular and lateral corners where the flow exits the hinge, but also in the adjacent corner where the fluid dives in the hinge.

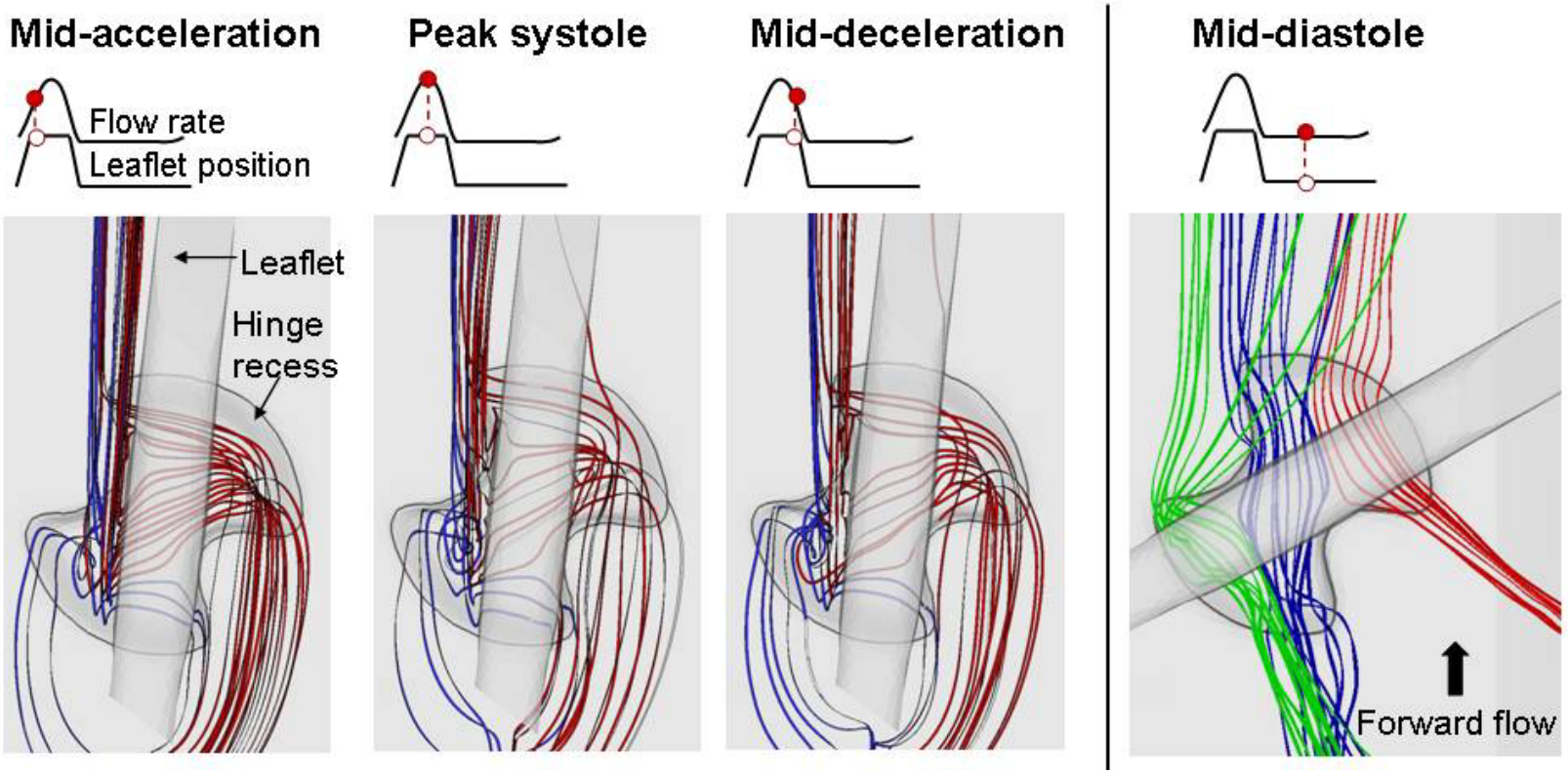

Figure 4-49: Three-dimensional instantaneous streamtraces at mid-acceleration, peak systole, mid-deceleration, and mid-diastole. [CM hinge design with a regular hinge gap width].

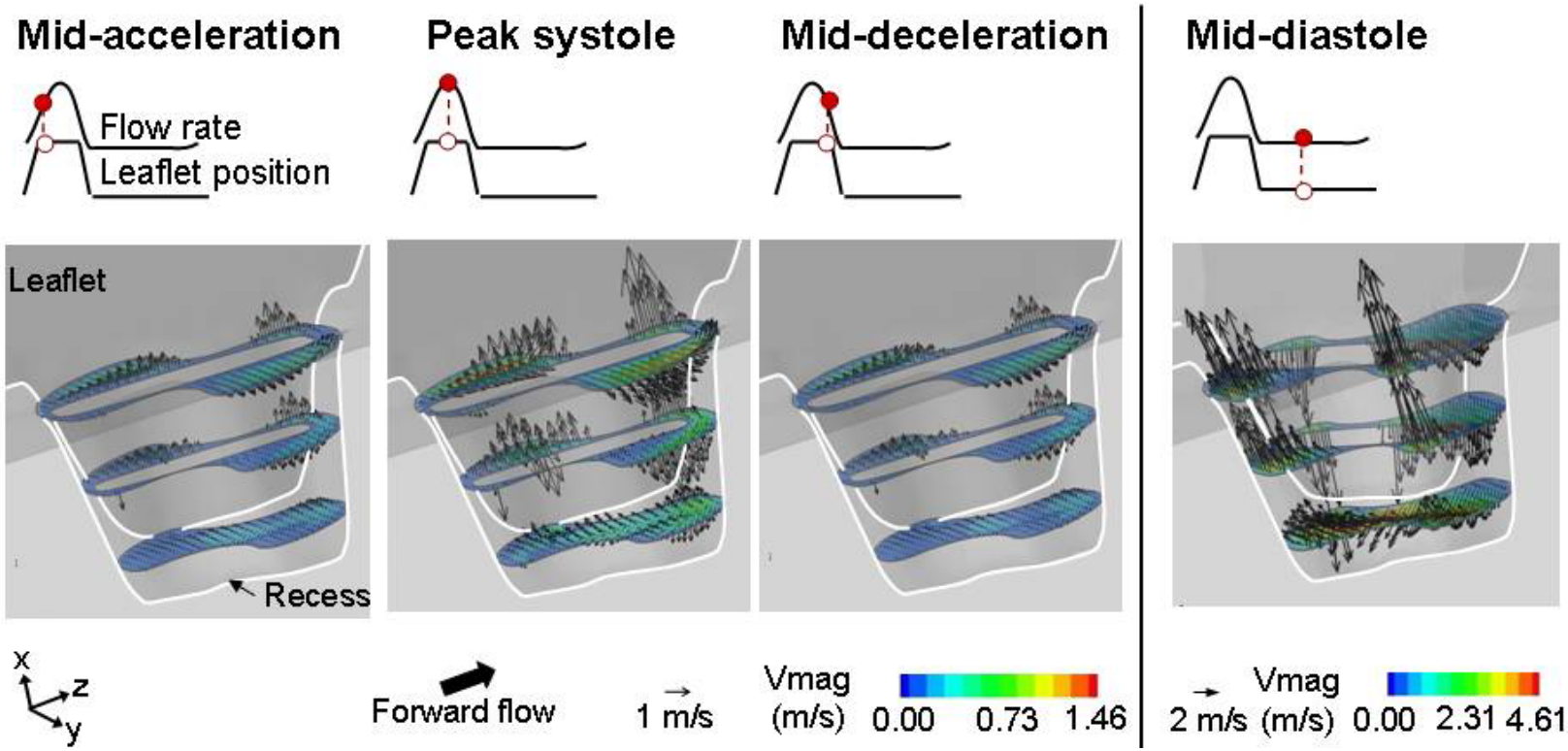

Figure 4-50: Three-dimensional velocity vectors with three dimensional velocity magnitude contour plots along four planes within the hinge recess and at four instances of the cardiac cycle. Note that the x-axis is not to scale and has been stretched to allow visualization of the flow fields. [CM hinge design with a regular hinge gap width].

Comparison of the velocity vector fields throughout the cardiac cycle underscore that the velocity magnitudes are the largest during the leakage phase when the leaflet is in its closed position. The peak velocity magnitude reaches 1.46 m/s at peak systole and 4.61 m/s at mid-diastole. Similarly, the three-dimensionality of the flow is more pronounced during the leakage phase compared to the forward flow phase (Figure 4-50 and Table 4-3).

Table 4-3: Maximum velocity magnitude and velocity component range throughout the hinge recess at mid-acceleration, peak systole, mid-deceleration, and mid-diastole [CM hinge design with a regular hinge gap width]

		CM hinge with a regular hinge gap width			
		Across entire hinge recess			
		Mid-acceleration	**Peak systole**	**Mid-deceleration**	**Mid-diastole**
Velocity range (m/s)	**u**	[-0.15;0.27]	[-0.42;0.67]	[-0.17;0.26]	[-3.01;3.34]
	v	[-0.33;0.24]	[-0.80;0.63]	[-0.32;0.28]	[-1.82;3.49]
	w	[-0.14;0.50]	[-0.36;1.45]	[-0.14;0.62]	[-4.60; 0.13]
Max. velocity magnitude (m/s)		0.51	1.46	0.62	4.61

To assess the global distribution of the shear stress in the hinge and near-hinge region, Figure 4-51 shows the iso-surfaces of the principal shear stress for the same four instances in time as above. Animations of the iso-surfaces at peak systole and mid-diastole are also provided (CM_Isosurfaces_MidDiastole.mov and CM_Isosurfaces_ PeakSystole.mov).The overall flow features being similar throughout the forward flow phase, it is of no surprise that the shear stress distribution is similar at mid-acceleration, peak systole, and mid-deceleration. However, the velocity magnitude inside the hinge recess was found to be dependent on the systolic bulk valvular flow rate and, thus, the

shear stress levels are also dependent on the flow rate. Consequently, the shear stress structures are similar at all three instants of the forward flow phase depicted, but the shear-stress values are higher at peak systole because of the large bulk valvular flow rate at this instant. For example, the shear stress iso-surfaces of 250 dyn/cm^2 at peak systole are similar to the iso-surfaces of 100 dyn/cm^2 at mid-acceleration and mid-deceleration. Similarly, the shear stress iso-surfaces of 500 dyn/cm^2 at peak systole are similar to the iso-surfaces of 250 dyn/cm^2 at mid-acceleration and mid-deceleration. Specific comparison of the 250 dyn/cm^2 iso-surface at mid-acceleration and mid-deceleration shows that the iso-surface downstream of the aortic pocket extends further downstream at mid-deceleration than at mid-acceleration. This may be due to the presence of flow instabilities in the lateral corner of the hinge during flow deceleration, as previously underscored by the 3D streamtraces.

Throughout systole, the iso-surfaces underline that the region of elevated shear stresses are located outside of the hinge recess rather than within. In particular, the principal region of elevated shear stresses is identified immediately upstream of the ventricular corner, close to the leaflet edge. Another smaller region of high shear is seen downstream of the adjacent corner. The maximum shear stress levels during the forward flow phase are observed at peak systole and reach 1,060 dyn/cm^2 within the recess and 1,800 dyn/cm^2 in the near-hinge region.

During the leakage phase, the distribution and magnitude of shear stress is different from that observed during the forward flow phase. As expected, the maximum shear stresses are seen on the wake of the leakage jets identified in both Figure 4-49 and Figure 4-50: downstream of the ventricular corner and downstream of the tip of the lateral corner. Also visible in Figure 4-51 are two additional regions of elevated shear

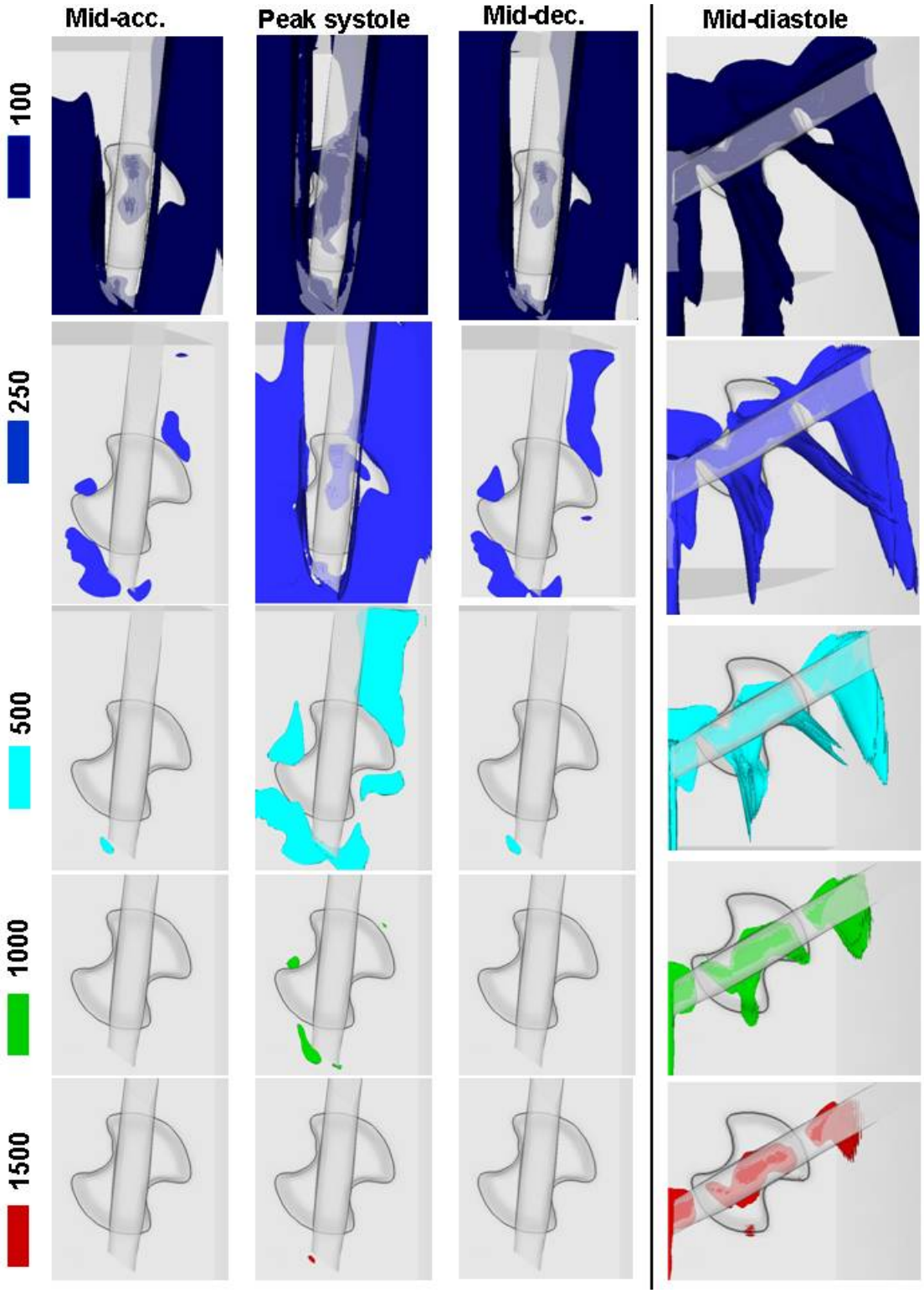

Figure 4-51: Iso-surfaces of shear stress levels at mid-acceleration, peak systole, mid-deceleration, and mid-diastole. The iso-surfaces are plotted for 100 dyn/cm^2 (dark blue), 250 dyn/cm^2 (blue), 500 dyn/cm^2 (light blue), 1,000 dyn/cm^2 (green), and 1,500 dyn/cm^2 (red). [CM hinge design with a regular hinge gap width].

stresses outside of the hinge recess. These regions correspond to the flow leaking through the gap, known as the peripheral gap, formed by the leaflet and the housing surface.

Localized regions of shear stress of 1,000 and 1,500dyn/cm^2 are identified during the forward flow phase outside of the hinge recess. However, during the leakage flow phase, the iso-surfaces for these same shear stress levels are very large with a main iso-surface observed within the hinge recess, underneath of the leaflet ear. Overall, the maximum shear stresses during the leakage phase are higher than those computed during the forward flow phase. These maximum stresses reach at mid-diastole 5,910 dyn/cm^2 within the recess and 8,985 dyn/cm^2 in the near-hinge region. The observed differences in shear stress distribution and magnitude suggest that the leakage phase will be more detrimental to blood elements than the forward flow phase.

4.4.2 Detailed description of the hinge flow fields

The following section provides a detailed description of the hinge flow fields throughout the cardiac cycle by presenting the flow along selected planes at multiple instants of time. In order to gain further insight into the dynamic of the flow, the reader is referred to the accompanying animations to clearly visualize the temporal variations of the described flow structures (animations CM_2Dvectors_V-o-p.mov and CM_2Dvectors _Vmag.mov at the same planes within the hinge recess].

Leaflet opening phase

This section focuses on the early phase of the cardiac cycle during which the leaflet spans 55^o to move from its fully-closed to its fully-open position. The leaflet

opening motion is rapid and only lasts during the first 88 ms of the cardiac cycle (whose entire duration is 860 ms). The hinge flow fields during the first 88 ms of the cardiac cycle are therefore dependent upon not only the slowly-increasing bulk valvular flow but also the abrupt motion of the leaflet. To best visualize the hinge flow dynamics during this phase, Figure 4-52 and Figure 4-53 show the hinge flow fields at four instances, spanning from 20 ms to 88 ms into the cardiac cycle. The first figure presents the velocity magnitude distribution at the flat level, the 195 μm, and the 390 μm-levels. Figure 4-53 displays the two-dimensional in-plane velocity vectors superimposed on the out-of-plane velocity distribution along the same three levels.

At early systole (20 ms), the leaflet is still in the near-fully closed position. A forward flow pattern of low magnitude is seen to develop in the ventricular and aortic corners as the bulk valvular flow rate starts to increase. The out-of-plane velocity distribution at the flat level indicates that the flow dives in the recess in the ventricular corner (u-velocity component extremum of -0.13 m/s) and flows out of the recess through the aortic corner (extremum of 0.17 m/s). This forward flow pattern underneath the leaflet ear is clearly visible at the 390 μm-level. The maximum velocity magnitude of the flow at this level is 0.60 m/s. The tip of the lateral corner is characterized by a forward flow with a large out-of-plane motion. In this region, the flow is seen to accelerate as it dives in the recess through the gap formed by the recess wall and the leaflet. The velocity magnitude and out-of-plane u-velocity component in this tip at the flat level reach up to 0.31 m/s and -0.25 m/s, respectively. On the other hand, the tip of the adjacent corner is associated with a jet that exits the hinge recess. The maximum velocity magnitude and out-of-plane velocity component in this tip are 0.40 m/s and 0.31 m/s, respectively.

As the leaflet opens further (42 and 57 ms), a forward flow pattern develops in the ventricular and lateral corners of the hinge (right-hand side of the leaflet in Figure 4-53). The direction of the flow in these corners appears to be mainly dictated by the leaflet surface at the flat level and the recess wall at 195 μm below the flat level. In contrast to the fast flow observed on the right-hand side of the leaflet, the flow structures on the left side of the leaflet (in the adjacent and aortic corners) are much slower. These lower velocities are due to the flow separation that occurs behind the leaflet. The flow at the bottom of the hinge recess (the 390 μm-level in Figure 4-53) shows a forward flow pattern of low magnitude that is primarily oriented towards the adjacent (right) side of the hinge. Comparison of the velocity magnitude distribution at 20 ms, 42, and 57 ms indicates that the velocity magnitude throughout the hinge recess decreases at 42 ms compared to early systole (20 ms) and then increases until the end of the leaflet opening phase.

At the end of the leaflet opening phase (88 ms), the flow in the adjacent corner of the hinge is deflected towards the lateral (right) side of the hinge as it impinges the recess wall. This flow feature, seen at the flat level, translates into the formation of a clockwise rotating flow structure clearly visible at the 195 μm-level. The forward flow pattern seen in the lateral corner at 42 ms and 57 ms increases in strength at the end of the leaflet opening phase. At deeper levels within the hinge recess, this forward flow is deflected towards the aortic corner as it collides with the downstream wall of the lateral corner. This flow then exits the hinge recess from the downstream-most (left) tip of the aortic corner with a large out-of-plane motion. In this tip, the velocity magnitude and the out-of-plane u-velocity component at the flat level reach up to 0.19 m/s and 0.15 m/s, respectively. At this instant in time, the velocity magnitude at the flat level reaches up to 0.40 m/s in both the adjacent corner and the lateral corner.

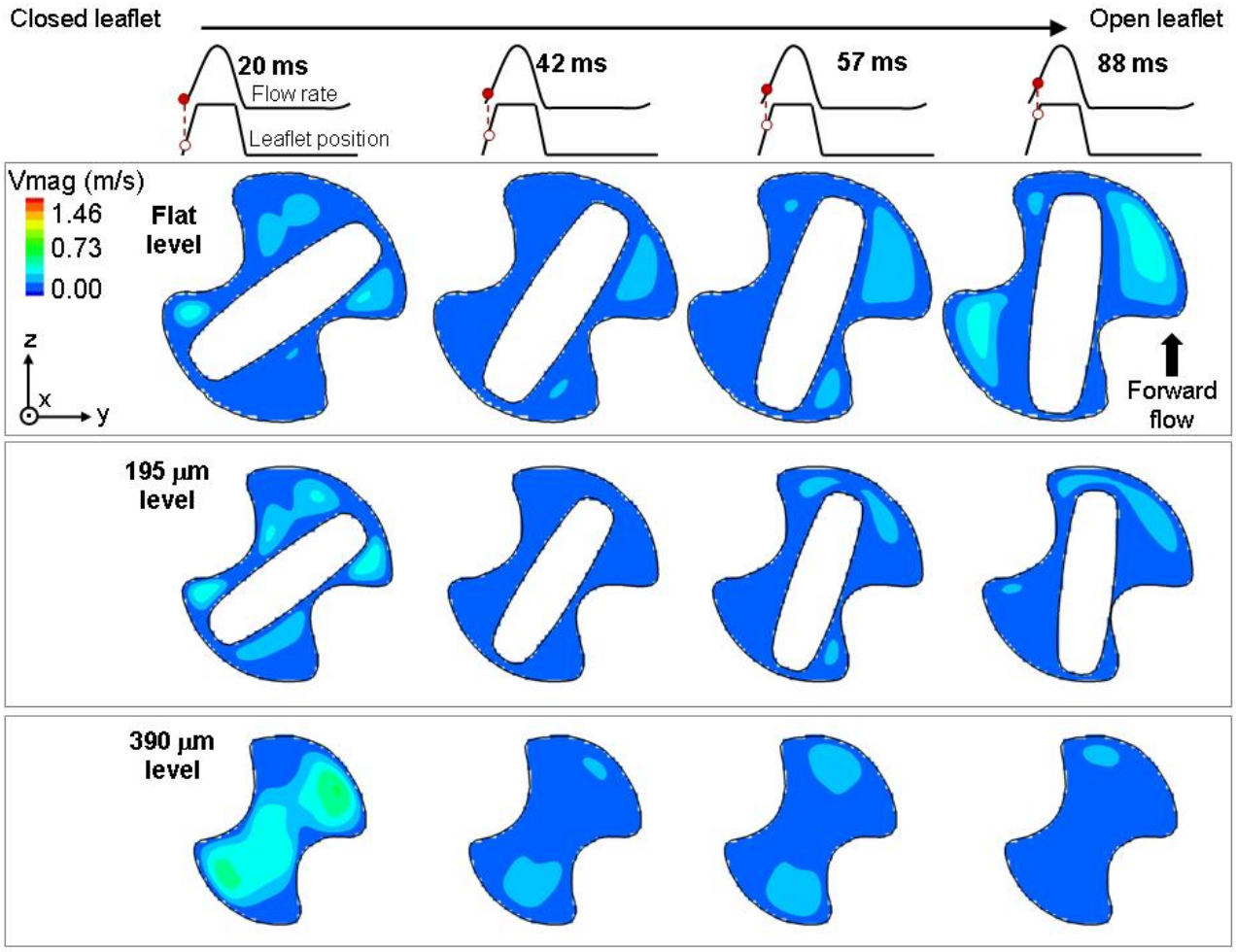

Figure 4-52: Three-dimensional velocity magnitude at the flat level, 195 μm, and 390 μm below the flat level at four instances of the leaflet opening phase. [CM hinge design with a regular hinge gap width]

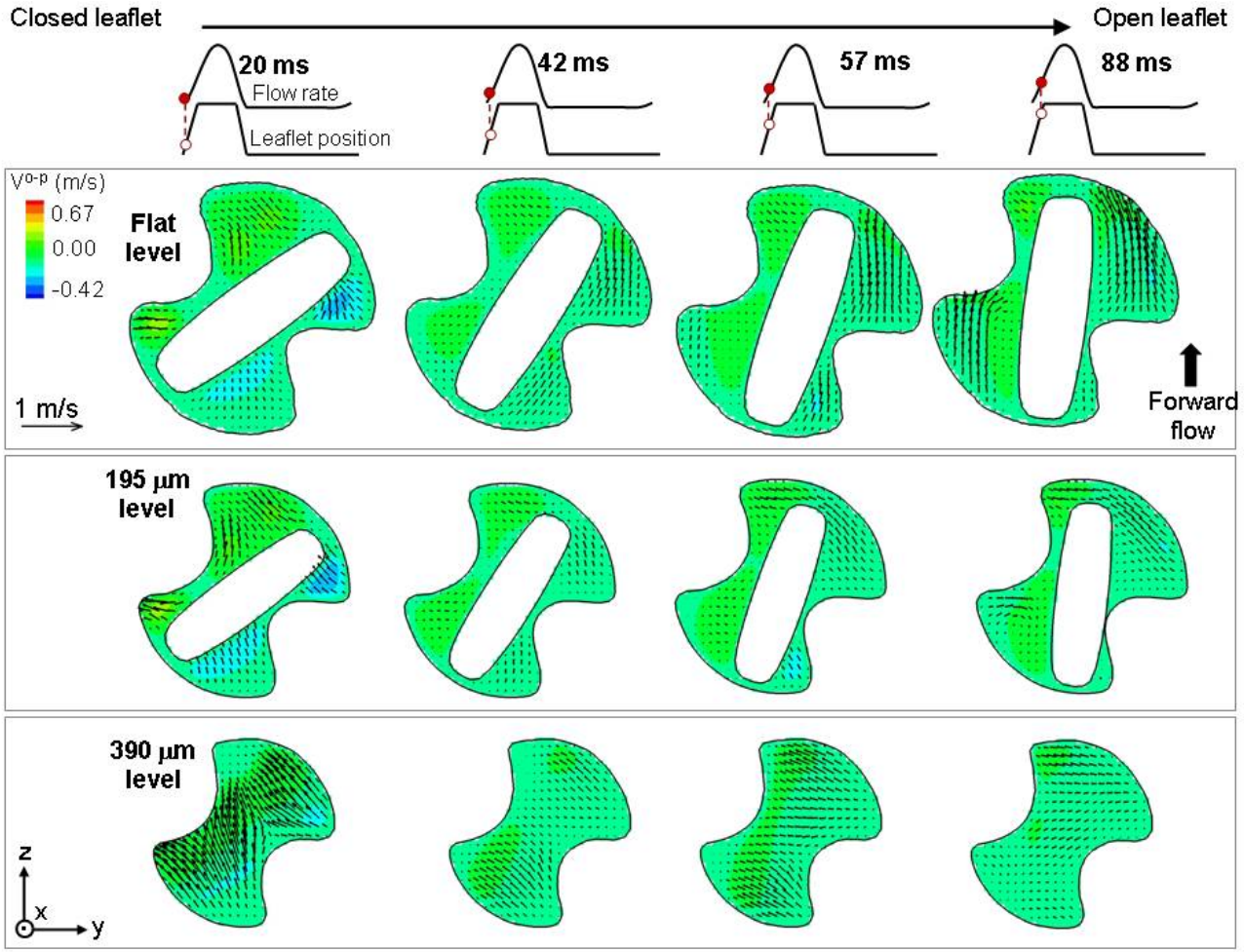

Figure 4-53: Two-dimensional in-plane velocity vectors with out-of-plane velocity contours at the flat level, 195 μm, and 390 μm below the flat level during the leaflet opening phase. [CM hinge design with a regular hinge gap width]

The complete opening of the leaflet induces a reversal in flow direction at the bottom of the hinge recess. This is visible at the 390 μm-level in Figure 4-53 but also in the hinge center plane displayed in Figure 4-54. The strong forward flow pattern visible at 20 ms decreases in strength and reverses direction. As the leaflet reaches its fully open position (88 ms), a reversed flow of low magnitude may be identified at the bottom of the hinge, in the central region of the recess. At early systole (20 ms), the magnitude of the forward flow pattern is 0.60 m/s. At the end of the opening phase, the magnitude of the observed reverse flow pattern decreases to only 0.11 m/s. This slow reverse flow pattern is primarily oriented towards the adjacent side of the hinge. Along the hinge central plane, at the bottom of the hinge recess, the out-of-plane v-velocity component ranges from -0.10 to -0.05 m/s.

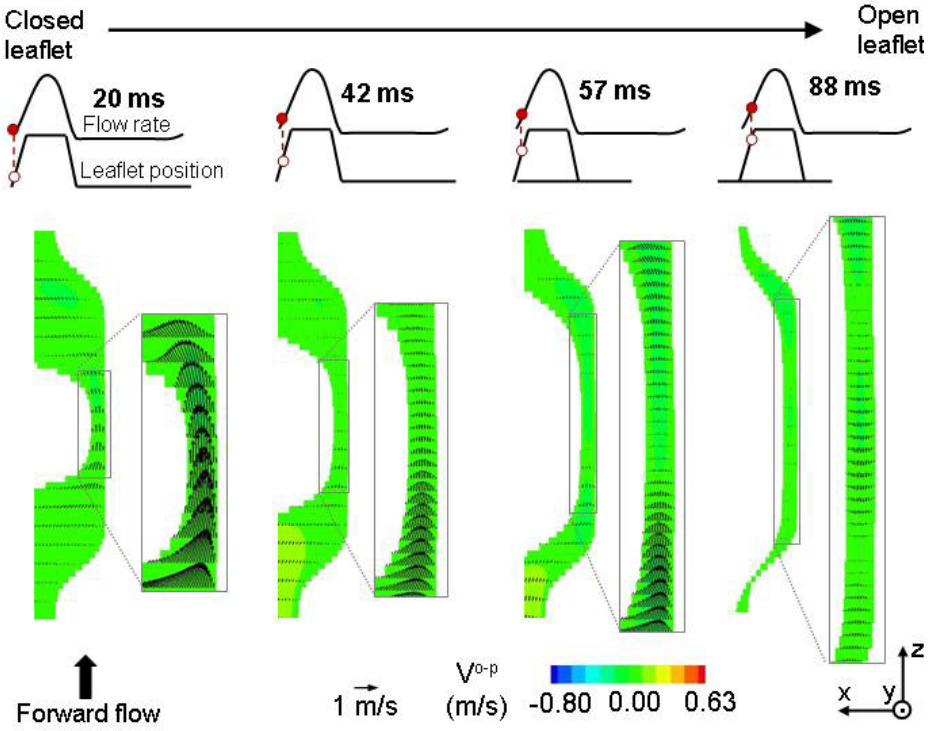

Figure 4-54: Two-dimensional in-plane velocity vectors with out-of-plane velocity contours along the central plane of the hinge during the leaflet opening phase. [CM hinge design with a regular hinge gap width]

Fully-open leaflet phase

The leaflet opening phase is followed in the cardiac cycle by the fully-open phase that spans from 88 ms to 330 ms. As was underscored by the streamtraces presented in Figure 4-49, the flow structures during the fully-opened phase are fairly self-similar; the main difference from one instant to the next being that the velocity magnitudes scale with the magnitude of the bulk valvular flow rate. Moreover, the de-stabilizing effect of the decelerating flow at the end of the fully-open leaflet phase was noted, in particular in the lateral corner of the hinge.

With these observations in mind, this section provides a thorough description of the hinge flow structures at three instances of the fully-open phase (namely mid-acceleration, peak systole, and mid-deceleration) all together. Emphasis is placed on specific differences observed between the three depicted instances. Figure 4-55, Figure 4-56 and Figure 4-57 show the flow fields within the hinge recess at the flat level, the 195 μm-level and the 390 μm-level, respectively. For each level, the velocity magnitude distribution and the in-plane velocity vectors superimposed on the out-of-plane velocity contours are provided.

The three-dimensional streamtraces depicted in Figure 4-49 from mid-acceleration to mid-deceleration shows a complex flow pattern, characterized by a larger recalculating flow pattern in the adjacent corner of the hinge. This flow pattern is visible at all levels within the hinge recess throughout the fully-open phase (Figure 4-55, Figure 4-56 and Figure 4-57). The in-plane velocity vector fields clearly indicate that the incoming forward flow collides with the downstream-most wall of the adjacent corner and turns towards the lateral side of the hinge. This in turn induces the formation of a clockwise rotating flow. This is particularly apparent in Figure 4-56 where the rotating flow is evident at the 195 μm-level at peak systole.

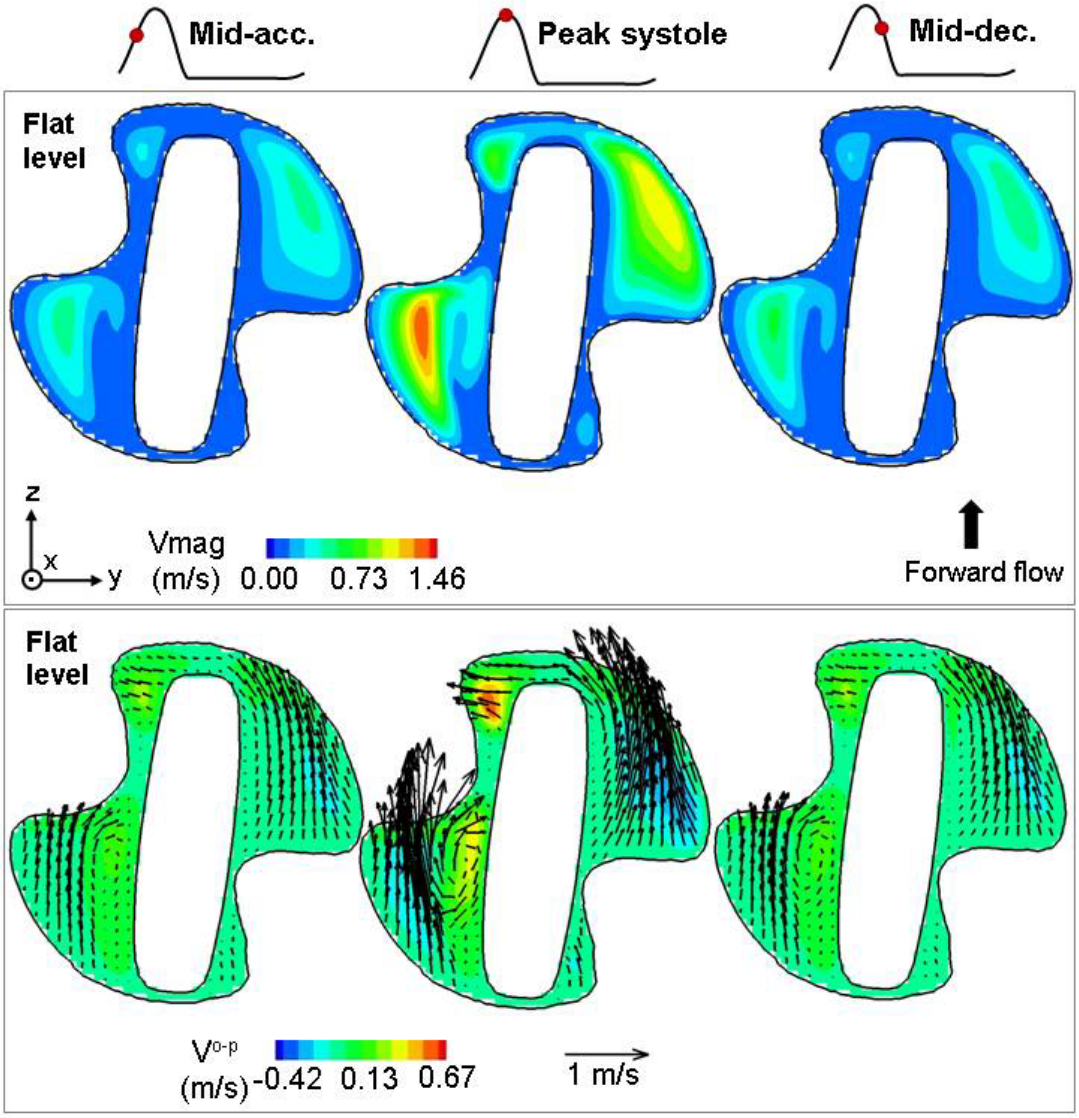

Figure 4-55: Three-dimensional velocity magnitude (top row) and two-dimensional in-plane velocity vectors with out-of-plane velocity contours (bottom row) at three instances of the cardiac cycle at the flat level. [CM hinge design with a regular hinge gap width]

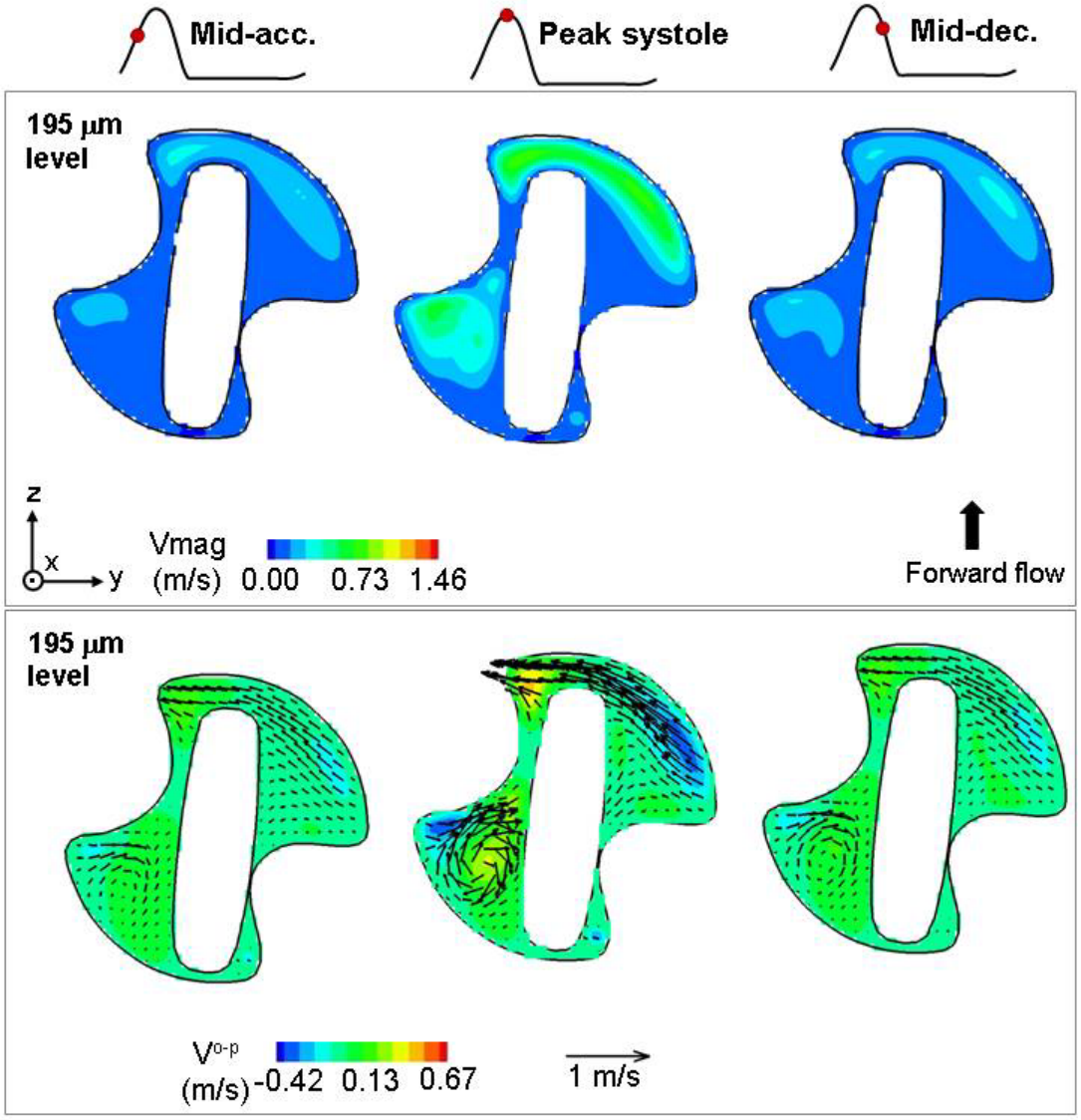

Figure 4-56: Three-dimensional velocity magnitude (top row) and two-dimensional in-plane velocity vectors with out-of-plane velocity contours (bottom row) at three instances of the cardiac cycle at 195 μm below the flat level.
[CM hinge design with a regular hinge gap width]

This clockwise rotating structure, first identified in Figure 4-49, is depicted by the blue area seen in the adjacent corner of the hinge at the 195 μm-level. This rotating flow structure is best visualized using out-of-plane vorticity contour plots. At peak systole (shown in Figure 4-58), the rotating flow structure at the 195 μm-level corresponds to the circular region of negative vorticity located in the center of the adjacent corner. This flow structure is seen to form at the end of the opening phase (Figure 4-53), is the largest at peak systole, and decreases in strength at mid-deceleration. Throughout the fully-open phase, the rotating structure is seen at the bottom of the hinge recess (the 390 μm-level) but is less evident than at the flat level and the 195 μm-level.

The streamtraces in the adjacent corner exit the hinge recess with a large out-of-plane motion from the downstream-most part of the corner (Figure 4-49 and Figure 4-50). This is further confirmed by the out-of-plane velocity distribution where the u-velocity component in this region reaches 0.15 m/s, 0.38 m/s, and 0.16 m/s at mid-acceleration, peak systole and mid-deceleration, respectively. The large negative out-of-plane velocity components noted along the upstream-most wall of the adjacent corner are due to the flow diving inside the hinge recess, as highlighted by the trajectory of the streamtraces provided in Figure 4-49. In this region, the extremum out-of-plane u-velocity component is -0.07 m/s at mid-acceleration, -0.17 m/s at peak systole and -0.08 m/s at mid-deceleration. The same region in the ventricular pocket of the hinge (lateral-most or right-most tip of the ventricular corner) is, on the other hand, associated with low out-of-plane velocity component and low velocity magnitudes (up to 0.23 m/s at the flat level at peak systole).

The streamtraces presented in Figure 4-49 suggest that part of the fluid dives into the lateral corner, follows the curved downstream wall of the hinge before exiting the recess from the left-most tip of the aortic corner. This corresponds to the region of

elevated velocity magnitude and large out-of-plane velocity component seen in the tip of the aortic corner. The flow in this region accelerates as it exits the hinge recess with a strong out-of-plane motion. At flat level, the maximum out-of-plane velocity component at peak systole is 0.66 m/s. At mid-acceleration and mid-deceleration, the flow in this region is weaker and the out-of-plane velocity component does not exceed 0.27 m/s.

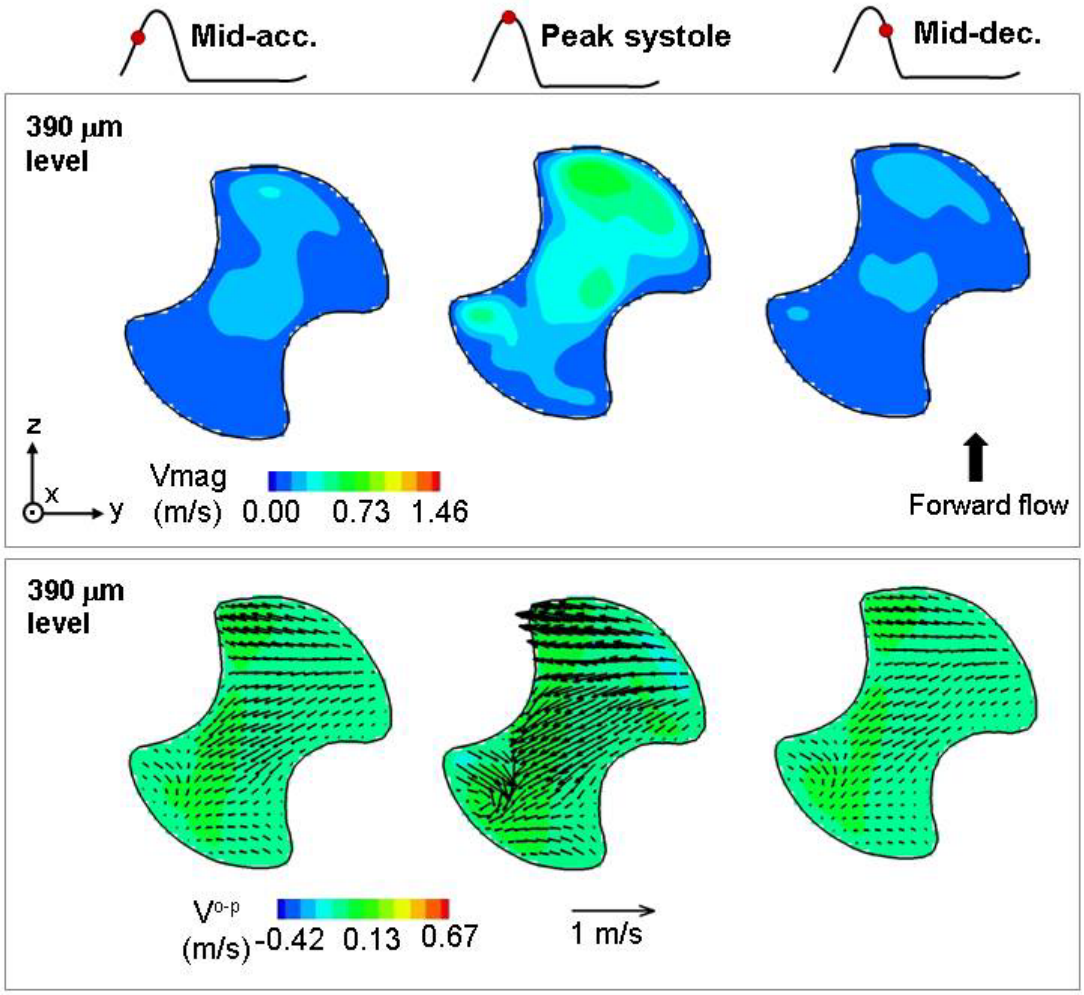

Figure 4-57: Three-dimensional velocity magnitude (top row) and two-dimensional in-plane velocity vectors with out-of-plane velocity contours (bottom row) at three instances of the cardiac cycle at 390 μm below the flat level.
[CM hinge design with a regular hinge gap width]

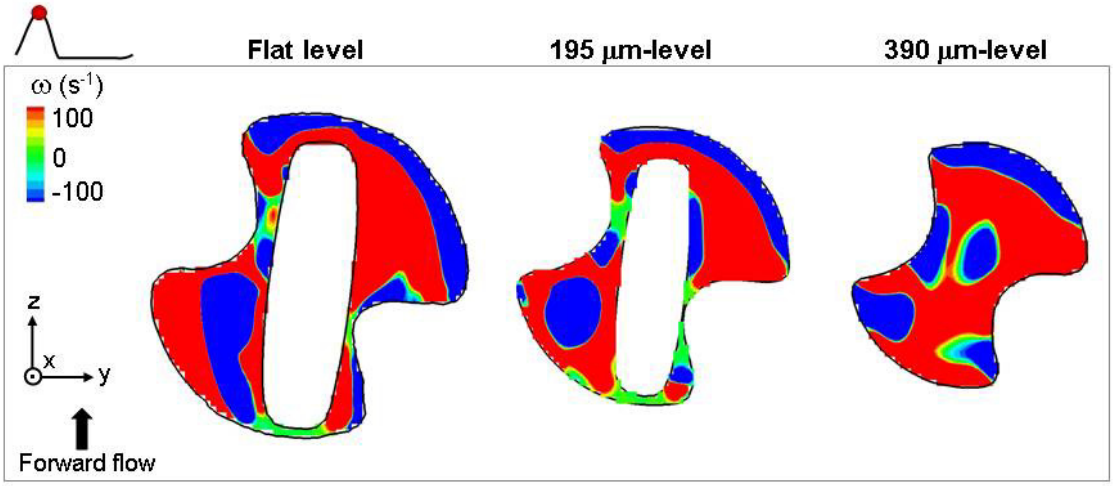

Figure 4-58: Out-of-plane vorticity contours along three planes parallel to the flat level within the hinge recess at peak systole.
[CM hinge design with a regular hinge gap width]

The main flow pattern characterizing the systolic hinge flow fields is the reverse flow developing in the lateral corner of the hinge and extending underneath the leaflet ear (Figure 4-49). This translates into a forward flow pattern with a strong axial component visible at the flat level of the lateral corner. In this region, the maximum velocity magnitude reaches 0.47m/s, 1.12 m/s, and 0.51 m/s at mid-acceleration, peak systole, and mid-deceleration respectively. At deeper levels within the lateral corner, the forward flow impinges the downstream wall of the hinge and is reoriented towards the aortic corner of the hinge. This induces the formation of the reverse flow pattern visible throughout the bottom of the hinge recess.

A closer inspection of the flow fields at the intermediate level (195 μm-level in Figure 4-56) reveals the velocity vector distribution slightly differs at mid-acceleration, peak systole and mid-diastole. At peak systole, the fluid along the downstream wall of the lateral corner collides with the leaflet and then flows back along the leaflet surface in the direction of the ventricular pocket of the hinge. This induces the formation of a slow counter-clockwise rotating flow structure. This flow structure, evident at peak systole, is also visible at mid-deceleration, but does not exist at mid-acceleration. This correlates

with the three-dimensional streamtraces shown in Figure 4-49 that reveal the presence of a streamlined flow in the lateral corner at mid-acceleration and a more complex flow pattern, with a flow swirl, at peak systole and mid-deceleration.

Further insight into the flow fields can be gained by considering cross-sectional views of the hinge. Because of the similitude in flow distribution at mid-acceleration, peak systole and mid-diastole, Figure 4-59 displays the flow fields along the adjacent, central, and lateral planes of the hinge at peak systole. The flow reversal observed at the bottom of the hinge recess throughout the fully-open leaflet phase is best seen in the hinge central plane. The in-plane velocity vectors reveal that this reverse flow pattern has a near-parabolic profile. This parabolic profile is also observed at mid-acceleration and mid-deceleration (not shown). The reverse flow is the strongest at peak systole, with a peak velocity magnitude at 0.51 m/s and a maximum out-of-plane v-velocity component of -0.45 m/s computed along the hinge central plane. The velocity magnitude of the reverse flow is lower at mid-acceleration and mid-deceleration, with a peak at 0.23 m/s and 0.19 m/s, respectively. The out-of-plane velocity component is also lower with a maximum of -0.21 m/s at mid-acceleration and -0.17 m/s at mid-deceleration. The change in flow direction underneath the leaflet ear can also be seen in the vorticity contour distribution along the central plane of the hinge (Figure 4-59)

The cross-sectional view through the adjacent plane shows a strong forward flow pattern, with a reversal of the flow observed near the downstream wall of the recess as the flow impinges the wall. This flow pattern corresponds to the recirculation region identified with the streamtraces in the adjacent corner (Figure 4-49). This recirculating pattern was found to rotate clockwise and it is therefore expected to see a region of strong positive out-of-plane v-component (up to 0.55 m/s at peak systole) along this cross-sectional plane.

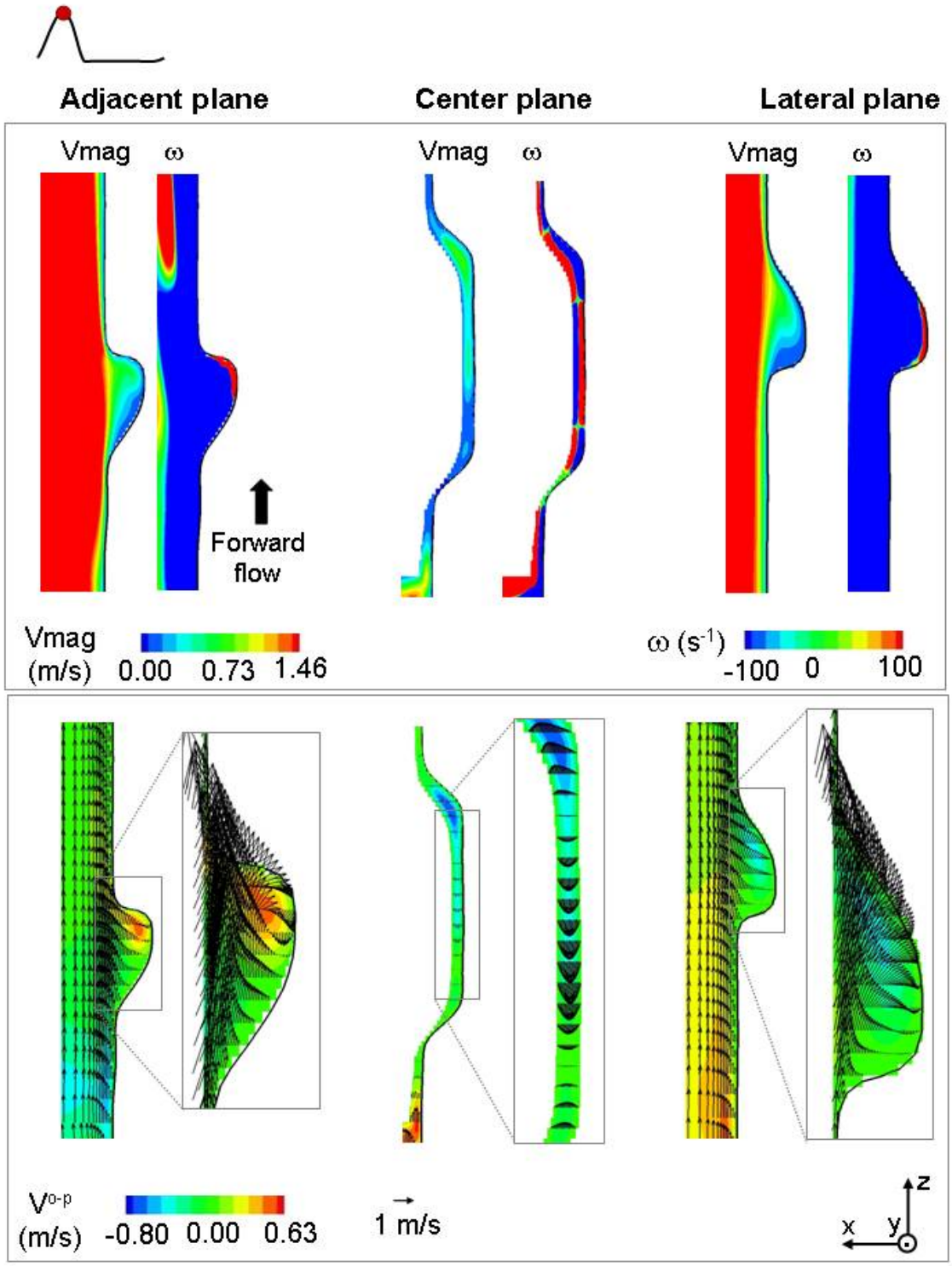

Figure 4-59: Cross-sectional views of the hinge recess at peak systole. Three-dimensional velocity magnitude and out-of-plane vorticity contours are shown on the top row. The bottom row displays the two-dimensional in-plane velocity vectors superimposed on the out-of-plane velocity contours.
[CM hinge design with a regular hinge gap width]

The lateral plane, on the other hand, shows that the flow is mainly directed forward except near the upstream recess wall where a flow reversal of low magnitude is present. This reverse flow pattern corresponds to the region of positive vorticity observed along the hinge recess wall. The out-of-plane flow motion within the hinge recess along this plane is smaller than in the adjacent plane, with a maximum out-of-plane v-velocity component of 0.45 m/s. It should be noted that the flow swirl observed in the lateral corner of the hinge (Figure 4-49) is located near the leaflet surface and is thus not visible in the lateral plane.

Leaflet closing phase

The flow events depicted in this section occur during the leaflet closing phase, therefore after the mid-deceleration phase but before the mid-diastole phase described in the general overview (section 4.4.1). The leaflet closing phase lasts 55 ms during which the leaflet moves from its fully-open position (at 330 ms) to its fully-closed position (385 ms). The combined effect of the rapid motion of the leaflet and the decelerating bulk valvular flow rate gives rises to complex unsteady flow features.

Figure 4-60 and Figure 4-61 show the hinge flow fields during the leaflet closing phase at 348 ms, 372 ms, and 382. The first figure focuses on the flat level while the latter presents the flow structures deeper into the hinge recess, at 195 and 390 μm below the flat level.

At the beginning of the leaflet closing phase (348 ms), a slow reverse flow with little out-of-plane motion is seen throughout the flat level. At this instance, the maximum velocity magnitude at the flat level is computed in the lateral corner with a peak of 0.10 m/s. The out-of-plane u-velocity component at the flat level is also low and ranges from -0.03 m/s to 0.04 m/s.

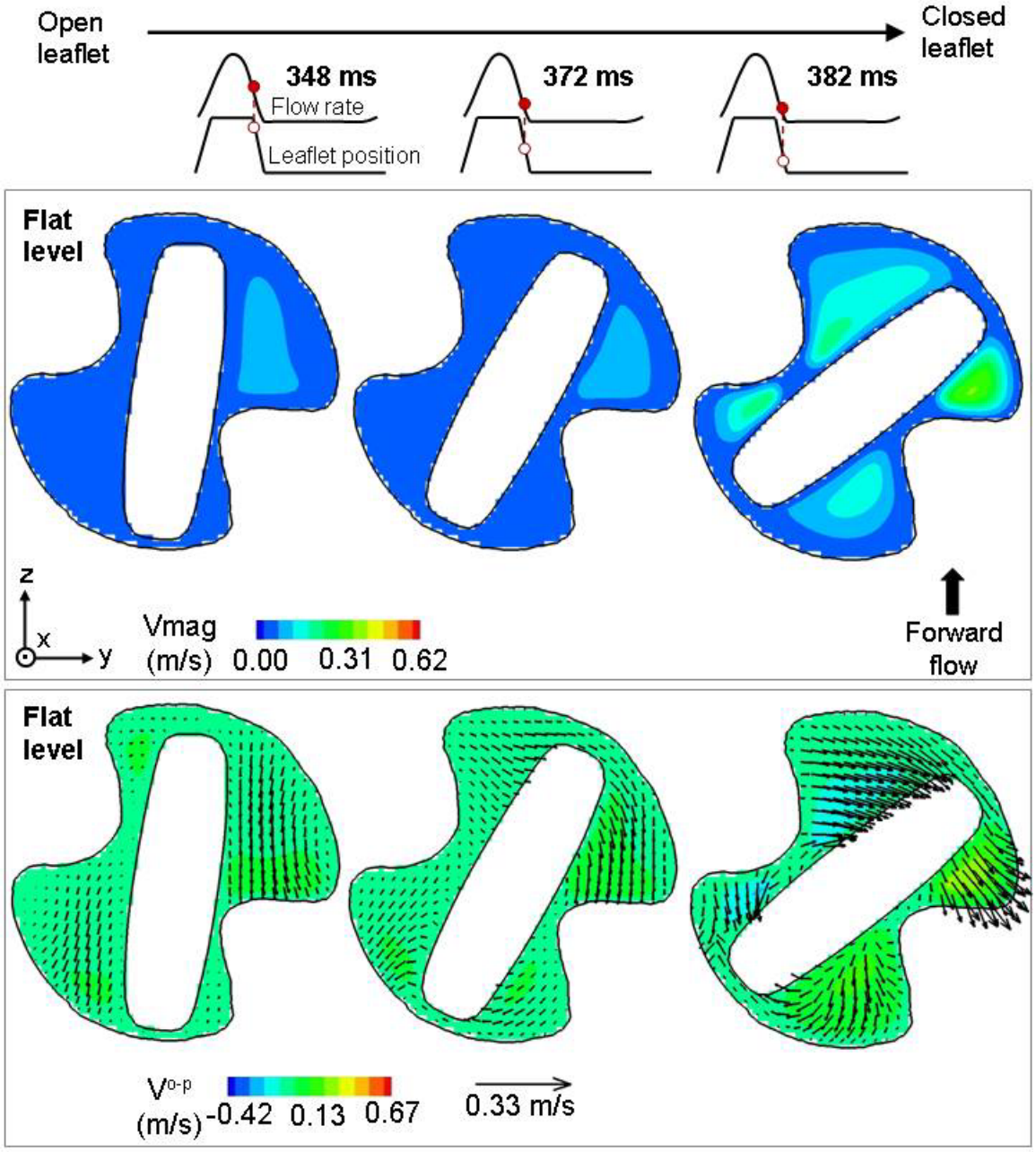

Figure 4-60: Three-dimensional velocity magnitude (top row) and two-dimensional in-plane velocity vectors with out-of-plane velocity contours (bottom row) at the flat level during the leaflet closing phase. [CM hinge design with a regular hinge gap width]

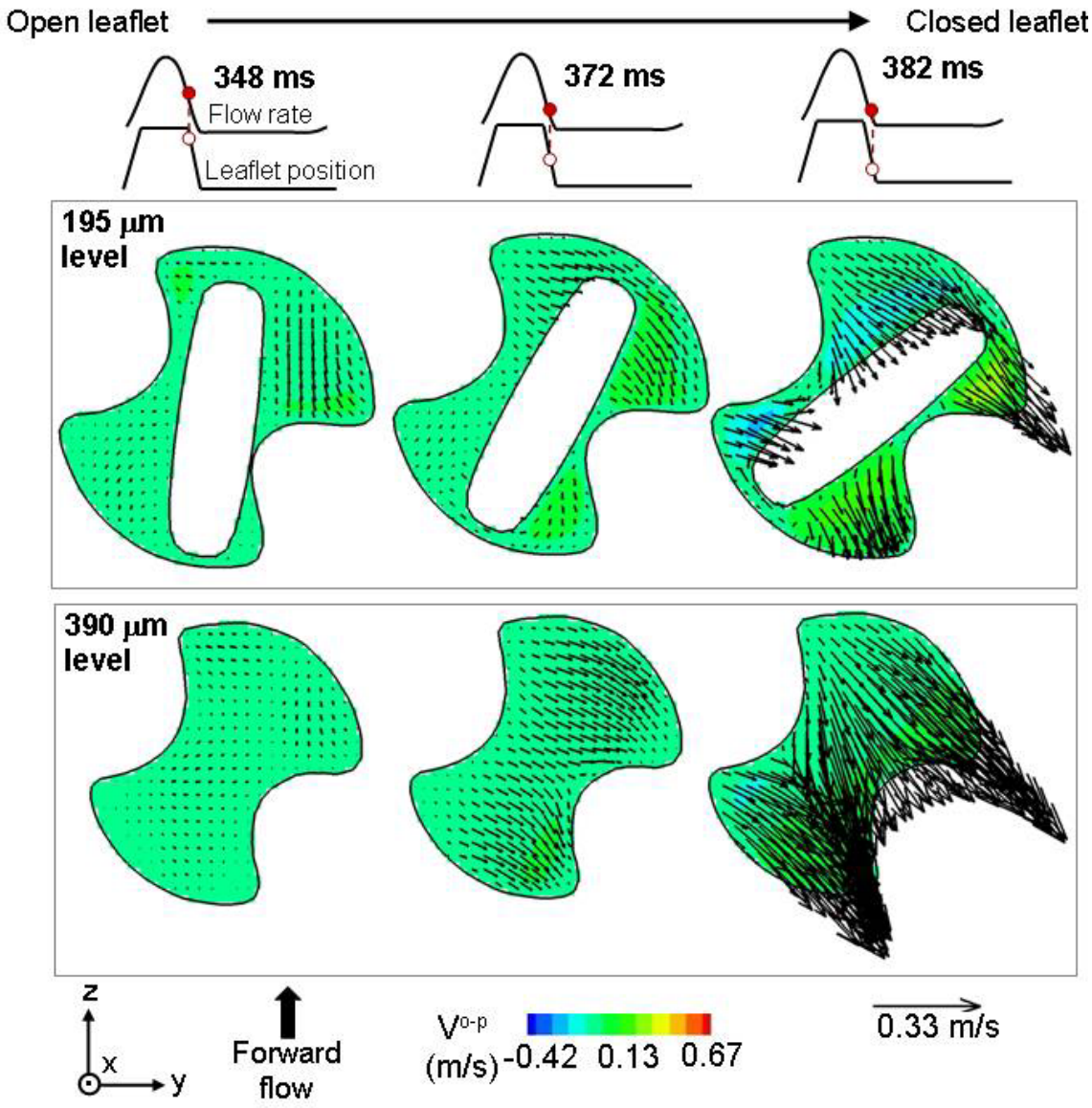

Figure 4-61: Two-dimensional in-plane velocity vectors with out-of-plane velocity contours at 195 μm and 390 μm below the flat level during the leaflet closing phase. [CM hinge design with a regular hinge gap width]

As the leaflet starts to close further (372 ms), its effect on the hinge flow field becomes evident at the flat level in the ventricular and lateral corners of the hinge as the flow appears to have an overall clockwise direction, which corresponds to the leaflet movement. At deeper levels within the hinge recess, the effect of the moving leaflet is less and a reverse flow predominantly oriented towards the lateral side of the hinge is clearly visible at the 390 μm-level. The velocity magnitudes at this instance are slightly higher than at 348 ms but the out-of-plane flow motion remains low, with the out-of-plane u-velocity component ranging from -0.05 m/s to 0.07 m/s at the flat level.

At the end of the leaflet closing phase (382 ms), the leaflet has nearly reached its fully-closed position. The reverse flow in the aortic corner appears to be primarily oriented towards the lateral side. The out-of-plane velocity component distribution at the flat level along with the velocity vectors at deeper levels within the hinge recess clearly indicate that the flow in the adjacent corner dives inside the recess and exits the hinge primarily from the tip of the lateral corner. This is supported by the positive u-velocity component observed in this tip. The velocity magnitude and the out-of-plane velocity component in the tip of the lateral corner reach 0.37 m/s and 0.32 m/s at the flat level, respectively. Part of the flow entering the recess from the aortic corner exits the hinge from the adjacent corner of the hinge. This yields a fast-flowing reverse flow at the bottom of the hinge recess as the flow squeezes between the leaflet and the recess wall. This reverse flow exhibits a parabolic-profile as shown in Figure 4-62.

Still at 382 ms, the flow is also seen to dive inside the hinge through the left tip of the aortic corner. In this region, the extremum out-of-plane velocity component reaches –0.24 m/s at the flat level. This flow then exits the hinge recess from the ventricular corner, with a peak out-of-plane velocity component of 0.14 m/s at the flat level.

Overall, higher velocity magnitudes and larger out-of-plane motion are seen throughout the hinge recess at the end of the leaflet closing phase compared to the beginning. The maximum velocity magnitudes at 382 ms reach up to 0.62 m/s.

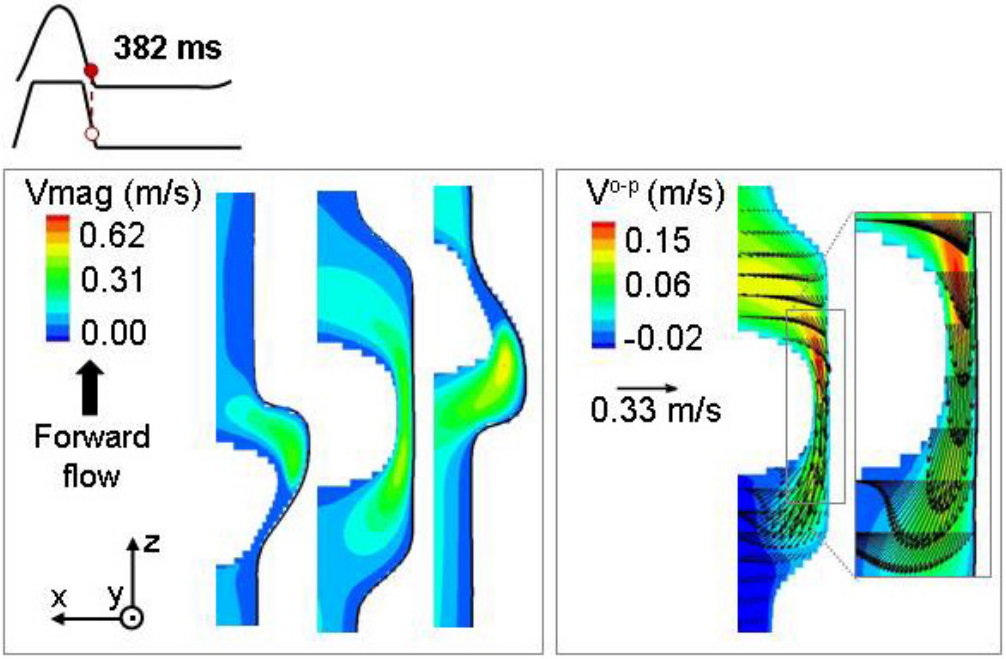

Figure 4-62: Three-dimensional velocity magnitude contours along three cross-sectional planes of the hinge (left) and the in-plane velocity vectors distribution along the hinge central plane (right) at late systole (382 ms).
[CM hinge design with a regular hinge gap width]

Fully-closed leaflet phase

The leaflet reaches its fully-closed position at 385 ms in the cardiac cycle and a constant flow rate then leaks through the closed valve. To best visualize the hinge flow pattern during the fully-closed leaflet phase, Figure 4-63 shows the three-dimensional velocity magnitude and the in-plane velocity vectors superimposed on the out-of-plane velocity component contours along three planes within the hinge recess at mid-diastole.

As the flow dives into the hinge in the aortic pocket, it goes underneath the leaflet ear and exits the recess from the ventricular corner. This leads to the formation of a strong axial leakage jet which is observed at all levels within the hinge recess (Figure 4-63). This is also seen in the trajectories of the blue streamtraces (Figure 4-49) that show a leakage flow pattern in the ventricular corner of the hinge. The maximum velocity magnitude and out-of-plane velocity component in the ventricular corner reach 4.05 m/s and 2.50 m/s, respectively, at the flat level.

A second leakage jet, with a larger out-of-plane motion, is clearly visible in the tip of the lateral corner. This leakage jet corresponds to the set of red streamtraces depicted in Figure 4-49. Part of the flow diving in the recess in the aortic corner accelerates as it squeezes between the leaflet surface and the recess surface and then exits the recess through the tip of the lateral corner. In this tip, the out-of-plane u-velocity component reaches 3.35 m/s at the flat level and the velocity magnitude 4.61 m/s. As previously noted for the leakage jet emanating from the ventricular corner, the lateral leakage jet is visible at all levels within the hinge recess.

Finally, the velocity vector distribution indicates the presence of a strong localized flow in the tip of the adjacent corner suggesting the diving of the flow in the recess. The out-of-plane u-velocity components in this tip are large with an extremum of -2.05 m/s at the flat level. The maximum velocity magnitude in this region is 2.75 m/s. A close inspection of the hinge recess reveals that the flow in this region has a strong axial component at the flat level but is primarily oriented towards the ventricular corner at deeper levels within the recess. This correlates with the green streamtraces (Figure 4-49) that show the flow entering the hinge from the tip of the lateral corner and exiting it though the ventricular corner.

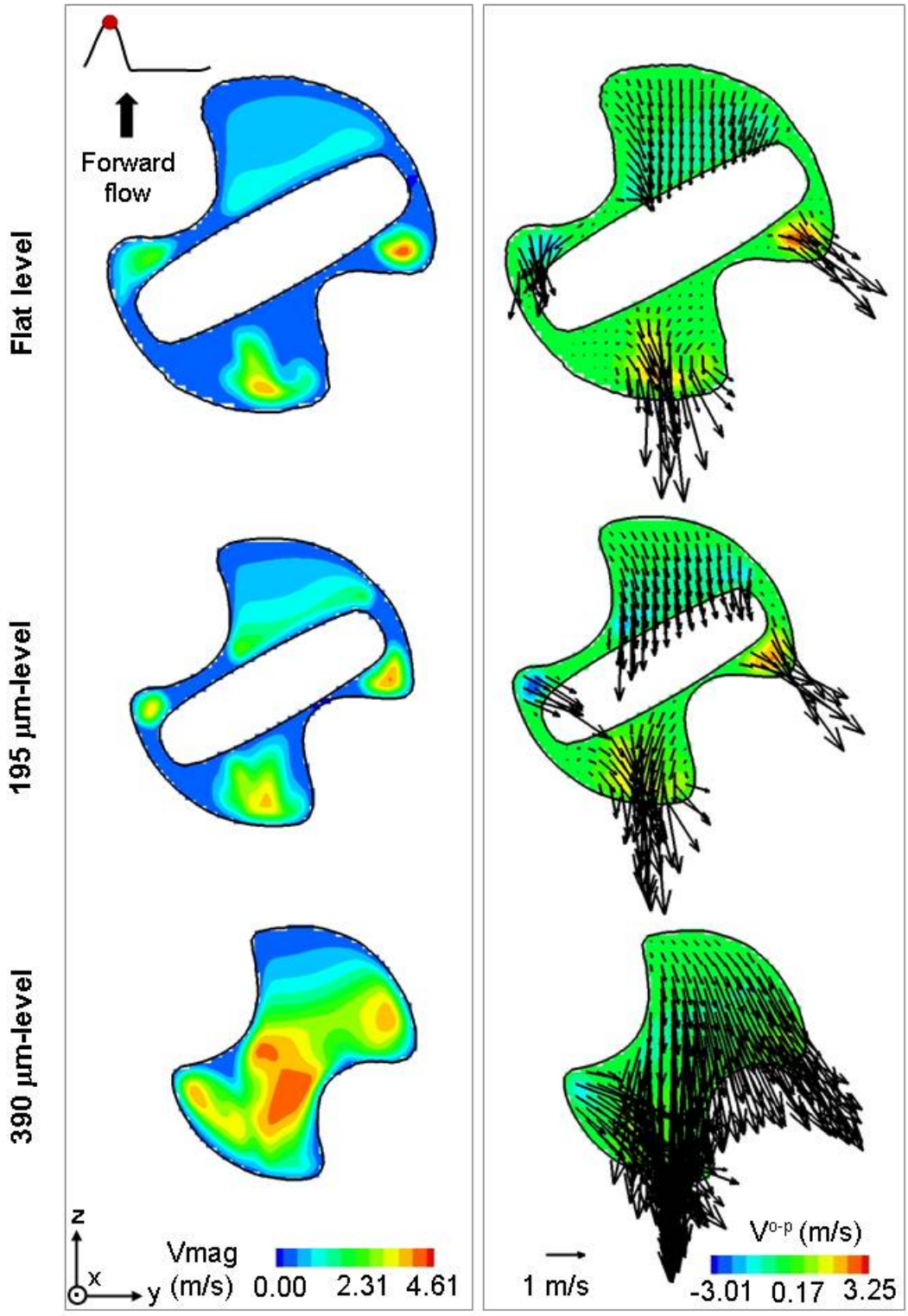

Figure 4-63: Two-dimensional in-plane velocity vectors with out-of-plane velocity contours at the flat level, 195 μm, 390 μm below the flat level at mid-diastole. [CM hinge design with a regular hinge gap width]

These leakage flow patterns can be identified in the out-of-plane vorticity contour plot provided in Figure 4-64. The juxtaposed layers of negative and positive vorticity in the adjacent, ventricular and lateral corners of the hinge at the flat level are characteristic of flow jets. Moreover, the large region of positive vorticity seen at the 390 μm-level corresponds to the fast-paced flow entering the hinge through the tip of the adjacent corner.

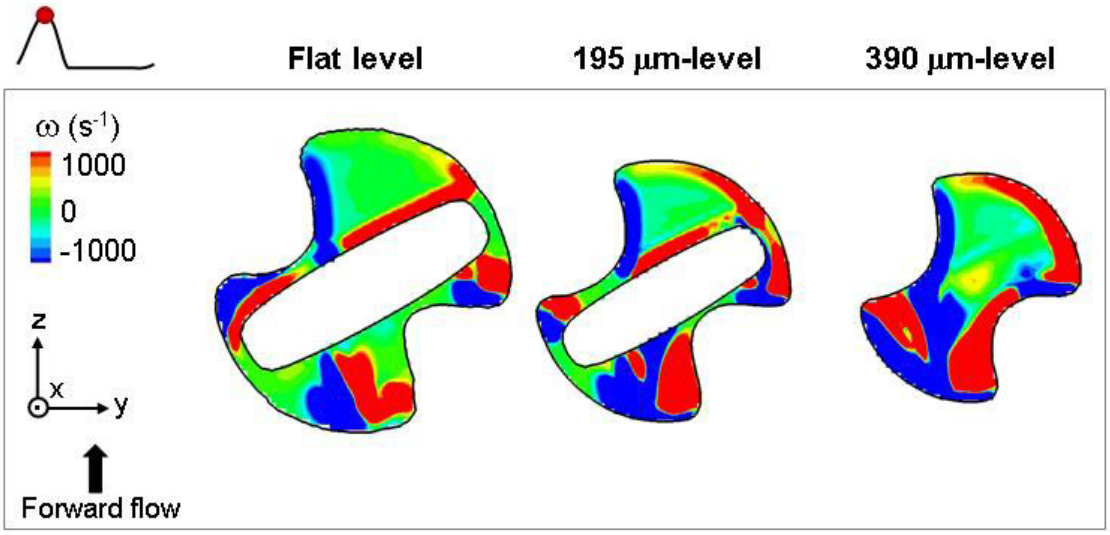

Figure 4-64: Out-of-plane vorticity contours along three planes parallel to the flat level at mid-diastole. [CM hinge design with a regular hinge gap width]

Cross-sectional views through the hinge recess provide further information on the flow structures present within the hinge recess during the fully-closed leaflet phase (Figure 4-65). The in-plane velocity vectors along the adjacent plane correspond to the flow diving in the recess from the left-most tip of the adjacent corner. This jet was seen to be predominantly oriented towards the ventricular corner (Figure 4-63), and thus large positive out-of-plane v-velocity values are seen along the adjacent plane. The maximum v-velocity component reaches 3.23 m/s.

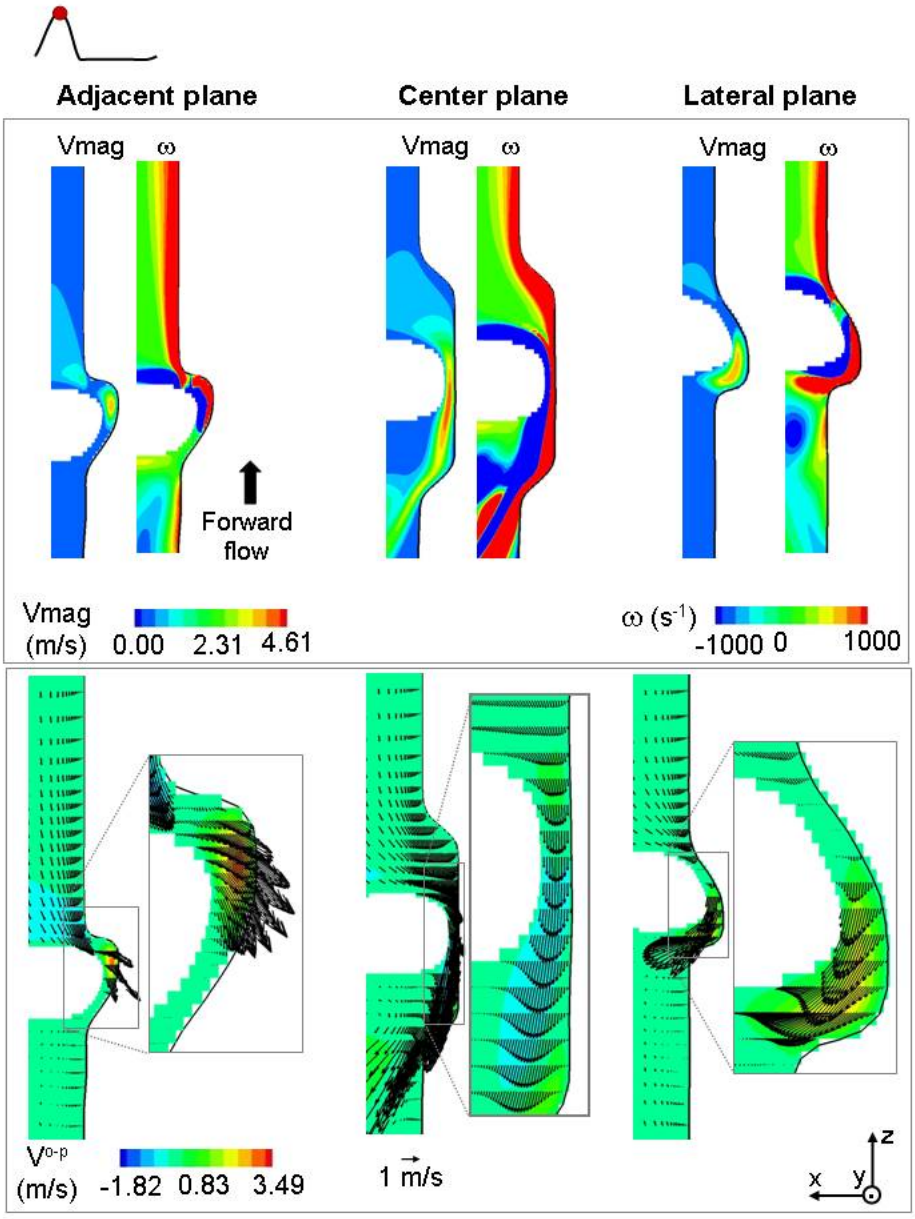

Figure 4-65: Three-dimensional velocity magnitude (top row) and two-dimensional in-plane velocity vectors with out-of-plane velocity contours (bottom row) along the adjacent, central, and lateral planes of the hinge at mid-diastole.
[CM hinge design with a regular hinge gap width]

The leakage jet emanating from the ventricular corner is seen in the central plane. The in-plane velocity vector distribution underscores the near-parabolic profile of this jet. The extremum velocity magnitude and out-of-plane v-velocity component along this plane are 4.56 m/s and -0.73 m/s, respectively. The lateral plane, on the other hand, shows that the leakage jet in the lateral corner has a profile skewed towards the leaflet ear with an out-of-plane v-velocity component up to 2.35 m/s. This correlates with Figure 4-49 that underlines that the ventricular jet has a more axial direction (smaller v-velocity component) than the lateral jet.

4.4.3 Detailed description of the shear stress distribution

The images provided in Figure 4-51 and the animations CM_Isosurfaces _MidDiastole.mov and CM_Isosurfaces_PeakSystole.mov present the global shear stress distribution in the hinge and the near-hinge region at key instances of the cardiac cycle. The following section provides a detailed description of the shear stress fields at four key instances of the cardiac cycle so as to gain further insight into the shear stress associated with the hinge fluid dynamics. Figure 4-66 and Figure 4-67 show the principal shear stress contour maps along four planes outside and within the hinge recess at mid-acceleration, peak systole, mid-deceleration, and mid-diastole. Animations complement this figure by illustrating the temporal variations of the shear stress distribution throughout the cardiac cycle (CM_Shear_Stress_Contours.mov at four planes within the hinge recess). The local shear stress maxima are provided for each of these contour maps. The shear stress contours maps during the forward flow phase are presented first and are followed by a description of the shear stress distribution during the leakage flow phase. This sections ends with the temporal variations of the maximum shear stress levels in the hinge and the near-hinge region.

Forward flow phase: The iso-surfaces revealed a similar shear stress distribution throughout the forward flow phase but the magnitude of these shear stresses were found to be dependent on the bulk valvular flow rate. This is further confirmed by the local maxima provided on the shear stress fields which highlight that the maximum shear stress levels during the forward flow phase are obtained at peak systole. Moreover, the iso-surfaces showed two main regions of elevated shear stress during systole: 1) immediately upstream of the ventricular corner, close to the leaflet edge; and 2) downstream of the adjacent corner. These two regions are visible in the shear stress contour map along the plane located outside of the hinge recess (top row of Figure 4-66). Along the plane shown, the maximum shear stress level at peak systole is 830 dyn/cm^2 downstream of the adjacent corner and 730 dyn/cm^2 upstream of the ventricular corner. The hinge recess itself, as suggested by the absence of high shear stress iso-surfaces, is associated with lower shear stress values.

At the flat level (Figure 4-66), the maximum shear stress levels are seen near the downstream wall of the adjacent corner. The wall of the lateral corner is also associated with elevated shear stresses, but of slightly lower magnitude. Both of these regions correspond to the flow impinging on the recess wall. A third region of elevated shear stress is seen along the upstream wall of the aortic pocket.

At deeper levels within the hinge recess (Figure 4-67) the highest shear stress levels are observed in the aortic pocket of the hinge. Elevated shear stresses are present along the wall of the aortic pocket and near the downstream surface of the leaflet, where the flow squeezes between the leaflet surface and the recess wall. Nonetheless, the region of high shear stress identified at the flat level in the adjacent corner is still visible at deeper levels but the magnitude of shear stress in this region is lower than at the flat level.

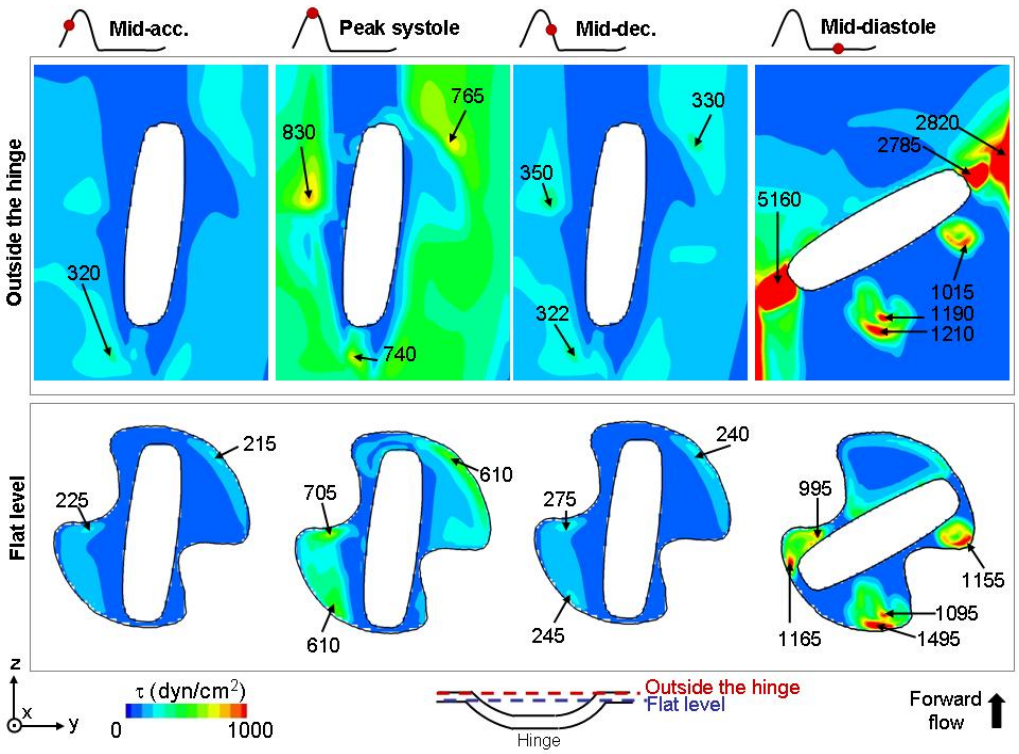

Figure 4-66: Shear stress distribution at four instances of the cardiac cycle. The top row shows a plane located outside the hinge recess, near the leaflet edge surface as depicted in the schematic. The bottom row corresponds to the flat level. [CM hinge design with a regular hinge gap width].

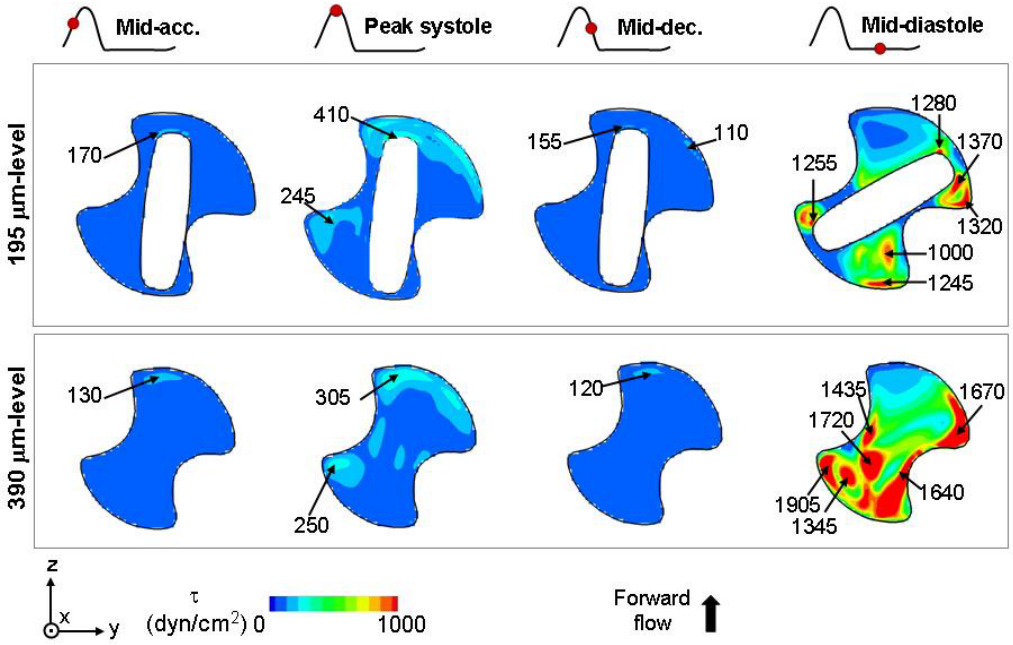

Figure 4-67: Shear stress distribution at four instances of the cardiac cycle at 195 μm and 390 μm below the flat level. [CM hinge design with a regular hinge gap width]

Figure 4-68 shows the shear stress distribution along three cross-sectional planes. This figure further highlights that throughout the forward flow phase, the maximum shear stress levels are not found inside but outside the hinge recess. The regions along the housing wall and located immediately upstream and downstream of the hinge are consistently associated with higher shear stress levels than the hinge recess itself. Further comparison of the shear stress distribution reveals that the shear stress levels are consistently higher downstream than upstream of the hinge recess. For instance, at peak systole, shear stresses up to 875 dyn/cm^2 and 1,365 dyn/cm^2 are reported along the adjacent plane upstream and downstream of the hinge, respectively.

Leakage flow phase: As previously highlighted by the iso-surfaces (Figure 4-51), the shear stress distribution during the leakage flow phase is drastically different from that observed during the forward flow phase. Large region of elevated shear stress levels are seen outside of the hinge recess, in particular on either side of the closed leaflet (top row in Figure 4-66). These regions of high shear stresses correspond to the leakage jets emanating from the peripheral gap of the valve (i.e. the gap formed by the surface of the closed leaflet and the valve housing). Along the plane located outside the hinge recess, along the leaflet surface, the shear levels reach 5,160 dyn/cm^2.

Within the hinge recess, the shear stress distribution is closely related to the flow structures present during the leakage phase. Regions of elevated shear stresses are seen in the ventricular and lateral corners, where strong leakage jets were identified. Similarly large shear stress levels are also seen in the tip of the adjacent corner where a fast-paced flow with large out-of-plane motion was noted. At the flat level, the maximum shear stress levels are 1495 dyn/cm^2, 1155 dyn/cm^2, and 1165 dyn/cm^2 in the ventricular, lateral and adjacent corners respectively. At deeper levels within the hinge recess, the associated shear stress levels are much higher.

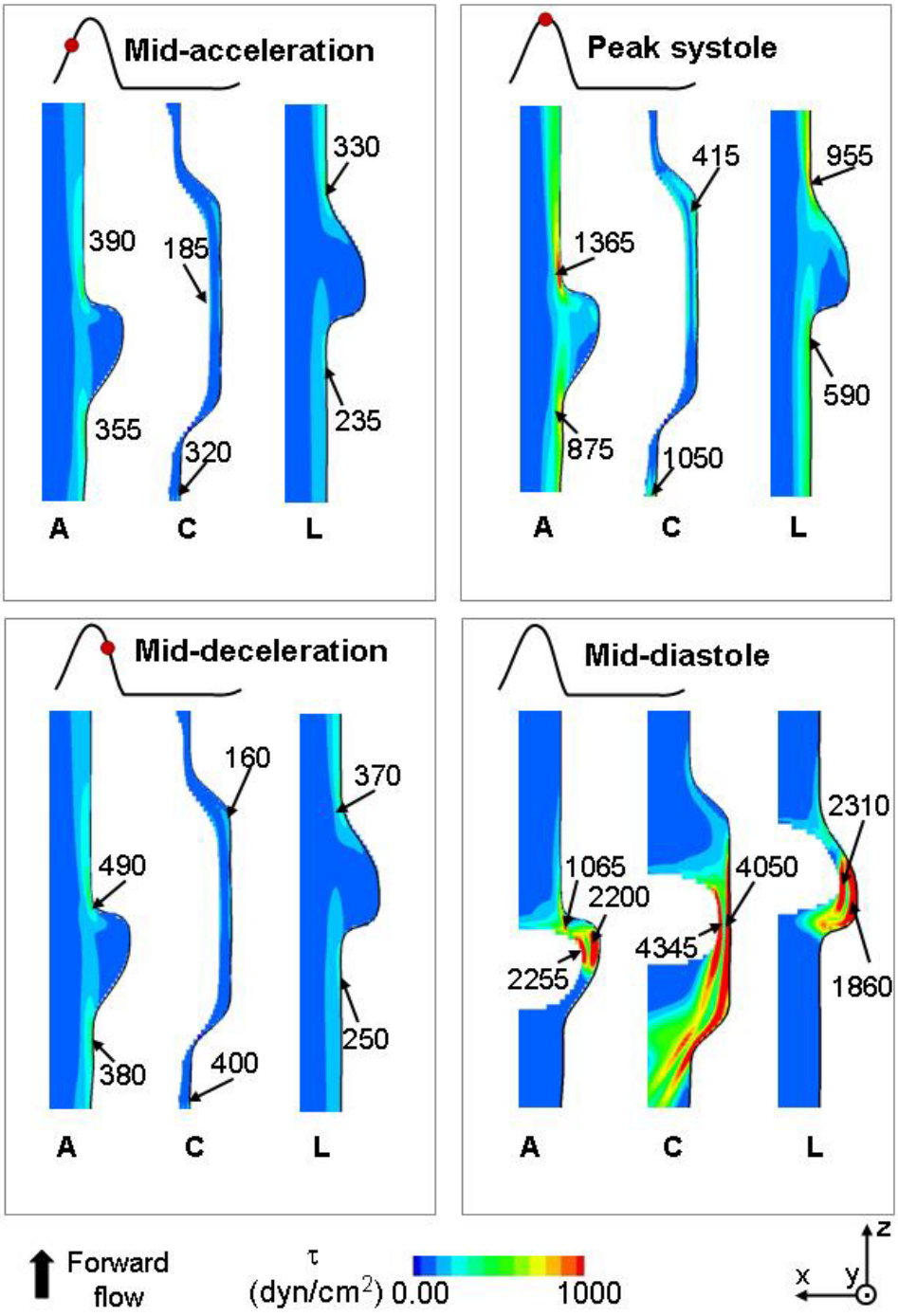

Figure 4-68: Shear stress distribution throughout the cardiac cycle along three cross-sectional planes: the adjacent (A) plane, the central (C) plane, and the lateral (L) plane. [CM hinge design with a regular hinge gap width].

At the bottom of the hinge recess, along the wall of the lateral corner, shear stress levels reach up to 1,905 dyn/cm^2. Cross-sectional views through the hinge (Figure 4-68) clearly highlight that the regions of elevated shear stresses are located in the wake of the leakage jets, in particular along the center plane where the wake of the ventricular leakage jet is visible. Along this plane, shear stresses up to 4,345 dyn/cm2 are computed within the hinge recess. Overall, the shear stress contour maps show that during the leakage flow phase, the wake of the leakage jets and the region within the hinge recess defined by recess wall and the leaflet surface are associated with elevated shear stress.

Temporal Variations:

Figure 4-69 shows the temporal variations of the maximum shear stress in the hinge and near hinge region from the onset of systole to mid-diastole. The red curve corresponds to the hinge recess alone while the black curve corresponds to the hinge recess and its vicinity (as depicted in blue in the two schematics shown below the graph).

During the forward flow phase, both curves follow a similar parabolic-like trend, thus indicating that the maximum shear stress closely follows the variation in bulk valvular flow rate. When the leaflet closes (385 ms), the maximum shear stresses increase abruptly and then reach a plateau. Figure 4-69 highlights that it is during the leakage phase that the highest shear stresses are computed. The maximum shear stresses during the forward flow phase occur at peak systole, with a maximum of 1,060 dyn/cm^2 within the hinge recess and 1,800 dyn/cm^2 in the hinge vicinity. At mid-diastole, the maximum shear stress level reaches 5,910 dyn/cm^2 in the hinge recess and 8,985 dyn/cm^2 in the hinge vicinity

The black curve is seen to be consistently above the red one except during the leaflet opening (from 0 to 88 ms) and the leaflet closing phase (from 330 to 385 ms). This indicates that, except during the phases when the leaflet moves, the highest shear stress values are present outside of the hinge recess rather than within. This is in agreement with the iso-surfaces (Figure 4-51) and shear stress contour plots (Figure 4-67 and Figure 4-68) which underscored the presence of elevated shear stress levels near the hinge but outside of the recess. During the forward flow phase, the elevated shear stress values are located immediately upstream of the leaflet. During the leakage flow phase, these higher shear stresses are seen in the wake of the leakage jets.

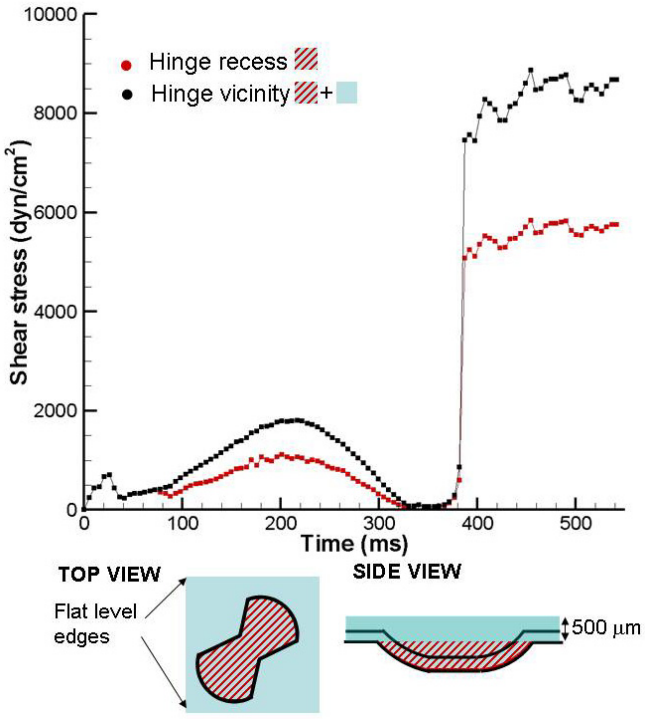

Figure 4-69: Variations of the maximum principal shear stress within the hinge recess (red) and in the hinge vicinity (black) as a function of time.
[CM hinge design with a regular hinge gap width].

Finally, the differences in flow dynamics and associated shear stresses between the leaflet opening and closing phases are clearly seen in Figure 4-69. The opening motion of the leaflet during the first 88 ms of the cardiac cycle induces complex and unstable flow patterns which yield a complex shear stress field distribution. This explains the variation in maximum shear stress observed at early systole in Figure 4-69. During the leaflet closing phase, on the other hand, the bulk valvular flow rate is lesser than during the leaflet opening phase. This leads to slower flow fields and smaller shear stress levels compared to the leaflet opening phase.

4.5 Lagrangian analysis of the hinge flow fields

4.5.1 Introduction

The following section presents the Lagrangian analysis of the hinge flow fields for all three hinge designs. Using the simulated flow fields, the trajectories of the blood elements are computed according to the methodology described in section 3.5. In order to clearly visualize the trajectories of the particles crossing the hinge recess, approximately 300 particles are released within the hinge recess every 15 ms from early systole to mid-diastole (515 ms). Particles are released 34 times during this time period. The position of these particles are then tracked with time, in order to 1) estimate the particle trajectories and the shear stresses experienced by the particles along these trajectories 2) compute a surrogate measure of the thromboembolic potential of the hinge using existing blood damage models.

For each one of the three hinge designs, the description and analysis of the particle trajectories are provided first. To best visualize the estimated trajectories of the blood elements and the flow structures, two sets of images are provided whenever necessary. The first set of images illustrates the particle pathlines, that is to say the

trajectory followed by each individual particle from the seeding time onwards. The second set of figures makes use of particle streaklines to display instantaneous snapshots of all the seeded particles at a given instance of the cardiac cycle. By definition, a streakline is the locus of points of all the particles that have continuously passed through a particular spatial point. This is similar to injecting dye continuously at a given location and observing how the dye moves along with the fluid motion. The visualization of the streak-lines is herein possible due to the fact that the particles are released at similar location throughout the cardiac cycle. The schematic provided in Figure 4-70 explains exactly how these streakline-like plots are obtained.

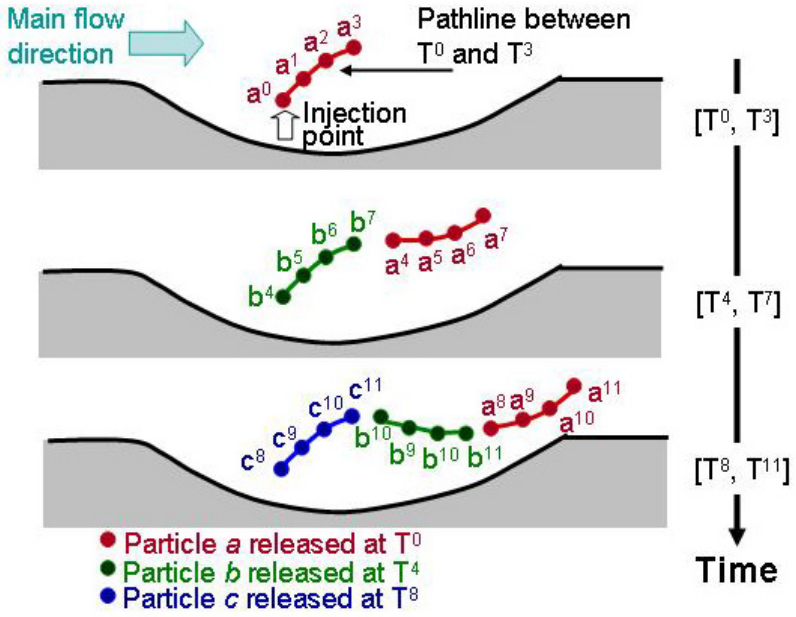

Figure 4-70: Schematic illustrating the streakline-like display. Three particles (a, b, c) are released from the same location at times T^0, T^4 and T^8, respectively. The pathlines of these particles are plotted at consecutive time intervals: the position of the particles *P* at the instant of time *t* is noted as P^t. For instance, a^5 corresponds to the position of the particle *a* at the instant *5.*

In brief, the cardiac cycle is divided into time intervals and for each of these time interval, the particle pathlines are plotted. These figures are complemented by some animations (Large_View_Streaklines.mov and Zoom_View_Streaklines.mov for each hinge design) to illustrate the unsteadiness of the flow.

The Lagrangian analysis of the flow is followed by a description of the estimated thromboembolic potential. There, blood damage indices (BDI), based on previously published blood damage models are computed, and histograms of the BDI distribution of the particles are given.

4.5.2 SJM hinge with a regular hinge gap width

Prior to looking closely at the details of the flow structures and particle trajectories within the hinge recess, a global view of the numerical domain is provided in Figure 4-71. The streaklines, as explained in the schematic provided in Figure 4-70, are shown at various instances of the cardiac cycle, spanning from early systole to early diastole. The reader is referred to the accompanying animation SJMReg_Large_View_Streaklines.mov and SJMReg_Zoom_View_Streaklines.mov. The streaklines are color-coded by the particle release time; the particles released at early systole are shown in blue and those released at early diastole in red.

During the early phase of the cardiac cycle, the valvular flow rate is low and the particles remain in the near-hinge region. As the bulk valvular flow rate increases, the particles travel further downstream. It is interesting to note that while the particles released at mid-systole (green) are dragged by the main stream away from the valve region, the particles released at early systole (blue) get entrapped in the recirculating flow structure that forms in the sinus region. During the deceleration phase, the less elongated aspect

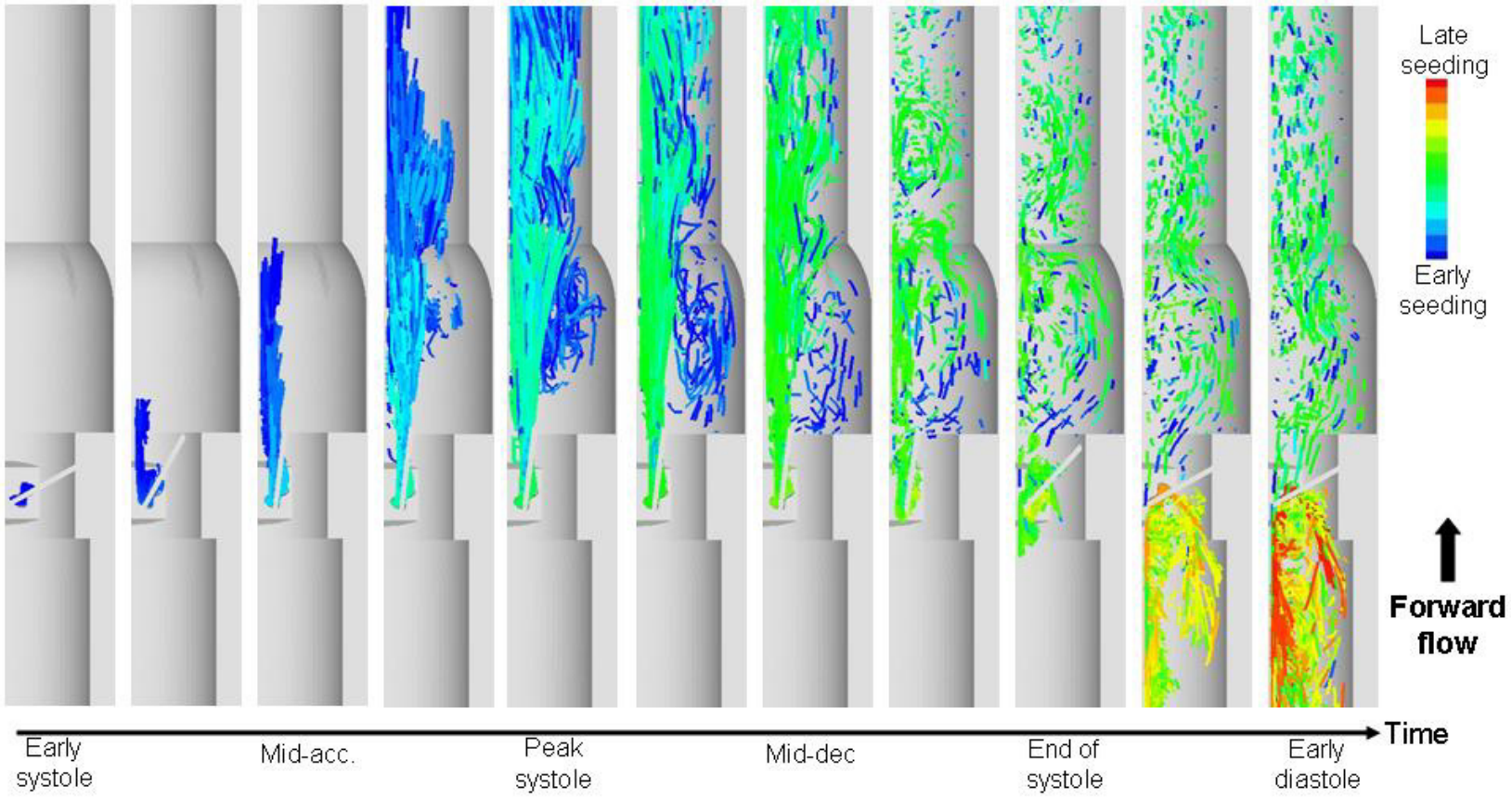

Figure 4-71: Particle streaklines as a function of time. The streaklines are color-coded with the seeding time of the particles. The particles released at early systole are shown in blue and those released at early diastole in red. [SJM hinge design with a regular hinge gap width]

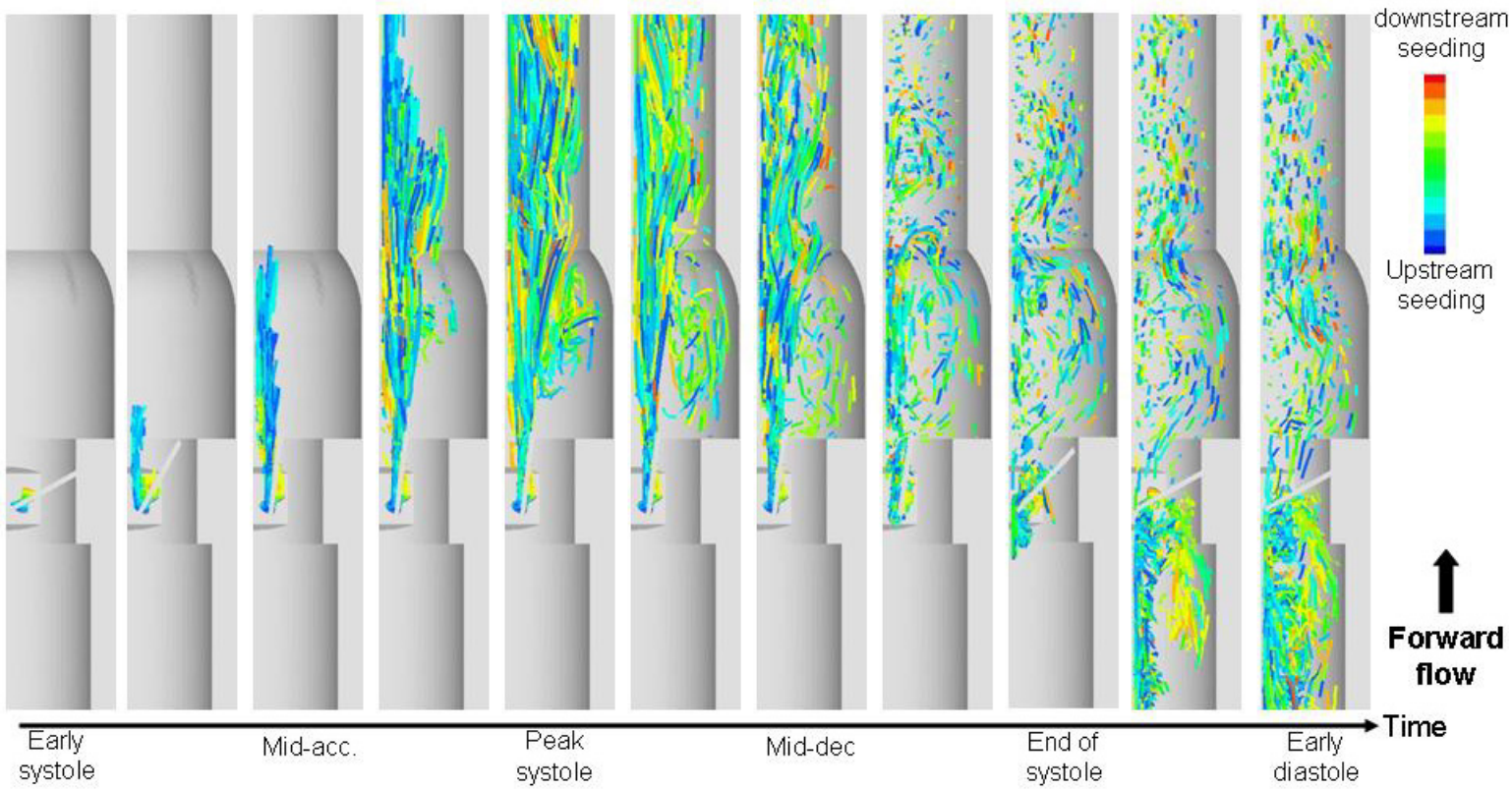

Figure 4-72: Particle streaklines as a function of time. The streaklines are color-coded with the initial position of the particle at the time of injection. The particles seeded the furthest upstream are shown in blue and the particles the furthest downstream in red. [SJM hinge design with a regular hinge gap width]

of the streaklines downstream of the valve reveal the rise of more chaotic flow structures attributed to the destabilizing effect of the decelerating flow. The particles furthest downstream of the valve get entrapped in small eddies forming point-like streaklines. Closer to the valve a larger coherent recirculation spans the entire sinus. At the end of systole, the flow has started to reverse, and the particles released at that point in time (light green) indicate the formation of leakage jets emanating from the hinge region. These leakage jets persist throughout diastole and all particles released after valve closure travel upstream towards the ventricular section of the numerical domain.

Figure 4-72 shows the same streaklines as in Figure 4-71, but color-coded with the initial position of the particles at the time of release. The blue and red particles correspond to the particles seeded the furthest upstream and downstream of the hinge, respectively. Incidentally, due to the design of the recess, this coloring may also be viewed as the seeding-position with respect to the open leaflet: particles in tints of blue and green are released on the adjacent side of the hinge (on the left of the open leaflet), near the b-datum line, while the yellow-red particles are released on the lateral side of the hinge (on the right of the leaflet). During systole, all particles are seen to be dragged with a strong axial flow component towards the sinus region where particle mixing is observed (Figure 4-72). This mixing holds during diastole. It is interesting to note that, when the leaflet is in its fully closed position, the lateral (right) leakage jet contains primarily red-yellow particles while the flow near the b-datum line transports the blue-green particles. The very limited amount of mixing between those two jets in the early stages of diastole corroborates the observations made earlier in the Eulerian analysis of the flow, and notably the formation of well defined flow structures pinpointed in Figure 4-4 and Figure 4-19.

Figure 4-73 shows a close-up view of Figure 4-72 centered on the hinge recess itself in order to clearly visualize and identify the main hinge flow structures. Figure 4-74,

complements Figure 4-73 with a side-view of the same streaklines, which clearly highlights the three-dimensionality of the blood element trajectories throughout the cardiac cycle. During the leaflet opening phase, the particles emanating from the hinge recess are seen to be mainly oriented along the mainstream direction.

Particles seeded in the ventricular side of the hinge (color-coded in blue in Figure 4-73 and Figure 4-74) are seen to exit the recess from the left-most side of the adjacent corner with a strong out-of-plane motion. On the opposite, particles emanating from the aortic corner (color-coded in yellow-red) flow closer to the valve housing, with lesser of an out-of-plane component. These particles are constrained along the housing wall, by the open leaflet on the one-hand, and by the flow and particles emanating from the ventricular corner on the other.

An interesting flow feature that was noted in the Eulerian analysis was the presence, throughout the fully-open leaflet phase, of a flow reversal at the bottom of the hinge recess (section 4.2). This characteristic flow can clearly be identified in Figure 4-73 and Figure 4-74 by tracking the particles color-coded in light blue and green. At early systole, the flow reversal is not yet visible and these particles flow from the ventricular side of the hinge towards the aortic side. However, during the fully open leaflet phase (depicted by the images at mid-acceleration, peak systole, mid-deceleration), these particles change direction and transit from the lateral to the adjacent corner of the hinge where they merge with the blue ventricular streaklines before exiting the hinge recess.

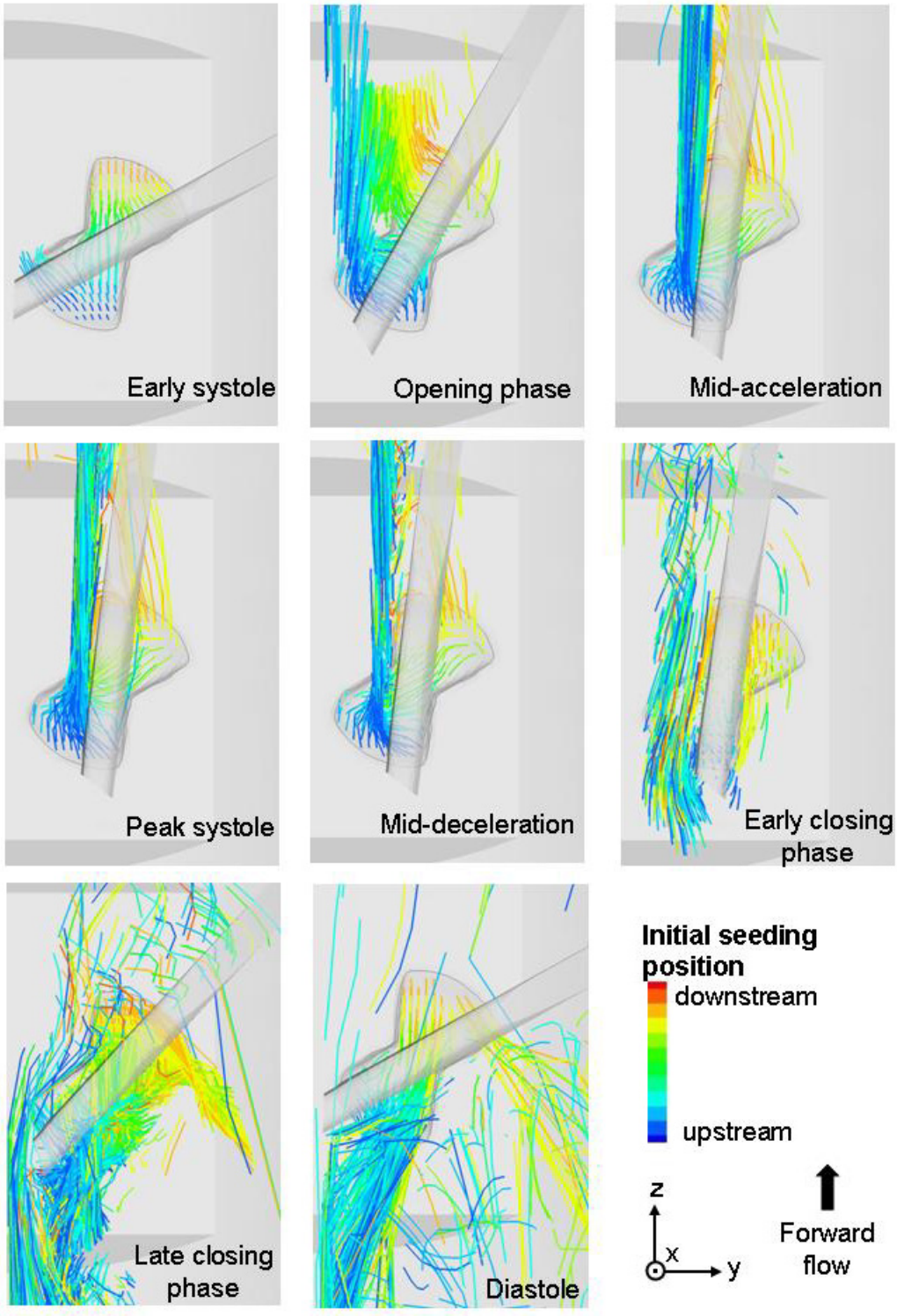

Figure 4-73: Particle streaklines as a function of time. The streaklines are color-coded with the initial position of the particle at the time of injection. The particles seeded the furthest upstream are shown in blue and the particles the furthest downstream in red. [SJM hinge design with a regular hinge gap width]

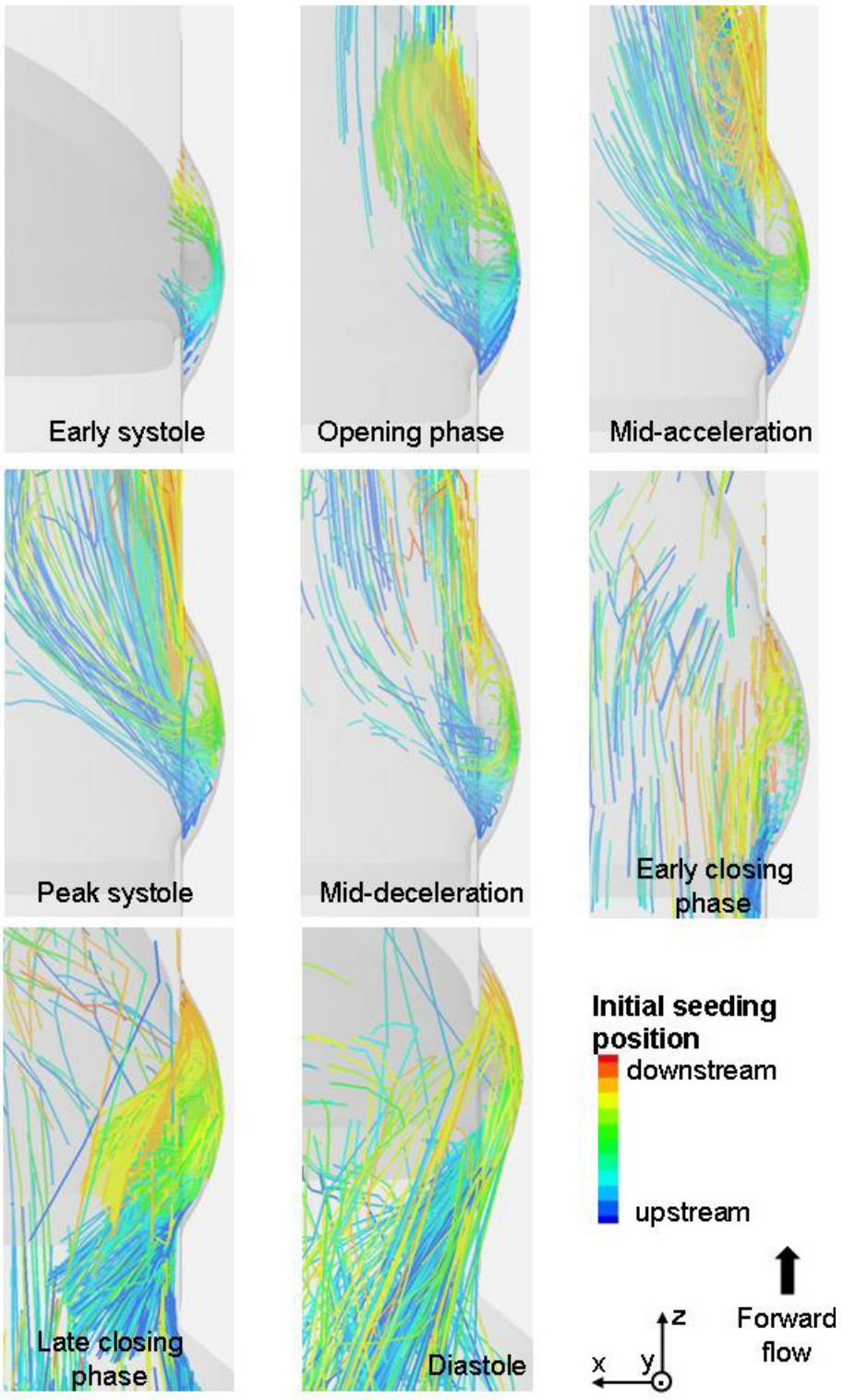

Figure 4-74: Particle streaklines as a function of time. The streaklines are color-coded with the initial position of the particle at the time of injection. The particles seeded the furthest upstream are shown in blue and the particles the furthest downstream in red. [SJM hinge design with a regular hinge gap width]

The exact position through which the particles exit the hinge in the adjacent corner is seen to vary with time: during the leaflet opening phase, particles preferentially exit the recess near the tip of the adjacent corner while during the fully open leaflet phase their exit-point is located in the downstream most- part of the adjacent corner.

Of main interest is the position of the red and yellow streaklines emanating from the lateral corner of the hinge. These streaklines indicate the presence of a forward flow pattern that crosses below the leaflet downstream of the hinge recess. Similarly to the reverse flow at the bottom of the hinge recess, this flow pattern may be attributed to the low pressure on the left side of the leaflet induced by the flow separation.

As the leaflet starts closing, the flow changes direction and the streaklines emphasize the existence of a reverse flow throughout the hinge recess. The particles that had already traveled in the sinus region revert their path and move back towards the hinge region. This corresponds to the streaklines seen in the top part of the images provided in Figure 4-73. Once the leaflet reaches its fully-closed position and the net cross-valvular flow rate increases to its diastolic leakage value, the streaklines suggest the presence of two highly three-dimensional strong leakage jets: one of them emanating from the lateral corner (with mostly yellow-red particles) and the second one from the ventricular corner (blue-tinted particles). The overall position of the streak-lines outside of the two jets underscores, as expected, the complex flow that exists on the aortic side of the closed leaflet.

Streaklines are used to provide a deeper insight into the flow structures that form inside the hinge recess during the cardiac cycle. They provide an intuitive mean to inspect a flow field, as they may be seen as the trace left by a dye injection at a given instant in time. However, in order to understand the thromboembolic complications associated with the implantation of BMHVs, it is important to follow individual blood elements, estimate their trajectories at they cross through the hinge recess and the

shear stress levels they experience along those paths. Accordingly, the following paragraphs no longer depict instantaneous snapshots of the flow and particles, but rather focus on the trajectories of the seeded particles and their history depending upon their release-time.

Figure 4-75 displays the pathlines of particles seeded at four instances of the cardiac cycle, namely early systole, peak systole, mid deceleration, and diastole. In this figure, each column shows the top and side views of the trajectories followed by the particles that are seeded at each of those specific instances. The trajectories are then color-coded with time. For instance, the pathline of a particle seeded at early systole (left-most column) is color-coded in blue at the initial position of the particle (inside the hinge) and in red at the location occupied by the particle at early diastole. Note that the leaflet is shown in both its fully-open and fully-closed position. The sparseness of the red/orange paths in the left most column reveals that only very few of the particles seeded at early systole are in the vicinity of the hinge during the early part of diastole. The same observation holds true for the particles seeded at peak systole (second column in Figure 4-75). These two observations combined indicate that the particles that cross the hinge recess between early and peak systole travel sufficiently far away from the hinge recess for only very few of them to leak back through the closed leaflet. Taking a closer comparative look at those two left-most columns, it may be noted that the few particle-paths that come back and leak through the hinge in the first column are color-coded in shades of orange, while they are color-coded in shades of yellow in the second column. This indicates that, as expected, the particles that perform a first pass through the hinge early in systole travel further downstream of the hinge than those seeded in a later phase. At peak systole, most of the particles are seen to exit the hinge recess from the adjacent corner of the hinge due to the flow reversal present at the bottom of the hinge recess.

At mid-deceleration phase, the bulk valvular flow rate is lower than that at peak systole. This phase is followed by the leaflet closing phase during which the main flow through the valve starts to reverse. The variations in flow through the valve are clearly seen in the particle trajectories. As can be seen in the third column of Figure 4-75, the particles seeded at mid-deceleration are dragged downstream of the valve but quickly reverse direction, and flow back to the ventricular side at valve closure. This is evidenced by the yellow-color of all pathlines seen on either side of the leaflet ear, color which corresponds to the leaflet closing phase,

Finally, the trajectories of the particles seeded at early diastole (right column) clearly illustrate the leakage jets emanating from the hinge region and indicate that only the particles in the lateral corner form the lateral leakage jet (right). The vast majority of the particles seeded within the hinge after valve closure are seen to preferentially exit the recess from the ventricular corner, forming the ventricular (left) jet.

Of prime interest is the visualization of the shear stress levels experienced by the particles along their trajectory. Figure 4-76 displays the same particle pathlines as in Figure 4-75 but color-coded by the principal shear stress levels. Note that the maximum of the color-scale is set to 1,000 dyn/cm^2 to identify critical regions with elevated potential for blood damage. In the Eulerian analysis, shear stresses of 1,000 dyn/cm^2 and above were noted at peak systole outside of the recess between the leaflet and recess surfaces and within the hinge recess alongside of the adjacent and lateral corner walls. While shear stresses above 1,000 dyn/cm^2 were limited to confined regions during systole, they occupied a large portion of the recess and near hinge region during diastole, notably in the wake of the leakage jets and at the bottom of the hinge recess.

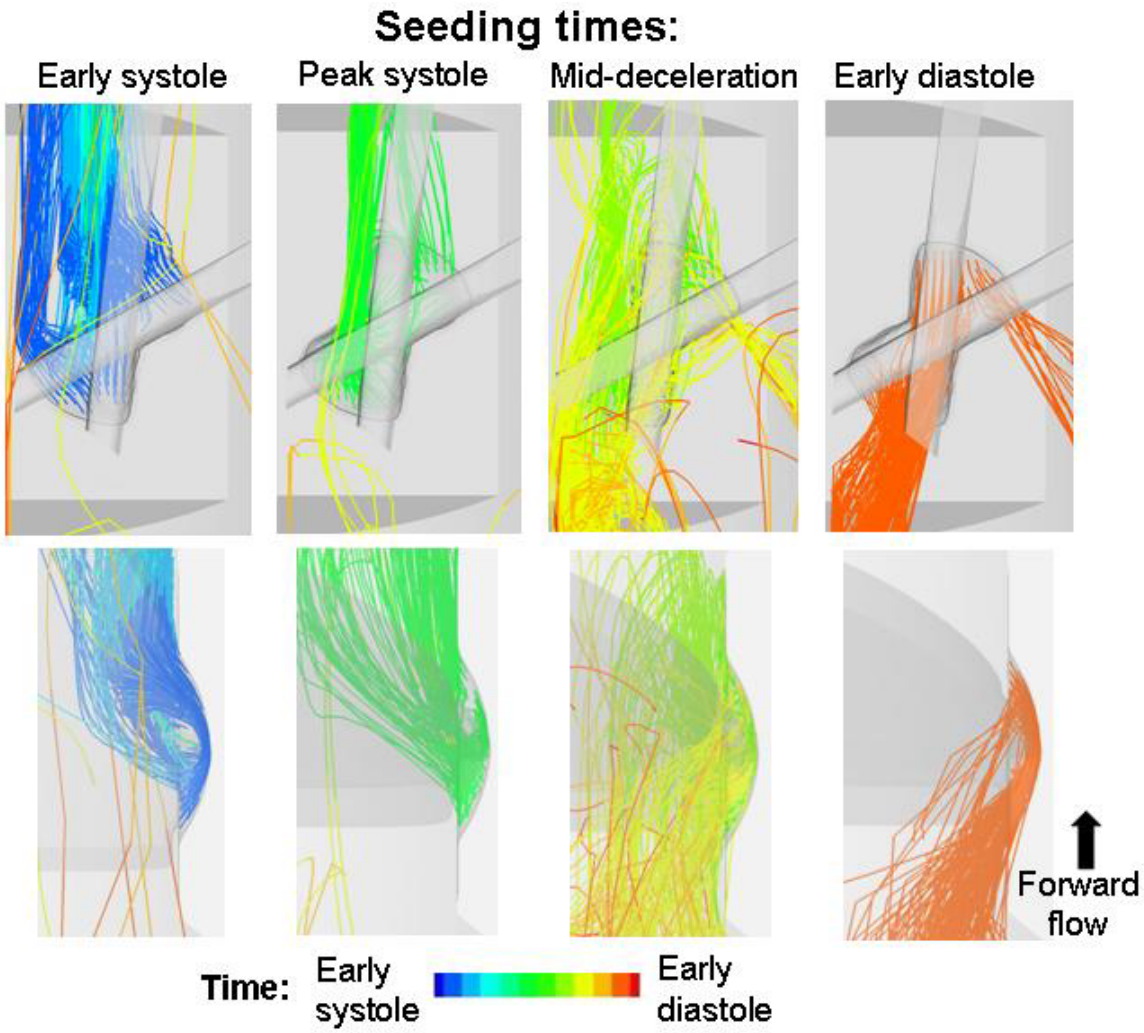

Figure 4-75: Particle pathlines for four sets of particles seeded at different instances of the cardiac cycle, namely early systole, peak systole, mid deceleration and diastole. Each column shows the trajectories followed by the particles seeded at that specific instance. The pathlines are then color-coded with time. Accordingly the pathline of a particle seeded at early systole will be blue at the origin (inside the hinge) and red at the location occupied by the particle at early diastole. The top row represents the top view of the hinge and the bottom row the side view.
[SJM hinge design with a regular hinge gap width]

More precisely, shear stresses values reached up to 1,310 dyn/cm^2 within the hinge recess and 2,080 dyn/cm2 in the near hinge region at peak systole, while at mid-diastole shear stresses up to 6,515 in the hinge recess and 8,535 dyn/cm^2 in the hinge vicinity were found.

These differences in shear stress distribution induce some variations in shear stress along the particle trajectories. The easiest correlation between the shear stress maps provided in the Eulerian description of the flow and the shear stress history of a particle may be achieved by considering the shear stress levels experienced at the time of seeding. Considering the shear stresses experienced at seeding by a family of particles released at the same instance in time throughout the hinge, provides a discrete representation of the Eulerian shear stress maps. During the forward flow phase, it is the particles seeded at peak systole (left column in Figure 4-76) that experience the largest shear stress during the early part of their trajectory. It is evident that the particles seeded at peak systole along the upstream and downstream wall of the hinge are associated with elevated shear stress levels. Nonetheless, the particles that experience the highest shear stress levels during the early part of their pathlines are the ones that are seeded at or after valve closure. This is clearly shown in the third and fourth columns of Figure 4-76. The particles located in the aortic side of the hinge cross the recess underneath the closed leaflet and experience especially high shear stresses, as indicated by the red-colored section of the pathline at the bottom of the hinge recess.

Considering the pathlines as a whole and not only immediately after particle injection, it is evident that the particles seeded at systole experience elevated shear stresses as they flow back through the recess during the leakage flow phase and get entrapped in the wake of the leakage jets emanating from the hinge recess. However, only a limited number of particles seeded between early systole and mid-deceleration actually leak back through the hinge and experience the elevated diastolic forces.

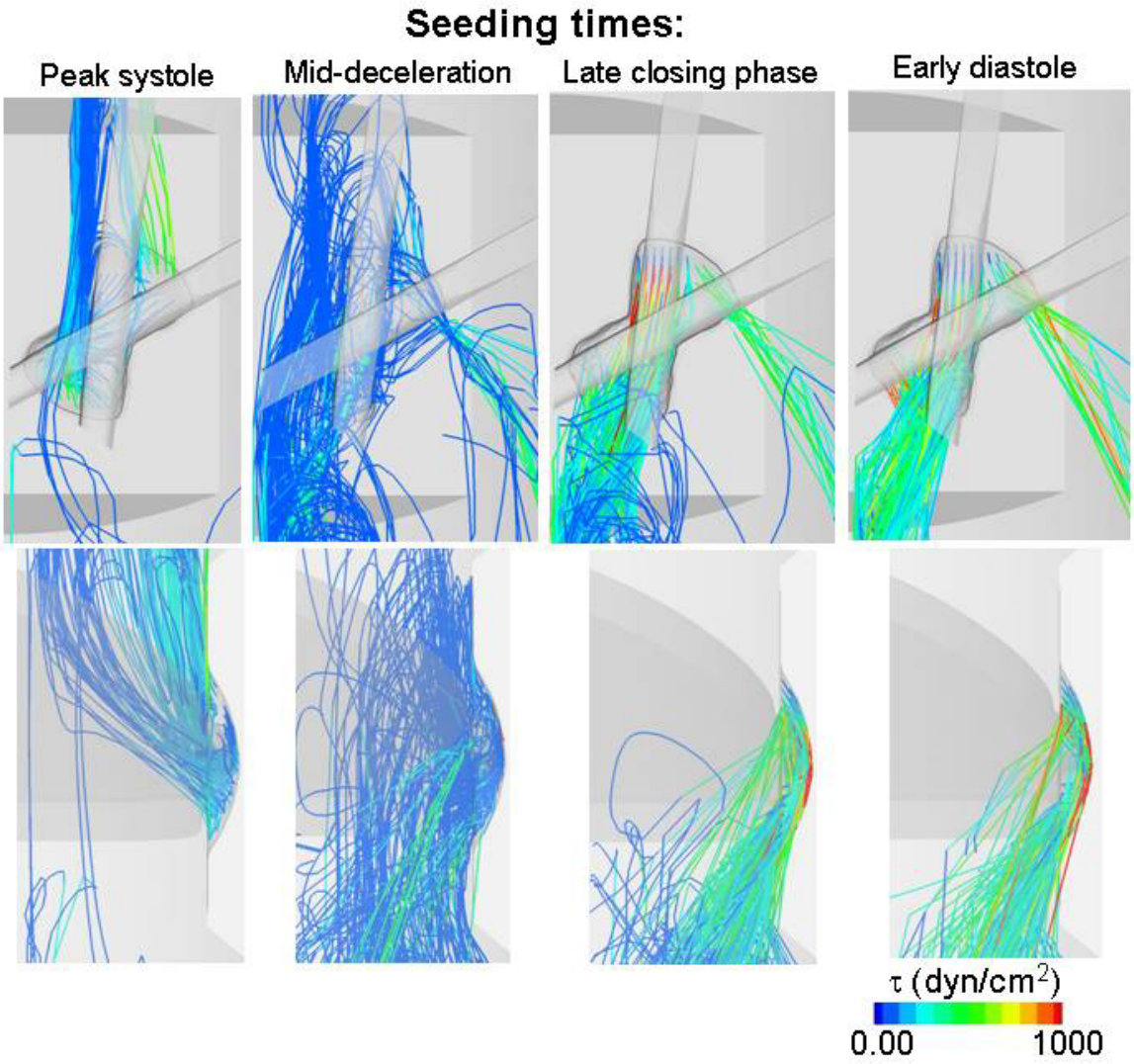

Figure 4-76: Particle pathlines for four sets of particles seeded at different instances of the cardiac cycle. Each column shows the trajectories followed by the particles seeded at that specific instance. The pathlines are color-coded with the principal shear stress levels. The top row represents the top view of the hinge and the bottom row the side view. [SJM hinge design with a regular hinge gap width]

From mid-deceleration onwards, a significant portion of the particles seeded within the hinge recess flow back towards the ventricle. A close inspection of the pathlines indicates that while particles seeded at mid-deceleration reverse direction and travel back towards the hinge; most of the particles do not flow through the regions of elevated shear stresses. However, as expected, this is not the case for the particles seeded during the later phases of the cardiac cycle. The particles that are in the hinge at valve closure and diastole get entrapped in the strong diastolic leakage jets and therefore experience elevated shear stresses after their seeding time. However, as the particles move to the ventricular side of the domain, further away from the valve housing and the leakage jets dissipates, the shear stresses along the pathlines lower. Overall, this indicates a higher propensity for hemolysis and platelet activation for the particles crossing the hinge during diastole compared to systole.

The maximum shear stress levels experienced along the particle trajectory is computed and the distribution of maximum shear stress levels is provided in Figure 4-77. It is clear that most of the particle experience a maximum shear stress below 1,000 dyn/cm^2 while only a small portion are subjected to a shear stress above 1,000 dyn/cm^2 , up to 3,250 dyn/cm^2. It is worthwhile noting that this maximum shear stress value of 3,250 dyn/cm^2 is about half of the maximum shear stress level noted in the Eulerian analysis. A lower maximum shear stress in the Lagrangian analysis is expected since the particles seeded inside the hinge recess are not bound to cross the localized regions of very high shear stresses that were identified during the leakage phase in the hinge and near hinge region. This further highlights the relevance of a Lagrangian approach to analyze the hinge flow fields and relate them to blood damage potential. While a specific hinge design may be associated with high shear stress levels, it is the propensity of the blood elements to flow through these regions of elevated shear stresses that influence the ultimate thromboembolic potential.

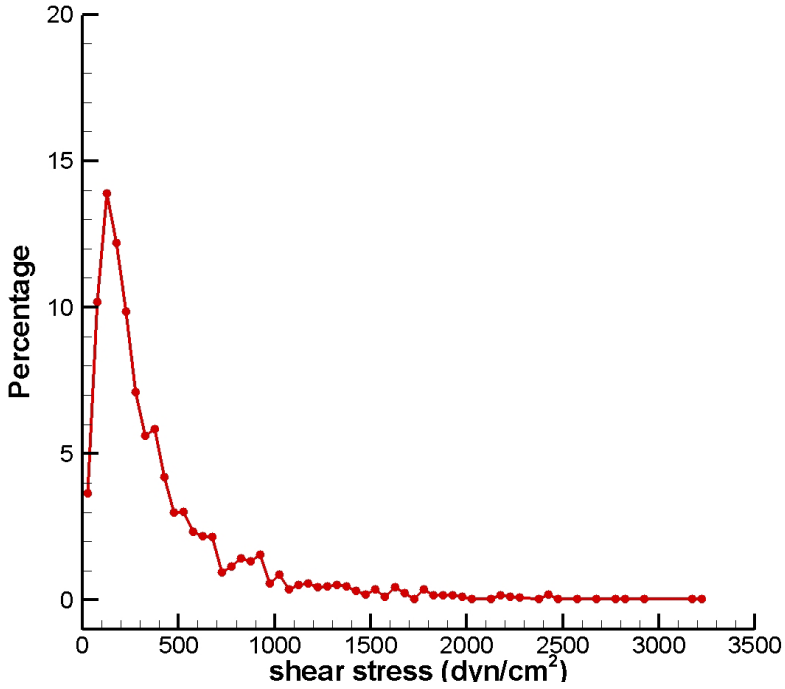

Figure 4-77: Distribution of the maximum shear stress experienced along the particle trajectories. [SJM hinge design with a regular hinge gap width]

In order to obtain a surrogate measure of the thromboembolic potential associated with the hinge flow fields, two blood damage models are applied to estimate the potential for platelet activation and hemolysis (section 3.6.2). The equations to compute the blood damage index for platelet activation BDI^{PL} and the blood damage index for hemolysis BDI^{H} are recalled hereafter:

$$BDI^{PL}{}_{\mathcal{P}} = \sum_i 3.31x10^{-6}\,\Delta t_i^{\,0.77}\,\tau_i^{\,3.075} \qquad \text{Equation 4-1}$$

$$BDI^{H}{}_{\mathcal{P}} = \sum_i 3.62x10^{-5}\,\Delta t_i^{\,0.785}\,\tau_i^{\,2.416} \qquad \text{Equation 4-2}$$

The total damage corresponds to the sum along each particle trajectory of the weighted product of the exposure time by the shear stress experienced. In this

approach, the particle trajectories are considered to be representative of either platelet or red blood cell paths. Consequently, the particles associated with large BDI^{PL} are also associated with large BDI^{H}. The computed BDI^{PL} and BDI^{H} are presented in Figure 4-78. Most of the particles are seen to be associated with a low BDI however, a few particles are associated large BDI and these correspond to the particles crossing the hinge recess during the diastolic phase.

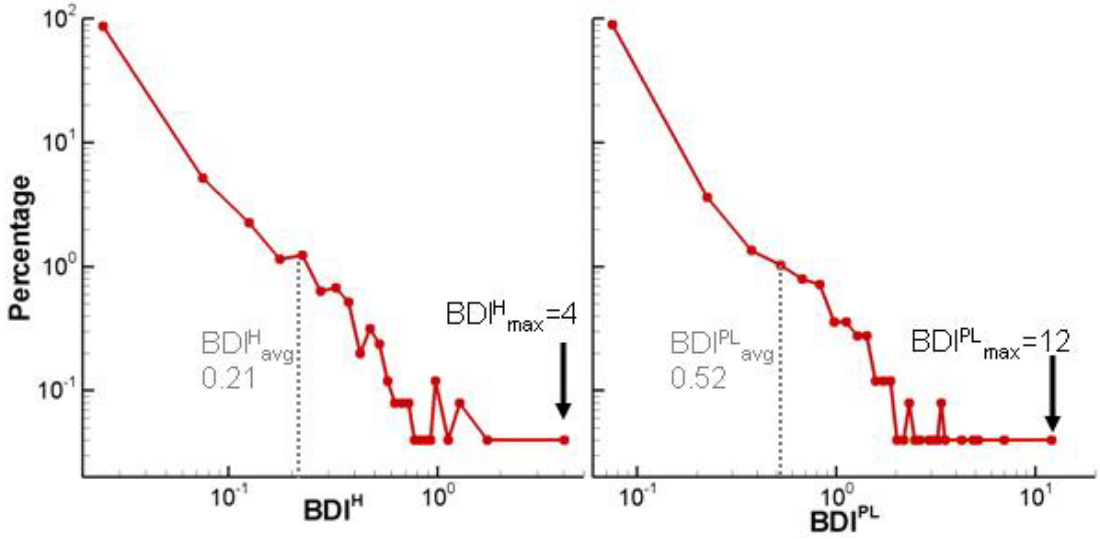

Figure 4-78: Distribution of the blood damage indices for hemolysis and platelet activation as a function of the particle percentage.
[SJM hinge design with a regular hinge gap width]

4.5.3 SJM hinge with a large hinge gap width

As was the case with the SJM regular hinge, streaklines are shown first to provide a better understanding of the location of the seeded particles and their dynamic interplay during the cardiac cycle. The reader is referred to Figure 4-70 for the exact definition of the streaklines shown herein. A global view of the numerical domain is provided in Figure 4-79, where streaklines are shown at as function of time, from early systole to early diastole. In this figure, the streaklines are color-coded by the particle

release time; the particles released at early systole are shown in blue and those released at early diastole in red. Animations SJMLarge_Large_View_Streaklines.mov SJMLarge_Zoom_View_Streaklines.mov complement Figure 4-79.

At early systole, the valvular flow rate is low and the particles remains in the vicinity of the hinge. As the flow rate increases, the particles are dragged further downstream of the valve. It is interesting to note that, throughout the leaflet opening and fully-open leaflet phases, the forward flow emanating from the hinge recess is primarily located on the adjacent (left) side of the leaflet. A close inspection of streaklines during systole underlines that the particles released at mid-systole (green) travel downstream away from the valve whereas the particles injected earlier, during the first part of systole (blue particles), get entrapped in the recirculating flow structure that forms in the sinus region.

As the cross-valvular flow rate decelerates, the streaklines are less elongated and more chaotic flow structures form downstream of the valve due to the destabilizing effect of the decelerating flow. The large recirculation region that appeared at mid-systole downstream of the valve is seen to span the entire sinus after mid-deceleration.

As the leaflet closes, the flow through the numerical domain starts to reverse, and the particles released at the end of systole indicate the formation of a large leakage jet in the adjacent (left) side of the hinge. All particles released after leaflet closure are seen move upstream, towards the ventricular section of the numerical domain.

In order to evaluate the mixing of the flow, the streaklines presented in Figure 4-80 are color-coded with the initial position of the particles at the time of release.

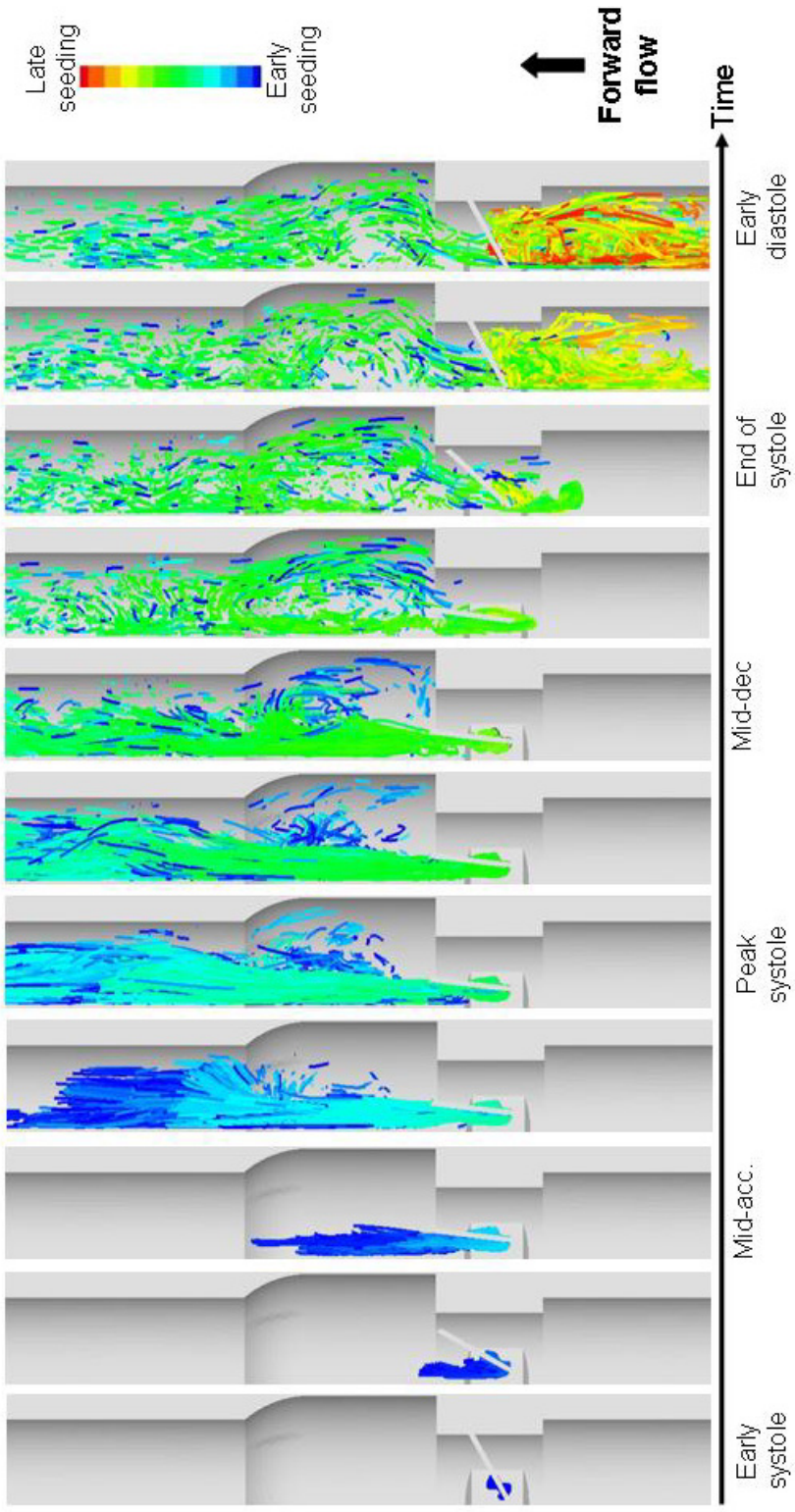

Figure 4-79: Particle streaklines as a function of time. The streaklines are color-coded with the seeding time of the particles. The particles released at early systole are shown in blue and those released at early diastole in red. [SJM hinge design with a large hinge gap width]

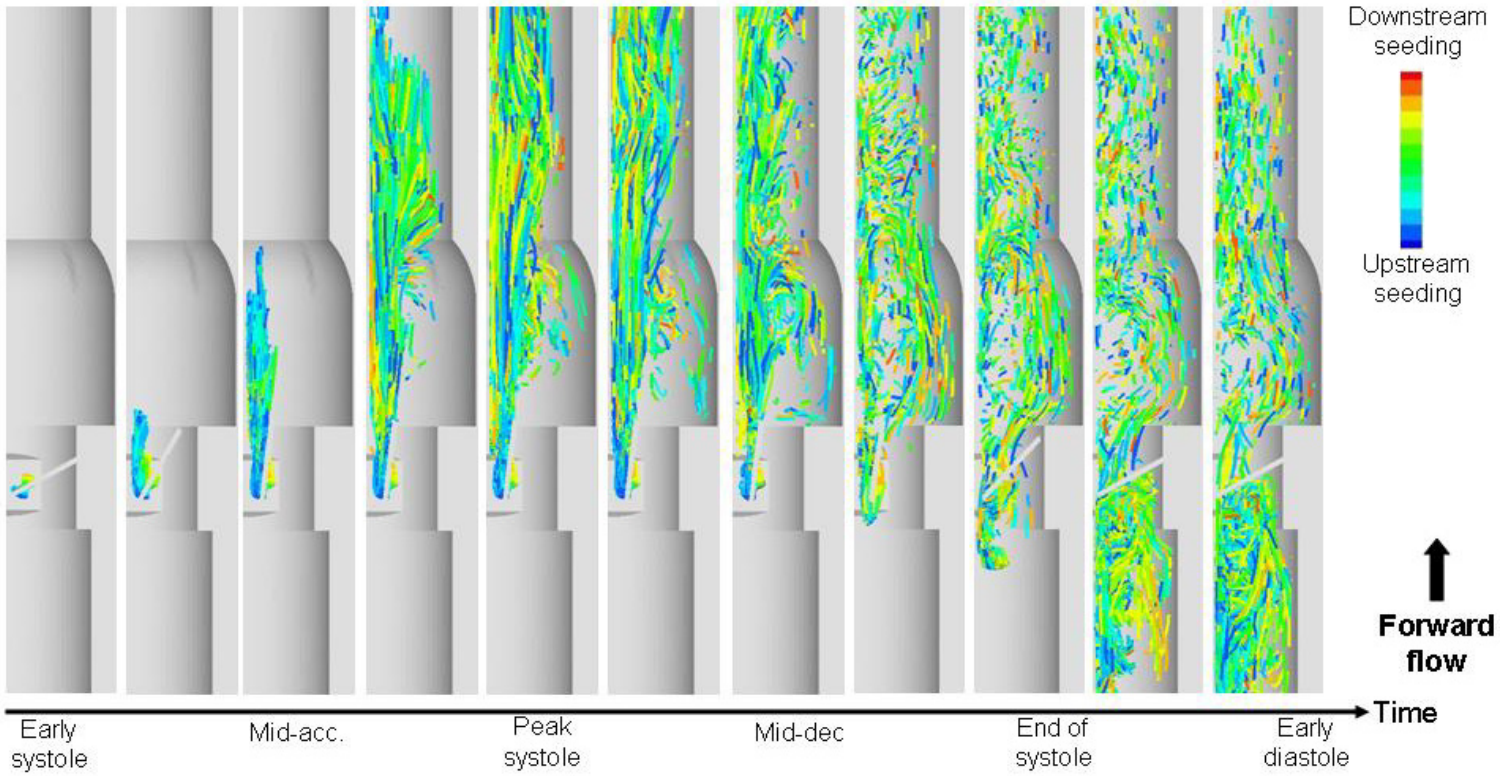

Figure 4-80: Particle streaklines as a function of time. The streaklines are color-coded with the initial position of the particle at the time of injection. The particles seeded the furthest upstream are shown in blue and the particles the furthest downstream in red. [SJM hinge design with a large hinge gap width]

Accordingly, in Figure 4-80, the blue streaklines correspond to the particles released the furthest upstream, on the ventricular side of the hinge, whereas the streaklines color-coded in red correspond to the particles seeded the furthest downstream, on the aortic side of the hinge. Due to the design of the hinge recess, it should be noted that the color distribution may also be viewed as the seeding-position with respect to the open leaflet; the blue and green streaklines representing particles seeded on the left side of the leaflet, and the yellow and red streaklines corresponding to those seeded on the right side.

From early systole to mid-deceleration, all particles seeded in the hinge are dragged downstream by the main stream and thus the streaklines reveal a strong axial flow component. However, a close inspection of the streaklines indicates that immediately downstream of the valve, the red particles seeded in the lateral (right) side of the hinge are the one located the furthest on the left side of the numerical domain (fourth panel in Figure 4-80). This suggests that the flow in the right side of the hinge has a strong lateral-adjacent (right-left) component. Particle mixing is evident in the sinus region and downstream of the sinus during the entire deceleration phase, spanning from peak systole onwards. This downstream mixing is seen to hold during the leaflet closing phase and diastole. Once the leaflet has reached its fully closed position, the streaklines on the ventricular side of the numerical domain, upstream of the valve, underscore the presence of a strong mixing of the flow.

Figure 4-79 and Figure 4-80 show the streaklines from a global perspective. In order to look closely at the details of the flow structures within the hinge recess, Figure 4-81 shows a close-up view of Figure 4-80 centered on the hinge recess itself. To visualize the three-dimensionality of the element trajectories in the near hinge region, Figure 4-82, complements Figure 4-81 by providing a side-view of the same streaklines.

During the leaflet opening phase, the blue streaklines in Figure 4-81 and Figure 4-82 are seen to be mainly oriented along the mainstream direction, implying that particles seeded in the ventricular side of the hinge exit the recess from the left-most side of the adjacent corner with a strong out-of-plane motion. On the other hand, the streaklines forming on the aortic side of the hinge (yellow-red) underscore the presence of a lesser three-dimensional flow with a larger lateral-adjacent component.

The Eulerian analysis of the flow reveals a change in flow direction at the bottom of the hinge recess during the fully-open leaflet phase: a flow reversal was noted at mid-acceleration and mid-deceleration, while at peak systole, this flow reversal was substituted for a forward flow pattern (section 4.3). This characteristic change in flow direction at the bottom of the hinge recess can clearly be identified in Figure 4-81 and Figure 4-82 by tracking the particles color-coded in light blue and green. During the opening phase, the flow reversal is not yet visible and the particles tinted in light blue and green travel from the ventricular side to the aortic side of the hinge. Once the valve has reached its fully open position (mid-acceleration in Figure 4-81 and Figure 4-82), these particles are seen to transit from lateral to the adjacent corner of the hinge where they merge with the dark blue ventricular streaklines before exiting the hinge recess. This observation also holds at mid-deceleration. However, at peak systole, these same particles resume the main stream direction and flow directly from the ventricular to the aortic side of the hinge. This change in flow direction during the fully-open leaflet phase impacts the flow in the lateral corner of the hinge. While the reverse flow observed at mid-acceleration and mid-deceleration is associated with smooth streaklines in the lateral corner of the hinge, the forward flow pattern characterizing the hinge bottom at peak systole induces a complex flow pattern in the lateral corner as suggested by the entangled green streaklines.

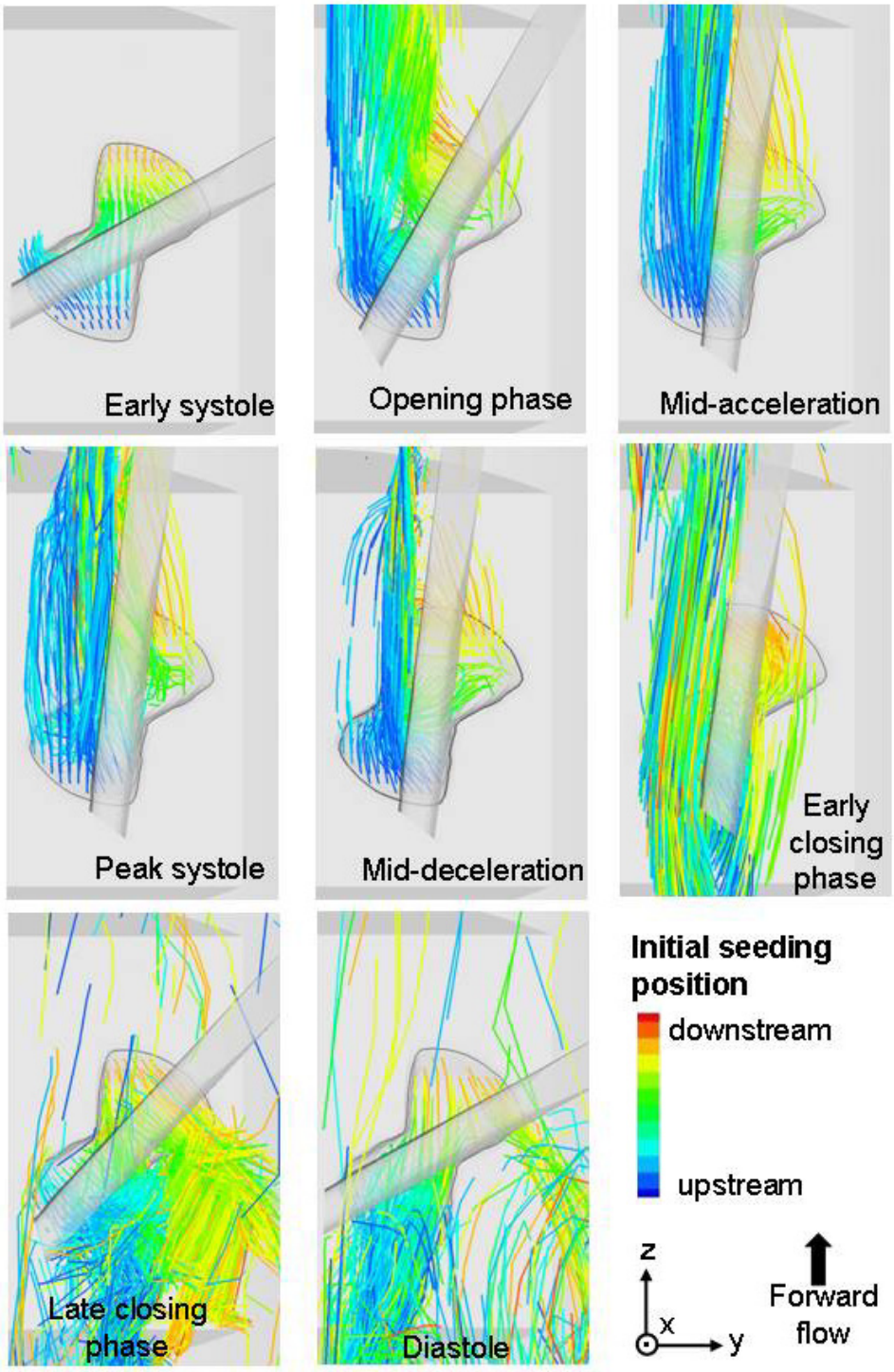

Figure 4-81: Particle streaklines as a function of time. The streaklines are color-coded with the initial position of the particle at the time of injection. The particles seeded the furthest upstream are shown in blue and the particles the furthest downstream in red. [SJM hinge design with a large hinge gap width]

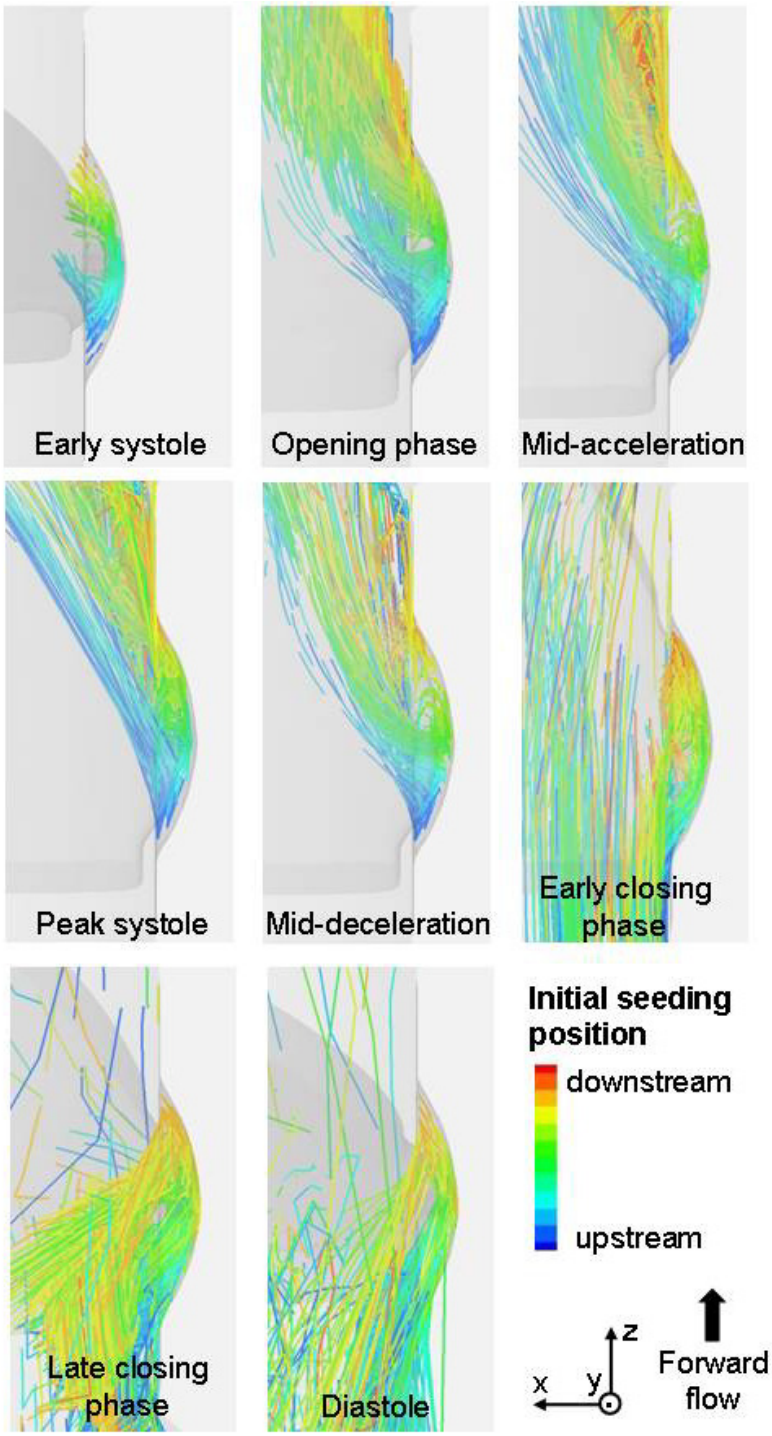

Figure 4-82: Particle streaklines as a function of time. The streaklines are color-coded with the initial position of the particle at the time of injection. The particles seeded the furthest upstream are shown in blue and the particles the furthest downstream in red. [SJM hinge design with a large hinge gap width]

As the leaflet starts to close, the global flow direction switches and the net cross-valvular flow rate becomes negative. The streaklines during the early closing phase emphasize the existence of a strong reverse flow throughout the hinge recess. The increase in net cross-valvular flow rate during the leaflet closing phase translates into the formation of a strong and highly-three dimensional leakage flow pattern, primarily oriented towards the lateral (right) side of the domain at the end of the closing phase. The particles that had already traveled in the sinus region change direction and move back towards the hinge. This corresponds to the streaklines seen in the top part of the images provided in Figure 4-81.

During diastole, the leaflet is closed and the cross-valvular flow rate has reached its diastolic leakage value. At this instance, the streaklines suggest the presence of two strong three-dimensional leakage jets, the first one emanating from the lateral corner and the second one from the ventricular corner. The overall position of the streak-lines outside of the two jets underscores the complexity of the flow that exists on the aortic side of the closed leaflet. Comparison of the streakline distribution during diastole and during the late phase of the leaflet closing reveals some differences. The motion of the leaflet induces a highly three-dimensional flow with a large lateral-adjacent (left-right) component, whereas during diastole the three-dimensionality of the flow is lesser (smaller out-of-plane u-component) and the leakage jets are primarily oriented along the main stream direction. The difference in flow direction is particularly evident for the flow emanating from the ventricular side of the hinge.

Inspection of the streaklines provides a mean to gain deeper information into the flow structures that arise inside the hinge recess during the cardiac cycle. Nonetheless, following individual blood elements and estimating their history is essential to analyze the hinge flow fields from a blood cell stand-point and understand hinge flow-related

thromboembolic complications. Consequently, the following paragraphs center on the trajectories of the seeded particles and their history depending upon their release-time.

Figure 4-83 displays the pathlines of particles seeded at early systole, peak systole, mid deceleration, and early diastole. In this figure, each column shows the top and side views of the trajectories taken by the particles that were seeded at each of those specific instances. The trajectories are color-coded with time: the pathline of a particle seeded at early systole (first column) is color-coded in blue at the initial position of the particle (inside the hinge) and in red at the location occupied by the particle at early diastole.

The trajectories of the particles exiting the hinge recess at early systole are seen to be greatly influenced by the hinge recess design. As the particles are dragged forward by the main stream, they are impinging upon the downstream wall of the adjacent corner and exit the hinge from either the tip of the adjacent corner or the aortic corner. This is clearly visualized by the presence of two distinct sets of pathlines in Figure 4-83 (first column). Of all the particles seeded within the hinge recess at early systole and also at peak systole (second column), only a few are seen to be in the near-hinge region at early diastole. This suggest that the particles travelling through the hinge during the first half of systole move sufficiently far away from the valve for only very few of them to leak back through the closed leaflet during early diastole.

At mid-deceleration phase, the bulk valvular flow rate is lower than that at peak systole. This phase is followed by the leaflet closing phase during which the main flow through the valve starts to reverse. Consequently the particles seeded at mid-deceleration (third column) are dragged downstream of the valve but quickly reverse direction and flow back to the ventricular side at valve closure. This is evidenced by the yellow-color of the pathlines in the near hinge region, which corresponds to the leaflet closing phase. The pathlines of these particles at later time (orange-red) reveal that most

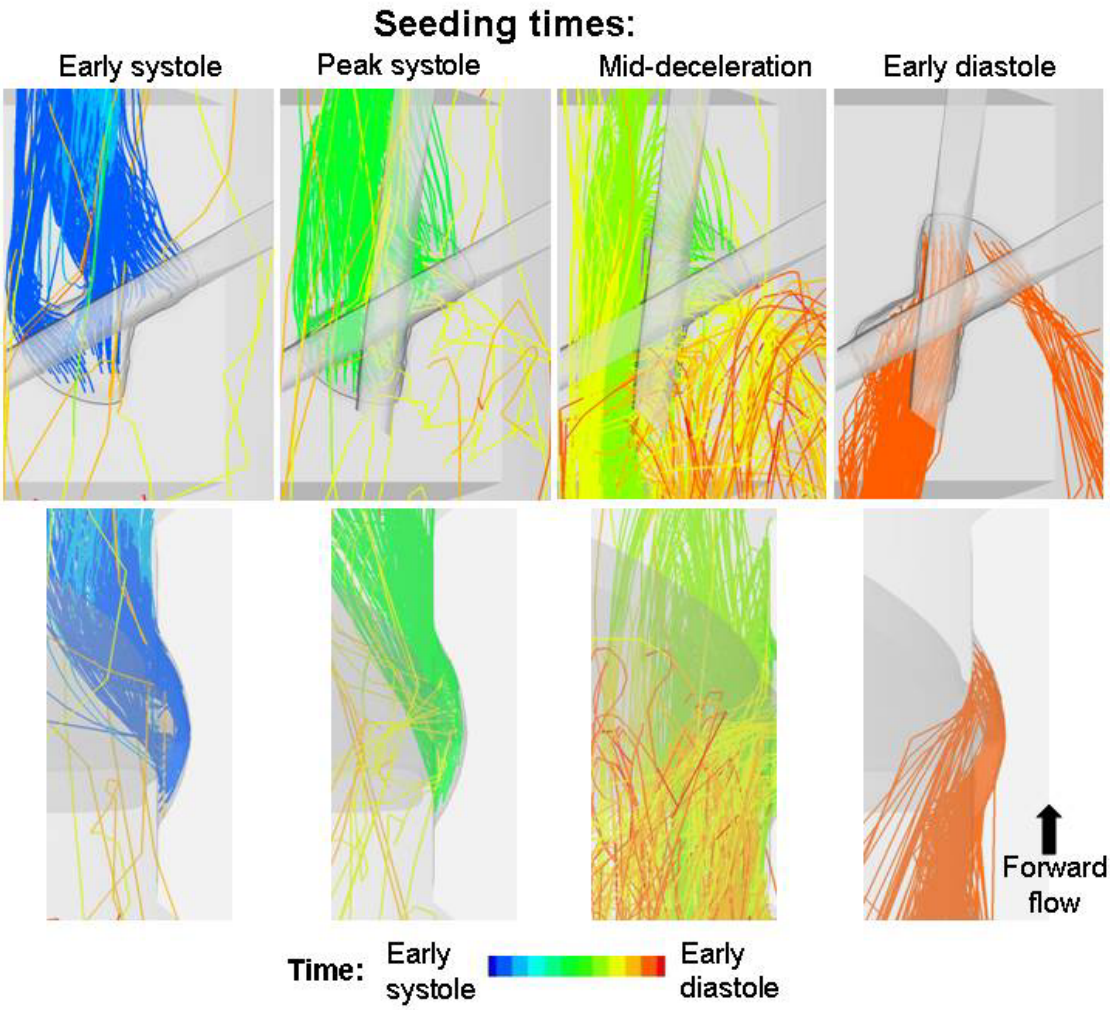

Figure 4-83: Selected particle pathlines for four sets of particles seeded at different instances of the cardiac cycle, namely early systole, peak systole, mid deceleration and diastole. Each column shows the trajectories followed by the particles seeded at that specific instance. The pathlines are then color-coded with time: the pathline of a particle seeded at early systole is blue at the origin (inside the hinge) and red at the location occupied by the particle at early diastole. The top row represents the top view of the hinge and the bottom row the side view.
[SJM hinge design with a large hinge gap width]

of the particles are on the ventricular side of the leaflet and follow complex trajectories. It should be noted that the trajectory of the particles seeded at the bottom of the hinge recess between mid-acceleration and mid-deceleration corroborates with previous findings (section 4.3.2) and indicate a change of flow direction within the hinge recess (not shown in Figure 4-83). Finally, the trajectories of the particles seeded during the early part of diastole (right column) clearly illustrate the presence of well-defined leakage jets emanating from the hinge region.

In order to visualize the shear stress levels experienced by the particles along their trajectory, Figure 4-84 displays the particle pathlines color-coded by the principal shear stress levels. In order to have a mean of assessing detrimental shear stress from benign shear stress levels, the maximum of the color-scale is set to 1,000 dyn/cm^2. As a reminder, the Eulerian analysis of the shear stress distribution pinpointed several regions in the hinge and near hinge region associated with shear stresses above 1,000 dyn/cm^2. During the forward flow phase, a localized region of elevated shear stresses was identified immediately upstream and outside of the recess, in the gap between the leaflet and recess surfaces. Moreover, elevated shear stresses were also found along the walls of the adjacent and lateral corners. On the other hand, during the leakage flow phase, the elevated shear stresses were seen in the wake of the leakage jets and at the bottom of the hinge recess.

Accordingly, particles seeded at different locations and times are bound to experience different shear stress levels along their trajectories, as shown in Figure 4-84. The particles are seeded within the recess at different instances of the cycle and therefore differences in shear stress levels are already visible immediately after seeding. Particles released at early systole (first column) experience near-zero shear stress levels during the early part of their trajectory. However, this is not the case for the particles seeded at peak systole (second column). These particles are seen to experience higher

shear stresses right after seeding. It is evident that the particles seeded along the upstream and downstream wall of the hinge are associated with elevated shear stress levels, which is in agreement with the shear stress maps provided in the Eulerian description of the flow (section 4.3.3). Comparison of the particle trajectories indicates that, of all particles seeded during the forward flow phase, it is the particles released at peak systole that experience the largest initial shear stresses. Nonetheless, the particles that experience the largest shear stress levels at seeding are those seeded at valve closure (fourth column) and at early diastole (fifth column in Figure 4-84). The particles seeded at the bottom of the hinge recess at these two instances experience elevated shear stress as highlighted by the red-colored pathlines. Particles seeded at early diastole in the lateral corner of the hinge are also seen to experience shear stress levels above 1,000 dyn/cm^2.

Differences in shear stress exist along the entire pathlines and not only in the initial part of the trajectories. During the forward flow phase, most particles travel away from the hinge and do not flow back through the recess during the leakage flow phase. They thus experience low shear stress levels along their trajectory. However, it is clear from Figure 4-84 that all particles that get entrapped in the wake of the leakage jets emanating from the hinge recess experience elevated shear stress levels. This is particularly evident for the particles seeded from valve closure onwards (two right-most columns in Figure 4-84). These particles are exposed to elevated shear stresses for a long time as they experience elevated shear stress at the seeding time but also afterwards while they travels towards the ventricular side, dragged by the leakage jets. Further away from the hinge, the leakage jets dissipate and consequently the shear stress levels along the particle pathlines lower. Overall, Figure 4-84 clearly underscores that the propensity for blood cell rupture and damage is higher for the particles crossing the hinge during diastole compared to those crossing it during systole.

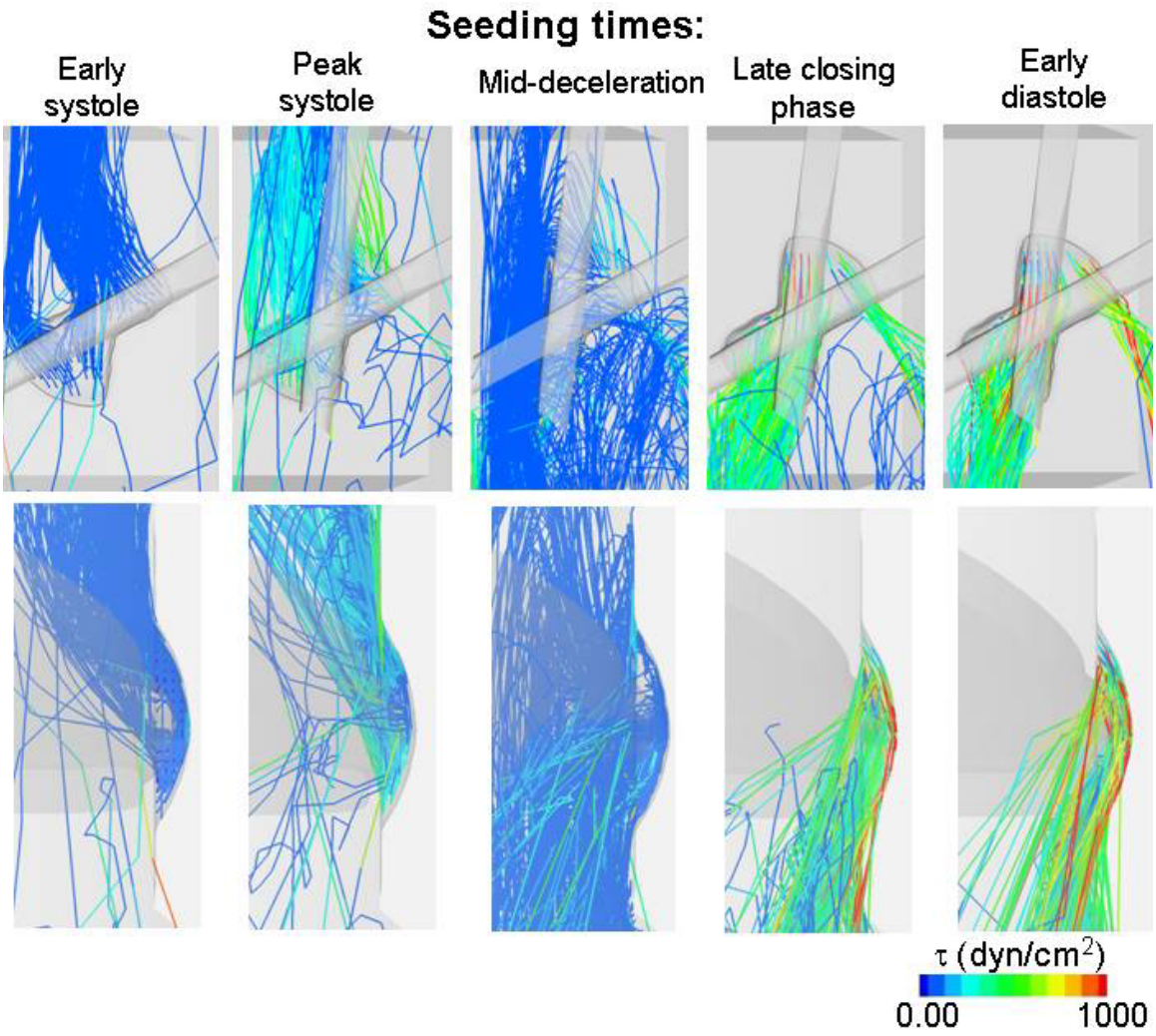

Figure 4-84: Selected particle pathlines for four sets of particles seeded at different instances of the cardiac cycle. Each column shows the trajectories followed by the particles seeded at that specific instance. The pathlines are color-coded with the principal shear stress levels. The top row represents the top view of the hinge and the bottom row the side view. [SJM hinge design with a large hinge gap width]

The maximum principal shear stress levels experienced along the particle trajectory is computed and the distribution of maximum shear stress levels is provided in Figure 4-85. It is evident that most of the particle experience a maximum shear stress below 1,000 dyn/cm^2 while only a small portion are subjected to a shear stress above 1,000 dyn/cm^2. The maximum shear stress computed reaches 3,025 dyn/cm^2. This value is lower than the maximum shear stress reported in the Eulerian analysis of the flow. At mid-diastole, the peak shear stress levels were found to be 5,445 dyn/cm^2 inside the hinge recess and 6,320 dyn/cm^2 in its immediate vicinity. These levels were estimated to be lower during the forward flow phase with a maximum of 1,430 dyn/cm^2 inside the recess and 1,730 dyn/cm^2 in the hinge vicinity. The Eulerian analysis of the flow revealed the existence of regions of large shear stress levels in the hinge and near hinge region. However, the particles seeded in the hinge region are not bound to travel through these localized region of elevated shear stresses. Consequently, the overall maximum shear stress experienced by the particles crossing the hinge is lower than the peak levels estimated from the Eulerian study of the flow.

Two blood damage models (equations 4-1 and 4-2) are applied along each particle trajectory to estimate the potential for platelet activation and hemolysis. In this approach, the particle trajectories are considered to be representative of either platelet or red blood cell paths. As a result, the particles associated with elevated blood damage index for platelet activation (BDI^{PL}) are also associated with large blood damage index for hemolysis (BDI^{H}). The computed BDI^{PL} and BDI^{H} are presented in Figure 4-86. The maximum computed BDI^{H} reaches 1.28 while the maximum BDI^{PL} is 4.13. Figure 4-86 clearly underscores that most particles are associated with a low BDI. This is expected since, as noted earlier, particles are not constrained to cross regions of elevated shear stresses. Only the particles that are subjected to elevated shear stresses are likely to be associated with a large BDI.

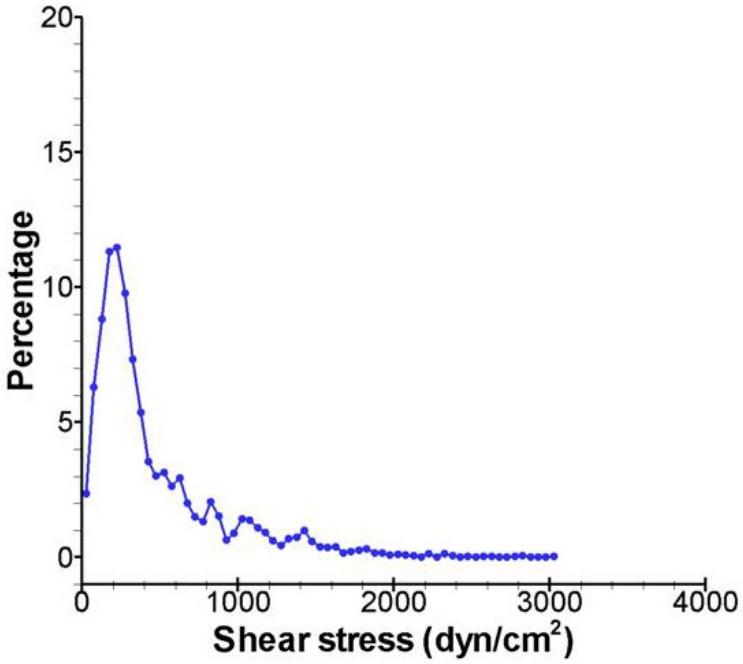

Figure 4-85: Distribution of the maximum shear stress experienced along the particle trajectories. [SJM hinge design with a large hinge gap width]

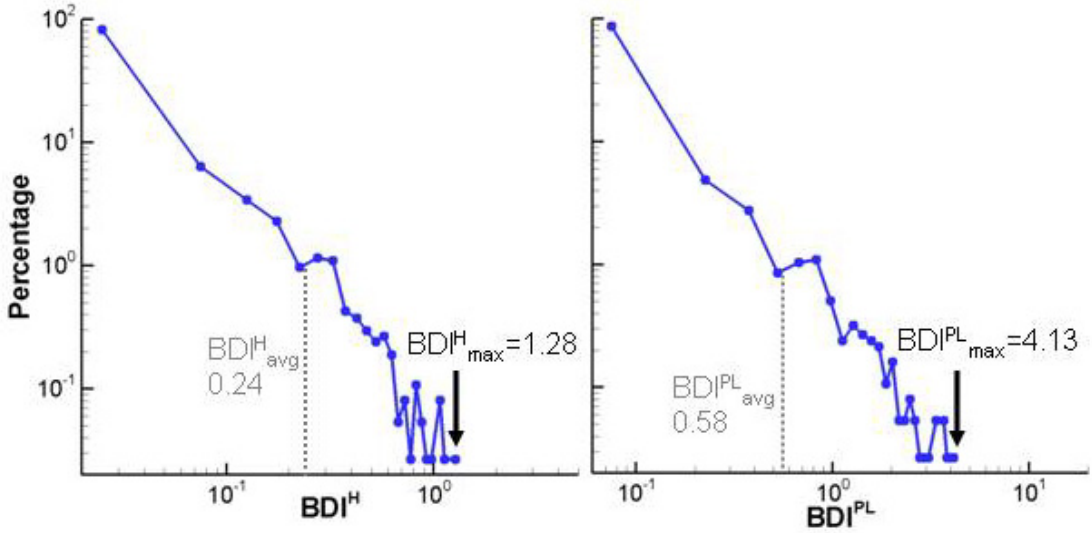

Figure 4-86: Distribution of the blood damage indices for hemolysis and platelet activation as a function of the particle percentage.
[SJM hinge design with a large hinge gap width]

4.5.4 CM hinge with a regular hinge gap width

A structure similar to that employed with the SJM hinge designs is used herein to present the Lagrangian results of the CM hinge design. The streaklines are presented first from a global perspective before focusing on the hinge recess itself. Figure 4-87 displays the streaklines at various instances of the cardiac cycle from early systole to early diastole. The streaklines are color-coded by the particle release time, such that the particles released at early systole are shown in blue and those released at early diastole in red. Animations CM_Large_View_Streaklines.mov and CM_Zoom_View _Streaklines.mov complement the figures provided in this section.

At the beginning of the cardiac cycle, the particles seeded within the hinge recess are seen to be dragged downstream by the slowly increasing main stream flow. Part of these particles released early in the cycle (blue particles) gets entrapped in the recirculating flow structure that forms in the sinus region. The particles released at a later time are carried away by a fast flowing main stream flow and thus travels downstream of the valve without being entrapped in the sinus vortex. This is clearly seen with the particles released at peak systole (light green particles).

During the deceleration phase however, the valvular flow rate decreases resulting in lower particle velocities as shown by the less elongated aspect of the streaklines. The particles released during this phase (dark green color) get entrapped in the decaying sinus vortex. Overall, the streakline distribution during the late systole is chaotic due to the destabilizing effect of the decelerating flow.

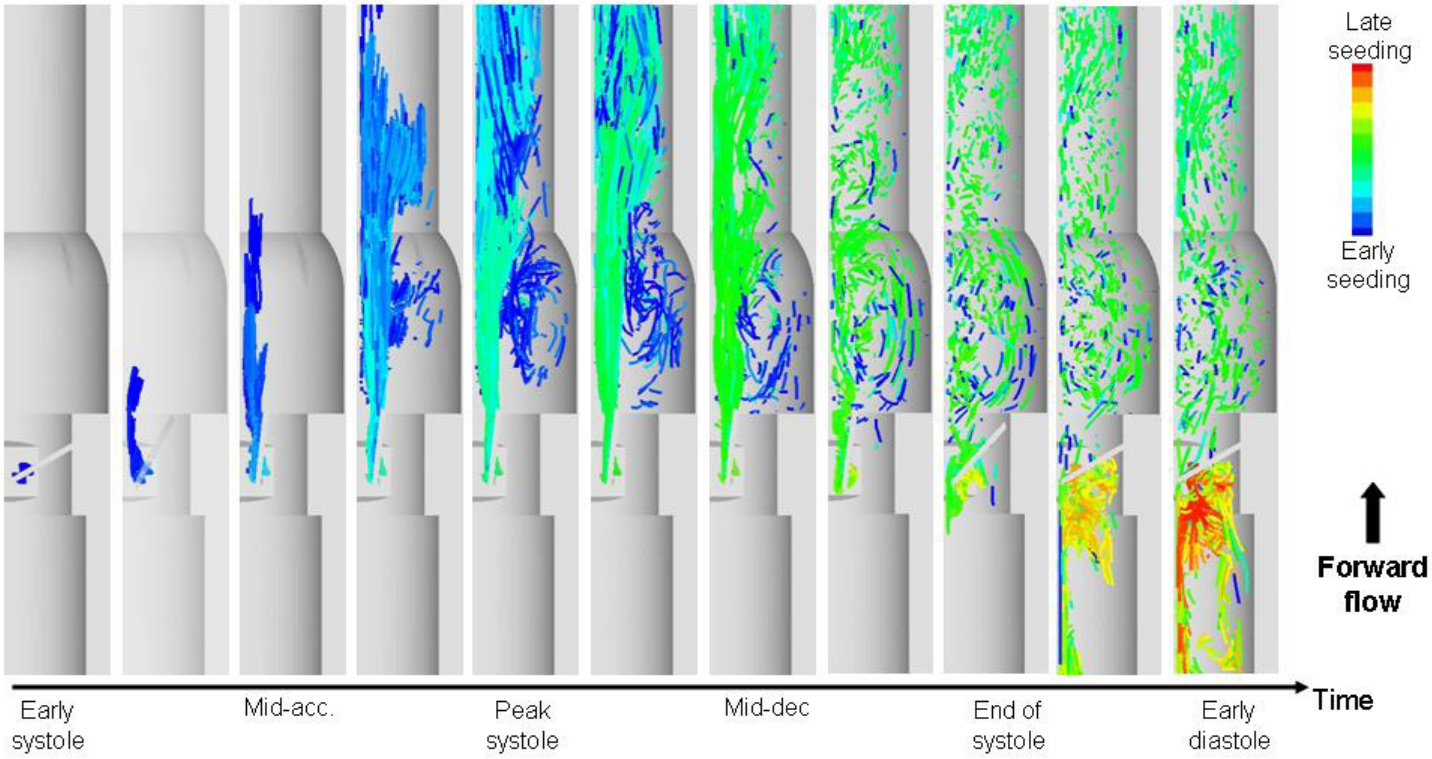

Figure 4-87: Particle streaklines as a function of time. The streaklines are color-coded with the seeding time of the particles. The particles released at early systole are shown in blue and those released at early diastole in red. [CM hinge design with a regular hinge gap width]

At the end of systole, the flow has started to reverse, and the particles released at that point in time (light green) indicate the formation of reverse flow jets leaking from the hinge region. These leakage jets persist throughout diastole and all particles released from valve closure onwards travel upstream towards the ventricular section of the numerical domain. The particles that were released during the early phase of the cardiac cycle are the only ones visible in the aortic section of the domain. The point-like streaklines of these early particles suggest the presence on the aortic side of a complex slow-moving flow containing small eddies.

To visualize the mixing of the flow crossing through the hinge region, Figure 4-88 shows the same streaklines as those presented in Figure 4-87 but the streaklines are color-coded with the initial position of the particles at the time of release. The blue and red particles correspond to the particles seeded the furthest upstream and downstream of the hinge, respectively. Incidentally, due to the design of the recess, the blue-green and yellow-red particles also correspond to the particles seeded on the left and on the right of the open leaflet, respectively.

During systole, the particles are carried away from the valve with a strong axial flow component. A close inspection of the flow patterns emanating from the hinge suggests a cross-over of the upstream and downstream particles (third panel in Figure 4-88): the red particles, originally seeded downstream on the right of the leaflet, are seen to travel on the left side of the forward flow jet, while the blue particles, originally seeded upstream on the left, are seen on the right side.

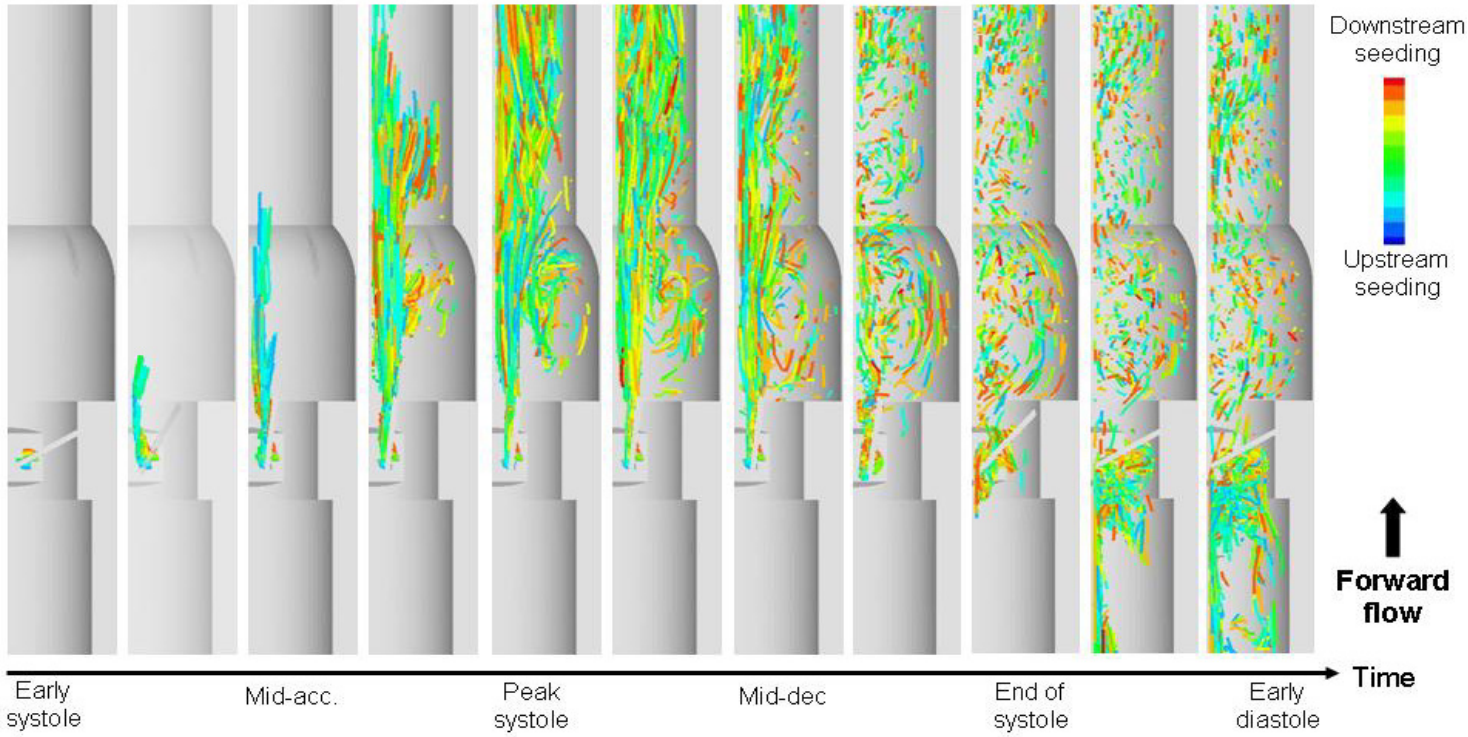

Figure 4-88: Particle streaklines as a function of time. The streaklines are color-coded with the initial position of the particle at the time of injection. The particles seeded the furthest upstream are shown in blue and the particles the furthest downstream in red. [CM hinge design with a regular hinge gap width]

In the sinus region, the particles entrapped in the coherent vortex structure were initially released from both the upstream (blue) and downstream (red) region of the hinge, suggesting a good mixing of the flow. This mixing is seen to hold during the leaflet closing phase and diastole. When the leaflet is in its fully closed position, strong leakage jets are observed. While the adjacent (left) jet appears to be primarily formed by the particles seeded in the left (blue, green), particles seeded in the right side (yellow, red) are also observed. Conversely, a few blue and green particles may be observed within the lateral (right) jet. Both observations suggest a complex mixing flow pattern in the near-hinge region.

To elucidate the flow features within the hinge recess, Figure 4-89 provides a close-up view of Figure 4-88 centered on the hinge recess itself. While Figure 4-89 shows a top view of the hinge, Figure 4-90 accompanies it by providing the side view of the hinge in order to visualize the three-dimensionality of the flow.

During the leaflet opening phase, the particles exit the hinge recess from two well-defined regions of the hinge: the tip of the adjacent corner for the upstream (blue) particles and the tip of the aortic corner for the downstream (red) particles. The streaklines in these two regions indicate that the flow is mainly oriented along the mainstream direction. In both cases, particles exit the hinge with a relatively low out-of-plane motion (Figure 4-90) compared to later instances during the cardiac cycle.

The Eulerian analysis revealed the presence, throughout the fully-open leaflet phase, of a flow reversal at the bottom of the hinge recess (section 4.4.2). This flow features is clearly shown by the particles color-coded in light blue and green in Figure 4-89 at mid-acceleration, peak systole, and mid-deceleration. This reverse flow pattern is believed to be due to the local depressurization induced by the flow separation along the leaflet surface. This depressurization also explains the presence of red and yellow streaklines crossing below the leaflet downstream of the hinge recess.

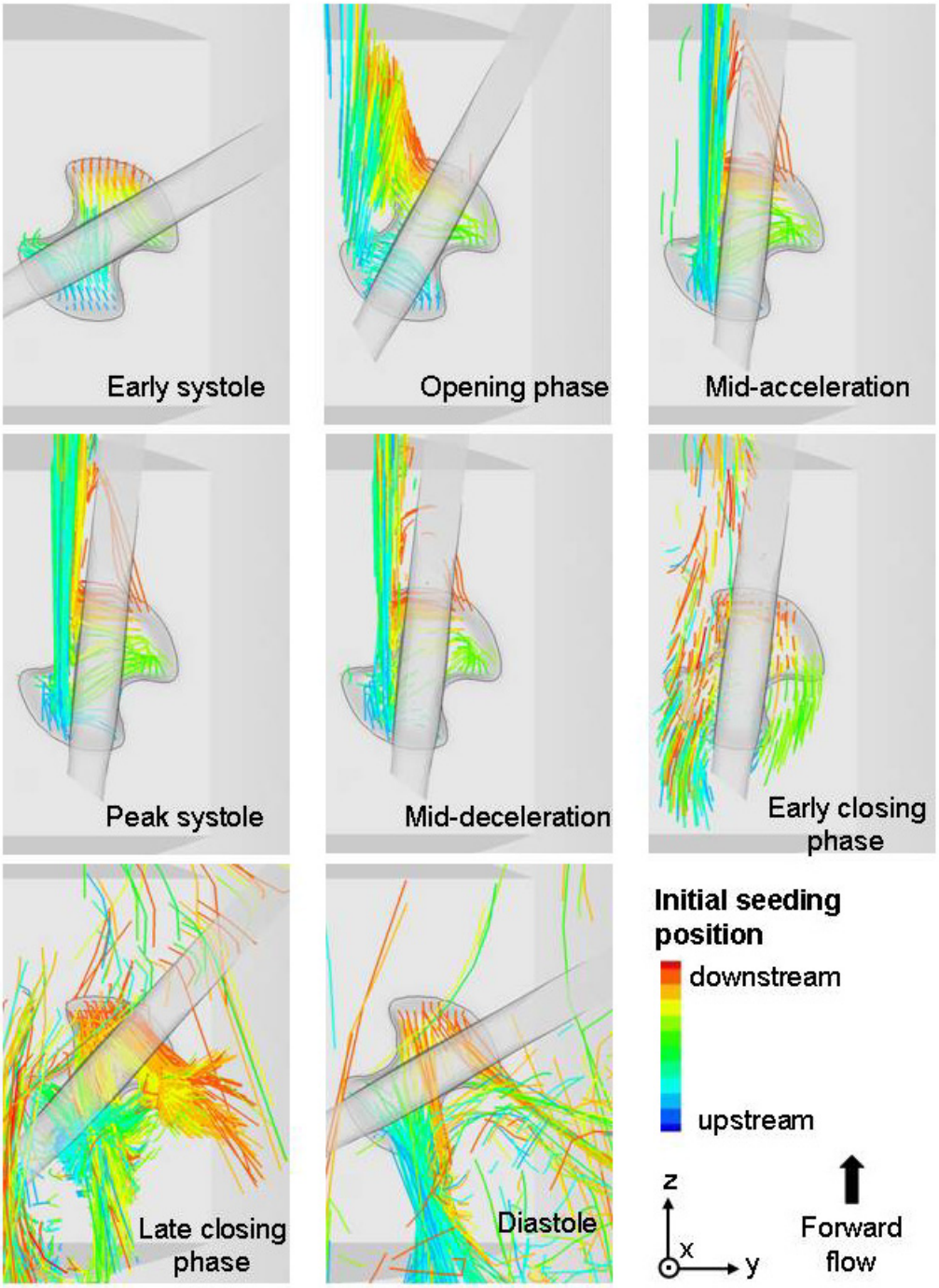

Figure 4-89: Particle streaklines as a function of time. The streaklines are color-coded with the initial position of the particle at the time of injection. The particles seeded the furthest upstream are shown in blue and the particles the furthest downstream in red. [CM hinge design with a regular hinge gap width]

The Eulerian description of the hinge flow fields revealed the existence of a clockwise rotating flow structure in the adjacent corner of the hinge. This rotating structure was found to persist throughout the fully-open leaflet phase, developing during the acceleration phase and being the strongest at peak systole. This recirculation region, combined with the large out-of-plane motion, leads to helical-like streaklines in the adjacent corner. However, as the particles exit the recess, the out-of-plane component becomes dominant and the recirculating pattern vanishes.

During the leaflet closing phase, the flow changes direction as underscored by the orientation of the streaklines emanating from the hinge recess and directed towards the ventricular side of the numerical domain (early closing phase in Figure 4-89). The particles that had already traveled downstream of the valve change direction as well and move back towards the hinge. This is indicated by the presence of the streaklines immediately downstream of the hinge recess (top part of the panels corresponding to the leaflet closing and diastolic phases in Figure 4-89). During the fully-closed leaflet phase, the streaklines suggest the presence of three strong leakage jets. The downstream (red) particles appear to form two distinct leakage jets. On the one hand, the red particles located the furthest on the right travel towards the lateral corner and exit the hinge from the tip of the corner, forming the lateral leakage jet. On the other hand, the red particles seeded further on the left side transit from the aortic corner towards the ventricular corner where they exit the hinge recess. Finally, the last leakage jet corresponds to the particles released in the adjacent corner of the hinge and moving out of the recess from the ventricular corner. Inspection of Figure 4-90 indicates that all of these three jets are highly three-dimensional. The apparently random disposition of the streaklines outside of the jets underscores the complex flow that exists on the aortic side of the closed leaflet.

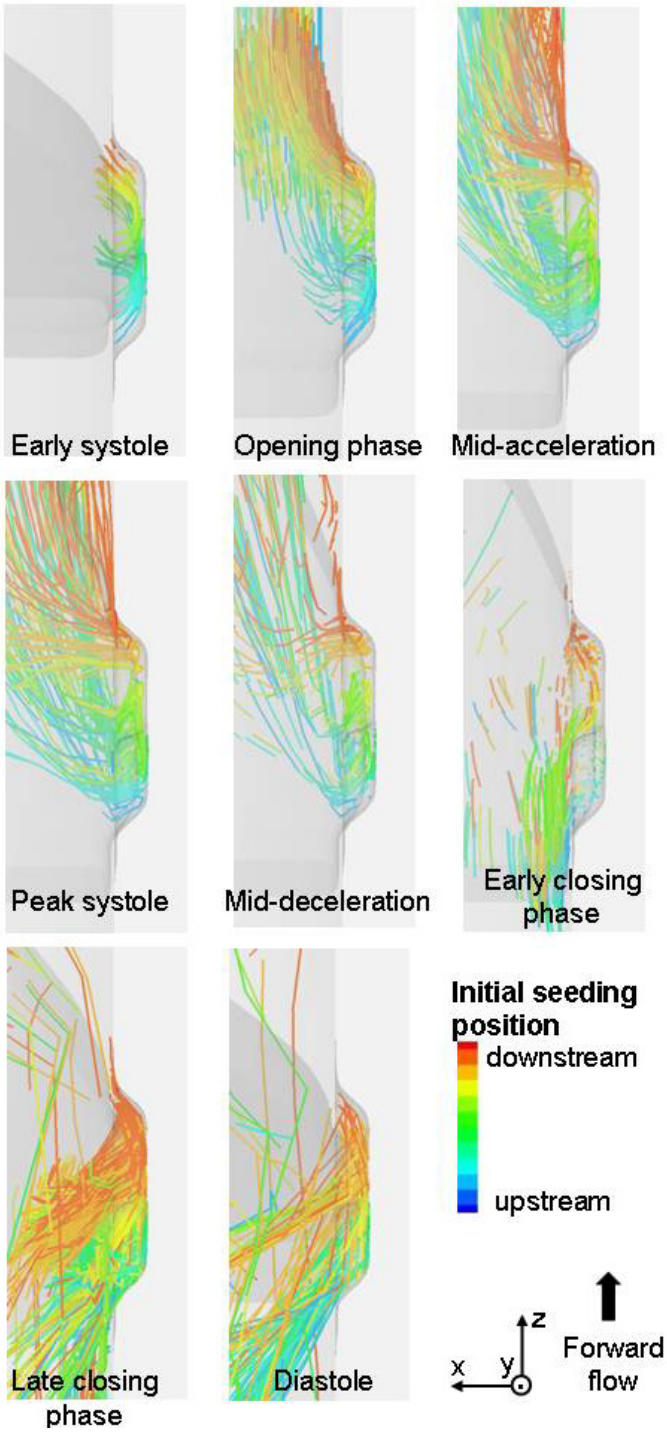

Figure 4-90: Particle streaklines as a function of time. The streaklines are color-coded with the initial position of the particle at the time of injection. The particles seeded the furthest upstream are shown in blue and the particles the furthest downstream in red. [CM hinge design with a regular hinge gap width]

Intrinsically, a streakline corresponds to the trace left by a dye continuously injected from the same location. The streaklines therefore provide a deeper insight into the flow structures that form inside the hinge recess during the cardiac cycle. However, as emphasized previously in the description of the SJM results, the streaklines do not correspond to the actual trajectories followed by individual particles traveling through the hinge recess. Following individual particles and estimating the shear stress levels they experience along their path is essential to analyze the flow fields from a blood cell standpoint and understand the thromboembolic complications associated with the hinge flow fields. Accordingly, the following paragraphs center on the trajectories of the seeded particles depending upon their release-time.

Figure 4-91 shows the pathlines of particles seeded at early systole, peak systole, mid-deceleration, and early diastole. Each column shows the top and side views of the trajectories taken by the particles seeded at each of those specific four instances. The trajectories are color-coded with time: the blue-colored section of the pathline corresponds to the position occupied by the particle at early systole whereas the red-colored section of the path represents the particle position at early diastole.

Of all particles seeded at early systole only a few are seen to be in the near hinge region at the end of systole. This is evidenced by the few orange and red pathlines in the first column in Figure 4-91. Similarly, only a few particles seeded at early systole (second column) are seen to be in the near hinge region at late systole. This suggests that most particles crossing the hinge recess during the early part of systole are likely travel so far downstream of the valve that they do not leak back through the hinge once the leaflet is closed.

Most of the particles seeded at peak systole are seen to exit the hinge recess from the adjacent corner of the hinge due to the flow reversal present at the bottom of the hinge recess. This flow reversal, not seen at early systole, persists throughout the

fully-open leaflet phase. The streaklines revealed the crossing of the flow underneath the leaflet, immediately downstream of the hinge recess. This crossing is clearly observed with the streamlines as well, as shown by the streamlines emanating from the lateral corner at peak systole and traveling towards the left side of the domain.

The pathlines of the particles seeded at mid-deceleration are very complex due to the low valvular flow rate at the seeding time followed by the reversal of the bulk valvular flow occurring immediately after during the closing leaflet phase. These two events combined prevent the particles from traveling far downstream of the hinge recess. The crossing of the flow identified with the peak systole particles downstream of the lateral corner is not seen here due to the lower valvular flow rate. The particles seeded at mid-deceleration are seen to principally exit the hinge recess from the adjacent corner. As previously stated for the particles seeded at peak systole, this is due to the flow reversal present at the bottom of the recess. The particles exiting the hinge recess quickly reverse direction and leak back towards the ventricular side of the domain, mostly through the adjacent (left) side of the domain.

Finally, the trajectories of the particles seeded during diastole (right column) illustrate the presence of leakage jets emanating from the hinge region. Particles traveling from both the aortic and adjacent corners merge in the ventricular corner to form a strong, highly three-dimensional leakage jet, while the particle seeded in the lateral corner form a smaller and more localized leakage jet that emanates from the tip of the lateral corner.

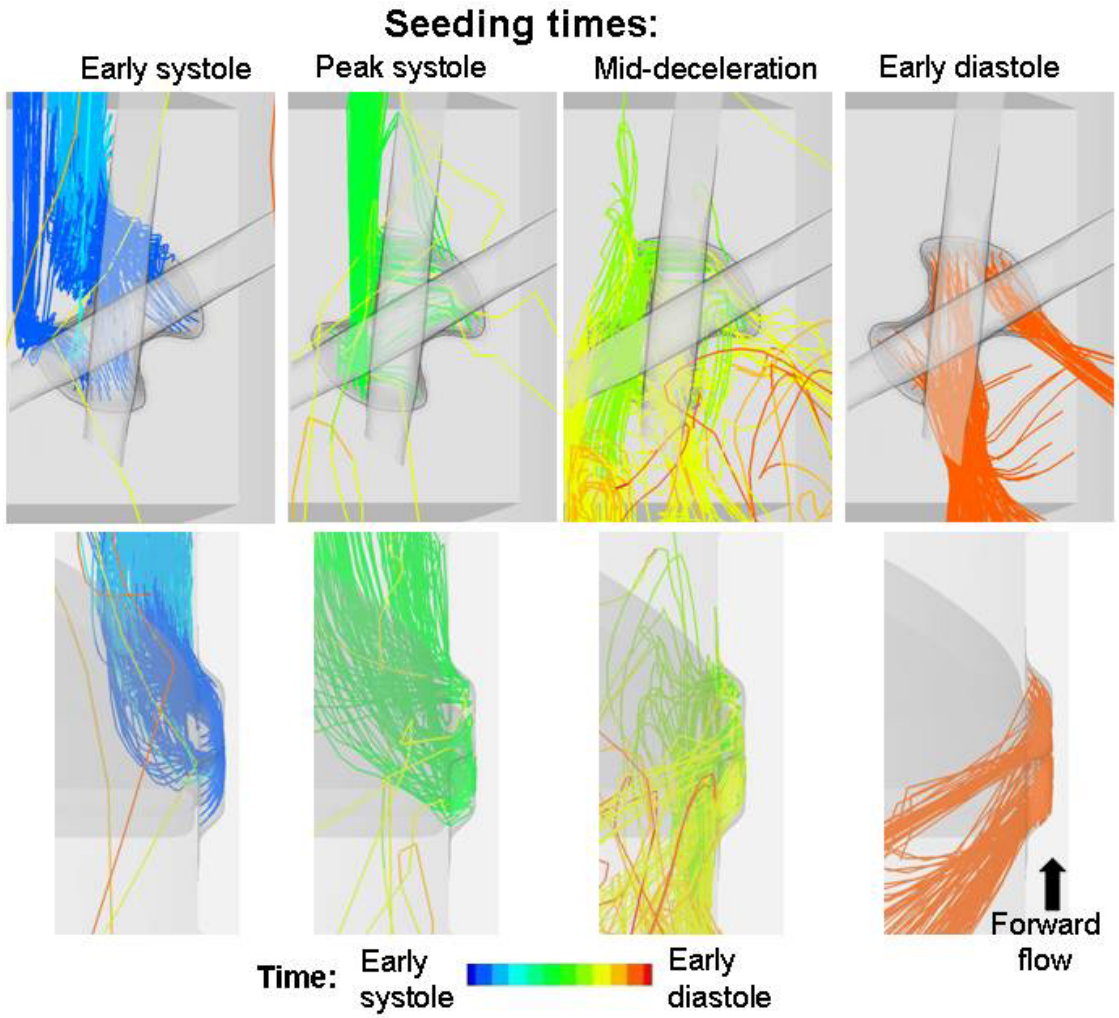

Figure 4-91: Selected particle pathlines for four sets of particles seeded at different instances of the cardiac cycle, namely early systole, peak systole, mid deceleration, and early diastole. Each column shows the trajectories followed by the particles seeded at that specific instance. The pathlines are then color-coded with time. Accordingly the pathline of a particle seeded at early systole will be blue at the origin (inside the hinge) and red at the location occupied by the particle at early diastole. The top row represents the top view of the hinge and the bottom row the side view.
[CM hinge design with a regular hinge gap width]

In order to visualize the shear stress experienced by the particles along their trajectories, Figure 4-92 displays the particle pathlines color-coded by the principal shear stress levels. Note that the maximum of the color-scale is set to 1,000 dyn/cm^2 to identify critical sections of the trajectories where the potential for blood damage is elevated.

In order to easily correlate the shear stress maps provided in the Eulerian description of the flow (section 4.4.3) and the shear stress history of a particle, the shear stress levels experienced by the particles immediately after seeding are described first. Of all the particles released during the forward flow phase, it is the particles seeded at peak systole (second column in Figure 4-92) that experience the largest shear stress during the early part of their trajectory. It is clearly visible that the particles seeded in the adjacent corner and along the downstream wall of the lateral corner are associated with large shear stress levels (second column in Figure 4-92). This is in agreement with the shear stress maps provided in the Eulerian description of the flow that showed regions of large shear stresses in the same two regions at peak systole (section 4.4.3). Nonetheless, the particles that experience the largest shear stress levels at seeding are those seeded after valve closure (fourth and fifth columns in Figure 4-92). The particles seeded at the bottom of the recess at late closing phase and early diastole experience shear stress above 1,000 dyn/cm^2 as highlighted by the red-colored pathlines.

Further inspection of the entire pathlines and not the initial part of the trajectories emphasizes that the particles that experience the highest shear stress levels are those who get entrapped in the leakage jets present from the end of the leaflet closing phase onwards. For instance, it is evident that the particles seeded during the forward flow phase do not experience large shear stresses at the exception of the particles leaking back and getting entrapped in the wake of the leakage jets during diastole. Only a limited portion of the particles seeded between early systole and mid-deceleration actually leak back through the hinge and experience the elevated diastolic forces.

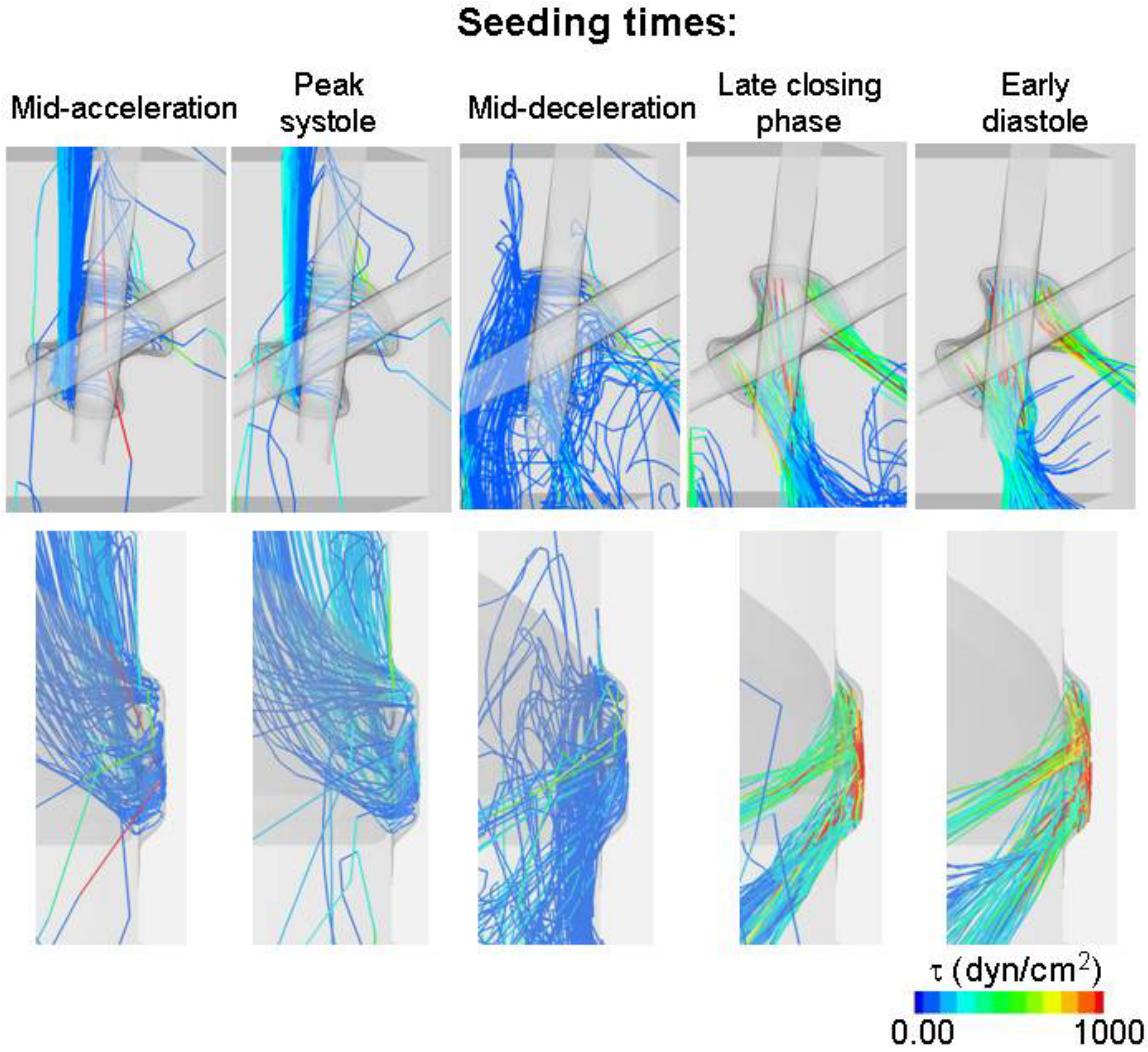

Figure 4-92: Selected particle pathlines for five sets of particles seeded at different instances of the cardiac cycle. Each column shows the trajectories followed by the particles seeded at that specific instance. The pathlines are color-coded with the principal shear stress levels. The top row represents the top view of the hinge and the bottom row the side view. [CM hinge design with a regular hinge gap width]

From mid-deceleration onwards, on the other hand, a significant number of particles flow back towards the ventricle. Nonetheless, a closer inspection of the pathlines indicates that while particles seeded at mid-deceleration reverse direction and move back towards the hinge; most of the particles do not cross through the regions of elevated shear stresses.

All particles seeded at valve closure and early diastole get entrapped in the strong diastolic leakage jets and therefore experience elevated shear stresses after their seeding time. However, it should be pointed out that, as the particles move away from the valve and the leakage jets dissipate, the shear stresses along the pathlines lower. Overall, this suggests a higher propensity for blood cell rupture and damage for the particles crossing the hinge during diastole compared to those traveling through the hinge during systole.

The maximum shear stress levels experienced by each particle along its trajectory is computed. These maximum shear stresses for all particles combined are provided in Figure 4-93 in the form of a distribution plot. Peak shear stress levels could be expected to reflect the maximum values reported during the Eulerian analysis of the CM flow fields (section 4.4.3). In that Eulerian analysis, the peak systolic shear stress levels were found to be 1,060 dyn/cm^2 within the recess and 1,800 dyn/cm^2 in the hinge vicinity. The peak levels during diastole were higher, with a maximum of 5,910 dyn/cm^2 in the recess and 8,985 dyn/cm^2 in the hinge vicinity. However, these maxima do not correspond to the actual maxima experienced by the particles traveling through the hinge. Indeed the particles seeded within the hinge region do not necessarily cross the localized regions of elevated stresses identified during the leakage phase in the hinge and near-hinge region. It is clear from Figure 4-93 that most of the particle experience a maximum shear stress below 1,000 dyn/cm^2 while only a small portion are subjected to a shear stress above 1,000 dyn/cm^2 , up to 3,975 dyn/cm^2.

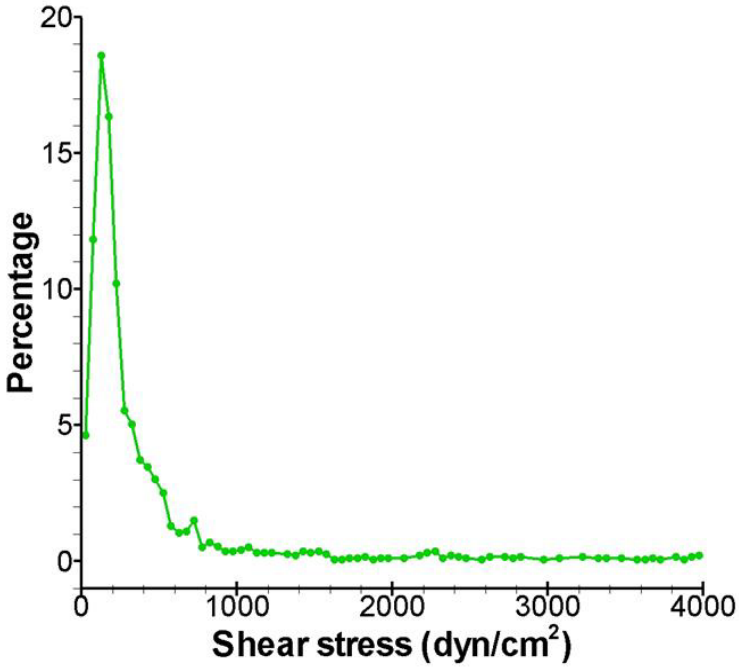

Figure 4-93: Distribution of the maximum shear stress experienced along the particle trajectories. [CM hinge design with a regular hinge gap width]

As previously explained in sections 4.5.2 and 4.5.3 describing the Lagrangian results of the SJM hinge designs, a blood damage index for platelet activation (BDI^{PL}) and another for hemolysis (BDI^{H}) are computed by considering the shear stress exposure along each particle trajectory. In this approach, the particles are assumed to model both platelets and red blood cells, and thus the particle trajectories are considered to be representative of either platelet or red blood cell paths. The BDI^{PL} and BDI^{H} are computed for each particle trajectory and the overall distribution of these two indices is provided in Figure 4-94. As expected, the distribution is similar for both BDI^{PL} and BDI^{H}. Because particles do not necessarily cross regions of elevated shear stresses, it is unsurprisingly that most particles are found to be associated with a low BDI. The maximum computed BDI^{H} reaches 3.82 while the maximum BDI^{PL} is 14.8.

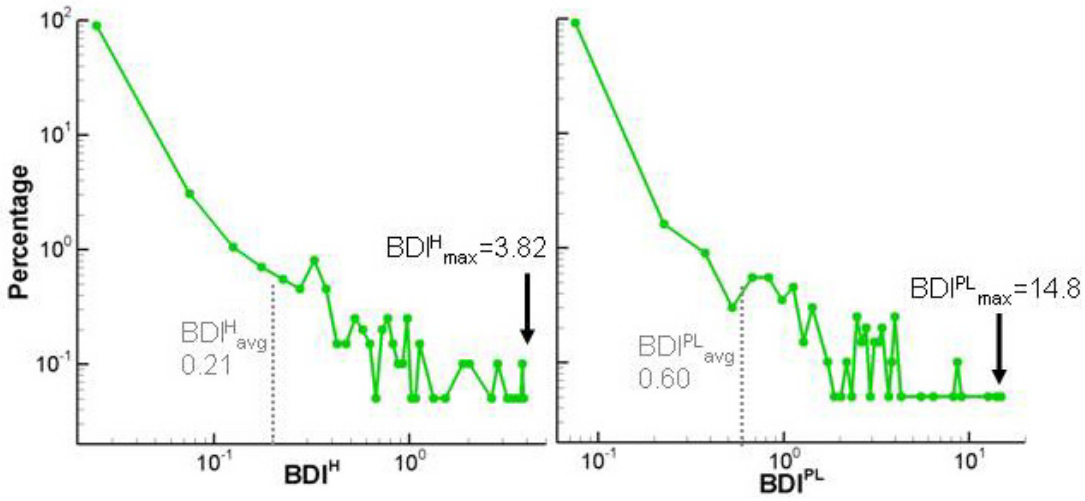

Figure 4-94: Distribution of the blood damage indices for hemolysis and platelet activation as a function of the particle percentage.
[CM hinge design with a regular hinge gap width]

CHAPTER 5

DISCUSSION

5.1 Validation and boundary conditions

In this study three-dimensional, time-accurate simulations are carried out to model the flow through the hinge recess of three BMHV hinge configurations under physiologic aortic flow conditions. Imposing physiologic boundary conditions is of prime importance to assess the *in vivo* performance of a specific hinge design. By performing a one-way coupling between a large-scale model and the hinge solver and using knowledge of the human physiology, the present study reproduces the hemodynamic environment of the hinge as closely as possible.

During the forward flow phase, the hinge has little effect on the bulk flow through the open valve, so that a one-way coupling between the large-scale and the hinge flow solver was deemed appropriate. However, such an approach is not applicable during diastole. The exact leakage flow rate through the closed valve is dependent on the trans-valvular pressure gradient and the resistance offered to the flow by the hinge, the b-datum gap and the peripheral gap. This in turn is dependent on the geometry and dimensions of these gaps. Conducting the large-scale simulations with a valve model that includes hinge recesses and gaps similar in size to those present in clinical valves, while concurrently achieving a good spatial resolution, would exceed currently available computational resources. The gap dimensions in the large-scale model therefore had to be increased. The gap dimension was about sixe times larger than in actual clinical valve, with a gap of approximately 900 μm compared to about 150 μm, and

consequently a physiological trans-valvular pressure gradient could not be achieved. As a result, prescribing the velocity profile from the large-scale simulations as boundary conditions for the present hinge study during the leakage flow phase was not deemed suitable. Instead, the boundary conditions were set so as to impose a trans-valvular pressure gradient of approximately 80 mmHg, which corresponds to a normal physiologic pressure drop. However, one instance of time that this modeling approach does not allow to capture is the instant of valve closure. In this work, this instant is modeled by prescribing the leaflet kinematics from the large-scale simulations, while pressure and flow smoothly transition towards their diastolic value. In reality, at this instance of time, the closing of the leaflets yields a sudden pressure build up, which would require a full two-way coupling between the large-scale and the hinge solvers to synchronize leaflet kinematics and the local hemodynamics.

Nonetheless, the numerical solver is capable of capturing the main flow features present in the hinge and near-hinge region. To assess the accuracy with which the numerical solver is capable of predicting these hinge micro-flow fields, the simulated flow fields are compared to experimental data. The comparison focuses on the St. Jude Medical valve with a regular hinge gap width for which experimental data are available under physiological aortic flow conditions similar to those modeled in the present study.

5.1.1 Validation of the global near-hinge flow features

Before delving into the flow patterns observed within the hinge recess, the flow field outside the hinge recess is presented and compared with experimental data to confirm that the flow solver is capable of capturing the main flow features present in the near-hinge region. An excellent agreement was achieved between both modalities.

Figure 5-1 displays the numerical flow fields obtained with the current numerical solver at five instances of the cardiac cycle outside the hinge recess, approximately 500 μm above the flat level. During the forward flow phase, two strong forward flow jets emanate from the lateral and central orifices and extend on either side of the leaflet (Figure 5-1). The magnitude of these jets is closely related to the cross-valvular bulk flow rate and reaches its maximum at peak systole, with the lateral jet extending further downstream of the valve than the central jet. A region of low flow is visible in the wake of the open leaflet immediately downstream of the hinge region. This flow separation leads to a complex flow pattern downstream of the valve central orifice.

These flow features are in excellent qualitative agreement with the recent experimental results of Dasi *et al.* [62]. For reference, the flow fields measured *in vitro* immediately downstream of the valve along the valve center plane are provided at five instances of the cardiac cycle in Figure 5-2. In that experimental study, the authors report the flow dynamics along the central plane of a SJM bileaflet mechanical heart valve in an axisymmetric aorta. This central plane is actually outside of the current numerical model, such that a direct comparison of the numerical and experimental results is limited. Nonetheless, qualitative comparison of the main flow structures is possible. In particular, the experimental results show that the lateral jet at peak systole extends further downstream than the jet emanating from the central orifice, as noted in the current numerical study. The formation of the two forward flow jets is accompanied by that of a flow separation region in the wake of the leaflet. This flow separation, reported in the experimental data, is expected due to the angle of the leaflet with respect to the axial flow direction.

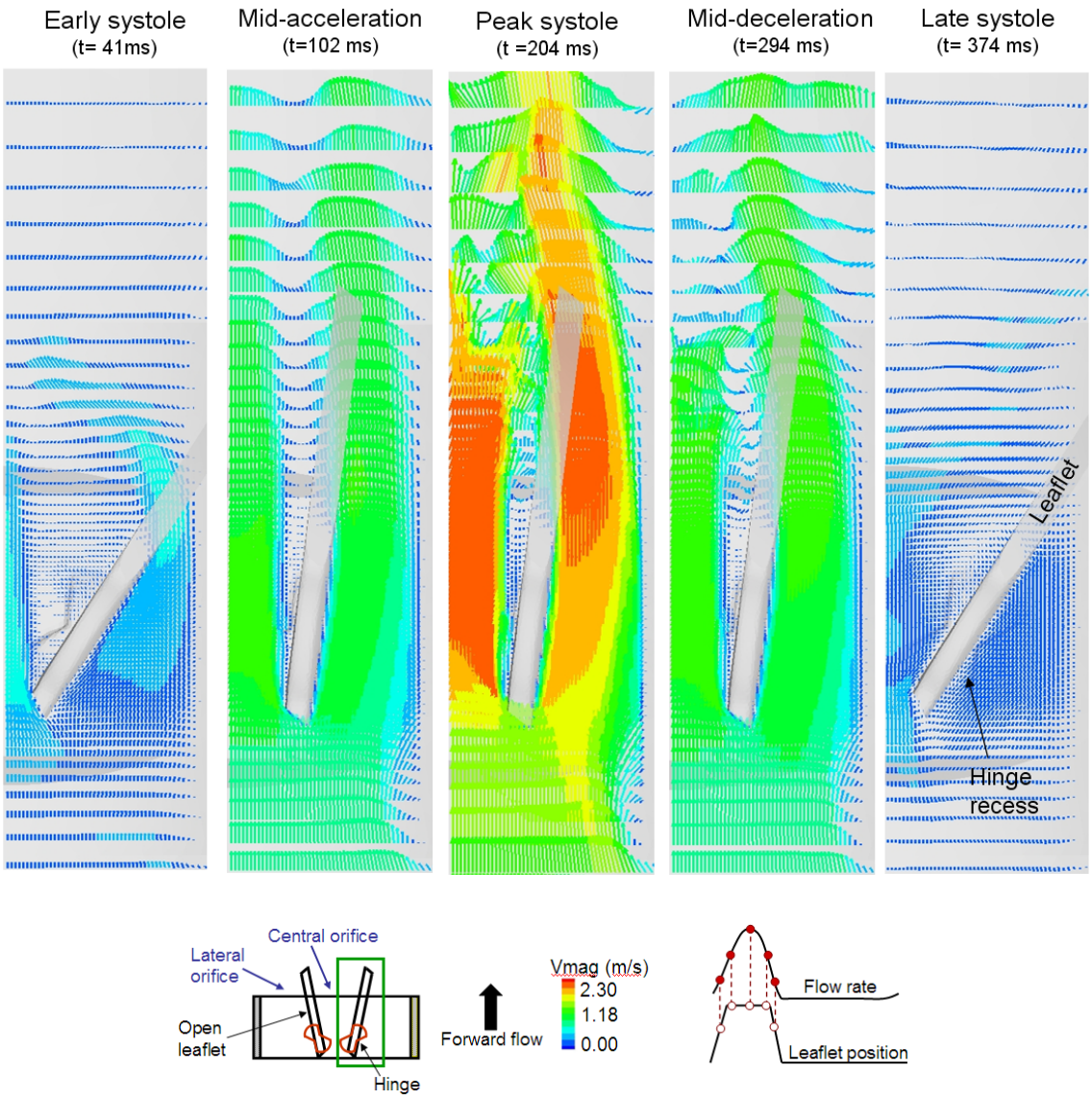

Figure 5-1: Flow fields obtained at 500 μm above the flat level, outside the hinge recess at five instances of the cardiac cycle. The valve model used here is the SJM hinge with a regular hinge gap width. The circles on the flow rate and leaflet position curves indicate the instances of the cardiac cycle displayed and the corresponding leaflet position. The three-dimensional instantaneous velocity vectors are color-coded with the velocity magnitude.

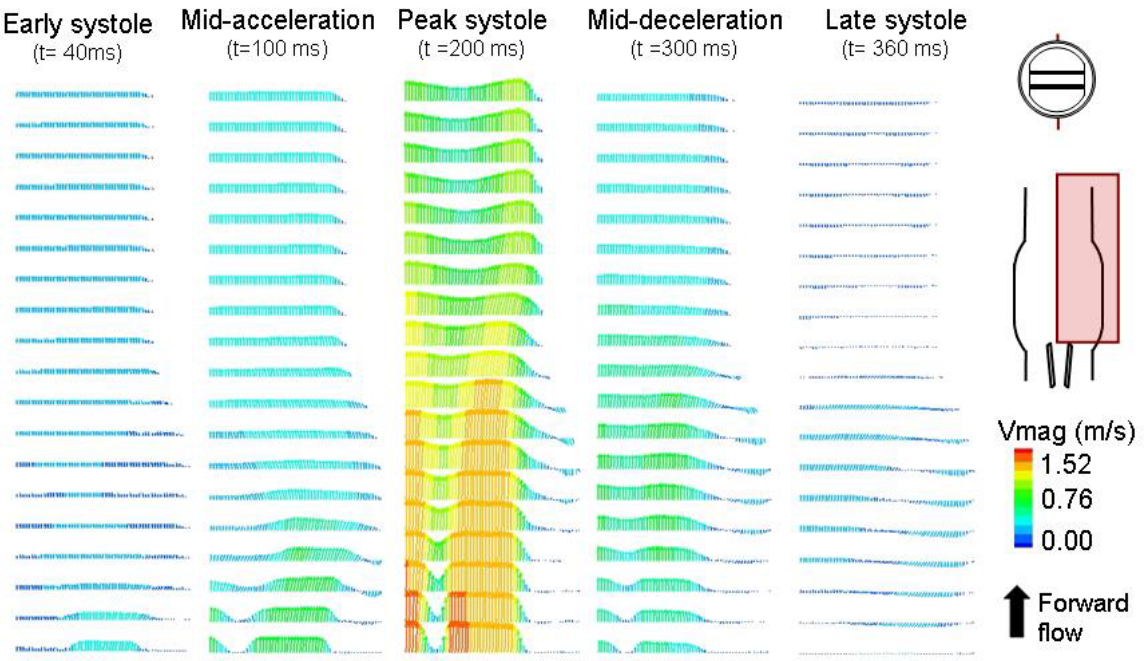

Figure 5-2: Experimental flow fields along the valve center plane at five instances of the cardiac cycle [62]. Particle Image Velocimetry technique was used to characterize the valvular flow field. The position of the flow fields with respect to the valve geometry is shown in the top right schematics. The two-dimensional phase-averaged velocity vectors are color-coded with the two-dimensional velocity magnitude.

During the deceleration phase, a flow reversal region is observed in the numerical data set on the right side of the lateral jet. This was also reported in the experimental results, where a reverse flow was seen near the valve housing during the deceleration phase despite a net positive flow rate through the valve. Such a flow reversal corresponds to a Womersley flow profile where a region of reverse flow is typically present during the deceleration phase along the wall of a pipe subjected to pulsatile flow. Finally at the end of systole, the leaflet starts to close and a reverse flow of low magnitude is visible throughout both experimental and numerical domains. Once the valve is totally closed, strong leakage jets emanate from the hinge, the peripheral gap (between the valve housing and the leaflet surface), and the b-datum gap (in the valve center, between the closed leaflets. (Figure 5-3 and Figure 5-4). Such a leakage flow pattern computed numerically was previously reported experimentally [36, 84-86]. Overall, the comparison of the numerical and experimental results indicates that the numerical solver is capable of capturing the main flow patterns present outside of the hinge recess.

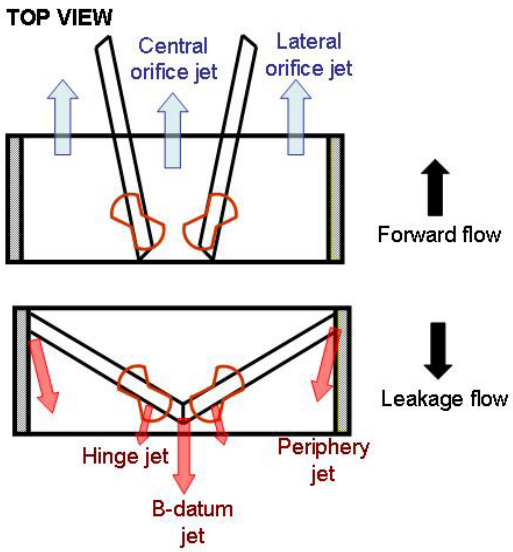

Figure 5-3: Schematic indicating the position of the forward and leakage flow jets.

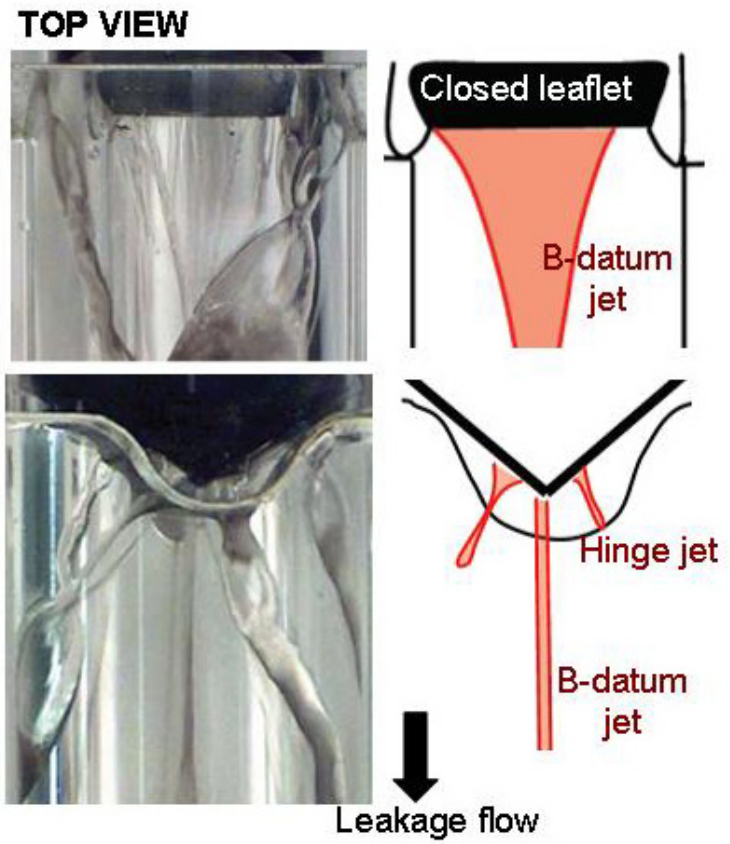

Figure 5-4: Images of a static leakage experiment perform to visualize the position of the three-dimensional leakage jets emanating from a closed SJM valve. The valve is subjected to a constant pressure head of 120 mmHg. The hinge and b-datum leakage jets are clearly seen. [87]

5.1.2 Validation of the hinge flow features

A closer inspection of the flow within the hinge recess itself indicates that the computed flow features are also in qualitative agreement with previous experimental data. Of particular interest is the experimental study of the St. Jude Medical hinge flow fields under aortic flow conditions conducted by Simon *et al.* using laser Doppler velocimetry measurements [36]. Figure 5-5 shows the simulated and experimental hinge flow structures at the flat level side-by-side for four instances of the cardiac cycle. The same layout is adopted in Figure 5-6 to compare numerical and experimental results at

390 μm below the flat level. Both figures only display the two-dimensional in-plane velocity vectors since experimental data acquisition was limited to two-dimensions.

Forward flow phase comparison: Similarly to the present numerical results, the experiments by Simon *et al.* show the existence, during systole, of a strong forward flow at the flat level, in the lateral corner of the hinge. The adjacent corner on the other hand is characterized by a less streamlined flow, composed of a forward jet of lesser magnitude and a small recirculation region near the leaflet surface (Figure 5-5). This recirculation region, leading to the formation of a clockwise helical flow pattern was clearly seen in previous flow visualization experiments (courtesy of Medtronic Inc) where H bubbles were continuously released immediately upstream and downstream of the hinge (Animation H_Bubble_Flow_Vis.mov, top row in Figure 5-7). Comparison of the hinge flow pattern at deeper levels within the hinge recess (390 μm below the flat level in Figure 5-6) shows good agreement in the overall direction of the flow. The clock-wise rotation observed in the adjacent corner in the numerical results is also seen in the experiments. Likewise, the deflection of the flow towards the adjacent corner in the ventricular corner of the hinge is visible in both the numerical and experimental results. The reverse flow observed in the lateral corner of both data sets, as well as in the flow visualization experiments (top row in Figure 5-7) further reinforces the good qualitative agreement between the two modalities. Finally, it should be noted that the experimental study by Simon *et al,* along with previous experimental work [35, 88], reports the presence of a flow reversal of low magnitude between the leaflet ear tip and the bottom of the hinge recess that persists throughout systole even at its peak. This reverse flow was captured for the first time using numerical simulations by Shu *et al.* [47] and is again observed in the present study.

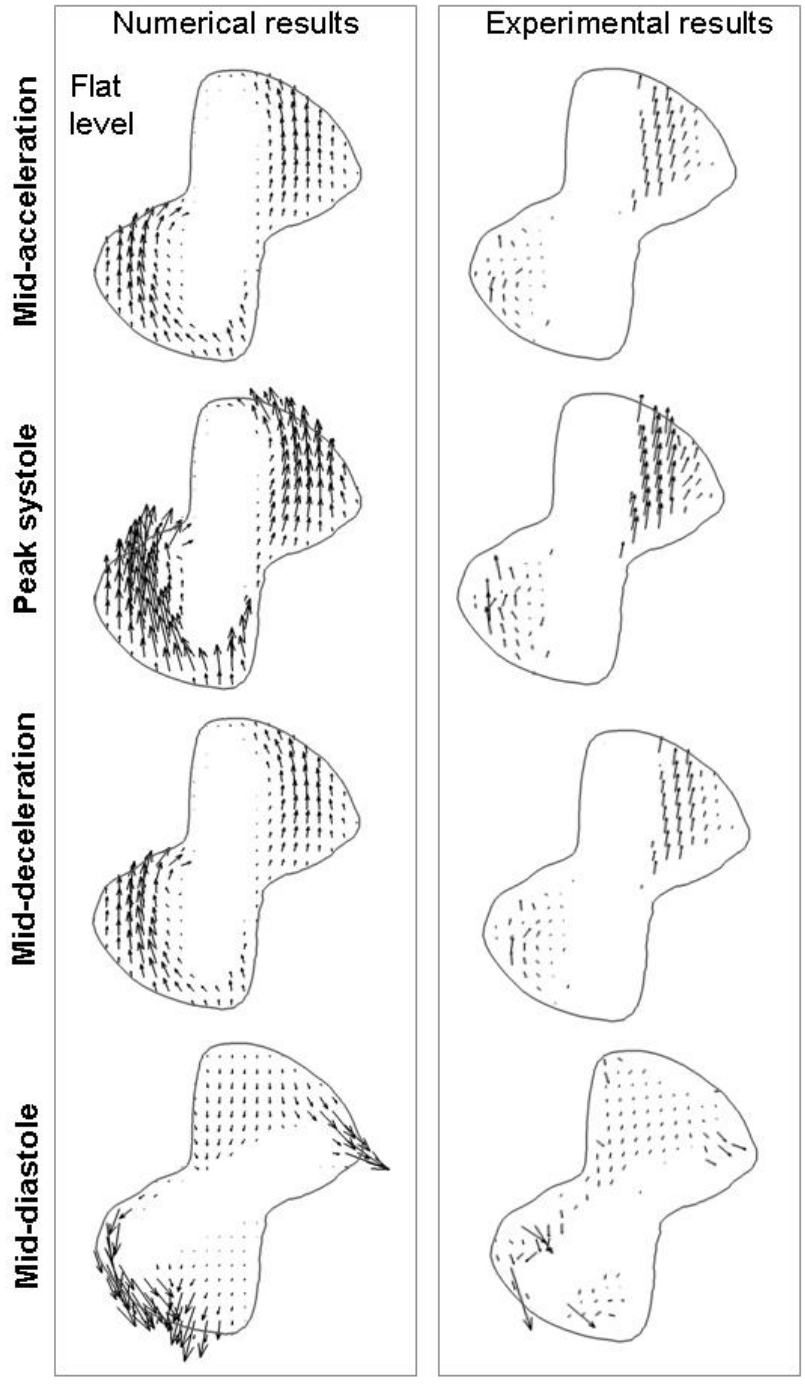

Figure 5-5: Comparison of the simulated (left) and experimentally (right) measured in-plane velocity vectors at the flat level at four instances of the cardiac cycle. [SJM hinge design with a regular hinge gap width].

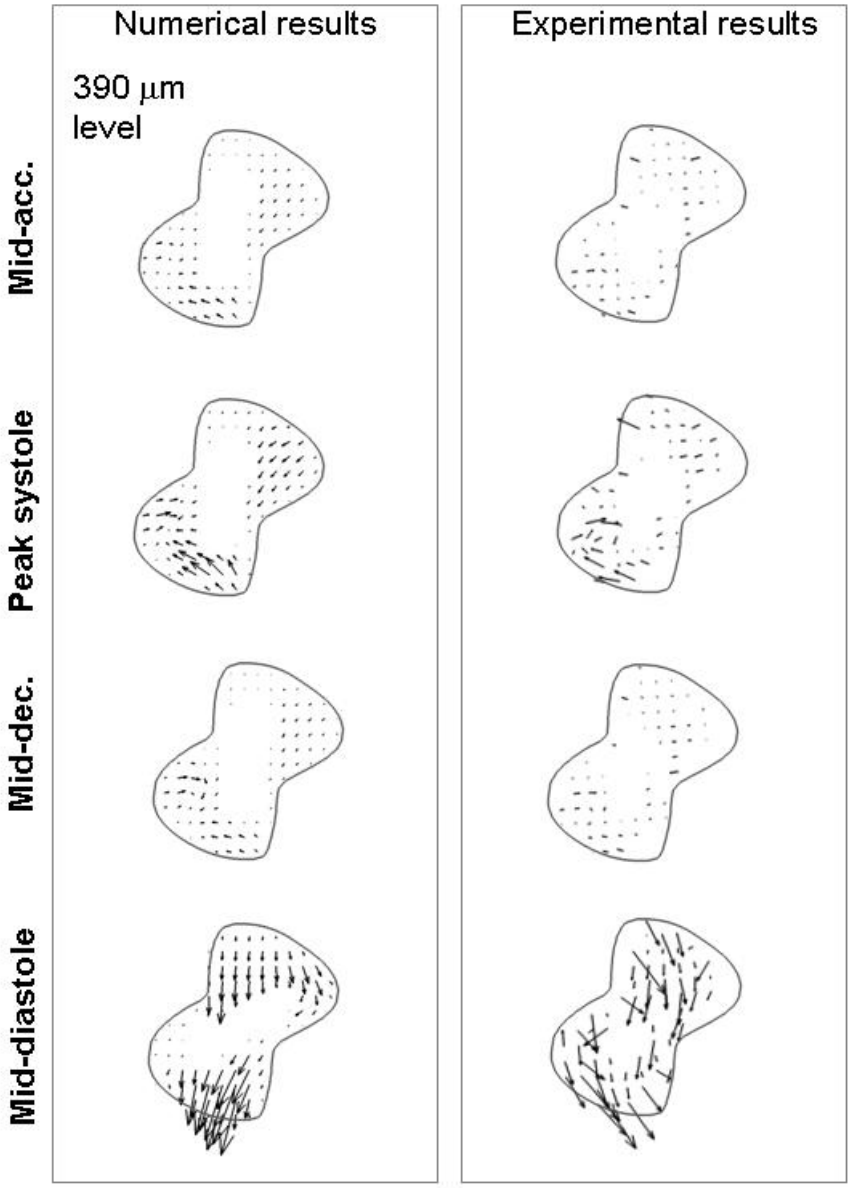

Figure 5-6: Comparison of the simulated (left) and experimentally (right) measured in-plane velocity vectors at 390 μm below the flat level at four instances of the cardiac cycle hinge flow structures. [SJM hinge design with a regular hinge gap width].

This further underlines the capabilities of the current numerical solver in modeling the intricacy of the hinge flow fields (see sections 5.2 and 5.3). Moreover, this flow reversal seen at the bottom of the hinge recess highlights the need for performing full three-dimensional hinge simulations rather than simple two-dimensional studies in order to accurately model the complex hinge flow patterns.

From a quantitative viewpoint, the maximum velocity magnitude reported within the hinge recess during the forward flow phase is 1.75 m/s in the experiments and 1.54 m/s in the simulations. This, along with the flow structure analysis, indicates that the velocity magnitude and the general flow distribution during the forward flow phase inside the hinge recess are similar to those obtained experimentally.

Leakage flow phase comparison: During the leakage phase, good qualitative agreement is also noted between the measured and simulated flow patterns. Both experiments and simulations revealed two main leakage flow patterns on either side of the leaflet ear and oriented towards the lateral side of the hinge. These leakage flow patterns in the lateral and adjacent corner of the hinge are visible at all levels within the hinge recess, as suggested by the vector fields at the flat level and at the 390-μm level (Figure 5-6).

A third leakage flow pattern is seen at the flat level in the numerical results but not in the experimental data set. This can be attributed to the poor experimental spatial resolution. It is likely that the leakage jet was not captured *in vitro*, as suggested by the small number of data points present within the ventricular corner at the flat level. Nonetheless, at deeper levels within the hinge recess (at the 195-μm level not shown and at the 390-μm level in Figure 5-6), the direction of the velocity vectors suggests the presence of this ventricular leakage jet *in vitro.* This jet, emanating from the ventricular

corner of the hinge was clearly capture in *in vitro* flow visualization experiments, as shown in Figure 5-7 (bottom row).

Differences in velocity magnitude exist between the experimental and numerical data sets at mid-diastole. While the experimental study reported a maximum velocity magnitude of 2.27 m/s during the leakage phase [36, 87], the simulations show a maximum velocity field nearly twice as high with a peak of 4.66 m/s when neglecting the out-of-plane component that is not captured in the experiments. Again, such a discrepancy might be attributed to the poor spatial resolution of the experiments, where high velocity points might have been missed by the coarse measurement grid. However, it is more likely because of a possible difference in hinge gap width between the numerical and experimental valve models, as small changes in the gap clearance would have a strong effect on the flow magnitude. For instance, in the present numerical study, the peak velocity magnitude within the hinge recess is 4.75 m/s with a SJM valve with a regular hinge gap (150 μm) with and 5.26 m/s with a large hinge gap width (250 μm). Moreover, the leaflet motion in the numerical model is limited to rotation, while, in the experimental data sets, the leaflets are free to rotate but also to translate up and down along the leaflet axis. This extra degree of freedom, along with variations in manufacturer tolerance, explains the possible difference in gap clearance and thus on flow magnitude. In addition, the variations in the aortic flow profile in the experiments and the limitations imposed by the numerical boundary conditions might explain the observed difference in flow magnitude. A full two-way coupling between the large-scale and hinge solvers is expected to yield a closer comparison between the experimental and the numerical data. Such a true multi-scale implementation, however, is beyond the scope of this work.

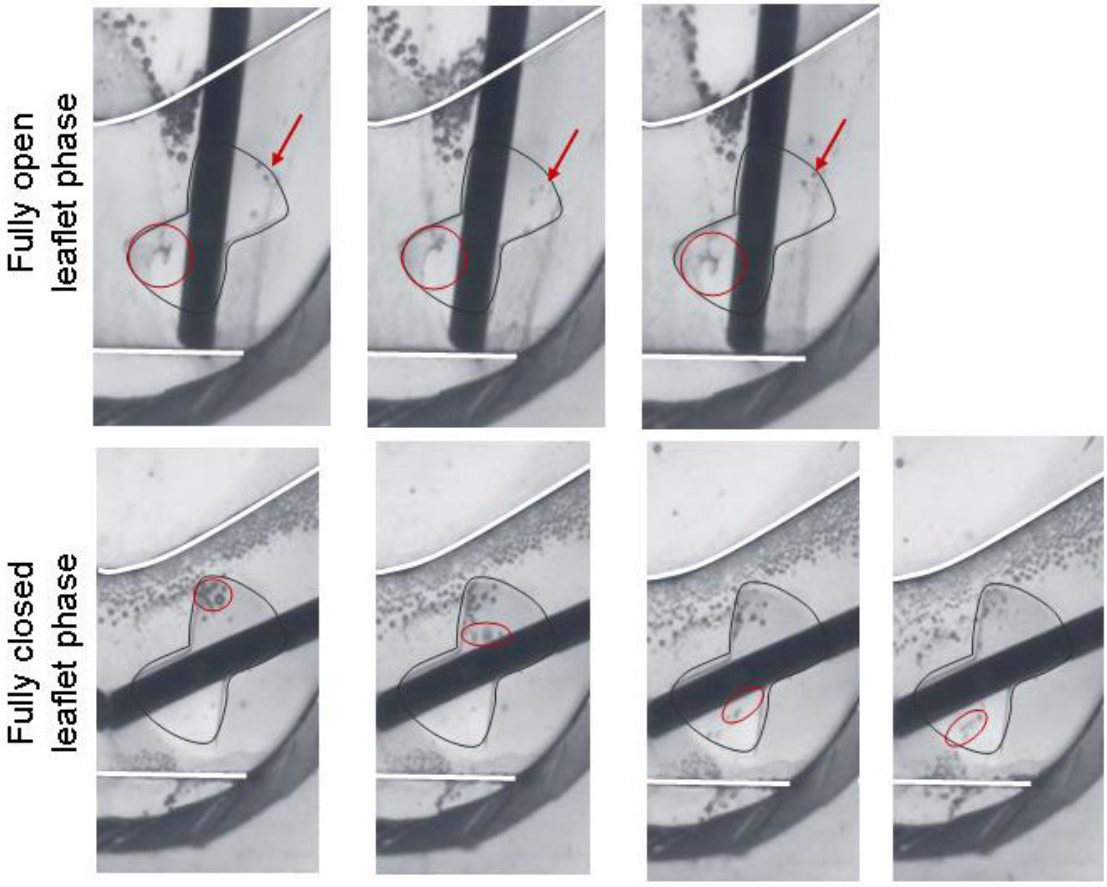

Figure 5-7: Qualitative flow visualization of the hinge flow fields in a SJM valve using hydrogen bubbles (courtesy of Medtronic, Inc). The H bubbles are released immediately upstream and downstream of the hinge, along the two lines shown in white. The top and bottom rows show instantaneous images of the flow during the fully open and fully closed leaflet phase, respectively. The main flow features are highlighted in red.

5.2 Effect of the hinge gap width on the hinge flow fields

The effect of the hinge gap width on the flow fields and the associated thromboembolic complications is investigated using two hinge models whose only difference in design stems from the prescribed gap width. Both models are based on the St. Jude Medical (SJM) design, the first one with a regular hinge gap width, while the other has a larger than regular hinge gap width. For ease of reading, the SJM hinge with a regular hinge gap width will be dubbed from hereon the SJM regular hinge. Similarly, the SJM hinge with a large hinge gap width will be called the SJM large hinge.

The micro-computed tomography scan of a 23 mm SJM valve was used to generate both of regular and large SJM hinge models. In the SJM regular hinge, the leaflet was positioned such that the distance between the leaflet ear and the housing recess wall was 150 μm. In the SJM large hinge, the same leaflet and hinge recess geometries were used but the leaflet was shifted out of the hinge recess by 100 μm so as to have a hinge gap width of approximately 250 μm.

Currently clinically used SJM valves have a regular hinge design on the order of 150 μm. The clinical long-term follow-up studies of these valves reveal good clinical performance with low thromboembolic complications [89, 90]. The SJM large hinge, with its oversized hinge gap width, falls outside the manufacturing tolerance range used by St. Jude Medical Inc and thus would not be considered for implantation. Hence, no clinical data is available for this hinge configuration. Nonetheless, researchers have attempted to investigate *in vitro* the effect of the hinge gap width on valve performance. Travis *et al.* found that the valve with a smaller or larger than regular hinge gap width were associated with more platelet secretion and anionic phospholipid expression than the same valve with a regular hinge gap width. The authors concluded that the hinge gap width had a significant effect on platelet damage initiated by leakage flow [34]. *In*

vitro assessment of the hinge fluid dynamics highlighted the effect of the hinge gap width on the hinge washout and shear stress levels [91]. Previously published studies therefore suggest that the variation of the hinge gap width has an effect on shear stress levels and flow-induced blood damage. The present numerical investigation aims at gaining a better understanding of the influence of this design parameter by identifying the differences in hinge flow features, shear stress distribution, and potential for hemolysis and platelet activation between the SJM regular and large hinges. Accordingly, the following analysis focuses on the influence on the hinge gap width first on the hinge flow fields and then on the shear stress distribution throughout the cardiac cycle. This section analyses the similarity in flow structures and shear stress distribution between the two designs, but emphasis is placed upon the differences, as these may explain possible variations in thromboembolic complication rates. The section analyses both the Eulerian and Lagrangian results and attempts to compare the potential for hemolysis and platelet activation of the two SJM hinges.

5.2.1 Hinge flow fields

Forward flow phase

During the leaflet opening phase, similar flow patterns are seen at all levels within the recess of both regular and large hinge designs except in the adjacent corner of the hinge. In the SJM regular hinge the formation of a clockwise rotating helical flow structure in the adjacent corner is evident at the end of the leaflet opening phase. This flow structure then persists throughout the fully open leaflet phase (feature *a* in Figure 5-8). In the SJM large hinge, on the other hand, the flow field in the adjacent corner during the leaflet opening phase is characterized by a small separation region in the wake of the leaflet and a strong forward flow pattern that impinges on the wall of the

hinge recess. The flow in this adjacent corner is found to be largely unsteady during the fully open phase, with in particular the formation of a counterclockwise flow structure that is only seen at peak systole (feature *A* in Figure 5-8). These differences in flow features between the two hinge configurations, which appear as early as the leaflet opening phase and persist throughout the fully open phase, are likely to induce variations in blood cell residence time and thus in the propensity for thrombus formation.

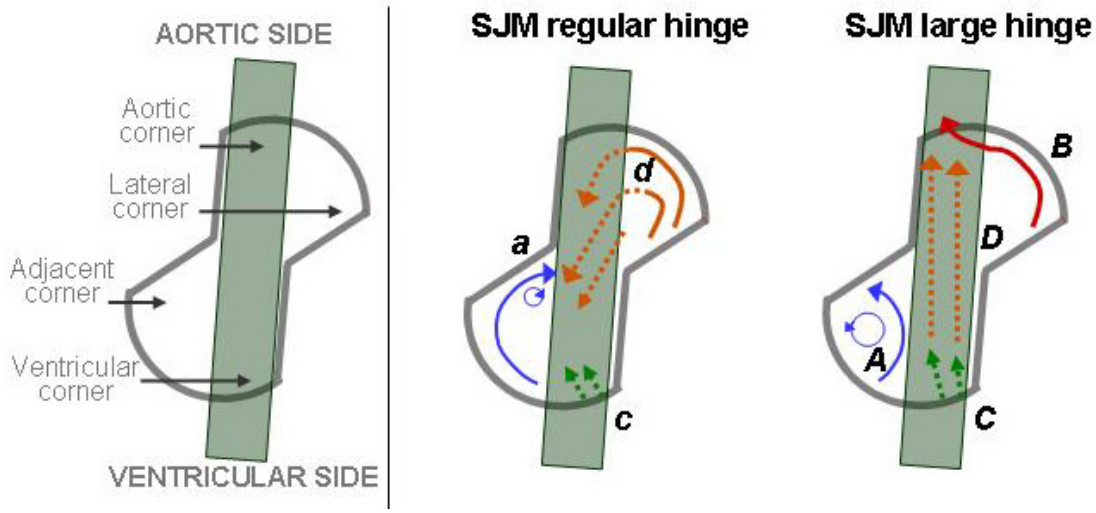

Figure 5-8: Characteristic flow features observed at peak systole in the SJM hinge design with a regular and a large hinge gap width. Note that each flow pattern is associated with a particular color and a letter for easy visualization and referencing. The nomenclature used to describe the hinge design is recalled on the left schematic.

It is during the fully-open leaflet phase, and in particular at peak systole (Figure 5-8) when the cross-valvular bulk flow rate is the largest, that the differences in flow structures and magnitudes are the most pronounced. The most outstanding difference in flow patterns is observed at the bottom of the hinge recess. In the case of the SJM regular hinge, a flow reversal of low magnitude is seen to form in this region at the end of the leaflet opening phase. This reverse flow pattern, first noted in the Eulerian

analysis of the flow, was further emphasized with the particle pathlines in the Lagrangian description. Despite the strong forward cross-valvular flow rate that exists during systole, this reverse flow persists throughout the fully open phase even at peak systole when the cross-valvular flow rate is the highest (feature *d* in Figure 5-8). This flow reversal may be attributed to a region of low pressure located in the aortic surface of the leaflet due to the detachment of the main stream in this region. This region of low pressure results in a negative pressure gradient between the lateral and adjacent corners of the hinge, thereby inducing the flow reversal observed at the bottom of the recess, with fluid going from the lateral to the adjacent corner. In the SJM large hinge on the other hand, this flow reversal is observed at mid-acceleration and mid-deceleration but not at peak systole, when it is replaced by a forward flow pattern (feature *D* in Figure 5-8). The larger hinge gap width offers lower resistance to the flow than the regular hinge gap width. This lower resistance, combined with the large valvular flow rate at peak systole, explains the change of flow direction observed at the bottom of the recess in both Eulerian and Lagrangian description of the flow. It should be noted that the hinge Reynolds number, based on the hinge gap width and the maximum hinge velocity is on the order of 120 and 60 for the SJM large and regular hinges, respectively. These low Reynolds numbers indicate that the flow is far from the transitional and turbulent regimes. It is therefore of no surprise that the flow at the bottom of the hinge recess, in both SJM configurations and whether it is a forward or reverse flow, exhibits a near-parabolic profile.

The difference in flow pattern at the bottom of the hinge recess noted at peak systole induces some differences in both the adjacent and lateral corners. The adjacent corner is characterized by a strong out-of-plane flow motion in both hinges. However, a close inspection of the particle paths reveals that, in the SJM regular hinge, the exit point of the particles in this corner is very localized as all particles get entrapped in the clock-wise helical-like flow. This is illustrated on the schematic by the presence of a small

circle on the downstream side of the adjacent corner (feature *a* in Figure 5-8), which correspond to the rise of the helical flow, and the aforementioned exit point. On the other hand, as was mentioned at the beginning of this section, the flow in the SJM large hinge spans the entire adjacent corner and demonstrates significant levels of unsteadiness throughout systole. The particles seeded the furthest downstream get caught in the counter-clockwise rotating flow while the one seeded upstream exit the hinge with a strong axial component, without entering the rotating structure. The flow structures observed in the adjacent corner appear to be directly related to the flow present at the bottom of the hinge recess. The change of flow direction at the bottom of the hinge induces a change in the recirculation direction. The counter-clockwise rotating flow structure noted in the SJM large hinge at peak systole results from the forward flow pattern present at the bottom of the hinge. The reverse flow pattern at the bottom of the SJM regular hinge, on the other hand, is associated with a clockwise rotating flow. Expectedly, a clockwise flow pattern is also noted in the SJM large hinge at mid-acceleration and mid-deceleration, when the bottom of the hinge recess is characterized by the presence of a reverse flow pattern.

As for the lateral corner, in the SJM regular hinge, it is characterized by a smooth streamlined flow, whereas, in the SJM large hinge, it exhibits a more complex flow patterns as underlined by the presence of entangled particle pathlines. This entangled aspect of the pathlines is due to the change in flow direction at the bottom of the hinge recess. During mid-acceleration and mid-deceleration, the reverse flow at the bottom of the hinge is associated with a streamline flow in the lateral corner. However, as this reversal flow disappears and is replaced by a forward flow, the particles in the lateral corner are also forced to change direction, leading to the observed complex pathlines. In the SJM regular hinge on the other hand, the reverse flow is present throughout the fully-open phase and thus a streamlined flow is seen in the lateral corner throughout the fully-

open leaflet phase. Such differences in flow structures and consequently in particle pathlines throughout the hinge recess are expected to yield variations in the residence time of blood elements within the hinge recess between the two SJM hinge designs.

Interestingly, the local change of pressure present on the left side of the leaflet due to the flow separation not only induces the flow reversal at the bottom of the hinge recess but also explains the presence of a forward flow pattern that crosses below the leaflet downstream of the hinge recess. This flow cross-over, observed with the particle streaklines and pathlines, is evident in both the SJM regular and large hinge.

The forward flow phase ends with a deceleration phase during which the cross-valvular flow rate starts to decrease. This phase is destabilizing in nature and yields to flow instabilities, observed within the hinge recess but best seen in the sinus region by the chaotic distribution of the short streaklines downstream of the valve (Figure 4-71).

The observed differences in flow patterns between the two hinge configurations are associated with some variations in velocity magnitude within the hinge recess. While at both mid-acceleration and mid-deceleration, the peak velocity magnitude within the recess is larger in the SJM regular hinge, it is in the SJM large hinge that the maximum velocity magnitude is reported at peak systole (Table 4-1 and Table 4-2). One could conclude that the hinge flow is overall faster in the SJM regular hinge than in the SJM large hinge at all instances of the forward flow phase except peak systole. However, a close inspection of the velocity magnitude distribution within the hinge recess (Figure 5-9) indicates that the velocity distribution within the hinge recess does not directly correlate with the peak velocity magnitude. Indeed, throughout the forward flow phase, the regions associated with low velocity magnitudes are larger in the SJM regular (Figure 5-9), whereas the regions of elevated velocities are larger in the SJM large hinge. This indicates that the velocities are generally lower in the SJM regular hinge, thus suggesting a higher propensity for thrombus build-up compared to the SJM large

hinge. Conversely, the relatively larger peak velocities noted in the SJM large hinge at peak systole might favor hinge washout. One could also argue that larger velocities could also dislodge thrombi, which would increase the risk for thromboembolism. However, as will be discussed in the subsequent paragraphs, both hinges are characterized by elevated velocities during diastole. As a result thrombus dislocation would most likely occur in diastole, irrespective of the maximum velocities observed here during the forward flow phase.

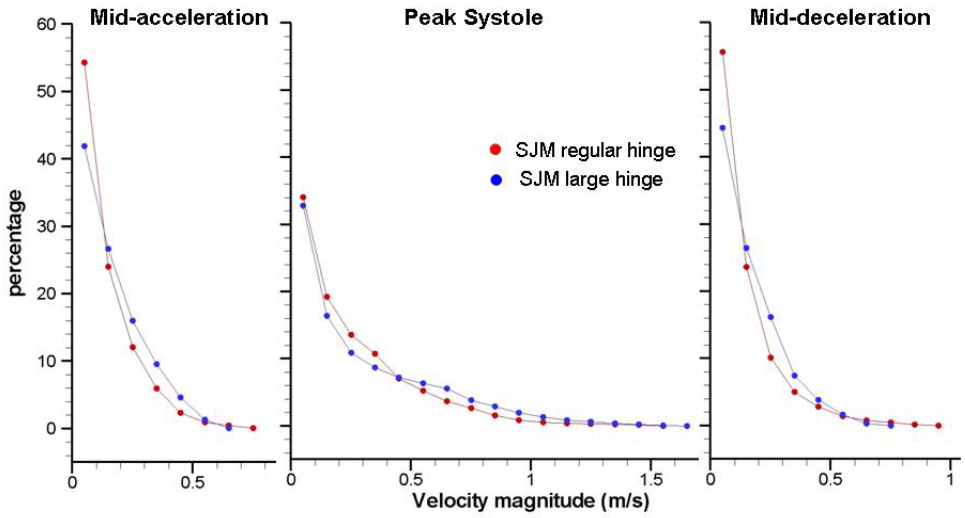

Figure 5-9: Velocity magnitude distribution within the hinge recess. Plotted is the percentage of hinge grid nodes as a function of the velocity magnitude.

Leaflet closing and the leakage flow phases

The fully-open leaflet phase is followed by the leaflet closing phase that is characterized by the onset of the leakage flow patterns observed throughout diastole. During the leakage flow phase (Figure 5-10), the flow structures in the SJM regular and large hinges appear to be comparable: 1) the leakage jets have a similar main direction;

2) the ventricular jet is consistently stronger than the adjacent jet. This is clearly visible with the pathlines of the particles released at early diastole (Figure 4-75 and Figure 4-83).

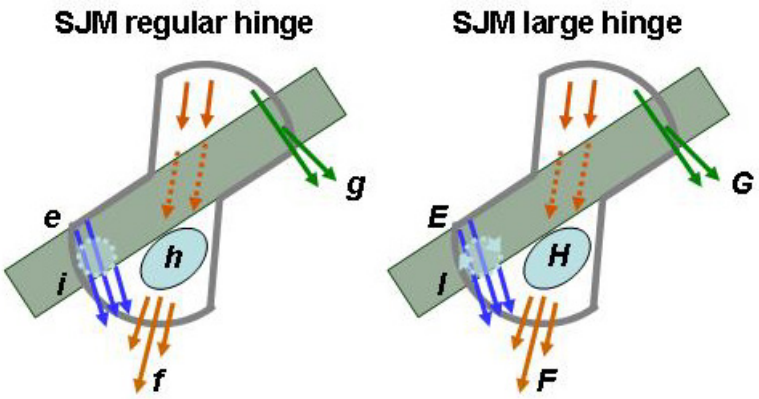

Figure 5-10: Characteristic flow features observed at mid-diastole in the SJM hinge design with a regular (left) and a large (right) hinge gap width. Note that each flow pattern is associated with a particular color and a letter for easy visualization and referencing.

Despite similar overall flow patterns and comparable relative distribution of the velocity magnitude in the two hinge designs, the reported velocity values are higher in the SJM large hinge than in the SJM regular hinge (Figure 5-11). This observation corroborates the earlier experimental findings by Leo et al. [91], who reported larger peak velocities in the SJM large hinge than in the SJM regular hinge under mitral flow conditions. At first, one could have expected the exact opposite phenomenon, with a smaller hinge gap width yielding higher velocities. This, however, would have overlooked the underlying pumping mechanism of the heart, which imposes a varying ventricle pressure rather than a varying valvular flow rate. Thus, two valves with different designs do not experience a similar leakage flow rate during diastole, but rather a similar trans-valvular pressure gradient. Moreover, since the SJM large hinge features larger gaps

than the SJM regular hinge, this hinge model offers a lower flow resistance compared to its counterpart. As a result, applying the same physiologic diastolic pressure drop of approximately 80 mmHg across the two valves yields a larger diastolic flow rate in the SJM large hinge than it does in the SJM regular hinge. This ultimately translates into faster and more three-dimensional flow in the SJM large hinge compared to the SJM regular hinge. This difference in blood velocity during diastole is clearly illustrated by the particle streaklines, which form longer streaks in the SJM large hinge compared to the SJM regular hinge, testifying for the fact that blood particles entrapped in the hinge leakage jets travel a longer distance away from the SJM large hinge than from the SJM regular hinge for a same time frame.

This difference in diastolic flow rate also yields small differences in flow structures, in particular during the leaflet closing phase (Figure 4-16 and Figure 4-17 for the SJM regular hinge, and Figure 4-39 and Figure 4-40 for the SJM large hinge). The hinge flow fields in the SJM regular hinge are seen to be strongly dominated by the motion of the leaflet, while in the SJM large hinge, the effect of leaflet motion is overshadowed by that of the elevated trans-valvular flow rate. For example, the effect of the moving leaflet is clearly visible in the aortic corner of the SJM regular hinge, with a clockwise flow motion due to the clockwise rotation of the leaflet, but not in the SJM large hinge. Similarly, the ventricular jet is present in the ventricular corner of the SJM large hinge from the beginning of the leaflet closing phase onwards, but only appears in the SJM regular hinge after the leaflet has completely closed.

In addition to the dynamic differences observed during the leaflet closing phase, the adjacent corner of the two hinge designs features distinct flow structures during the entire leakage flow phase. The strong adjacent leakage jet persisting near the flat level of the SJM regular hinge is associated with a flow detachment, which yields a small region of nearly stagnant flow at deeper levels within the adjacent corner (feature *i* in

Figure 5-10). The velocity vectors in the SJM large hinge, on the other hand, indicate the existence of a localized region of a faster-flowing clockwise rotating flow at the same location (feature I in Figure 5-10). Comparison of the velocity distribution (Figure 5-11) further enforces this observation, showing that the SJM regular hinge is associated with a larger percentage of low velocities than the SJM large hinge. Such a difference is of importance as regions of low flow, and in particular region of recirculating low flow, are thought to favor thrombus formation by enhancing cell-to-cell contact.

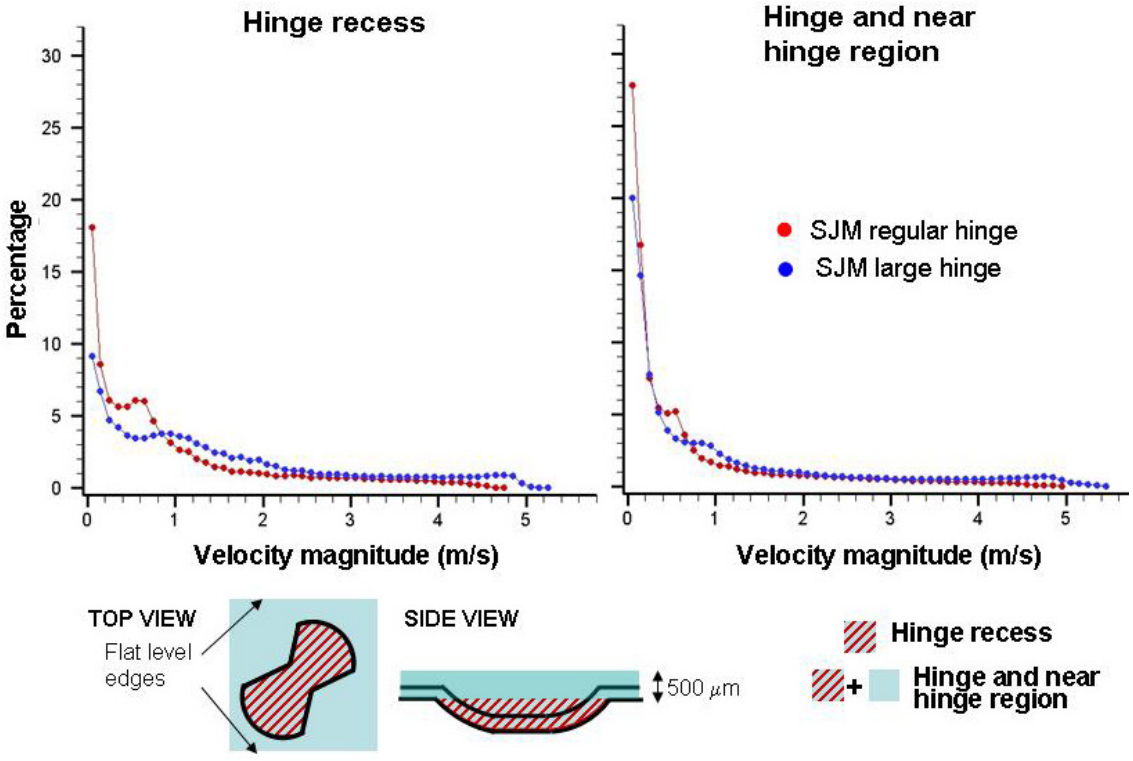

Figure 5-11: Velocity magnitude distribution within the hinge recess (left) and in the hinge vicinity (right) at mid-diastole. The hinge recess and the hinge and near-hinge regions are defined in the schematics shown below the graph.

5.2.2 Shear stress distribution

Forward flow phase

Comparison of the iso-surfaces during the forward flow phase shows similar global distribution between the SJM large and regular hinges. In order to get a better insight into the shear stress distribution within the hinge recess of these two SJM models, Figure 5-12 shows the probability density function (PDF) of the shear stress in the hinge and near hinge regions at three instances of the forward flow phase. It is evident from this figure that the shear stress distributions are similar for both valves, following similar trends in the hinge and its vicinity throughout all reported instances of the forward flow phase. Nonetheless, a few differences may be noted among the two hinge designs in the detailed distribution of the low and elevated shear stress regions. These differences are discussed hereafter.

Throughout systole and for both SJM hinges, the PDF of the shear stress in the hinge vicinity exhibits a plateau-like pattern at low shear stress levels (up to 300 dyn/cm^2). This plateau suggests the presence of shear stress levels up to 300 dyn/cm^2 in a significant portion of the hinge and near hinge region, this portion being slightly larger in the SJM large than in the SJM regular hinge. A close look at the iso-surfaces of low shear stress values (100 and 250 dyn/cm^2) supports these findings as these iso-surfaces are generally larger in the SJM large hinge compared to the SJM regular hinge. Even shear stress levels as low as 100 dyn/cm^2 may be detrimental to platelets and induce activation. However, only long exposure time (on the order of 10^2s [91]) to these low shear stress levels are believed to induce platelet activation. Therefore the difference in low shear stress distribution between the two SJM hinges is not thought to be critical in the overall hinge-related thromboembolic potential.

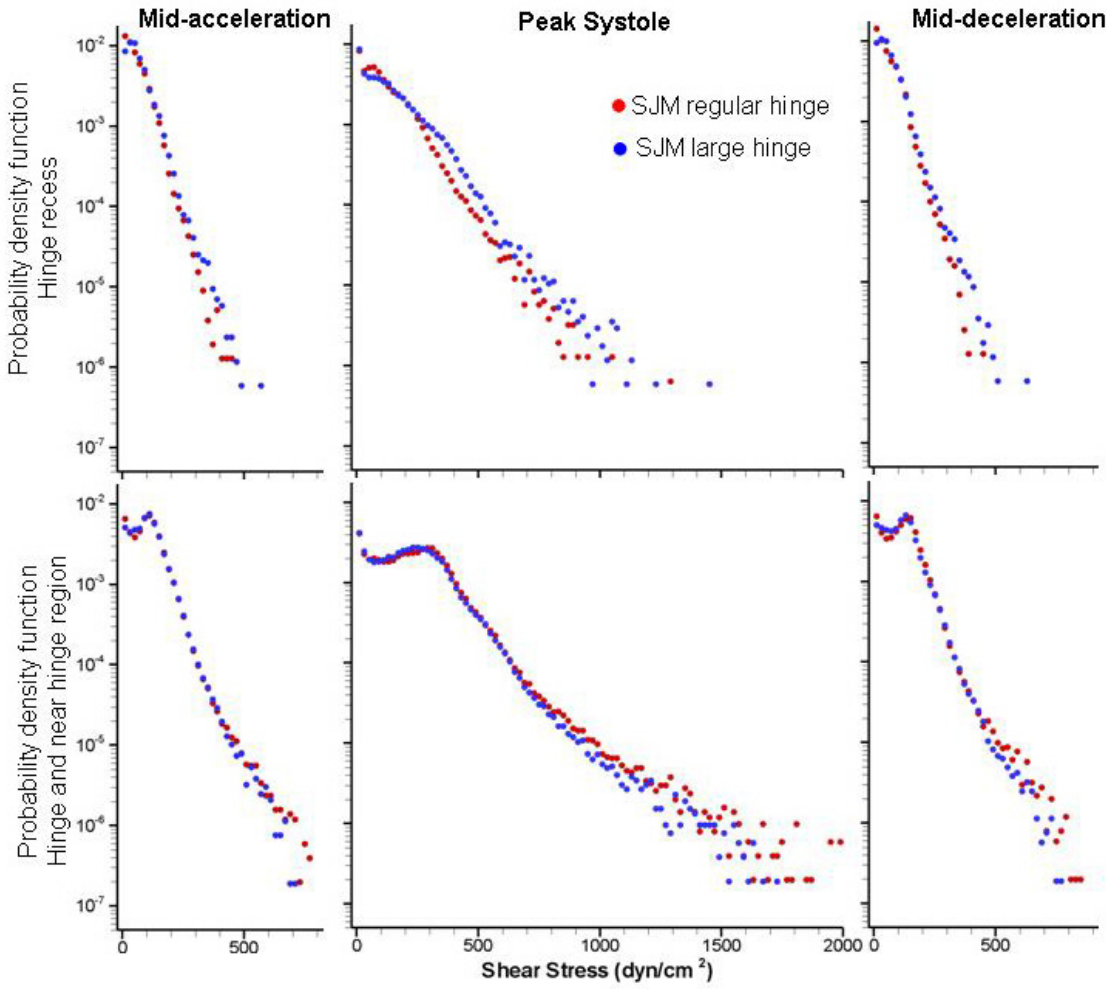

Figure 5-12: Probability density function of the shear stress within the hinge recess (top row) and in the hinge and its vicinity (bottom row) at three instances of systole.

Of more interest are differences in the distribution of regions of elevated shear stresses as they are likely to have a stronger impact on thrombus formation. Iso-surfaces of elevated shear stress levels (1,000 dyn/cm^2 and 1,500 dyn/cm^2), are seen during the forward flow phase in both hinge models not within the hinge recess but immediately upstream, at the edge of the gap formed by the leaflet and the flat level surfaces. This is further quantified in Figure 5-12, where the PDF within the hinge recess doesn't extend as far in the high shear stresses as the PDF of the hinge vicinity. Moreover, the iso-surface distribution indicates that the zone of elevated shear stress is larger for the SJM regular than for the SJM large hinge models. This is clearly seen in the PDF of the hinge and near hinge region where the red curve at peak systole is seen to lie above the blue curve at elevated shear stress levels. This difference might be attributed to a difference in the valve design. The SJM large hinge is identical to the SJM regular hinge except for the leaflet being shifted out of the hinge recess by a hundred microns. This not only results in an increased gap width within the hinge recess, but also outside of the recess, between the leaflet and the flat level. This geometrical difference induces some variations in the flow resistance, and consequently, despite the similar incoming valvular flow rate, the velocities in the gap formed by the leaflet and the housing surfaces differ. The velocities in this region are therefore slightly smaller in the SJM regular hinge than the SJM large hinge. These differences in velocity distribution lead to variations in the shear stress distribution.

As previously noted, the shear stress levels within the recess itself are lower than those found outside of the hinge. This holds true for both hinge configurations. While the PDF of shear stress in the hinge vicinity (bottom row in Figure 5-12) indicated slightly larger shear stresses for the SJM regular hinge compared to the SJM large hinge, this trend is inverted when focusing on the hinge recess itself (top row in Figure 5-12). Examination of the PDF within the two hinge recesses clearly indicates that, low shear

stress levels notwithstanding, the SJM large hinge recess is associated with slightly larger regions of elevated shear stress than the SJM regular hinge recess. This difference in shear stresses within the hinge recess might be attributed to the differences in hinge flow structures depicted above, where higher velocities and therefore higher shear stress levels are present in the SJM large hinge during the fully-open leaflet phase.

Overall, the greatest shear stress levels during the forward flow phase are seen at peak systole for both hinge configurations. Within the hinge recess itself, larger region of elevated shear stress exist in the SJM large hinge compared to the SJM regular hinge. This might imply a higher propensity for platelet activation and hemolysis within the SJM large hinge recess compared to the SJM regular hinge. This trend is inverted outside of the hinge recess as the SJM regular hinge is associated with larger portions of elevated shear stress than the SJM large hinge.

Leakage flow phase

During the leakage flow phase, flow features drastically different from the systolic flow fields were observed. As expected, this led to drastically different distribution of shear stresses during diastole compared to systole, but comparable distribution between the two SJM hinge configurations. In both hinge models, regions of elevated shear stresses were found outside of the recess in the wake of the leakage jets. Within the hinge recess itself, the shear stress distribution reveals four main regions of elevated shear stresses in both hinge models, namely: 1) along the wall of the ventricular corner; 2) in the tip of the lateral corner; 3) along the wall of the adjacent corner; and finally 4) at the bottom of the hinge recess. The location of these high shear stresses clearly

suggests that the curvature of the recess wall along with the design of the leaflet ear play a key role in the shear stress distribution.

The PDFs of the shear stress levels in the hinge and near hinge region of both SJM hinges are provided in Figure 5-13. Up to 3,000 dyn/cm^2, the PDFs of the SJM large hinge are greater than for the SJM regular hinge, both inside the hinge recess and in the near hinge regions. This indicates that the SJM large hinge exhibits larger areas of shear stresses of 3,000 dyn/cm^2 or less than the SJM regular hinge. This is clearly visualized in the iso-surface plots (Figure 4-6 and Figure 4-28) that qualitatively show that for all plotted shear stress levels (from 100 to 1,500 dyn/cm^2), the iso-surfaces are larger and extend further in the ventricular direction in the SJM large hinge model compared to the SJM regular hinge model. For larger shear stresses, however, the trend is inverted and a larger portion of the hinge and near hinge regions of the SJM regular hinge is associated with shear stress levels above 3,000 dyn/cm^2.

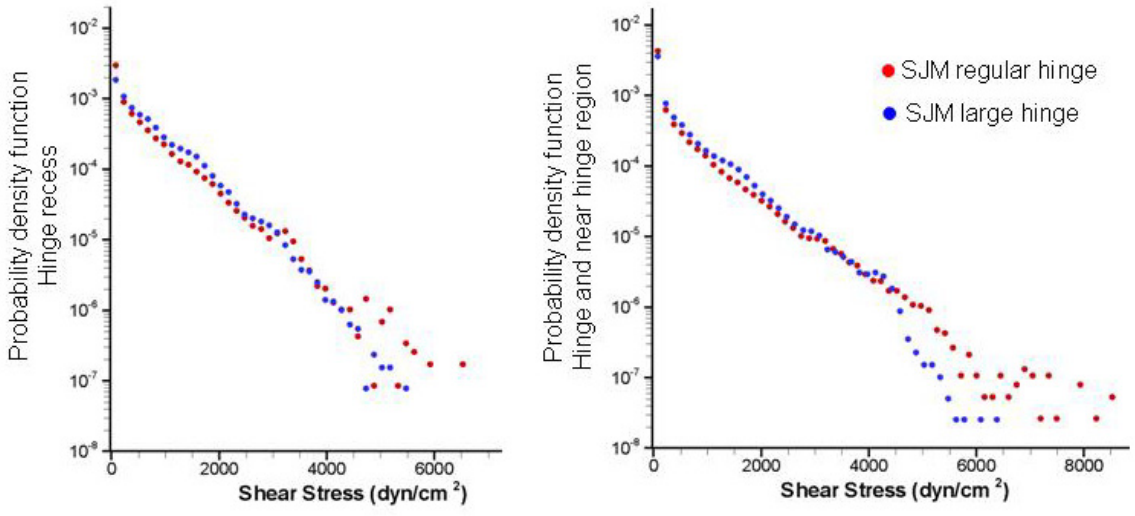

Figure 5-13: Probability density function of the shear stress (log-scale) within the hinge recess (left) and in the hinge and its vicinity (right) at mid-diastole.

Based on the above observations for the forward and leakage flow phases, one might conclude that the thromboembolic potential due to the flow in the hinge recess itself is slightly higher for the SJM large hinge while that associated with the near-hinge flow is greater for the SJM regular hinge. Modeling the shear stress distribution is essential to determine the potential for blood cell trauma, hemolysis and platelet activation associated with the hinge flow fields. However, only an assessment of the exposure time to specific shear stress levels would permit the true estimation of the environment experienced by the blood cells and allow for a comparison of the thromboembolic potential of a specific hinge design with respect to another. Indeed, localized region of elevated shear stress, in a fast flowing environment could yield a low exposure time and thus induce a low risk for blood damage. The following section aims at addressing this point by providing a comparative analysis of the Lagrangian results obtained for the SJM regular and large hinge models.

5.2.3 Hinge flow and blood damage

The Eulerian description of the shear stress fields in the hinge and near-hinge region provides detailed maps of the shear stress and helps in pinpointing regions with elevated potential for blood damage. This information may then be used to improve the hinge design and develop hinges with lesser risk of blood damage. However, in order to understand the thromboembolic complications associated with the implantation of BMHVs, it is important to estimate the shear stress levels experienced by particles along their trajectories as they cross through the hinge recess.

Particles were seeded at similar instances of time in both SJM hinge designs and the maximum shear stress levels experienced along their trajectories were computed. These maximum shear stress levels were consistently found to be lower than those

reported in the Eulerian analysis of the flow. For instance, for the SJM regular hinge, the maximum shear stress levels along the particle trajectories was found to be 3,250 dyn/cm^2, while the Eulerian analysis indicated a maximum shear stress of 6,515 dyn/cm^2 within the hinge recess and 8,535 dyn/cm^2 in the near-hinge region. This indicates that the particles seeded inside the hinge recess are not forced to travel through the localized regions of elevated shear stresses present in the hinge and its vicinity. This underscores the relevance of a Lagrangian approach to analyze the hinge flow fields and relate them to blood damage potential. While a specific hinge design may be associated with high shear stress levels, it is the propensity of the blood elements to flow through these regions of elevated shear stresses that influence the ultimate thromboembolic potential. However, it should be pointed out that in this study approximately 300 particles were seeded within the hinge recess and released at different time instants. This corresponds to a particle density of approximately 200 particles/mm^3. A single cubic millimeter of blood contains about 4,000 to 6,000 red blood cells and 200 to 500 platelets. It is expected that the release of a larger number of particles, with a density closer to that of real blood, within the hinge recess would increase the probability for a particle to cross the most detrimental flow region and thus lead to an overall peak shear stress levels along the pathlines that is higher and closer to the Eulerian peak value.

Nonetheless, because the particles were seeded with the same density and in similar locations in both hinge configurations, the present approach allows the comparison of the hinge performance. Comparative assessments of the different seeding and particle trajectories clearly indicate that, for both SJM hinge designs, the particles that cross the hinge after valve closure experience higher shear stress levels than those crossing the hinge during systole. This in turn suggests an overall higher propensity for blood cell damage for the particles crossing the hinge during diastole, independent of the hinge design.

In order to investigate the effect of the hinge gap width on the shear stress levels experienced by blood elements crossing the hinge recess, Figure 5-14 shows the cumulative distribution of the maximum shear stress levels along the particle trajectories. In this plot, all particles are considered, independently of their seeding time, for both hinge designs. Specifically, Figure 5-14 represents the percentage of particles experiencing a maximum shear stress level larger than a set value. For instance, Figure 5-14 indicates that 14% of the particles crossing the SJM large hinge are subjected to a maximum shear stress level greater than 1,000 dyn/cm^2. In the SJM regular hinge, the corresponding percentage is only 8%. It is evident that, up to 1,500 dyn/cm^2, the histogram bars are larger for the SJM large hinge compared to the SJM regular hinge, while at larger shear stress levels, the distribution is similar. This suggests that a larger portion of the particles seeded in the SJM large hinge experience detrimental conditions compared to the SJM regular hinge. As a result, this suggests a larger propensity for shear-induced red blood cell damage and platelet activation in the SJM large hinge.

The performance of the two hinges from a blood-cell point of view are further quantified by computing two blood damage indices, one characterizing the potential for hemolysis BDI^H and another one for platelet activation BDI^{PL}. These indices correspond to the sum along each particle trajectory of the weighted product of the exposure time by the shear stress experienced according to the equations provided in section 3.6.2. In this approach, the particle trajectories are considered to be representative of either platelet or red blood cell paths. The cumulative distribution of blood damage index for both hemolysis and platelet activation in the SJM regular and large hinges are presented together in Figure 5-15.

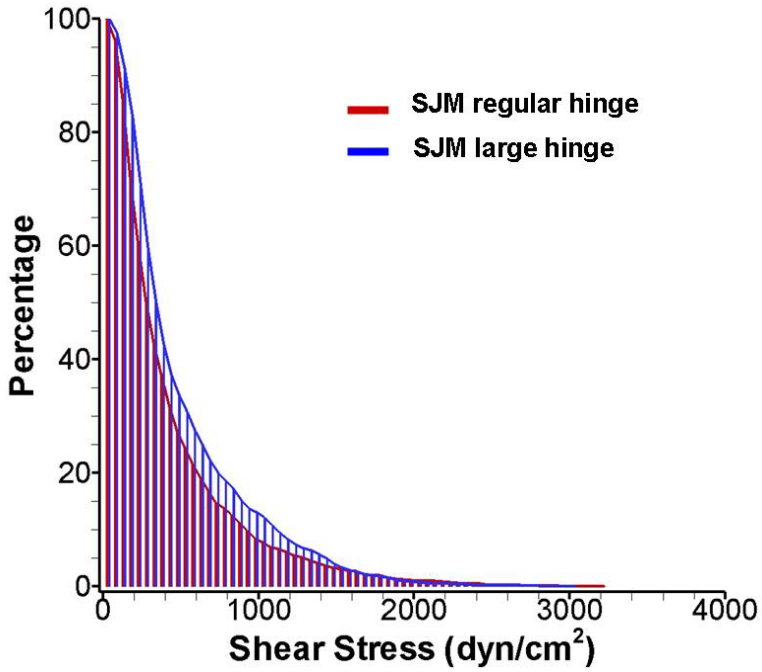

Figure 5-14: Cumulative distribution of the maximum shear stress experienced along the particle trajectories for the SJM regular and large hinges. The histogram shown in blue pertains to the SJM large hinge while the red one corresponds to the SJM regular hinge.

This cumulative distribution corresponds to the percentage of particles experiencing a BDI larger than a particular value. For instance, Figure 5-15 indicates that 5.5 % of the particles crossing the SJM large hinge are associated with a BDI^{H} of 0.22 or higher while this percentage is 4.6 % in the SJM regular hinge. The overall distribution of BDI is similar in both hinge configurations with, as expected, a decaying distribution from small BDI to large BDI, with a larger percentage of particles experiencing small BDI than large BDI. For all BDI^{H} up to 0.65 and all BDI^{PL} up to 2, the histogram bars representing the SJM large hinge are above those of the SJM regular hinge. This indicates that a larger portion of the particles are experiencing BDI^{H} from 0 to 0.65 and BDI^{PL} from 0 to 2 in the SJM large hinge compared to the SJM regular hinge. This cumulative distribution reveals a slightly higher propensity for hemolysis and platelet activation within the SJM large hinge. However, inspection of the distribution's

tail shows that this trend is inverted for higher values of BDI. Nonetheless, it should be emphasized that higher BDI values are associated with small particle percentage (of less than 1%) suggesting that only a few particles are actually experiencing these elevated BDIs.

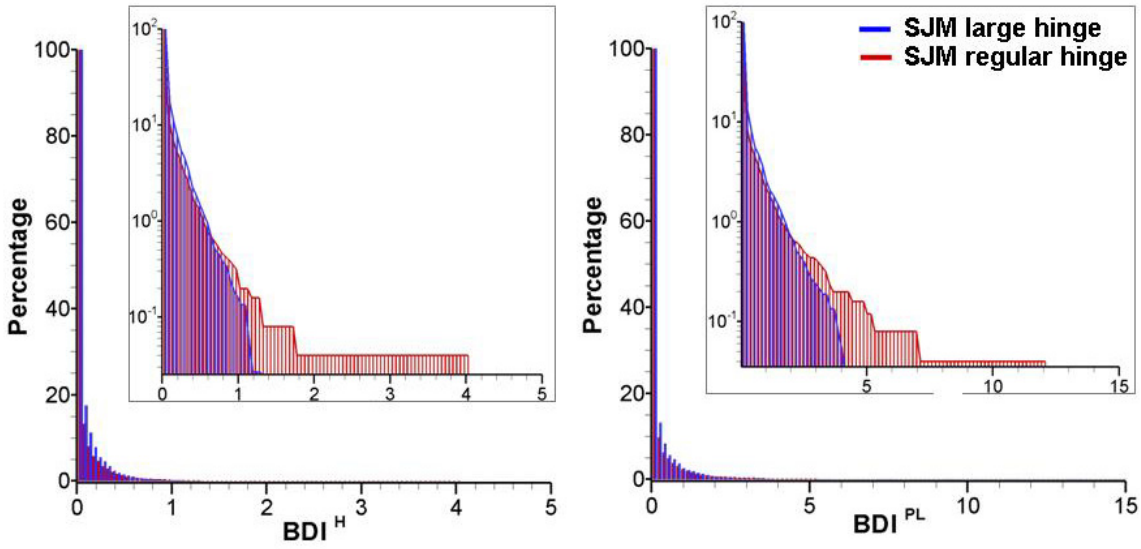

Figure 5-15: Cumulative distribution of the blood damage indices for hemolysis (left) and platelet activation (right) as a function of the particle percentage. The histogram shown in blue pertains to the SJM large hinge while the red one corresponds to the SJM regular hinge. The cumulative distribution plotted on a log scale is provided for both blood damage indices.

5.2.4 Concluding remarks

The comparative analysis of the flow in both hinge configurations presented herein indicates that velocities are generally lower in the SJM regular hinge compared to the SJM large hinge. This suggests a higher propensity for platelet aggregation in the SJM regular hinge, by enhancing cell-to-cell contact. Conversely, the large velocities in the SJM large hinge might prohibit thrombus formation by providing a good washout of

the hinge. This observation, however, can not be compared to clinical or *in vitro* data as no study, to date, have attempted to specifically quantify the risk for thrombus formation in these two hinge designs.

Comparative assessment of the different seeding and particle trajectories clearly indicate that, for both SJM hinge designs, the particles that cross the hinge after valve closure experience higher shear stress levels than those crossing the hinge during systole. This in turn suggests an overall higher propensity for blood cell rupture and damage for the particles crossing the hinge during diastole, independently of the hinge design.

The maximum shear stresses experienced along the particle trajectories indicate that a larger portion of the particles seeded in the SJM large hinge are subjected to detrimental flow conditions compared to the SJM regular hinge. As previously underscored exposure time is a key parameter in influencing hemolysis and platelet activation, as low shear stresses applied for a long exposure time could be just as detrimental as high shear stresses applied for a short time period. Nonetheless, the larger peak shear stresses observed along the particle paths in the SJM large hinge did translate into higher BDI. This is clearly shown in the distribution of the BDI which indicate that for the most part the particles seeded in the SJM large hinge experienced higher BDI than those in the SJM regular hinge. Exception should be noted for the high BDI values, for which the trend is inverted. However, these probabilities represent only very few of the seeded particles (less than 1%) and conclusions drawn from few individual particles are to be taken cautiously.

Overall, the performance of the two hinge recesses appears to be similar, whereas *in vitro* blood studies have shown that large hinge gap width might be more detrimental to blood elements. However, it should be pointed out that the *in vitro* blood experiments solely focused on the leakage phase, while the cumulative BDI reported

herein include the forward flow phase. Moreover, the blood elements in the experimental flow loop make several passes throughout the hinge. The differences in wash-out, flow stagnation and shear stresses though small may accumulate over the repeated number of passes. In addition, while the particle seeding achieved in this study reached the limits of our computational power, it is still limited when compared to the density of the red blood cells or platelets flowing through the hinge. A finer particle seeding, with more particles released more frequently during the cardiac cycle, is expected to provide a better sampling of the regions of elevated shear stresses or flow entrapment and deeper insight into the effect of the hinge gap.

5.3 Effect of the hinge design on the hinge flow fields

In order to assess how hinge design impacts the flow structures and associated thromboembolic potential, this section provides a comparative assessment of the hemodynamics of two different hinge designs, namely the St. Jude Medical (SJM) and CarboMedics (CM) hinges. The leaflet and hinge geometry of these two hinge models are obtained from micro-computed tomography. In both models, the distance between the leaflet ear and the bottom of the hinge recess, known as the hinge gap width, is set to a nominal value of 150 μm, which corresponds to a regular hinge gap width.

Previous clinical studies have shown that the SJM valve has excellent clinical results, with low valve-related complications [89]. Several clinical studies have also concluded that the CM valve has satisfactory clinical performance [92-95]. However, Akins showed that the clinical performance of the CarboMedics valve based is just behind the SJM on incidence of thromboembolism [90]. This difference in performance between the SJM and CM valves may be attributed to the differences in hinge design, and subsequently in hinge flow dynamics. Identifying the differences in hinge flow fields

and relating these to potential for blood cell damage is therefore crucial to identify specific design features that are either favorable or detrimental to blood elements and to the overall clinical performance of the valve. Such an insight is required to optimize the hinge design from a blood-cell standpoint.

As a result, the following discussion is divided into three main sections so as to provide a thorough analysis of the influence of the hinge design on three different hemodynamic metrics. More precisely, each section will focus, in order, on the effect of the hinge design throughout the cardiac cycle on 1) the hinge flow fields; 2) the shear stress distribution; and 3) the estimated hinge blood damage potential. The first two sections present the similarity in flow structures and shear stress distributions but emphasis is placed upon the differences between the two different hinge designs. The last section focuses on the analysis of the Lagrangian results to assess and compare the potential for hemolysis and platelet activation of the two hinges.

Before delving into the analysis of the hinge performance, it is essential to have a good understanding of the geometrical similarities and differences between the two selected hinge designs. The geometric characteristics of each of the two hinges are therefore recalled herein (Figure 5-16). The SJM hinge is characterized by a smooth streamlined butterfly geometry with smooth contours. It consists of a semicircular leaflet ear, which mates to a recess of similar shape in the valve housing. This mated-sphere pivot design allows the leaflet appendage to sweep all areas of the pivot depression. The CM hinge design, on the other hand, has a butterfly geometry similar to that of the SJM hinge, but with sharper corners and more angulated edges. The design of the CM hinge is such that the projection of the leaflet within the recess cannot sweep the entire hinge area, leaving an unswept area in each of the four corners of the hinge. Finally, the SJM and CM hinges do not differ only in geometrical features, but also in dimensions. As can be seen in Appendix B.3, the volume encompassed by the CM hinge is smaller than that

of the SJM hinge. The CM hinge outline at the flat level is clearly smaller than that of the SJM hinge, and the depth of the CM recess (up to 525 μm) is lesser than that of the SJM recess (685 μm). The dimensions of the periphery gap, between the flat level and the leaflet surface edge also varies, with an approximate gap of 55 μm and 100 μm in the CM model and the SJM model, respectively.

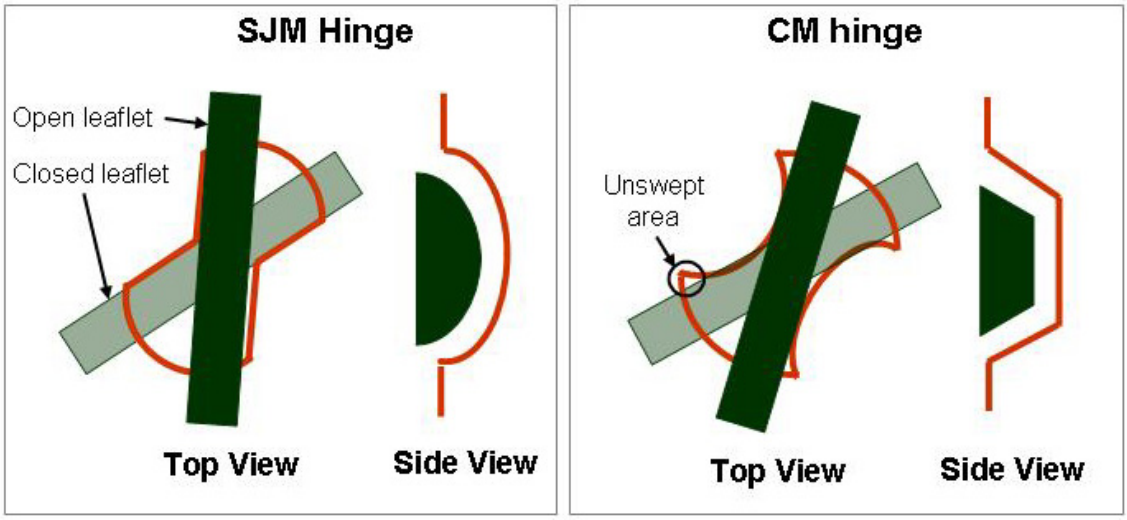

Figure 5-16: Schematics highlighting the main features of the SJM hinge design (left) and the CM hinge design (right)

5.3.1 Hinge flow fields

Forward flow phase

During the leaflet opening phase, the flow features are similar throughout the hinge recess, with a forward flow pattern developing in the lateral corner and more complex flow features forming in the adjacent corner due to the flow separation

occurring in the wake of the leaflet. Differences in flow features become apparent at mid-acceleration and exist throughout the fully open leaflet phase.

The most striking difference in flow features is seen in the adjacent corner. The incoming flow impinges on the downstream wall of the adjacent corner and as a result is deflected towards the lateral side of the hinge. Because of the confined geometry of the CM hinge, this leads to formation of a well-defined clockwise rotating flow that occupies the entire adjacent corner. This rotating flow is seen throughout the fully open leaflet phase and varies in magnitude with the valvular flow rate, its strength being the largest at peak systole (feature *A* in Figure 5-17). This rotating flow, combined with the large out-of-plane motion, leads to the formation of helical-like streaklines spanning the entire adjacent corner of the CM hinge. However, as the particles exit the recess, the out-of-plane component becomes dominant and the rotating pattern vanishes. In the SJM regular hinge, on the other hand, a close inspection of the particle paths reveals that the rotating pattern is less pronounced and the exit point is localized in the downstream-most part of the adjacent corner (feature *a* in Figure 5-17). Recirculating flow region are known to promote thrombus formation by favoring cell-to-cell contact and platelet aggregation. The flow features observed in the adjacent corner therefore suggest a longer blood cell residence time and consequently a greater thrombogenic risk for the CM hinge compared to the SJM regular hinge.

Additional variations in flow features are also noted in the aortic and ventricular corners. These differences can clearly be attributed to the variations in designs, in particular to the curvature of the hinge corner tips. For instance, in the lateral corner of the hinge, the forward flow pattern is redirected towards the aortic corner as it impinges on the recess wall. In the CM hinge design this flow redirection translates into the formation of a strong isolated jet in the tip of the aortic corner (feature *B* in Figure 5-17).

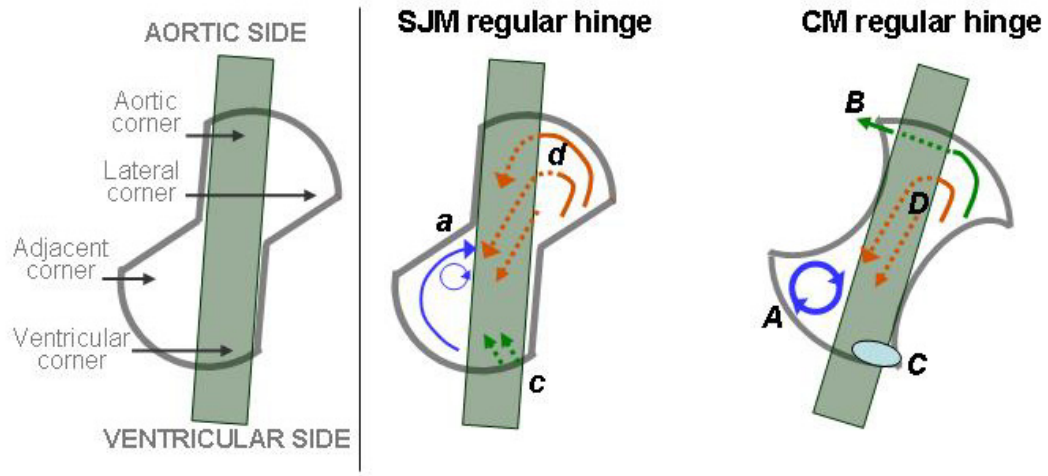

Figure 5-17: Characteristic flow features observed during the forward flow phase in the SJM hinge design (left) and the CM hinge design (right). Note that each flow pattern is associated with a particular color and a letter for easy visualization and referencing.

Indeed, the CM hinge corners are not entirely swept by the leaflet ear. When the leaflet is in its fully open position, an “unswept” area exits in the tip of the aortic corner through which fluid can flow and accelerate leading to the formation of an isolated jet, which is best seen with the particle pathlines (Figure 4-91). Conversely, in the SJM regular hinge design such an unswept area doesn’t exist as the SJM hinge is designed such that the flat surface of the leaflet comes to a “flat-to-flat” contact with the flat surface of the hinge corners. As a result, no leakage jet is seen in the tip of the SJM aortic corner. The difference in design between the curved CM hinge and the straight SJM hinge is also responsible for the differences in flow structures observed in the ventricular corner. The SJM ventricular corner is characterized by a fast-paced flow diving inside the hinge. The ventricular corner of the CM hinge, on the other hand, exhibits an isolated region of low flow that persists throughout the fully-open leaflet phase (features *c* and *C* in Figure 5-17). This region is best visualized with the particle streaklines where along the ventricular corner wall underneath the leaflet ear no

streaklines are seen. This region of low flow is associated with an elevated risk for platelet aggregation and is therefore thought to play an important role in the overall thromboembolic potential of the CM hinge design.

Interestingly, in both hinge configurations, a reverse flow pattern is visible at the bottom of the hinge recess throughout the forward flow phase at the exception of the early part of the leaflet opening phase (features *d* and *D* Figure 5-17). As previously noted in section 5.2.1, this flow reversal may be attributed to a region of low pressure located in the aortic surface of the leaflet due to the detachment of the main stream flow in this region. This region of low pressure induces a negative pressure gradient between the lateral and adjacent corners. This eventually leads to the flow reversal observed at the bottom of the hinge recess, with fluid going from the lateral to the adjacent corner. This flow reversal, present in both hinge models, exhibits a near-parabolic profile, suggesting that the hinge flow falls into the laminar regime. This is expected since the hinge Reynolds number, based on the hinge gap width and the maximum hinge velocity is on the order of 70 for the SJM regular hinge and 60 for the CM hinge.

The local depressurization present on the left side of the leaflet during the forward flow phase also explains the presence of a flow cross-over immediately downstream of the hinge underneath of the leaflet. This flow cross-over is best observed with the particle streaklines and pathlines where particles seeded in the lateral corner travel downstream of the hinge and flow back in the direction of the aortic corner. This characteristic flow pattern is evident in both the SJM regular and the CM regular hinges.

The differences in flow features observed between the SJM and CM hinges are associated with some variations in velocity magnitude. Comparison of the maximum hinge velocity magnitude (Table 4-1 and Table 4-3) indicates that throughout the forward flow phase, the peak velocity magnitudes are larger in the SJM regular hinge. This is consistent with the overall velocity distribution within the hinge recess (Figure 5-18).

Figure 5-18 clearly indicates that the largest velocities are consistently seen in the SJM regular hinge. During mid-acceleration and mid-deceleration, for all velocities above 0.5 m/s the green curve consistently lays below the green curves, indicating that the regions associated with large velocities are smaller in the CM regular hinge. At peak systole, it is clear that the distribution of regions associated with velocities above 0.75 m/s is similar between the two hinges. This suggests a better washout of the SJM hinge induced by the large velocities compared to the CM hinge.

A close inspection of the distribution at low velocities suggest that the regions of low velocity magnitudes (less than 0.5 m/s during mid-acceleration and mid-deceleration and less than 0.75 m/s at peak systole) are slightly larger in the CM hinge. This observation suggests a higher propensity for thrombus build-up compared to the SJM regular hinge.

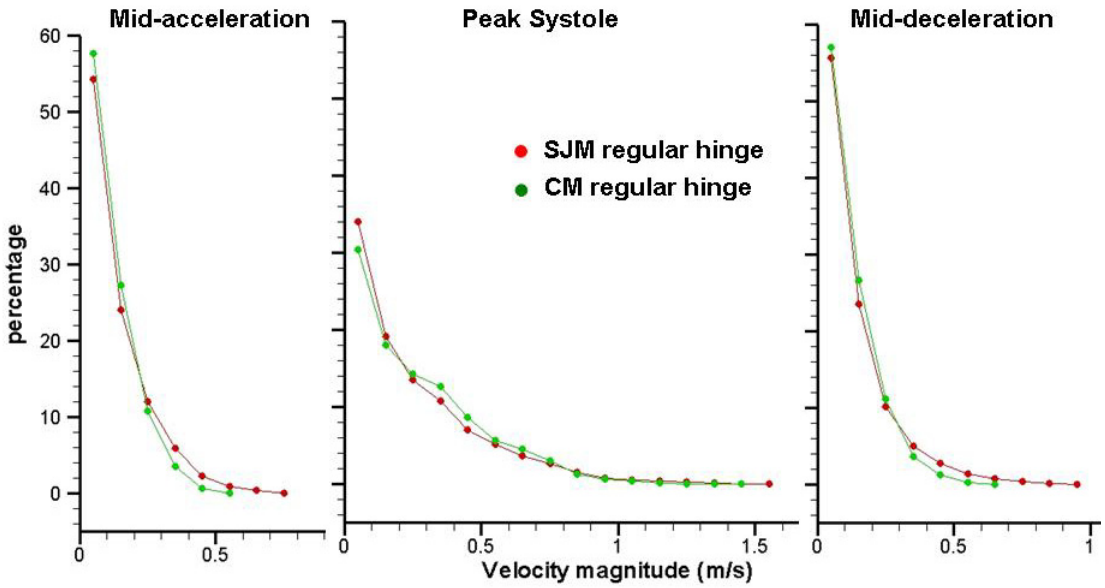

Figure 5-18: Velocity magnitude distribution within the hinge recess. Plotted is the percentage of hinge grid nodes as a function of the velocity magnitude.

Leakage flow phase

The forward flow phase ends with the leaflet closing phase during which the leaflet moves from the fully-open to the fully-closed position and the net inflow through the valve reduces. During the leaflet closing phase, the flow field in both hinge configurations appears to be strongly dominated by the motion of the leaflet. Indeed, the effect of the moving leaflet is clearly visible in the aortic corner where a clockwise flow motion is seen due to the clockwise rotation of the leaflet (Figure 4-16 and Figure 4-60).

The closing phase is characterized by the formation of the flow patterns that are present throughout the leakage flow phase, in particular the three main leakage flows seen in the lateral, ventricular, and adjacent corners. Similarly, to what was observed during the forward flow phase, the differences in flow structures in the hinge corners are mostly imparted by the design differences: curved-shaped angulated corners for the CM hinge vs. a smooth corner design for the SJM one. For instance, in the CM hinge, the flow in the adjacent corner is seen to accelerate as it dives inside the hinge through the unswept area in the corner tip (feature *E* in Figure 5-19). At that point the flow is bounded by the hinge recess on one side and the leaflet surface on the other. As it impinges on the recess wall, this localized and bounded flow is redirected towards the ventricular corner from where it exits the hinge recess (feature *F* in Figure 5-19). Contrary to the CM hinge model, the flow in the SJM adjacent corner appear to be largely influenced by the flow leaking through the periphery gap (the gap formed by the flat level and the leaflet surface). The direction and strength of the adjacent SJM leakage jet corresponds to the flow immediately outside of the hinge recess (feature e in Figure 5-19). This difference could be attributed to the difference in periphery gap dimensions, the SJM model featuring a larger gap than the CM model (100 μm vs. 55 μm).

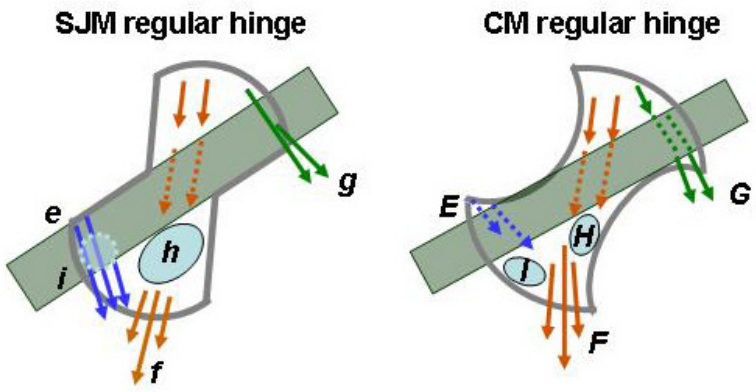

Figure 5-19: Characteristic flow features observed during the leakage flow phase in the SJM hinge design (left) and the CM hinge design (right). Note that each flow pattern is associated with a particular color and a letter for easy visualization and referencing.

The difference in flow pattern in the adjacent corner of the hinge explains the differences observed in the ventricular corner. The CM adjacent jet is seen to merge with the ventricular flow at the bottom of the hinge recess. This induces a change of direction in the ventricular leakage jet compared to the SJM hinge. A close inspection of the pathlines emanating from the ventricular corner reveals that the CM ventricular jet is nearly aligned along with the mainstream flow direction while the SJM leakage jet is preferentially oriented towards the adjacent side of the hinge (features *F* and *f* in Figure 5-19).

Comparison of the flow in the lateral corner of the hinge reveals that the SJM and CM lateral leakage jets have a strong out-of-plane motion and are oriented along the same main direction. The main difference between these two leakage jets lie in their position with respect to the hinge design, and thus can be attributed to the variations in design of the corner tips. The CM lateral jet (feature *G* in Figure 5-19) stems from the unswept area in the lateral CM hinge corner. It is isolated from the neighboring flow in the aortic corner by the leaflet ear and hinge recess surfaces and spreads through the

entire aortic corner tip. In the SJM hinge on the other hand, the lateral jet is located along the downstream wall of the lateral corner (feature *g* in Figure 5-19).

In addition to the differences in leakage jet position and orientation, the two hinge recesses exhibit distinct regions of low flow. A flow jet appears due the squeezing of the flow through a small orifice. The formation of a jet of elevated velocity magnitude is associated with a flow separation and the presence of low flow regions on the side of the jet. These regions of low flow are clearly seen in both hinge configurations due to the ventricular and adjacent leakage jets. In the two hinge models, the fast-flowing ventricular jet originating from the aortic side of the hinge detaches from the leaflet surface and thus induces the formation of a low flow region in the ventricular corner along the leaflet wall. Because of the larger dimensions of the SJM hinge with respect to the CM hinge, this region of low flow appears to be larger in the SJM hinge (features *h* and *H* in Figure 5-19). This observation is further reinforced by the comparison of the velocity distribution (Figure 5-20) that indicates that that the SJM regular hinge is associated with a larger percentage of low velocities than the CM hinge.

In both hinge designs, another region of low flow is also observed in the adjacent corner. This region of low flow results in both hinges from a flow separation induced by the adjacent leakage jet. However, the location of this low flow region differs between the CM and SJM hinges. The adjacent CM jet is clearly seen to detach from the leaflet surface and exit the hinge from the ventricular corner, thereby yielding a small low flow region along the ventricular leaflet wall in the adjacent corner (feature *I* in Figure 5-19). In the SJM hinge, on the other hand, the strong adjacent jet persisting near the flat level induces a flow separation that is characterized by a small region of low flow in the tip of the adjacent corner (feature *i* in Figure 5-19).

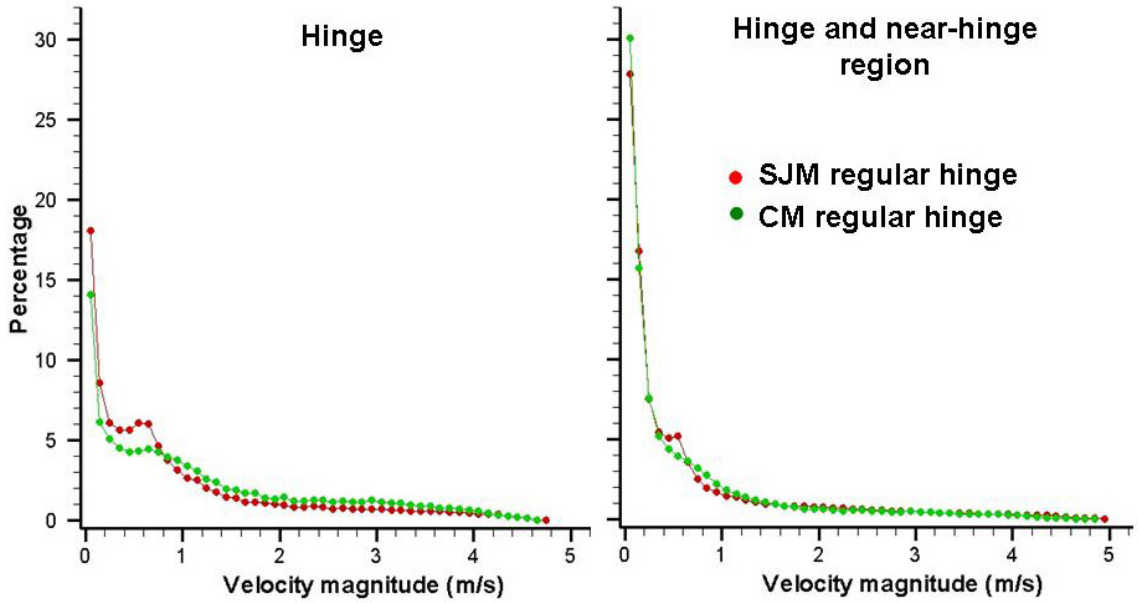

Figure 5-20: Velocity magnitude distribution within the hinge recess (left) and in the hinge vicinity (right) at mid-diastole.

The variations in hinge design were seen to induce some variations in flow patterns throughout the cardiac cycle. In particular, most of the observed differences could be related to the difference in hinge corner design. The curved vs. flat corner was seen to significantly impact the hinge flow features, not only the strong leakage jets emanating from the hinge but also the resulting regions of flow separation. These region flow separation, and thus of low flow, are thought to favor thrombus formation by enhancing cell-to-cell contact, therefore differences in the extent of low flow regions are likely to induce some differences in the hinge thromboembolic potential. Therefore, based on the above observations, the SJM hinge might have a slightly larger potential for platelet aggregation during diastole compared to its counterpart the CM hinge.

5.3.2 Shear stress distribution

Forward flow phase

The overall shear stress distributions (Figure 4-22 and Figure 4-23 for the SJM regular hinge, and Figure 4-66 and Figure 4-67 for the CM hinge) during the forward flow phase are similar between the CM and the SJM regular hinges. In order to gain further insight into the shear stress associated with the fluid dynamics of these two hinge designs, Figure 5-21 shows the probability density function (PDF) of the shear stress in the hinge and near hinge regions at three instances of the forward flow phase.

This figure clearly highlights that the shear stress distributions are similar for both hinges, following similar trends in the hinge and its vicinity at mid-acceleration, peak systole, and mid-diastole. It also underscores that the greatest shear stress levels during the forward flow phase are seen at peak systole for both hinge configurations. The shear stress PDFs corresponding to the hinge and near-hinge region display a plateau-like pattern at low shear levels (for shear stresses below 150 dyn/cm^2 at mid-acceleration and mid-deceleration and below 300 dyn/cm^2 at peak systole) for both hinge designs. This plateau indicates that a significant portion of the hinge and its vicinity is associated with shear stress levels lower than 300 dyn/cm^2. Previous studies have shown that low shear stress levels can be detrimental to platelets and induce platelet activation if the blood elements are subjected to these conditions for a long time [81, 82]. Leo *et al.* refer to an exposure time on the order of 10^2s and a shear stress of 100 dyn/cm^2 for platelet activation to occur [91]. Because of the extended exposure time required to induce blood trauma at low shear stress, the regions of low shear stress levels seen in both hinge designs are not thought to participate to a large degree to the thromboembolic potential of the hinge.

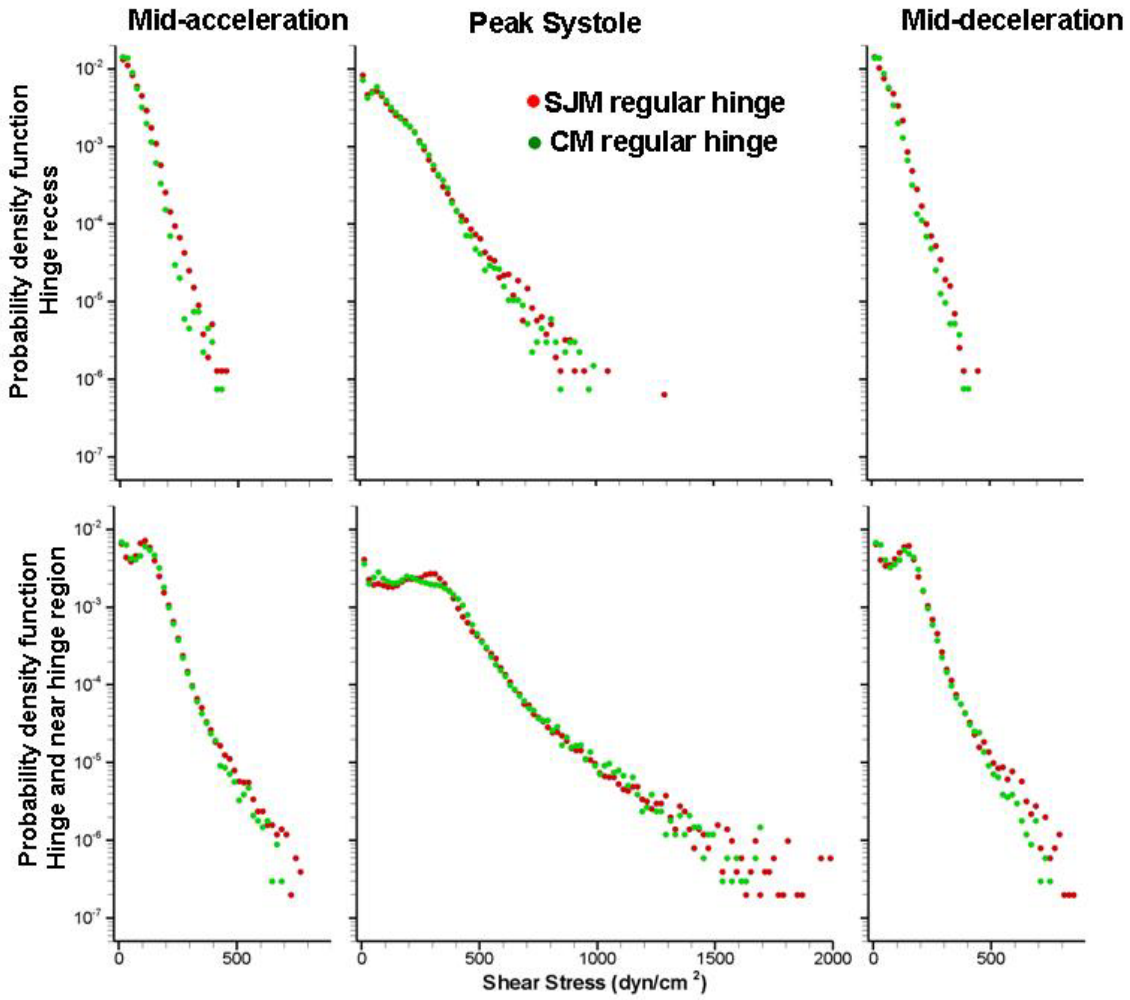

Figure 5-21: Probability density function of the shear stress within the hinge recess (top row) and in the hinge and its vicinity (bottom row) at three instances of systole.

For higher shear stress levels, the PDFs in the hinge and near hinge-region exhibit a linear decay. The nearly superimposed red and green PDFs underline that a similar shear stress distribution exists between the two hinge models for all shear stress above 300 dyn/cm^2. Nonetheless, a close inspection of the tail of the PDFs at mid-acceleration and mid-deceleration reveals that the SJM regular hinge is associated with large zones of elevated shear stress (above 500 dyn/cm^2) compared to the CM hinge. Such a trend is also observed in the PDFs of the hinge recess alone, where the red symbols (corresponding to the SJM regular hinge) appear to be consistently above the green symbols (which depict the CM hinge). This implies that the propensity for platelet activation and hemolysis associated with the SJM hinge design might be slightly higher during the forward flow phase than that of the CM hinge.

Leakage flow phase

During the leakage flow phase, the hinge flow features are totally different from those observed during the forward flow phase. This leads to drastically different shear stress distribution as highlighted by the iso-surface plots provided in Figure 4-6 and Figure 4-51. In both hinge models, the regions of elevated shear stresses are mostly found outside of the recess in the wake of the leakage jets. The shear stress distribution between the CM and SJM hinges are therefore comparable, except in the wake of the ventricular leakage jet where difference in jet orientation was noted. Nonetheless, the shear stress PDF in the hinge and near hinge region (Figure 5-22) indicates a similar distribution of shear stress in the CM and SJM hinge. For both hinge models, the shear stress levels are five to six times greater during diastole than during systole, suggesting that the leakage flow phase is the most detrimental phase of the cardiac cycle.

It is inside the hinge recess itself that the differences between the two hinge designs are the most pronounced. The shear stress distribution within the recess reveals in both hinge models four main regions of elevated shear stresses, namely: 1) the adjacent corner tip; 2) the lateral corner tip; 3) along the wall of the ventricular corner; and finally 4) at the bottom of the hinge recess. It is interesting to note that, at the flat level and at the 195-μm level, the peak shear stresses appear to be higher and the region of high shear stress larger in the SJM hinge (Figure 4-22 and Figure 4-23) compared to the CM hinge (Figure 4-66 and Figure 4-67). However, this trend is inverted at deeper level within the recess where, for instance, at the 390-μm level a larger portion of the CM hinge (Figure 4-67) is occupied with elevated shear stress compared to the SJM hinge (Figure 4-23). A comparison of the iso-surface plots (Figure 4-6 and Figure 4-51) underscores that for a similar shear stress level, the iso-surfaces within the recess are larger in the CM hinge compared to the SJM hinge. This is further confirmed by the PDFs of the shear stress within the hinge recess (Figure 5-22) that clearly indicate that the regions of elevated shear stress are overall larger in the CM hinge than in the SJM hinge. This might be attributed to the differences in hinge design. The smooth streamlined SJM hinge profile, with a gradual change in geometry reduces the propensity for flow separation. In contrast, the angulated CM hinge features sharp corner that may disrupt the flow. Thus, the larger shear stress values noted in the CM hinge design is consistent with the hinge geometry. This clearly suggests that blood elements passing through the CM hinge may experience more severe flow conditions than those passing through the SJM hinge, and consequently that the CM hinge may have a higher potential for blood cell trauma, hemolysis, and platelet activation than the SJM hinge during the diastolic phase. This finding correlates well with previously published

experimental studies which concluded based on a purely fluid dynamics assessment that, under mitral [32] and aortic conditions [36], the Reynolds shear stress were larger in the CM hinge and thus the thromboembolic potential might be larger in the CM hinge compared to the SJM hinge.

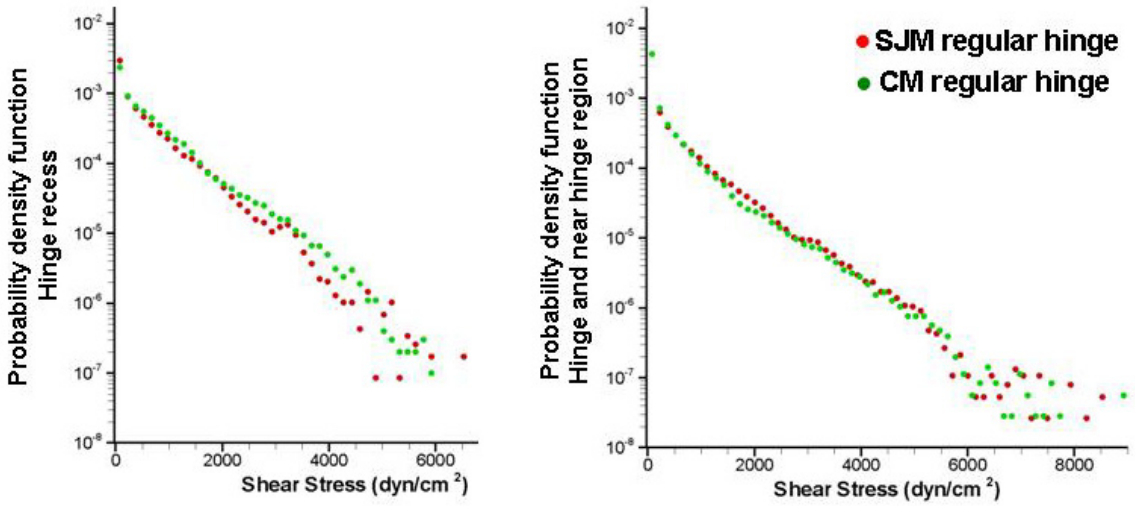

Figure 5-22: Probability density function of the shear stress (log-scale) within the hinge recess (left) and in the hinge and its vicinity (right) at mid-diastole.

The above observations underscore that the differences in shear stress distribution within the SJM and CM hinges are larger during the leakage flow phase compared to the forward flow phase. This implies that the hinge design might play a larger role on the shear stress distribution, and thus on platelet activation and hemolysis, during diastole compared to systole. Moreover, the systolic flow patterns reveal the presence of a large recirculation region in the CM hinge that is not seen in the SJM hinge. Such a recirculation region is known to promote thrombus formation. Consequently, in order to minimize blood trauma and thrombosis, the hinge design might

have to be optimized to reduce large shear stresses during the leakage flow phase and limit recirculating flow during the forward flow phase.

However, such a conclusion drawn only on the shear stress and flow distributions is to be taken with caution as residence time and shear stress exposure time have been identified as key parameters in determining the risk for thrombus formation, platelet activation, and hemolysis. The following section therefore aims at addressing this point by comparing the Lagrangian results of the CM and SJM regular hinges.

5.3.3 Hinge flow and blood damage

It is of prime importance to identify regions of elevated shear stresses in the hinge and near-hinge region in order to locate areas of the hinge where design improvement could be performed. Such information may be obtained by considering detailed maps of the shear stress obtained from the Eulerian description of flow. However, previous studies have shown that hemolysis and platelet activation not only depend on shear stress levels but also exposure time. Therefore, history of blood elements crossing through the hinge region should be taken into consideration in order to have a comprehensive understanding of the flow-induced thromboembolic complications of BMHVs. Knowledge of the paths taken by the particles flowing in the near hinge region can be used to estimate the shear stress levels experienced along each particle path and to relate shear stress levels with exposure time.

Approximately 300 particles were seeded at regular intervals in time in both the SJM regular and the CM hinge designs and their position was tracked with time. Comparative assessment of the different seeding and particle trajectories clearly indicate that of all the particles, those crossing the hinge after valve closure experience higher shear stress levels than those crossing the hinge during systole. This observation is in

agreement with the Eulerian shear stress maps, which revealed lower shear stress values during systole compared to diastole for both valve designs. This specifically designates the leakage flow phase as the most detrimental flow phase of the cardiac cycle, indicating an overall higher propensity for blood cell rupture and damage for the particles crossing the hinge during diastole, independently of the hinge design.

The maximum shear stress levels experienced along the particle trajectories were computed and the cumulative distribution of these maxima is provided in Figure 5-23. Note that in this plot, all particles are considered, independently of their seeding time. Figure 5-23 provides the percentage of particles experiencing a maximum shear stress levels larger than a set value. For instance, Figure 5-23 indicates that 24% of the particles crossing the SJM regular hinge are subjected to a maximum shear stress levels greater than 500 dyn/cm^2 whereas, in the CM regular hinge, the corresponding percentage is lower at 18%. It is evident that, up to 1,000 dyn/cm^2, the histogram bars are larger for the SJM regular hinge compared to the CM regular hinge, while at larger shear stress levels, this trend is inverted. This indicates that a larger portion of the particles seeded in the CM hinge experience detrimental conditions compared to the SJM regular hinge. This in turn suggests a larger propensity for shear-induced blood cell damage and activation in the CM hinge.

It is noteworthy to mention that the maximum shear stress experienced by the particles along their trajectory is 4,000 dyn/cm^2 with the CM hinge and 3,250 dyn/cm^2 with the SJM hinge. As previously underscored in section 5.2.3, these maxima are lower than those reported in the Eulerian analysis of the flow. As a reminder, the Eulerian analysis of the SJM regular hinge indicated a maximum shear stress of 6,515 dyn/cm^2 within the hinge recess and 8,535 dyn/cm^2 in the near-hinge region. The maximum shear stresses in the CM hinge were on the same order of magnitude, with a peak value of 5,910 dyn/cm^2 in the hinge recess and 8,985 dyn/cm^2 in the hinge vicinity. It is

unsurprising that the shear stress levels along the particle trajectories are lower than those seen in the Eulerian map, since the particles are not bound to travel regions of high shear stresses. Furthermore, in this study, only 300 particles are released within the hinge recess every 15 ms. A finer seeding, with a larger number of particles and more frequent releases, is expected to increase the probability for particles to cross the most detrimental region, thereby leading to an overall peak shear stress levels along the pathlines that is higher and closer to the Eulerian peak value. Nevertheless, because particle seeding was similar in both hinge configurations, analysis of the particle trajectories and histories in both hinge designs allows the assessment and comparison of the hinge performance.

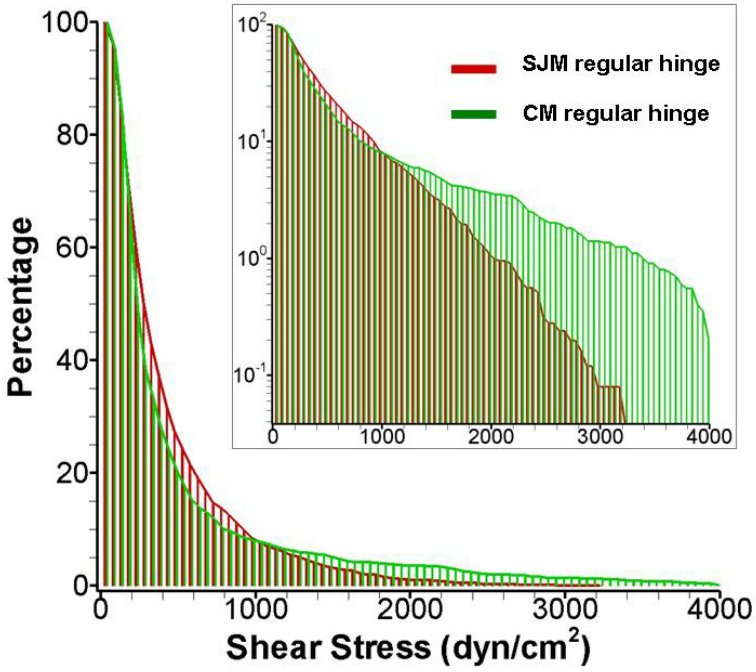

Figure 5-23: Cumulative distribution of the maximum shear stress experienced along the particle trajectories for the CM and SJM regular hinges. The histogram shown in green pertains to the CM regular hinge while the red one corresponds to the SJM regular hinge. The cumulative distribution plotted on a log scale is also provided.

Previous blood studies have shown that the estimation of shear stress levels alone is not sufficient to understand hemolysis and platelet activation. Researchers have emphasized the need to consider shear stress levels in conjunction with exposure time to obtain a more realistic estimate of the blood damage potential. With this in mind, two previously-published blood damage models, combining exposure time and shear stress levels (section 3-6-2), were applied to the Lagrangian results to obtain a measure of hemolysis and platelet activation. Two indices were computed, a blood damage index for hemolysis (BDI^{H}) and another one for platelet activation (BDI^{PL}). It is important to recall here that the particles considered in the present Lagrangian analysis are weightless point particles that represent indistinctly red blood cells and platelets.

These two indices, BDI^{H} and BDI^{PL}, were computed along all particle trajectories, independently of their seeding times, and their cumulative distribution was estimated. The cumulative distribution corresponds to the percentage of particles experiencing a BDI larger than a particular value and is provided, for both SJM and CM hinge designs, in Figure 5-24. The overall distribution of BDI is similar in both hinge configurations, with as expected a decaying distribution from small BDI to large BDI. It is evident that, at the exception of small BDI levels for which the distribution is similar ($BDI^{H}<0.1$ and $BDI^{PL}<0.45$), the histogram bars representing the CM hinge are consistently above those of the SJM large hinge. This strongly suggests that the CM hinge has a higher propensity for hemolysis and platelet activation compared to the SJM hinge.

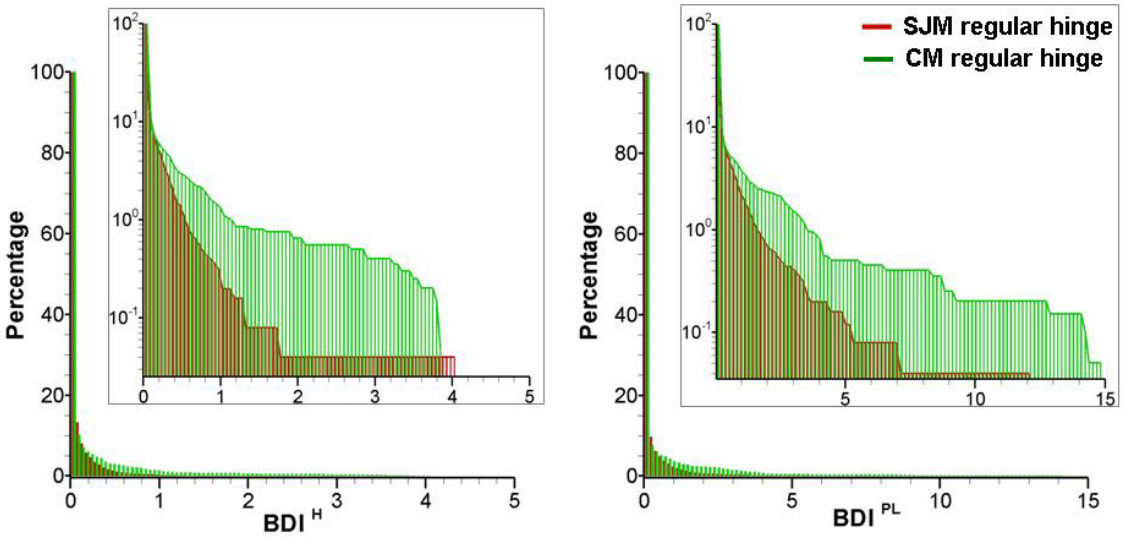

Figure 5-24: Cumulative distribution of the blood damage indices for hemolysis (left) and platelet activation (right) as a function of the particle percentage. The histogram shown in green pertains to the CM regular hinge while the red one corresponds to the SJM regular hinge. The cumulative distribution plotted on a log scale is provided for both blood damage indices.

5.3.4 Concluding remarks

The above discussion underscores the considerable influence of the hinge design on the flow features, the shear stress distribution, and the resulting blood damage potential. These flow and shear stress analyses collectively suggest that overall the CM hinge design is the least optimal from a blood-cell standpoint. Comparison of the flow performance of the SJM and CM hinges suggests the existence of a good washout of the SJM hinge and regions of low flow with long residence time in the CM hinge. Flow washout is important to dislodge possible thrombi and avoid platelet aggregation while regions of low flow, on the opposite, are known to favor cell-to-cell contact and platelet aggregation. Moreover, compared to the SJM regular hinge, the CM hinge exhibited a greater propensity for platelet activation and hemolysis. This correlates well with previous *in vitro* and clinical studies which suggests that the CM hinge induces more

detrimental flow conditions than the SJM hinge [32, 36], and higher clinical complication rate for the CM hinge [90].

From a design perspective, the curved tip of the CM corners was found to promote the formation of localized flow jets with large shear stress levels. Corner featuring straight wall rather than curved wall might therefore be more favorable. As underscored by the present study, the smooth streamlined profile of the SJM hinge, which exhibits a gradual change in geometry, reduces the propensity for flow separation, and therefore region of low flow, while ensuring a good washout of the entire hinge recess. In contrast, the angulated design of the CM hinge disrupts the flow and promotes flow separation, favoring region of low velocities and large shear stresses, which are known to be detrimental to blood elements. These geometrical considerations correlate with previous experimental findings on the pro-coagulant properties of flow fields through various orifices [96], which showed that abrupt geometry is more detrimental to blood elements than smooth geometry.

5.4 Implications of the Current Study for Hinge Design Optimization

In the present study, the effect of the hinge design on the flow fields, and subsequently on the platelet activation and hemolysis potential, was investigated. Two main geometrical factors were considered, the curvature of the recess and leaflet walls and the dimension of the hinge gap width. To this purpose, the performance of a SJM hinge with a regular and a large hinge gap width and the performance of a CM hinge were compared and related to previously-published clinical data. This comparative assessment permits us to draw several conclusions essential to the improvement of the hinge design of bileaflet mechanical heart valves. Three main parameters are to be considered to improve on the design of the hinge: 1) high shear stress levels should be

minimized to reduce blood damage, 2) regions of low velocities, and in particular region of low recirculating flow, should be diminished to limit thrombus formation, and 3) regions of high velocities should be favored as they ensure a good washout on the hinge. However, it should be pointed out that such regions of large velocities might not only be associated with large shear stresses but also dislodge thrombi increasing the risk for thromboembolism. The optimization parameters are thus closely related, making the design of an optimal hinge recess a challenging exercise.

The analysis of the shear stress distribution clearly pinpoints the diastolic phase as the most detrimental phase of the cardiac cycle, independent of the hinge design. Indeed, the Eulerian assessment of the flow revealed that the shear stress levels are higher and occupy larger areas after valve closure than during the forward flow phase. Similarly, a close inspection of the shear stress history indicated that the particles were subjected to the largest shear stress levels when leaking back through the valve during diastole. It is therefore evident that platelet activation and hemolysis are most likely to occur during the leakage flow phase. Elevated shear stresses, above the threshold for blood damage, were also computed during the forward flow phase. Unlike the diastolic regions of elevated shear stresses, these systolic regions of high shear stresses did not pertain to the hinge recess itself, irrespective of the hinge design under consideration. Rather, the high systolic shear stresses were identified immediately upstream of the hinge, in the gap formed by the leaflet and housing surface.

For all three hinges, the forward flow phase was associated with slower velocity magnitude than the leakage flow phase. This suggests a higher risk for thrombosis during systole. Indeed, regions of low flow are known to promote thrombus formation by increasing residence time within the hinge recess and enhancing cell-to-cell contact. Hinge design should therefore seek to minimize regions of low flow. This is all the more

important if fast-paced flows appear in similar regions at a later time of the cardiac cycle. These rapid flows, while providing a good washout of the hinge, may dislodge thrombi and therefore increase the risk for thromboembolism.

From a design point of view, the above observations imply that in order to reduce the potential for thromboembolism, the hinge recess should be conceived so as to reduce high shear stresses during the leakage phase to minimize blood cell trauma, and reduce the extent of the regions of low velocities during systole to prevent thrombosis.

Several parameters may be considered when optimizing the performance of the hinge design. Simple variations in dimension may play an essential role in the overall performance of the design. Previous researchers have shown that the hinge gap width has a significant effect on platelet damage [34], and reported higher blood cell trauma in hinges with small and large hinge gap width compared to those with a regular gap width. Consequently, a hinge design with an optimal hinge gap width may exist and help in improving the hemodynamics and reducing the potential for thrombosis, platelet activation, and hemolysis. It should be pointed out, however, that in an experimental set-up the effect of hinge gap width alone is difficult to isolate due to the degrees of freedom of the leaflet. Indeed, in actual clinical valves, the leaflets are not only free to rotate but also to translate within the hinge recess, in particular up and down along the leaflet axis. Herein, the effect of the hinge gap width is investigated, by considering two identical SJM hinges and solely varying the dimension of the gap width. Comparative analysis of the hemodynamics of the two hinge configurations indicated some differences not only in velocity distribution but also in shear stress distribution. A slightly larger portion of the particles seeded in the SJM large hinge experienced detrimental conditions compared to the SJM regular hinge. This translated into small differences in blood damage indices between the two hinge configurations. However, it should be underscored that only a

single cardiac cycle was considered in this study. In reality, the heart beats 70 times per minute, and as such, the cumulative effect of repeated exposure to slightly different shear stress levels may ultimately translate into significant performance differences between the two hinge configurations. The range of possible dimensions for the hinge gap width is intrinsically dependent on the manufacturing constraints. A thorough investigation of a wide range of hinge gap width that the valve manufacturer could realistically envision to produce would constitute the necessary parametric studies to determine the optimal hinge gap width.

Dimensional parameters should not be overlooked in the design of new hinge regions. However, as was demonstrated here by the larger differences observed between the SJM and CM hinge designs compared to the differences between the two SJM hinges of varying gap width, the influence of the overall hinge design itself is likely to overshadow the impact of the dimensions. Clinical studies corroborate this observation and have shed some light on the design parameters that may influence the valve success rate. The Medtronic Parallel (MP) valve was found to have unacceptably high thrombosis complication rates while the CM and SJM valves have good clinical outcomes, with the SJM valve exhibiting less thrombogenic complications than the CM hinge [90]. The hinge design of the MP valve explains its poor performance. Indeed, the complex hinge design with sudden expansion and contraction regions is thought to disrupt the flow, leading to detrimental regions of low flow and high shear stresses [26, 97]. Similarly, the difference in the clinically observed thrombogenic complications between the SJM and CM hinge are considered to be due to the difference in hinge design, and thus in hinge flow fields. This is in agreement with the present study which underscores the large influence of the hinge design on the flow fields, shear stress distribution and resulting blood damage potential. Regions of low flow were found to occur predominantly in the CM hinge, suggesting a higher propensity for thrombosis

than in the SJM hinge. Moreover, the comparative analysis of the particle history suggests a higher incidence for platelet activation and hemolysis in the CM hinge. These findings not only suggest that the SJM design is more optimal than the CM valve design from a blood-cell standpoint, but also points to the importance of the hinge geometry. From a design perspective, the SJM design provides a streamlined hinge profile characterized by a gradual change in geometry. Blood flowing through the hinge follows the smooth inside surface of the hinge, thus reducing the propensity for flow separation and regions of low flow, as noted in the present study. In contrast, the angulated design of the CM hinge disrupts the flow, promoting flow separation and favoring region of low velocities. These geometrical considerations lead to the conclusion that abrupt changes in curvature and sharp angles should be avoided in favor of smooth shape transitions. Finally, the curved tip of the CM corners was found to promote the formation of localized flow jets with large shear stress levels, which are known to be detrimental to blood elements. Using straight rather than curved corners might therefore be more favorable, ensuring that the leaflet ear sweeps the entire hinge recess and avoiding the formation of localized high velocity jets.

It is important to recall, that despite its good clinical performance, SJM valve can still cause thromboembolic complications and patients with such an implant must undergo lifelong anti-coagulation therapy. Hence, even though, it is established that smooth streamlined hinge geometry functions better than abrupt design, improvement of the smooth geometry of SJM hinge recess is still possible. The present study shows four main regions within the hinge recess that are associated with elevated shear stresses during the leakage flow phase. These regions are the wall of the ventricular corner, the tip of the lateral corner, the wall of the adjacent corner; and finally the bottom of the hinge recess. All these four regions are located in the vicinity of the recess wall, which suggests that the wall curvature play a key role in the shear stress distribution. Testing

different smooth hinge designs with varying wall curvature would be of interest to determine the optimum curvature to minimize shear stress levels. Optimization of the curvature of the recess wall should be done in conjunction with that of the leaflet ear. Inspection of the shear stress distribution revealed that elevated regions of shear stresses were also present, during the leakage flow phase, along the wall of the leaflet ear. Particular emphasis should therefore be placed on the design of the leaflet ear to minimize the large shear stresses that are present in this region. Additionally, the close inspection of the flow fields in the SJM recess underscores the presence of regions of low flow, known to be favorable to platelet aggregation. These regions of low flow were identified as region of flow separation induced by fast flowing jets detaching from the valve housing. Modifying the hinge design to reduce the formation of flow jets is expected to in turn reduce the formation of low flow regions. Moreover, to minimize flow separation, one may envision altering the hinge geometry near the flat level at the edge of the recess. Abrupt edges would yield immediate flow separation while a more rounded edge would reduce it. Change in the curvature of the hinge edges may therefore improve the propensity for platelet aggregation and thrombus formation. Optimal curvature of the hinge wall and edges will result in a tradeoff between a slow transition in geometry and imposing sufficient constraints on the leaflet ear to maintain it in position. The aforementioned improvements, focused solely on the hinge recess could possible be combined with modifications in the near-hinge region, such as including a bi-level flat level. The dual-level flat level, characteristic of the Medtronic Advantage valve, has been shown *in vitro* to be beneficial and reduce the potential for stagnation region [98]. Altering the hinge recess but also the near hinge region by including a bi-level flat design feature, is expected to improve the hinge performance and thus reduce the overall valve thrombogenic complication rate.

Finally, another aspect of the hinge optimization that should not be disregarded is the implant location. The present study focuses on the aortic position, but previous experimental studies have shown that the implant location is a critical design parameter [36, 87]. Prosthesis implanted in the aortic or mitral positions are not subjected to the same flow and pressure conditions, and thus the hemodynamics in the hinge region differs. In order to achieve further reductions of thrombosis rates and to limit the need for lifelong anticoagulation therapy, importance of the implant location may have to be emphasized during the conception and design phase of future valve prostheses.

The above discussion underscores several possible areas of improvements to reduce flow-induced hemolysis, platelet activation, and thrombosis in the hinge region. It is evident that conceiving an optimal hinge design, with minimal thrombogenic potential, requires large parametric studies to investigate the individual or combined influence of various design parameters. Performing these studies *in vitro* would be time-consuming and require the manufacturing of every prototype envisioned. Numerical approaches, such as the numerical framework developed in the present study, applied to a wide range of hinges would allow for a rapid and cost-efficient assessment of the fluid dynamics performance of different designs and eventually help in determining the optimal hinge design.

CHAPTER 6

LIMITATIONS

6.1 Boundary conditions

A one-way coupling is implemented between a large-scale FSI model and the present hinge model. During the forward flow phase, this coupling is achieved by imposing the systolic velocity profiles extracted from the large-scale simulation of the bulk flow through a BMHV as inflow boundary conditions for the micro-scale hinge model. During the leakage flow phase, on the other hand, the flow boundary conditions are set such that the resulting cross-valvular pressure gradient reaches a physiologic value of approximately 80 mmHg at mid-diastole. This approach ensures that the physiologic environment of the hinge is reproduced as closely as possible. However, one instance in time that this modeling approach does not allow to capture is the instant of valve closure. In this study, this instant is modeled by 1) prescribing the leaflet motion computed by the large-scale FSI solver, with the exclusion of the leaflet rebound occurring right after valve closure and 2) gradually increasing the cross-valvular pressure and flow rate to their diastolic value. In reality, experimental studies have shown that the abrupt closure of the leaflet against the valve housing gives rise to a sudden increase in velocity magnitude and cross-valvular pressure gradient. Numerical modeling of this sudden pressure build-up could only be achieved by simultaneously simulating the leaflet kinematics and the local hemodynamics. As discussed in Chapter 5, this would require the implementation of a full two-way coupling between the large-scale and the micro-scale hinge flow solvers.

The sudden increase in cross-valvular pressure gradient at valve closure is believed to be associated with elevated shear stresses that are detrimental to blood elements. Smoothing the valve closure flow dynamics by progressively transitioning the flow and pressures from their systolic to their diastolic values will thus most likely yield an underestimation of the shear stresses experienced by the blood elements, and in turn to an underestimation of the hinge thromboembolic potential. However, all investigated hinge designs suffers from the same limitation. As a result, the hinge ranking drawn from the current work based on hemodynamic and thromboembolic performance of the hinge designs is expected to be comparable to the one that would have been drawn with the inclusion of the exact valve closure instant modeling. Nonetheless, a study specifically focusing on valve closure would shed more light into the influence of the hinge design during this particle instant of the cardiac cycle.

6.2 Leaflet motion

In actual clinical BMHVs, the leaflet is free to both rotate and translate within the hinge recess. While the translational motion of the leaflet is considered to have a minor, if not negligible, effect on the bulk valvular flow field, this motion is believed to have an impact on the hinge flow fields. Even so, this translational motion is ignored in the present hinge study due to the coupling approach between the large-scale and hinge model. Indeed, the leaflet motion imposed in the present micro-scale hinge studies is directly extracted from the large-scale FSI simulations. In these large-scale simulations, any translational motion was neglected and the leaflet was assumed to only have one degree of freedom: rotation around a fixed hinge axis. Moreover, previous studies have shown that the motion of the two leaflets of a same BMHV is not synchronized and that variations in leaflet motion exist between the two leaflets and from cycle-to-cycle [62].

Capturing numerically the complex leaflet motion, including the translational and rotational motion and the cycle-to-cycle variations, constitutes a numerical challenge itself. This would not only require conducting simulations over multiple cycles, but also modeling the entire valve domain, and each of the four hinges, as the assumption of valve symmetry would not hold. Moreover, such simulations would require a highly refined numerical mesh, in particular in the peripheral gap region to appropriately model the leakage flow features during diastole. A two-way coupling between the large and small-scale flow solvers, as described in Chapter 8, is expected to provide the necessary numerical tool to model the complexity of the leaflet motion. It should also be noted that in the present study, the leaflet rebound that occurs immediately after valve closure was neglected. It is anticipated that the leaflet motion plays a major role in the hinge fluid dynamics and on the flow-induced blood damage. More realistic representation of the leaflet motion is thus expected to yield a more accurate estimation of the hinge performance.

6.3 Spatial and temporal considerations

In the present study, the fluid domain was discretized with a Cartesian non-uniform grid of nearly 6 million grid nodes. By selectively stretching the Cartesian grid, a minimum of 80,000 nodes could be obtained in the fluid region of the hinge recess itself. The current grid reaches the limit of the computational resources currently available and, thus, a detailed grid refinement study, with even finer grids, could not be performed. It is expected that the ever-improving capabilities of computer clusters and the implementation of a two-way coupling approach, as described in Chapter 8, would allow to further improve the spatial resolution within the hinge and mesh refinement studies focusing on the hinge region could thus be undertaken.

In this study, the simulations were limited to a single cardiac cycle and only the first half of the cardiac cycle, from early systole to mid-diastole, was modeled. Simulations over several cardiac cycles would minimize the influence of the initial conditions. Moreover, modeling of several cardiac cycles would permit the investigation of possible cycle-to-cycle variations. It should also be noted that the temporal discretization of the cardiac cycle dictates to a certain extent the exposure time during which the blood elements are subjected to specific fluid shear stress forces. The blood elements in reality experience the instantaneous fluctuations of the viscous shear stresses. It is therefore essential to perform the simulations with good temporal resolution to suitably estimate the shear stress history and blood damage potential of the blood elements.

6.4 Hinge and valve models

In the present numerical simulations, the BMHV, and thus its associated flow fields, are considered symmetric. The planes of symmetry are used to reduce the overall computational domain so as to only model only one of the four hinges with high spatial resolution. However, as was observed in the numerical results reported herein as well as in earlier qualitative static leakage flow experiments [87], the leakage jets emanating from the hinge region through the closed valve are highly three-dimensional. Because of the proximity of the hinges on each side of the leaflets and the three-dimensionality of the flow emanating from the hinge, it is suspected that the hinge flows interact with one another during diastole. Modeling one half of the valve and thus a pair of hinges, rather than a quarter of the valve and a single hinge, would help in elucidating the possible hinge flow interactions.

The numerical model used in the large-scale FSI simulations is composed of a BMHV inserted in between a straight pipe, figuring the left ventricle (LV), and a straight chamber with an axisymmetric expansion representing the aorta and its sinus region. The numerical model used in the current hinge simulations corresponds to a section of the large-scale model. Accordingly, the LV and the aorta are also considered as straight rigid pipes. However, in the human anatomy, the geometry of the left side of the heart is far more complex, with a conical-like LV and a curved aortic arch. The aortic geometry, as well as the valve orientation with respect to the aorta geometry have been shown to have an impact on the bulk valvular flow field [99-102] and are thus likely to also impact the hinge flow fields. Moreover, during the cardiac cycle as the heart contracts and relaxes, the annulus plane of the aortic valve moves, the aortic root expands and contracts, and more importantly the LV greatly deforms in shape. Considering a straight, rigid static pipe both upstream and downstream of the aortic valve is thus a limitation of the numerical model.

Regarding the hinge geometries themselves, both the SJM and CM hinges are reconstructed from the micro-computed tomography (CT) scans of two clinical valves. This reverse-engineered approach to generate the hinge geometrical features is believed to yield the best possible computational meshes in order to closely model the hinge region of actual clinical valves. Moreover, the micro-CT is also used to estimate the nominal hinge gap width. However, it should be underlined that because of the very own existence of these recess-leaflet gap within each of the leaflet hinges, the leaflets are actually “free-floating” and are able to move. Therefore, the measured hinge gap width might not exactly correspond to the hinge gap width originally intended by the manufacturer. This, combined with the unknown manufacturing tolerances, implies that differences in nominal hinge gap width between the numerical model and the clinical valve might exist.

In order to investigate the effect of the hinge gap width on the flow fields, two identical SJM hinges with distinct hinge gap widths are studied. The only difference between the two hinges lies in the position of the leaflet with respect to the bottom of the hinge recess. However, the shifting of the leaflet within the hinge recess not only changes the hinge gap dimensions but also the peripheral gap (gap between the leaflet and the valve housing). The effect of the hinge gap width is thus herein combined with that of the periphery gap dimension. In order to isolate the effect of the hinge gap width on the hinge flow fields, a more rigorous approach would have been to redesign the leaflet ear rather than shifting the entire leaflet out of the recess. This could have been achieved by reducing the length of the leaflet ear without affecting the remainder of the leaflet. Eventually, parametric studies could be conducted to assess the optimal length to width ratio for the leaflet ear, or for instance the optimal curvature for the ear and hinge recess surfaces. However, such design optimization is beyond the scope of the current study. The results presented herein lay the grounds for hinge design optimization and demonstrate the strength of the developed numerical framework, paving the ground for futures parametric studies.

6.5 Blood properties

In the present numerical solver, the blood is modeled as an incompressible single-phase Newtonian flow. Assuming Newtonian properties and neglecting the multi-phase characteristic of the blood allows for a comparison of the numerical results with experimental findings. Indeed, *in vitro* experimental studies of the hinge flow fields are commonly conducted with a Newtonian working fluid generally made of 79% saturated aqueous sodium iodide solution, 20% glycerin, and 1% water by volume [30, 31, 36, 91, 97, 98]. This blood analog fluid has a kinematic viscosity of 3.5 cSt that matches that of

blood at high-shear rates and its refractive index is commonly adjusted to allow the use of optical measurement technique and avoid optical distortion. In reality blood is a particulate fluid and exhibits non-Newtonian properties, both of which are un-captured with the viscosity-matched fluid used in the experimental setting. Previous researchers have determined that at relatively high rates of shear, the blood viscosity can be considered constant [103]. In large blood vessels, such as the aorta, the shear rate is well above the accepted threshold of 100 s^{-1} and, thus, a Newtonian description of the flow is acceptable. However, in small blood vessels, such as arterioles and capillaries, the shear rate is very low. There, the blood exhibits a non-linear relationship between shear stress and shear rate and thus shows non-Newtonian flow properties. The complex hinge region features small gaps, but the hinge is also characterized by fast-flowing blood, in particular during the leakage flow phase. As a result, the shear rate in this region exceeds the threshold of 100 s^{-1}. However and more importantly, because of the small dimension of the hinge, large cell-to-cell interactions are expected between the red blood cells and platelets. These interactions are known to strongly influence the overall trajectory and behavior of the particles. As a result, the validity of the Newtonian single-phase flow assumption used to describe the flow in the hinge recess is limited.

6.6 Particle tracking algorithm

The transport of blood elements by the hinge flow fields is assessed by performing a Lagrangian analysis of the flow. Approximately 300 particles are seeded at regular time intervals within the recess of all three hinge configurations and the position of these particles is tracked with time. Because the particles are seeded with the same density and in similar locations, this methodology permits to compare the performance of the three hinges. However, while the particle seeding achieved in this study reaches the

limits of our computational power, it is still limited when compared to the density of the red blood cells or platelets flowing through the hinge. The particles are released within the hinge recess at an approximate density of 200 particles/mm^3. A single cubic millimeter of blood contains about 4,000 to 6,000 red blood cells and 200 to 500 platelets. A finer particle seeding, with a larger number of particles released more frequently, is expected to provide a better sampling of the hinge flow features and deeper insight into the influence of the hinge design. It should be pointed that a single cardiac cycle was considered to estimate the particle trajectories. However, to get a better representation of the shear stress history experienced by blood elements crossing through the hinge recess, several cardiac cycles should be considered as blood elements may stay in the vicinity of the valve and make several passes through the hinge region over several cardiac cycles before flowing away in the circulatory system.

Moreover, it should be pointed out that in this analysis, several assumptions are made. The particles are assumed to be neutrally buoyant weight-less point particles that are passively advected by the flow. Their trajectories are assumed to be representative of both red blood cells (RBC) and platelet trajectories. In reality the motion of RBC and platelets are expected to differ due to their difference in size, shape and mechanical properties. Moreover the particulate property of the blood is believed to play a key role in the blood cell distribution and global flow fields due to the cell-to-cell, cell-to-valve and cell-to-surrounding fluid interactions.

The shear stress along the trajectories of the point particles is considered to be representative of the shear stress experienced by a red blood cell or platelet flowing along the same trajectory. In reality, the blood cells are not single points but have a volume and thus the shear stress is expected to vary along the membrane surface. This is especially true in the case of the red blood cells, which are approximately four times as large as platelets and have a highly deformable membrane. The relatively large

volume occupied by a single red blood cell and the deformable membrane are likely to induce some differences between the computed shear stress values representative of the cell center and the actual true shear stress experienced by the cell.

Nonetheless, the proposed approach provides a good approximation of the thromboembolic potential of the hinge recess. Modeling particulate blood flow, with realistic hematocrit level and taking into account cell-to-cell interactions constitutes a challenge of its own. To date, most particulate blood flow models are limited to two-dimension [104]. Three-dimensional models have been developed as well, but even most advanced studies to date are still performed at lower than physiological levels of hematocrit with limited number of red blood cells in simple straight pipes of very small volume (less than 1 μl) [105, 106]. Extending these three-dimensional models to clinically relevant hematocrit levels and to blood volumes as large as the fluid domain considered in the present simulations is thus beyond current numerical capabilities.

In brief, the current study presents a numerical framework for the detailed investigation of the micro-scale hinge flow fields and their associated thromboembolic potential. This framework aims at improving the clinical success of bileaflet mechanical heart valve by providing a mean to reduce the hinge thrombo-embolic potential and thus easily optimize hinge design. Most of the limitations cited above point towards possible improvements to better model the actual hemodynamics experienced by the platelets and red blood cells. Exact modeling of valve closure dynamic, particulate flow simulations, use of realistic blood properties, and fine parametric variations of the leaflet and recess designs constitute as many directions that could be investigated in future studies.

CHAPTER 7

CONCLUSIONS

The present study demonstrates that numerical approaches provide the essential framework to estimate the hemodynamic performance and thromboembolic potential associated with a given hinge design, and more importantly to pinpoint areas of possible design improvement. Such numerical tools applied to a wide range of hinge designs are essential to improve and refine the geometrical hinge features and eventually reduce the propensity for thromboembolic complications associated with current BMHVs. This study further underscores the intricacy of the hinge flow fields with high three-dimensionality and important levels of unsteadiness. Sophisticated computational fluid dynamics tools implemented at the micro-scale level are thus paramount to conducting of hinge optimization studies, in order to ensure that all relevant temporal and spatial length scales are properly captured and that the associated results are of clinical relevance.

Computational approach

The current study presents a numerical solver capable of performing full three-dimensional pulsatile simulations on a dense computational mesh to appropriately capture the complex spatial and temporal three-dimensional hinge flow structures. The complexity and unsteadiness of the flow in the hinge recess arise from the pulsatility of the flow, the complexity of the recess geometry, and the flow-dependent motion of the valve leaflets. The present numerical methodology allows for high accuracy pulsatile simulations to be performed by 1) employing a second order accurate, unsteady, implicit flow solver, 2) making use of an immersed-boundary formulation to capture all

geometrical intricacies, and 3) using a pseudo multi-scale approach for optimally decomposing the computational domain and prescribing realistic leaflet motion and flow boundary conditions. Decomposition of the valve flow domain into the bulk flow fields on the one hand and the hinge-specific model on the other, allowed for very high spatial resolution with a mesh spacing on the order of 8 μm within the hinge recess. This approach addresses the shortcomings of earlier hinge investigations, which either used two-dimensional domain, coarse grids or highly idealized geometries and flow conditions. This approach, combined with a Lagrangian methodology, allows for the first time for the full resolution and analysis of the 3D flow motion within realistic hinge designs.

In order to closely reproduce the *in vivo* hinge flows, the inflow/outflow boundary conditions were carefully selected so as to replicate the physiological aortic flow environment as best as possible. A pseudo multi-scale approach was therefore implemented by performing a one-way coupling between large-scale and small-scale simulations. This approach consisted of two main parts: 1) extracting the boundary conditions for the hinge simulations from the Fluid-Structure-Interaction (FSI) simulations of a BMHV bulk flow and 2) imposing physiologic pressure drop during the closed phase. Such an approach ensured that realistic physiologic flow conditions were applied in the hinge solver and consequently that the complex *in vivo* hinge flow features were reproduced as closely as possible. Comparison of the computed flow features were found to be in good agreement with previous Laser Doppler Velocimetry experimental data acquired in the hinge region of a clear-housing BMHV valve.

Finally, Micro-Computed Tomography was used to extract the geometrical features of the hinge geometry from actual clinical valves and generate accurate computational meshes. This approach provided the necessary realistic hinge geometry

models to perform numerical simulations and accurately assess the performance of the hinge design.

The carefully selected physiologic flow boundary conditions, the realistic hinge recess geometries, the three-dimensional pulsatile simulations, and the fine numerical mesh permitted to conduct a three-dimensional study of the hinge recess with elevated spatial and temporal resolution and provide details at a level not achievable by experiment alone. The Lagrangian analysis of the hinge flow fields, combined with existing blood damage models, provided the necessary mean to compute surrogate measures of the levels of platelet activation and hemolysis induced by the hinge flow fields.

Main characteristic of the hinge flow fields

The present study provided a thorough insight into the flow structures within three different hinge recesses and in their vicinity while subjected to physiological aortic conditions. Good qualitative agreement was achieved between the computed hinge flow fields and experimental Laser Doppler Velocimetry data. The numerical findings highlighted the complexity and three-dimensionality of the hinge flow fields throughout the cycle, which couldn't be fully assessed using *in vitro* experiments alone. Detailed analysis of the three-dimensional hinge flow fields, description of the principal shear stress distribution and assessment of the particle pathlines in the hinge and near-hinge region permit to draw some general conclusions on the fluid dynamics of the hinge.

Independently of the hinge design, several main flow phenomena were identified as detrimental to the blood elements for all three investigated hinge designs. The shear stress distribution and the Lagrangian flow analysis pointed to the diastolic phase as the most detrimental phase of the cardiac cycle. During this phase and due to the large shear stress levels computed, the potential for platelet activation and hemolysis is

expected to be the highest. The bottom of the hinge recess and the wake of the leakage jets were identified as the most harmful regions from a blood-cell standpoint. During the forward flow phase, the shear stress levels were lower. Nonetheless, peak systole was identified as a possible phase for blood damage to occur as shear stress levels above the threshold for platelet activation were computed in the near hinge region. Characterization of the shear stress levels is important to assess the risk for blood cell trauma. However, another important parameter to consider is the risk for thrombosis. Regions of low and recirculating flow, thereby with important risk for platelet aggregation and thrombosis, were identified during systole in all three hinges. These observations clearly indicate that, regardless of the hinge design, the systolic phase is prone to thrombosis while the diastolic phase is plagued by an elevated risk for hemolysis and platelet activation.

Comparative assessment of the hemodynamic performance of different hinge designs.

In the present study, the influence of the hinge design on the flow fields and the thrombogenic potential was investigated. Two major geometrical parameters were considered: 1) the role of the hinge gap width was evaluated by estimating the performance of a SJM hinge with a regular and a large hinge gap width and 2) the effect of the wall curvature was assessed by comparing the performance of a St. Jude Medical hinge with that of a CarboMedics hinge. The computed hinge flow fields and resulting blood damage indices were related to previously-published clinical data.

Effect of the hinge gap width

Comparison of the flow distribution between the two SJM hinges pinpointed to lower velocities in the SJM regular compared to the SJM large hinge. This in turn,

suggested a slightly higher propensity for platelet aggregation in the SJM regular hinge by enhancing cell-to-cell contact.

The Eulerian shear stress distribution indicated that the peak shear stress levels were larger in the SJM regular hinge, but, shear stress is to be considered with exposure time to truly estimate the potential for blood cell trauma. Consequently, particles seeded in the hinge recess were tracked with time. Analysis of the shear stress history experienced along the particle paths did not permit to specifically designate one hinge design as superior than the other. However, previous blood studies have concluded that a large hinge gap width might be more detrimental to blood elements. It is therefore suspected that the influence of the hinge gap width on the flow fields exists but is minor. It is expected that a finer particle seeding, with more particles released more frequently and tracked over several cardiac cycles, would to provide deeper insight into the effect of the hinge gap width by highlighting the differences existing between the two hinge configurations.

Effect of the recess wall curvature

Contrary to the hinge gap width, the hinge design, and in particular the curvature of the recess wall, was found to have a considerable influence on the flow features, the shear stress distribution, and the resulting blood damage potential. The performance of the CM hinge was hindered by two major shortcomings. The CM hinge was found to be associated with regions of low flow with long residence time while good flow washout was noted in the SJM hinge. Regions of low flow favor cell-to-cell contact and platelet aggregation and therefore suggest a higher potential for thrombosis in the CM hinge. Secondly, the particles crossing the CM hinge recess were found to experience more detrimental flow conditions than the particles crossing in the SJM hinge. The resulting blood damage indices were therefore higher in the CM hinge compared to the SJM

hinge. This clearly indicated a greater propensity for platelet activation and hemolysis in the CM hinge. These two observations together suggest that the CM hinge design is the less optimal from a blood-cell standpoint. This correlates well with previous *in vitro* and clinical studies which suggest that the CM hinge induces higher clinical complication rate than the SJM hinge.

Design considerations

The present comparative assessment of three hinge configurations permits to extract some essential information regarding possible improvements of the hinge design of bileaflet mechanical heart valves. Several parameters may be considered to optimize the performance of the hinge design. Simple variations in dimension may play a small, yet essential role in the overall performance of the design. A thorough investigation of a wide range of hinge gap widths would constitute the necessary parametric study to determine the ideal hinge gap width.

Dimensional parameters are important but their impact of the flow is lesser than that of the overall hinge design itself. The present study clearly underscores the large influence of the hinge design on the flow fields, the shear stress distribution, and the resulting blood damage potential. The CM hinge was found to have a higher propensity for thrombus formation compared to the SJM hinge. This suggests that abrupt hinge design disrupts the flow, thereby promoting flow separation, regions of low velocities, and in turn, thrombosis. Smooth streamline hinges, with gradual changes in the geometry should therefore be preferred to angulated geometries.

The design of the hinge corners themselves was also established to play an important role in the overall performance of the hinge. The curved tip of the CM corners promoted the formation of localized jets and large shear stress levels, which are known

to be detrimental to blood elements. From a design perspective, corners featuring straight wall rather than curved wall might therefore be more favorable.

It is evident from these geometrical considerations, that smooth geometries should be favored to abrupt geometries to minimize the complication rates induced by the hinge flow. Concordant with that statement, the SJM hinge, which is characterized by such a smooth streamlined geometry, was the best design of the present study. Nonetheless, the SJM hinges are still known to cause thromboembolic complications and patients with such an implant must undergo lifelong anti-coagulation therapy. Hence, improvement of the smooth geometry of SJM hinge recess is still possible. The present studies identified few regions within the hinge recess associated with elevated shear stresses. These regions, all located along the recess wall, point to the wall curvature as a possible parameter for improvement. Moreover, elevated shear stresses were also found near the wall of the leaflet ear. Optimization of the curvature of the recess wall should therefore be done in conjunction with that of the leaflet ear in order to minimize shear stress levels and reduce the risk for platelet activation and hemolysis. Additionally, regions of low flow were identified in the SJM hinge, suggesting room for possible improvement and reduction of the risk for thrombosis. These regions of low flow were mainly due to flow separation following the formation of strong flow jets. Altering the edges of the hinge recess, by incorporating more rounded edges, or modifying the near hinge region, by including a bi-level flat level such as that in the Medtronic Advantage valve, could potentially reduce flow detachment and thus limit the formation of low flow regions.

Potential of computational tools to be used as optimization tools

The comparative assessment of the three hinge designs performed in the present study allowed drawing several conclusions on possible hinge design

improvement and subsequent reduction in flow-induced hemolysis, platelet activation and thrombosis. However, conceiving the ideal hinge design would require parametric studies in order to test a large number of prototypes and determine the most optimal design. The numerical framework, developed herein, allows such parametric studies to be performed rapidly. The Eulerian analysis provides instantaneous information on the hinge flow fields and shear stress distribution and help pinpointing detrimental regions of the hinge, while the Lagrangian analysis appears as the necessary complement to truly understand the flow environment experienced by the blood elements flowing through the hinge recess. Hence, this study not only provided some insight into design improvement, but underscored the potential for numerical approaches for refining and improving existing bileaflet mechanical heart valves.

CHAPTER 8

RECOMMENDATIONS

8.1 Multi-scale modeling

One of the main challenges to simulate the BMHV flow fields stems from the large-disparity of characteristic length scales, ranging from several millimeters in the valve diameters down to a few hundred microns in the hinge recess. Ideally, the micro and large-scale flow features should be solved simultaneously to accurately predict the complex BMHV fluid mechanics. However, with the currently available computational resources and numerical algorithms, it is impossible to perform full multi-scale simulations of the BMHV flows while retaining a good spatial and temporal resolution. It is expected that with the ever-growing and improving capabilities of computer cluster this challenge will be overcome. A full two-way coupling approach between the large-scale and micro-scale solvers will provide the required mean to simultaneously and accurately compute the bulk valvular flow fields and the hinge fluid dynamics. A couple of approaches can be envisioned to perform such sophisticated simulations.

Accurate modeling of both the micro and large-scale flow features requires the use of a suitable numerical mesh, whose resolution is constrained by the smallest characteristic scale to be captured. In the simulations of the bileaflet mechanical heart valve flows, the mesh resolution is thus dependent on the scale of the hinge flow features. However, using a single highly-refined grid to discretize the entire computational domain and ensure that the hinge flow fields are accurately modeled is unrealistic. Instead of using a single grid, one may envision employing a Chimera

overset grid method. This method consists of constructing a grid system made up of blocks of overlapping grids: one block could correspond to the bulk flow domain, while smaller blocks with a finer mesh resolution could be specifically used to discretize the hinge and near-hinge region. Such a Chimera overset approach would permit to represent the hinge recess independently from the bulk flow domain, thereby ensuring a high spatial accuracy in the hinge region without tremendously increasing the computational effort due to the use of unnecessarily refined mesh in the bulk of the flow. The large-scale flow solver could then be applied to the coarse block, while the highly refined block could be treated with the hinge flow solver.

Another possible approach would consist of implementing an adaptive mesh refinement method. Such a method allows the use of high resolution grids only at the physical locations where they are required. The main concept behind this method is the sub-division of selected grid cells to achieve the necessary resolution in specific regions of the computational domain. Adaptive mesh refinement methods could therefore be applied to locally increase the grid resolution in the hinge region.

The implementation of a Chimera overset grid method or an adaptive mesh refinement method would make it possible to simultaneously capture the large-scale and small-scale flow features. This would address the limitations of the present study (chapter 6), by alleviating the need for valve symmetry assumption and by accurately capturing the instant of valve closure. These two methods would also ensure a high spatial mesh resolution in the hinge For instance, with a Chimera overset grid method, the grid corresponding to the hinge region could be limited to the immediate vicinity of the hinge recess and not include upstream and downstream extensions. In the present study, despite the advantage of using selectively stretched grid, the need to include these upstream and downstream extensions as domain inlet and outlet yielded a total grid size of 5.9 million grid nodes with only 80,000 nodes within the fluid region of the

hinge recess. A drastic gain could thus be obtained by limiting the domain of interest, and mesh refinement studies focusing on the hinge region could thus be undertaken, without drastically increasing the overall memory requirements.

Additionally, the geometry of the heart model upstream (left ventricle) and downstream (aorta) of the valve has been shown to impact the valvular fluid dynamics [99-101]. An optimized meshing approach is expected to lead the way for the hemodynamics simulations of valves under physiologic conditions and in anatomically accurate geometries.

8.2 Particulate and non-Newtonian nature of blood

Blood is known to be a multi-phase fluid that exhibits non-Newtonian properties. Due to the large dimensions of the valve diameter with respect to the blood elements, simulations of the valvular bulk flow fields assuming a single-phase Newtonian flow is deemed a reasonable approximation of the blood flow. However, in small gaps such as those present in the hinge recess of BMHV, the non-Newtonian effect of the flow is thought to be non-negligible. Modifications of the current numerical solver to include the non-Newtonian effect of the flow in the hinge recess are expected to yield more realistic hinge flow patterns.

In the present study, an attempt is made towards the assessment of the thromboembolic potential of the three hinges by performing a Lagrangian particle analysis combined with existing blood damage model. However, the current analysis models the blood elements as weightless point-particles that are passively advected by the surrounding fluid. Simulating the full and accurate dynamics of the blood elements crossing the hinge region requires the implementation of a highly sophisticated model that incorporate the effects of the particulate nature of blood, by 1) considering a fluid

with platelets and red blood cells at physiologic concentration and with realistic membrane properties, 2) modeling cell-to-cell and cell-to-valve surface interactions, 3) taking into account cell membrane deformation and possible tearing. Researchers have tried to develop such models, but to date these models are still limited to two-dimensional simulations [104]. As emphasized above, the simulations of blood element motion with such a level of complexity are contingent on the development of improved and efficient numerical algorithms and the augmentation of the computational power. However, should such multi-phase simulations be possible, fully-coupled large-scale and micro-scale simulations with multi-phase particulate flow are expected to still require tremendous computational capabilities. Multi-phase simulations performed in a one-way-coupling setting, where the boundary conditions are obtained from large-scale simulations, would yield further insight into the blood cell behavior in the hinge recess and constitute the necessary first step towards the completion of multi-scale multi-phase simulations.

8.3 Numerical result validation

The development of highly sophisticated numerical solvers capable of capturing all scales present in the flow (from the large scale down to the cell levels) should be performed gradually and each step should be carefully validated against experimental results. The current numerical results are compared to Laser Doppler Velocimetry (LDV) measurements. However, LDV is a point-wise measurement technique that only provides two-dimensional flow information at selected locations. An improvement would be the use of micro-Particle Image Velocimetry (PIV) or Magnetic Resonance Imaging (MRI) techniques as complementary methods for validation. MRI or micro-PIV in the hinge region would efficiently provide detailed maps of the general flow field features at

specific instances of the cardiac cycle. These two modalities, however, are both Eulerian measurement techniques and thus may not be used to estimate blood element trajectories. The efficacy of the particle tracking algorithm in modeling the Lagrangian particle trajectories should therefore be verified with another modality. Flow visualization techniques relying on dye injection or hydrogen bubble could be used.

Finally, the calculated hinge thromboembolic potentials also require validation. These potentials constitute a surrogate measure of the actual hemolysis and platelet activation levels induced by the hinge region of the BMHVs and could be verified with controlled *in vitro* blood experiments [34, 96, 107, 108]. Comparison of the numerically-computed and experimentally-assessed blood damage potentials for a similar set of hinge designs should yield a similar trend and designate the same hinge designs as optimal or worst. Such a comparison would ensure that the calculated potential is relevant and can be used as a decisive parameter in the numerical optimization of the hinge design.

8.4 Numerical solver application

The influence of the design of the hinge recess and leaflet ear on the micro-scale hinge flow fields and the associated thromboembolic potential is estimated in the present study by comparing three hinge geometries with different recesses, leaflet ears and hinge gap width. The present numerical solver may be used to perform a larger parametric study and identify the hinge geometrical features that are most or least detrimental to the blood elements. The hinge recess of the two most commonly implanted BMHVs, the SJM and CM valves, are studied here. A thorough numerical investigation of the Medtronic Parallel (MP) hinge, which is known to have unacceptably high thromboembolic rate, would provide useful information on which features are to be

avoided to improve hinge performances. The investigation of drastically different hinge designs such as the hinge of the ATS Open Pivot valve, which features an open protruded convex hinge rather than a recessed hinge, would also be of interest. The assessment of the MP and ATS hinges, combined with the present assessment of the SJM and CM recessed hinges, would give tremendous insight into possible improvement of the hinge designs and give the basis for performing a relevant parametric study assessing a variety of design parameters. Such a parametric study is essential to improve existing valves or even design novel valves in order to eventually remove, or at least reduce, the need for anticoagulation therapy in patients with implanted BMHVs. This numerical parametric study would reduce the cost and time required to introduce new prostheses by limiting the need for prototype manufacturing and bench testing to only the valve designs that have been numerically optimized.

8.5 *In vitro* blood experiments

In the present study, a surrogate measure of the hinge thromboembolic potential is computed by combining the shear stress history along cell trajectories with previously-published empirical blood damage models. A validation of this approach and further information on flow-induced blood damage could be obtained by performing specifically-tailored *in vitro* blood experiments. This is a challenging prospect largely due to the opacity of the blood, the difficulty to track individual blood cells, and the large dimensions of the hinge region with respect to blood elements. Nonetheless, advances in cell imaging techniques, improvements in the area of fluorescent tracking, and development of sophisticated image analysis tools and adequate software [109-112] hold considerable promise for the characterization of blood cell motion and trauma in regions such as the hinge recess. For instance, fluorescently labeled Ca2+ has been shown to

be a suitable mean to visualize the activation and aggregation of platelets in real time. Similarly, red blood cells can be tracked by dying their membranes with, for example, fluorescent DiI [110]. Fluorescent inorganic semiconductor nano-crystals, known as quantum dots, are also used to visualize the trajectory of particles flowing in blood. [113]. As a result, controlled *in vitro* blood studies where the hinge region is isolated and adequate tagging and tracking of blood cells is performed, is expected to provide the required experimental results for validating the numerical models. These studies, combined with ad-hoc blood assays for hemolysis, platelet activation, and clot formation would provide valuable experimental information to be used in the development and validation of blood damage models and subsequent assessment of the hinge thromboembolic potential.

APPENDIX A

NUMERICAL METHODS

A.1 Overall structure of the code

Figure A-1 describes the overall structure of the code. Two input files are required to provide the code with the body surface and fluid domain information. The immersed surfaces are discretized using unstructured triangular meshes. The nodes defining these triangular meshes and their connectivity are provided via two input files, *ibmdata0* for the valve chamber and the valve housing surfaces and *ibmdata1* for the leaflet surface. The input file *grid.dat* corresponds to the Cartesian fluid domain.

The output files of the code are pairs of binary files that contain the velocity, pressure and node classification information at specific iterations of the simulations. The nomenclature used to name these files is the following: *prefix_field_suffix_0.dat* and *prefix_field_suffix_0.dat.info.* The prefix indicates the type of information contained in the file (*u* for the Cartesian velocity field, *v* for the Contravariant velocity field, *p* for the pressure field and *nv* for the node classification as explained in Appendix A.2). The suffix provides the iterations of the simulations at which this information was computed. For instance *pfield02960_0.dat* and *pfield02960_0.dat.info* provides the pressure field at the iteration 2960. These binary files can be post-processed using the code *data.c* to generate Tecplot files.

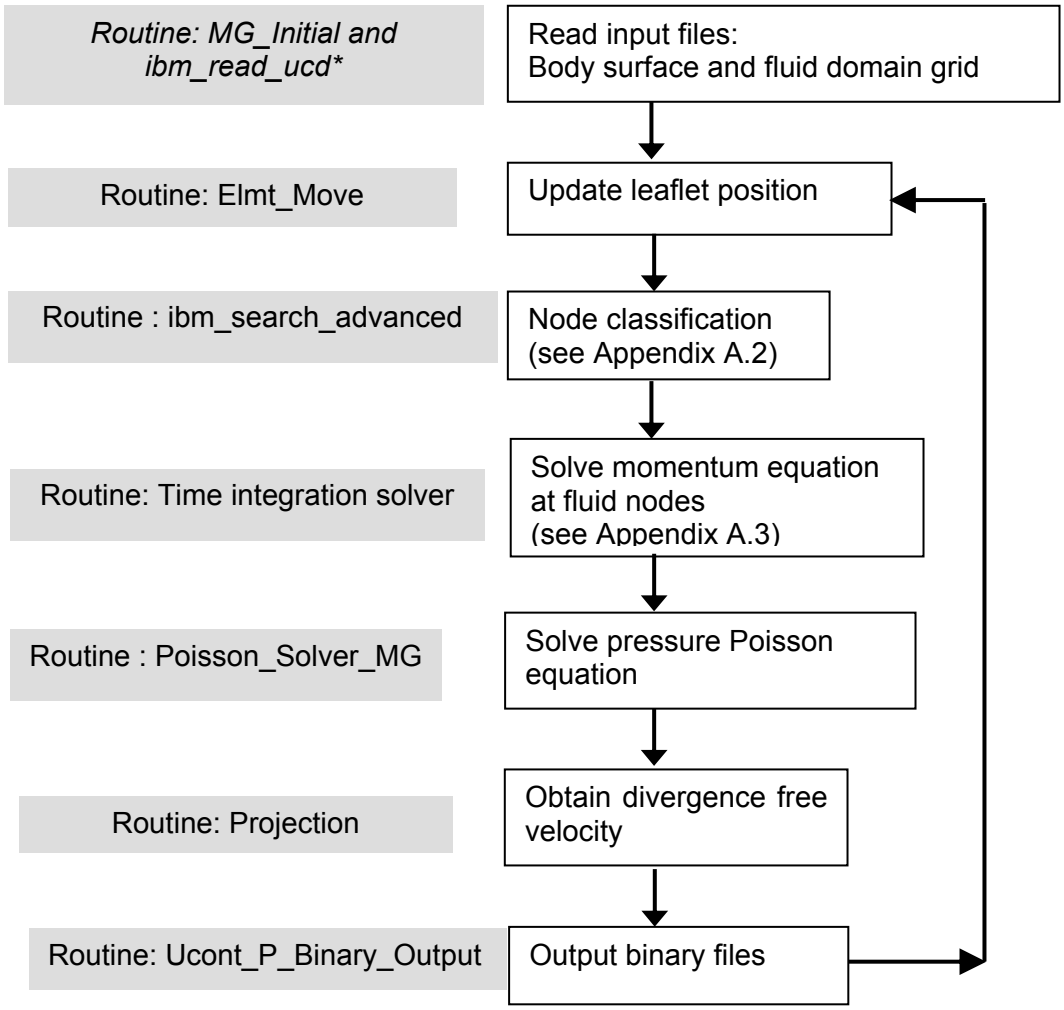

Figure A-1: Overall structure of the code.

A.2 Node classification algorithm

A.2.1 Preliminary node classification into two broad categories (inner or outer nodes)

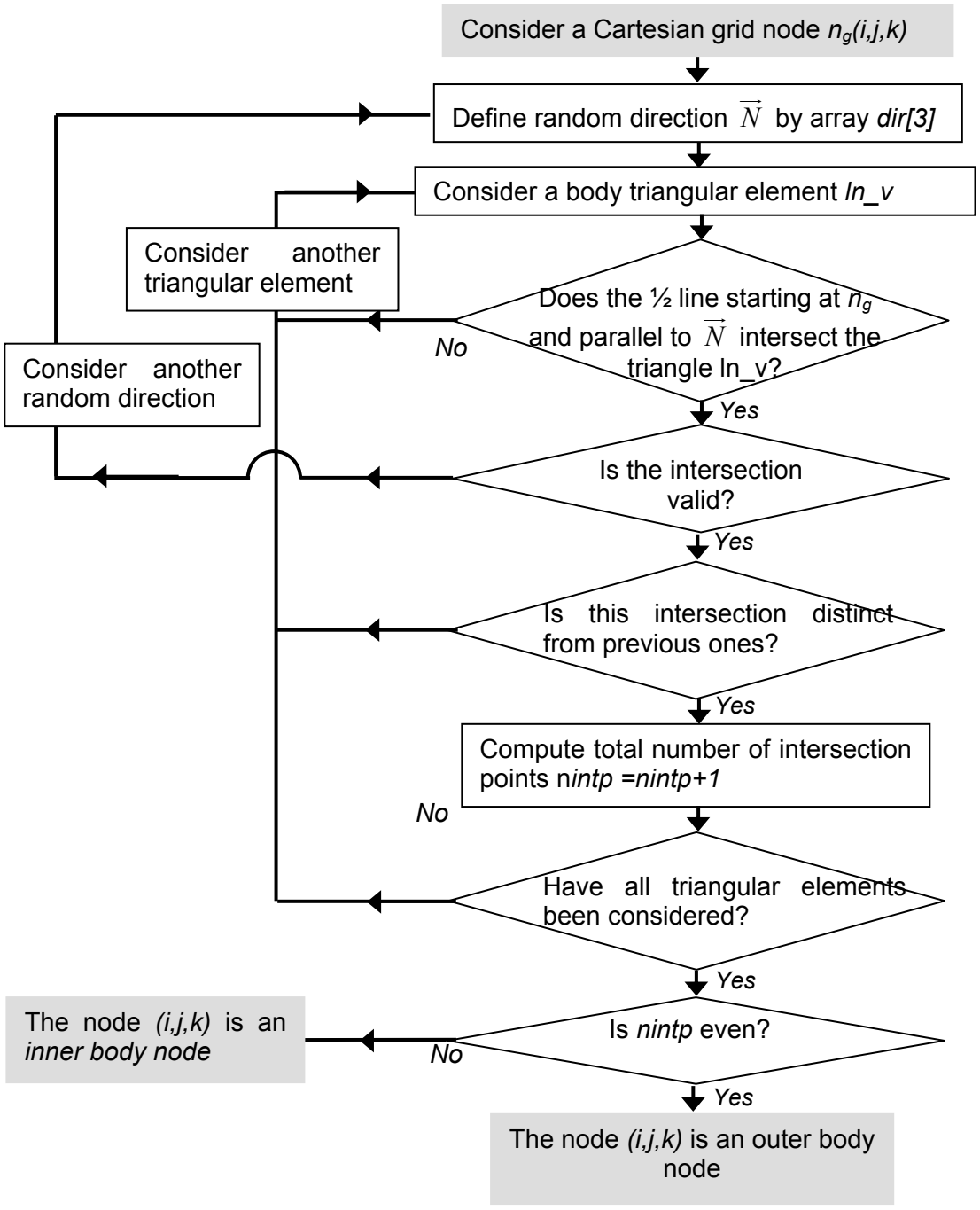

Figure A-2: Flow charts describing the main steps of the preliminary node classification.

A.2.2 Final node classification into three categories (inner body nodes, fluid nodes or near boundary (nb) nodes)

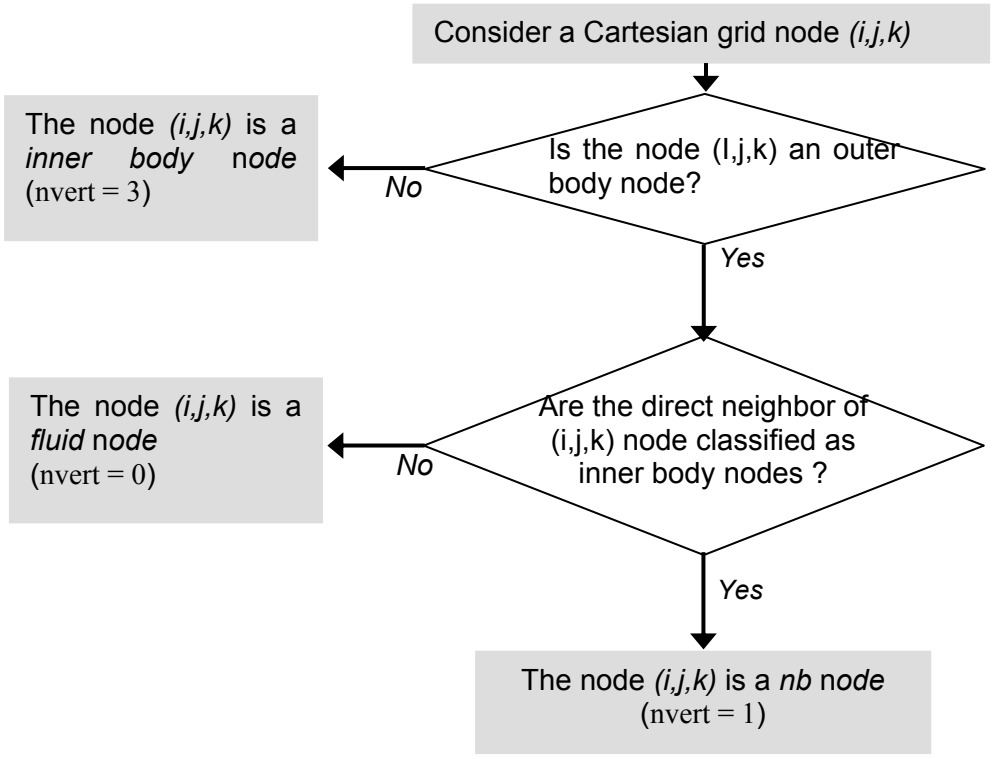

Figure A-3: Flow chart representing the steps of the final node classification.

The node classification algorithm is implemented using the following four main subroutines defined in *main.c*: i*bm_search_advanced*, *randomdirection*, *point_cell_advanced, intsect_triangles*.

A.3 Numerical approach to obtain the right-hand side of the Navier Stokes equations.

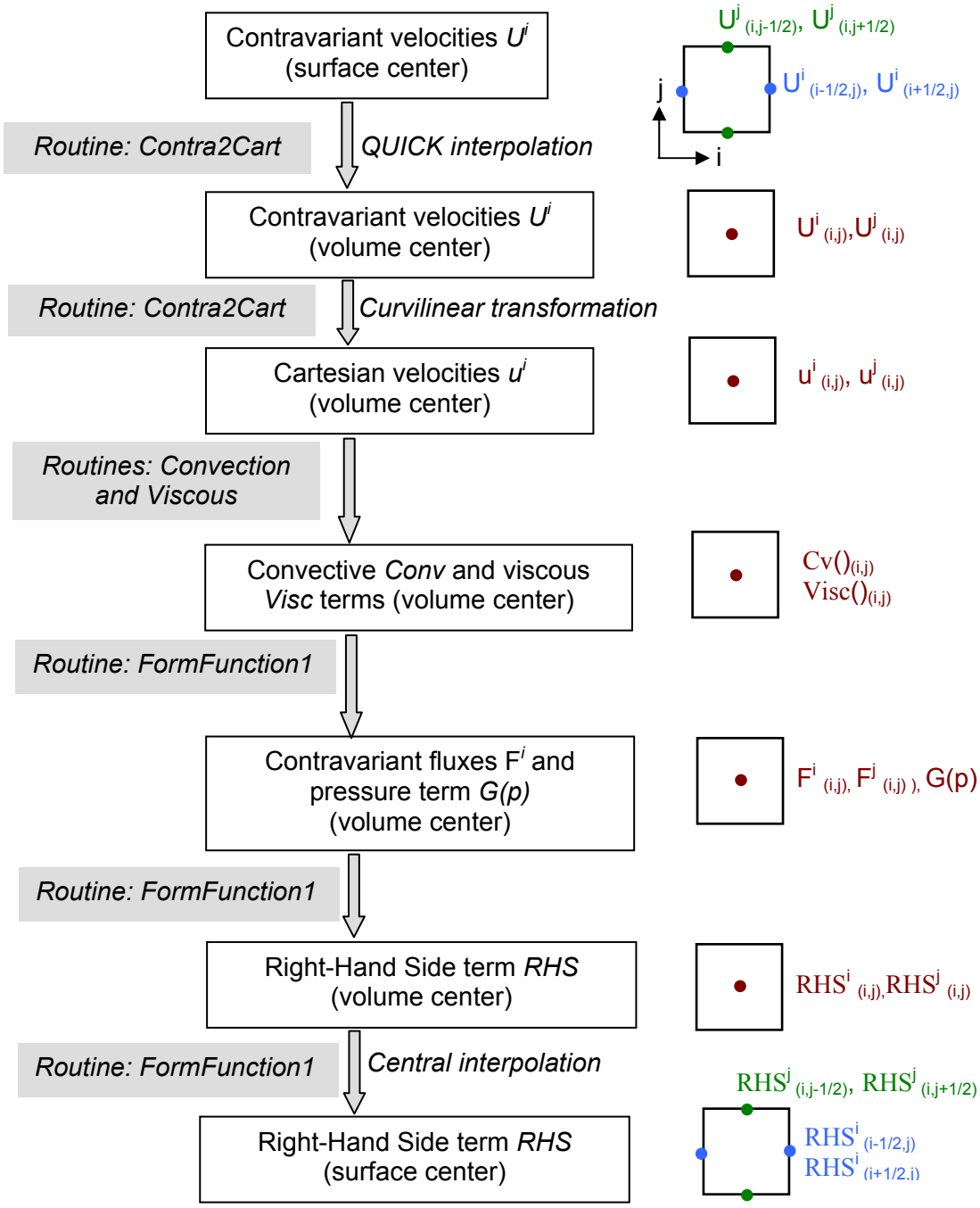

Figure A-4: Flow chart summarizing the main steps of the numerical approach to compute the right hand side term (including convective, viscous and pressure gradient terms) at the surface centers. Note that the full three-dimensional governing equations were solved, but for clarity, two-dimensional schematics are presented here.

A.4 Interpolation schemes

The full three dimensional governing equations were solved, but for clarity, the figures in this section are two dimensional schematics.

Quadratic Upstream Interpolation for Convective Kinematics (QUICK): The interpolation method to obtain the Contravariant fluxes at the volume center based on the information at the surface center is a QUICK one-dimensional interpolation scheme. Considering the *i*-direction, the Contravariant fluxes at the volume center (node *i*) are calculated from the values at the surface centers (half nodes *i-3/2, i-1/2* and *i+1/2*) with:

$$V^1_{i,j,k} = \frac{1}{8}\left(6\,V^1_{i-1/2,j,k} - V^1_{i-3/2,j,k} + 3\,V^1_{i+1/2,j,k}\right) \text{ for i>1} \qquad \text{Equation A-1}$$

$$V^1_{i,j,k} = \frac{1}{8}\left(6\,V^1_{i+1/2,j,k} - V^1_{i+3/2,j,k} + 3\,V^1_{i-1/2,j,k}\right) \text{ for i=1} \qquad \text{Equation A-2}$$

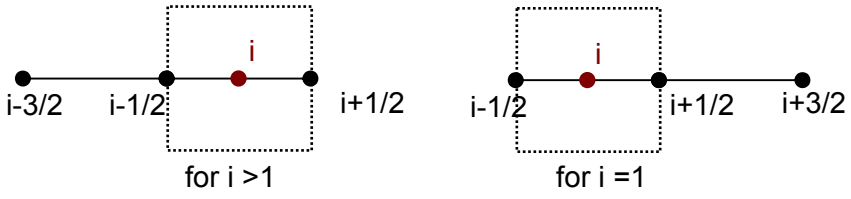

Figure A-5: Illustration of the QUICK interpolation scheme.

A similar interpolation scheme is used for the *j*- and *k*-directions. Once the Contravariant fluxes are known at the volume center, the Cartesian velocity at the volume center can be obtained using Equation 3-10.

Central differencing: To reconstruct the contravariant flux terms F^i at the surface center (half nodes i+1/2) based on the flux terms known at the volume center (nodes *i and i+1*), the following scheme is employed:

$$F^1_{i+1/2,j,k} = \frac{1}{2}\left(F^1_{i+1,j,k} + F^1_{i,j,k}\right) \text{ for } i<i_{max}\text{-}1 \qquad \text{Equation A-3}$$

A similar interpolation scheme is used for reconstructing the Contravariant flux terms F^j and F^k along the *j*- and *k*-directions, respectively.

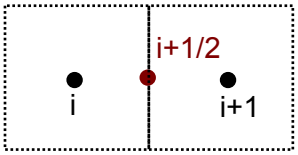

Figure A-6: Illustration of the central differencing scheme.

A.5 Simulation parameters.

A list of all parameters required by the numerical solver is provided. The values of these parameters are read in the file *control.dat*. The listed values correspond to the settings that were used for the hinge simulations conducted as part of this thesis.

Main parameters

tio 10	Intervals for solution output
imm 1	1- immersed body present, 0- no immersed body
ren 6000	Reynolds number
cfl 1.0	CFL number
vnn 1.0	Von Neumann number
dt 0.0027	non-dimensionalized time step defined as *Deltat / (L/U)*
time_bin 10000	Number of time steps to discretize the cardiac cycle
rsteps 10000	Number of time steps to be computed
rstart 9000	Time step at which to restart the computation

Scaling and positioning parameters

chact_leng 25.4 Characteristic length to normalize computational grid
chact_leng_valve 25.4 Characteristic length to normalize immersed surface
translation_value_x 0 x-axis translation imposed to all immersed bodies
translation_value_y 0 y-axis translation imposed to all immersed bodies
translation_value_z 0 z-axis translation imposed to all immersed bodies
gap_width_shift 0.0 x-axis translation imposed to the leaflet (in mm) to vary the hinge gap width
leaflet_shift_z -0.04458 z-axis translation imposed to the leaflet (in mm)
leaflet_shift_y 0.164 y-axis translation imposed to the leaflet (in mm)
leaflet_shift_x 0.09 x-axis translation imposed to the leaflet (in mm)

maximum_inflow_rate 2.427316e+01 Peak systolic flow rate

Flow solver: multigrid grid level parameters

mg_level 3 Number of levels to be used
mg_coarse_ksp_type fgmres Implement the Flexible Generalized Minimal Residual method (Flexible GMRES) for the coarse grid
mg_coarse_gmres_restart 20 Set number of iterations at which GMRES restarts
mg_coarse_ksp_max_it 25 Maximum number of iterations for the coarse grid
mg_k_semi 1 Coarsening direction

Flow solver: KSP solver for Poisson equation

ps_ksp_type fgmres Implement the Flexible Generalized Minimal Residual (GMRES) method
ps_ksp_gmres_restart 20 Set number of iterations at which GMRES restarts
ps_ksp_atol 1.e-8 Set absolute tolerance of residual norm
ps_ksp_rtol 1.e-5 Set convergence tolerance by defining the minimum relative decrease in tolerance norm from initial
ps_ksp_max_it 100 Maximum number of iterations
ps_ksp_truemonitor Print true residual norm || b-Ax ||
ps_mg_coarse_ksp_type bcgs Implement the Bi-Conjugate Gradient Squared (BCGS) method for the coarse grid
ps_mg_levels_1_ksp_type richardson Define the Krylov subspace method for level 1 as richardson method
ps_mg_levels_2_ksp_type richardson Define the Krylov subspace method for level 2 as richardson method
ps_mg_levels_3_ksp_type fgmres Define the Krylov subspace method for level 3 as the Flexible Generalized Minimal Residual method.

Flow solver: SNES solver for momentum equation solver

snes_monitor Print residual norm at each iteration for SNES
snes_rtol 1.e-4 Set convergence tolerance by defining the minimum relative decrease in tolerance norm from initial
snes_max_it 25 Maximum number of iterations
ksp_monitor Print residual norm at each iteration for KSP
ksp_rtol 1.e-3 Set convergence tolerance by defining the minimum relative decrease in tolerance norm from initial
ksp_max_it 150 Maximum number of iterations

APPENDIX B

NUMERICAL MODELS

B.1 Large-scale Numerical Models

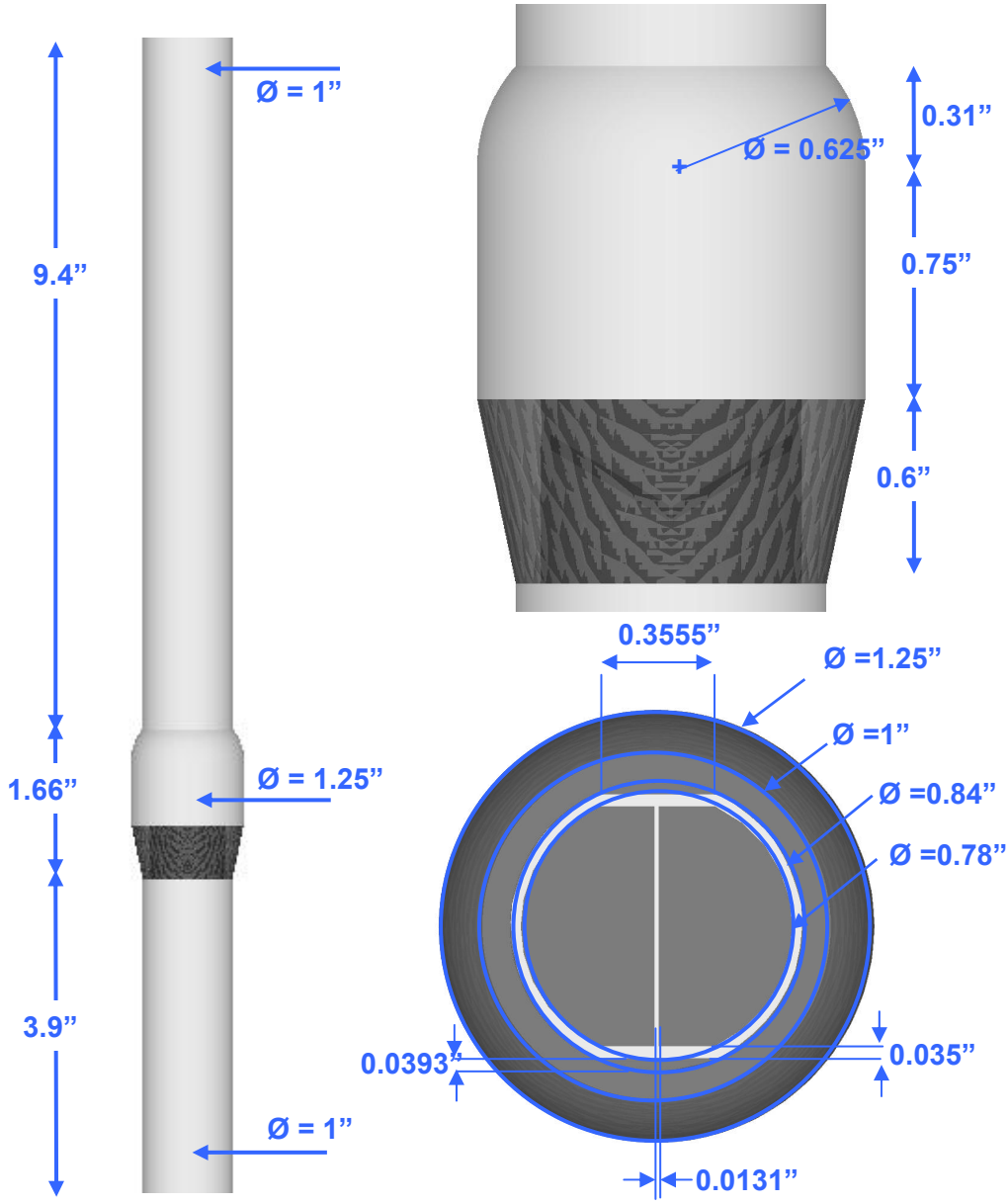

Figure B-1: Large-scale numerical model: the bileaflet mechanical heart valve is inserted into a simplified aorta consisting of a straight tube with an axisymmetric expansion representing the sinus region. Dimensions are provided in inch.

B.2 Hinge Numerical Models

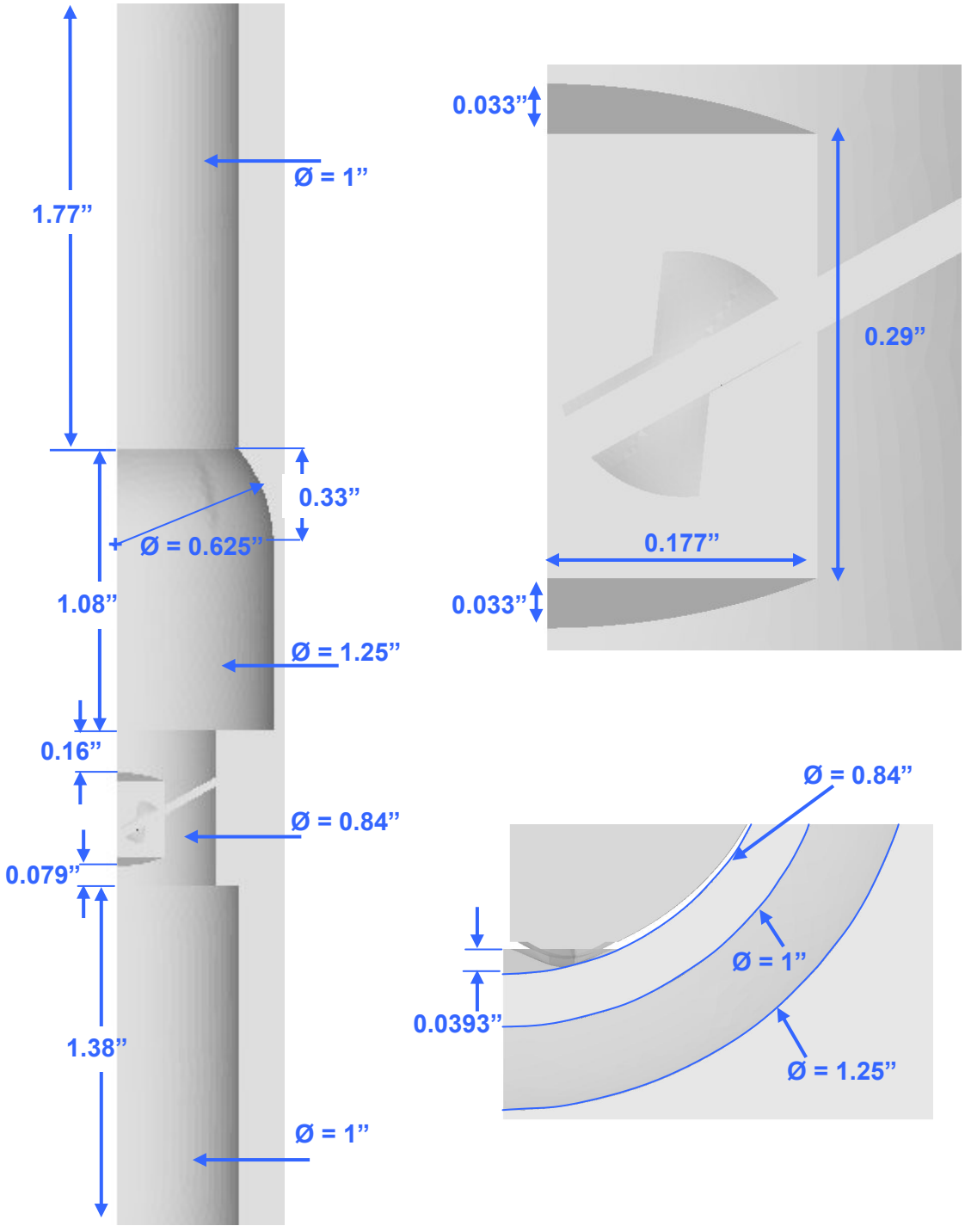

Figure B-2: Hinge numerical model: the model for the hinge simulations corresponds to a section of the large-scale numerical model presented in Figure B-1. The dimensions are provided in inch.

B.3 Hinge Designs

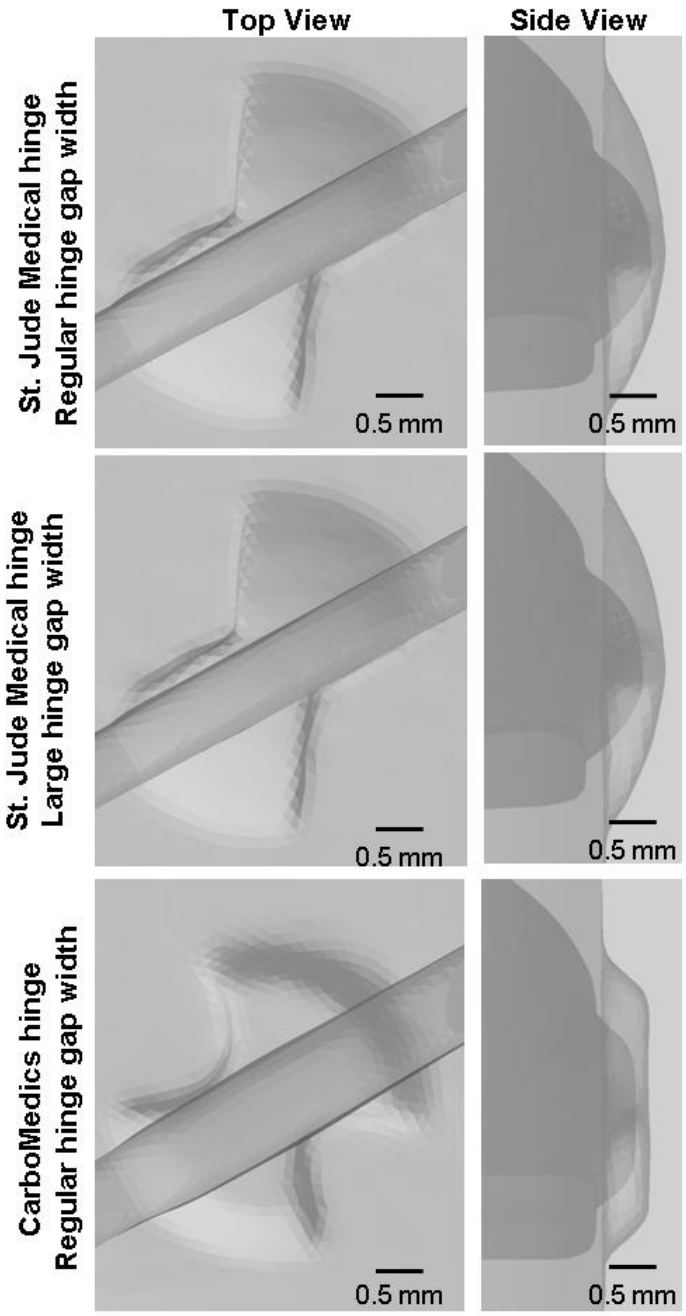

Figure B-3: Comparison of the three hinge designs. Note that the images are to scale.

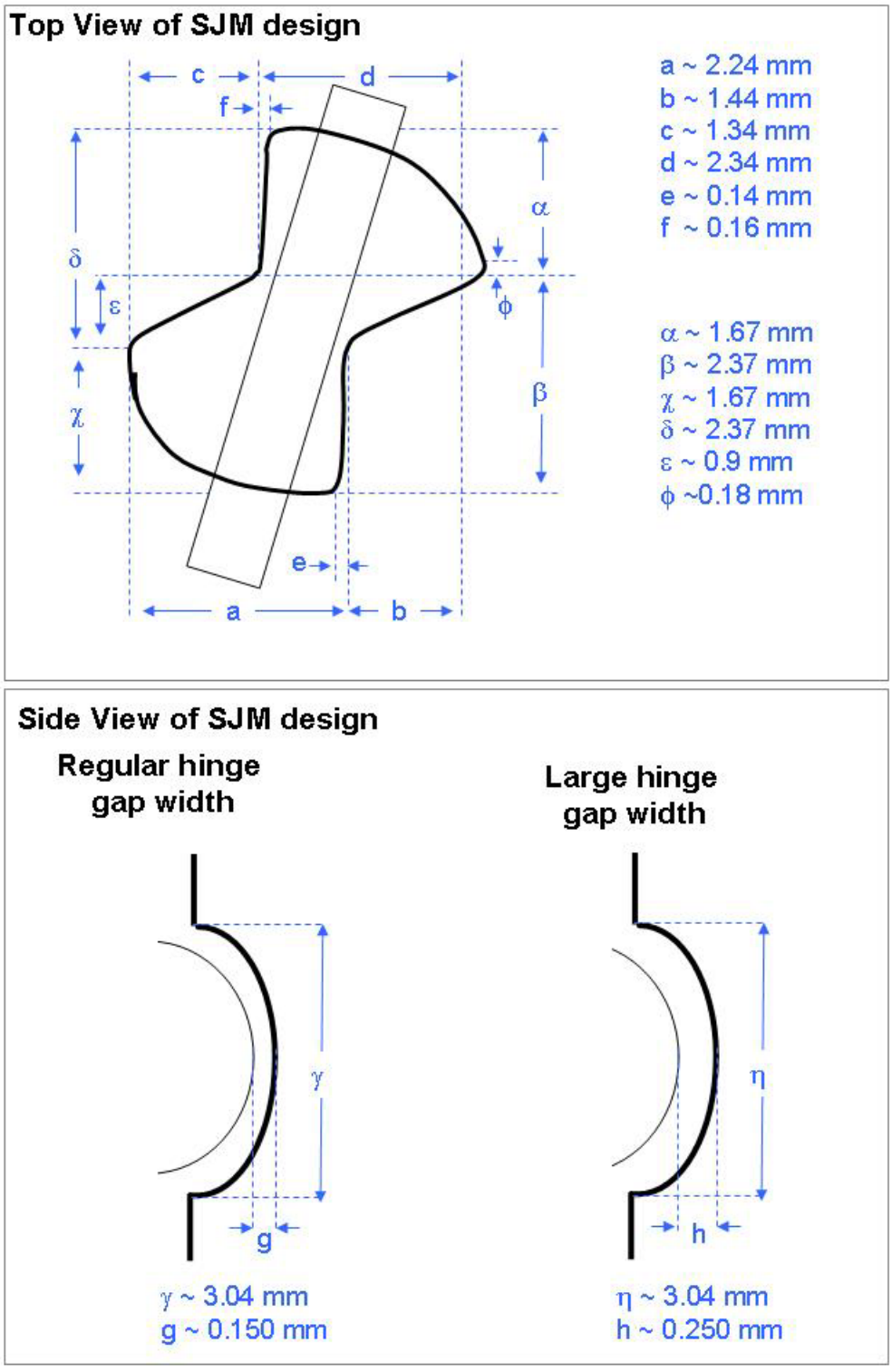

Figure B-4: Approximate dimensions (in mm) of the SJM hinge design, for both the large and regular hinge gap width configurations.

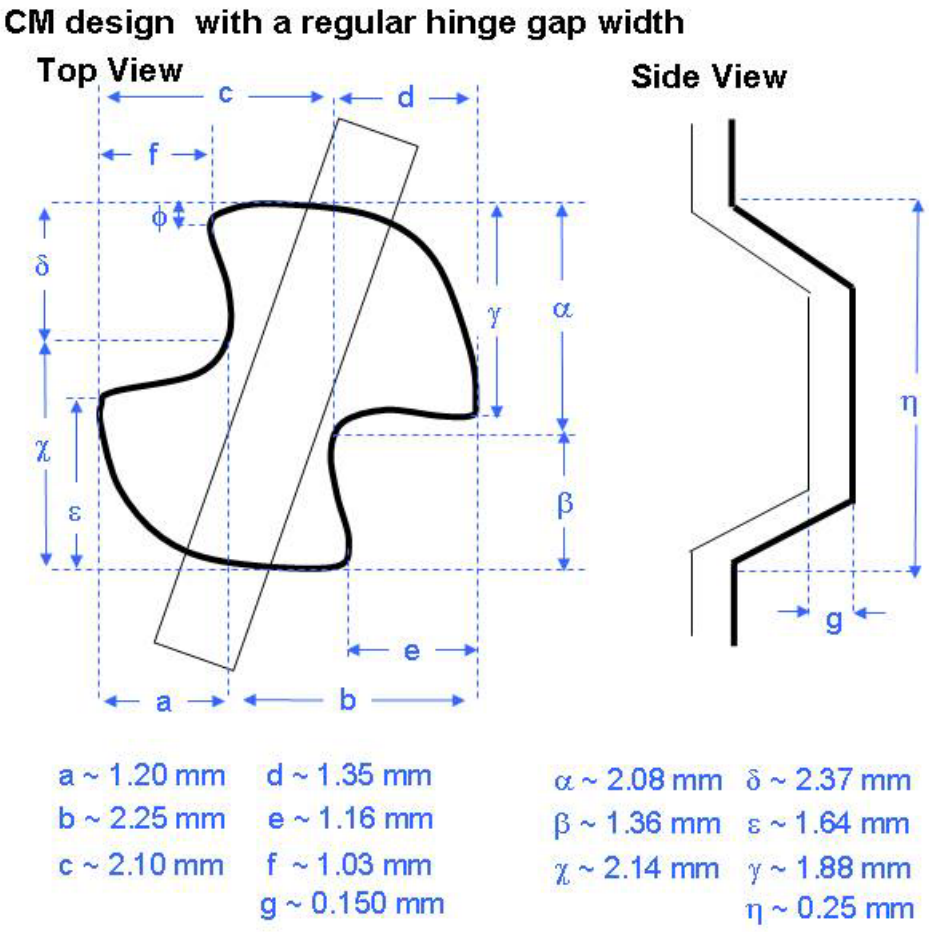

Figure B-5: Approximate dimensions (in mm) of the CM hinge design with a regular hinge gap width.

B.4 Overall approach to generate the hinge numerical model

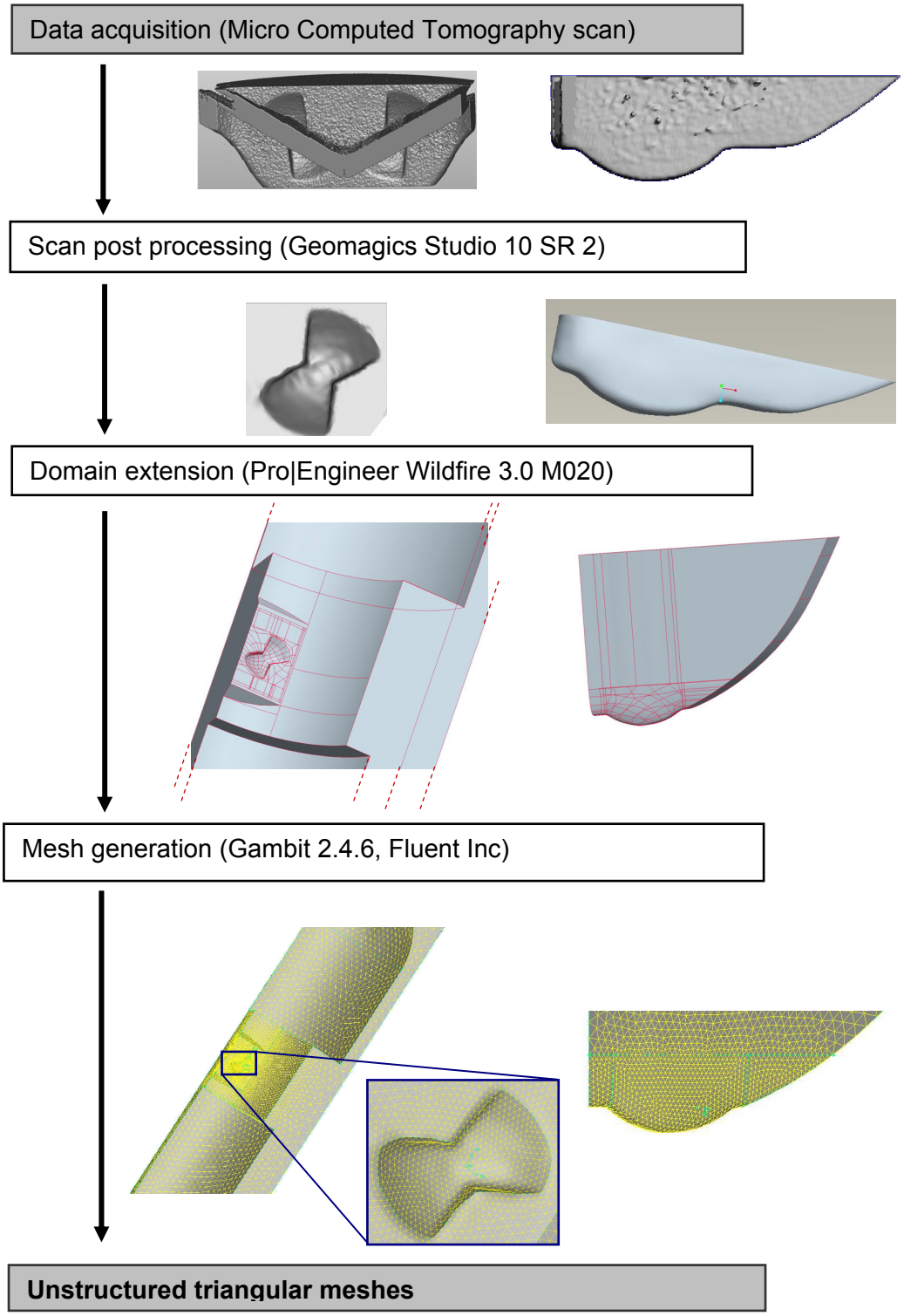

Figure B-6: Flow chart illustrating the methodology to obtain the hinge numerical mesh from the micro-computed tomography scan of a bileaflet mechanical heart valve. Note that the images are not to scale.

APPENDIX C

GEOMAGICS GUIDELINE

The following two sections describe the steps to obtain from a micro-computed scan a surface model from which a computational mesh may be generated using Geomagics Studio software (Geomagics Studio 10 SR2). Section C.1 presents the post-processing of the leaflet geometry and the different issues that may be encountered. Section C.2 focuses on the hinge recess.

C.1 Post-processing of the leaflet

1 – Open the STL file of the micro Computed tomography scan

File > Open

2 - Decimate the model to reduce the number of triangles without compromising surface details. This is particularly useful when the model contains an excessive number of triangles.

Polygons >Decimate

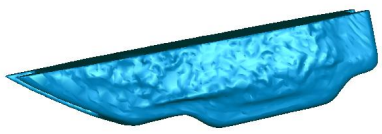

Figure C-1: Decimated model of a leaflet

3 - Remove the top plane of the leaflet using "*Section by Plane".* Do not close the intersection. The function "Section by plane" superimposes a plane on the model and removes all triangles on one side of the plane. The easiest methods to position the plane are:

- *Pick Boundary.* The selected boundary specifies the location of the superimposed plane

- Three Points: Three points can be selected on the model and are used to define the section plane.

- System plane: The plane can be chosen as a plane parallel to the coordinate system planes (X-Y plane, X-Z plane, YZ plane). The plane can then be translated to its desired location.

Polygons >Section by Plane

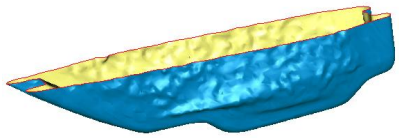

Figure C-2: Decimated model of a leaflet with the top plane removed

3 - If needed, remove all triangular elements that are noise (floating triangles that are not part of the hinge and recess surfaces)

Edit > Selection Tools > Lasso and *delete*

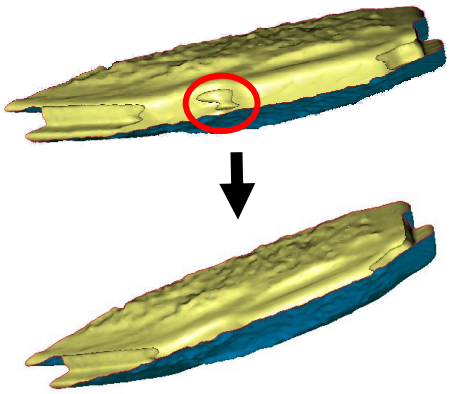

Figure C-3: Three-dimensional view of the leaflet showing the interior of the leaflet, before and after performing the noise removal step.

4 – If needed, reconstruct the sides of the leaflet

- Select and delete all sections of the leaflet sides that were not properly scanned

  Edit > Selection Tools > Lasso and *delete*

- Reconstruct the side of the leaflet based on the curvature of the leaflet at the edge using the "*Fill Holes"* command. This function detects the presence of holes and constructs a polygon mesh over each hole. The "fill partial" method is here the preferred method as it allows the user to specify which portion of the hole to be filled.

  Polygons > Fill Holes >Fill Partial icon button

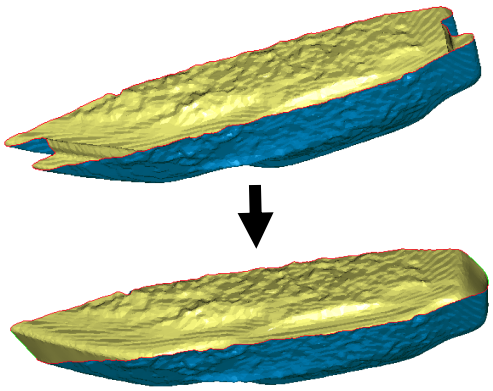

Figure C-4: Three dimensional view of the model, before (top) and after (bottom) reconstructing the leaflet sides.

5 - Relax the model to adjust the crease angle between the triangles such that the mesh becomes smoother.

Polygons >Relax

6 - In case where the scan is very noisy, additional clean-up of the leaflet surface may be required. In regions of low curvature (nearly flat) that are particularly noisy, delete the triangular elements and fill the newly-created hole. The function "*Fill holes*" detects the presence of holes and constructs a polygon mesh over each hole. The "Fill" icon button should be used to select and fill the holes.

Edit > Selection Tools > Lasso and *delete*

Polygons > Fill Holes >Fill icon button

7 – If needed, perform a final clean-up of the leaflet sides by using "SandPaper" and "Defeature". "SandPaper" reconstructs the polygon mesh to have smoother surfaces and gentler curves. "Defeature" deletes triangles in a selected area of the model and inserts a more orderly mesh. Both of these functions should be use only in regions where the curvature is minimal to avoid altering the design of the model.

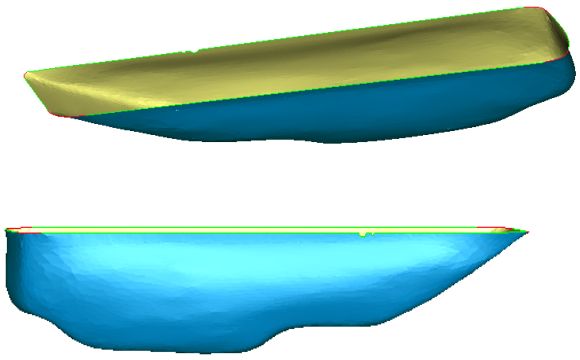

Figure C-5: Smooth surface of the leaflet model

7 – If the top boundary of the leaflet is not straight, the “Fill Partial” option of the “Fill Holes” function may be used to straighten the surface. The function “Section by plane” could also be used as it superimposes a plane on the model and removes all triangles on one side of the plane, thereby generating a straight boundary. At this point the model is ready for surface fitting.

Polygons > Fill Holes >Fill Partial icon button

Polygons >Section by Plane

8 –Switch from “*Polygon Mode*” to “*Shape Phase*”

Edit > Phase >Shape Phase

9 - Construct patches on the model. Patches are four-sided subdivisions of the model that are approximately equilateral.

- Detect the curvature of the model to optimize the positioning of the patches. This is achieved using “Detect curvature” which automatically places lines on areas of curvature.

  Contour > Detect curvature

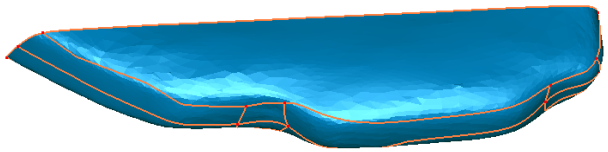

Figure C-6: Leaflet model with curvature lines

- Construct the patches

  Patches > Construct patches

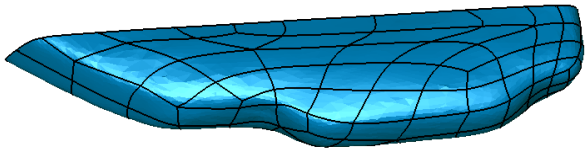

Figure C-7: Patch distribution on the leaflet model

- Repair the patches using “Repair Patches”. This function locates problematic regions of a patch layout and provides several repair methods.

  A patch layout is classified as problematic if exist intersecting paths (an intersecting path causes two patches to share one location of the model), poor patch angles (a poor patch angle is significantly greater or less than 90 degrees), high-degree corners (high-degree corner are similar to poor patch angles and are seen when many patches share the same vertex) or high deviation patches (a high-deviation patch is very different in shape from the other patches).

  The repair methods are relax linear, relax curvilinear, delete and fill, relax and project, subdivide patches.

  Patches > Repair Patches

- If “Repair Patches” is not sufficient, use “Edit Patches” and “Shuffle Patches” to help in repairing problematic patches. “Edit Patches” modifies the paths of individual patch lines to create a more effective patch layout, by moving vertices or redistributing vertices along each patch. “Shuffle Patches” rearranges the patches that surrounds a specific line or vertex.

Patches > Edit Patches

Patches > Shuffle > Patches

10 – Construct a grid on every patch using “Construct grids”. Note that all patches in the model will have this resolution. For a given resolution, a denser grid is achieved by having a smaller patch and a sparser grid by having a larger patch. Small patches should therefore be used where precise surfacing, and thus great overall grid density, is needed. Large patches should be used where grid density is less important.

Grids > Construct grids

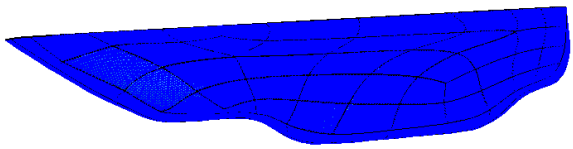

Figure C-8: Grid on the leaflet model

11 – Generate a NURBS surface in each patch of the model using “Fit Surfaces”.

NURBS > Fit Surfaces

Figure C-9: Final leaflet surface

12 – Perform transformations to the model as needed. The model may be reoriented, scaled or mirror using "*Scale Model*", "*Reorient Model*", *"Reset Model*" or "*Mirror Model*". "*Scale Model*" reduces or enlarges the active object by a numerical factor. This is an adjustment to the data, not just a change of perspective. "*Reset Model*" restores the model's position in the world coordinate system to its position before any alignment or rotation. "*Mirror Model*" duplicates the model on the other side of a mirroring plane. The original model may be kept (thus resulting in a symmetrical model) or deleted (thus leading to an inverse model).

Edit >Scale Model.

Edit >Reorient Model

Edit >Reset Model

Edit >Mirror Model

13 – Export the resulting surface into an IGES file.

File > Save As> IGES format

C.2 Post-processing of the hinge region

1 - Open the STL file of the micro Computed tomography scan

File>Open

2 - Cut the model to only keep the region of interest, here the hinge recess

- Select and delete all unneeded elements of the scan

Edit > Selection Tools > Lasso and delete

- Remove the back plane of the hinge volume using "*Section by Plane"* without closing the intersection. The function *"*Section by plane" superimposes a plane on the model and removes all triangles on one side of the plane. The easiest methods to position the plane are:

  - *Pick Boundary*. The selected boundary specifies the location of the superimposed plane

  - Three Points: Three points can be selected on the model and are used to define the section plane.

  - System plane: The plane can be chosen as a plane parallel to the coordinate system planes (X-Y plane, X-Z plane, YZ plane). The plane can then be translated to its desired location.

  Polygons >Section by Plane

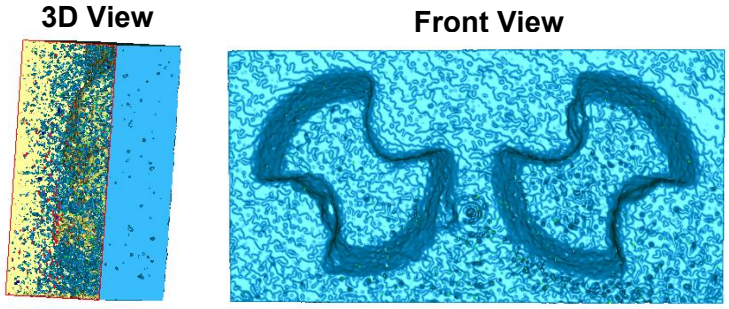

Figure C-10: Original hinge geometry obtained from micro-Computed Tomography. The 3D view shows the region of noise.

3 - Decimate the model to reduce the number of triangles without compromising surface detail. This is particularly useful when the model contains an excessive number of triangles.

Polygons >Decimate

4 - If needed, remove all triangular elements that are noise (floating triangles that are not part of the hinge and recess surfaces)

- Select and delete the triangles

Edit > Selection Tools > Lasso and delete

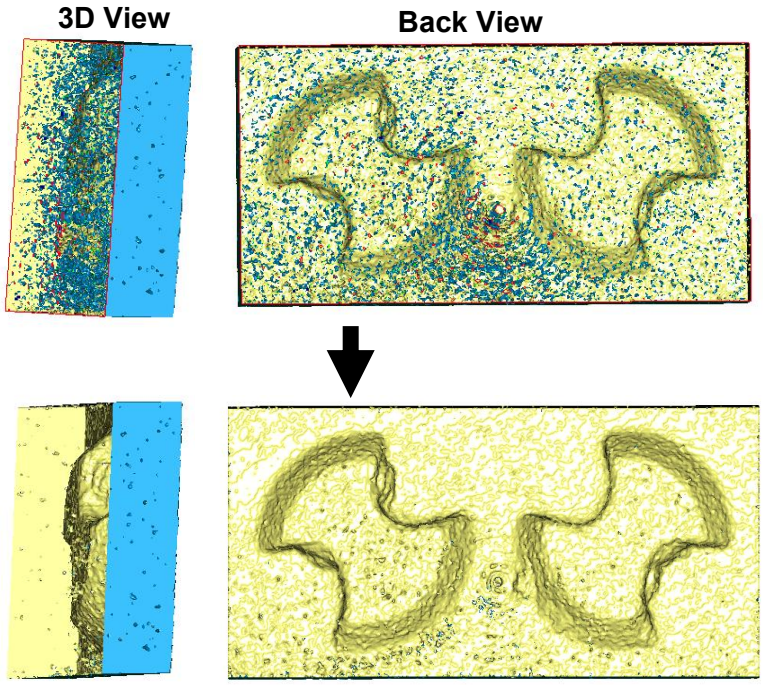

Figure C-11: Hinge model before (top) and after (bottom) noise removal

5 - If needed, fill the holes in the model using "*Fill Holes".* This function detects the presence of holes, and constructs a polygon mesh over each hole. Using the "Fill" icon button, the holes to be filled can be selected.

Polygons > Fill Holes >Fill icon button

6 - Relax the model to adjust the crease angle between the triangles such that the mesh becomes smoother

Polygons >Relax

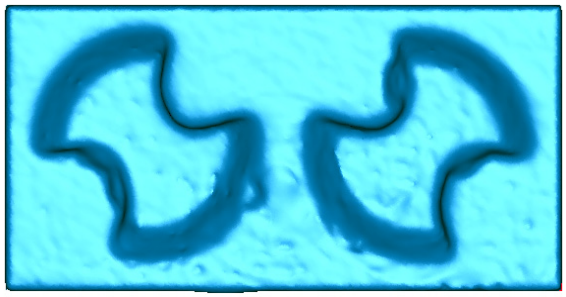

Figure C-12: Hinge model after relaxation

7 - If large holes are present or if section of the model is to be reconstructed, models may be merged.

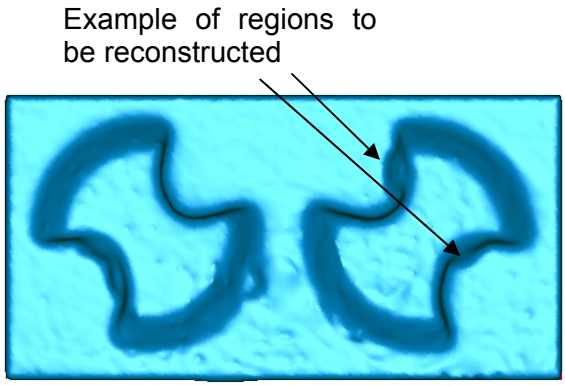

Figure C-13: Regions of the hinge model that have to be reconstructed

- Load a second model and add it to the current file without removing the current model.

  File > Import

- Position the second model with respect to the first one using "*Transform*". This function allows translating or rotating the model as desired. The "*translation*" tool may be used to set the desired motion of the model away from its current position in all

three axe directions. The "*rotation*" tool may be used to set the desired rotation of the model. Note that here only the reconstruction of the right hinge recess of model #1 is shown.

Tools >Transform >Edit transform

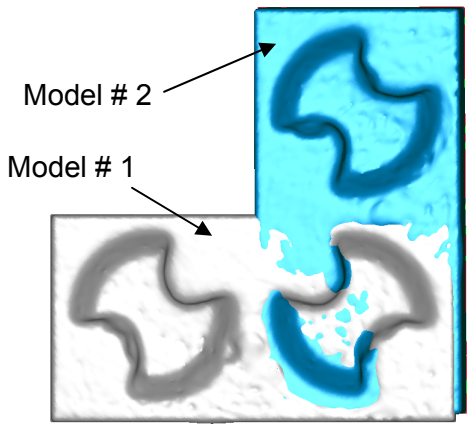

Figure C-14: Positioning of the models that are to be merged

- Delete the sections of the models that are not needed and keep only the sections that are to be merged

Edit > Selection Tools > Lasso and delete

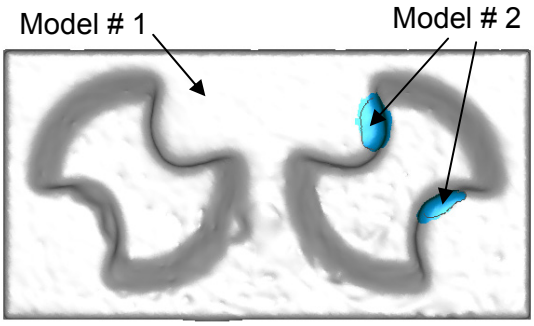

Figure C-15: Trimmed models before merging step

- Merge the two models using “Merge”. This function merges two or more selected polygon models into a single composite model. This function automatically performs noise reduction, global registration, and uniform sampling. It then creates a polygon model named Merged.

  Polygons > Merge

- If needed, fill the remaining holes between the merged models using “Fill Holes”. This function detects the presence of holes and constructs a polygon mesh over each hole. The “Fill” icon button allows selecting the holes that are to be filled.

  Polygons > Fill Holes >Fill icon button

8 - Perform a final clean-up of the model using “SandPaper” and “Defeature”. “SandPaper” reconstructs the polygon mesh to have smoother surfaces and gentler curves. “Defeature” deletes triangles in a selected area of the model and inserts a more orderly mesh. Both of these commands should be used only in region where the curvature is minimal to avoid altering the design of the model.

Polygons > Sandpaper

Polygons > Defeature

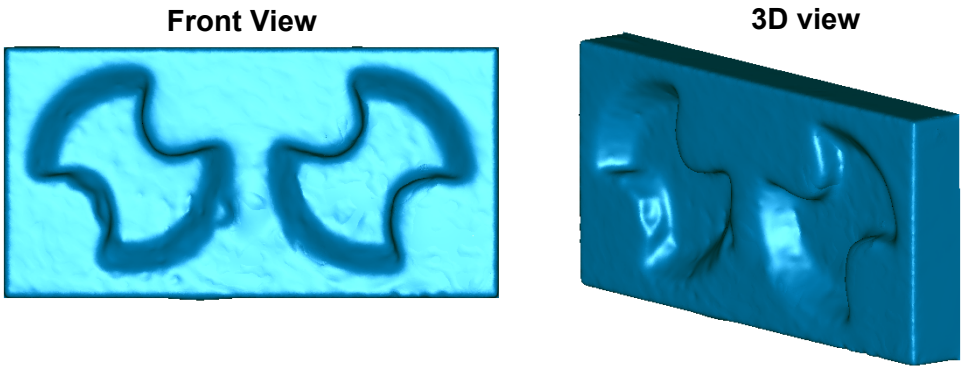

Figure C-16: Smooth surface of the hinge region

9 - Cut the model using "*Section by Plane"* so as to only retain the surface where lie the recesses. Do not close the intersection. The function "Section by plane" superimposes a plane on the model and removes all triangles on one side of the plane. The easiest methods to position the plane are:

- *Pick Boundary.* The selected boundary specifies the location of the superimposed plane

- Three Points: Three points can be selected on the model and are used to define the section plane.

- System plane: The plane can be chosen as a plane parallel to the coordinate system planes (X-Y plane, X-Z plane, YZ plane). The plane can then be translated to its desired location.

Polygons >Section by Plane

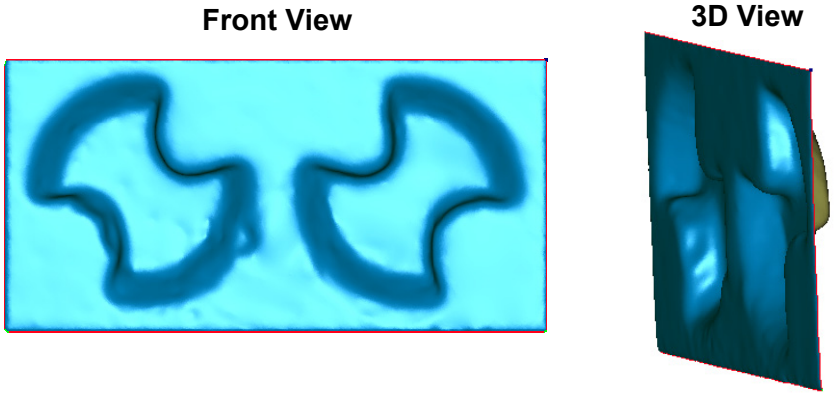

Figure C-17: Final model of the hinge region

10 - Switch from "*Polygon Mode*" to "*Shape Phase*"

Edit > Phase >Shape Phase

11 - Construct patches on the model. Patches are four-sided subdivisions of the model that are approximately equilateral.

- Detect the curvature of the model to optimize the positioning of the patches. This is achieved using the command “Detect curvature” which automatically places lines on areas of curvature.

  Contour > Detect curvature

- Construct the patches

  Patches > Construct patches

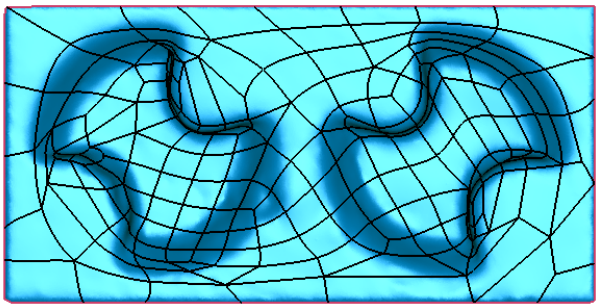

Figure C-18: Patch distribution on the hinge model

- Repair the patches using “Repair Patches”. This function locates problematic regions of a patch layout and provides several repair methods.

A patch layout is classified as problematic if exist intersecting paths (an intersecting path causes two patches to share one location of the model), poor patch angles (a poor patch angle is significantly greater or less than 90 degrees), high-degree corners (high-degree corner are similar to poor patch angles and are seen when many patches share the same vertex) or high deviation patches (a high-deviation patch is very different in shape from the other patches).

The repair methods are relax linear, relax curvilinear, delete and fill, relax and project, subdivide patches.

Patches > Repair Patches

- If “Repair Patches” is not sufficient, use “Edit Patches” and “Shuffle Patches” to help in repairing problematic patches. “Edit Patches” modifies the paths of individual patch lines to create a more effective patch layout, by moving vertices or redistributing vertices along each patch. “Shuffle Patches” rearranges the patches that surrounds a specific line or vertex.

  Patches > Edit Patches

  Patches > Shuffle > Patches

12 – Construct a grid on every patch using “Construct grids”. Note that all patches in the model will have this resolution. For a given resolution, a denser grid is achieved by having a smaller patch and a sparser grid by having a larger patch. Small patches should therefore be used where precise surfacing, and thus great overall grid density, is needed. Large patches should be used where grid density is less important.

Grids > Construct grids

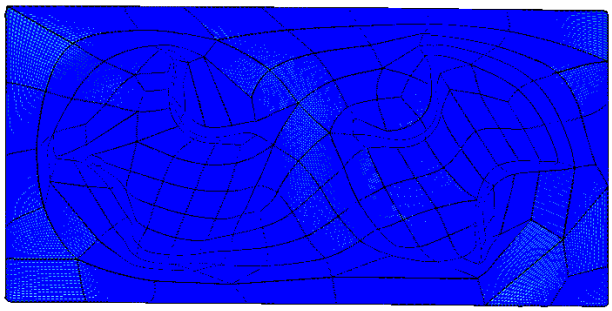

Figure C-19: Hinge model with the grid

13 – Generate a NURBS surface in each patch of the model using “Fit Surfaces”.

NURBS > Fit Surfaces

Figure C-20: Final surface of the hinge region

14 - Export the resulting surface into an IGES file.

File > Save As> IGES format

APPENDIX D

LIST OF ANIMATIONS

The following appendix contains the final naming protocol and a brief description of the animations accompanying this thesis. All the animations are QuickTime movies. The movies pertaining to the SJM regular hinge, the SJM large hinge and the CM hinge are labeled SJMReg, SJMLarge, and CM, respectively. For each valve design, several animations are provided:

- Animations of the principal shear stress fields (Table D-1)
- Animations of the hinge flow fields along selected planes (Table D-2)
- Animations of the Lagrangian results (Table D-3)

An animation of the hinge flow fields visualized experimentally (H_Bubble_Flow_Vis.mov, courtesy of Medtronic Inc) is provided to qualitatively compare the hinge flow structures computed in the present thesis and with those seen *in vitro*. In the flow visualization experiment, hydrogen bubbles are continuously released upstream and downstream of the hinge recess of a St. Jude Medical valve. The path of these hydrogen bubbles is used to identify the flow structures forming inside the hinge recess.

Table D-1: Description of the principal shear stress distribution animations

Movie Description	Movie Name
Principal Shear Stress Iso-surfaces Animations of the iso-surfaces of the principal shear stress levels at two specific instances of the cardiac cycle. The iso-surfaces are color-coded with the shear stress levels from 0 to 1,000 dyn/cm^2.	*At peak systole:* Isosurfaces_PeakSystole.mov
	At mid-diastole: Isosurfaces_MidDiastole.mov
Principal Shear Stress Contours Temporal variations of the principal shear stress distribution at four different levels within the recess. The maximum of the contour scale is set to 1,000 dyn/cm^2.	*At the flat level:* StressContours_Flat.avi
	At 195 μm below the flat level: StressContours_195micron.mov
	At 390 μm below the flat level: StressContours_390micron.mov
	At 585 μm below the flat level: StressContours_585micron.mov

Table D-2: Description of the animations corresponding to the Eulerian description of the hinge flow fields

Movie Description	Movie Name
2D velocity vectors with 3D velocity magnitude contours Temporal variations of the two-dimensional in-plane velocity vectors along selected planes within the hinge recess. The velocity vectors are superimposed on the three-dimensional velocity magnitude contours.	*At the flat level:* 2Dvectors_Vmag_Flat.mov
	At 195 μm below the flat level : 2Dvectors_Vmag_ 195micron.mov
	At 390 μm below the flat level: 2Dvectors_Vmag_ 390micron.mov
	At 585 μm below the flat level: 2Dvectors_Vmag_ 585micron.mov
2D velocity vectors with out-of-plane velocity component contours Temporal variations of the two-dimensional in-plane velocity vectors along selected planes within the hinge recess. The velocity vectors are superimposed on the out-of-plane velocity component contours.	*At the flat level:* 2Dvectors_Vop_ Flat.mov
	At 195 μm below the flat level: 2Dvectors_Vop_ 195micron.mov
	At 390 μm below the flat level: 2Dvectors_Vop_ 390micron.mov
	At 585 μm below the flat level: 2Dvectors_Vop_ 585micron.mov
3D exploded view of the hinge flow fields Exploded view of the hinge showing the temporal variations of the three-dimensional velocity vectors along four planes located within the hinge recess. The three-dimensional velocity vectors are superimposed on the three-dimensional velocity magnitude contours.	3DView_3DVectors_3Dvmag.mov

Table D-3: Description of the animations of the Lagrangian results

Movie Description	Movie Name
3D streaklines Particles are released regularly from the hinge recess. The corresponding streaklines are color-coded by the release time of the particles: the particles released at early systole are shown in blue, the ones released at early diastole are shown in red.	*Top view of the entire numerical domain:* Large_View_Streaklines.mov
	Top view focusing on the hinge recess: Zoom_View_Streaklines.mov

REFERENCES

1. Yoganathan, A.P., Lemmon, J., and Ellis, J.T., *Heart Valve Dynamics*, in *The Biomedical Engineering Handbook, Second Edition*. 1995. p. 29/1-29/15.

2. Piehler, H.R., 2000."The Future of Medicine: Biomaterial". Material Research Society Bulletin: pp. 67-70.

3. Rosamond, W., Flegal, K., Furie, K., et al., 2008."Heart Disease and Stroke Statistics□2008 Update: A Report from the American Heart Association Statistics Committee and Stroke Statistics Subcommittee". Circulation, **117**: pp. e25-e146.

4. Black, M.M. and Drury, P.J., *Mechanical and Other Problems of Artificial Valves*, in *Current Topic in Pathology*, Berry, C., Editor. 1994, Springer-Verlag Berlin Heidelberg. p. 127-159.

5. Yoganathan, A.P., Leo, H.-L., Travis, B.R., et al., *Heart Valve Bioengineering*, in *Encyclopedia of Comprehensive Structural Integrity (Csi)*, Science, E., Editor. 2003. p. 795–796.

6. Grunkemeier, G.L. and Anderson, W.N.J., 1998."Clinical Evaluation and Analysis of Heart Valve Substitutes". Journal of Heart Valve Disease, **7**(2): pp. 163-169.

7. Walker, P. and Yoganathan, A.P., 1992."In Vitro Pulsatile Flow Hemodynamics of Five Mechanical Aortic Heart Valve Prostheses". European Journal of Cardiothoracic Surgery, **6**(Suppl): pp. S113-S123

8. Harker, L. and Slichter, S., 1970."Studies of Platelet and Fibrinogen Kinetics in Patients with Prosthetic Heart Valves". The New England Journal of Medicine, **283**: pp. 1302-1305.

9. Skoularigis, J., Essop, M., Skudicky, D., et al., 1993."Frequency and Severity of Intravascular Hemolysis after Left-Sided Cardiac Valve Replacement with Medtronic Hall and St. Jude Medical Prostheses, and Influence of Prosthetic Type, Position, Size, and Number". American Journal of Cardiology, **71**: pp. 587-591.

10. Vallana, F., Rinaldi, S., Galleti, P.M., et al., 1992."Pivot Design in Bileaflet Valves". ASAIO Journal, **38**: pp. M600-M606.

11. Chien, S., *Red Cell Membrane and Hemolysis*, in *Cardiovascular Flow Dynamics and Measurements*, Normann, N.H.C.H.A.N.A., Editor. 1977, University Park Press: Baltimore.

12. *Blood*, in *Fundamentals: Anatomy and Physiology, Fifth Edition*, Martini, Prentice Hall. p. 474-496.

13. Nevaril, C.G., Lynch, E.C., Alfrey, C.P., et al., 1968."Erythrocyte Damage and Destruction Induced by Shearing Stress". Journal of Laboratory and Clinical Medicine, (71): pp. 784.

14. Leverett, L.B., Hellums, J.D., Alfrey, C.P., et al., 1972."Red Blood Cell Damage by Shear Stress". Biophysical journal, **12**: pp. 257-273.

15. Blackshear, P.L., *Mechanical Hemolysis in Flowing Blood*, in *Biomechanics: Its Foundation and Objectives by Fung Y.C., Perrone N., Anliker*, Hall, P., Editor. 1972: Englewood Cliffs, NJ. p. 501-525.

16. Sutera, S.P. and Mehrjardi, M.H., 1975."Deformation and Fragmentation of Human Red Blood Cells in Turbulent Shear Flow". Biophysical journal, **15**: pp. 1-10.

17. Hellums, J.D. and Brown, C.H.I., *Blood Cell Damage by Mechanical Forces*, in *Cardiovascular Flow Dynamics and Measurements*, Normann, N.H.C.H.A.N.A., Editor. 1977, University Park Press: Baltimore. p. 799-822.

18. Sallam, A.M. and Hwang, N.H.C., 1984."Human Red Blood Cell Hemolysis in a Turbulent Shear Flow: Contribution of Reynolds Shear Stresses". Biorheology, **21**: pp. 783-797.

19. Lu, P.C., Lai, H.C., and Liu, J.S., 2001."A Reevaluation and Discussion on the Threshold Limit for Hemolysis in a Turbulent Shear Flow". Journal of Biomechanics, **34**: pp. 1361-1364.

20. Born, G.V.R., 1962."Aggregation of Blood Platelets by Adenosine Diphosphate and Its Reversal". Nature, **194**: pp. 927-929.

21. Born, G.V.R. and Cross, M.J., 1963."The Aggregation of Blood Platelets". Journal of Physiology, **168**: pp. 178-195.

22. Brown, C.H., Leverett, L.B., Lewis, C.W., et al., 1975."Morphological, Biochemical, and Functional Changes in Human Platelets Subjected to Shear Stress". J. Lab. Clin. Med. , **3**: pp. 462-474.

23. Bernstein, E.F., Marzec, U., and Johnston, G.G., 1977."Structural Correlates of Platelets Functional Damage by Physical Forces". Trans. Am. Soc.Artif. Intern. Organs, **23**: pp. 617-625.

24. Anderson, G.H., Hellums, J.D., Moake, J.L., et al., 1978."Platelet Lysis and Aggregation in Shear Fields". Blood Cells, **4**(3): pp. 499-511.

25. Shipkowitz, T., Ambrus, J., Kurk, J., et al., 2002."Evaluation Technique for Bileaflet Mechanical Valves". Journal of Heart Valve Disease, **11**(2): pp. 275-282.

26. Gross, J.M., Shu, M.C.S., Dai, F.F., et al., 1996."A Microstructural Flow Analysis within a Bileaflet Mechanical Heart Valve Hinge". Journal of Heart Valve Disease, **5**(6): pp. 581-590.

27. Ellis, J.T., Healy, T.M., Fontaine, A.A., et al., 1996."An in Vitro Investigation of the Retrograde Flow Fields of Two Bileaflet Mechanical Heart Valves". Journal of Heart Valve Disease, **5**(6): pp. 600-606.

28. Sallam, A.M. and Hwang, N.H.C., 1984."Human Red Blood Cell Hemolysis in a Trubulent Shear Flow: Contribution of Reynolds Shear Stresses". Biorheology, **21**: pp. 783-797.

29. Gao, Z.B., Hosein, N., Dai, F.F., et al., 1999."Pressure and Flow Fields in the Hinge Region of Bileaflet Mechanical Heart Valves". Journal of Heart Valve Disease, **8**(2): pp. 197-205.

30. Ellis, J.T., Travis, B.R., and Yoganathan, A.P., 2000."An in Vitro Study of the Hinge and near-Field Forward Flow Dynamics of the St. Jude Medical® Regent™ Bileaflet Mechanical Heart Valve". Annals of Biomedical Engineering, **28**: pp. 524-532.

31. Ellis, J. and Yoganathan, A.P., 2000."A Comparison of the Hinge and near-Hinge Flow Fields of the St. Jude Medical Hemodynamic Plus and Regent Bileaflet Mechanical Heart Valves". Journal of Thoracic and Cardiovascular Surgery, **119**: pp. 83-93.

32. Leo, H.-L., He, Z., Ellis, J.T., et al., 2002."Microflow Fields in the Hinge Region of the Carbomedics Bileaflet Mechanical Heart Valve Design". The journal of thoracic and cardiovascular surgery, **124**(3): pp. 561-574.

33. Ellis, J.T., 1999."An in Vitro Investigation of the Leakage and Hinge Flow Fields through Bileaflet Mechanical Heart Valves and Their Relevance to Thrombogenesis". Georgia Institute of Technology. Atlanta, GA

34. Travis, B.R., Marzec, U.M., Leo, H.-L., et al., 2001."Bileaflet Aortic Valve Prosthesis Pivot Geometry Influences Platelet Secretion and Anionic Phospholipid Exposure". Annals of Biomedical Engineering, **29**(8): pp. 657-664.

35. Leo, H.-L., 2005."An in Vitro Investigation of the Flow Fields through Bileaflet and Polymeric Prosthetic Heart Valves". Biomedical Engineering Department. Georgia Institute of Technology. Atlanta

36. Simon, H.A., Leo, H.-L., Carberry, J., et al., 2004."Comparison of the Hinge Flow Fields of Two Bileaflet Mechanical Heart Valves under Aortic and Mitral Conditions". Annals of Biomedical Engineering, **32**(12): pp. 1607–1617.

37. King, M.J., Corden, J., David, T., et al., 1996."A Three-Dimensional, Time-Dependent Anaylsis of Flow through a Bileaflet Mechanical Heart Valve: Comparison of Experimental and Numerical Results". Journal of Biomechanics, **29**(5): pp. 609-618.

38. King, M.J., David, T., and Fisher, H., 1997."Three-Dimensional Study of the Effect of Two Leaflet Opening Angles on the Time-Dependent Flow through a Bileaflet Mechanical Heart Valve". Medicine Engineering Physics, **19**(3): pp. 235-241.

39. Redealli, A., Bothorel, H., Votta, E., et al., 2004."3-D Simulation of the St. Jude Medical Bileaflet Valve Opening Process: Fluid-Structure Interaction Study and Experimental Validation". Journal of Heart Valve Disease, **13**(5): pp. 804-813.

40. Cheng, R., Lai, Y.G., and Chandran, K.B., 2003."Two-Dimensional Fluid-Structure Interaction Simulation of Bileaflet Mechanical Heart Valve Flow Dynamics". Journal of Heart Valve Disease, **12**(6): pp. 772-780.

41. Cheng, R., Lai, Y.G., and Chandran, K.B., 2004."Three-Dimensional Fluid-Structure Interaction Simulation of Bileaflet Mechanical Heart Valve Flow Dynamics". Annals of Biomedical Engineering, **32**(11): pp. 1471-1483.

42. Ge, L., Jones, S.C., Sotiropoulos, F., et al., 2003."Numerical Simulation of Flow in Mechanical Heart Valves: Grid Resolution and the Assumption of Flow Symmetry". Journal of Biomechanical Engineering, **125**: pp. 709-718.

43. Wang, J.W., Yao, H., Lim, C.J., et al., 2001."Computational Fluid Dynamics Study of a Protruded-Hinge Bileaflet Mechanical Heart Valve". Journal of Heart Valve Disease, **10**(2): pp. 254-263.

44. Kelly, S.G.D., 2002."Computational Fluid Dynamics Insights in the Design of Mechanical Heart Valves". Artificial organs, **26**(7): pp. 608-613.

45. Kelly, S.G.D., Verdonck, P.R., Vierendeels, J.A.M., et al., 1999."A Three-Dimensional Analysis of Flow in the Pivot Regions of an Ats Bileaflet Valve". The international Journal of Artificial Organs, **22**(11): pp. 754-763.

46. Shu, M.C.S., Gross, J.M., O'rourke, K.K., et al., 2003."An Integrated Macro/Micro Approach to Evaluating Pivot Flow within the Medtronic Advantage Bileaflet Mechanical Heart Valve". Journal of Heart Valve Disease, **12**(4): pp. 503-512.

47. Shu, M.C.S., O'rourke, K.K., Coppin, C.M., et al., 2004."Flow Characterization of the Advantage® and St. Jude Medical® Bileaflet Mechanical Heart Valves". Journal of heart valve disease, **13**(5): pp. 814-822.

48. Almomani, T., Udaykumar, H.S., Marshall, J.S., et al., 2008."Micro-Scale Dynamic Simulation of Erythrocyte-Platelet Interaction in Blood Flow". Annals of Biomedical Engineering, **36**(6): pp. 905-920.

49. Chan, W.K., Wong, Y.W., Ding, Y., et al., 2002."Numerical Investigation of the Effect of Blade Geometry on Blood Trauma in a Centrifugal Blood Pump". Artificial organs, **26**(9): pp. 785-793.

50. Song, X.W., Throckmorton, A.L., Wood, H.G., et al., 2004."Quantitative Evaluation of Blood Damage in a Centrifugal Vad by Computational Fluid Dynamics". Journal of Fluids Engineering - Transaction of ASME, **126**(3): pp. 410-418.

51. Apel, J., Paul, R., Klauss, S., et al., 2001."Assessment of Hemolysis Related Quantities in a Microaxial Blood Pump by Computational Fluid Dynamics". Artificial organs, **25**(5): pp. 341-347.

52. Balducci, A., Grigioni, M., Querzoli, G., et al., 2004."Investigation of the Flow Field Downstream of an Artificial Heart Valve by Means of Piv and Ptv". Experiments in fluids, **36**(1): pp. 204-213.

53. Krishnan, S., Udaykumar, H.S., Marshall, J.S., et al., 2006."Two-Dimensional Dynamic Simulation of Platelet Activation During Mechanical Heart Valve Closure". Annals of Biomedical Engineering, **34**(10): pp. 1519-1534.

54. Raz, S., Einav, S., Alemu, Y., et al., 2007."Dpiv Prediction of Flow Induced Platelet Activation - Comparison to Numerical Predictions". Annals of Biomedical Engineering, **35**(4): pp. 493-504.

55. Heuser, G. and Opitz, R., 1980."A Couette Viscometer for Short-Time Shearing of Blood". Biorheology, **17**(1-2): pp. 17-24.

56. Bludszuweit, C., 1995."Model for a General Mechanical Blood Damage Prediction". Artificial organs, **19**(7): pp. 583-589.

57. Giersepen, M., Wurzinger, L.J., Opitz, R., et al., 1990."Estimation of Shear Stress-Related Blood Damage in Heart Valve Prostheses- in Vitro Comparison of 25 Aortic Valves". International Journal Of Artificial Organs, **13**(5): pp. 300-306.

58. Lim, W.L., Chew, Y.T., Chew, T.C., et al., 2001."Pulsatile Flow Studies of a Porcine Bioprosthetic Aortic Valve in Vitro: Piv Measurements and Shear-Induced Blood Damage". Journal of Biomechanics, **34**: pp. 1417-1427.

59. Gilmanov, A. and Sotiropoulos, F., 2005."A Hybrid Cartesian/Immersed Boundary Method for Simulating flows with 3d, Geometrically Complex, Moving Bodies". Journal of Computational Physics, **207** pp. 457-492.

60. Ge, L. and Sotiropoulos, F., 2007."A Numerical Method for Solving the 3d Unsteady Incompressible Navier-Stokes Equations in Curvilinear Domains with Complex Immersed Boundaries". Journal of Computational Physics, **225**(2): pp. 1782-1809.

61. Borazjani, I., Ge, L., and Sotiropoulos, F., 2008."Curvilinear Immersed Boundary Method for Simulating Fluid Structure Interaction with Complex 3d Rigid Bodies". Journal of Computational Physics, **227**(16): pp. 7587-7620.

62. Dasi, L.P., Ge, L., Simon, H.A., et al., 2007."Vorticity Dynamics of a Bileaflet Mechanical Heart Valve in an Axisymmetric Aorta". Physics of Fluids, **19**: pp. 067105(1) - 067105(17).

63. Sotiropoulos, F. and Abdallah, S., 1991."The Discrete Continuity Equation in Primitive Variable Solutions of Incompressible-Flow". Journal of Computational Physics, **95**: pp. 212-227.

64. Ferziger, J. and Peric, M., 1999,*Computational Methods for Fluid Dynamics*. Berlin: Springer.

65. Shyy, W. and Vu, T.C., 1991."On the Adoption of Velocity Variable and Grid System for Fluid Flow Computation in Curvilinear Coordinates". Journal of Computational Physics, **92**: pp. 82-105.

66. Gilmanov, A., Sotiropoulos, F., and Balaras, E., 2003."A General Reconstruction Algorithm for Simulating Flows with Complex 3d Immersed Boundaries on Cartesian Grids". Journal of Computational Physics, **191**(2): pp. 660-669.

67. Balay, S., Buschelman, K., Eijkhout, V., et al., *Petsc Users Manual*. 2004, Argonne National Laboratory.

68. Kelley, C.T., 1995,*Iterative Methods for Linear and Nonlinear Equations*. Frontiers in Applied Mathematics. Philadelphia: Society for Industrial Mathematics. 180.

69. Balay, S., Buschelman, K., Gropp, W.D., et al. *Petsc Web Page*. http://www.mcs.anl.gov/petsc [cited January 2009].

70. Saad, Y. and Schlutz, M.H., 1986."Gmres: A Generalized Minimal Residual Algorithm for Solving Non-Symmetric Linear Systems ". SIAM J. Sci. Stat. Comput., **7**: pp. 856-869.

71. Simoncini, V. and Szyld, D.B., 2003."Flexible Inner-Outer Krylov Subspace Methods". SIAM J. Sci. Stat. Comput., **40**(6): pp. 2219-2239.

72. Oosterlee, C. and Washio, T., 1998."An Evaluation of Parallel Multigrid as a Solver and a Preconditioner for Singularly Perturbed Problems". SIAM Journal on Scientific Computing **19**(1): pp. 87-110.

73. Trottenberg, U., Oosterlee, C.W., and SchuLler, A., 2001,*Multigrid*. San Diego Academic Press.

74. Dumont, K., Vierendeels, J.A.M., Kaminsky, R., et al., 2007."Comparison of the Hemodynamic and Thrombogenic Performance of Two Bileaflet Mechanical Heart Valves Using a Cfd/Fsi Model". Journal of Biomechanical Engineering, **129**: pp. 558-565.

75. Holme, P.A., Orvim, U., Hamers, M.J.A.G., et al., 1997."Shear-Induced Platelet Activation and Platelet Microparticle Formation at Blood Flow Conditions as in Arteries with a Severe Stenosis". Arteriosclerosis, Thrombosis, and Vascular Biology, **17**: pp. 646-653.

76. Tambasco, M. and Steinman, D.A., 2003."Path-Dependent Hemodynamics of the Stenosed Carotid Bifurcation". Annals of Biomedical Engineering, **31**: pp. 1054-1065.

77. Tambasco, M., 2002."Lagrangian Hemodynamics of the Stenosed Carotid Bifurcation". The University of Western Ontario. London, Ontario

78. Giersiepen, M., Wurzinger, L.J., Opitz, R., et al., 1990."Estimation of Shear Stress-Related Blood Damage in Heart Valve Prostheses- in Vitro Comparison of 25 Aortic Valves". International Journal Of Artificial Organs, **13**(5): pp. 300-306.

79. Wurzinger, L.J., Opitz, R., and Eckstein, H., 1986."Mechanical Blood Trauma: An Overview". Angeiologie, **38**: pp. 81-97.

80. Wurzinger, L.J., Opitz, R., Blasberg, P., et al., 1985."Platelet and Coagulation Parameters Following Millisecond Exposure to Laminar Shear Stress". Thrombosis and Haemostasis, **54**: pp. 381-386.

81. Hung, T.C., Hochmuth, R.M., Joist, J.H., et al., 1976."Shear-Induced Aggregation and Lysis of Platelets". Trans. Am. Soc.Artif. Intern. Organs, **22**: pp. 285-91.

82. Ramstack, J.M., Zuckerman, L., and Mockros, L.F., 1979."Shear-Induced Activation of Platelet". Journal of Biomechanics, **12**(2): pp. 113-25.

83. Wurzinger, L.J., Opitz, R., Wolf, M., et al., 1985."Shear Induced Platelet Activation - a Critical Reappraisal". Biorheology, **22**(5): pp. 399-413.

84. Dasi, L.P., Murphy, D.W., Glezer, A., et al., 2008."Passive Flow Control of Bileaflet Mechanical Heart Valve Leakage Flow". Journal of Biomechanics, **41**(6): pp. 1166-1173.

85. Ellis, J., 1999."An in Vitro Investigation of the Leakage and Hinge Flow Fields through Bileaflet Mechanical Heart Valves and Their Relevance to Thrombogenesis". Mechanical Engineering. Georgia Institute of Technology. Atlanta

86. Meyer, R.S., Deutsch, S., Bachmann, C.B., et al., 2001."Laser Doppler Velcimetry and Flow Visualization Studies in the Regurgitant Leakage Flow Region of Three Mechanical Mitral Valves". Artificial organs, **25**(4): pp. 292-299.

87. Simon, H.A., 2004."Influence of the Implant Location on the Hinge and Leakage Flow Fields through Bileaflet Mechanical Heart Valves". Chemical and Biomolecular Engineering Department. Georgia Institute of Technology. Atlanta

88. Shu, M.C.S., Gross, J.M., O'rourke, K.K., et al., 2003."An Integrated Macro/Micro Approach to Evaluating Pivot Flow within the Medtronic Advantage (Tm) Bileaflet Mechanical Heart Valve". Journal of Heart Valve Disease, **12**(4): pp. 503-512.

89. Zellner, J.L., Kratz, J.M., Crumbley, A.J., et al., 1999."Long Term Experience with the St Jude Medical Valve Prothesis". Annals of Thoracic Surgery, **68**: pp. 1210-1218.

90. Akins, C.W., 1995."Results with Mechanical Cardiac Valvular Prostheses". Annals of Thoracic Surgery, **60**: pp. 1836-1844.

91. Leo, H.L., Simon, H.A., Dasi, L.P., et al., 2006."Effect of Hinge Gap Width on the Microflow Structures in 27-Mm Bileaflet Mechanical Heart Valves". Journal of Heart Valve Disease, **15**(6): pp. 800-808.

92. Jamieson, W.R.E., Fradet, G.J., Miyagishima, R.T., et al., 2000."Carbomedics Mechanical Prosthesis: Performance at Eight Years". Journal of heart valve disease, **9**(5): pp. 678-687.

93. Aagard, J., Tinglef, J., Andersen, P.V., et al., 2003."Fourteen Years' Experience with the Carbomedics Valve in Young Adults with Aortic Valve Disease". Journal of Heart Valve Disease, **12**(1): pp. 81-86.

94. Minakata, K., Wu, Y.X., Zerr, K.J., et al., 2002."Clinical Evaluation of the Carbomedics Prosthesis: Experience at Providence Health System in Portland". Journal of Heart Valve Disease, **11**(6): pp. 844-850.

95. Dalrymple-Hay, M.J.R., Pearce, R.K.S., Dawkins, S., et al., 2000."Mid-Term Results with 1,503 Carbomedics Mechanical Valve Implants". Journal of Heart Valve Disease, **9**(3): pp. 389-395.

96. Fallon, A.M., Dasi, L.P., Marzec, U.M., et al., 2008."Procoagulant Properties of Flow Fields in Stenotic and Expansive Orifices". Annals of Biomedical Engineering, **36**(1): pp. 1-13.

97. Ellis, J., Healy, T.M., Fontaine, A.A., et al., 1996."Velocity Measurements and Flow Patterns within the Hinge Region of a Medtronic Parallel Bileaflet Mechanical Heart Valve with Clear Housing". Journal of Heart Valve Disease, **5**(6): pp. 591-599.

98. Saxena, R., Lemmon, J., Ellis, J., et al., 2003."An in Vitro Assessment by Means of Laser Doppler Velocimetry of the Medtronic Advantage Bileaflet Mechanical Heart Valve Hinge Flow". Journal of Thoracic and Cardiovascular Surgery, **126**(1): pp. 90-98.

99. Sotiropoulos, F. and Borazjani, I., 2009."A Review of the State-of-the-Art Numerical Methods for Simulating Flow through Mechanical Heart Valves". Medical and Biological Engineering and Computing, **47**: pp. 245–256.

100. Borazjani, I. and Sotiropoulos, F., 2009."High Resolution Fluid-Structure Interaction Simulations of Flow through a Bi-Leaflet Mechanical Heart Valve in an Anatomic Aorta". Annals of Biomedical Engineering, (Submitted).

101. Bluestein, D., Li, Y.M., and Krukenkamp, I.B., 2002."Free Emboli in the Wake of Bileaflet Mechanical Heart Valves and the Effects of Implantation Techniques". Journal of Biomechanics, **35**(12): pp. 1533-1540.

102. Chandran, K.B., Khalighi, B., Chen, C.J., et al., 1983."Effect of Valve Orientation on Flow Development Past Aortic-Valve Prostheses in a Model Human Aorta". Journal of Thoracic and Cardiovascular Surgery, **85**(6): pp. 893-901.

103. Chandran, K.B., Rittgers, S.E., and Yoganathan, A.P., 2006,*Biofluid Mechanics: The Human Circulation*: CRC Press. 432.

104. Govindarajan, V., Udaykumar, H.S., and Chandran, K.B., 2009."Two-Dimensional Simulation of Flow and Platelet Dynamics in the Hinge Region of a

Mechanical Heart Valve". Journal of Biomechanical Engineering, **131**(3): pp. 031002.

105. Macmeccan, R.M., Clausen, J.R., Neitzel, G.P., et al., 2009."Simulating Deformable Particle Suspensions Using a Coupled Lattice-Boltzmann and Finite-Element Method". Journal of Fluid Mechanics, **618**: pp. 13-39.

106. Dupin, M.M., Halliday, I., Care, C.M., et al., 2007."Modeling the Flow of Dense Suspensions of Deformable Particles in Three Dimensions". Physical Review E, **75**(6): pp. -.

107. Fallon, A.M., Marzec, U.M., Hanson, S.R., et al., 2007."Thrombin Formation in Vitro in Response to Shear-Induced Activation of Platelets". Thrombosis Research, **121**(3): pp. 397-406.

108. Fallon, A.M., Shah, N., Marzec, U.M., et al., 2006."Flow and Thrombosis at Orifices Simulating Mechanical Heart Valve Leakage Regions". Journal of Biomechanical Engineering-Transactions of the Asme, **128**(1): pp. 30-39.

109. Eden, E., Waisman, D., Rudzsky, M., et al., 2005."An Automated Method for Analysis of Flow Characteristics of Circulating Particles from in Vivo Video Microscopy". Ieee Transactions on Medical Imaging, **24**(8): pp. 1011-1024.

110. Reyes-Aldasoro, C.C., Akerman, S., and Tozer, G.M., 2007."Measuring the Velocity of Fluorescently Labelled Red Blood Cells with a Keyhole Tracking Algorithm". Journal of Microscopy, **229**(1): pp. 162-173.

111. Higgins, J.M., Eddington, D.T., Bhatia, S.N., et al., 20009."Statistical Dynamics of Flowing Red Blood Cells by Morphological Image Processing". PLoS Computational Biology, **5**(2): pp. 1-10.

112. Jeong, D.H. *Visual Analysis on Red Blood Cells*. http://www.vrissue.com/portfolio/RBCVis/RBCVis.htm [cited April 2009].

113. Voura, E.B., Jaiswal, J.K., Mattoussi, H., et al., 2004."Tracking Metastatic Tumor Cell Extravasation with Quantum Dot Nanocrystals and Fluorescence Emission-Scanning Microscopy". Nature Medicine, **10**(9): pp. 993-998.